IAA INSTRUMENTATION

SID/FS-0000-v8.0

April 22 of 2008

PROJECT:

SIDE: SUPER IFU DEPLOYABLE EXPERIMENT

TITLE:

SIDE FEASIBILITY STUDY

AUTHORS

A list of the authors of this document can be found in Annex B. The list is divided by Institutions and, within each institution, the names are listed in alphabetical order. The names included in the list have been provided by the Co-Is of the Consortium institutions. All the institutions and groups are defined and listed in the Management Chapter (see Chapter 4) of this document. See also Annex A where we acknowledge colleagues, institutions and companies who also contributed to the project.

APPROVAL CONTROL

Control	Name	Function	Date	Signature
Revised by:	Marco Azzaro, Francisco Prada	PM, PI	1-12-2007	
Approved by:	Francisco Prada	PI	1-12-2007	
Authorised by:	Marco Azzaro	PM	1-12-2007	

ACRONYMS

2dF	2 degree Field Survey
A&G	Acquisition and guiding
ACS	Advanced Camera for Surveys
ADC	Atmospheric Dispersion Corrector
AGB	Asymptotic Giant Branch
AGN	Active Galactic Nuclei
ALHAMBRA	Advanced, Large, Homogeneous Area, Medium Band Redshift Astronomical (Survey)
AO	Adaptive Optics
API	Application programming interface
AR	Anti-Reflection
ASAP	Advanced System Analysis Program
BAO	Baryon Acoustic Oscillations
BH	Black Hole
CAF	Characterization Filter
CAHA	Centro Astronómico Hispano Alemán
CCD	Charge Coupled Device
CDM	Cold Dark Matter
CMOS	Charged metal oxide semiconductor
COF	Correction Filter
CoG	Center of Gravity
Co-I	Co-Investigator
CSIC	Consejo Superior de Investigación Científica
CTE	Coefficient of Termal Expansion
DART	Dwarf Abundances and Radial velocities Team
DAS	Data Acquisition System
DC	Dark Current
DE	Dark Energy
DES	Dark Energy Survey
DETF	Dark Energy Task Force
DF	Data Factory
DFP	SIDE Data Factory Pipeline
DM	Dark Matter
DSC	Dust and Security Cover
ELG	Emission Line Galaxies

EMIR	Espectrógrafo Multiobjeto InfraRojo
ESA	European Space Agency
ESO	European Southern Observatory
EW	Equivalent Width
F-Cass	Folded Cassegrain Focus
FE	Finite Elements
FEA	Finite Elements Analysis
FLAMES	Fiber Large Array Multi Element Spectrograph
FMOS	Fiber Multi Object Spectrograph
FOV	Filed of view
FP	Focal Plate
FPA	Focal Plane Array
FPR	Fiber Positioner Robot
FRD	Focal Ratio Degradation
FRIDA	InFRared Imager & Dissector for A.o.
GAIA	Global Astrometric Interferometer for Astrophysics
GC	Galactic Cluster
GCS	GTC control system
GRB	Gamma Ray Burst
GTC	Gran Telescopio de Canarias
HSC	Hyper Suprime Cam
HW	Hardware
IAA	Instituto de Astrofísica de Andalucía
IAC	Instituto de Astrofisica de Canarias
ICM	Intra-Cluster Medium
IDT	Instrument Definition Team
IEEC	Institut d'Estudis Espacials de Catalunya
IEEE	Institute of Electrical and Electronics Engineers
IFAE	Institut de Fisica d'Altes Energies
IFS	Integral Field Spectroscopy
IFU	Integral Field Unit
IGM	Inter Galactic Medium
IMBH	Intermediate Mass Black Hole
INAOE	Instituto Nacional de Astrofísica, Óptica y Electrónica
IR	Infra Red
IRMOS	Infrared Multi Object Spectrograph
ISM	InterStellar Medium
JWST	James Webb Space Telescope
KIDS	KIlo Degree Survey (VLT Survey Telescope)
KMOS	K-band Multi-Object Spectrograph
LAE	Lyman-Alpha Emitters
LBG	Lyman-Break Galaxies
LCU	Local Control Unit

LGRB	Long-duration Gamma Ray Bursts
LIRG	Luminous InfraRed Galaxies
LISA	Laboratory of Imaging Sensors for Astronomy
LM	Local Manager
LRG	Luminous Red Galaxy
LRU	Line Replaceable Unit
LSS	Light Scattering Spectroscopy
LSST	Large Synoptic Survey Telescope
LVDS	Low voltage differential signalling
MCT	Mercury Cadmium Telluride
mIFU	Mini Integral Field Units
Mini-IFU	Mini Integral Field Units
MIR	Middle InfraRed
MMT	Multiple Mirror Telescope
MOS	Multi Object Spectrograph
MPMNT	Mean Preventive Maintenance Night-Time
MTBF	Mean Time Between Failures
MTTR	Mean Time To Repair
MW	Milky Way
N&R	Nod & Read
N&S	Nod & Shuffle
NA	Nominal Aperture
NFCS	Nasmyth Focal Station Coordinate System
NIR, nIR	Near Infrared
NP	Nasmyth Platform
NR	Nasmyth Rotator
OH	hydroxyl radical
OOB	Out-Of-Band
OSIRIS	Optical System for Imaging and low Resolution Integrated Spectroscopy
PI	Principal Investigator
PIFS	Palomar Integral Field Spectrograph
PM	Project Manager
PMAS	Potsdam Multi Aperture Spectrophotometer
QE	Quantum Efficiency
QSO	Quasi Stellar Object
RAL	Rutherford Appleton Laboratory
ROI	Region Of Interest
RV	Radial Velocity
SAC	Scientific Advisory Committee of GTC
SDSS	Sloan Digital Sky Survey
SED	Spectral Energy Distribution
SEGUE	Sloan Extension for Galactic Underpinnings and Evolution
SFH	Star Formation History

SFR	Star Formation Rate
SIDE	Super Ifu Deployable Experiment
SIFU	Super Integral Field Unit
SNR	SuperNovae Remnant / Signal to Noise Ratio
ST	Science Team
SW	Software
SZ	Sunyaev-Zel'dovich
TBC	To Be Confirmed
TBD	To Be Defined
TIS	Total Integrated Scatter
TV	Television
UB	Universidad de Barcelona
UCM	Universidad Complutense de Madrid
UFL	University of Florida
UIST	UKIRT Imaging Spectrometer
UKIRT	U.K. InfraRed Telescope
UNAM	Universidad Nacional Autonoma de Mexico
UVES	Ultraviolet & Visual Echelle Spectrograph
VF	View Factor
VIMOS	VIsible MultiObject Spectrograph
VIS	Visible wavelength band
VISTA	Visible and Infrared Survey Telescope for Astronomy
VLIRG	Very Luminous InfraRed Galaxy
VLT	Very Large Telescope
VPH	Volume Phase Hologram
VSOP	Variable Star One-shot Project
VVDS	VIMOS VLT Deep Survey
WFC	Wide Field Corrector
WFI	Wide Field Imager
WFMOS	Wide Field multi-object spectrograph
WG	Working Group
WP	Working Package
WRT	With Respect To
XMM	X-ray Multimirror Mission

TABLE OF CONTENTS

1 SUMMARY

1.1 The SIDE project

1.1.1 Foreword

The many people and groups involved in writing this SIDE Feasibility Study document present here the result of about two years of intense work, aiming to define the project in detail to prove its scientific and technical viability. We all hope that the global idea, the scientific possibilities, the instrument baseline and its affordability can be fully understood through these dense pages and that our effort has produced a sensible and clear Feasibility Study document for GTC to review and evaluate.

1.1.2 SIDE project overview

The SIDE project aims to build a second-generation instrument for the GTC on La Palma (Canary Islands, Spain). The main aim of the instrument is to be a common-user instrument of intermediate resolution, with a high efficiency in multi-object spectroscopy through a large number of fibers and a wide field of view, as well as 3D (IFU) spectroscopy. All this would be possible over the range from visible to near infrared. In particular, there is the unique possibility for visible and IR observations to be performed simultaneously for certain ranges.

SIDE will provide low resolution (R = 1500, 4000, 5000) and high resolution (R = 8000, 15000, 29000). The low resolution spectrograph is called “Dual VIS-NIR” because it will be capable of simultaneous observations in the Visible and near Infrared bands (0.4 – 1.7 μ) by using a dichroic. The high resolution device is called Hi-Res VIS spectrograph as it works in the Visible band only (0.35 – 0.87 μ). SIDE will work in three observing modes: MOS, SIFU and mIFU. The Dual VIS-NIRspectrograph will work in all three modes (MOS, SIFU and mIFU), while the Hi-Res VIS will be fed only by MOS and mIFU units. Due to the large number of fibers, the Dual VIS-NIRspectrograph will be a set of ~10 identical spectrographs, located, together with the Hi-Res spectrograph in a dedicated and conditioned room mounted on the telescope structure.

Table 1 shows a resume of the basic parameters of SIDE:

Location	GTC 10.4m Nasmyth focus
FOV	MOS: 20' diameter mIFU: 3"x 3" each over an 8' focal plane SIFU 30"x 30"
Instrument observing modes	MOS, SIFU, mIFU
N. of science units	~1000 MOS ~2500 fibers in SIFU ~27 mIFUs of 36 fibers each
Resolution, spectral coverage and mode	1500 < R < 30000 spectral window: 350-1700 nm Nod&Read observing mode

Table 1. Basic parameters of SIDE.

The preferred location for the MOS units, configured by a Fiber Positioner Robot, is the Nasmyth focus of GTC, with 20' of FOV and some 950 science units. The preferred location for the SIFU and mIFU units is the Folded Cassegrain focus, with about 2500 fibers for the SIFU and about 27 mIFUs.

The goal of SIDE is to provide the GTC community with new and unique observing capabilities, i.e.

- Intermediate spectral resolution
- Survey spectroscopy
- 3D spectroscopy

The project is leaded by the Instituto de Astrofísica de Andalucía (IAA-CSIC), based in Granada, Spain. After the project received support from the GTC SAC, a Science Team and an Instrument Definition Team were formed and the basis of the instrument were defined. The Feasibility Study phase, which started the 1st of December of 2006, is funded by the Spanish MEC and the GTC, together with the Consortium members support.

After the first kick-off meeting in Sevilla (Sept. 2006), the SIDE Consortium was formed and several institutions from Spain, Mexico and USA committed themselves for the project. At present, 10 Institutions with worldwide recognized prestige form the SIDE Consortium:

1. Instituto de Astrofísica de Andalucía (IAA-CSIC)
2. Instituto de Astrofísica de Canarias (IAC)
3. Institut d'Estudis Espacials de Catalunya (IEEC)
4. Institut de Física d'Altes Energies (IFAE)
5. Instituto Nacional de Astrofísica de Óptica y Electrónica (INAOE)
6. Universitat de Barcelona (UB)
7. Universidad Nacional Autónoma de México (UNAM)
8. Universidad Complutense de Madrid (UCM)
9. University of Florida (UFL)
10. Lawrence Berkeley National Laboratory (LBNL)

Figure 1 shows the basic flow of light through the instrument: light enters the instrument at the two foci behind the A&G boxes (Nasmyth and Folded Cassegrain) for MOS and mIFUs and SIFU respectively.

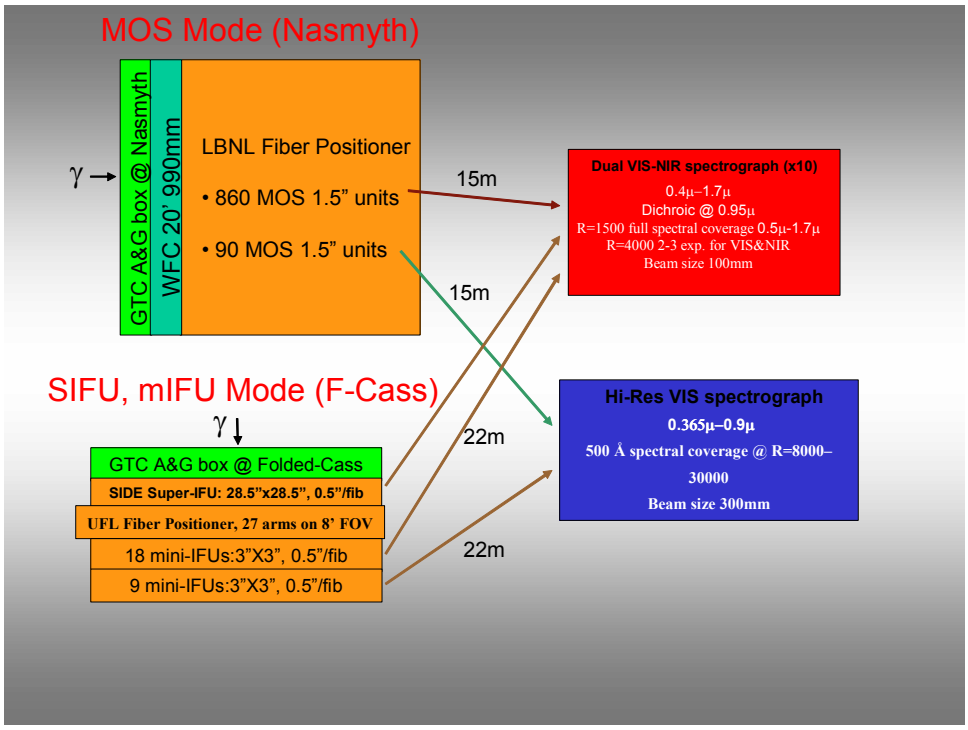

Figure 1. Basic flow of light through the instrument.

SIDE has been presented by the end of October 2006 to the GTC SAC and has the support of the GTC Project Office (see letter by GTC Director General, Annex **¡Error! No se encuentra el origen de la referencia.**). A progress report on the Feasibility Study phase has been given to the GTC SAC in March 2007 and another progress report was given in November 2007. The Feasibility Study phase has finished on December 1st 2007 with the submission of the present document.

The challenge of the project is to guarantee that SIDE at GTC will arrive on time to be competitive with similar instruments planned for other major telescopes and to lead survey and 3D spectroscopy science in the next decade. For the time being, the timetable has been totally fulfilled.

A great variety of Science Cases could be addressed with SIDE, of which a detailed discussion is presented in Chapter 2 of this Proposal.

2 SIDE SCIENCE JUSTIFICATION

2.1 Introduction

2.1.1 SIDE philosophy

The main aim of SIDE is to be a GTC common-user instrument with a high efficiency as survey multi-object spectrograph, both through large number of fibers and wide field of view, and also 3-D IFU spectroscopy. All this would be possible over the range from visible to near-infrared wavelengths working at intermediate spectral resolution. In particular, it will offer the possibility for visible and IR observations to be performed simultaneously for certain spectral ranges.

A great variety of science cases could be addressed with SIDE, covering from Cosmology, Stellar Physics, Solar System and Extragalactic Astronomy of which some are reported in the list given here.

Science in MOS mode:

- Galaxy redshift surveys: large scale structure, dark energy, galaxy formation
- Galaxy clusters, AGNs, QSOs and IGM at high z
- Galactic structure and evolution: radial velocities and metallicities (bulge, disc, globular clusters and tidal streams)
- Target follow-up of SDSS, ALHAMBRA, COMBO-17/GEMS, VISTA, ….
- Stellar populations and star formation rates of massive galaxy samples
- dSph, M31, M33 and Local Group studies

Science in IFU mode:

- Ionized gas in galaxies
- Jet kinematics and physical conditions
- Quasar and GRB hosting galaxies
- HII regions, post-AGB, HH, PNe
- Solar system: comets and planetary atmospheres
- Mass distribution in galaxies

- PNs in M31 and Local Group galaxies
- Stellar populations and gas kinematics
- Study of objects with high-z Lyα emission
- Gravitational lenses

2.1.2 Role and availability of photometric data in 2010+

Given the limited worldwide installed survey spectroscopic capacity, photo-z's are essential for

- Measuring the global evolution of galaxies
- Pre-selecting galaxy samples for detailed spectroscopic studies
- Measuring cosmological parameters from large-scale structure or gravitational lenses

Massive surveys in these fields are starting that all rely on photo-z's as a quality bottleneck (see ESA/ESO report on Fundamental Cosmology 2006). As we push into a regime where even tiny systematics are critical for the results, we need to have perfect understanding of this tool. A recent comparison of alternative photo-z tools has shown unexplained systematics and complementary strengths and weaknesses, which still need to be overcome. In either case, a massive amount of photometric data with ~0.03 photo-z accuracy ($s_z/(1+z)$) will be obtained in the optical and NIR with SDSS-II, CFHT-LS, various VISTA surveys, Subaru SuprimeCam, DES and Pan-STARRS. There will be no shortage of s_z~0.03 data. All science that can be done with photo-z's of that accuracy could be done with data obtained until 2011.

If higher redshift resolution is needed, we can resort to spectroscopy or to HiFi-photo-z's as obtained from medium-band imaging (e.g. COMBO-17, ALHAMBRA). Such data is interesting for large surveys of

a) Dependence of galaxy characteristics on environment

b) Metallicity and dynamics data (require spectroscopy)

c) Higher-accuracy cosmological measurements

There will be a lot of hype about (a) in the next five years. We now know the basic evolution of galaxies (luminosities, color, morphology) from z=1 to 0, but we hope to find out the physical causes from looking specifically at the role of environment. So far, this is possible only to z~0.2 with good quality. In the 2dFGRS survey, the galaxy luminosity function shows little environmental variation among galaxies of M_B<-19. Virtually all the trends are among faint galaxies. Hence, one needs to both go deep and have very small redshift errors. Note, that basic photo-z surveys without good characterization of the environment will play a big role in studying the z=[1,5] universe now and in the near future.

There will be interest in (b) with relations to morphology and the co-evolution of stellar mass, dynamical mass, morphology and SED, with massive surveys at z=[0,1] and glimpses into the high-z universe as far as possible. Also, there is the question of environmental definition: does environment just speed up galaxy evolution, or does it alter the route a galaxy takes (i.e. is a galaxy at a fixed stage in development as described by one parameter, different in another parameter, when compared to a galaxy in a different environment?).

(c) attracts people as it is more about fundamental physics following simple equations rather than about the complexities of wet galaxy science involving gas and other hard-to-ever-model-right factors. The evolution of LSS is going to be studied from super-massive photo-z surveys ($10^{7.5}$ objects) and massive spectroscopic ones ($10^{5.5}$ objects) very soon.

2.1.3 Competition for SIDE from photometric redshifts or spectroscopic surveys

HiFi-photo-z's are useless for (b) and too expensive for (c). However, they could do a good job for (a), certainly for selected high-density environments such as super-cluster regions. General 3-D environment needs to be defined at a level of redshift accuracy that might only be provided by spectroscopy in the end.

Some spectroscopic surveys are underway, which can do all three points (a)-(c) well. In the next five years we expect data from the following sources:

VVDS and DEEP-2 are benchmarks for the 2007/8 data sets. They have good depth and resolution (DEEP-2), but are probably only reasonably complete (up to 50% level) to z~1.2.

The BOSS survey at SDSS, the WiggleZ project and the Shanks et al. LRG survey both at AAOmega will do a good job at z=[0.5,0.8] on LSS and BAOs.

FAST-SOUND with FMOS at Subaru could do $10^{5.5}$ star-forming galaxies at z=[1.3,1.7]. However, it still needs an imaging data base involving VISTA after the pilot project is done from the UKIDSS UDS. It should do a good job on LSS, BAO, SFH and metallicity history over this period.

They are not a single dataset, but together they will do a very good job in cosmology overall (LSS/BAO) and define environment, metallicities and dynamics as well as possible at z=[0.5,~1.5] (or as well as possible with fibers for some issues). Further projects in the near-future will look at lower-redshift environments in large super-cluster and field volumes, using optical instruments for that (AAOmega, VST-16, etc.).

Instrumentally, there is the threat of the WFMOS competition as a direct optical competitor instrument to SIDE, which together with FMOS in the NIR covers 0.3-1.8 micron for many objects. The competition of both instruments at 8-m-telescopes, with the slower-than-SIDE NIR instrument being ready now, and the faster-than-SIDE optical instrument coming later, could be very strong indeed. FMOS will stay at the Northern hemisphere, while WFMOS still is pending of funding.

We believe that the main challenge to SIDE activities is the spectroscopic competition. There are some scientific and technical aspects to look at, such that we guarantee that we choose the right strategy to build a competitive instrument to lead survey spectroscopy in the next decade. We must identify unique capabilities such as the simultaneous MOS visible + NIR coverage and the wide field of view IFU 3D spectroscopy.

A full comparison of SIDE with its long term competitors is presented in detail below in Section 3.1.5.

2.1.4 Complementary role of photometric and spectroscopic data

Photometry is badly needed to get well-defined object SEDs, to do K corrections properly and to fine-tune any (with narrow slits/apertures/fibers necessarily modest) spectroscopic flux calibration. It also allows lensing analysis and pre-selection of desired spectroscopic samples.

Any massive SIDE spectroscopy survey should consider running in one or two fields of then existing massive spectroscopic surveys (i.e. the z=[0.5,0.8]-LRG survey by Shanks et al. in the SDSS-II field, or the "FAST-SOUND" z=[1.3,1.7]-ELG survey by Totani, Dalton, Glazebrook et al., SDSS BOSS fields, etc). This would have the advantage of double-checking on redshifts, interlopers, completeness, flux calibration, etc.

The ESA/ESO Working Group report on Fundamental Cosmology mentions the need for very massive spectroscopic capacities, mostly in order to provide the fine-tuning calibration of super-massive photo-z surveys. The idea is to have a billion photo-z's on several thousand square degrees (VST-KIDS or Pan-STARRS for example), and to have a low filling-factor coverage of spectroscopic cross-checks than can do a spatially resolved recalibration tuning to optimize the photo-z's over a large area survey. For this purpose a spectrograph is needed that covers a much larger FOV than SIDE to get the source density right. Optical/NIR capabilities will here be relevant for different redshift regimes. However, it is not well understood for us, from a very fundamental point of view, the need for the redshift survey to cover the imaging survey area uniformly with a low filling factor. The universe is supposed to be isotropic. While indeed the foreground dust extinction and the imaging calibrations are not going to be isotropic, they should be well enough controllable, that spectroscopy obtained for photo-z training purposes needs to be only massive and representative enough; it could cover denser objects packages covering a looser grid of regions, and this would be feasible with SIDE.

In the next Chapters, we present the result of the work done so far by the seven SIDE science working groups whom carried out an extensive survey of the science window opportunities for the project, has provided detailed justification of the science requirements and performed a tentative identification of desirable competitive projects for SIDE.

2.2 Energetic Phenomena

2.2.1 Current status and open questions in the field

This is a time in which cosmic evolution studies are undergoing a major step forward thanks to cosmological surveys and new technological facilities. The basic goal of such surveys is

the building of catalogues containing the photometry of all the detected objects, and the deduced spectral energy distribution (SED) and redshift (z) values. With this information, it is possible to address many different issues in cosmic evolution of different system types, starburst and active galaxies in particular.

A limitation of survey studies is the need to investigate the integrated, global properties of the systems, which might not provide a realistic view of the star forming history and their evolution. On the other hand, while most galaxies that are actually forming are too far away for detailed studies of their stellar populations, their local counterparts, such as nearby starburst and colliding galaxies, are far easier targets.

Nearby starburst and active galaxies are fascinating objects in their own right. They are, moreover, ideal sites to overcome the limitations mentioned above. They allow the detailed study of the physics of phenomena that occurred much more frequently in the past: mergers/interactions, star formation activity, and nuclear activity. They are complex systems, which must be asserted through the study of their spatial properties. A variety of phenomena such as inflows, outflows, interactions/mergers, etc imprint profound signatures in the observed properties of the stellar populations and the interstellar medium (ISM) which need to be investigated in two spatial dimensions for a proper assessment of their impact during the formation and evolution of the systems.

The need for Integral Field Spectroscopy (IFS) has been thus recognized for a long time, since it allows to characterize and model the spatially extended properties of gas and stars (kinematics, ionization, age/metallicity of stellar populations, etc). It is also necessary to extend the detailed studies of star forming and active galaxies at high z, to investigate whether low z objects observed at high spatial and physical resolution can be good analogues of star formation and nuclear activity at high-z.

Although our comprehension of galaxy evolution has advanced in a significant way, important questions remain open: What is the triggering mechanism of the nuclear activity in galaxies? What is the role of feedback in galaxy formation and evolution? How important is galaxy merging to the star-formation history and mass-assembly of galaxies? Is the physics of star formation the same at high and low redshift? How is the accreted material in active galaxies fueled inwards? Can we draw an evolutionary diagram for active galactic nuclei (AGN)? What version of the unification model for different types of active galaxies is valid? What is the connection between nuclear activity and galaxy evolution? What is the relationship between the super-massive black hole (BH) and the host galaxy? How are AGN jets produced and collimated?

2.2.2 Future prospects. The next 10 years.

The increasing number of Integral Field Unit (IFU) and MOS facilities on telescopes of different apertures emphasizes the growing importance of this mode of spectroscopy, particularly in this era of large 8-10 m class telescopes and adaptive-optics systems. The next decade will see the development of wide-field monolithic IFU units such as the 2nd generation VLT instrument MUSE (2011), together with multiple deployable IFU systems (e.g. KMOS on VLT 2010 or VIRUS on the 9.2m Hobby Eberly Telescope, HET in 2009). The combination with laser guide star adaptive optics, which is already a powerful technique (e.g. OSIRIS on Keck, NIFS on Gemini, SINFONI on VLT), will keep advancing (MUSE).

The first IFS deployed in space will become a reality (NIRS, MIRI on the James Webb Space Telescope in 2013).

Such developments are critical to address the existing open issues and the new scientific challenges opened by ongoing and future surveys as well as new technological facilities.

Detailed integral field spectroscopic studies of nearby galaxies have advanced relatively slowly compared to the associated technology and a broad range of scientific issues (see section 2.2.4) remain to be explored. The situation for distant galaxies is even worse.

Moreover, a whole new window is being opened by ongoing surveys performed at different wavelengths. On one hand, new object classes are being discovered in large numbers, which requires, and will require during the next decade, the intensive use of integral field spectrographs on 8-10m class telescopes to complement the survey studies. A clear example is the long-searched type 2 quasar population, whose existence was predicted from the statistics of Seyfert 1 and 2 galaxies and from those of radio galaxies and radio-loud quasars. Only recently have large samples of type 2 quasars been found (Zakamska et al. 2003) using data from the Sloan Digital Sky Survey (SDSS) and the concerted use of both the MIR and the X-ray emissions.

On the other hand, new technological facilities have revealed phenomena, unnoticed before in nearby galaxies. As an example, the Galaxy Explorer (GALEX) satellite has uncovered a population of early type galaxies with blue UV/optical colors. Almost all are AGN (Kauffmann et al. 2006). IFS studies can be very valuable to characterize such phenomena.

The SAURON survey on nearby galaxies has demonstrated the power of integral field spectroscopy to view into the structure of galaxies (see various papers on this project). The fossil record of formation held in nearby galaxies is a powerful resource and IFS is the ideal way to probe this. The next natural step is to look back in time, towards higher redshifts, when interactions between galaxies were more frequent and galaxies looked different from today.

The possibilities for integral field spectroscopy in the next decade are endless.

2.2.3 The opportunity window for SIDE

Since most of the science described in this section is based on the SIFU unit and the mIFU modes of SIDE, we will focus our discussion in this section on the potential of SIDE with these two modes of observation.

The scientific topics considered in this section would benefit enormously from a wide field integral field unit working both in the optical and the near-infrared. The IF spectrographs available today can already be combined to map numerous galaxy properties (kinematics, electron density, metallicity, stellar populations...). However, a limitation of many of these instruments is their small field of view (FOV). Most IF spectrographs available today on 8-10m class telescopes have typically a FOV of (maximum) several arcsec (see Table 2 and Table 3 in section 2.12). They are moreover, optimized to work in the NIR or the optical.

Many galactic systems show important phenomena in extranuclear regions across spatial scales of kpc and up to100 kpc, which (depending on redshift), would require a wide FOV (≥30”X30”) integral field unit for an efficient and adequate characterization of its properties. Two examples are shown in Figure 2 and Figure 3.

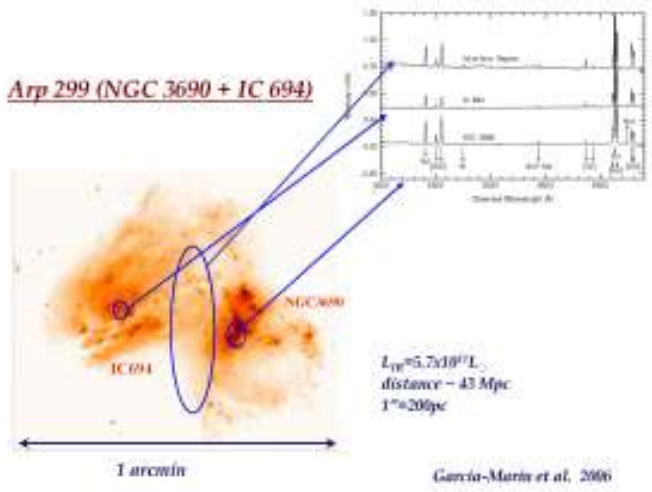

Figure 2. The famous ARP 299 interacting system is shown together with several spectra extracted from different apertures. This example shows the potential of large FOV integral field spectrographs to study nearby interacting systems.

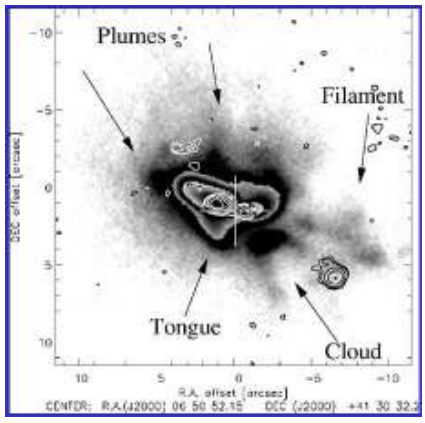

Figure 3. Narrow band image obtained with Keck (Reuland et al. 2003) of a giant Lyα nebula at z=3.8. The nebula extends for more than 20’’. Such giant nebulae contain rich information on the formation process and early evolution of very massive elliptical galaxies. The ≈30’’x30’’ FOV of SIDE’s SIFU would be ideal for this study, extending to (at least) 1.4μm to cover more emission lines.

The space density of some interesting object classes at intermediate and high *z* (several to several hundred sources per square arcminute depending on redshift and flux detection limit) further supports the interest of wide field IF spectrographs. For instance, the main science driver of MUSE (FOV 1'x1') will be the investigation of Lyα emitters at high *z*. The predicted space density is 287 galaxies per sq. arcminute for Lyα fluxes > $3x10^{-19}$ erg s^{-1} cm^{-2} at $z \geq 2.8$. The space density of IR-bright galaxies ($LIR>10^{11}L_{\odot}$) in current Spitzer cosmological surveys is 5-7 sources $arcmin^{-2}$ (Pérez-González, private communication).

VIMOS on VLT, working in the optical, is the IFS on an 8-10m class telescope with the largest FOV (54''x54''), although this maximum FOV is possible only at a very low spectral resolution (R~250). FLAMES-ARGUS (optical), also on VLT is next with a maximum FOV of 11.5''x7.5'' at spectral resolution $R \geq 11000$.

The need for wide FOV integral field spectrographs on 8-10m class telescopes is compelling. This fact is reflected by the current development of instruments such as MUSE (VLT, FOV 1'x1') and VIRUS (HET), which, in addition to the multi-deployable IF system, it will have a central IFU with continuous coverage of 3.5'x3.5'.

SIDE, with the possibility to work with a maximum FOV of ~30"x30" will have one of the largest FOV on 8-10m class telescopes (the largest at >1μm), with the added advantage, compared with instruments such as VIRUS, MUSE or VIMOS, of working within a much wider spectral range, extending between 4000 Å and 1.7μm with the possibility of simultaneous VIS-NIR spectroscopy.

Many important advances during the next decade will come from the study of statistical samples of faint astrophysical objects. A mini-IFU mode would allow simultaneous integral-field spectroscopy of several sources, which would greatly increase the efficient use of GTC. Similar facilities exist already (GIRAFFE on VLT, optical, $R \geq 11000$) or are under development (KMOS on VLT 1-2.45 μm, R~3500; VIRUS on HET, 3400-5700 Å, R~1000). As we will discuss in more detail in Sect. 3.2.7, a mini-IFU mode for SIDE on GTC would be of great value. The possibility to observe in the spectral range 4000 Å to 1.7μm (at least) at R~3000-5000 would make it a unique facility.

2.2.4 Science cases

In this section we discuss topics within the area of "Extragalactic Energetic Phenomena" which would benefit from the availability of SIDE. Since issues related to statistical studies (for which the MOS mode is critical) of starburst and active galaxies at different *z* are discussed in other chapters, we will mostly focus on the potential of detailed spectroscopic studies of individual sources in two spatial dimensions. These would make use of the integral field (SIFU) and mini-IFU SIDE modes. In this section we present open scientific questions on different fields and the limitations of current studies. In Sect. 2.2.7 we will propose the way SIDE could be used to investigate such issues.

2.2.4.1 MOS observing mode

N/A (see above).

2.2.4.2 mIFU observing mode

See applications in 2.2.4.3 depending on subject area.

2.2.4.3 SIFU observing mode

Starburst galaxies

In 1978 Larson and Tinsley found that strongly interacting galaxies tend to be bluer than isolated ones of the same type. They attributed the excess blue light in these "starburst galaxies" to newborn stars and argued that tidal interactions have induced vigorous bursts of star formation in these galaxies. Since then a lot of progress has been made in understanding the nature of starbursts and the circumstances that trigger the star formation activity. The principal role of mergers and interactions is now established beyond doubt. It is now also clear that mergers/interactions and starburst activity played a more important role in the past than in the local universe.

Many questions remain open regarding starburst galaxies, which can be addressed with NIR-optical IF spectroscopy on 8-10m class telescopes. From super stellar clusters (initial mass function, properties of the stellar population, formation process, role on the star forming activity of galaxies, etc) to interacting systems (star formation histories, dynamics of the interaction, feedback processes, etc), numerous interesting issues can be addressed with an instrument such as SIDE.

Many high z galaxies are forming stars at rates exceeding 100 $M_{\odot}$ yr^{-1} mostly spread over the entire galaxy, whereas in the nearby universe the starburst intensity activity is at leastan order of magnitude lower and mainly confined to the nuclear regions of the galaxies. In spite of this vast difference in energetics, local starburst galaxies serve as good yardsticks in understanding their high redshift counterparts.

Infrared (IR) bright galaxies are a particular example of star forming galaxies. These are luminous (LIRGs, L_{IR}=L[8-1000μm] = 10^{11}-10^{12} $L_{\odot}$) and ultraluminous (ULIRGs, $L_{IR} > 10^{12}$ $L_{\odot}$) IR galaxies. Their importance has been recognized since their discovery more than 30 years ago (Rieke & Low 1972). IR bright galaxies are thought to be responsible for the bulk of the cosmic IR background and play a major role in the cosmic star formation and accretion histories (Elbaz et al. 2002, Le Floc'h et al. 2005).

The process of merging with accompanying super-starbursts that produces LIRGs and ULIRGs appears to be an important stage in galaxy evolution, possibly even converting spiral galaxies into ellipticals (e.g., Genzel et al. 2001) and possibly giving rise to quasars (Sanders et al. 1988). However, the mechanisms that trigger the starburst and AGN activites as well as trends with the interaction stage are not well established yet (e.g. Alonso-Herrero et al. 2006). See Figure 4.

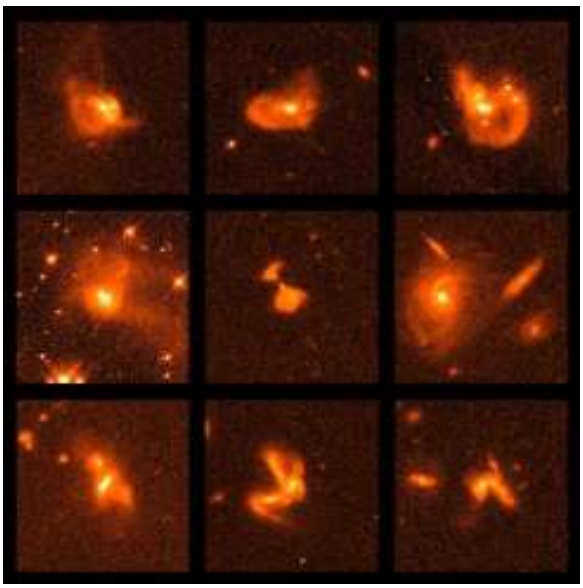

Figure 4. HST WFPC2 (F814W filter) images of a sample of ULIRGs whose morphologies appear to be a consequence of $\geq$ 2 mergers (Borne et al. 2000). SIDE would be ideal to investigate the spectroscopic properties of these systems. The FOV of each individual panel is 30"x30"., i.e. the maximum FOV planned for the SIDE's SIFU. The option of a 15"x15" FOV at ~0.5 sampling could be an (additional) interesting alternative when more detailed spatial information is required. The possibility to observe in the optical and well into the NIR with the same instrument would also be ideal. Although existing facilities (e.g. the IFUs on VLT and Gemini) are already capable of of addressing some issues related to this systems, a larger FOV and wider spectral range would offer clear advantages.

Other questions are: What is the origin of the IR luminosity, starbursts or AGN? Since, high z ULIRGs are likely to dominate the cosmic IR background, this issue has important cosmological implications. What are the star forming and chemical enrichment histories of IR bright galaxies? What is the dynamical mass of the host galaxies? What is the role of starburst induced-superwinds as a feedback mechanism?

IFS studies of LIRGs are very limited, since locally they have mostly used the long-slit technique (e.g., Veilleux et al. 1995). Detailed, spatially resolved spectroscopic studies of IR bright galaxies have focussed so far only on small samples (e.g., Colina et al. 2005) and have been biased towards some famous objects (e.g., Arp299 García-Marín et al. 2006). The situation for distant IR bright galaxies is even less advanced, as it is only in the last few years that we are starting to identify them in large numbers and gather sufficient information to understand their global properties (morphologies, observed colours, stellar masses, etc).

Super stellar clusters

The Hubble Space Telescope (HST) made a major breakthrough in understanding the nature of star formation in starburst galaxies by resolving the central region of the prototypical starburst M82 (see Figure 5) into hundreds of nuclear star clusters, now known as Super Star Clusters (SSCs). Since then, SSCs have been detected routinely in starburst regions. It has been proposed that SSCs are young globular clusters, forming in the present day Universe.

We know today that SSC represent a substantial fraction of new stars formed in a starburst event. Typically hundreds of SSCs are found in starbursts galaxies. Although many of them are immersed in the nuclear region, SSC are distributed over the whole galaxy. They have masses of 104-6 M□ and sizes <15 pc, i.e. (comparable to those of globular clusters) and apparent magnitudes mv<20.

Numerous issues remain unsolved about SSC. For example, how are stellar and cluster initial mass functions related? How are they influenced by the star formation history? What are the effects of stellar feedback? What is the relationship between the properties of SSC and the environments from which they form? Is the an evolutionary link with globular clusters?

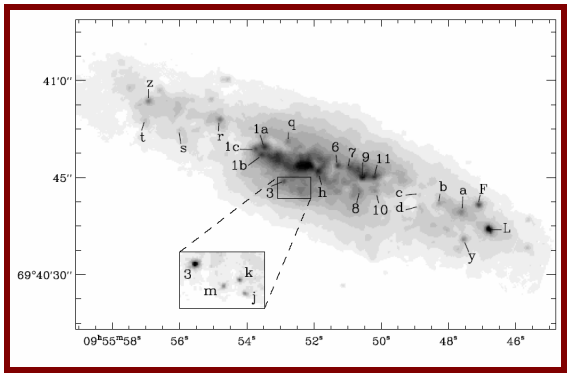

Figure 5. HST image of the nuclear region of M82. SSCs are marked (Borne et al. 2000).

Most studies of SSC to date have been based on long slit high spectral resolution spectroscopy (Keck telescope, e.g. McGrady & Grahamn 2007) and HST imaging (Borne et al. 2000). Due to their small sizes, high spatial resolution observations are critical to address some of the questions related to SSCs. On the other hand, high spectral resolution, (R > 20000) is necessary to measure their dynamical masses, one of the most important open questions related to SSC, fundamental to investigate whether there is an evolutionary link with globular clusters. Ground based, high signal to noise integral field spectroscopy of SSC at a spectral resolution of R~4000 can be very valuable, specially combining optical and NIR observations. This would allow to characterize the stellar population in the SSCs (ages and metallcities), investigate the presence of supernovae, characterize the extinction, etc (see Sec. 2.2.8).

Active galaxies

Nuclear activity reflects processes and physical conditions in the immediate vicinity of a black hole and its influence can be noticed in scales between light days and up to hundreds of kpc. It spans over 12 orders of magnitude in time and space and can be observed throughout much of the Universe, from the Galactic Center to z>6.

There is increasing recognition that the evolution of active galactic nuclei (AGN) and their host galaxies are intimately linked. Not only are the masses of the central super-massive black holes strongly correlated with the properties of the host galaxy bulges, but the redshift

evolution of the global star formation history of the field galaxy population also shows marked similarities with the redshift evolution of the AGN population. Although AGN-triggered feedback mechanisms and galaxy mergers are widely claimed to explain the trends, some observational results question these popular ideas (e.g. Li et al. 2006, Krongold et al. 2006). Many issues remain open regarding active galaxies. What is the impact of galaxy mergers on the triggering of the nuclear activity? How does the triggering proceed in detail? How are star formation and AGN activity linked and how does this depend on the host galaxy and environmental properties? How powerful is the feedback effect caused by AGN outflows, and how does it compare with other mechanisms (e.g. SNe)? How does the feedback depend on the properties of the AGN? What drives the outflows associated with AGN: relativistic jets? quasar-driven winds? (see Figure 6).

IF studies of active galaxies have been carried out for a number of years already (e.g.García-Lorenzo et al. 2001, Villar-Martín et al. 2007). Compared to the complexity of the AGN family, which includes numerous types of different objects (Seyferts, LINERS, radio galaxies, etc, etc), such studies have been very scarce. This situation is especially critical at higher redshift ($z>0.5$).

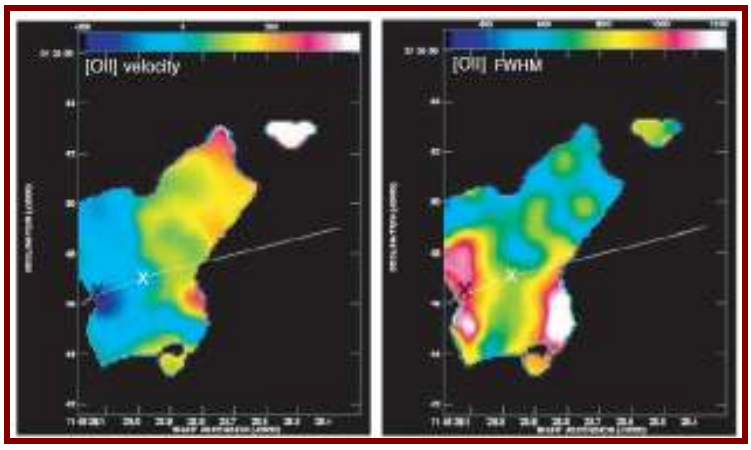

Figure 6. (Solorzano Iñarrea et al. 2002). It is possible that all massive ellipticals have gone through a radio-active phase, appearing as radio galaxies. The figure shows optical Taurus Tunnable Filter (WHT) of the radio galaxy 3C265 at z=0.8. The FOV is 14"x15" or ~110 kpc x1 00kpc.The kinematics of the ionized gas reveals the presence of very high velocity gas, probably accelerated by the radio structures, which might be ejected from the host galaxy. IFS studies of active galaxies at different *z* at both optical and NIR wavelengths can be critical to understand this and other types of feedback mechanisms.

Also, as we explained in Sec. 2.2.2, thanks to new technological facilities and/or ongoing and future surveys, a whole new window is being opened for IF spectroscopic studies of active galaxies by the finding of new AGN types, like type 2 quasars.

Gamma ray bursts

Since 1993, Gamma-ray Bursts (GRBs) have been classified into two subgroups according to the observed duration and hardness-ratio derived from their gamma-ray spectra: short-hard (SGRB) and long-soft (LGRB) events.

LGRBs originate at cosmological distances with energy releases of 10^{51} ergs (corrected by the teaming factor, Castro-Tirado et al. 1999). The first X-ray detections of SGRB afterglows in 2005 in combination with optical and radio detections have suggested that they release less energy than the LGRBs (i.e. energy releases of 10^{49} erg) and that they may originate from the coalescence of neutron star (NS) or NS-black hole (BH) binaries at cosmological distances. In fact, GRB 060121may be the most distant SGRB found so far (de Ugarte Postigo et al. 2006). A significant fraction of GRBs seem to be intrinsically faint. However the fact that they could be intrinsically dark events (Gorosabel et al. 1999) remains an open question. In some cases, it has been suggested that the cause of the reddening is dust extinction in the host galaxy (Castro-Tirado et al. 2007). On the other hand, ultra-high redshift events appear quite faint because of Lyman-α blanketing affecting the optical passbands.

The multiwavelength emission that follows the gamma-ray burst (the “afterglow”) satisfies the predictions of the ``standard'' relativistic fireball model and the central engines that power these extraordinary events are now considered to be the collapse of massive stars as recently proven by the spectroscopic signature of a peculiar, very energetic supernova (SN 2003dh, Willingale et al. 2004) in the nearest “classical” GRB afterglow detected so far, at z=0.17. Their potential as cosmological tools is now widely recognized, since they can be detected at very high redshift (z>6, e.g. Haislip et al. 2006. See also Figure 7).

With the forthcoming *GLAST* mission (to be launched in spring of 2008), the number of GRBs detected at high z could increase significantly. *SWIFT* is already detecting a significant fraction (10%) of events at *z*>4. Sinergy with *GLAST* (and possible other missions) will allow this number to increase (*GLAST* is expected to detect about 100 events/yr).

Obtaining optical and NIR IF spectroscopic data of GRB optical afterglows in less than 2 hr after the event occurrence is critical to determine the redshift (based on absorption/emission features). The continuum slope can thus be characterized and the reddening estimated. It will be possible to derive star-forming rates, chemical abundances, the study of intervening systems, etc.

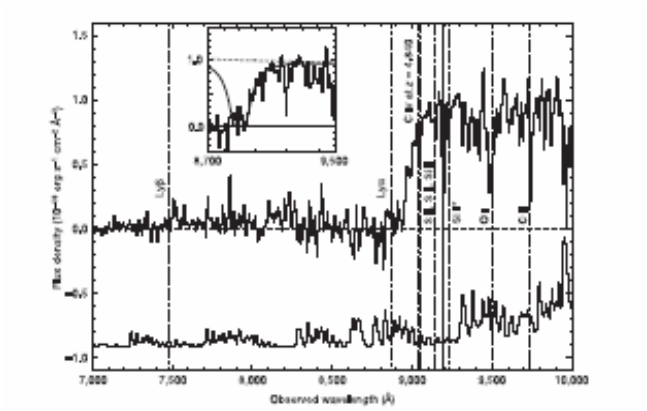

Figure 7. GRBs are powerful cosmological tools. This is a spectrum obtained with the SUBARU telescope of the afterglow of the GRB 050904 at z = 6.239 (Kawai et al. 2006). Notice the rich absorption line spectrum beyond the Lyman break, which provides information about both the host galaxy and intervening absorption systems.

2.2.5 Input photometric catalogue: optimum target population

More applicable to MOS. Examples of objects samples to be studied with SIFU/mIFU modes, related to "Extragalactic Energetic Phenomena" are mentioned across this chapter.

2.2.6 Target number density and optimal number of fibers

Applicable to MOS. See 2.2.7 for specifications on FOV and sampling (fiber size) for SIFU and mIFUs in next section.

2.2.7 Justification of the spectral resolution and wavelength coverage

Most of the science issues related to Extragalactic Energetic Phenomena require the characterization of the spectral gas and stellar properties in two spatial dimensions to obtain information on metallicities, dynamics, ionization mechanism, stellar ages, extinction, etc. The widest possible spectral range from the blue to the NIR is desirable for numerous reasons: depending on age, metallicity and mass, the stellar continuum peaks at different wavelengths and it shows absorption features which appear in different parts of the spectrum. On the other hand, the rich emission line spectra of the different gaseous phases (neutral, molecular, coronal, warm ionized) span a very broad range so that optical and NIR are both very valuable to identify and characterize their properties. Also, the effects of dust extinction often distort our view of the object properties. The impact of dust extinction must be evaluated and a combination of optical and NIR spectroscopy is critical for this.

Finally, SIDE greatest potential, both in MOS and IF modes, will be to investigate galaxy evolution. When we look at distant galaxies, some of the standard stellar population indicators and gas emission lines will be red-shifted towards the NIR so that the widest possible spectral coverage from the optical to the NIR is desirable to ensure as much as

possible that we can use at least some common indicators (e.g. [OII]λ3727, 4000 Å break, Hα, etc) at different redshifts.

All these ideas are reflected in Table 2 and Table 3, which have been adapted from Lehnert (2006) and d'Odorico (2007) oral presentations. The wavelengths of the main indicators (continuum features, absorption and emission lines) of stellar and gas properties within SIDE spectral range are shown for different redshifts up to z<13. The only difference between both tables is that in Table 2 we have considered the nominal spectral range proposed for SIDE (~3600Å-1.7μm) and in Table 3 we have considered a possible spectral range under discussion (~4000Å-1.4μm), see Section 3.10.1 on the SIDE Dual VIS-NIR spectrograph. Both tables show the potential of an instrument such as SIDE, thanks to the possibility of not only characterizing the SED over a broad spectral range, but also the combination of pairs of indicators at different wavelengths. As an example, the use of emission lines in the optical and NIR will be often unique to characterize reddening (e.g. Pβ/Hα, Hα/Hβ depending on redshift), the presence of supernovae in low *z* objects ([FeIIλ]1.257μm/Hβ), gas metallicities ([OII], Hβ, [OIII] for *z*~1-1.5), presence and properties of coronal gas [FeXIII]λ1.075μm/Hβ, etc.

Given the nature of the science proposed here, it is essential to cover as broad a spectral range as possible in a single exposure and with good enough S/N. In general, a spectral resolution of R~4000 is enough, making sure at the same time that we work efficiently between OH lines. The possibility to work at lower spectral resolution (~several hundreds) would also be valuable for cases where this is not an issue.

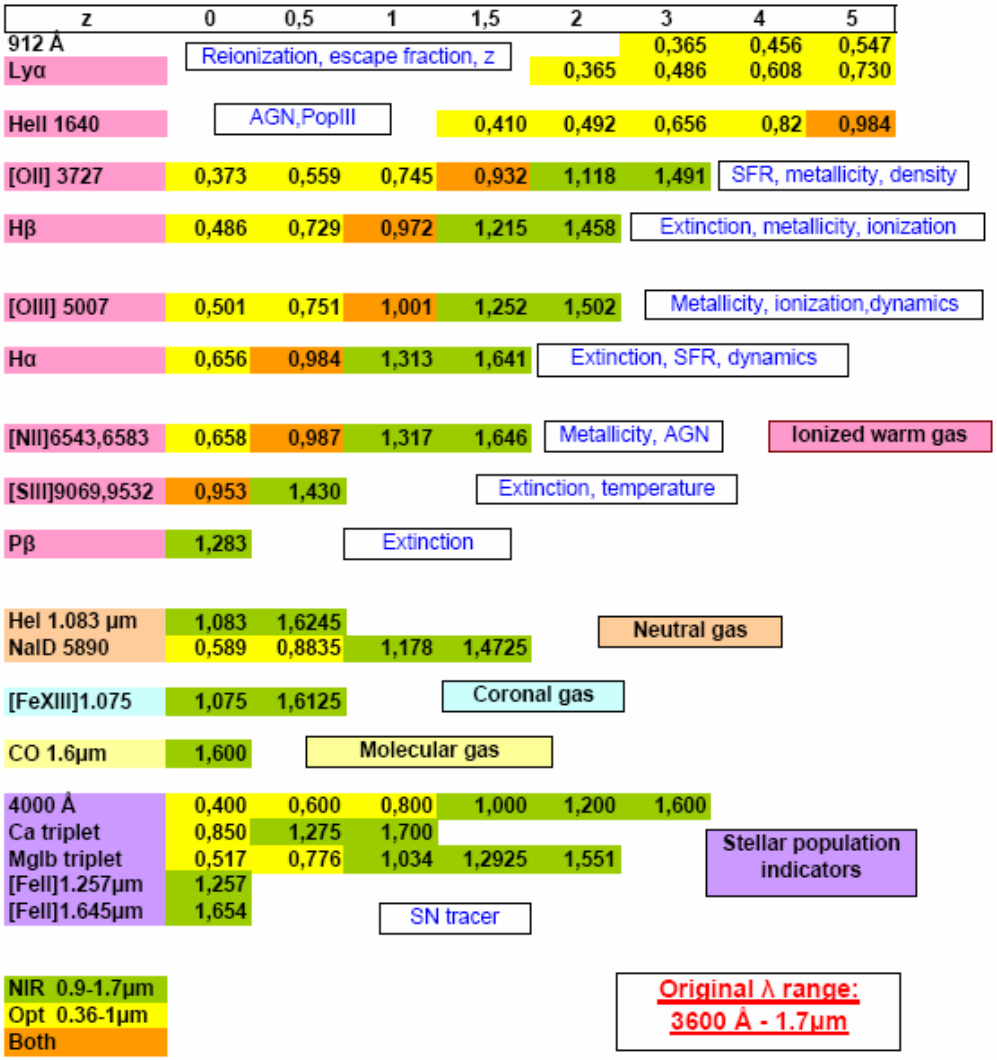
z
0
0,5
1
1,5
2
3
4
5
912 Å
Lyα
Reionization, escape fraction, z
0,365
0,365
0,486
0,456
0,608
0,547
0,730
HeII 1640
AGN,PopIII
0,410
0,492
0,656
0,82
0,984
[OII] 3727
0,373
0,559
0,745
0,932
1,118
1,491
SFR, metallicity, density
Hβ
0,486
0,729
0,972
1,215
1,458
Extinction, metallicity, ionization
[OIII] 5007
0,501
0,751
1,001
1,252
1,502
Metallicity, ionization,dynamics
Hα
0,656
0,984
1,313
1,641
Extinction, SFR, dynamics
[NII]6543,6583
0,658
0,987
1,317
1,646
Metallicity, AGN
Ionized warm gas
[SIII]9069,9532
0,953
1,430
Extinction, temperature
Pβ
1,283
Extinction
HeI 1.083 µm
NaID 5890
1,083
1,6245
0,589
0,8835
1,178
1,4725
Neutral gas
[FeXIII]1.075
1,075
1,6125
Coronal gas
CO 1.6µm
1,600
Molecular gas
4000 Å
Ca triplet
Mglb triplet
[FeII]1.257µm
[FeII]1.645µm
0,400
0,600
0,800
1,000
1,200
1,600
0,850
1,275
1,700
0,517
0,776
1,034
1,2925
1,551
1,257
1,654
Stellar population indicators
SN tracer
NIR 0.9-1.7µm
Opt 0.36-1µm
Both
Original λ range:
3600 Å - 1.7µm

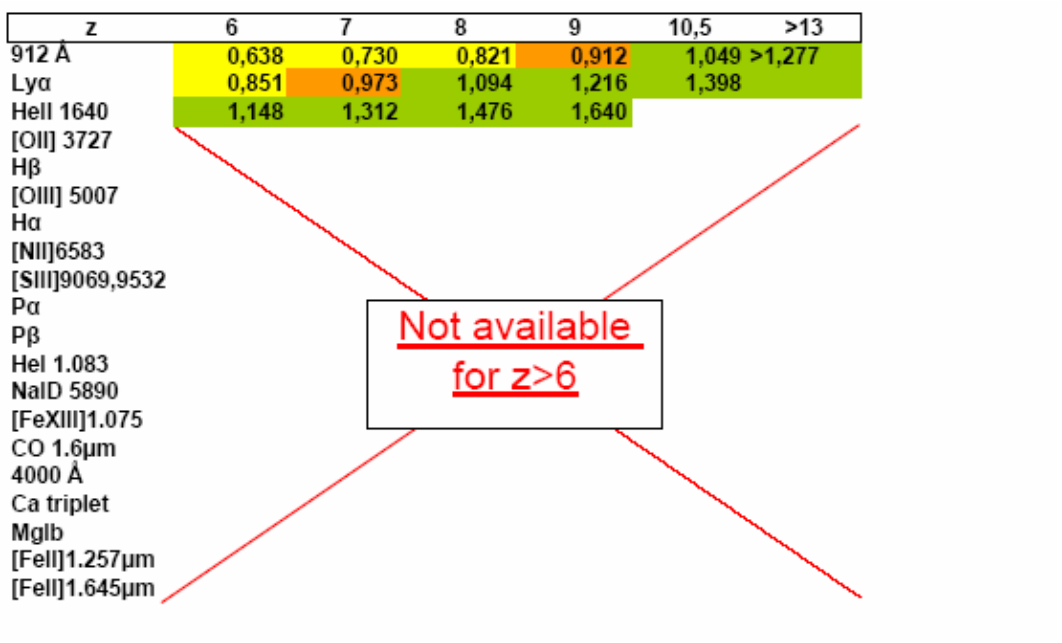

Table 2. (Previous page also) Emission and absorption spectral features, indicators of stellar and gaseous properties, for different redshifts. Notice the richness of such features over the spectral range nominally defined for SIDE (~3600 Å-1.7μm), both in the optical and NIR. A colour code is used to distinguish (top-left) between indicators that characterize properties of stars (light purple), warm ionized gas (pink), neutral gas (peach), coronal gas (light blue) and molecular gas (light yellow). For different redshifts, the wavelength values of the spectral features are highlighted in green, yellow or orange, depending on whether they would be observable in the NIR, optical or both bands with SIDE.

z	0	0,1	0,5	1	1,5	2	2,5	3	4
912 Å									0,456
Lyα							0,426	0,486	0,608
HeII 1640					0,410	0,492	0,574	0,656	0,82
[OII] 3727		0,410	0,559	0,745	0,932	1,118	1,304		
Hβ	0,486	0,535	0,729	0,972	1,215				
[OIII] 5007	0,501	0,551	0,751	1,001	1,252				
Hα	0,656	0,722	0,984	1,313					
[NII]6543,6583	0,658	0,724	0,987	1,317					
[SIII]9069,9532	0,953	1,049							
Pβ	1,283								
HeI 1.083 µm NaID 5890	1,083	1,1913							
[FeXIII]1.075	1,075	1,1825							
CO 1.6µm									
4000 Å	0,400	0,440	0,600	0,800	1,000	1,200			
Ca triplet	0,850	0,935	1,275						
MgIb triplet	0,517	0,5687	0,7755	1,034	1,293				
[FeII]1.257µm	1,257								
[FeII]1.645µm									

Revised λ range:
4000 Å - 1.4µm

NIR 0.9-1.4µm
Opt 0.4-1µm
Both

Table 3. (Previous page also) Same as Table 1 but for a spectral range of 4000Å – 1.4μm, under consideration for the SIDE Dual VIS-NIR spectrograph

2.2.8 Optimum observing strategy and procedure

For the projects discussed here, the typical strategy and procedure does not differ from that of standard IF observations. The IF mode to be used would depend on the project and object characteristics, to find the best compromise between field of view and spatial sampling (30"x30" at ~1" sampling vs. 15"x15" at 0.5" sampling). Dithering techniques could be applied in order to improve the spatial resolution when desired.

The possibility to observe simultaneously in the optical and NIR would be highly desirable, because of the obvious saving in exposure time. On the other hand, it would ensure, for instance, identical pointings over the entire spectral range (although atmospheric dispersion should be considered carefully here).

The use of the mini-IFUs can be very valuable for projects in which an intermediate mode between MOS and IF would allow to achieve an ideal compromise between FOV, number of targets (several tens) and the need for some spatial information on each target. For example, the Antennae interacting nuclei are separated by several arcminutes. The location of mini-IFUs at specific locations of star-forming clusters and diffuse regions of star formation is a very interesting alternative to the MOS mode (see Figure 8).

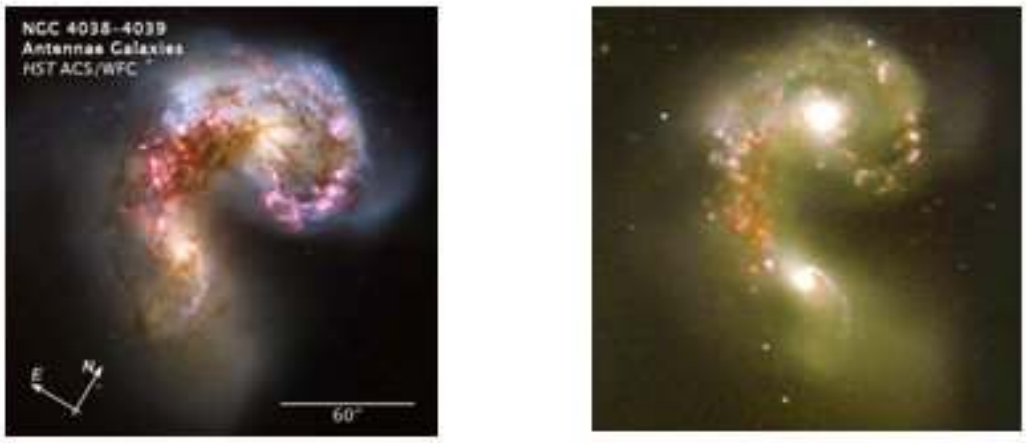

Figure 8. Left: ACS/WFP HST image of the Antennae system of interacting galaxies. Images taken in 4 different optical filters have been combined. Right: J,H,Ks combined image (SOFI-NTT). During the collision, billions of stars will be formed. The brightest and most compact of these star bright regions are called super stellar clusters. Notice the heavy extinction effects. An interesting possibility to investigate this and similar systems with SIDE, would make use of the mini-IFUs distributed at different locations to include both the SSC and regions of diffuse star formation. Due to the variety of stellar indicators depending on age and metallicity from optical to NIR wavelengths (see text), covering such a wide spectral range as proposed for SIDE would be very valuable.

Another important benefit of this IFS mode is the possibility to account for the effects of atmospheric dispersion. An ideal configuration of the mini-IFUs mode would require a FOV per mIFU large enough to ensure that for many distant objects some sky area is included (e.g. 4”x4”). As a guide, typical angular sizes revealed by Spitzer for intermediate redshift (z~0.5) IR galaxies is 2-3” (Pérez-González, private communication), a spatial sampling good enough to capitalize on the best seeing conditions (~0.2" per fiber) , and a large number of mini-IFUs. However, keeping in mind the minimum fiber size stated for SIDE (we have assumed 0.4”) and the expected number of fibers (1000), a compromise has to be found, since a FOV of 4”x4” would result in too few mIFUs (10) at 0.2”/fiber. Alternatively, a configuration of 20 mini-IFUs of 2.8”x2.8” FOV each with a spatial sampling of 0.4”/fiber might be an interesting alternative to be considered. With dithering, both the individual mIFU FOV and the spatial sampling could be improved. For comparison, KMOS (VLT) will have 24 mini-IFUs (2.8”x2.8” per mini-IFU at 0.2” sampling, working in 1-2.4 range) and FLAMES-GIRAFFE (VLT) has 15 (2”x3” FOV per mini-IFU at 0.5” sampling).

2.2.9 References

Alonso-Herrero A., Rieke G., Rieke M., Colina L., Pérez González P., Ryder S., 2006, ApJ, 650, 835
Band-Hawthorn J., 2007, in *Stellar populations as building blocks of galaxies.* Proceedings IAU Simposium No. 241, A. Vazdekis & R. Peletier Eds.
Borne K., Bushouse H., Lucas R., Colina L., 2000, ApJ, 529, L77
Castro-Tirado, A. J. et al. 1999, Sci 283, 2069
Castro-Tirado, A. J. et al. 2007, A&A 475, 101
de Ugarte Postigo, A. et al. 2006, ApJ 684, L83

Colina, L., Arribas, S., Monreal-Ibero, A. 2005, ApJ, 621, 725
Elbaz D., Cesarsky C. J., Chanial P., Aussel H., Franceschini A., Fadda D., Chary, R. R., 2002, A&A, 384, 848
D'Odorico v., 2007, in ESO Workshop on Obscured AGN Across Cosmic Time.
Seeon, Germany, 5-8 June 2007
García-Marín, M. et al. 2006, ApJ, 650, 850
García-Lorenzo B., Arribas S., Mediavilla E., 2001, A&A, 378, 787
Genzel, R. et al. 2001, ApJ, 563, 527
Gorosabel, J. et al. 1999, A&A 339, 719
Haislip J. et al. 2006, Nature, 440, 181
Kauffmann G. et al. 2006, accepted for the GALEX special issue of ApJS (astro-ph/0609436)
Kawai N. et al. 2006, Nature, 440, 184
Krongold Y., Nicastro F., Elvis M., Brickhouse N., Binette L., Mathur S., Jiménez-Bailón E., 2007, ApJ, 659, 1022
Larson R., Tinsley B, 1978, ApJ, 219, 46
Le Floc'h, E. et al. 2005, ApJ, 632, 169
Li C., Kauffmann G., Lan W., White S., Heckman T., Ping Y., 2006, MNRAS, 373, 457
McCady N., Graham J., 2007, ApJ, 663, 844
Reuland et al. 2003, ApJ, 592, 755
Rieke, G. H. & Low, F. J. 1972, ApJ, 176, L95
Sanders, D. B., Soifer, B. T., Elias, J. H., Neugebauer, B., \& Matthews, K. 1988, ApJ, 328, L35
Veilleux, S. et al. 1995, ApJS, 98, 171
Villar-Martíin M., Sánchez S.F., Humphrey A., Dijkstra M., di Serego Alighieri S., De Breuck C., González-Delgado R., 2007, MNRAS, 378, 416
Willingale R., Osborne J., O'Brien P., Ward M., Levan A., Page K., 2004, MNRAS, 349
Zakamska N. et al. 2003, AJ, 125, 2125
Zheng, X., Hammer, F., Flores H., Assémat F., Pelat D. 2004, A\&A, 421, 847

2.3 First Objects & IGM

2.3.1 Introduction

Two large, almost orthogonal, populations of high-redshift galaxies in formation have been discovered in the last decade: the blue starburst galaxies (with moderate star-formation rates) that do not suffer significant attenuation by dust, and are identified in deep optical imaging through their celebrated Lyman-break; and the heavily-obscured dusty starbursts (with extremely high star formation rates) that have been detected in deep far-infrared to mm surveys. The spectral energy distribution of the extragalactic background radiation shows that, after subtracting the diffuse cosmic microwave background which originates from the last-scattering surface at z~1089, the integrated emission in the Universe is dominated by two components of approximately equal energetic relevance: that emitted at optical-ultraviolet (UV) wavelengths, and that emitted at far-infrared to millimeter wavelengths. The great importance of measuring the integrated extragalactic background is that it can place strong constraints on the rates of star formation, the production of metals and the nature of objects in the early Universe that remain inaccessible to direct detection by the current generations of telescopes.

Understanding the evolutionary history and spatial distribution of these two orthogonal populations, within which also lie the first astronomical objects in the early-Universe (Population III stars, primeval galaxies and AGN), and their relative contributions to the extragalactic background, are therefore two of the fundamental goals of modern observational cosmology.

Identifying the first objects to form with the first 300 - 3000 Myr ($15 < z < 2$) following the Big Bang has been a significant motivating factor, and a major contributor to the justification for funding the largest optical/IR telescopes that have recently been constructed (Subaru, Gemini, VLT, Keck, GTC ….), and to those of the future (e.g. JWST and design studies for ground-based 30-m to 50-m diameter Extremely Large Telescopes). The same is true of the next generation of ground-based and satellite-borne millimeter-FIR experiments (LMT, ALMA, Herschel, Planck, ACT, SPT …), and those operating at low radio-frequencies (LOFAR, SKA).

The underlying expectation behind this high-impact science-goal, still to be proven observationally, is that the formation of the first (massive, hot Population III) stars, and the first galaxies and AGN, was a brief evolutionary phase that re-ionized the neutral primordial gas within the underlying dark matter distribution of the early Universe. The success of the on-going and future planned optical-IR searches for these first objects relies on the fact that the redshifted UV photons are not scattered by the zero- (or extremely low-) metallicity primordial gas. Contrastingly, however, these models also predict that the conversion of molecular gas into subsequent generations of young, massive stars and/or it's accretion to fuel a black-hole during the early formation of galaxies is expected to quickly convert from a UV-bright epoch of structure formation to a dusty and heavily-obscured episode. This rapid increase in the metallicity (and opacity) of the high-z Universe could occur within only 10-50 Myr after the formation of the first stars.

It is precisely this strong absorption of the UV-optical photons by dust grains (injected into the ISM by the strong winds and supernovae of the Population III, and later Population II stars), and hence strong re-radiation at longer rest-frame wavelengths, that also provides the current generation of mid-IR, FIR and millimeter wavelength instruments with the opportunity to also reveal these powerful bursts of activity in the early Universe. Thus the simultaneous searches for optical/IR continuum and emission-lines (rest-frame Ly-alpha) for the earliest low-metallicity and UV-bright galaxies (in the rest-frame), and the follow-up to the FIR-millimeter wavelengths searches for the essentially coeval dust-obscured phase of star-formation, provide a powerful combination of techniques and opportunities that the GTC and SIDE can exploit in the near future.

2.3.2 Current status and open questions in the field

Galaxy formation also yields important clues to the nature of the reionization mechanism and epoch of reionization, which WMAP (Spergel et al. 2004) places at z~ 10-15. The search for these first re-ionizing objects, dusty, or otherwise, pristine, which are expected at z>>7 is a significant challenge for observational astronomy, and one to which both the largest mm-FIR and optical-NIR facilities are being applied.

In recent years the optical-NIR surveys have gathered small samples of z~6-7 blue starbursts (with moderate star-formation rates, i.e. a few $M_{\odot}$ /yr), close to the end of the reionization epoch (e.g. Hu et al. 2002). These galaxies, selected through the Lyman break technique as optical drop-out galaxies, show an intrinsically blue UV rest-frame spectrum, as measured from observed near-IR colours. Extending the searches beyond z~7 requires very deep observations in NIR bands, where z~7-10 faint (H_{AB}~27) candidates can be found (e.g. Bouwens et al. 2005). By concentrating these searches on regions with strong gravitational lensing provided by rich foreground galaxy clusters, they can take advantage of the strong magnification (factors of a few to 15) that can improve the efficiency of the follow-up spectroscopic studies (e.g. Richard et al. 2006). Indeed recent deep optical-NIR imaging in the last 12 months towards nearby rich clusters may have already demonstrated the success of this technique (see Figure 9). Although still conducted as pilot programs with small (~30) candidate samples and information derived from, primarily, photometric-redshifts, there are now preliminary claims of the detection of normal starburst galaxies in the redshift range $7 < z < 12$, i.e. back to earlier re-ionization epochs (Pelló et al. 2007). Ellis et al. 2007, following a similar technique, blindly searching for emission lines towards strong lensing clusters, have also claimed a spectroscopic detection of the most-distant galaxy yet discovered, at z~10.

Creating new large colour-selected samples of primaeval galaxies at z~7-12 will now be a challenge for the new generation of deep GTC optical-NIR surveys. Due to the high surface density of candidates towards lensing clusters (~ 30 sources in ≤10 sq. arcmins) there exists the obvious requirement for a sensitive multi-object fiber-fed spectrograph to provide the necessary spectroscopic confirmation of these extreme redshifts.

Whilst we already understand that the optical-UV background is emitted by a combination of normal galaxies and quasars, the origin of the FIR-mm background is still waiting to be fully-resolved by the next generation of satellite-borne and ground-based FIR-mm telescopes/instruments: for example Herschel (and the proposed cryogenically-cooled FIR telescopes, e.g. SPICA), WISE, the 50-m Large Millimeter Telescope (LMT) and the Atacama Large Millimeter Array (ALMA). Together these facilities will conduct extremely deep, small area surveys (0.1 – 1 sq. degrees) to their respective confusion-limits, and much

more extensive, shallower surveys (100's of sq. degrees to all-sky). This wide dynamic-range of area and depth in the next generation of surveys is critical to the identification of all the populations that contribute to the extragalactic background over the entire cosmic history.

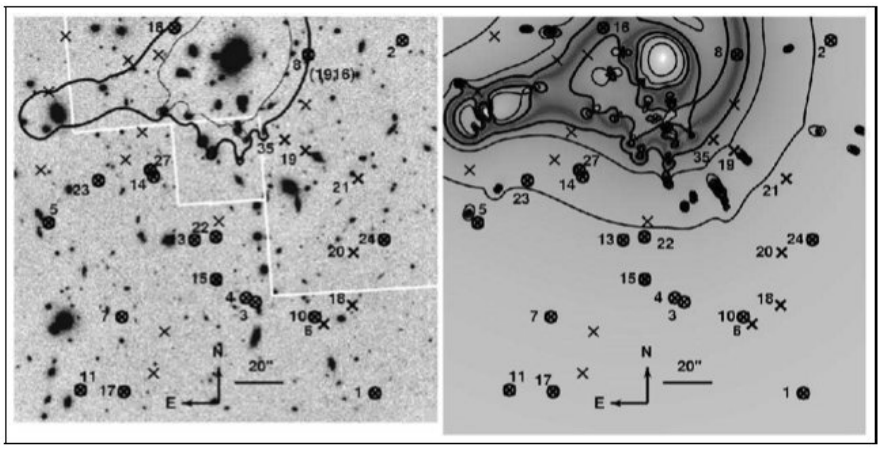

Figure 9: Left: 2'.5 x 2'.5 H-band image of the lensing cluster Abell 1835 (z=0.252) showing the location of the critical lines at z = 1.5 (thin solid curve) and z = 10 (thick solid curve). First/Second-category dropouts are circled and fourth-category objects are not labeled. Right: location of the same objects relative to the magnification across the field. Contours are overplotted for magnification values of 1, 2 and 3 magnitudes, computed assuming sources at z = 9, although the position of these lines is weakly sensitive to source redshift within the relevant range $6 < z < 10$.

During the last 10 years, various facilities and sub-mm cameras (SCUBA on 15-m JCMT; MAMBO on 30-m IRAM; Bolocam on 10-m CSO; AzTEC on 15-JCMT) have achieved approximately 200 secure detections of dusty, heavily-obscured galaxies undergoing extremely high-rates of star formation (>>500 $M_{\odot}$/yr) at submm-mm wavelengths. Commonly referred to as Submillimeter Galaxies (SMGs), this population are believed to be the high-redshift progenitors of massive elliptical galaxies caught in the act of formation. At the confusion-limit of these telescopes, approximately 1-3mJy (depending on the wavelength), the surface density of SMGs is ~ 3000 sources per sq. degree. Assuming a uniform distribution, and no clustering, this implies that there 300-400 sources within each SIDE FOV. Due to the sensitivity of the SMG surveys, however, only the brighter population (S > 3 mJy at 1.1mm, or S > 6mJy at 850um) have been routinely detected with a reduced surface density of ~40 SMGs within the SIDE FOV.

Understanding the physical nature and evolutionary history of the SMG population requires a comprehensive series of coordinated multi-wavelength follow-up observations. The spatial-resolution of these current submm-mm surveys is ~10-30 arcsecs which, given the noise properties of the maps, implies a typical positional uncertainty of +/- 3 arcsecs for the extracted SMG sources from the reconstructed maps. Inspection of deep radio, optical and IR surveys demonstrates that one can expect to find numerous candidates (a few to > 10 sources, depending on the sensitivity), consistent with positional error of the SMGs. To date these observations have been extremely time-consuming, due to the requirement to first identify the radio counterparts, under the reasonable assumption that both the radio and the rest-frame

FIR (observed submm-mm) emission have a spatial and temporal-correlation within regions of strong star formation. Taking advantage of the higher resolution interferometric radio observations, the optical-IR counterparts are then identified in broad-band images, followed by spectroscopic observations of the individual target. With these (and other) data one can in principle measure photometric and spectroscopic redshifts, determine the age and mass of the dominant stellar populations, characterize the morphology, measure dynamical masses, gas masses and the evolutionary history, as well as the AGN fraction within this SMG population.

Recent mid-IR surveys from Spitzer that have suggested that the observed MIPS 24μm emission provide a more efficient method to select the SMG counterpart. Yet whilst some success has been achieved, with the spectroscopic and photometric measurements of the redshift distribution for ~100 of the brightest SMGs (Chapman et al. 2005, Aretxaga et al. 2007), and detections of the molecular gas content in < 20 SMGs (Tacconi et al. 2006) ambiguities remain in the redshifts and counterparts and it has been extremely difficult to characterize the rest-frame UV and optical properties of their stellar populations and ionized gas content.

2.3.3 Future prospects

2.3.3.1 The next five years

The early generation of SMG surveys covered ~ 10 – 200 sq. arcmins. The recently completed SHADES (SCUBA Half Degree Extragalactic Survey) on the JCMT, and the AzTEC 1.1mm surveys of SMGs towards biased and un-biased (blank) fields have now mapped 200 – 1800 sq arcmins. The forthcoming extensive catalogs (> 1000 targets) from these AzTEC surveys will shortly require follow-up. Already it is clear that multi-object spectrographs (using masks) and single IFUs on Gemini, Subaru, VLT etc do not provide a sufficient multiplexing capability to efficiently observe the counterparts SMGs, nor to observe the companion populations of galaxies within the common dark-matter haloes of these progenitor elliptical galaxies. Whatever the situation today, it is a fact that in the next 5 years the significant increase in the sensitivities, spatial-resolutions and areas of the next generation of submm-mm and radio surveys will result in the need for larger-format and more sensitive multi-object optical spectrographs to measure redshifts and the UV-optical properties of this population.

As Figure 10 illustrates, the situation will rapidly become increasingly difficult. In 2008, SCUBA-2, a next-generation monolithic-array (6400 pixels of superconducting transition-edged sensors - TES) continuum camera, operating at 850 and 450um, will be commissioned on JCMT. The mapping-speed of SCUBA-2 will be ~200 times faster than SCUBA. Since the confusion-limit of SCUBA-2 will remain ~2mJy, this mapping speed can be translated directly to a factor of 200 increase in the number of detected sources. Furthermore in 2009, the AzTEC camera (which has already been commissioned and generated significant catalogs, >> 1000 SMG sources, from surveys with the JCMT and the 10-m Atacama Submillimeter Telescope Experiment) will be installed on the 50-m LMT. Taking advantage of the significantly greater collecting area and resolution, the LMT will be able to conduct 0.5-1.0 sq. degree surveys to a much lower confusion-limit (< 0.1 mJy). A single LMT Key Project survey of this order is expected to detect 20,000 – 50,000 sources, or ~10 per sq.

arcmin. Given the steepness of the 1.1mm source-counts, wider-area and shallower surveys with the LMT will produce similarly large catalogs in the same integration-time.

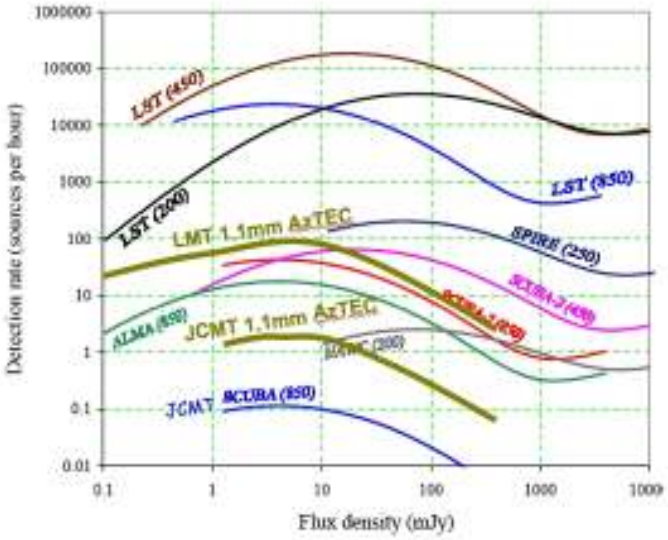

Figure 10: Detection rate of sources at FIR to mm wavelengths (in parentehesis, in microns) by different existing, planned and proposed facilities (adapted from Blain et al. 2002). The current survey speeds are indicated by SCUBA on JCMT & AzTEC on JCMT. The next generation of surveys by ALMA, SPIRE on Herschel, SCUBA-2 on the 15-m JCMT, AzTEC on the 50-m LMT, and a large 30-m submm telescope (LST) are expected map areas of 1-1000 sq. degrees, providing sources-catalogs of >>100,000 dusty galaxies that will require intensive spectroscopic follow-up by optical-NIR facilities such as the 10.4-m GTC and SIDE.

The higher S/N and improved resolution of such an LMT survey will provide improved positional errors (~ +/- 1 arcsec) of the SMGs.

In the context of SIDE on the GTC, there is an obvious need for an instrument that has of order 1000 MOS fibers to measure the rest-frame UV-optical emission from the more numerous fainter SMGs that will be detected in future surveys by the LMT. No evidence yet exists, but it is possible that the fainter SMGs at millimeter wavelengths may be brighter at observed optical wavelengths (due to less or more patchy dust-obscuration). Furthermore for those SMGs that have a positional uncertainty > 1 arcsec, then small bundles of fibers (mIFUs over a 4 x 4 arcsec FOV) are the ideal way to measure redshifts, emission line-ratios, continuum emission and stellar absorption features.

2.3.3.2 Beyond the next five years

The first-light suite of LMT instrumentation will be delivered to the telescope in 2008-2009. In the case of continuum mapping, the 144-pixel feedhorn-coupled AzTEC camera will be the primary instrument. It is planned however to develop a monolithic filled-array to fill the full field-of-view. Requiring only 6000-10000 pixels, the proven technology of TES detectors already exists and hence it expected that by 2013 a second generation large-format camera for the LMT will be commissioned. Such an instrument will have a further increase

in mapping speed by a factor of > 10, at which point the demand for a multi-object spectrograph with at least the baseline capabilities of SIDE (~1000 MOS fibers) will be essential.

On a similar timescale all the Herschel and Planck survey data will be publically available, as well as the all-sky FIR AKARI surveys. To complement these FIR galaxy and cluster surveys, the South-Pole Telescope (SPT) and the Atacama Cosmology Telescope (ACT) will also have completed their blank-field searches for high-z redshift clusters (z >> 1) via the millimeter-wavelength detection of the Sunyaev-Zeldovich effect. Both SPT and ACT have on-going optical surveys at southern equatorial declinations that are accessible to the GTC. SIDE spectroscopy of the over-densities of mm-wavelength and optical galaxies identified towards these cluster signatures will provide an important and efficient means to determine the redshift and velocity-dispersion (mass) of these evolving high-redshift clusters. Although many other facilities will be coming on-line in the next 5 years and beyond 2013, LOFAR, ALMA and SKA deserve special mention. At the core of their scientific-cases are the detections of primordial HI and CO towards the first stars and galaxies at the epoch of reionization. Although redshifts of these first objects are directly measured from the line-transitions that arise from the neutral HI and molecular CO gas, SIDE on the GTC will provide the opportunity to complement these unique radio-mm data and provide information on the ionised state of the gas involved in the first stages of structure formation.

2.3.4 The opportunity window for SIDE

The uniqueness of SIDE is that it provides sensitive spectroscopy of the orthogonal UV-optical and FIR-submm galaxy populations that have high surface-densities. The large SIDE FOV will typically contain a few hundred to 1000 targets. SIDE can efficiently deliver spectroscopic surveys over many sq. degrees of contiguous area or individual pointings.

2.3.5 Science cases

Deep surveys that identify sites of galaxy formation in both blank-fields and strongly biased fields towards high-z over-densities (such as those signaled by AGN and clusters) will be accomplished in the next decade. Existing data show that these surveys will have a mix of the FIR-mm dust-enshrouded galaxies and blue low-metallicity galaxies that co-exist in the same fields, and that represent the orthogonal high-z starburst populations discovered though complementary multi-wavelength imaging. The simultaneous studies of their redshift distributions, luminosity functions, clustering and morphological evolution in the field and in rich clusters will confront galaxy formation models. Large-area imaging surveys, of up to ~100 sq. deg. are being proposed by the next generation facilities. An equivalent increase in the performance of the optical-NIR spectroscopic follow-up will be required to derive maximum profit from these initial discovery surveys that will produce samples of tens to hundreds of thousands of galaxies in formation back to the epoch of re-ionization. An efficient way to simultaneously determine the redshifts (up to z~10) of these targets over a large field FOV (~20') is thus required. A powerful way is also necessary to follow-up selected targets of interest through detailed spectroscopic observations that will address the physical properties of the dust-enshrouded and low-metallicity galaxies in formation.

2.3.5.1 MOS observing mode

Blank field populations of dusty and blue high-z starbursts can efficiently be studied with this MOS mode. The number counts of dusty starbursts at high-z (see Figure 11) indicate that the current surveys at $S_{1.1mm}$>2mJy, such as those carried out with the AzTEC camera in the 15-m JCMT (e.g. Austermann et al. 2007) are discovering blank-field FIR ultraluminous galaxies with surface-densities of ~400-900 sources per sq. deg, allowing for a factor of 2–3 conversion between the 850μm and 1.1mm flux densities. Hence the expected number of sources per SIDE FOV is ~40–90. Surveys carried out towards high-z overdensities, however, show a factor of ~10 increase in the millimeter source-counts, even at z~4 (Hughes et al. 2007). Surveys carried out with the LMT, close to the confusion limit, $S_{1.1mm}$ >0.3 mJy will contain >10000 sources per sq. deg, giving a target base of > 1000 sources per SIDE FOV.

The abundance of mm-wavelength targets, from the LMT and other instruments (e.g. SCUBA-2), over the SIDE FOV guarantees that an optimal use of the order of ~few hundred to 1000 fibers can be made per unit exposure time using only dusty galaxies as targets. If we include the blank-field, optically-bright population of galaxies in formation and other objects, then the strategic value of the 1000-fiber MOS-mode of SIDE is clearly demonstrated.

Typical blank-field dusty starburst at high-z are faint at optical-NIR wavelengths with R(AB)~20-26 mag for a sample at z~ 1 to 4 (Chapman et al. 2005), and these are likely to be brighter for the neighbouring unobscured galaxies in the environments (common dark-matter haloes) of the primary mm-wavelength targets.

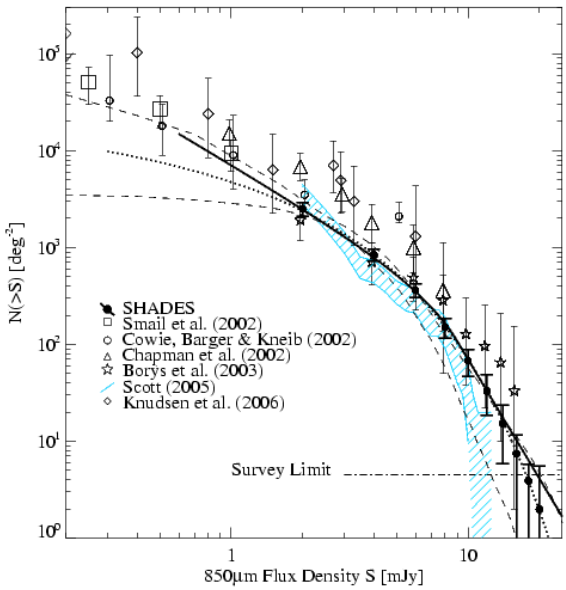

Figure 11: Number counts at 850μm derived from a variety of sub-mm surveys (from Coppin et al. 2006). 1.1mm counts can be estimated from the flux-ratio, F(850μm)/F(1.1mm) ~2.5.

An important issue to consider for the blue starbursts at z>7 is the relationship between photometric depth and surveyed area which is needed to identify a representative number of candidates, or to reach a meaningful non-detection limit. Because of the small fields of view of current space and ground-based optical cameras, a large uncertainty exists at the bright

end of the luminosity function, which is the dominant contributor to the bright end of the number counts at such redshifts (see Figure 12). We consider some reasonable extrapolations (to be confirmed by forthcoming observations which should be available when SIDE starts operations). An L* galaxy at z~4 will have H(AB)~25 at z~7.5. A direct extrapolation of the current z~6-7 UV luminosity function in blank fields (with a turnover observed towards the bright end of the luminosity function compared to z~3-4) yields a few (~<10 per redshift bin of 1) "bright" sources in the SIDE FOV with H(AB)~24.5-25.5 up to z~8.

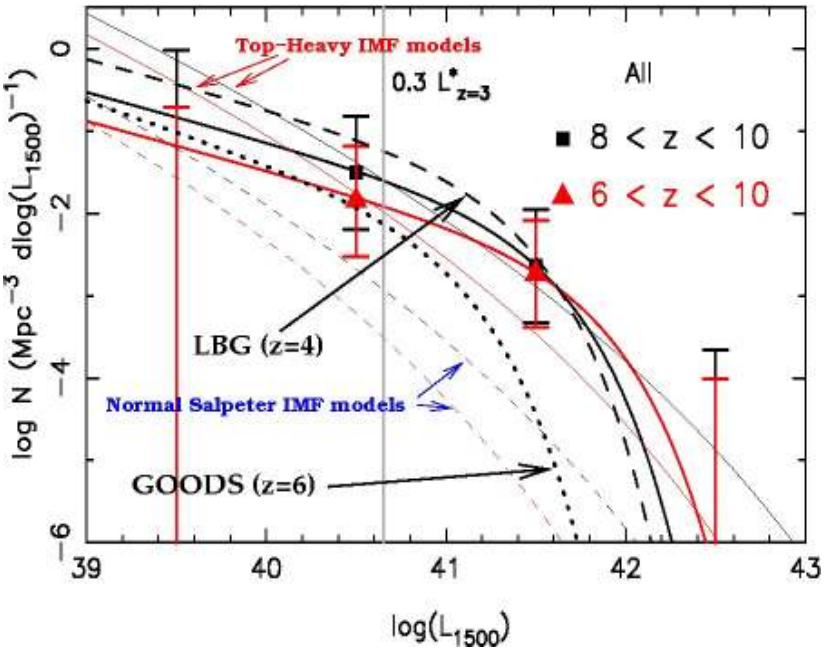

Figure 12: (from Pelló et al. 2007) Luminosity Function of z>6 Lyman break galaxies inferred from the photometric sample of Richards et al (2006), and comparison with the luminosity function at z~4 of Steidel et al. (2003) and the fit of Bouwens & Illingworth (2006). Also displayed are the results of a toy model, based on the Press-Schechter formalism, with all haloes converting a constant fraction ~0.1 of their baryonic mass into stars between z=17 and z=6, Two ``extreme" IMFs are considered: a standard Salpeter and a top-heavy IMF (50-500 $M_{\odot}$ stars). These estimations take into account the visibility time of bursts t~ 10^6 yr through a duty-cycle correction factor.

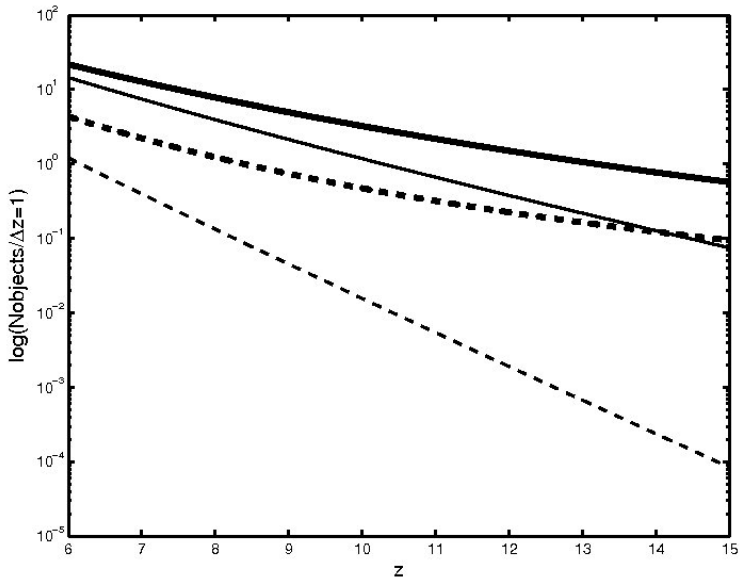

Figure 13: Comparison of the expected number counts of galaxies in a 6x6' FoV, centered on a blank field (thin lines) and on a strong lensing field (z(cluster)=0.25, thick lines), up to H(AB)~25.5, per dz=1.0 bin. We use extreme values of the observed L(1500) luminosity function: an upper "optimistic" limit (solid lines) and a low "pessimistic" value (dashed line).

Clearly, if one targets strongly-lensed areas around intervening clusters to identify and study the blue starbursting galaxies at z>7, the magnitudes can be a few times brighter. The MOS mode can be efficiently used to explore the regions around the critical magnification lines in strong-lensing clusters (like those in Figure 9). The survey could be a "blind" spectroscopic search of for emission-lines, setting the fibers along the critical lines of a given z, since the positions of these critical lines are well constrained by the mass model of the cluster with an appropriate accuracy. Alternatively "pointed" observations could be conducted, following the photometric pre-selection of candidates found in (ultra)deep imaging surveys of the lensing clusters. Note that the detection of magnitude-limited samples of z>7 galaxies is a factor between a ~3-20 more efficient in lensing clusters than in blank fields, and the relative efficiency increases with the redshift of the sources. SIDE will also allow a simultaneous acquisition of optical and IR spectra for a complete survey of Lyman-alpha emitters over the full redshift domain where lensing clusters reach maximum magnification efficiency (Figure 13).

2.3.5.2 mIFU observing mode

Often the counterparts to the high-z submillimeter galaxies cannot be identified without ambiguity in the follow-up imaging surveys. In general this is due to the unfavorable low resolutions of current single-dish mm-FIR telescopes (6” – 18” at 1.1mm at the 50-m LMT and 15-m JCMT, or 17 – 34” at 250–500μm by SPIRE in Herschel). The positional accuracies of the sources are typically a few arcsecs depending on the noise-properties of the map, the wavelength and telescope. It is therefore common to find radio/IR/optical counterparts within a third of the beam-size (e.g. Ivison et al. 2007). Multi-wavelength colour selection can help to identify the counterparts, as one expects red optical-IR colours for dusty galaxies. Multiple optical candidates are often found if one does not include high-resolution interferometric mm to radio follow-up campaigns. In both instances (inaccurate positions, or multiple candidates) positioning a small bundle (4”x4”) of fibers or mini-IFU at the location

of the ambiguously associated sources of the FIR-mm survey is sufficient to acquire the objects of interest, and other nearby objects that could be associated with the primary target (see for instance, Figure 14, where a SCUBA source has 2 alternative radio identifications, and one of them, in turn, has several optical counterparts).

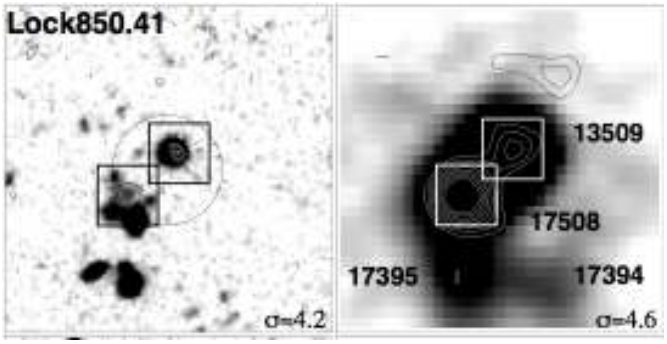

Figure 14: 25 × 25-arcsec postage stamp of a SCUBA source (Ivison et al. 2007). Greyscale R-band and 24-μm data are shown in the left- and right-hand panels, respectively, superimposed with radio 1.4GHz contours. Circles indicate 2 σ positional uncertainties of the SCUBA sources. Solid boxes indicate robust identifications, where the probability of chance association P<0.05 is based on the radio or 24-μm counts, or a combination of the two. Dashed boxes indicate tentative associations.

Mini-IFUs are also of use in the search for extended emission around powerful starbursts (e.g. Swinbank et al. 2005), and determining the fraction of escape photons in these systems that place constraints their contribution to re-ionization. Around several of several of these intense starbursts, strong diffuse Lyman-α regions have been identified. A mini-IFU of ~4"x4" (at z=2 corresponding to ~28 x 28kpc) will allow SIDE to detect the extended emission in individual components believed to be ejecting strong galactic winds.

A combination of ~30 to 50 mini-IFUs and a few hundreds MOS fibers in the same field can provide a very powerful configuration to simultaneously target ambiguous and unambiguous colour-selected high-z candidate sources in the same field, and to search for extended Lyman-α emission in bonafide z>7 photometrically-determined candidates. Blind searches for extra Lyman-α emitters that do not necessarily have a strong continuum along the critical magnification lines in clusters can also be conducted with the mini-IFU mode of SIDE.

2.3.5.3 SIFU observing mode

The SIFU mode, as MOS, can target specific regions of clusters to search along the critical lines of magnification for z>7 galaxies, without leaving gaps between the fibers, as in the MOS case.

Because optical and IR spectra could be acquired simultaneously, in some cases it should be possible to obtain detailed 3D spectroscopy of z~1-6 highly magnified/multiple images lying on the IFU FOV. Concentrating on such images is an interesting separate project, allowing SIDE to conduct high spatial-resolution measurements of velocity-fields and hence

dynamical masses, spectrophotometric properties in order to establish the gas and stellar components, etc.

2.3.6 Input photometric catalogue: optimum target population

The target populations will be composed of a few hundreds of blue starbursts and a few thousand to tens of thousands of dusty starbursts discovered over a coordinated series of blank fields (typically ~1-30 sq. deg) and biased surveys towards known over-densities (e.g. high-z AGN and clusters). About a dozen strong lensing moderate-z clusters will also be targeted to search along the critical lines of magnification, observing a few hundred blue starbursts at z>7 that have been either colour-selected from existing optical-IR catalogs, or simply by blindly searching for emission. These data will constrain luminosity functions and their influence on the epoch of re-ionization. The catalogs will produce faint objects of R(AB)~22-26 mag and H(AB)~22-24 to follow-up spectroscopically with SIDE.

2.3.7 Target number density and optimal number of fibers

The combination of surveys (see 2.3.5) guarantees that these scientific cases can take full advantage of the order of ~few hundreds to 1000 MOS fibers per SIDE FOV. The project would benefit from the maximum number of fibers available simultaneously (close to 1000), and it is the high-surface density of these dust-obscured submm galaxies and low-metallicity blue galaxies combined with the large FOV that provides a unique niche for SIDE in galaxy formation studies.

2.3.8 Justification of the spectral resolution and wavelength coverage

The targets of these science-cases are faint (R>22) and small (typically less than 2”), and thus the MOS and mIFU modes with fibers of large diameter ~1.2” – 1.5” would be better suited for these projects by minimizing the atmospheric diffraction effect and maximizing the simultaneous spectral coverage over the field. Maximum spectral coverage is required since the redshift of the sources is often only estimated and based on photometric-colors. Consequently these estimates can potentially span a large range, $1 < z < 10$. The spectroscopic searches will be focused on detecting primarily Ly-α in emission, but also other prominent UV-optical lines in typical starbursts and AGN (C-IV1500, C-III]1909, OII3727, Hβ). Low resolution (R~1000-5000) will be the primary observing mode of these faint dust-enshrouded mm galaxies and low-metallicity blue galaxies.

2.3.9 References

Aretxaga I. et al. 2007, MNRAS, in press (astro-ph/0702503).
Austermann J. et al. 2007, ApJ, in preparation.
Blain A.W et al. 2002. PhR, 369, 111.
Bouwens R.J. & Illingworth G. D. 2006, NewARev, 50, 152.
Bouwens R.J. et al. 2004, ApJ, 616, L79
Chapman S. et al. 2005, ApJ,
Coppin K. et al. 2006, MNRAS, 372, 1621.
Hu E. et al. 2002, ApJ, 568, L75.
Hughes D.H. et al. 2007, AAS, 209, 8307.
Ivison R.J. et al. 2007, MNRAS, in press (astro-ph/ 0702544).
Pelló R. et al. 2007, RevMexAA Conf. Ser., 29, 132.

Richard J. et al. 2006, A&A, 456, 861l
Spergel D.N. et al. 2007, ApJS, 170, 377.
Steidel C. et al. 2003, ApJ, 592, 728.
Swinbank et al. 2005, MNRAS, 359, 401.
Tacconi L. et al. 2006, ApJ, 640, 226.

2.4 Galaxy Evolution

2.4.1 Current status and open questions

Understanding how galaxies form and evolve is one of the most fundamental issues in astronomy. Many efforts have been done and many new instruments have been built with the aim of determining the morphological-dynamical, chemical and spectral evolution of galaxies. SIDE is an instrument concept that can revolutionize our understanding of these three aspects of galaxy evolution.

According with the "Galaxy Evolution across the Hubble time" symposium holding during the General Assembly in Prague in 2006 there are still many open questions in the domain of galaxy evolution. Some of these are:

- How and when was the present Hubble sequence of galaxies established?
- When the mass of galaxies was assembly?
- What is the efficiency of the star formation history through the Hubble time and how the star formation is linked to the galaxy morphology?
- What is the role of the environment in the evolution and transformation of galaxies?

Optical and NIR observations of nearby and far-away galaxies with SIDE can contribute significantly to answer these key questions of galaxy evolution. Many projects can be carried out with SIDE.

Here, however, we explain in details only projects dedicated to:

- Detection and study of high-redshift galaxies
- Properties of galaxies at intermediate redshift
- Nuclear Activity and its role on the evolution of galaxies
- The role of environment in the formation and evolution of galaxies
- The chemical evolution of galaxies

2.4.2 Future prospects

Most of the properties of galaxies are really derived at optical wavelengths. Spectroscopic surveys is the best tool to determine the evolution of stellar mass, dynamical mass, metallicity and spectral energy distribution of galaxies.

SDSS survey has proved this. A big advance has been obtained in the last five years in the determination of the stellar population properties and the ionized gas in galaxies due to the large sample of galaxies observed by Sloan in its spectroscopic mode. However, Sloan is limited at nearby galaxies ($z<0.3$) and bright galaxies. To understand how galaxies evolve, many spectra of galaxies at intermediate and high-redshift need to be observed.

Many phot-z surveys are being done in this decade. They will be able to constrain the evolution of the luminosity function, color and morphology of galaxies at intermediate redshift. However, spectroscopic surveys are needed to constrain the dynamical and stellar mass and metallicity of galaxies. Spectroscopy at rest-frame optical wavelengths is, for example, badly needed if we want to distinguish between red evolved galaxies and dusty young systems (see Section 2.4.4).

SIDE is the ideal instrument for studying how galaxies evolve due to its intermediate spectral resolution (R=4000), its spectral coverage (Optical and NIR), and its capability to observe a large number of objects simultaneously in its MOS observing mode. SIFU and mini-IFU modes are also relevant to get the kinematics and properties of the ionized gas and stellar populations of galaxies. By its sensitivity, SIDE will be able to observe a large number of high-redshift galaxies up to z=6 (or beyond) in the Lα line (see section 2.4.4 for a science case). These qualities make SIDE an unique instrument for next 10 years.

2.4.3 Opportunity window for SIDE

a) MOS observing mode: Properties of galaxies at intermediate redshift

MOS is the ideal observing mode of SIDE for developing this project. The capability of observing several hundreds of objects with simultaneous spectral covering at optical and NIR with an intermediate spectral resolution makes of SIDE the instrument to do a large survey of galaxies in the redshift interval of 0.8-1.5.

Observing parameters required for this project are:

- Spectral range: Optical rest frame. At z=0.8—1.5, the optical range 3600—7000 Å will be observed in 6500 Å —1.7 μm.
- Spectral resolution: Spectral synthesis requires a resolution of 1000, but due to the sky line contribution at the Z and NIR bands, an intermediate resolution of R=4000 is needed.
- Simultaneous observations of the optical and NIR is needed to cover the same galaxy area and to avoid problems with the flux calibration.
- Fiber sizes. At z= 1, 1 arcsec corresponds to 8 kpc. The stellar light radius (R_{half}) of these galaxies is 0.5 arcsec; so, a fiber of 1.5 arcsec is needed to avoid loss light.
- Number of fibers: A large number of observed galaxies are required to obtain statistic results. The objects density at z=1 estimated using COMBO17 data is about galaxies/arcmin^2 (see section 2.4.6.2). So, with SIDE FOV, more than 400 galaxies can be observed with MOS.
- SIDE limiting magnitudes: Assuming a fiber size of 1.5 arcsec, a seeing of 0.7 arcsec, a (final) resolution of 1000, it is expected to detect with a S/N= 3 galaxies with I_{fiber}= 23.2 mag, J_{fiber}= 21.4 mag in 2h.

These capabilities of SIDE will allow us to do a large survey of galaxies at z=1 and probably producing an impact equivalent to the SDSS in the local universe.

b) Mini-IFU observing mode: Properties of galaxies at intermediate redshift

The mini-IFU observing mode of SIDE is the ideal to perform detailed analysis of the properties of galaxies at intermediate redshift. Observing parameters for this project are:

- FOV of the mIFU: at least (2-3) arcsec x (2-3) arcsec due to the size of the extended ionized gas in these galaxies and the distance scale.
- Fiber sizes of 0.3-0.4 arcsec are needed for sampling the seeing.
- At least 10-20 mini-IFU are required to be able of obtaining statistic significant data.

c) SIFU observing mode: Nuclear Activity and its role on the evolution of galaxies

The SIFU observing mode of SIDE is the ideal to perform detailed analysis of the properties of QSOs and Starbursts.

- FOV of 15x15 arcsec is needed for mapping these objects since many of them are multiple systems. At z=0.5, 1 arcsec is 6 kpc, and the ionized gas can be extended up to 20 kpc.
- Sampling of 0.3 arcsec/fiber is needed to subtract the PSF contribution due to the QSO.
- Simultaneous covering at the I and J band will allow us to observe [OIII] and Hα in objects at z=0.5.

2.4.4 Science cases

Many projects can be carried out with SIDE in the field of Galaxy Evolution. Here, however, we explain in details only projects dedicated to:

- Detection and study of high-redshift galaxies
- Properties of galaxies at intermediate redshift
- Nuclear Activity and its role on the evolution of galaxies
- The role of environment in the formation and evolution of galaxies
- The chemical evolution of galaxies

2.4.4.1 High redshift galaxies: Star Formation in the Young Cosmic Web

Massive surveys for large-scale structure (LSS) exist at redshift 0.1 and will exist across redshift 0 to 1 by 2011. In the young universe (z=5.7 is 1 Gyr after the Big Bang) we now find routinely Lyman-break galaxies (LBG) and Lyman-alpha emitters (LAE), whereby a very large fraction, growing with redshift, of the LBGs are LAEs. Subaru-based imaging has put Japanese astronomy firmly on the map of high-quality astronomy with imaging datasets of high-z LAEs and LBGs, and new funding for better imagers helps to keep the lead. Spectroscopy is mostly done for statistical confirmation rates and contamination checks, but not possible for really large samples. Many teams now focus on the redshift 0.5 to 2 universe to study evolution of LSS with a view to Baryonic Oscillations, and plan surveys for gravitational lensing tomography centered on redshifts <1 as well. There are no attempts for large high-redshift LSS surveys that are impossible without SIDE or WFMOS at Subaru. However, the subject of the "first star formation" at high redshift is relevant for understanding star and galaxy formation. Also, we need to prepare the ground for more detailed studies of high-redshift galaxies with the next generation Space Telescope JWST. Furthermore, it is desirable to test theoretical predictions of the early Universe such as those from the Millennium simulations. The correlation function of galaxies at high-z also

constrains the power spectrum of initial fluctuations. The subject thus touches cosmology, formation of galaxies and star formation at the same time.

Objectives:

• To obtain a 3-D map of star-formation in a $(500\ Mpc)^3$ volume of the 1 Gyr old Universe from 50,000 galaxy spectra in 60 nights of GTC/SIDE observations.

• To measure the star-formation-density relation, correlation function, and early evolutionary trends from 800 to 1300 Myr after the Big Bang.

• To relate the results to the later evolution observed in lower-redshift surveys and to compare them with the Millennium simulation of various "wet galaxy physics".

Critical issues:

• It is not clear how to transform Lα luminosity into SFRs, and by when we will be able to observe [OII] (K-band) or Hα or FIR.

• It is not clear how to get stellar masses via NIR photometry for these objects (continuum detections would be very beneficial).

• Imaging observations should be finished before spectroscopy commences so the full range of redshift is covered in one go.

• We can start with the pilot project and enlarge to the full project of five footprints (or seven, geometrically optimal) after first results.

2.4.4.2 Galaxies at intermediate redshift: Stellar Populations and the kinematic properties of galaxies

Until now, there is not too much information about the stellar populations and kinematics properties of galaxies in the intermediate redshift interval ($0.7<z<2$). The main reason is related with the lack of suit instrumentation to work in the Z and J and H bands. In this decade, we have advanced significantly to the study of the galaxies at $z > 2.5$, discovered through the Lyman break technique, and as well as in faint galaxies ($R < 24$) at $z < 0.7$. But the stellar populations and kinematics properties of the galaxies at intermediate redshift need to be determined to know how the galaxies assemble and evolve to end at $z=0$, and to investigate the history of galaxy mass assembly and star formation. The chemical evolution of these galaxies is also relevant. So, the determination of the metallicity is needed.

Many samples of high-redshift galaxies ($z>1$) are selected at optical wavelengths, as a result we select only those galaxies that are bright in the rest-frame UV. So, LBG that are starbursts and they show a strong UV continuum are easily detected at the optical. But galaxies with a post-starburst population (100Myr -1Gyr) are relatively weak at the UV, and the stellar populations can be only characterized observing the optical rest frame. In fact, most of our understanding about the stellar populations properties of galaxies comes from the analysis of the spectra range 3500-7000 A that is quite rich in hydrogen, helium, and metallic lines. But this spectral range is observed in the Z, J and H bands in galaxies at $z=1.5$. On the other hand, Spitzer surveys have found that most of the IR selected galaxies are VLIRs ($\log L_{ir}$

=11-12 L_{sun}). These galaxies made a significant contribution to the galaxy population in the intermediate redshift interval (Le Floch et al. 2005; Pérez-González et al. 2005). We expect that these galaxies will be similar to the local VLIRGs and ULIRGs. So, they are probably merger systems with starburst and/or post-starburst signatures that are in the process of converting spirals in elliptical galaxies. Because they are too red systems, due to the extinction, they can only be distinguished from galaxies with an intrinsic red population (older than several Gyr) by fitting the stellar population absorption features (see Figure 15). Post-starbursts populations show deep Balmer absorption and weak metallic lines (González Delgado et al. 2004).

Complete surveys including blue and red galaxies at intermediate redshift need to be done, to find out which is the fraction of red evolved galaxies with respect to (dusty) (post-) starburst galaxies. The stellar populations kinematics properties have to be obtained. The specific objectives and SIDE opportunity window are explained here.

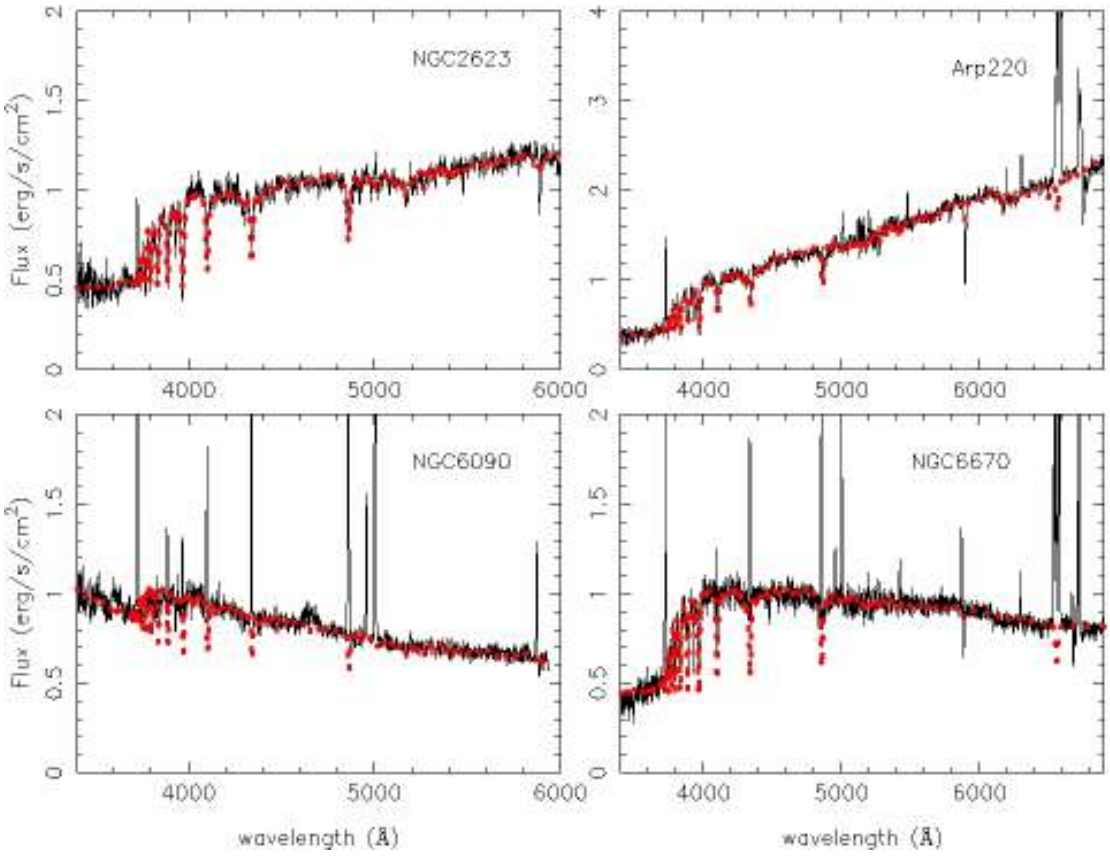

Figure 15 Several examples of nearby VLIRGs and ULIRGs. The best models fits are plotted in red. (Plot taken from González Delgado 2007).

a) MOS observing mode: Stellar population properties of galaxies at intermediate redshift

The only way to break the age-extinction degeneracy in red galaxies is doing spectral synthesis at the rest-frame optical range (see Figure 15). Photometry is not enough to distinguish between red evolved galaxies and (dusty) (post-) starburst galaxies. The age and the extinction of the stellar population can be determined, and then an estimation of the luminosity mass can be obtained. Age determination for galaxies at intermediate and high redshift provides an accurate clock for galaxy formation at early times.

Specific Objectives

- Stellar population properties: To determine the age, extinction, and mass through the spectral synthesis of the optical continuum, Balmer break, and absorption stellar lines. In particular, the high order Balmer lines (HOBL) are expected to be in absorption in most of the VLIRGs and ULIRGs systems, and they are a very good age indicator for post-starbursts.
- The ionized gas physical conditions and properties of galaxies with emission lines. To determine:
    - Extinction of the ionized gas through Hα/Hβ ratio
    - The SFR from Hα
    - Metallicity of the ionized gas
    - Emission lines ratios such as [OIII]/Hβ, [NII]/Hα , [SII]/Hα, [OI]/Hα, and [OII]/[OIII]. They are relevant to distinguish between star formation galaxies and AGN.
    - The gas velocity dispersion through the FWHM of (Hα). Then, an estimation of the dynamical masses of these galaxies is possible.

b) Mini-IFU observing mode: Kinematics of galaxies at intermediate redshift
Specific Objectives

- Kinematics of the ionized gas Hα and [OIII].
- Determination of the dynamical mass of these galaxies.
- To built the Tully-Fisher relationship.
- To find out and study outflows of the ionized gas

2.4.4.3 Nuclear Activity and its role on the evolution of galaxies: Evolutionary link between ULIRGs, Radio Galaxies, QSOs and elliptical galaxies

Today there is increasing evidence that the evolution of massive galaxies is linked to their nuclear activity. This evidence is supported by: 1) the similarities between the evolution of the QSO luminosity density and the star formation rate (Boyle & Terlevich 1998); 2) the tight correlation between the black hole (BH) mass and the bulge stellar velocity dispersion (Ferrarese & Merrit 2000). These results imply that the creation and evolution of a BH (presumably associated to a QSO) is intimately connected to that of the galaxy bulge. Furthermore, they also suggest a Starburst-AGN connection due to the co-existence in a

galaxy of circumnuclear starbursts and QSO activity. In the context of the hierarchical galaxy evolution models these results can be explained in terms of accretion: as galaxies merge together to form large units, gas is driven into the nuclear regions and triggers both star formation and AGN activity.

However, some additional ingredients that has to be considered in the formation and evolution of galaxies, in particular if we want to understand the "downsizing effect". In fact, the feedback processes and outflows from the starbursts and the AGNs can play a strong effect in the evolution of galaxies. Outflows can drive hot ionized gas out the central regions of the galaxies and effectively quench star formation. If so, outflows can be the key ingredient in the hierarchical models to explain why the most massive galaxies seem to be formed at high-redshift and they have the oldest stellar population.

Strong evidence has been found connecting nuclear activity and mergers in VLIRGs-ULIRGs. It is found that ULIRGs are mergers in the later stages (Veilleux et al. 1999). Kinematics observations of ULIRG mergers have proved that they are ellipticals in formation (Genzel et al. 2001). In fact, mergers can drive an evolutionary sequence from cool ULIRGs to warm ULIRGs in their way to becoming quasars. Thus, mergers go first through a starburst phase, followed by a dust enshrouded Seyfert phase, then the dust is cleaned by the AGN and starburst wind actions, and finally ULIRGs are shown as QSOs (Sanders et al. 1988).

Evidences of circumnuclear starbursts have been also found in surveys of QSO host galaxies. They have revealed that the host galaxy colors are significantly bluer than those of elliptical galaxies. These colors are consistent with an intermediate age population, that was probably associated to a starburst triggered 1 Gyr ago. These QSOs shows merger/interaction features in their hosts.

Specific Objectives

The goals are to study the stellar populations and properties of the ionized gas in different VLIRGs, ULIRGs and QSOs samples. Specific objectives are:

- The spatial distribution of the properties of the host stellar populations. The high-order Balmer lines, the CaII H and K, G band, Mgb and the Balmer break, together with evolutionary synthesis models (González Delgado et al. 2004) and spectral synthesis techniques will be used to determine the stellar properties (age, mass, luminosities, extinction) of the QSO hosts. These properties will be compared with those of ULIRGs. In particular, ages can be used as a clock to set the possible evolution between ULIRGs, post-Starburst QSOs and elliptical galaxies.
- The spatial distribution of the extended ionized gas. 3D spectroscopy is an essential tool to resolve spatially and spectrally the broad and the narrow line emission regions. A 3D decoupling procedure is used to isolate the host and the nuclear spectra, and to map the extended ionized gas by means of the most important emission lines, such as Hα, Hβ, [NII], [OIII], [OII], [OI] and [SII]. The morphology of these regions together with the emission line ratios will be used to distinguish between gas photo-ionized by the AGN or by young stellar components. Kinematics of the extended ionized gas can put constrains the properties of feedback processes (e.g. outflows) in these objects.

2.4.4.4 The role of the environment in the evolution of galaxies: Deep Multi-Object Spectroscopy of cluster galaxies

The study of galaxy evolution in different environments is a necessary step in order to understand the role played by the environment along the cosmic history. In particular, the investigation of the role star formation history has played in the evolution of galaxies in dense environments make necessary for us to observe a representative sample of cluster galaxies in the nearby universe. It has been claimed that cluster of galaxies are "dead" environments in the sense that no star formation related activity is to be expected in them. Recent results however point towards a different scenario in which star formation is a key ingredient in order to understand the formation history of these structures. In addition, appropriate spatial sampling of dense structures, clusters and super-clusters, within a wide, spectroscopically driven, study can provide precious information on open questions such as the effect of cosmic variance in current galaxy formation scenarios in the dense parts of the universe. On the other hand, phenomenological environmental effects among galaxies --such as tidal interactions, tidal stripping, strangulation, among others--, or from the interaction of galaxies with the intra-cluster medium, can produce big changes on the observable properties of galaxies, producing serious implications for their evolution. At this point, a novel approach proposed in this project is the extensive study of samples of dwarf galaxies in dense environments, given their relevance on current scenarios of galaxy formation in different environments and epochs. Future developments in the field include increasing the spatial sampling, observing larger areas of the clusters, reaching well beyond the Virial radius, and increasing the sensitivity with an extension to the lower luminosity galaxies (dwarfs), making use of 2D spectroscopy with large telescopes.

2.4.4.5 The chemical evolution of galaxies: Chemical evolution in 3D. Metallicity gradients in spiral galaxies

The derivation of accurate metallicity gradients in galaxies constitutes the basic input for the study of the chemical evolution of galaxies. Traditionally, abundance gradients of galaxies have been derived for their stellar population and also for their interstellar medium, neutral and ionized. The derivation of the chemical composition of the stars of a galaxy is particularly difficult, even for 10m class telescopes, when individual stars outside of the Galaxy or the Magellanic Clouds are studied; though some notable observational efforts have been carried out recently to study bright stars in nearby spiral galaxies --such as M33, M31 or NGC 300, among others— leading to precious constraints for their abundance gradients. For the vast majority of the observable galaxies, the stellar metallicity information usually comes from integrated spectroscopic observations; these are frequently translated into metallicity with the help of evolutionary synthesis models, among other tools.

The abundance of the elements in the gaseous phase of a galaxy represents their present day abundances. In this respect, HII regions provide the most useful abundance indicator, since they can be easily observed going from nearby objects up to the very distant galaxies, thanks to their rich emission line spectrum. Up to date, one-dimensional (1D) radial abundance gradients across the disks of spiral galaxies have been derived using spectroscopy of individual HII regions located at different galactocentric radii. However, thanks to the increased 2D capabilities of modern spectroscopic instrumentation, a sufficient 2D sampling and coverage of the galaxy disks could be achieved. This aspect can represent, de facto, a major step forward in this research field, mainly in order to provide theoretical models with

the necessary constraints, since their predictions, at this stage, appear beyond presently available observations.

Another very important aspect of chemical abundances research is the derivation of the most accurate chemical abundances, making use of direct derivations of the electron temperature from collisionally-excited lines, and of the precise measurements of the very faint fluxes expected for the metallic recombination lines. These data from the optical to NIR range are most needed in order to complement to and compare with the abundance derivation for extragalactic HII regions using mid-infrared lines; these derivations appear reduced to a handful of nearby galaxies.

An aspect frequently overlooked is the loss of spatial resolution for distant galaxies. This fact implies that their spectra are integrating all the emission produced in the disk and nucleus. In this respect, the 2D spatially resolved observations proposed in this project can provide useful data to empirically constrain the modeling of integrated spectra and derive appropriate metallicity values for most distant galaxies.

At present, there is no firm derivation of the actual slope of the radial abundance gradient in the inner region (say radius<4Kpc) of a spiral galaxy (including the Milky Way!). Even more difficult to explore, with the data presently available, are hypothesis such as possible changes in azimuth of the slope of the abundance gradient, or the existence of abundance anisotropies in the disks near their central regions, as a possible consequence of gas flows.

Recent hydro-D models of disk galaxies provide new constraints on their formation mechanisms and secular evolution. Most notably, recent models results predict the formation of 2D, or even 3D, galactic disk structures, associated to possible mass flows in/to/from the disks. These are an example of most recent model predictions for galaxy evolution, which appear of extraordinary relevance for chemical evolution studies. We are in a position to produce this step forward in the study of the chemical evolution of the interstellar medium of galaxies "in 3D", in the next years.

2.4.5 Input photometric catalogue

2.4.5.1 High redshift galaxies

The Japanese HyperSuprimeCam (HSC) is now funded for Subaru and contacts with the WFMOS team aim for beneficial synergy. If WFMOS were delayed there would be an opportunity for SIDE to take the place. Collaboration with Japanese groups would be highly desirable to access HCS data, especially if we can offer a powerful spectroscopic capability. HSC is projected to have a circular field of view with 2 deg diameter and 0.2" pixels. The sensitivity plateau covers 700-1000 nm but good performance is expected from 600 to 1100 nm. It is anticipated that narrow-band filters will be available to satisfy the needs of high-z galaxy science. It is an 18 million US-$ project. First light is anticipated for 2011.

2.4.5.2 Intermediate redshift galaxies

One possible catalogue for this project is the ALHAMBRA survey (Moles et al. 2005). This survey is done by the Spanish community using the guarantee time at the 3.5m telescope of

CAHA observatory. The survey is done with LAICA and a set of 20 adjacent medium-band filters that cover the visible range. These filters, together with three standard near-infrared ones and the OMEGA-2000 (NIR) cameras, allow for a detailed measurement of the spectral energy distribution and redshift of 6.6x10^5$ galaxies with I <25 (60% completeness level), and z_{med} = 0.7 (see Figure 16). The survey covers eight separate regions of the sky, with a total area of 4 square degrees. More than 50000 galaxies are expected to detect in the redshift range 0.7-1.4 and I_{AB} < 24 .

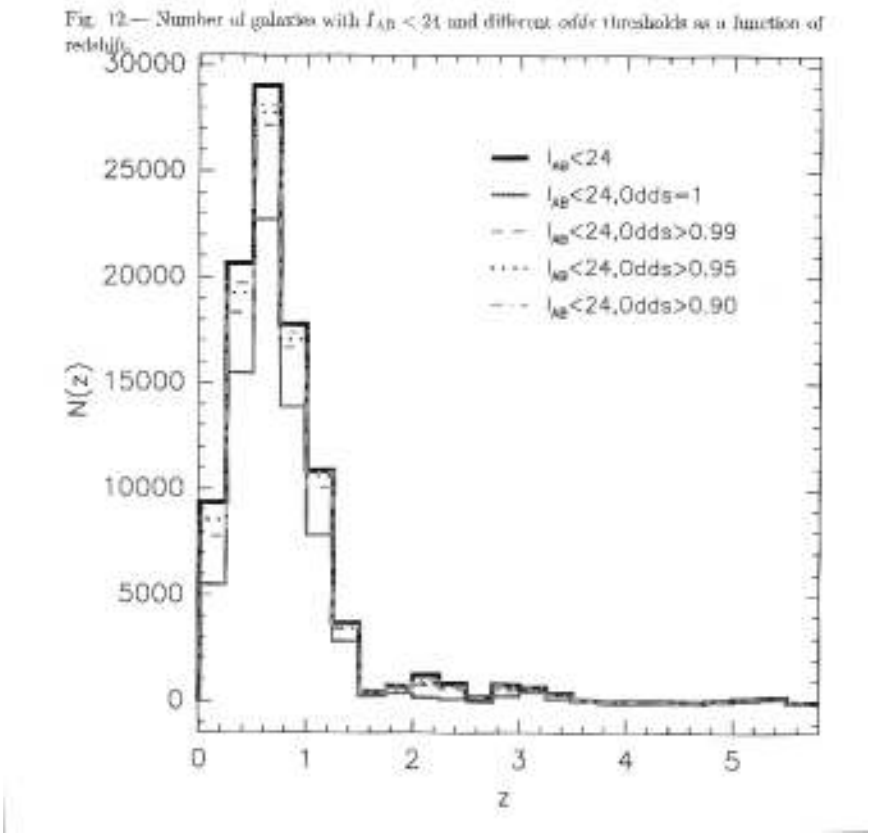

Figure 16 This plot is provided by the ALHAMBRA core team.

2.4.5.3 AGNs and Starbursts samples

Brotherton el al. (1999) have identified a class of QSOs and its spectrum is a chimera because it displays the broad MgII 2800 Å emission line and a strong continuum characteristic of classical QSOs, but their optical continuum display a large Balmer break, prominent high-order Balmer absorption lines, and CaII K and H lines. They called it a post-Starburst QSO because its stellar component is consistent with a 400 Myr old population. The bolometric luminosity of the post-starburst and the QSO is consistent to have been a ULIRG a few 100 Myr ago. HST images reveal that the QSO host resembles a merger remnant. Thus, this object could be in a transition phase between ULIRGs and classical QSOs. The SDSS survey has revealed a significant number of Post-starburst QSOs. These objects could be in a transition phase between ULIRGs and classical QSOs. These SDSS QSOs have redshift between 0.25 and 0.8.

Sample of VLIRGs and ULIRGs at redshift z=0.25-0.8 will be selected from the FIRST catalogue (Stanford et al. 2000)

2.4.5.4 Cluster galaxiey sample

It has been produced a complete sample of nearby (z<0.25) northern hemisphere clusters of galaxies that we have already observed with photometry (narrow and broad band) (Vílchez et al in preparation). In order to derive their population of galaxies presenting signatures of recent star formation a survey has been undertaken on these clusters database and a starburst and post-starburst target list is being produced. Typically, over 300-500 target objects per cluster field (typically 0.25x0.25 deg^2) are measured and catalogued, with a sensitivity equivalent to detecting a (post-)starburst galaxy with 3 - 5 A equivalent width.

An example of source detection & target production (see Figure 17) showing the sample of objects selected for the cluster Abell 779, using their measured Hα equivalent width as a selection constraint of the targets

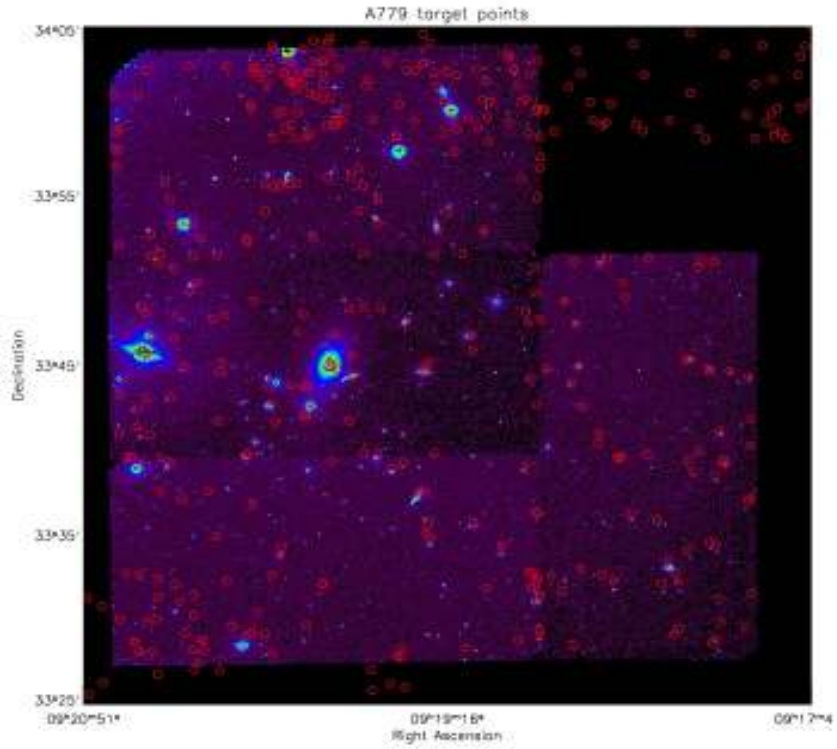

Figure 17 Sample of objects selected for the cluster Abell 779.

2.4.5.5 The chemical evolution of galaxies

This project proposes the derivation of all the necessary information on chemical abundances across the whole face of the galaxies disks, in 3D. We propose making use of the powerful multiplexing spectroscopy capabilities that will be provided by SIDE in order to derive chemical abundance gradients for our sample of galaxies, including different types, for which extensive samples of HII regions and Planetary Nebulae are already defined in 2D. Sample

targets vary depending on the galaxy considered in each case. However, typical target density for our nearby spirals can be estimated from the available imaging of HII regions, giving rise to figures of the order 1000-2000 objects per disk (i.e. over equivalent radii of some 0.3 deg). For more distant galaxies, the size of the fibers plays an important role; nonetheless, for the purposes of this project both, MOS and IFUs (m or S) spectroscopy are equally valid to reach our goals, depending on the acquired Signal to Noise ratio. Again, object morphology will be the guiding property in order to select a given observing mode.

2.4.6 Target density

2.4.6.1 High-redshift galaxies

Previous Subaru SuprimeCam work, typically on 800 sq. arcmin fields yielded plenty of 2003-2006 papers on the properties of the high-z LAE and LBG population. In summary, Table 4 shows the numbers of LAEs per sq. arcmin per unit redshift (with NB filters magnitude limits as below, dominated by line emission).

z=4.8	0.6 at i(710/10) < 25.7 AB mag
z=5.7	1.0 at i(815/12) < 26.0 AB mag
z=6.5	0.55 at z(920/13) < 26.0 AB mag

Table 4 Numbers of LAEs per square arcmin per unit redshift.

The spectroscopy of such objects allows confirmation of the Lα line if ~8000 sec are spent on Keck/DEIMOS or 15000 sec on Subaru/FOCAS. We foresee that with the high throughput planned at 700-900 nm, a 6000 sec exposure on SIDE (max. 1/3 night including all overhead) would secure redshifts for these objects.

Five atmospheric (semi-) windows are available for best performance (see Table 5), and with a single pointing 2 deg round field we get (H_0=70 km/s/Mpc, Ω_m=0.3, Ω_λ =0.7)

lambda / width (nm)	z range	z range	r.side.comoving	volume geometry
696/23	z=[4.6,4.8]	~135 Mpc/deg	~550 Mpc/z	round 270 x 110 Mpc deep
752/20	z=[5.1,5.27]	~137 Mpc/deg	~505 Mpc/z	round 275 x 85 Mpc deep
816/24	z=[5.6,5.8]	~142 Mpc/deg	~450 Mpc/z	round 280 x 90 Mpc deep
856/14	z=[6.0,6.1]	~143 Mpc/deg	~420 Mpc/z	round 285 x 42 Mpc deep
914/27	z=[6.4,6.62]	~145 Mpc/deg	~380 Mpc/z	round 290 x 80 Mpc deep

Table 5: Available windows and parameters for each.

If we are prepared for third-night shots with 1 candidate per sq. arcmin across 680-930 nm, and SIDE has a round 20' FOV, then we need to do 36 tiles with SIDE = 12 clear nights. We'd get ~300 objects per shot with over-densities up to 500, maybe? This could be combined with foreground objects if the density is too small. A better alternative would be to combine it with LBGs from a less constrained but similar redshift range, thus more than doubling the object density. The resulting total dataset after subtracting interlopers would be:

z=4.8: ~1400 objects
z=5.2: ~1500 objects
z=5.7: ~2300 objects
z=6.1: ~ 800 objects
z=6.5: ~1400 objects

plus possible LBGs of which only 30-40% would fall within the redshift limits of the atmospheric windows, but which would enrich the dataset. A problem is how we get their redshifts reliably if they don't have Lα emission. This remains to be understood. We could think big and do five HSC circular footprints in a 2x2 pattern plus filling the middle with a further pointing and a bit of overlap, getting almost a box with 4 x 4 deg, or roughly 15 sq. deg. total area and >40,000 objects in five volumes of 500 x 500 Mpc^2 and various depths as above (see Figure 18 for a z=5.2 cosmology simulation). This would cost five Subaru footprints with narrow-bands and 60 clear nights at SIDE.

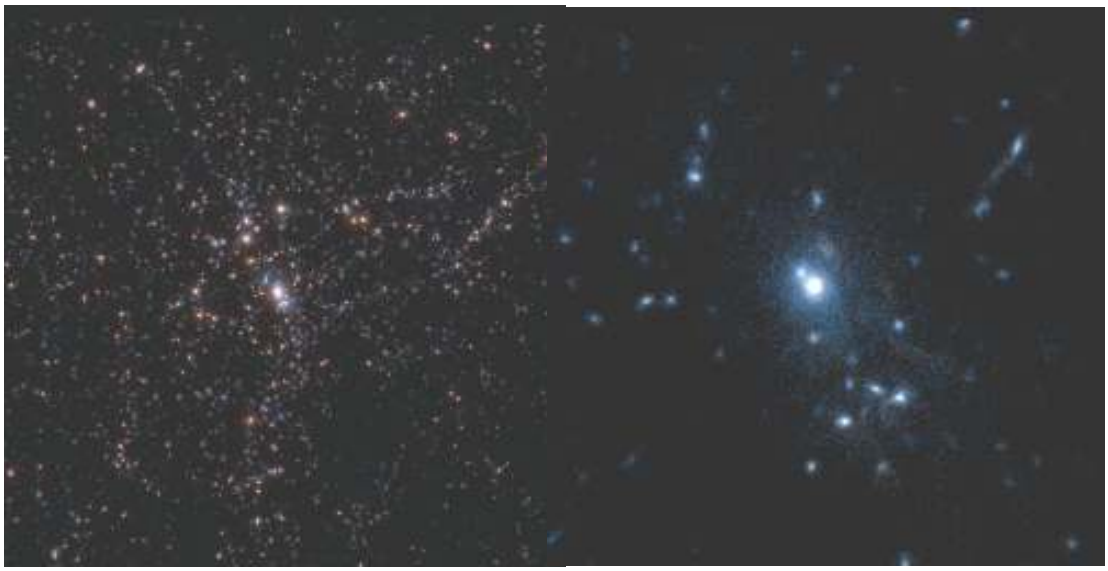

Figure 18. An example of how the galaxies look like in a Lambda Cold Dark Matter universe at z=5.2. Left panel: full sky mock image of 5 Mpc comoving size. Right panel: a mock CCD image of 1000x1000 pixels (500 kpc comoving in a side) of a massive galaxy has been obtained from a combination of U, B and V rest frame filter images of the spectral energy distribution emitted by stars generated in The MareNostrum Galaxy formation simulation (http://astro.ft.uam.es/marenostrum). This simulation is currently the largest numerical simulation of galaxy formation done so far with more than 2 billion computational elements representing the different fluids of the Universe (dark matter, gas and stars). The computational box of this simulation corresponds to 50 /h comoving Mpc. The image shows a small area of 5 Mpc across around the brightest object in the simulation. The amount of substructure in the galaxy distribution is quite remarkable. These kind of simulations are, despite their technical difficulties, the most useful tools to predict the distribution and abundance of Lyα emitters at different redshifts. We plan to use this simulations and other as a basic tool to construct mock catalogs to design the best observational strategies for SIDE spectroscopic follow-up operations.

2.4.6.2 Intermediate-redshift galaxies

Using COMBO 17 (Wolf et al. 2003) colors and photometric redshift data, we estimate the density of galaxies with J < 21 mag (corresponding to R-band) in the redshift interval $0.8<z<1.3$ is about 1.23 galaxies/arcmin^2. So, in the SIDE FOV about 400 galaxies will be. So, a minimum of the several hundred fibers is required for this project.

2.4.7 Spectral resolution and wavelength coverage

Most of the projects on Galaxy Evolution require the determination of the properties of the stellar population, and the ionized gas. This means that we need a large spectral coverage, at least the rest-frame optical wavelengths for galaxies at intermediate redshift. Rest-frame UV range is also very useful to constrain the properties of galaxies at high-redshift.

- Lα is the strongest emission line to be detected in the spectra of high-redshift galaxies. This line can be observed at optical wavelengths in galaxies up redshift $z<8$. Higher redshift ($z=14$) galaxies can be observed in the J and H bands.
- The determination of the stellar population properties of galaxies at intermediate redshift requires the observations of the Balmer break, the Balmer lines, and metallic lines (such as CaII K and H, G band and Mgb). To derive the ionized gas properties and metallicities of galaxies needs the observations of the collisional emission lines, such as [OII]3727, [OIII]5007, [NII]6584,6548, and the Balmer lines. Ha and Hb lines are required to estimate the extinction of the ionized gas. And the optical continuum from 3600 to 7000 Å to constrain the age and the extinction. Thus, for galaxies at intermediate redshift ($z=0.8$-1.5), the optical range 3600—7000 Å will be observed in 6500 Å —1.7 μm.

The studies of the stellar populations properties in galaxies require of 1000, but due to the sky line contribution at the Z and NIR bands, an intermediate resolution of R=4000 is needed.

2.4.8 Optimum observing strategy and procedure

All the observing modes of SIDE (MOS, IFU and mini-IFU) are applicable for the projects presented in this chapter. The setup observational constrains will be specified for each project. The possibility to observe simultaneously at optical and NIR (J, H) is probably the most unique capability of SIDE for these projects, since it will allow us to get the rest-frame optical spectra of galaxies at intermediate redshift.

2.4.9 Further considerations about SIDE opportunity window for galaxy surveys

SIDE is an excellent instrument for spectroscopy of galaxies at redshift ~1, since the peak S/N is achieved in the I-band. This corresponds to the region around 400 nm in restframe, which is the most important region for stellar age analysis and provides measures of D_{4000} and the Hδ line index. Certainly, the other Balmer lines are required to measure Balmer decrements to constrain dust extinction, and indeed SIDE can access the whole spectrum for full spectral fitting to reconstruct stellar age distributions for any individual galaxy.

S/N=5/pixel in SIDE means S/N=(5, 2.6)/Å in (I, J)-band at R~1500, and (8.5, 4.5) at R~4000, respectively. The last half-magnitude bin in the SDSS spectroscopic dataset has

S/N~5/pixel (>3/pixel) in g-band, and ~15/pixel (>10/pixel) in r- and i-bands. The SDSS resolution is 69.03 km/sec/pixel, so for a survey at z~1 the SDSS limits translate into S/N>(2, 6, 6)/Å in (I, J, H). This limit is achieved after one hour in the R~4000 setting for a galaxy of I=23 and J=19.8, but at no redshift <5 there are such red galaxies. Hence, it makes sense to require a higher S/N detection in restframe B/g-band, i.e. observed-frame I-band, and relax the requirements for J and H. Below, we ask for a limit of S/N=5/Å in the observed-frame I-band to obtain spectra of SDSS-type quality.

Table 6 shows the possibilities for surveys targeting redshift 1 (or nearby):

Category	S/N/Å I-band	Setup / shots	Range [λ] and [z] with OII-Hα	M_{lim} for 1h exposure	M_{lim} in 1n= 8h exposure
Pure fast redshift determination	1.5	R~1500 1 shot	0.53-1.7 μ z=[0.44,1.55]	I=23.3 J=20.7	I=24.4 J=21.8
SDSS quality S/N, narrow z range	5	R~4000 2 shots	0.62-1.37 μ z=[0.68,1.07]	I=22.0 J=19.4	I=23.1 J=20.5
SDSS quality S/N, wide z range	5	R~4000 3 shots	0.51-1.37 μ ∔ 1.44-1.70 μ z=[0.42,1.07] + z=[1.25,1.63]		
Ideal stellar population analysis	25	R~4000 2 shots	0.62-1.37 μ z=[0.68,1.07]	I=20.3 J=17.7	I=21.4 J=18.8
Ideal stellar population analysis, wide z range	25	R~4000 3 shots	0.51-1.37 μ ∔ 1.44-1.70 μ z=[0.42,1.07] + z=[1.25,1.63]		

Table 6 Possibilities for surveys targeting z = 1.

In all above setups at least one spectral line will appear at any redshift out to 2.6. In each of the above categories a couple of alternative surveys are possible trading off area vs. depth. The primary aim is to go to redshift 1, but we have to include wider ranges to keep the fibers busy when we don't go deep enough.

We assume that we keep 800 fibers on objects in any pointing and the other 200 on sky. We assume a survey with 75 clear nights, and 8 hours of full exposure time per night. We start from the COMBO-17 redshift and aperture magnitude distribution to determine the redshift and luminosity ranges. We use the COMBO-17 three-field catalogue, which is enhanced by the A901 cluster (but corrected by taking an effective area of 0.84 sq.deg. = 10 SIDE

footprints, instead of true 0.78 sq.deg.). 12 SIDE footprints cover 1 sq. degree, so SIDE is ideal for objects with surface density of >9500/sq.deg. (below L* is for z=1). Table 7 shows a possible list of surveys proposed with SIDE.

Survey code	S/N/Å I-band	Objects in 75 n	Area sq.°	Fraction of obj's to I_{lim}	% gal z>0.8	Range [z] complete	Complete to M_{abs} / tail to
Z1-wide	1.5	480,000	50	15% to 23.3	40%	0.93-1.07	L*+1 /+2
Z1-deep	1.5	60,000	0.3	5% to 24.4	? %	Complete	-
S2-w	5	80,000	8.5	26% to 22.6	25%	0.71-1.07	L*+0.5 /+2
S2-d	5	22,000	2.3	15% to 23.3	40%	0.93-1.07	L*+1.2 /+2
Pop2-w	25	13,000	1.4	44% to 21.9		Inefficient	
Pop2-d	25	4,300	0.5	28% to 22.5	25%	0.68-1.07	L*+0.5 /+2
Pop3-w	25	8,700	1.0	44% to 21.9	17%	0.42-1.07	L* /+3?

Table 7 Possible SIDE survey list.

The survey with the largest volume is **Z1-wide**, which is probably not competitive by 2015 for a BAO measurement due to a similar FMOS survey (FAST-SOUND) having finished by then. The scientific use is unclear, if only redshifts can be obtained, although the galaxy numbers sound impressive right now.

The **Z1-deep** survey to I=24.4 (I_{AB}<24.9) would be similarly deep as the new VVDS-ultra-deep project that aims to obtain 900 VLT spectra to I_{AB}<24.75 from 0.55 to 0.95 μ. But with 60,000 spectra it would be 60x larger and as large as the entire VVDS today. These data would have legacy value as the deepest large statistical galaxy sample for some time, and would be perfect for very deep photo-z calibration as well as providing redshift distributions for gravitational lensing statistics and spectroscopic properties of faint galaxies. It would be very powerful to conduct this survey on a field where ultra-deep multi-wavelength data exist already.

The **S2-w** survey to I=22.6 would be complete to L*+0.5 for 80,000 galaxies in a shell around z~0.9 with depth Δz~0.36 (co-moving volume of 0.02 Gpc^3 for h=0.7). The data quality would be SDSS-like, but the sample size only 10% of it. If this survey is desired to be larger, ¼ million galaxies could be observed with 225 clear nights over 25 sq. deg., just larger than 2dF, but less deep in luminosity. Version **S2-d** might be preferred due to greater and more even depth, completeness to L*+1.2 despite the smaller volume.

The **Pop2-w** survey is too shallow to be targeting a selected redshift range, and only **Pop3-w** would make sense but cut the sample size by a third.

The **Pop2-d** survey to I=22.5 would deliver superb S/N for composite stellar population analysis of individual galaxies. The ideal sample was mentioned to be 10,000 galaxies near z~1 with superb quality of calibration (Panter) and is preferred over a million galaxies with meagre data. However, 10,000 galaxies would require 175 clear nights.

Nested or combined surveys can help to achieve several goals with less observing time. In Table 8 we explore to what extent the **S2-d** survey contains **Pop2**-type high-S/N data on brighter objects already and compare it to the other survey samples:

Survey code	S/N/Å I-band	Objects in 75 n	Area sq.°	I_{lim}	Range [z] complete	Complete to M_{abs} / tail to
S2-w	5	80,000	8.5	22.6	0.71-1.07	L*+0.5 /+2
S2-d	5	22,000	2.3	23.3	0.93-1.07	L*+1.2 /+2
S2-d/Pop2	(25)	900	2.3	21.6	0.93-1.07	L* -0.5 /+0.3
Pop2-d	25	4,300	0.5	22.5	0.68-1.07	L*+0.5 /+2

Table 8 Comparison between different surveys on bright objects.

The brightest 4% of the galaxies in S2-d would have Pop2-type high-S/N data, but only for galaxies brighter than L*. Adding a deeper nested Pop2-d survey could reach out to fainter luminosities. Surveys could always be nested with some limited savings.

The LBL robot positioner allows for small adjustments of object positions across the field between exposures to track the effect of differential refraction at the mean wavelength of observation, which is a subtle stretching of the image scale in the focal plane along the parallactic angle. Hence, the only critical problem caused by the absence of an ADC in SIDE is the spread of the object's spectrum in the focal plane, which exceeds the fiber size when wide spectral ranges are combined with large zenith distances (d_{zen}). Survey fields can always be selected to culminate near zenith over La Palma. However, we prefer to obtain spectroscopy in fields, where now or in a few years time plenty of deep imaging data exist for a wide wavelength range, such as from CFHT-LS, UKIDSS or VISTA.

In a 2-shot setup of the R~4000 mode we choose to observe 0.62-0.76 μ with 0.95-1.20 μ simultaneously at low airmass (d_{zen} < 35 deg) and 0.75-0.95 μ with 1.10-1.37 μ at larger airmass (d_{zen} < 50 deg). These d_{zen} ranges ensure that the light entering the fiber does not originate from too different parts of the galaxy as required for stellar population analysis. In the Z1-deep survey we only wish to measure redshifts and tolerate small losses of S/N so that d_{zen} < 35 deg is no problem for the entire range of 0.51-1.7 μ (for details see Fig. 45). This suggest several attractive survey options:

Attractive option 1: **Z1-deep:** A nice choice would be the COSMOS field (10h, +2 deg) that is visible for about 6 hours per night at $d_{zen} < 50$ deg and for 3 hours at $d_{zen} < 34$ deg. There are deep Subaru, HST and further multi-wavelength data available. Other options include the XMM/LSS-Subaru-UKIDSS-Ultra-deep survey field at (2h, -4 deg).

Attractive option 2: **S2-w** or **S2-d:** Use CFHT-LS W4 field (also in UKIDSS DXS and a VVDS field) at (22h 18m, +1 deg) that will have 8.75 sq.deg. of ugrizJK data to r=25.9, z=24.8 and J=22.5 (5σ point source limits).

Attractive option 3: A small-area **Pop2** survey should be done in the COSMOS field to capitalize on the combination of HST-quality morphologies with excellent SIDE spectra and further multi-wavelength data (X-ray to FIR). The redshift range also contains a few already known clusters in the COSMOS data set.

Table 9 shows possible surveys with comments:

Survey code	S/N/Å I-band	Objects in 75 n	Area sq.°	Range [z] complete	S/N/Å J-band	Comments
Z1-wide	1.5	480,000	50	0.93-1.07	0.5-0.9	Contains 5 BO cells + 5 Coma clusters. Purpose?
Z1-deep	1.5	60,000	0.3	Complete		60x VVDS-ultra-deep, photo-z calibration, n(z), do on COSMOS field?
S2-w	5	80,000	8.5	0.71-1.07	1.5 - 3	10% of SDSS @ z~0.9, complete to L*+0.5
S2-d	5	22,000	2.3	0.93-1.07		10% of 2dFGRS @ z=1, complete to L*+1.2, incl. 900 obj's at Pop2-d level
Pop2-d	25	4,300	0.5	0.68-1.07	7.5 - 15	Ideal data to reconstruct individual SF histories, do on COSMOS field?

Table 9 Commented summary of possible surveys.

2.4.10 References

Boyle, B.J. & Terlevich, R.J. 1998, MNRAS, 293, L49

Brotherton, M.S., van Breugel, W., Stanford, S.A., Smith, R.J., Boyle, B.J., Miller, L., Shanks, T., Croom, S.M., Filippenko, A.V. 1999, ApJ, 520, L87

Ferrarese, L. & Merritt, D. 2000, 539, L9

Genzel, R., Tacconi, L.J., Rigopoulou, D., Lutz, D., Tecza, M. 2001, ApJ, 563, 527

González Delgado, R.M. 2007, ASP Conf. Series, in press (eds. Knapen, Mahoney, Vazdekis)

González Delgado, R.M., Cid Fernandes, R., Pérez, E., Martins, L.P., Storchi-Bergmann, T., Schmitt, H., Heckman, T., Leitherer, C. 2004, ApJ, 605, 127

Le Floc'h, E., Papovich, C., Dole, H., et al. 2005, ApJ, 632, 169

Moles, M. et al. 2005, astro-ph//0504545

Pérez-González, P.G. et al. 2005, ApJ, 630, 82

Sanders, D.B., Soifer, B.T., Elias, J.H., Madore, B.F., Matthews, K., Neugebauer, G.; Scoville, N. Z. 1988, ApJ, 325, 74

Stanford, S. A., Stern, D. van Breugel, W., De Breuck, C. 2000, ApJS, 131, 185

Veilleux, S., Kim, D.-C., Sanders, D.B. 1999, ApJ, 522, 113

Wolf, C., Meisenheimer, K., Rix, H.-W., Borch, A., Dye, S., Kleinheinrich, M., 2003, A&A, 401, 73

2.5 Galactic Structure & the Local Group

2.5.1 Current status and open questions in the field

The remarkable gain in precision on astronomical observations on the ground and in space, supported by interpretative efforts and theoretical work has led us to crucial discoveries in the last decades. The galactic bar, the existence of the thick disk or the properties of the dark matter halo, are excellent examples on that. Looking at the future, several are the key astronomical questions: do large galaxies form from accumulation of many smaller systems which have already initiated star formation? Does star formation begin in a gravitational potential well in which much of the gas is already accumulated? Does the bulge pre-date, postdate, or is it contemporaneous with, the halo and inner disk? Is the thick disk a mix of the early disk and a later major merger? Is there a radial age gradient in the older stars? Is the history of star formation relatively smooth, or highly episodic? Is the SFH varying within the same galactic type, depending on the environmental conditions? Answers to such questions will come from an optimal combination of space (Gaia, SIM, JWST) and ground-based observations with 8-10m class telescopes. In the optical domain, future space mission (see Sect. 2.5.2) will provide unprecedented astrometric data for stars up to ~20 magnitude. The acquisition of the third component of the space velocity, the radial velocity, up to this limiting magnitude will be essential for future galactic kinematic and dynamical studies. As stated by Binney (2005) we can only claim to understand the structure of the Galaxy when we have a dynamical model galaxy that reproduce the data. Furthermore, kinematical data need to be combined with the measurement of individual element abundances to place a direct insight into the past accretion events that led to the formation of our galaxy. Multiwavelength data, mostly optical and infrared are needed to test the galaxy formation models in a qualitative manner.

The evolution of the interstellar medium (ISM) and the system of stars is fundamentally coupled through star formation, stellar evolution, and stellar death. A comprehensive examination of various phases of the ISM, their mutual interactions and couplings, and the mechanisms by which stars inject matter and energy back into the ISM is required to understand the chemical enrichment of the Universe, the evolution of galaxies and the formation of stars and planets. Objects within our own Galaxy and the Local Group provide the best opportunity to probe cosmic recycling. Studies targeting HII regions, stellar wind bubbles, SNR and supershells, have the goals of measure the composition of these regions and to characterize systematic variations with location within the Galaxy, to map the excitation and kinematic conditions of the various phases of the ISM and to characterize the stellar content of the star forming regions. The continuous increasing in sensitivity, angular resolution and spectral coverage of the observations are fundamental elements for our understanding the interactions between gas and stars.

There have been particularly exciting developments in the last decades to characterize the today's known galaxies in our Local Group, excellent laboratories in which individual objects can be studied in detail (see Van den Bergh, 2000). Among others, the discovery of the Sagittarius dwarf and the spheroidal companions of the Milky Way and Andromeda, the application of CCD detectors to study the stellar populations or the deep high-resolution observations with the Hubble Space Telescope. The study of the Local Group will help us to

see how galaxies evolve over timescales in excess of 10 billion years, with the older stars providing critical information on the physical conditions of the early Universe (see Sect. 2.5.3 for open questions in the field).

2.5.2 Future prospects

2.5.2.1 The next five years

Here is a list of the most relevant large key projects on galactic structure and LG. A more exhaustive compilation can be found in de Zeeuw (2005).

DART – Dwarf Abundances and Radial velocities Team - Large programme at ESO, to analyse the chemical and kinematic behaviour of individual stars in a representative sample of dSphs in the Local Group in order to derive their star formation and chemical enrichment histories (WFI imaging and intermediate resolution VLT/FLAMES spectra).

IPHAS + VPHAS - Photometric galactic plane Survey in Hα and ugri (Drew et al.., 2005) useful to trace both, the young population, for galactic spiral structure studies, and the old population, to characterize stellar streams. IPHAS has at present 100 million objects, ~50000 of them being Hα emitting. (Schedule: IPHAS first release 2007 ; VPHAS observations for 2007-2009).

RAVE – Spectroscopic survey to measure radial velocities and stellar atmosphere parameters of up to one million stars using the 6dF/1.2m telescope of the Anglo-Australian Observatory. The RAVE program started in 2003, obtaining medium-resolution spectra (median R = 7500) in the Ca-triplet region for stars in the range 9<I<12. 80% of the radial velocities have uncertainties better than 3.4 km/s.

SPITZER - Imaging and spectroscopy in the 3.6 to 160 micron range. Spitzer has some large Legacy projects devoted to the Galaxy, like GLIMPSE (a 240 sq. deg. survey of the inner galactic plane), MIPSGAL or Gouldsbelt.

EMIR GALEP Central Programme will obtain IR spectroscopy of many thousands galaxy sources to understand the structures in the inner galaxy. The IR spectra, R=4250-4000 at H&K respectively, will allow to classify a significant fraction of the stellar content of the galactic plane. An additional goal of this project is the measurement of radial velocities to 7-20 km/s accuracy.

2.5.2.2 Beyond the next five years

Gaia, ESA mission (2011-2016) - Astrometry, Photometry and Spectroscopy. From the astrometric instrument Gaia will obtain parallax and proper motions for 10^9 stars up to G=20. With a pixel size of 0.059 arcsec , the crowding limit is about 3 million stars per square degree (Baade's window). Detailed performances are quoted in de Bruijne (2005). As an example, a KIII GC'star with V=15 will have a 15 % error in distance at 10 kpc. This star, at a 6 kpc heliocentric distance on the galactic plane, with Av=5 and V=19 will have $\sigma_\pi \sim 90$ μas, $\sigma_\mu \sim 70$ μas/yr which translate to a tangential velocity error of about 8km/s.

Performances of the spectrograph for radial velocities derivation using the Ca II lines at 8400-8700A (R=10000-11500, TBD) are not yet fixed. At present, a RV accuracy ~ 10-20 km/s is expected for a KIII, V=16 star (Wilkinson et al., 2005). No spectrum is free from superposition of faint stars and overlaps between bright stars (V<17) in 20 % of cases at 10^3 star deg^{-2} are expected. The satellite launch is scheduled for late 2011with five years mission operation. A final catalogue release is expected for 2017 and preliminary releases are on discussion.

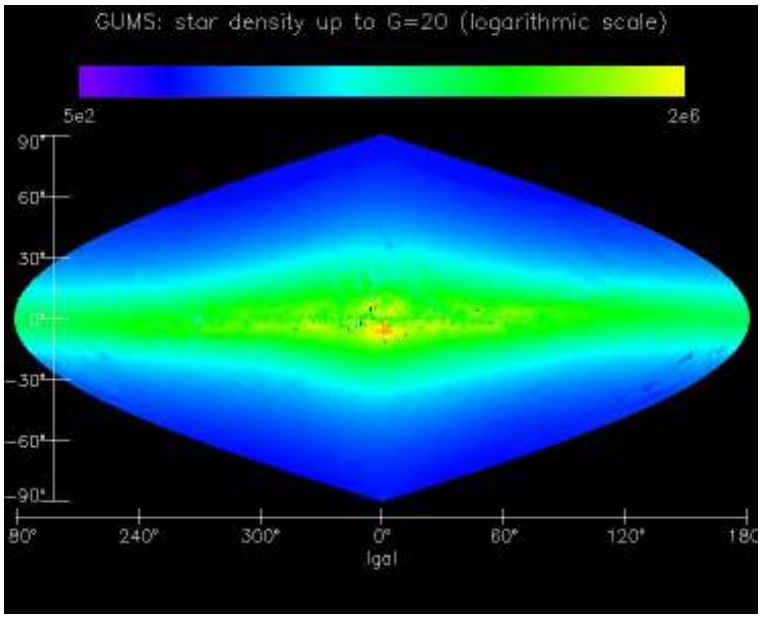

Figure 19: Star density up to G = 20 Gaia mag. as predicted by the Besançon Galaxy Model and the 3D extinction model of Drimmel et al. (2003) (V=G for (V-I)=0; V=G+1 for (V-I)=2.5)

JWST Space infrared observatory optimised for diffraction-limited performance in the near-IR (1 - 5 micron) region with extensions to the visible (0.6 - 1 micron) and mid-IR (5 - 28 micron). Its main scientific drivers are exploring the formation of stars and galaxies in the remote Universe at the earliest times and to study the formation of planetary systems and the origins of life, but as a observatory it can provide important information to decipher the history of our surroundings. A JWST "Design Reference Mission" contains up to 25 scientific programs. Among them we can find attempts to answer some relevant questions like the age of the oldest stars in our galaxy and the LG or the evolutionary and chemical history of our neighbourhood. JWST will help to learn how and when the central bulge and disc of the Milky Way form and to investigate if LG galaxies form in a similar way and at a similar time. JWST offers unique capabilities in imaging and obtaining IFU spectroscopy at 1.7 - 28 μm as well as MOS spectroscopy (up to some 100 objects in a 9x9 arcmin field at R about 1000). The launch of the JWST is forecast for 2013.

2.5.3 Science Case 1: The "missing dwarfs satellite problem"

2.5.3.1 Current status and open questions in the field

The Cold Dark Matter (CDM) cosmological model predicts that massive galaxies such as the Milky Way and Andromeda should be surrounded by large numbers of dark matter dominated satellite halos. At present, this prediction is in disagreement with observations, with a factor about 4 too few discovered dwarf galaxies over a significant range of masses. Distinguishing among the large range of cosmological and astrophysical solutions being proposed requires a huge space and on-ground observational effort. Current computational efforts of N-body simulations of a Milky Way-size galaxy (234 million particles) – see Diemand et al (2007) – push hard to be checked in the observational domain. See also Kravtsov et al. (2005) for a detailed discussion.

Open questions in the field are: 1) How many gravitationally bound dark matter dominated systems has the MW?, 2) Which are the properties of the tidally-disrupted systems? Are they at the faint end of the luminosity function? 3) Were the dwarf galaxies we observe today more massive objects that have been reduced to their present appearance by dramatic tidal stripping?, 4) Thus the properties of the subhalos in MW simulations match observations? 5) Which is the variety of masses, luminosities and mass-to-light ratios of known and undiscovered systems?, 6) Is there a floor on the masses of dSphs?, 7) Is the dark matter halo independent of luminosity? (velocity dispersion is needed) 8) How the velocity dispersion tensor varies with the galactocentric distance?, 9) Is there evidence for a difference in the mean velocity between eastern and western parts of the satellite galaxy?, 10) Is a coherent rotation present in some of them?,9) Which is the dynamical evolution of the merging processes?, Can dark matter Milky Way galactic potential be traced from stellar streams kinematics?. Answer to these questions and new insights on the missing satellite problem are proposed as a key goal of SIDE/GTC.

The massive measurement (MOS mode) of stellar velocity vectors, with a robust statistical treatment of the velocity dispersion profiles, and the derivation of chemical composition (mIFU at high spectral resolution) and evolutionary state of the stellar populations of these ultra-faint Milky Way satellites are, with no doubt, a task for the next decade and an excellent opportunity window for SIDE. Instruments as DEIMOS/KeckII (disadvantages: slit masks, only 50-100 stars per mask), FLAMES/VLT (DART project, south hemisphere) and MIKE/Magellan (6.5m telescope, 128 fibers/channel) are competitive here but SIDE, with a factor ~10 in targets per pointing and ~1 magnitude fainter, will substantially overcome them.

General requirements to achieve science goals are: 1) accurate kinematics (see 2.5.3.3), 2) high resolution spectroscopy (see 2.5.3.4), 3) high spatial resolution to avoid crowding and contamination problems, 4) powerful techniques/methods to discriminate members of the dSph from foreground stars. SIDE data shall be complemented with follow up proper motion studies.

2.5.3.2 Target dwarfs galaxies and star selection

Thanks to the available photometric surveys at least 20 new dwarf galaxies have been discovered in the Milky Way and Andromeda systems in the last 3 years and it is expected that a large population will be discovered in future surveys. All new satellites discovered up to now are on the only 8000 square degrees covered by SDSS thus, a factor of about 6 on new discoveries are expected from future photometric surveys (Panstarrs, Sect. 2.5.8). The distribution of the discovered Milky Way dwarf galaxies as a function of galactic latitude suggest that at least ~4 systems remain to be discovered at low latitudes (Willman et al, 2004), where crowding, high reddening and foreground confusion are important. SIDE shall be competitive to manage these systems thus, besides to the capabilities of the MOS observing mode, a mIFU with 0.25 arcsec diameters fibers is required to avoid, as possible, contamination by close companions.

As an example, Figure 20 shows the metallicity-luminosity relation for dwarf galaxies in the LG. As will be argued in Sect.2.5.3.4, high spectral resolution is mandatory to reduce error bars in relation such this one. Furthermore, it shall be checked how metallicity spread inside each system affects the observed trends.

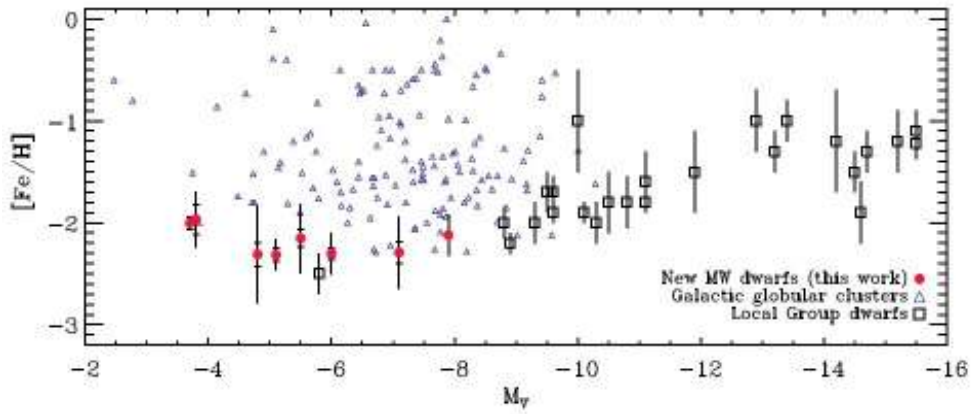

Figure 20: Metallicity-luminosity relation for dwarf galaxies in the local group (Simon & Geha, 2007)

The present observational challenger is to acquire data sets consisting of > 1000 stellar RVs extended over dSph. SIDE can be unique on that purpose. Target stars priorities inside each system will be established from the photometric surveys listed in Sect. 2.5.2.1 and specific observational campaigns. Broad band photometry allow to select high probability members based on their color, apparent magnitude and position (i.e. Martínez-Delgado et al., 2005).

Requirements for target stars selection are: 1) good spatial coverage and 2) accuracy in the relative astrometry better than 0.05" to avoid mis-centering effects (Gaia, PanStarrs, etc.) Independent repeated measurements of individual stars on overlapping sky areas will be needed to avoid systematic errors.

2.5.3.3 Kinematics: Low-Res in MOS and Hi-Res in mIFU observing modes

Low resolution spectroscopy in MOS observing mode provides enough accuracy for most of the kinematics science goals proposed here. A resolution of R=4000 implies a velocity resolution of 75 km/s when using the Ca II triplet absorption lines near 8500Å. Hoping to measure velocities at 10 % of resolution, , hanging upon system stability, a RV accuracy of about 7-8 km/s can be obtained. This median velocity uncertainties would be enough to statistically analyze the internal kinematics of the systems. Questions such as weather the dSphs are gravitationally bound (dark matter dominated) or they have been subject to tidal disruption effects can be answered and this accuracy is enough to tackle, using the correlation between velocity dispersion and absolute magnitude, if there is a floor in the masses of dSphs (Gilmore et al. 2007).

In case that SIDE can achieve a resolution of about ~25000 when using the Ca II triplet absorption lines near 8500A, thus a velocity resolution of 12 km/s. Again, hoping to measure velocities at 10 % of the resolution, results in a RV accuracy of about 1.2 km/s. Thus, measurements with the Hi-Res observing mode in m-IFU mode will: 1) Give high precision radial velocity measurement of cluster center members, 2) Test the MOS low resolution spectroscopy data for systematic trends, and 3) Evaluate the percentage of unresolved binary stars in the sample (see Olszewski et al. 1996 for this effect on the intrinsic velocity dispersion).

2.5.3.4 Evolutionary stages of the stellar populations: Hi-Res in mIFU observing mode

Mean metallicity and metallicity spread within the satellite are proposed to be derived from: 1) The Ca II triplet absorption lines, by combining the three EWs into a single quantity (Rutledge et al., 1997) , and 2) the MgI-triplet absorption feature (~5170Å), FeI and NiI lines at the 5130-5180 Å region.

Spectra for stars near the limiting magnitude (at about B,R ~21) with low S/N spectra (1hr integration has S/N~5 at this limiting magnitude) will not be suitable for measuring equivalent widths. Instead, line strengths via spectral indices can be used. Its correlation with stellar parameters such as effective temperature, surface gravities, chemical abundances of iron-peak and alpha elements allow to achieve constrains on membership and to trace the evolutionary stages of the stellar populations within a given dSph (Walker et al. 2007). Furthermore, composite indices, obtained summing different absorption lines corresponding to the same alpha element will allow to discriminate among star formation processes. Foreground stars can be removed with the use of the EW of the NaI-8183,8195 absorption lines, strongly dependent on surface gravity and temperature. As proposed by Gilbert et al. (2006), this feature can also be used to discriminate between dwarf and giants. In conclusion, accurate metallicity measurements are a strong requirement to detect and quantify both, the metallicity spread within the galaxy, which would suggest multiple star formation epochs and, when studying nearby stellar streams, its metallicity gradients in the inner and outer rings.

2.5.4 Science Case 2: Dynamical Parallaxes for Galactic Globular Clusters

The distances of galactic globular clusters are a fundamental parameter affecting diverse areas of astrophysics from stellar evolution to cosmology. They are needed to determine the

age and mass of a cluster, to make comparisons between globular cluster color-magnitude diagrams and post-MS stellar models, to test the galaxy formation scenarios and to constrain cosmological models. As an example, Chaboyer (1999) argued that a a change of 0.1 mag in the distance modulus of a GC change its age by about 10 %.

A number of methods have been devised to measure cluster distances. The most fundamental is, of course, trigonometric parallax. However, even with the Space Interferometry Mission, which will launch around 2015 on a 5 year mission, the precision will be about 10% at 10 kpc. GAIA, which is expected to begin operations around 2012, will provide distance precisions of 20% at 10 kpc. Another fundamental technique to measure distances is dynamical parallax, one of the few methods that do not rely on secondary calibrators. This method utilizes the proper motion and radial velocity distributions of cluster stars to measure the distance of the cluster. They are related via the simple equation

$$d\ (\mathrm{kpc}) = \sigma(\mathrm{RV,\ km/s}) / [47.35 * \sigma(\mathrm{pm,"/century})].$$

The relative proper motions of stars in galactic globular clusters are currently being measured by members of The ACS Survey of Galactic Globular Clusters Treasury project (Sarajedini et al. 2007a). We expect to have relative proper motions for thousands of stars in each of 65 clusters with precisions of 0.01"/century or less. As a future prospect, absolute proper motions from Gaia will contribute with a significant improvement on this field.

The precision of these dynamical distances does not change significantly for more distant clusters – it only depends on the precision of the radial velocities (and the intrinsic shape of the velocity profile). High precision radial velocities with SIDE/GTC will allow us to get more precise distances at larger than distances as compared with GAIA.

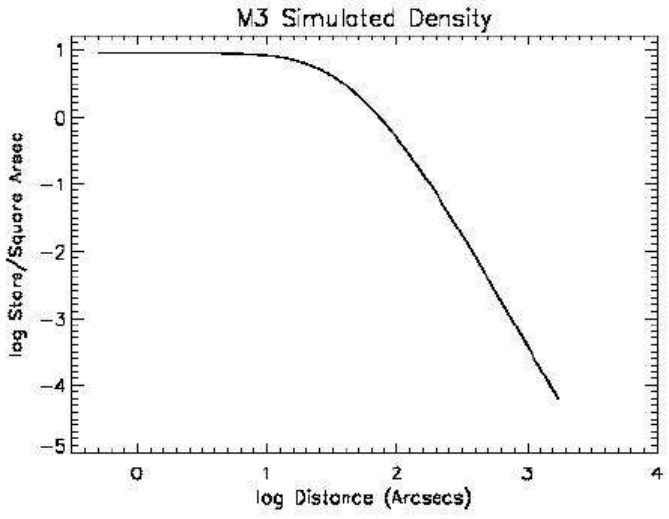

Figure 21: Simulation of M3 GC where the number of stars have been scaled to the HST ACS treasury program focused on Galactic globular clusters (Sarajedini et al. 2007a) which measures stars down to 0.2 of a solar mass in the furthest clusters. For M3, we go down to Mv ~ 9. These are 10 mags fainter than the stars we will observe with SIDE in this cluster

The distances of these clusters range from the nearest objects out to about 20 kpc. To use the equation of dynamical parallax to estimate distances for these globular clusters requires us to measure radial velocities of individual stars. Assuming a fiber diameter of 1.5" in MOS mode, Figure 21 shows that individual radial velocities for stars placed very near to the cluster center, up to a GC radius of about 1 arcmin, can be measured without a risky contamination by close companions.

2.5.4.1 MOS and mIFU observing mode

As discussed in McNamara et al. (2004) some difficulties exist with this dynamical distance method. Some of them are: 1) both radial velocity and proper motion dispersions change with distance from the cluster center, thus only those stars having both a radial velocity and a proper motion shall be used in the study; 2) velocity dispersion might not be isotropic, thus a dynamical model must be fitted and employed to guide the comparison; 3) computed distance can be altered in rapidly rotating systems, thus the complex inner rotation must be known, and 4) high-velocities and binaries shall be avoided when computing the velocity dispersion, they have to be detected. Observations with both MOS and the mIFU observing mode will sure contribute to overcome all these difficulties.

Simulations have been done to create synthetic globular clusters with structural parameters representative of real clusters. We observe the stars in these clusters with apertures 1" and 1".5 in diameter and examine how often there is more than 1 star in the aperture as a function of radial distance from the center of the cluster. Results are shown in Figure 22 for M3.

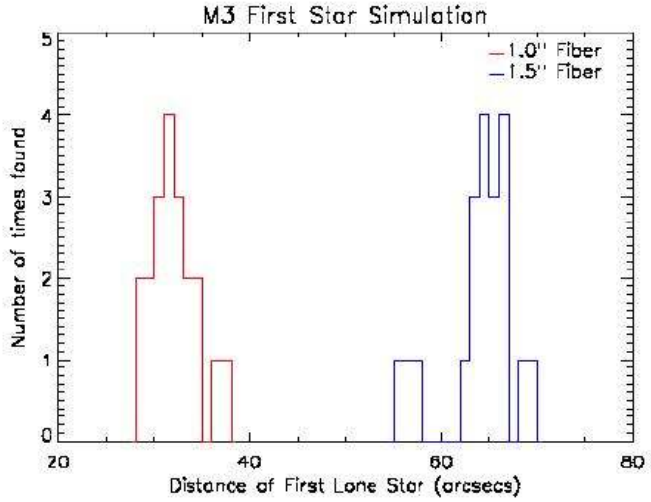

Figure 22: Distance of the first lone stars in M3 (simulated data). Aperture of 1" and 1.5" have been considered.

We propose to use MOS at the outer part of the GC and the mIFU mode to derive individual RV in the most central parts. For example with a mIFU with 28 fibers of 0.25" arcsec diameter each, RV of stars at a distance of 10-20" (TBC) from the GC center can be measured.

2.5.4.2 Justification of the spectral resolution and wavelength coverage

The radial velocity distribution of stars in GCs is typically around 10 km/s so for the velocity errors not to dominate the velocity dispersion, we need to measure individual stellar velocities to better than 3 km/s. With the possibility that SIDE Hi-Res Spectrograph will operate at a resolution of R~25000 on the CaII triplet (8500A) and of R=16200 at the MgI Triplet (~5160A), we expect to be able to measure individual radial velocities for late type stars with a resolution of ~12-20 km/s, thus with a radial velocity accuracy of ~1-2 km/s (hoping o measure velocities at 10 % of the resolution) for stars up to V=20. SIDE will provide a velocity distribution with the required precision to deliver cluster distances with 5% errors out to 20 kpc.

The exposure of this science case can not be finished without mention that SIDE will tremendously contribute to the knowledge of complementary aspects of GCs. Accurate derivation of velocity dispersion profiles –including the use of the SIFU mode at the central part of the clusters - will allow us to constrain important clues such us the amount of mass segregation, the dark matter content in their outer parts, the concentration of unseen material in the center and the challenging task to detect the presence of intermediate Mass Black Holes (IMBH). We can measure the mass of IMBH using SIDE but, how precise we need to measure velocities in order to constrain the mass of the IMBH? For a 10^3 M_{sun} BH (best case) and a 10^5 M_{sun} cluster, we need to go within 4 arcsec of the center of 47 Tuc (Baumgardt et al., 2005). This work can be completed with the detection and velocity gradient of the stars along the tidal tails will allow us to know the role the different dissolution processes have for cluster evolution.

2.5.5 Science Case 3: Milky Way Structure and Kinematics

In addition to the cases presented above, the science case for galactic structure will be the derivation of radial velocities for a large number of objects of the different galactic components. Accurate values for this parameter at the same level of the accuracy on the tangential components (Gaia, see Sect. 2.5.2.2) points for resolutions exceeding 15000. The actual design of the High Resolution Spectrograph fulfil these requirements having in mind that source confusion will be the main limits for our observations. The large number of fibers is just motivated by the gain in observing efficiency in highly populated areas.

An interesting observing mode for the Galactic Structure cases are the quick identification of the exact nature, e.g. complete spectral type, of many stellar objects underlying the population of the different targets and/or morphological components. Hence LRS in MOS mode is essential to this aim. From the above described science cases, it is clear that keeping the spatial resolution at the level of the optimum/median seeing at the GTC site should be also a must for the instrument in view of the high object density of the targets.

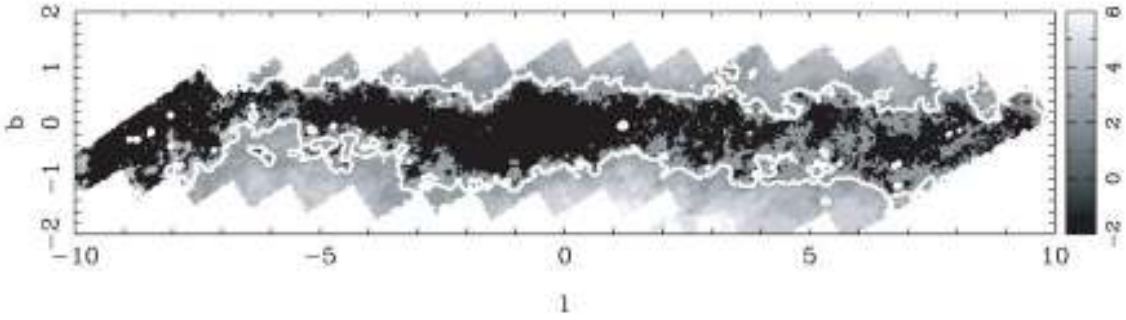

Figure 23: Absolute magnitude of bulge stars just reached at Gaia magnitude G=20 as a function of galactic(l,b) coordinates (units: degrees). The solid contour shows the iso-density of 100000 stars per square degree (Robin et al., 2005).

The optimal scientific exploitation of SIDE spectrometer, with hundredths of fibers, will be the observations of highly populated areas. Figure 23 shows the iso-density of 100000 stars per square degree predicted by the Besançon Galaxy model up to G(Gaia)=20 magnitude (V=21 for cool stars with (V-I)=2.5). We see that the thin layer on the galactic plane will have more than about 11000 stars in the MOS FOV (20'x20'). That results in a mean separation of ~10" between sources (~5" is the minimum separation among adjacent fibers).

2.5.6 Science Case 4: Gas kinematics & metallicity in HII regions in nearby Irregular Galaxies

2.5.6.1 Current status and open questions in the field

Nearby (<5 Mpc) galaxies provide us with excellent laboratories for the study of massive star cluster formation and its impact on the surrounding interstellar medium. Even though Galactic H II regions are better spatially resolved, the existence of distance uncertainties, moderate or large foreground extinctions, and superposition of different components along the line of sight greatly hamper their study. Furthermore, the most massive young clusters (Westerlund 1, Arches) are located behind extremely large (A_V > 10) quanties of dust. On the other hand, nearby galaxies provide us with a collection of easily accesible Giant H II regions whose velocity field can be used to understand the collective effect that hundreds of massive stars can have in their immediate environment.

SIDE at GTC will allow to have unprecedented accuracy (higher S/N) in the derivation of the spatial variations of intensity (flux per unit solid angle), central velocity (ν) and random mass motion (σ) of the ionized gas around the young massive star clusters and its distribution relative to the stars. Open questions are: 1) How is star formation triggered? 2) What are the properties of the surrounding shells and bubbles (radius, expansion speed, kinetic energy) Do theoretical models predict the observed shell-like structures and cavities? 3) How can the discrepancy between the total mechanical energy observed and that predicted from the evolutionary synthesis models be solved?

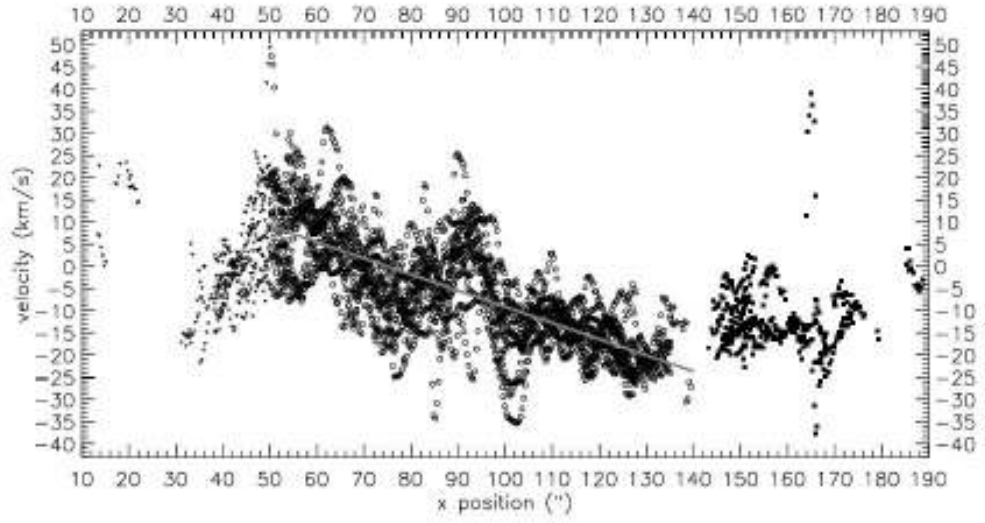

Figure 24: Rotation curve of NGC4214 in H_α (Maíz-Apellániz et al., 1999). Error bars are ~10 km/s, varying with the line intensity. The confusion in the figure is due to the 2" shift in the 12 parallel slits used in the observational campaign.

The opportunity window for SIDE is the combination of good spectral and spatial resolution and high S/N for the study of these H II regions. This is the unique way to study the multiple kinematic components originated by the wind and SNs, disentangling which of them are likely driving the ionized gas.

2.5.6.2 Target dwarfs galaxies and HII region's selection

This science case can be centered in the analysis of NGC4214, a well studied object. Other good observational programs could be centered on: 1) IC10, a irregular galaxy at distance of 660 kpc which proximity to the galactic plane has proved challenging; it has evidences of ongoing an extensive period of recent star formation, 2) the cometary dwarf irregular galaxy NGC 2366 (distance modulus of 27.6) where the high surface brightness giant HII region NGC 2363 is placed, 3) NGC 604 in M33 , 4) NGC 4449, and 5) the multiple giant HII regions in M101.

2.5.6.3 mIFU and SIFU observing mode

The gas kinematics is used to test how star formation is triggered. As an example, the 2D imaging of the velocity dispersion (σ) provides the means of discerning whether a multicore region is a single entity or results from the overlapping of different star-forming regions. A small diameter of the fibers is crucial to have good spatial resolution and to avoid contamination as large σ values of the emission lines may result from confusion with nearby unresolved red or blue secondary components of the gas. For most of the HII regions, the SIFU field of about 20"x20" is the most appropriate option. As high spatial and spectral resolution is needed, the central part of the shell in NGC4214-IA (see Figure 25) should be treated in mIFU mode. That would allow a detailed analysis of the faint kinematic

components, discussing the link between shell cavity and the galactic plane and the presence of a superwind.

Figure 25: NGC 4214 with the IA cavity, diameter of 10", at the center (HST image of 39"x43")

2.5.6.4 Justification of the spectral resolution and wavelength coverage

High spectral resolution is needed to accurately measure the splitting of the emission lines into several components as well as significant variations of the line widths. The spectral range 6390-6840 Å includes the Hα and [SII] 6717+6731 Å lines. This range enables one to construct maps of [SII]/Hα and He I 6678/Hα for the study of the 3D structure of the system (2d dimensional + 1D frequency). The spectral range 4665-5065 Å will be used to study the [OIII] 5007 Å line and Hβ (4861 Å).

2.5.7 Science Case 5: Kinematic properties of M33

2.5.7.1 Current status and open questions in the field

The Local Group galaxy M33 is a late-type dwarf spiral located at a distance of about 850 kpc. It is the nearest galaxy of its type by far allowing us to perform detailed studies of its stellar populations and structural components. Judging from the limited kinematical studies of star clusters in M33, it is clear that this galaxy contains clusters with the kinematical signature of a disk population and a halo population. The typical velocity precisions on which these results are based are in the 50 km/s range. A similar, though much less definitive result has been found for field stars in M33. Both of these types of studies are still in their infancy and a great deal of work still needs to be done. For example, it is unclear if the halo of M33 shows kinematical substructure similar to those of the Milky Way and M31 (its member star clusters exhibit an age range of between 5 and 7 Gyr). In addition, there is as yet no evidence, kinematical or otherwise, for a thick disk in M33. There is also the puzzle of M33's central regions which some have characterized as a bulge while others claim is simply a super star cluster. The current evidence suggests that, if this central star cluster contains a

black hole, its mass cannot be greater than 1000 solar masses. It is important to set a tighter constraint on this question by measuring the radial velocities of stars and star clusters in central regions of M33 with much better precision.

2.5.7.2 MOS and mIFU observing mode

To measure the kinematical properties of M33's structural components, it is most convenient to use its star cluster population. From ground-based observations with a seeing of 1", these clusters appear marginally resolved with typical FWHM values of few arcseconds (Sarajedini et al. 2007b).They can be easily confused with background galaxies. When considering HST images they are resolved into individual stars, making their identification as genuine cluster essentially unequivocal. A catalog of 451 star cluster candidates in M33 exist from which to select targets for spectroscopic work (Sarajedini and Mancone, 2007). There are also extensive stellar catalogs in place, and, in fact, Sarajedini et al. (private communication) are working on a new catalog of stars within a 1 degree field centered on M33.

Chandar et al. (2002) are able to identify a kinematical disk and halo among the M33 clusters using radial velocities with a precision of 20 km/s. In order to further differentiate between a disk, thick disk, halo, and substructures in the halo, we will need to push this velocity precision down to better than 5 km/s for hundreds of star clusters. This has been already done for 4 clusters using the Keck HiRes instrument (Larsen et al. 2002), but we require the MOS and mIFU mode of SIDE to enable the required large sample size. We estimate being able to observe approximately 50 M33 clusters in a typical MOS field of view.

2.5.7.3 Justification of the spectral resolution and wavelength coverage

In order to differentiate between the kinematical components of M33 (thin disk, thick disk, halo, tidal streams), we require a velocity precision of 5 km/s or better. To achieve this with the SIDE High Resolution Spectrograph, we will observe the clusters at a resolution of R=25000 in the spectral range of the near-infrared Calcium triplet (i.e. 8500A).

On the other hand, we would like to have spectral lines that tell us about the cluster age and metallicity. We would need to observe the Lick indices that can quantify these parameters, indices that usually require several thousand angstroms of wavelength coverage. Lick/IDS indices (see Lilly et al., 2006) at the intermediate resolution (R=5000) using MOS are proposed.

2.5.8 Input photometric catalogue: optimum target population

A non completed list of the on-ground photometric and spectroscopic surveys several of them being potential input data for SIDE is:

SDSS: Data Release 5 (Adelman-McCarthy et al., 2007), spatial coverage of 8000 square degrees. **SEGUE:** imaging and spectroscopy into the Milky Way, 3900 sq deg. **HST Treasury project** / Legacy survey: deep and uniform database of a large sample of Galactic GC - about 65 GCs, up to 20 kpc. Relative proper motions from ACS observations, archival and WFPC2. PM accuracy < 0".0001 /year (pixel size = 0.05"). Schedule: ACS stopped 2007.

Panoramic Survey Telescope and Rapid Response System survey (Pan-Starrs): four individual optical systems for a wide-field imaging survey with a spatial sampling of 0.3 arcseconds and a limiting magnitude of 24 (exposure time 30-60 seconds). Schedule: PS1: Prototype telescope: 1.80m Hawai (construction has been completed).
Large Synoptic Survey Telescope survey (LSST): 8.4m Cerro Tololo telescope that will provide digital imaging of faint astronomical objects with a AB magnitude limit of about 26-27. Schedule: Pending of approval, no development schedule yet.
UKIRT Infrared Deep Sky Survey (UKIDSS): The Large Area Survey, the Galactic Cluster Survey and the Galactic Plane Survey cover approximately 7000 square degrees to a depth of K~18. Filter set: ZYJHK and H2. Schedule: Started May, 2005; seven years sky survey.
Other surveys **: HyperSuprime** Survey at Subaru, **VLT Survey Telescope (KIDS,** VISTA, …), **VSOP** (hi-res spectroscopy of unstudied variable stars).

2.5.9 Justification of the spectral resolution and wavelength coverage

The relevant/indispensable spectral ranges to be covered with the Hi-Res mode of SIDE are centered in MgH (5200Å), Hα and CaI (6100-6200 Å), OI (7772 Å) – Jaschek et al. (1993) - y CaII (8500 Å). Regions of strong telluric absorption can be avoided: 6860-6925 Å, 7167-7320 Å, 7593-7690 Å and 8110-8320 Å. It is well known that the UV region of a stellar energy distribution (SED) contains relevant information about certain astrophysical parameters. As stated in Bond's review (1999), the spectral region near the Balmer Jump (3650 Å) provides unique information about the temperature of OB and the gravities of A-K stars and UV regions provide high sensitivity to metallicity in stars of F type and later. For AF-type stars, the region around 4000-5000 Å also contains information on stellar metallicity, separable from gravity effects at shorter wavelengths, F-type subgiants are crucial for age determination of stellar populations. For the determination of SFR and ages measurements, and hence of inferring evolutionary states, [alpha/Fe] abundances have to be derived. Strong features of these [alpha/Fe] elements, synthesized by alpha capture in SNeII, between 3500A-10000 Å are: MgI triplet, CaII H&K and molecular bands (OH, MgH, TiO). This non exhaustive list justify a blue and red hi-res spectrograph in the selectable wavelength ranges 3450-5750A and 5400-9000 Å respectively.

In Table 10 we give a summary of the Galactic Structure and LG spectral resolution and wavelength coverage needed for our studies.

Science case	Observing mode	Resolution	Lines/molecular band	Comments / requirements
MW Structure and kinematics (bulge, bar, arms, …)	MOS mIFU	R=5000 R=15000 - 25000	4000-9000A CaII triplet (8500A)	Radial Velocities & Spectral Type
MW galactic populations: chemical abundances	mIFU	R=15000 - 25000	MgI triplet, CaII H&K and bands (OH, MgH, TiO)	Metallicity & [alpha/Fe]
SF in young open clusters and associations	mIFU	R=15000 - 25000	6470-6790A, H_α, LiI6780A	Ages, SF history, Radial Velocities
Dynamic parallaxes of GC	MOS mIFU	R=5000 R=15000 - 25000	4000-9000A CaII triplet (8500A) & MgI triplet (5170A)	Radial velocities (σ_{RV} ~ 3 km/s)
Tidal Streams - kinematics	MOS	R=5000	4000-9000A	Radial velocities (σ_{RV} ~ 5-6 km/s)
Missing dwarfs satellite problem: chemical composition	mIFU	R=15000 - 25000	5130-5180A MgT,FeI and NiI CaII triplet	abundance gradients - [Fe/H]
Missing dwarfs satellite problem: kinematics	MOS mIFU	R=5000 R=25000	4000-9000A & CaII triplet	Radial velocities
HII regions in the LC: Chemical Composition	SIFU	R=2000-5000	4000-9000A	Peimbert et al. 2005
Gas kinematics of HII regions in Irregular galaxies	mIFU	R=15000-25000	6390-6840A 4665-5065A	3D kinematic structure
M33 star clusters: kinematics	mIFU	R=15000-25000	--	integrated spectra
M33 star clusters: age & metallicity	MOS	R=5000	--	Lick indices
Spectral library at the J-band (Bruzual, priv. com)	MOS	R=5000	9000-17000A	Stellar population synthesis

Table 10: Summary on the Galactic Structure and LG spectral resolution and wavelength coverage.

2.5.10 References

Adelman-McCarthy et al., 2007, submitted to ApJS
Baumgardt, H., Makino, J., Jut, P. 2005, ApJ 620, 238
Binney, J. 2005, ESA SP-576, 89
Bond, H. 1999, Where is the Information Located in Stellar Spectra?, Tech. rep., Space Telescope Science Institute, Baltimore

Chaboyer, B. 1999, in Post-Hipparcos Cosmic Candles, ed. A. Heck & F. Caputo (Dordrecht: Kluwer), 111
Chandar, et al. 2002, ApJ, 564, 712
De Bruijne, J. 2005, Gaia astrometric accuracy: TN Gaia-JdB-020, ESTEC, The Netherlands
De Zeeuw, T. 2005, ESA SP-576, 729
Diermand, J., Kuhlen, M., Madau, P. 2007, in press (astro-ph/0703337)
Drew, J. E., Greimel, R., Irwin, M.J. 2005, MNRAS 362, 753
Drimmel, R., Cabrera-Lavers, A. López-Corredoira, M.2003, A&A,409, 205
Gilbert, K.M., Guhathakurta, P., Kalirai, J.S. et al. 2006, ApJ 652, 1188
Gilmore, G. , Wilkinson, M.I.,Wyse, R.M., et al. 2007, ApJ, in press (astro-ph/0703308)
Jaschek, M., Jaschek, C., Andrillat, Y. 1993, A&AS 97, 781
Larsen, S.S., Brodie, J.P., Sarajedini, A., Huchra, J.P. 2002, AJ 124, 2615
Lilly, T., Fritze, U., Alversleben, V. 2006, A&A 457, 467
Maíz-Apellániz, J., Muñoz-Tuñón, C., Tenorio-Tagle, G. et al. 1999, A&A 343, 64
McNamara, B. et al. 2004, ApJ, 602, 264
Martínez-Delgado, D., Butler, D.J., Rix, H-W. 2005, ApJ 633, 205
Olszewski, E.W., Prior, C, Armandroff, T.E. 1996, AJ 111, 750
Peimbert, A., Peimbert, M., Ruiz, M.A. 2005, ApJ 634, 1056
Robin, A.C., Reylñe, C., Picaud, S., Schltheis, M. 2005, A&A 430, 129
Rutledge, G.A., Hesser,J.E., Stetson, P.B. 1997, PASP 109, 907
Sarajedini, A. et al. 2007a, AJ, 133, 1658
Sarajedini, A., Barker, M.K., Geisler, D. et al. 2007b, AJ 133, 290
Sarajedini, A., Mancone, C.L. 2007, AJ 134, 447
Simon, J.D, Geha, M., 2007, ApJ in press (arXiv:0706.0516v1)
Van den Bergh, S., 2000, "The Galaxies of the Local Group", Cambridge Univ. Press
Walker, M.G., Mateo, M., Olszewski, E.W. et al. 2007, astro-ph/0703284
Wilkinson, M.I., Vallenari, A., Turon, C. Et al. 2005, MNRAS 359, 1306
Willman, B., Governato, F., Dalcanton, J.J. et al. 2004, MNRAS, 353, 639

2.6 LSS & Cosmological Parameters

2.6.1 Current status and open questions in the field

2.6.1.1 General

Currently, the apparently most important questions in Cosmology and in the study of the Large-Scale Structure of the Universe are related to:

- The nature of Dark Energy (as well as its existence as the sole interpretation of the observed accelerated expansion of the Universe) and its interpretation within a fundamental physical theory.
- The nature of dominant form of matter, the Cold Dark Matter, and its precise amount.
- The statistical quantification of the large-scale structure of the universe at different epochs (clustering), since it encodes important length scales related to the horizon at last scattering and the acoustic baryon oscillations.
- Understanding the evolution of galaxies and clusters of galaxies, not only from the point of view of galaxy formation theories but also because they are proxies of the different cosmological parameters.

We anticipate that SIDE can provide a versatile instrument that its use can have an important impact on Dark Energy studies, but it could also have an important contribution to all of the previously posed issues, mainly through its capability to perform redshift surveys of hundred of thousands of high-redshift galaxies in a reasonable time. Such high-redshift surveys will be used in a complementary manner to address problems related to the important issues stated previously, but also to a wealth of themes, from galaxy evolution and transformation, to AGN processes, galaxy cluster dynamics and evolution, etc. We wish to note that two very extensive, recently released reports, have identified dark energy as a priority for future research: "Report of the Dark Energy Task Force (advising DOE, NASA and NSF), Albrecht et al., astro-ph/0609591, and "Report of the ESA/ESO Working Group on Fundamental Cosmology", Peacock et al., astro-ph/0610906.

Deep and large-area spectroscopic surveys are instrumental for the understanding of dark energy and determining with precision cosmological parameters by directly measuring the baryonic oscillation scale (BAO) at different redshifts. They can also provide, as an important added value, the necessary data to study a plentitude of large-scale structure and galaxy formation and evolution themes in the high-z universe. Large spectroscopic surveys are able to study the evolution of galaxies in ways that small samples cannot, by allowing us to investigate and understand the role of the environment on the galaxy properties, effects which indeed appear to be critical (as seen for example in environment studies with SDSS, DEEP2, and VVDS -- Blanton et al. 2003, Gomez et al. 2003, Cooper et al. 2006, 2007, Cucciati et al. 2007). Although, such large-areas surveys are telescope-time intensive, the scientific trade-off is huge.

An alternative and relatively more economic approach to measure dark energy is to use the large photometric surveys that have been proposed recently (DES: http://www.darkenergysurvey.org, Pan-STARRS: http://pan-starrs.ifa.hawaii.edu, LSST: http://www.lsst.org, SNAP: http://snap.lbl.gov DESTINY: http://destiny.asu.edu, DUNE: http://www.dune-mission.net). Such approach relies on broad-band photometric redshifts, which will reach accuracies of order $\sigma_z \sim 0.04(1+z)$. For such an approach to have possibilities of success it is instrumental to calibrate the photo-z determination algorithms with spectroscopic redshifts. Therefore, smaller area deep spectroscopic surveys, although cannot determine directly BAO's, are also of immense importance to calibrate photometric redshifts and establish the redshift distributions of the samples that will be used to study dark energy via weak lensing and photometric BAO techniques. For such studies to be able to derive the dark energy parameters to the necessary precision, the photo-z measurement uncertainties must be $<0.002(1+z)$ (for LSST or SNAP - Ma, Hu & Huterer, 2005) and therefore spectroscopic redshifts will provide the essential means for calibrating these photo-z's, either directly or indirectly via cross-correlation techniques (Newman 2007). Furthermore, such smaller spectroscopic surveys can be instrumental in determining a variety of cosmological relevant information, like the clustering properties of high-z X-ray selected AGN, the number density of voids as a function of redshift as well as providing the mass calibration of high-z cluster surveys.

We will divide below this section into five semi-independent sections, related to the different proposals of our working group, which are complementary and could be realized by a single deep large-area spectroscopic survey down to $R_{AB} \sim 24\text{-}24.2$ However, such a large-area survey is necessary only for the realization of the first proposal. The others could also be realized with selected smaller area spectroscopic surveys, which are not so telescope-time intensive.

2.6.1.2 Relevant LSS & Cosmology Themes to SIDE

Baryonic Acoustic Oscillation survey: The main future application of large-scale structure measurements to study cosmological parameters is the 'Baryonic Acoustic Oscillation' (BAO) measurements, which was identified by the U.S. Dark Energy Task Force (DETF) as one of the four most promising techniques to measure the properties of the dark energy and the one less likely to be limited by systematic uncertainties. BAOs are produced by pressure (acoustic) waves in the photon-baryon plasma in the early universe, generated by dark matter (DM) overdensities. At the recombination era (redshift $z \sim 1100$), photons decouple from baryons and free stream while the pressure wave stalls. Its frozen scale, which constitutes a "standard ruler", is equal to the sound horizon length, $r_s \sim 100\ h^{-1}$ Mpc (e.g. Eisenstein, Hu & Tegmark 1998). This appears as a small, ~10%, excess in the galaxy-galaxy or cluster-cluster power spectrum (and 2-point correlation function) at the scale corresponding to r_s. First evidences, at about 2.5σ significance, of this excess were recently reported (Eisenstein et al. 2005, Padmanabhan et al. 2006).

BAO measurements can be performed using either photometric or spectroscopic galaxy surveys: Photometric galaxy surveys can measure the angular scale of this ruler, determining $dA(z)/r_s$ with dA the angular distance, and therefore they constrain the geometry and matter-energy content of the universe. Spectroscopic galaxy surveys will measure the BAO scale along the line of sight and provide a direct measurement of the Hubble parameter, $r_s H(z)$, at different redshifts, which is more sensitive to the contents of the universe than integrated quantities like dA(z) or the luminosity distance dL(z), probed by SNIa. Regarding the

superiority of spectroscopic surveys, we note that except from the fact that photometric surveys throw away information via radial smearing, the same precision of the DE parameters can be obtained by spectroscopically covering ~10% of the corresponding photometric survey area. Finally, we note that it is important to estimate BAO's at high redshifts (z>1) because at such redshifts the power-spectrum is nearer to the linear regime (and thus suffers less from non-linear distortions) implying a higher precision in measuring BAO scales, while also at such high redshifts the maximum departure between the canonical w=-1 and evolving DE models occurs. Observations at different redshift intervals highly enhance the cosmological inference of BAO's (cf. Seo & Eisenstein 2003; 2007).

2.6.1.3 Calibration of large photometric redshift surveys

SIDE can also play an important role in the photometric approach to study the dark energy content of the universe. All of the proposed photometric surveys (DES, Pan-STARRS, LSST, SNAP, DESTINY, DUNE) will determine galaxy redshifts using broad-band photometry. In order, however, to reliably determine photometric redshifts (so-called photo-z's), calibration of the relevant algorithms is necessary. In particular, a precise knowledge of the bias and precision of the z-determination algorithms is mandatory in order to avoid degrading the weak lensing tomographical information (Ma, Hu & Huterer 2005). This will be achieved by comparing the measured photo-z's with accurate determinations of the redshifts of a fraction of the galaxies with spectroscopic techniques. Accurate calibration needs a spectroscopic fraction of order $O(10^{-3})$. Since some of the projects mentioned above, like DUNE, will survey about one billion galaxies, around a million spectra will eventually be needed. The ground-based surveys will gather about 300-500 million galaxies, and therefore, ~400,000 spectroscopic redshifts will be needed. Planned ground-based surveys will reach r~27 or greater, too faint for ground-based spectroscopy en masse; however, cross-correlation techniques can be used to calibrate photo-z's for even faint objects using spectroscopy of brighter samples at the same redshifts (Newman 2007). SIDE would be ideal for this, both contributing many more redshifts than currently available at $0.2 < z < 1.4$, and adding large numbers of redshifts at z>1.4, where few are available today, thanks to its IR multi-object spectroscopy.

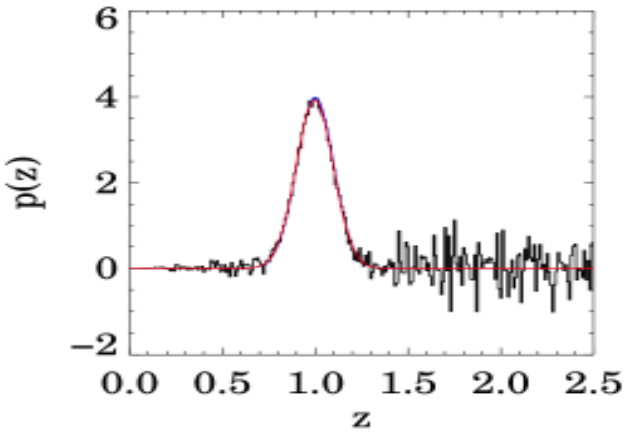

Figure 26: Recovery of the true redshift distribution for objects in a photo-z bin with surface density 10 objects/sq arcmin using spectroscopic-photometric cross-correlation techniques. The input distribution is in blue (not actually seen due to the excellent recovery; see below); one Monte Carlo realization of the recovery of the input distribution with realistic errors is shown in black; and a least-squares fit is shown in red, assuming either current redshift samples (left) or current samples plus a SIDE-like survey (right); only 7500 redshifts at z>1.5 are assumed, rather conservative for SIDE. With such a sample, this technique significantly outperforms the photo-z calibration accuracy required for LSST and SNAP (Newman 2007), even with z's of only bright galaxies (e.g. R< 24 vs. R>27 depth for LSST & SNAP).

2.6.1.4 High-z Galaxy Cluster Survey & Cluster mass calibrator

Clusters of galaxies occupy a special place in the hierarchy of cosmic structures, since they are the largest cosmic virialized (or nearly so) structures in the Universe. They arise from the collapse of initial density perturbations of a typical comoving scale of ~10 h^{-1}Mpc, which marks the transition between the non-linear and the linear or weakly non–linear gravitational dynamics regime. On smaller scales complex astrophysical processes, related to galaxy formation and evolution, dominate (gas cooling and heating, supernovae feedback, effects of active galactic nuclei, etc). The extensive use of clusters of galaxies as cosmological tools is owed exactly on the fact that they mark the transition between these two regimes. Below we indicate a few of the cosmological tests for which clusters of galaxies have or will be used:

- The clustering properties of the large–scale distribution of galaxy clusters and their redshift evolution provide information on the shape and amplitude of the power spectrum of the underlying DM distribution (e.g., Borgani 2007 and references therein). Furthermore, they can be used to determine, in the same way as galaxy surveys, wiggles in their $\xi(r)$ and P(k) due to BAO.

- The local cluster mass function, n(M,z), depends on Ω_m and the normalization of the power-spectrum, σ_8. One of the great successes of using clusters as Cosmological probes was exactly the correct determination of σ_8 (e.g., Schuecker et al. 2003; Vikhlinin et al. 2003), confirmed recently by WMAP3 (Spergel et al. 2006).

- The redshift evolution of n(M,z) is sensitive to the linear growth rate of density perturbations, and can therefore be used as a tracer of cosmic volume as a function of redshift which translate into constraints on the DM and DE density parameters (e.g., Newman et al. 2002; Rosati et al., 2002; Voit, 2005, and references therein). The key ingredient is to have a good measure of the cluster mass, as the cluster mass function depends exponentially on this quantity.

- The cluster mass-to-light ratio, M/L, can be used to estimate Ω_m once the mean luminosity density of the Universe is known, assuming that mass traces light similarly both inside and outside clusters (see Andernach et al. 2005 for a recent application of this method).

- The baryon fraction in nearby clusters has provided constraints on Ω_m (e.g., Fabian, 1991; White et al., 1993). Furthermore, assuming that the baryon fraction within clusters does not evolve, as gasdynamical simulations predict (e.g. Gottlöber and Yepes 2007), its determination at distant clusters can provide a geometrical constraint on DE (Allen et al., 2004).

Galaxy cluster surveys that probe the high redshift ($z>0.5$) universe can provide a wealth of information regarding the amount and nature of the dark matter and dark energy. To this end it is necessary to relate accurately the cluster virial mass with other cluster observables like the X-ray luminosity, the X-ray temperature, the Sunyaev-Zeldovich luminosity, etc. It is then the evolution of the accurately derived scaling relations (mass-temperature or mass-luminosity) which can be used as a cosmological proxy. Thus, the precision with which we will be able to measure high-z cluster masses is of outermost importance for such cosmological tests.

Furthermore, the cluster environment around high-z clusters can be used to investigate whether “Nature or Nurture” determines the galaxy morphology-density relation. Galaxy interactions and transformation, which could eventually dictate the morphology-density relation should happen at a higher rate and probably be very common at high redshifts. On the other side, it appears that at least locally the red-sequence is already in place in the outskirts of clusters of galaxies, implying that possible galaxy transformation processes happens in effect outside the densest cluster cores. Spectroscopic surveys of the environment of high-z clusters, for which SIDE is particularly suited for, can be used to characterize the dynamical state of high-z clusters and its evolution (using the velocity dispersion measurements), which in turn should play an important role in setting in the morphology-density relation (and the Butcher-Oemler effect).

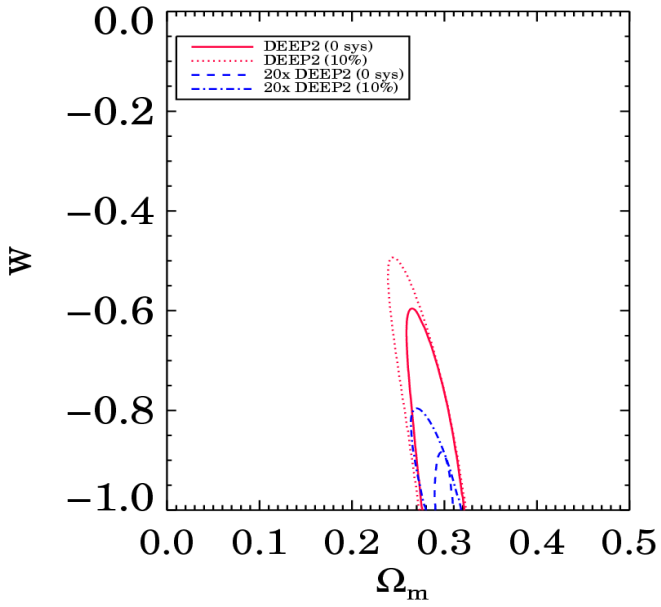

Figure 27: Constraints on the Dark Energy Equation-of-State parameter, w, and the cosmic matter density obtainable from measuring n(M,z) for groups in the DEEP2 Galaxy Redshift Survey (red) or a SIDE-like, 20 times larger survey (blue lines). Also, cluster kinematics measurements from SIDE will be critical for calibrating other cluster-based dark energy abundance tests (e.g. from red sequence or S-Z observations).

2.6.1.5 High-z X-ray AGN Clustering

Active Galactic Nuclei (AGN) can be easily detected out to high redshifts and thus their clustering properties can provide information on the large scale structure at such redshifts, the underlying matter distribution and the evolution with redshift of the AGN phenomenon. Optically selected AGN surveys miss however, large numbers of dusty systems and therefore provide a biased census of the AGN phenomenon. X-ray surveys, are least affected by dust providing an efficient tool for compiling uncensored AGN samples over a wide redshift range. Early studies of the X-ray AGN clustering, using Einstein and ROSAT data, produced contradictory results. Recently, there has been an effort to address this confusing issue and determine the clustering properties of both soft and hard X-ray selected AGNs, based on the XMM and Chandra missions (eg., Yang, et al. 2003, Yang, et al. 2006, Gilli, et al. 2005, Basilakos, et al., 2004, Basilakos, et al., 2005, Puccetti, et al., 2006, Miyaji, et al., 2006). However, most of these works either measure the angular correlation function and infer the spatial one via Limber's inversion, or measure the spatial correlation function but using rather limited redshift information. The outcome of these studies is a relatively large span of correlation length for the high-z X-ray AGNs (see Table 1 of Plionis & Basilakos 2007) which indicates that there sizes are still small enough to minimize cosmic-variance effects. The easy detection of high-z X-ray AGNs, in relatively short exposures ~10-50 ksec, imply that they can be used very efficiently as cosmological probes and indeed it has been shown that they can provide interesting cosmological constraints (eg. Basilakos & Plionis 2006, Plionis & Basilakos 2007; see Figure 28).

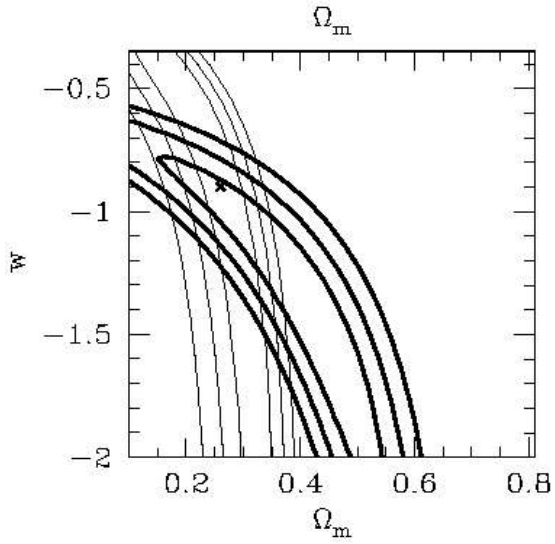

Figure 28: Present constraints on the Dark Energy Equation-of-State parameter, w, and the cosmic matter density obtained from combining the high-z X-ray AGN clustering results (thin contours) and the SNIa Hubble relation (thick contours). The uncertainties are large, which however could be significantly reduced by a large spectroscopic survey of the high-z AGNs.

However, the uncertainties due to the limited available redshift information and the small areas analysed (hence cosmic variance effects) prevents fully exploiting this approach, and in this respect SIDE (of which the FOV is similar in size to that of X-ray observatories) could provide the necessary high-z AGN redshifts, as an added value to a BAO or a Cluster survey (see below).

2.6.1.6 Constraining Dark Energy with the Evolution of Cosmic Voids

Patiri, Betancort-Rijo, Prada (2006) have developed a formalism that allows an accurate estimation of the number density of voids larger than a given radius for any given cosmological model. It has already been used to set strong constraints on the parameters σ_8 and Γ (=Ω h) by means of the present day void statistics found in the 2dFGRS. The same methodology can be used to obtain the void statistics at z ~ 1 and gain information about the evolution of the growth factor of the linear density fluctuations, D(z). This fluctuations depends both on the normalized dark energy density Ω_{DE}, and on its equation of state, parameterized by w ($p=w\,\rho$).

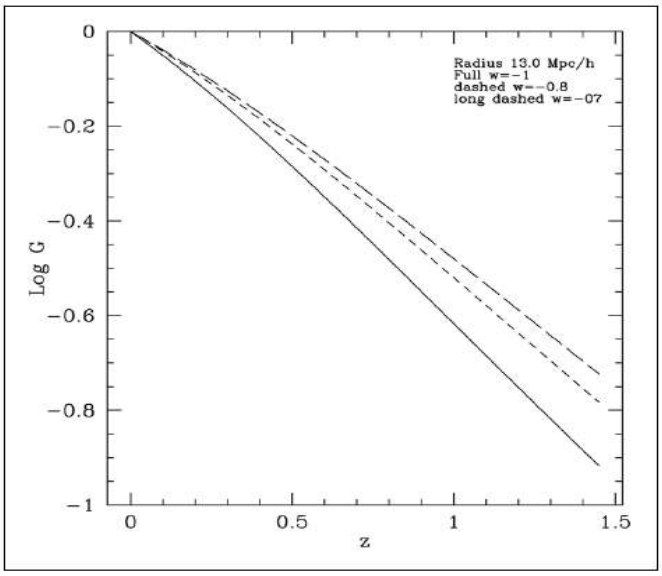

Figure 29: Number density of voids larger than 13h-1 Mpc normalized to one at z=0, G, as a function of z for three different equations of state of the dark energy (parameterized by w).

Assuming a flat model ($\Omega_M+\Omega_{DE}=1$) and $\Omega_M=0.3$, h=0.7, we have computed the dependence of the number density of voids larger than 13 h^{-1}Mpc defined by a galaxy sample with number density 4.6 10^{-3} $Mpc^{-3}h^3$ at z=1 normalized to the number density at present (see Figure 29). The strong dependence on w that is found suggests that the void statistics at z~1 may provide an accurate measurement of w.

The size of the survey needed to measure w, with a given accuracy, is estimated using only the largest voids, which contain most of the information about w. Only voids larger than R_0 are considered, which is chosen so that the RMS error of w, attains a minima:

$$RMSw(R) = \frac{(P_0(R)Vol(R))^{-1/2}}{d\ln P_0(R)/dw}$$

where $P_0(R)$ is the number density of voids larger than R (which is an implicit function of w) and Vol(R) is the available volume for voids within the survey. Minimizing this expression, the value of R_0 and its corresponding RMS error can be obtained for a given survey. If we want to measure w with some prescribed error, ε, the equation: $RMS(R_0)= \varepsilon$, determines the minimum size of the survey required to this purpose.

2.6.2 Future prospects

2.6.2.1 The next five years

In the next five years, no major advances in optical multi-object imaging spectrographs are expected. However, infrared MOS on 8-m class telescopes are now online (Subaru/MOIRCS) or coming soon (Keck/MOSFIRE). These IR MOS have limited field of view however (a few arcmin on a side), and in this respect SIDE will definitely make a difference. Thus we can comfortably expect that no optical MOS with ~5-10 times the

multiplexing of existing spectrographs on 8+ meter telescopes will occur in the next five years.

As far as imaging is concerned, considerable progress is expected in large-area, deep surveys in the next few years. Pan-STARRS and VISTA should begin their operation soon; DES, Hyper-SuPRIME, and ODI all hope to begin in the next 5 years, allowing deep multiband imaging of 1 deg^2 or more at a time. These surveys can provide parent imaging samples for future redshift surveys, like the ones we suggest for SIDE. We repeat that photometric BAO measurements cannot measure the radial modes, which allows one to estimate H(z).

Regarding clusters of galaxies, different approaches will be applied in the next few years to measure their masses based on galaxy richness, X-rays, lensing and the Sunyaev-Zel'dovich (SZ) effect. However, there is no current attempt for a cluster survey of velocity dispersion measurements, a region where SIDE can make a significant difference. In the next 5 years current cluster X-ray surveys will be consolidated and we will witness the first generation of SZ surveys, including ACT, Planck, DES and SPT. However, X-ray cluster surveys are mostly limited to $z<1$ because the signal gets weaker with redshift. SZ cluster surveys, which are insensitive to redshift, will be performed by the Atacama Cosmology Telescope (ACT) and the South Pole Telescope (SPT), while optical surveys like DES will measure the spatial density of massive clusters of galaxies as a function of redshift, which is a probe of dark energy. Both the ACT and SPT telescopes will start collecting data soon and are therefore going to provide a wealth of information on this method very soon. The DES optical survey will target the same area as SPT and thus provide photometric redshifts for about 10^4 clusters that SPT is expected to find. SIDE can be used to calibrate cluster mass, measured by other methods, since in the high-z regime X-ray measurements become extensively unreliable.

2.6.2.2 Beyond the next five years

Past the five year horizon, the multi-object spectrograph on JWST should cover the small-field/ultra-deep IR spectroscopy domain very well. However, it will be inefficient for wide fields, and therefore SIDE will still have an important role to play.

Large multi-object spectrographs take a great deal of time to plan and build. There are a couple of spectroscopic galaxy redshift survey proposals that will target the high-redshift regime from the ground, WFMOS which is being optimized for BAO studies (i.e. with a very wide field of view) on Subaru and HETDEX. However, there are lingering doubts about their time scales, and even about whether they will even happen. If they do go through they will target about 0.5-1 million galaxies at redshifts up to about 3.5, covering 200--300 deg^2 in the sky for survey volumes around $1\sim(Gpc/h)^3$.

In a longer time scale, there is also the ADEPT satellite proposal, a candidate for the DOE-NSF Joint Dark Energy Mission (JDEM), that, if approved, will perform an all-sky galaxy redshift survey using slit-less spectroscopy to sample almost $\sim 100\ (Gpc/h)^3$ with 100 million galaxies in the range $1<z<2$. If approved, ADEPT could be launched around 2015.

We also can expect large imaging campaigns which will find many transients (e.g. LSST or SNAP) and reach very great depths to occur more than 5 years from now. These surveys both will provide excellent datasets for target selection, and require large amounts of spectroscopy for calibration. IR coverage should be critical for objects faint in g and r (e.g. red sequence or highly extinct galaxies at $z>1$).

Finally, regarding clusters of galaxies, it is expected that the outcome of ACT, Planck, PanStars, SPT and DES will be complemented with different follow ups. This should include a SIDE cluster velocity dispersion survey, as we propose. We will probably also start seeing the use of weak lensing as mass calibrator for clusters surveys (eg DES).

2.6.3 The opportunity window for SIDE

1) Baryon oscillation surveys:

One of the most promising methods for probing dark energy is to use, as a standard ruler, the features imprinted in the large-scale structure from Baryon Acoustic Oscillations (BAO) in the early universe. This method has been shown to suffer much less systematics than competing techniques.

In order to reach the statistical accuracy needed to get relevant constraints on DE parameters, large volumes have to be surveyed. The DETF considered two classes of spectroscopic BAO surveys from the ground: a 2000 deg^2 survey covering $0.5<z<1.3$ and a 300 deg^2 survey covering $2.3<z<3.5$. The former survey would measure redshifts through the 4000 Å break, while the latter would use the Lyman break. In the intermediate redshift range $1.3<z<2.3$ it is difficult to determine reliably galaxy redshifts from the ground without IR capabilities. Therefore, SIDE has the key advantage of determining redshifts following the 4000 Å break into the infrared, which could be used to cover a large enough volume at $1.3<z<2.3$. Note, however, that not all galaxies in a given volume need to be measured: the rule of thumb is $nP>3$, where P is the power and n the co-moving galaxy density.

The essential ingredient for a successful BAO survey is wide areas, over which rare, bright galaxies at $z>1$ may be selected. Only sparse sampling of the galaxy distribution is needed, as the BAO scale is ~100 h^{-1} Mpc (comoving). With a ~0.4 deg FOV (vs. ~2 deg for WFMOS), SIDE would not be able to compete with WFMOS directly (BAO errors are driven by the volume covered, and with much larger area, WFMOS can cover much more volume more quickly). However, WFMOS is not a sure thing, and if it does not go forward or is heavily delayed, SIDE would be well-positioned to take up the slack.

Given the uncertainties surrounding HETDEX and, especially, WFMOS, and the time scale of ADEPT, it is safe to say that a galaxy redshift survey with SIDE covering about ~150 deg^2 in the sky with enough galaxies to get close to the cosmic variance limit in the redshift range $2.3<z<3.3$ is feasible and would be of great cosmological value. The IR capability of determining redshifts following the 4000 Å break into the infrared can be used to cover a large enough volume also in the $1.3<z<2.3$ range.

Furthermore, although the locations of the BAO peaks do not depend on the details of galaxy biasing and non-linear evolution, the amplitude of the BAO signal and the shape of the power-spectrum do. Therefore, in order to extract precision cosmological information and fully interpret BAO measurements, it would be necessary to understand systematic effects and biases. To this end it is necessary to understand:

(a) environmental effects, ie., the relationship of galaxies to their host dark matter halos,

(b) the nature and evolution of biasing between luminous galaxies, used to measure clustering on large scales, and the underlying dark matter distribution. The already planned

BAO surveys are very poorly suited for this task, since optimal BAO surveys, as discussed previously, sparsely sample luminous galaxies over large scales, much larger than the radius of their respective dark matter halos (≤1 Mpc). This tasks requires surveying not just the brightest galaxies at a given z, but also the fainter objects that fill out their common dark matter halos; and it requires dense, not sparse, sampling.

Therefore, even if WFMOS do go forward and a large-area spectroscopic SIDE survey is not pursued, smaller area spectroscopic SIDE surveys can be extremely important to address such issues. In fact, SIDE is a near-optimal instrument to investigate and eventually remove such biases, due to its high packing of fibers.

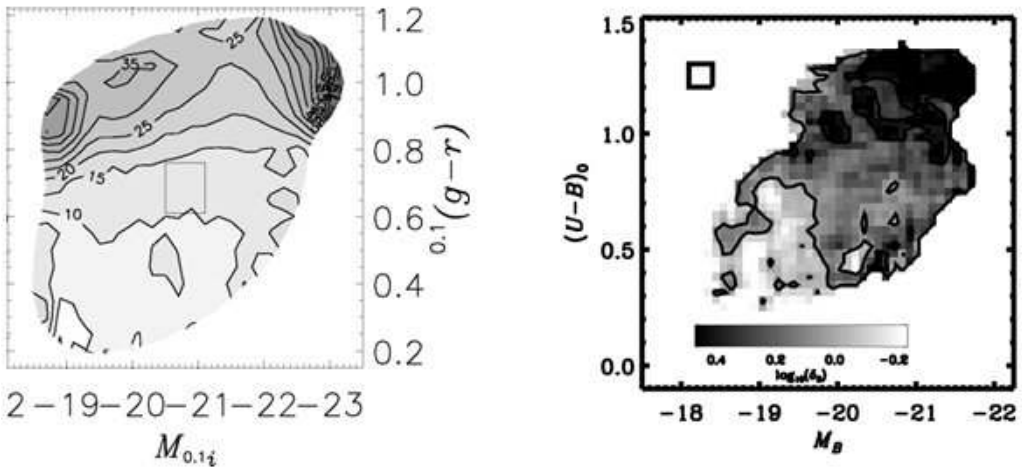

Figure 30: Average overdensity (or "environment") as a function of galaxy absolute magnitude and rest-frame color, at z~0.1 from SDSS (left, Blanton et al. 2005) and at z~1 from DEEP2 (right, Cooper et al. 2006). The overdensity measured is directly proportional to the linear bias. Much smaller environment errors are possible with the larger sample from SDSS, and analyses can be extended to rarer objects like the luminous red galaxies in SDSS (at the upper right corner of that plot), which will be the targets of BAO surveys. With a SIDE-based galaxy survey, we can achieve SDSS-like statistics at z~1, allowing an understanding of bias and its evolution at these redshifts, critical to interpretation of z~1 BAO datasets, while simultaneously providing critical constraints on galaxy evolution.

2) Calibration of large photometric redshift surveys:

Of the proposed spectroscopic galaxy redshift surveys only a few can reach the depth needed to match the large photometric surveys that will be used for Cosmological studies (i~24). Among those, the VIRMOS-VLT Deep Survey (VVDS) and the DEEP2 survey at Keck will provide about 100,000 galaxy redshifts with the required depth and accuracy. It therefore becomes clear that there is a need for an additional ~300,000 spectroscopic galaxy redshifts in the range $0.3<z<1.2$ in the time scale 2010-2015, that is, by the time DES and PanSTARRS will be in production mode. This is on top of the ~100,000 that will be provided by currently approved and funded surveys. We believe SIDE can provide most, maybe all, of these redshifts, as detailed in this document.

3) High-z Clusters of Galaxies:

A cluster follow up spectroscopic survey seems timely to address systematic issues of mass calibration that could alter the interpretation of the next generation of cluster surveys and therefore their cosmological implications for DE. SIDE can be used effectively, taking advantage of its 20' field, for targeted observations of a few hundred high-z (z~0.5-1.5) clusters, to map redshifts for ~1000 galaxies around them, to accurately determine the cluster velocity dispersion and thus the cluster mass via the virial theorem. The high galaxy sampling rate will also allow us to discriminate among dynamical relaxed or not clusters. This has an added value of providing significant information about the cluster outskirts, an important test-bed of galaxy evolution and transformation processes, but also on the evolution of cluster dynamics which in itself is an unanswered question, with important consequences for cosmology and structure formation theories. The dynamical state of high-z clusters will also provide another important parameter that should play an important role in affecting the morphology-density relation (and the Butch-Oemler effect).

These redshift measurements can be done targeting a few hundred of clusters in a given sample (ie, DES clusters or Planck SZ clusters). At the same time as an extra added benefit, we will have the background galaxy redshift distribution, which can be used for strong and weak lensing mass estimations, which however measure only the projected mass. This would be a further excellent tool to test DES, where we only expect to have photometric cluster lensing measures while the cluster mass calibration will be based on statistical weak lensing estimations.

The previous tasks can be accomplished also if a unique SIDE large-area spectroscopic survey goes ahead to study BAO's (according to the previous proposal), in which case a further important science case can be pursued, which is the serendipitously identification of high-z clusters of galaxies in redshift space, independent of photometry. This can prove to be an important task because our "biased" view of cluster identification at high-z's is based mostly on an already placed red-sequence or on ICM X-ray emission. Such searches, however, exclude a priori possible young, late-type galaxy aggregations, from being identified as cluster candidates and thus may provide a biased census of the cluster distribution and thus of the cluster mass function at high-z's which can have important consequences for cosmological tests which use the cluster N(M,z). Indeed, hints in this direction have been found recently in DEEP2 (Gerke et al. 2007).

4) Galaxy and AGN evolution:

SIDE redshift surveys, being either of one unique large-area or of smaller areas will simultaneously provide great amount of information on the demographics of galaxy evolution and their relationship to environment on the ~1 Mpc scales, which appears to very important in order to understanding transformation processes. SIDE can easily achieve 10 times the coverage of a DEEP2 or VVDS surveys, bringing us into a totally new, SDSS-like regime of accuracy of LSS and galaxy property measurements. The IR coverage of SIDE will simultaneously allow a variety of critical diagnostics of SFR, AGN activity, and metallicity at z~1, which makes it really appealing also for galaxy formation and evolution studies. Furthermore, by targeting also deep X-ray imaging fields we will be able to determine the clustering properties and the environment of high-z X-ray AGNs, an issue of current hot-debate, which could help us understand their formation and evolution, but can also be used as probes of the cosmological parameters (eg. Plionis & Basilakos 2007). Of current great interest is also the population of faint, sub-L* galaxies, in the range $0.1<z<0.5$, which are missed by the SDSS and the 2dF. Also, DEEP2, VVDS, and zCOSMOS cover too small

solid angles to get the rare, brighter galaxies, while AGES covers only one field, giving cosmic variance problems.

SIDE spectroscopic SDSS-like surveys of the distant universe -- with many hundreds of thousands of redshifts, and reaching large samples substantially fainter than L_*, will be of immense value, since projects like DEEP2 and VVDS are really only covering the tip of the iceberg at z~1 -- the very brightest galaxies.

We stress that as an added value of any such SIDE based redshift survey, we will also address the many open questions in galaxy formation and evolution, including: When, where, and how did galaxies quench and assemble into today's early-type galaxies? Did star formation cease early in them, or late? What role do AGN, mergers, etc. play in quenching? What has driven the radical decline in SFR since z~1? What fraction of today's galactic disks (Milky-Way like galaxies) were in place at z>1?

5) Constraining Dark Energy with the Evolution of Cosmic Voids:

To accomplish this project a redshift survey at z=1 with contiguous area of ~16 square degrees is optimum to obtain the required void statistics and constrain the value of w with an uncertainty of ~3%. In an ideal case a galaxy number density of $2x10^{-3}$ Mpc^{-3}, similar to the DEEP2 survey is necessary. This gives a total number of galaxies of about 250,000 down to R=23.5 mag. A spectral resolution of about 4000 will be sufficient to obtain reliable redshifts in the near-IR domain (0.7 to 1.2 microns). We believe that 2 hours exposures will be necessary to obtain a S/N of 3 per pixel which will provide not only redshifts but also good quality spectra that will allow to make quantitative studies of the physical properties of galaxies at z=1.

2.6.4 Science cases

We may sum up the various interrelated proposed projects into two main Science cases, each one of which serves a huge number of scientific themes:

- A Broad/BAO survey is to measure its signal in the distribution of galaxies and QSO line-of-sight absorbers up to redshifts z~3.5. In order to achieve this goal, we propose to carry out spectroscopic survey of ~150 deg^2 in order to directly measure BAO's in the radial direction. The data gathered will also serve to study a huge variety of other LSS and galaxy formation and evolution themes, among which we note a few of current interest of our working group: calibration of photometric-z methods, the evolution of galaxy and AGN properties, the clustering evolution of high-z X-ray AGNs and of other mass tracers, the evolution of the cluster mass function and cluster virialization, the void distribution, whose redshift evolution can also be used to derive cosmological parameters. This survey would represent a ~10x advance on current samples at redshifts from z~0.5 to 3.5.

- A Cluster survey is to take advantage of the 20' field of view to map redshifts for ~1000 galaxies around a few hundred high mass, z~0.5-1.0, clusters. These clusters may be drawn from a variety of upcoming samples (e.g. DES or Planck SZ clusters). We can then use the velocity dispersion of the cluster galaxy members to calibrate cluster masses and test their virialization state. At the same time we will have redshifts for the background galaxies (because of the 20' field of view). These can be

used to improve strong and weak lensing mass estimations. This would be an excellent tool to test DES where we only expect to have photometric cluster mass measures, with a cluster mass calibration based on statistical weak lensing estimates (for ensembles of clusters).

2.6.4.1 MOS observing mode

The MOS mode is critical for almost all large-scale structure studies and galaxy or cluster surveys. They cannot cover significant area without it. For BAO studies, it would be important for MOS mode to have as large a field of view as possible. All studies at $z>1.4$ and metallicity or star formation studies at $z>0.8$ would benefit greatly from IR coverage.

2.6.4.2 SIFU observing mode

The principal LSS driver for the IFU mode is searches for counterparts to QSO absorption systems. 0.5' is a reasonable scale for this (as absorbers appear to have an ~100 kpc extent). MOS modes may still be better for this, however, unless blind searches for extended gas are desired, or fiber collision constraints are strong.

2.6.5 Input photometric catalogue: optimum target population

There will be many possible choices of parent catalog for SIDE, thanks to all of the wide-area surveys occurring over the next 5+ years - e.g. DES, LSST and VISTA. It is possible to select separately optimized surveys of $z<0.7$, $z=0.7$-1.4, and $z>1.4$ targets with just gri photometry, as shown by DEEP2; this should not be a problem.

Ideally, targets for the redshift survey could be provided by a large imaging survey contemporary to SIDE with U band coverage, such as PanSTARRS-4. Examples of interesting target samples are: Lyman Break Galaxies (LBG) selected in colour-colour space in the redshift range $2.5<z<3.5$; QSOs in the redshift range $z>2.5$; and field galaxies at redshifts $z>0.5$ (at lower redshifts there is not enough volume for the observations to be constraining enough). All of these require good photometry, including good coverage in the U band, in order to measure photometric redshifts reliably.

A cluster survey could be undertaken with already-available optical cluster catalogues, starting with well-known very rich examples which have X-ray, SZ and/or lensing measurements. For instance, the clusters in the DES should be made public starting around 2012. Note that DES will be measuring not only ~20000 clusters, but also 300 million galaxies and 2000 supernovae by means of a deep survey (up to $z\sim1.2$) of about 5000 square degrees of the southern sky. It is planned to start operation in 2010 and survey the sky for at least 5 years

2.6.6 Target number density and optimal number of fibers

Given the SIDE/GTC field of view and the proposed survey requirement of large area coverage, the magnitude limit needs to be conservatively shallow. According to previous LBG surveys, the space density of high-z objects down to magnitudes $R_{AB}\sim24$ is approximately a thousand per square degree. For QSOs, the space density is around $100/deg^2$

down to g~24.5. For field galaxies at z>1, it is 9000/deg^2 down to R_{AB}~24. For the field of view of SIDE, approximately a tenth of a degree, that would mean having on average 100, 10, and 900 sources per plate of LBG, QSO and field galaxies, respectively.

In order to get an idea of the capabilities of the GTC-SIDE, it took DEEP2, with a multiplexing of ~120 objects at a time and net throughput ~30% on the Keck II Telescope, ~90 nights to obtain 50,000 spectra, targeting 60% of the z>0.75 galaxies to R_{AB}=24.1 (~3 sq/arcmin). This yields a sample with number density ~1/3 of that of SDSS. Therefore, we estimate that for ~10 times larger samples we would require ~1000 fibers (and ~100-150 nights), roughly. Finally, in order to get an idea of the spatial scale that corresponds to the angular size of the FOV and the fiber diameter as a function of redshift, see Figure 31 (for the ΛCDM standard model with h=0.72).

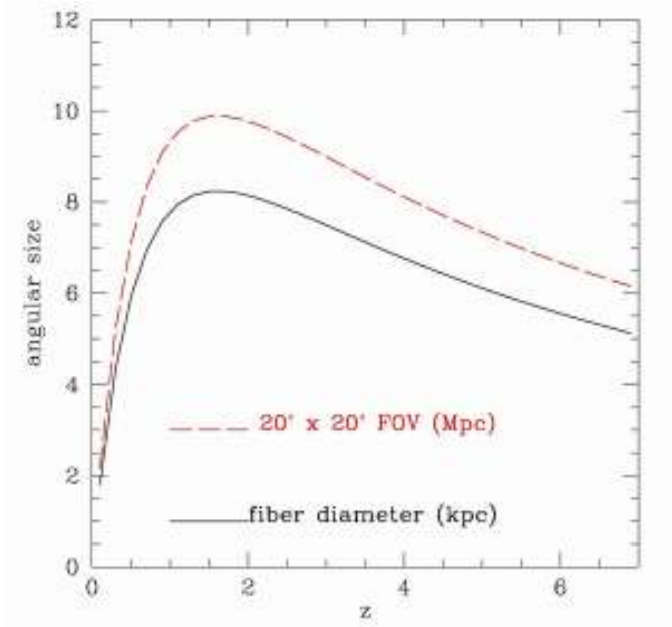

Figure 31: Angular size in Mpc of the SIDE FOV (red dashed line) and of the fiber diameter.

2.6.7 Justification of the spectral resolution and wavelength coverage

In order to be able to use efficiently the radial modes of BAO, a redshift resolution ~0.003(1+z) is needed. For this a moderate resolution R~ 1000 is enough, although R~λ/δλ ~2000 allows splitting of the [OII] doublet for secure redshifts even if that is the only feature seen. Higher resolutions than this help for sky subtraction (as skylines occupy a smaller and smaller fraction of the spectrum), and will also enhance the ability of a SIDE survey to constrain evolution and the spatial variation of the Fine Structure Constant using [OIII] 4959/5007 measurements (Newman et al. 2007). IR coverage is key for z >1.2; e.g. red sequence galaxies are optically faint at these redshifts, and very poorly covered by DEEP2 & VVDS (violating the R or I magnitude limit and/or yielding very poor redshift success because of the lack of photons below ~8500Å).

The wavelength coverage needed for tracking the Lyman break between z=2.3 and z=3.3 is between ~300 nm and ~400 nm, on the bluer edge of the sensitivity of the optical spectrograph, while to explore the redshift range 1.2<z<2.3 with the 4000 Å break, near infrared sensitivity is required, with a wavelength range between ~0.88 μm and 1.32 μm. A blue-sensitive spectrograph can efficiently obtain z's for dust-deficient star-forming galaxies at 1.5<z<2.5 (Steidel et al. 2004), but cannot cover the full population. For QSOs absorbers, one wants to sample the Lyman alpha forest at least in a region between 1050 and 1180A in the QSO rest-frame. This implies sampling from ~3700 A to get down to redshifts z=2.5 to ~6000 A to reach z=4.0. The resolution needed for QSOs is also higher. In principle R~5000 is the best choice but resolutions down to 2000 are also adequate.

2.6.8 Optimum observing strategy and procedure

We focus here on the Broad/BAO survey. According to public calculations performed for both the KAOS (now WFMOS) and the "Thousand Points of Light" projects, a spectrograph like SIDE would be able to measure accurately the redshifts of Luminous Red Galaxies at redshift z~3 with exposures of about one hour. Sampling the quasar Lyman alpha forest at adequate signal-to-noise may probably require longer exposures, although low signal-to-noise is not a show-stopper. Field galaxies observed in the near-infrared may also require longer exposures. Although a proper maximization of the survey would be needed, a good compromise seems to be a 150 deg^2 total area coverage, with ~1,5 hour exposures that would take approximately ~200 nights to complete (~40 nights per year for 5 years). The survey could be run on its own, pushing down the magnitude limit or subsampling lower redshift objects to get on the order of 1000 targets per plate, or could be run sharing the plates with other surveys. A stand-alone survey would require the simultaneous operation of the optical and infrared spectrographs. If this is not feasible, then using only the optical spectrographs would not fill the plate with targets unless z<1 objects are included or the magnitude limit is fainter than R~24. If it only uses the optical spectrographs, a survey can piggyback with other surveys sharing the same tiling. With such a survey design we will obtain information for ~2 x 10^5 LBGs, ~1.5 x 10^4 QSOs and ~10^6 field galaxies in 150 deg^2 in 200 nights. With this sample we expect to determine the sound horizon scale at ~3% for each of the LBG, QSOs absorbers and field galaxies samples at their given redshifts. These would be the best BAO constraints at high redshifts and very important in constraining models predicting variations of dark-energy characteristics with cosmic time; the data would simultaneously provide a wealth of information on galaxy evolution and clustering.

We note that in order to study galaxy biasing, environment and cluster velocity dispersions, it will be necessary to either close-pack fibers (<10" separations, corresponding to ~100 h^{-1} kpc at z=1) or repeatedly cover a selected number of regions with overlapping observations to include both central and satellite galaxies within dark matter halos.

As a complementary tool to design the target selection of objects at high redshift, we will use high-resolution modern N-body+gas simulations of galaxy formation which are the most useful tool to quantify the abundance of objects at different epochs. Large scale simulations which include the most relevant physics of the galaxy formation process are now feasible (eg. the MareNostrum Universe simulation collaboration http://astro.ft.uam.es/marenostrum). The results from these large scale numerical experiments will be used as templates for the most efficient design of the observing strategies with SIDE.

2.6.9 References

Basilakos, S., et al., 2004, ApJL, 607, L79,
Basilakos, S., et al., 2005, MNRAS, 356, 183,
Basilakos, S. & Plionis, M., 2006, ApJ, 650, L1
Blanton, M. R., et al. 2003, ApJ, 594, 186
Coil, A. L. et al. 2007, in preparation
Cooper, M. C., et al. 2006, MNRAS, 370, 198
Cooper, M. C., et al. 2007, MNRAS in press
Davis, M., et al. 2003, Proc. SPIE, 4834, 161 (astro-ph/0209419)
Davis et al. 2007, ApJL, in press
Eisenstein, Hu, & Tegmark 1998, ApJ, 504, L57
Eisenstein et al. 2005, ApJ 633, 560
Gerke, B.F., et al., 2007, MNRAS, 376, 1425
Gilli, R., et al. 2005, A&A, 430, 811
Gomez et al. 2003, ApJ, 584, 210
Gottlober, S. & Yepes, G., 2007, ApJ, 664, 117
Ma, Hu & Huterer, 2005, ApJ, 636, 21
Miyaji, T., et al., 2006, astro-ph/0612369
Newman, 2007, Ap.J., submitted
Newman et al. 2007, Phys. Rev. Letters, in prep.
Padmanabhan et al. 2007, MNRAS, 378, 852
Plionis, M. & Basilakos, S., 2007, arXiv: astro-ph/0701696
Puccetti, S., et al., 2006, AA, 457, 501
Seo, H.-J., & Eisenstein, D. J. 2003, ApJ, 598, 720
Steidel et al. 2004, AJ 604, 534
Yang, Y., et al. 2003, ApJ, 585, L85,
Yang, Y., Mushotzky, R.F., Barger, A.J., Cowie, L.L., 2006, ApJ, 645, 68,

2.7 Solar System

2.7.1 Current status and open questions in the field

Comets

Comets are among the most pristine bodies of the solar system and their studies can give precious hints on the formation of the solar system. They represent the population of small icy bodies in the formation disk. After their accretion at the epoch of the solar system formation, they were either ejected to large distances (5 x 10^4 AU) into the Oort Cloud, or they remained in their formation region, in the Edgewort-Kuiper belt, at heliocentric distances greater than 40 AU. Orbital integrations carried out for 4 billion years (Duncan and Levison 1997) have shown that a disk of scattered objects beyond the orbit of Neptune can be produced. These computations indicate that about 1% of the particles survive in this disk for the age of the solar system, and the objects in this disk could supply all of the observed Jupiter-family comets. Thus, in the history of the cometary observations the observed targets fall in 3 categories: dynamically new comets, long-period comets and short period (or Jupiter Family comets). The 1st ones are those injected in the inner Solar System for the first time since their formation, as it was the case for C/1999 T1 (McNaught-Hartley), C/2001 Q4 (NEAT), C/2002 T7 (LINEAR) or C/2006 M4 (SWAN); the 2nd ones are those with orbital period longer than 200 years as IRAS-Araki-Alcock, Liller 88A, Thiele 85M; whereas the JF comets are the most widely and repeatedly observed (9P/Tempel 1, 73P S-W3, 2P/Encke, 8P/Tuttle, etc) aiming to a meaningful characterization of these bodies.

In pursuit of clues to the origin of the Solar System, routinely observations of available comets must be conducted. Classically, in the optical and near-IR domain, observations of active comets allow us to derive the relative molecular abundances, dust-to-gas ratios, dust colour, gas and dust coma morphology, and other properties, including the dependence of these properties on heliocentric distance, as well as to establish correlations among these properties and others such as dynamical age, visual magnitude, or evolutionary effects.

From the sample available up to date and from a coherent set of ground-based observations, some conclusions can be drawn:

(i) there is no differentiation with depth in the cometary nucleus, although the Deep Impact experiment has shown this statement to be not true, and thus further investigation is needed,

(ii) most comets are very similar to each other in chemical composition,

(iii) the dust-to-gas ratio does not vary with the dynamical age of the comet,

(iv) there is little variation of relative abundances with heliocentric distance, implying that for the species we observe (CN, C_2, C_3, O^1D, NH_2 and NH) the role of density-dependent processes in the coma is small,

(v) there is also little variation from one apparition to the next for most short-period comets,

(vi) there are significant compositional grouping of comets, apparently related to place of formation, the dust-to-gas ratio is correlated with perihelion distance,

(vii) most of CN, most of C_2 and virtually no NH, are produced from grains in the coma rather from nuclear ices.

Beside these conclusions, there are also some evidences, which need further investigations, as

(viii) the mixing between water and other ices occur at the level of grains rather than at the molecular level,
(ix) there must be a large population of comets having very low activity,
(x) data appear to require mixing of cometesimals with different compositions into individual nuclei, with some nuclei containing nearly the full range of compositions while others contain a much smaller range of compositions.

Hence, numerous observations of short- and long-period comets have enabled us to derive ensemble properties of a considerable large sample of comets. However, recent observations of some short period comets as 9P/Tempel 1, the Deep Impact target, or 73P/S-W3, a splitted comet which suffered further splitting during the 2006 approach to the Sun, and of large period comets as C/1996 B2 Hyakutake, C/1995 O1 Hale-Bopp, C/2001 Q4 NEAT have opened a wide panorama to study comets as primitive bodies of the Solar System. No need to say, that the optical observations of comets are much more valuable in the frame of coordinated and multi-spectral campaigns.

Although much insight has been gained in the comprehension of the gas and dust coma, and cometary nuclei, some questions as still remain unanswered. Some of these are: at which depth are the different parent species located? What are the physical parameters (porosity, temperature) of the cometary material near the nucleus surface? Are some species produced directly from icy grains in the inner coma? Is amorphous water ice present inside the nucleus? The answer to these questions would provide constraints to the nature and composition of the material constituting the nuclei, and thus to unveil some of the mysteries of the Solar System formation and evolution.

Planetary atmospheres

Planetary atmospheres offer a wealth of physical phenomena ranging from the atmosphere dynamics to its chemistry and cloud and hazes properties. The variety of atmospheric characteristics spans from the cold and tenuous atmosphere of Mars to the dense and permanently cloud covered atmospheres of Venus and the Giant Planets. The different dynamical regimes, chemistry and thermal properties of these atmospheres provide natural scenarios to test and go beyond our current understanding of the behavior of the atmosphere of our own planet and are essential to the knowledge of Solar System formation and evolution.

2.7.2 Future prospects

2.7.2.1 The next five years

Space missions: ground based support to on-going or future space missions as Rosetta (ESA), Deep-Impact NeXT, EPOXI.

Complementary, that is multispectral, observations to space borne and ground-based observatories.

Regarding space mission to study planets and their environments, SIDE represents a key instrument to provide ground based support to ongoing and approved space missions such as Venus Climate Orbiter (JAXA, 2010-2012).

Additionally NASA has an ambitious program of Mars exploration with dedicated missions every two years. We can list for instance the following missions: Mars Reconnaissance Orbiter (NASA, 2006-2010) and Phoenix (Mars Lander, NASA, 2008).

2.7.2.2 Beyond the next five years

Coordinated observations in situ, thanks to the space missions mentioned previously, and from ground.

Multispectral observations of active comets.

Within the ESA programme, Cosmic Vision 2015-2025, a mission to a minor body of the Solar System seems to be of high interest to the scientific community. Thus, ground based support, as mission planning, and simultaneous observations at the encounter phase can guarantee a nice synergy between space missions and use of large telescopes.

Finally NASA and ESA are closing now their research programs for the decade 2015-2025 which contemplate several missions to explore the Solar System. Some of the likely proposed missions are:

- Venus in Situ Explorer (NASA, New Frontiers program).
- European Venus Explorer (ESA, Cosmic Vision program 2015-2025).
- KRONOS: Saturn atmospheric probe and deep atmosphere and interior remote sounding (ESA, Cosmic Vision program 2015-2025).
- A Mission to Europa and the Jupiter System (ESA, Cosmic Vision program 2015-2025).
- Several missions to Mars from NASA beyond the 2009 frontier.

While the atmospheres of Venus and specially Mars will be systematically observed from spacecrafts the study of the atmospheric phenomena of the Giant planets will largely remain the domain of Earth-based and Earth-orbiting telescopes. This is an area where a 10m telescope such as GranTeCan can greatly contribute to research in this area.

2.7.3 The opportunity window for SIDE

Comets

Optical observations of comet, especially narrowband images to cover typical gas emissions and clear continuum regions, do suffer of a severe problem: to obtain a good S/N is necessary a long integration time (in the order of tens of minutes for a relatively bright comet with integrated V mag ~ 10). This hampers any effort to have a complete 2D map of the inner gas and dust coma during a single run of observations, which at the same time, does not allow us to correlate gas-gas and gas-dust phenomena occurring at short time scales of one or two days.

SIDE mounted at the GTC represents a unique instrument to achieve a complete characterization of the cometary coma in terms of the gas and dust (see Figure 32) morphology (see Figure 33) and production rates.

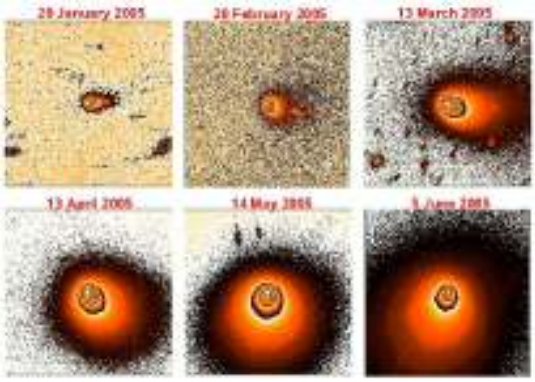

Figure 32: Activity evolution of comet 9P/Tempel 1 (Lara et al. 2006) as imaged with a R Johnson filter. A more meaningful study of the cometary activity can be achieved by using clear continuum regions as well as the gas emission bands.

Figure 33: Coma morphology evolution of comet 9P/Tempel 1 (Lara et al. 2006). They are obtained by processing (with a Laplace filter) the images shown in Fig. 1. Note that the study of the evolution of the different structures with time allows us to retrieve rotational parameters of the nucleus.

This characterization can also provide precious hints on the still unveiled nature of the comet nucleus. 3D spectroscopy of a cometary coma comprises the study of the resonant fluorescence of daughter species as CN, C_3, C_2, NH, NH_2 all of them with strong spectral signatures (bands) in the optical and near-IR range, O(1D) and CI(1D) atomic lines at 630.1 nm and 982.3/985.0 nm respectively, and of clear continuum regions (see Lara et al. 2001; 2004a; 2004b).

Planetary atmospheres

The multiobject spectra capabilities of SIDE can be used to simultaneously obtain spectra of planetary atmospheres at different locations of the planet linked with its meteorology. This allows obtaining a large variety of atmospheric data such as gas composition as a function of latitude and longitude related to atmospheric dynamics, thermal information in the near infrared at night-side on the hot atmosphere of Venus, and characterization of hazes and cloud layers on different planets.

The field of view of the instrument and its other characteristics suit the study of the atmospheres of Venus, Jupiter and Saturn. To a lesser extent, similar scientific objectives can be pursued on Uranus and Neptune.

Planet	**Diameter [arcsec]**	**Fiber cover [km]**	**Percentage over planet diameter**
Venus	10-60	200-1200	2-10%
Mars	4-15	450-1700	7-25 %
Jupiter	45-48	1500	1 %
Saturn	18-20	3300	3 %
Uranus	3.7	6670	13 %
Neptune	2.3	10670	21 %
Titan*	0.8-0.9	3300	64 %

Table 11: Data for planetary atmospheres observations. Assuming the fiber resolution of 1 arcsec each fiber could cover from a small to a significative portion of the planet area.

Table 11 lists the apparent size of the Solar System atmospheres as observed from the Earth. Assuming each fiber in the instrument covers 1 arc second several fibers can be used to spectroscopically map different regions of the planet. Concerning the Giant Planets, Jupiter and Saturn could be covered with enough spatial resolution to allow mid-resolution multi-spectral maps of them. Differentiation of Belt and Zones and specific research over meso-scale atmospheric features such as storms, hot-spots, vortexes and polar hazes should be among the research capabilities of the instrument. The small moon Titan could be observed simultaneously to Saturn with two fibers exploring hemispheric differences expected from seasonal effects. Uranus and Neptune could be covered by a small number of fibers identifying spectra variation with latitude and center to limb variation useful to investigate their cloud and hazes vertical distribution. The terrestrial planets Mars and Venus will constitute intermediate cases in resolution. For Venus, which orbit is interior to the Earth the best resolution would be obtained observing the night-side of the planet with low phase angles.

2.7.4 Science cases

Comets

As previously mentioned, species produced by photodissociation of others directly produced at the nucleus surface or from the grains have strong emission bands in the optical and near-IR range. From the luminosity of these emissions, one can derive:

(i) The production rate of these daughter and its most likely parent species (as done in Lara et al. 2001).

(ii) The scalength (or lifetime) for the parent and daughter species, provided the S/N is high at large distances from the optocenter. This distance depends on the selected species and with the present FOV of SIDE at its SIFU mode, only the daughter lifetime will be retrieved for C_3, C_2, NH and NH_2. The CN has an extremely long lifetime (>200 000 s), which means that for the typical expansion velocity of the gas of 0.7-1 km/s, we would need a FOV of about 140000 km. However, the advantage of having radial profiles at as many as 360 different projected directions on the sky can shed light on the interaction of the gas and dust meaning that some dust can be the precursor of species as CN and C_2 (see Lara et al. 2003).

(iii) In the case of a close Earth approach of a comet (meaning a very high spatial resolution) it will be possible to measure the expansion velocity of the gas and dust by studying the temporal evolution of the gas emissions intensity in small apertures (see Keller et al. 2005 and Kueppers et al. 2005).

(iv) Morphological study of the inner gas and dust coma. Evolution of the structures, if they exist, to retrieve information on the rotational parameters and state of the comet nucleus (Lara et al. 2006).

Table 12, Table 13, Table 14 and Table 15 list these species and continuum regions together with the wavelength ranges where their emission is placed. From a simple look to those tables, it is easy to realize the importance of an instrument as SIDE. The narrowband imaging of all of these transitions is impossible to carry out for two reasons: there are not available filters for all the bands, and the time required to have a complementary characterization of the gas and dust coma of an active comet is much longer than usually obtained at the telescope.

CN transition	**Δv =0**	**2-0**	**3-1**	**1-0**	**2-1**
Emission band	**3830-3905**	**7822-8039**	**8032-8213**	**9109-9323**	**9342-9528**

Table 12: CN transition and emission bands.

C_2 transition	Δν =0	Δν=-1	Δν=-2	Δν=-3
Emission band	4860-5210	5373-5667	9109-9323	9342-9528

Table 13: C_2 transition and emission bands.

NH_2 transition	(0,10,0)	(0,8,0)	(0,7,0)	(0,6,0)
Emission band	5673-5766	6274-6407	6600-6778	6960-7051

Table 14: NH_2 transition and emission bands.

Species	Emission band (A)
C_3	3975-4150
CH	4280-4340
Cont1	4820-4850
Cont2	5200-5250
Cont3	4390-4500
Cont4	5800-5845
Cont5	3700-3815
Cont6	6800-6900
Cont7	8500-9000

Table 15: Species and emission bands.

From these gas emission bands, one can retrieve the production rate of these species. A'Hearn et al (1995), from a survey of 85 comets, concluded that the ratio $Q(CN)/Q(C_2)$, Q being the gas production rate in s^{-1} derived for each comet allows to classify them as rich, classical or depleted in carbon bearing species, and that this classification seems to change with heliocentric distance (Schulz et al. 1998).

In terms of the dust analysis, the 3D spectroscopy also enables us to analyze the behavior of the continuum radial profiles versus the projected cometocentric distance ρ, at different azimuthal angles, as indicative of steady flow of long-lived grains ($B \sim \rho^{-m}$), B being the surface brightness and m ~1), or otherwise if m ≠1 there might be indications of fragmentation processes, evaporation of icy grains or non-steady dust production rate. See Figure 34.

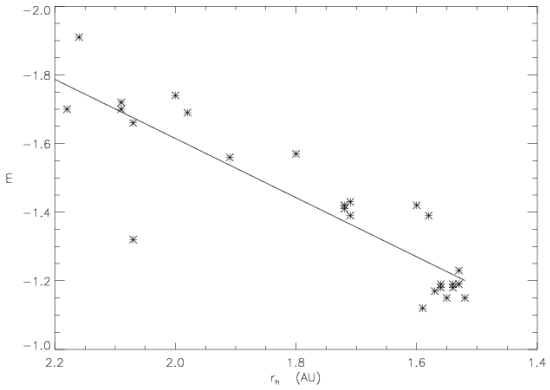

Figure 34: Values of the slope derived from linear fits of radial profiles of continuum surface brightness vs. projected cometocentric distance ρ at distances 3.1 < log ρ < 4.5, i.e. ρ between 1200 and 35 000 km, at the comet distance. Standard deviation of these fits is always below 1%. Solid line, representing a linear fit of m(rh) vs rh (standard deviation 8%) is included as merely indicative of such a behaviour.

Beside this dynamical analysis of the dust, color maps can be retrieved as several (to many) continuum regions can be selected from the spectra. From the color of the dust measured in the wider spectral range (from the visible to the near-IR) with the help of a radiative scattering model, it is be possible to obtain scattering of the dust, and hence some information on its nature (size distribution, albedo, chemistry...) (Kolokolova et al 2001, Icarus 153, 197). The observations will allow to detect spatial and temporal variations in the dust color (possibly due to its fragmentation and/or sublimation of its components), and provide a unique opportunity to study the evolution of cometary dust with nucleocentric and helocentric distance (see Figure 35).

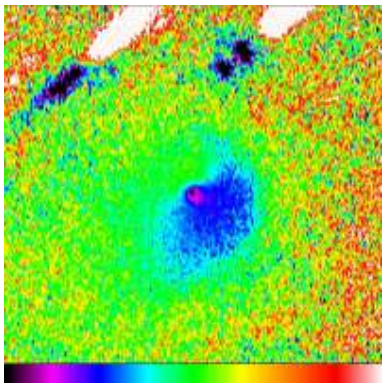

Figure 35: Two-dimensional colour map of the dust in the coma of 9P/Tempel 1 on July 4, i.e., ~14 h after impact. The look-up table is linear between 0 and 30% reddening. The FOV is 60000x60000 km at the comet distance centerd on the nucleus.

One more task that can be worked out with this instrument is obtaining comet nucleus composition and structure based on the characteristics of cometary dust. The high--resolution maps of cometary comae show that their colour and polarization experience dramatic changes in the near nucleus region (see e.g. Jockers, 1997). This leads to the conclusion that the cometary dust observed far from the nucleus represents not the original cometary material but the material processed by the solar radiation. The most likely change of cometary dust is

sublimation/destruction of its volatiles, ice and organics. Studying the changes that appear in the near--nucleus coma we can cautiously extrapolate the properties of cometary dust to the nucleus and obtain its characteristics. The higher the spatial resolution of such observations is the more correct characteristics of the nucleus material can be obtained. The methods that can be used for such extrapolations have already been developed. They include methods based on spectrophotometric long-slit observations of comae (Kolokolova et al., 2001b), simultaneous polarimetric and colorimetric imaging of comae (Kolokolova et al., 2001a), and on study of evolution of the near-infrared organic and mid-infrared silicate features (see, e.g. Hayward et al., 2000).

Another science case which would benefit from the 3D spectroscopy is the search for organic grains in cometary comae. Comets may have played an important role in depositing the organic matter that, between 4.6 to 3.6 billion of years ago, allowed the formation of life on the primordial Earth. Indeed the heavy cometary bombardment on the primordial Earth is believed to have deposited in only 100My 10^{16}-10^{18} kg of organic matter. For that reason the search of complex organic molecules in comets is one of aims pursued with ground- and space- based observations, as well as in situ experiments on board space missions.

During the last years, thank to new instrumentation and also because of fortunate passage of some bright comets, many complex molecules in the gas phase has been discovered both in the radio region, by detecting they rotational transitions, and in the near-IR by detecting their ro-vibrational transitions region (see for example Bockelée-Morvan et al., 2006; Crovisier et al., 2004; Mumma et al., 2003). However a large quantity of organic matter may be under the form of solid, as grains or embedded in silicate grains. The flyby mission of the Giotto spacecraft to the Halley comet more than two decades ago, revealed for the first time organic grains, as for example the so-called CHON particles. Those are tiny particles constituted by Carbon, Hydrogen, Oxygen and Nitrogen. It has been evaluated all the organic grains can contains almost 50% of the mass of organic matter present in Halley (Fomenkova, 1999).

The organic grains are believed to be also the responsible of the distributed source of gas in the comae. Indeed, in some comets, it has been observed that some parent molecules do not originate directly from the nucleus, but from some kind of distributed source. This distributed source cannot be another more complex molecule, a grand-parent, because its spatial distribution is not that of a grand-parent. For example a great part of formaldehyde in comet Hale-Bopp was produced from a distributed source, that has been suggested (Fray et al. 2006) to be the Polyoxymethylene (POM), a formaldehyde polymers. Recent results from the Stardust mission have shown that Polycyclic Aromatic Hydrocarbons (PAH), a large chain of Carbon and Hydrogen, are present in the cometary dust grains collected in the coma of comet Wild and returned to Earth (Sandford et al., 2007).

The spectroscopic detection by remote observation of those organic grains is extremely difficult because they scatter in large spectroscopic bands and their emission is always merged in the continuum emission of the normal refractory grains of the coma. It would be necessary to subtract the spatial distribution of the dust and gas spectra from the cometary spectrum in order to recover the spectrum of the possible organic grains. However this is not possible for normal long slit spectra, because the spatial distribution of the dust and gas emissions along the slit is *a priori* unknown. Our group developed a technique that allows to disentangle between emission of supposed organic grains from the refractory in images free of gas emission. The method is based to the assumption that most of organic grains will sublimate with a certain lifetime under the effect of solar radiation. So their profiles along the

nucleocentric distance (ρ), in the inner part, will be much steeper than the canonical ρ^{-1} of the normal dust. But this check can be only done on images in order to take into account of asymmetries in the coma (as those due to jets, fans…).

With this method applied on image observations with narrow and broad bands filters in regions free of gas emission, it has been possible to detect sublimating components in two comets: C/1999 WM1 and 9P/Tempel 1 (Tozzi et al. 2004; Tozzi et al. 2007), over the 6-7 exhaustively studied comets. As already mentioned, it is not possible to recover the spectrum, but only the scattering efficiency (the Af) at the central wavelengths of the filters used. By comparing this scatter efficiency vs wavelength with that of possible candidates, computed with a scattering model, it is possible to have hints on the composition of these sublimating components. In Figure 36 it is shown an example of the scattering efficiency of the sublimating components (dashed line), as detected in the comets 9/P Tempel 1, compared with that of the normal dust (full line).

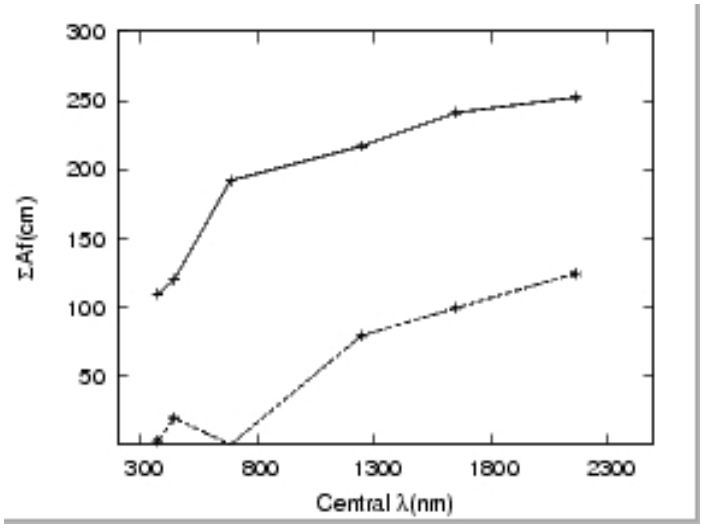

Figure 36: Scattering efficiency of the sublimating components (dashed line), as detected in the comets 9/P Tempel 1, compared with that of the normal dust (full line).

Only with a full spectrum of the sublimating component it would be possible to have a more sure identification of its nature. It is important to note that, even with the positive detection in two comets, there are still many questions to be understood that only with systematic observations of as many as possible comets can give clearer idea. For example why the detection has been only for these two comets, that moreover belong to different dynamical origin? Indeed C/1999 WM1 is a long period comet that originates from the Oort cloud, while 9P/Tempel 1 is a Jupiter Family Comet, originating from the Kuiper belt.

Only with a 3D spectroscopy, as that possible with SIDE mounted at GTC, it will be possible to recover the spectrum of any possible sublimating component. Indeed by reconstructing the images in each spectra bin of SIDE, it will be possible to separate the emission of the sublimating component from that of the normal refractory dust. Note that, while in the visible region it will possible to get the spectrum of the two components of the grains only in the regions free of gas emissions, the separate spectra can be fully recovered in the near-IR region, because here the emission of the gas is negligible. It will be then possible to compare

the recovered spectra with those of the possible candidates, obtained in laboratory, in order to identify the nature of these grains.

An approximate estimate of the dust production rate can be done by means of the customary Afρ parameter (A'Hearn et al. 1984) where A(θ) is the Bond albedo for the particular scattering angle, θ, of the observation, f is the filling factor of the grains in the FOV (number of grains per unit area times their mean-cross section divided by the area of the field of view), and ρ is the radios of the assumed circular field of view. The quotient $Af\rho/Q(H_2O)$ will indicate us, in a very approximate way but widely used, whether the nucleus of the observed comet is gas or dust enriched.

Planetary atmospheres

Venus: Venus is an Earth-like planet completely covered by clouds which circulate the planet at 65 km altitude. Its dense atmosphere reaches 90 bar pressure at the surface and 490 K due to a runaway green house effect. Because of the high temperatures the planet lower atmosphere is observable during night-side at infrared wavelengths. Traditionally, ground-based observations of the lower clouds of Venus have been obtained at 2.3 microns but the same clouds are observed at a narrow window centered at 1.74 microns (Allen and Crawford, 1984; Crisp et al. 1989).

There are other observation windows that can be used to access the surface and the lower atmosphere (see Table 16). The high-resolution spectra at different locations will provide information ranging from surface composition to atmospheric dynamics and cloud properties and lower atmosphere chemistry.

Night-side emissions are also observable at low phase angles and attempts to map them have been performed from the ground. The most intense night-side emission occurs at 1.267 microns (Connes et al. 1979) and is due to the de-excitation of oxygen molecules formed in the lower thermosphere at 100 km height. Other associated oxygen molecular emissions have been found at 1.58 microns but it is much weaker. Observations and characterization of these emissions are expected to provide a link between the dynamics of the upper clouds observed with CCD cameras in the ultraviolet at a 60-70 km height level and the lower thermosphere at 90-100 km heights (Bougher et al. 1997; Lellouch et al. 1997). The oxygen night-side emissions are also linked to the Sun's activity because free oxygen atoms are freed in the upper atmosphere by the ultraviolet flux from the Sun. The oxygen emissions from Venus are extremely variable in time and intensity and provide a puzzle in our current understanding of this atmosphere.

Wavelength (nm)	Day or night-side	Emission source	Processes
350-420	Day	Upper cloud deck and hazes	Reflected light
400-650	Night	Upper atmosphere	Herzberg II O2 airglow
558	Night	Upper atmosphere	Emission from atomic oxygen
850 and 900	Night	Surface	Thermal emission
800-990	Day	Lower limit of the upper cloud	Reflected light
1010	Night	Surface	Thermal emission
1100	Night	Surface	Thermal emission. Good for topography information
1180	Night	Surface	Thermal emission. Information about highest mountains
1269	Night	Upper atmosphere (90-100 km) + Deep clouds	Oxygen airglow mixed with emission from the lower atmosphere modulated by the lower cloud
1310	Night	Deep clouds	Thermal emission modulated by absorption over higher clouds
1740	Night	Deep clouds	Thermal emission modulated by absorption over higher clouds. Very high contrast

Table 16: Main observing windows in Venus within the range of the SIDE instrument.

Mars: Mars spectrum in the visible and near infrared is dominated by absorption features from O_2, H_2O and CO_2. Surface composition has been inferred from infrared spectroscopy onboard spacecraft missions, most notably with the OMEGA instrument on board Mars Express. The north is made largely of a silica-rich volcanic rock (felsic) and the south of basaltic rock relatively poor in silica (mafic); the soil and surface layer of exposed rocks contains oxides of iron, which give the planet its reddish color. From the spatial resolution of the fibers in the SIDE instrument and the spectral resolution it seems difficult for SIDE to significantly advance in this information. However and similarly to Venus, Mars presents a wealth of non local thermodynamic equilibrium emissions that can be characterized and mapped with an instrument such as SIDE. In particular, Mars spectrum shows the signature of the 1.267 microns oxygen emission. Mars atmosphere is subject to seasonal effects with large-scale sublimation and condensation in the polar caps and periods of large-scale dust storms that can grow to gigantic storms that cover the entire planet. In these periods the

surface upper layers may be altered and the dust particles might be characterized by ground-based spectroscopy.

Jupiter and the Giant Planets: The spectrum of Jupiter in the range of 0.4 to 1.7 microns is dominated by Rayleigh scattering on blue wavelengths and methane absorption at wavelengths longer than 600 nm. Ammonia gas presents interesting absorption bands at 552, 645, 790, 930, and 1030 nm but the spectrum at 600 to 1.7 microns is dominated by methane absorption lines. Spectroscopy at short wavelengths can be used to investigate the nature of the chromophore agent which gives Jupiter and Saturn their characteristic brownish color and its link whit the atmospheric dynamics in particular locations such as Jupiter's Great Red Spot.

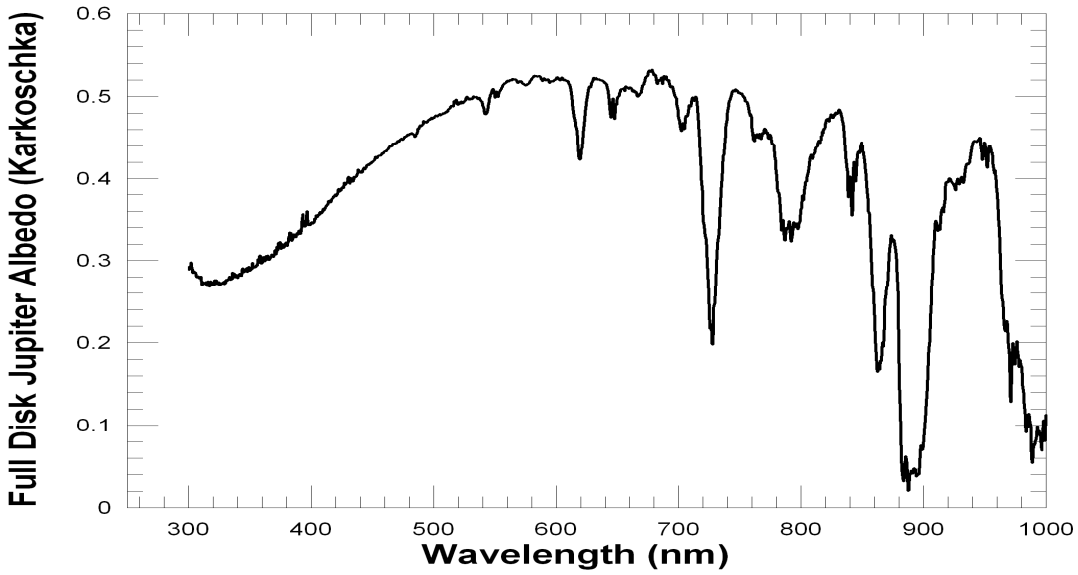

Figure 37: Jupiter spectrum showing distinctive bands due mainly to methane and ammonia gas (Karkoschka, 1998). MOS can be used to obtain spectra at different planetary locations (ie. The Great Red Spot, the Red Oval BA the Equatorial Belt and polar latitudes obtaining data that can be used to characterize the physical properties of haze and cloud particles and altitudes.

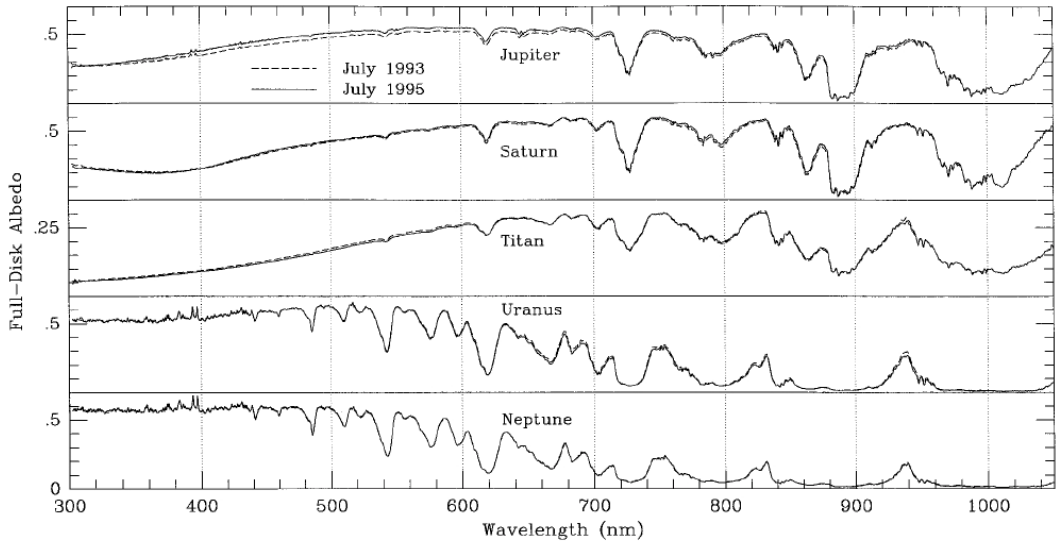

Figure 38: Full-disk albedo spectra of Jupiter, Saturn, and Uranus at 0.4 nm spectral resolution (Karkoschka, 1994, 1998).

Titan and Giant Planets satellites: Titan is the largest moon of Saturn and the only satellite on the Solar System that presents an atmosphere. Its surface temperature is only 90 K. The atmosphere is composed of nitrogen and a 5% of methane that can condense on this cold atmosphere driving a methane meteorological cycle. Titan is also covered by a permanent dense haze of hydrocarbon particles located at high altitudes and formed by the interaction of the methane with the solar ultraviolet radiation. Titan is one of the bodies in the Solar System with large astrobiological interest and has been visited in situ by the European spacecraft Huygens on January 2005. Although the apparent size of Titan is only slightly less than one fiber, two of them can be used together to obtain spectra of both hemispheres. Because Titan's axis is tilt 27º it presents seasonal variations as well as different cloud and hazes structures in both hemispheres.

Both Titan and other Giant Planets satellites without atmospheres can be observed essentially at no cost when also observing their central Giant Planet to obtain the albedo at a wide range of wavelengths.

2.7.5 Input photometric catalogue: optimum target population

Comets at heliocentric distances which have already developed a gas and dust coma. This distance is not firmly established, and there are comets which are highly active at ~3 AU (as S-W) whereas others show very low level of activity even at perihelion.

A bright comet with a favorable perihelion passage is recovered every 2 to 3 years, representing a unique opportunity for a thorough investigation of the gas and dust coma of the comet, and thus to put some constraints on the unknown nature of the nucleus.

2.7.6 Target number density and optimal number of fibers

Observations of active comets do not need an optimal number of fibers as the mode to be used is SIFU and it is constrained by the technical feasibility. Our needs are covered with the smallest possible size of the fibers and the largest number of fibers to have a large FOV. For example for the instrument set to ≈30“ x 30” with individual fiber size of 1’’, spatial resolution for an active comet at a geocentric distance of 1AU is ~725.3 km, and a total FOV of ~21,800 km. Most of the detectable structures in the dust coma are confined to ≤ 20,000 km, whereas the gas structures can span larger distances.

Problem: small FOV will not allow us to retrieve the scale length (or lifetime for an assumed velocity) of daughter species whose theoretical lifetime is larger than 30’. For very active comets at large geocentric distance, it would be possible to retrieve the lifetime for species as CN or C_2. On the other hand, lifetime of parent species mostly determines the shape of the profiles in the inner coma ($\rho \leq 20000$ km), thus enabling us to constrain the nature of the parent species whose photodissociation gives rise to the daughter species mentioned above.

2.7.7 Justification of the spectral resolution and wavelength coverage

Our scientific objectives are well covered with the proposed spectral resolution for SIDE as we can either select very wide emission bands or atomic lines of oxygen and carbon to characterize the dust and gas coma of the comet.

For the scientific objectives to be achieved in the study of planetary atmospheres and reflectance of the satellite surface, the spectral resolution provided by the instrument is appropriate. An important topic on planetary atmospheres that cannot be envisaged by SIDE is the study of the stratospheric and mesospheric winds by Doppler effect of the spectral lines. A resolution of ~100 000 (in the optical range) is necessary and it is well beyond the SIDE capabilities.

2.7.8 Optimum observing strategy and procedure

Comets

The gas and dust coma of an active will fill the FOV of the SIDE instrument in its SIFU mode, hence the acquisition of sky background cannot be done by the auxiliary fibers located at the edges, but pointing the telescope at several tens of arcminutes of the optocenter.

The real value of the 3D spectroscopy in the case of cometary science is when absolute flux calibration can be done, which means that the acquisition of the spectrophotometric standard stars has to be as accurate as possible such that the star flux falls in one fiber. If the flux calibration cannot be achieved, it is still possible

(i) to retrieve lifetime of parent and daughter species,

(ii) to study the behavior of the surface brightness profiles,

(iii) to detect the absence or presence of sublimating grains,

(iv) to carry out a morphological study of the coma (if structures are present and they are persistent and monitored, rotational parameters of the nucleus can be retrieved).

2.7.9 References

A'Hearn , M., et al. 1984, AJ 89, 579.
A'Hearn, M.F. et al. 1995, Icarus 118, 223.
Allen, D. A. and Crawford, J. W. 1984, Nature 307, 222.
Bockelée-Morvan, D., et al., 2006 in Comets II, 391, ed. Arizona press.
Bougher, S.W., et al. 1997, in Venus II: Geology, Geophysics, Atmosphere, and Solar Wind
Connes, P. et al. 1979, ApJ 233, L29.
Crisp, D., et al. 1989, Science 246, 506..
Crovisier, J., et al., 2004, A&A 418, 1141.
Duncan, M.J. and Levison, H.F. 1997, Science 276, 1670.
Hayward, T.L. et al 2000. ApJ 538, 428.
Fomenkova, M.N., 1999, Space Science Rev. 90, 109.
Fray et al. 2006, Icarus 184, 239.
Jockers, K. 1997, Earth, Moon and Planets 79, 221.
Karkoschka, E. 1994, Icarus 111, 174.
Karkoschka, E. 1998, Icarus 133, 134.
Keller, H.U. et al. 2005, Science 310, 281.
Kolokolova, L. et al. 2001a Icarus 153, 197.
Kolokolova, L. et al. 2001b, J. Geophys. Res. 106 (E5), 10113.
Kueppers, M. et al. 2005, Nature 437, 987.
Lara, L.M. et al., 2001, Icarus 150, 124.
Lara, L.M. et al., 2003, A&A 399, 763.
Lara, L.M. et al., 2004a, A&A 422, 717.
Lara, L.M. et al., 2004b, A&A 423, 1169.
Lara, L.M. et al., 2006, A&A 445, 1151.
Lellouch, E., et al. 1997, in Venus II: Geology, Geophysics, Atmosphere, and Solar Wind Environment. S.W. Bougher, D.M. Hunten, and R.J. Philips Editors *The University of Arizona Press*, Tucson (1997).
Mumma, M., et al., 2003, Adv. Space Res. 31, 2563.
Sandford et al., 2007, Science 314, 1720.
Schulz, R. et al. 1998, A&A 335, L46.
Tozzi et al. 2004, A&A 424, 325.
Tozzi et al. 2007, A&A submitted.

2.8 Stellar Physics

2.8.1 Current status and open questions in the field

Stars are fundamental constituents of galaxies. The stars formed in early times keep a fossil record of the first days in the Galaxy. The past SFH is recorded in the abundances of stars of different age and in the subsequent generation of stars. The dynamics of the galaxies, including mergers, tidal interactions and other effects are recorded in the dynamics of stars and stellar systems, like stellar streams and globular clusters. Massive stars, through their strong radiation fields and winds strongly influence the chemical and dynamical evolution of galaxies, while the behaviour of the IMF at very low masses has still to be confirmed as is crucial to understand the formation of planetary systems. Also the endpoints of massive stellar evolution (NS, BH) play an important role in the production of high energy and very-high energy radiation through accretion processes. The existence of intermediate mass BHs (IMBHs) is still an open issue despite the recent detection of several point sources with $L_x \sim 10^{39}$-10^{41} ergs/s in Local Group galaxies. They may represent the seeds from which supermassive BHs have formed in the core of galaxies.

The dynamics of systems like HMXRB and microquasars may give us the clues to understand systems like the AGNs and the environments of supermassive black holes in galaxies, while the UV radiation of very massive stars is crucial to understand the ionization of such systems and the behaviour of star forming regions, starbursts and superclusters.

Therefore it is clear that stars and stellar systems, being the fundamental blocks that form galaxies, are crucial to understand the formation, structure and evolution of galaxies and galaxy systems. The light we see, even from the farthest galaxies, comes from their stars. Interpreting the Universe at any z means interpreting the light coming either from single stars or from a combination of millions of them.

Open questions in stellar physics therefore seriously limit and compromise our understanding of the Universe. A few open questions, that need large telescope and databases to be answered are:

- Is there an upper IMF cut-off?
- Does the shape of the IMF depends on the physics of cloud collapse?
- Is there a minimum mass cut-off for the formation of substellar objects in isolation?
- How is the mass spectrum of NS and BHs (maximum and edges of the distribution)?
- How is the feedback between massive star formation and galaxy evolution?
- How does the stellar physics and evolution change at different metallicities?
- Are ULXs powered by IMBHs?

2.8.2 Future prospects

2.8.2.1 The next five years

During the next years a number of studies in the optical and IR will probably be finished and will provide a solid base for further studies in the stellar physics domain. A number of images of nearby galaxies have been obtained using the HST (mainly wit ACS, but not only) and surveys like the ARAUCARIA project (Gieren et al., 2004) are providing us with lots of targets for detailed abundances in nearby galaxies.

The IPHAS survey (Drew et al., 2005) has provided us with a lot of emission line objects in the Milky Way, as did the Local Group Census (Magrini et al., 2002) and the Survey of Star Forming Galaxies in the Local group (Massey et al., 2006). In the IR, 2MASS (Skrutskie et al., 1997) provides an excellent basis in the IR and will be improved by UKIDSS. For shorter and larger wavelengths we have access to space data, like the HST, Galex, Spitzer or those to be launched in the near future, like Herschel.

All these surveys provide us with an extraordinary database to explore the physics of the stars and their host galaxies. Therefore we have the targets needed to trace abundance patterns in the Milky Way and nearby galaxies and study the stellar evolution at different metallicities. To exploit these surveys, spectroscopic follow-up capabilities of large and intermediate resolution in 10m class telescopes are needed.

In the last years, we have recognized the existence of important moving groups in the Milky Way, that may reveal the fine details of the galactic dynamics. Spectroscopic work is currently under way in a few limited cases.

The mass distribution of neutron stars (NS) and black holes (BH) has a significant impact in several areas of modern Astrophysics such as constraining the equation of state of condensed matter (EOS) and testing models of supernovae explosion and close binary evolution. And this can be best done in X-ray transients (XRTs), a subtype of X-ray binaries which exhibit episodes of X-ray activity or outburst triggered by mass transfer instabilities in the accretion disc. In the interim, they remain in a quiescent state where the companion star dominates the optical flux. And dynamical studies of XRTs, performed since the onset of X-ray astronomy, have presented the best observational evidences that we have for the existence of stellar-mass BHs, with 20 confirmed cases (e.g. see Casares 2007). But this is just the tip of the iceberg of a hidden population of ~3000 dormant galactic BH binaries which are awaiting to be discovered through new X-ray outbursts.

In addition to the 20 known dynamical BHs, there are ~20 other BH candidates based on their X-ray temporal and spectral behaviour. Unfortunately, they have never been seen to reach quiescence, or they simply become too faint for an optical detection of the companion star, even with 10m class telescopes. However, we have devised (and are currently exploiting) a new strategy to allow the extraction of dynamical information during the X-ray active states. It utilises narrow high-excitation emission lines powered by irradiation on the companion star, in particular the strong CIII and fluorescence NIII lines from the Bowen blend at 4630-40. This technique was first applied to the NS LMXB Sco X-1 and the Doppler shift of the CIII/NIII lines enabled the motion of the donor star to be traced for the first time (Steeghs & Casares 2002). The use of this technique in other X-ray persistent binaries and XRTs in outburst has enabled us to prove the presence of a BH in GX 339-4 (Hynes et al.

2003) and find evidence for massive NS in X1822-371 (Muñoz-Darias et al. 2005), V801 Ara (Casares et al. 2006) and Aql X-1 (Cornelisse et al. 2007). High spectral resolution (R~5000-10000) is mandatory to resolve the sharp CIII/NIII transitions within the Bowen blend.

Despite this progress, our current knowledge of the shape of the BH and NS mass spectrum is biased by low number statistics and clearly many more detections are urgently needed. The strategy for the next few years is twofold (i) full exploitation of the above mentioned techniques (classical dynamical studies of quiescent XRBs and detection of fluorescence lines in persistent XRBs) needs to be continued (ii) alternative shortcuts need to be explored such as the use of the IPHAS catalogue with appropriate diagnostic diagrams to unveil the dormant population of XRBs through their red colours, strong Hα emission and cross-correlation with deep X-ray/NIR/radio catalogues.

The field of substellar objects (brown dwarfs and planets) has exploded dramatically since the discovery of the first systems in 1995 (Rebolo et al. 1995; Nakajima et al. 1995; Mayor & Queloz, 1995). To date, over several hundred brown dwarfs are known to populate the solar neighborhood (with surface temperatures in the interval 2500-800 K), a few tens of isolated planetary-mass objects have been identified in young star-forming regions, and over 110 planets are known orbiting nearby solar-type stars. Many efforts are currently being devoted to this field of research. Underlying this huge interest two major topics of substellar research can be identified: (i) understanding the formation and evolution of brown dwarfs, planets and planetary systems; and (ii) characterizing and understanding the substellar population of the Galaxy (e.g., by pushing the studies toward cooler objects with temperatures below 800 K). SIDE and GTC can make a significant contribution on this field.

2.8.2.2 Beyond the next five years

In five years, many of the above mentioned surveys will be finished, and the exploitation of the huge databases will be ongoing. Observations with the JSWT and Gaia will supply new targets. The exploitation of these data will need spectra of intermediate resolution (R= 5000-20000), very large SNR and large multiplexing capabilities. These spectra should be recorded in the optical, where the expertise, techniques and models of the astronomical community, developed during decades, are more accurate and provide us with a huge amount of parameters.

2.8.3 The opportunity window for SIDE

Few spectrographs are presently well suited for the work mentioned above. Most of them have either too low resolutions (to try to collect as many photons per pixel as possible, but rendering the interpretation of the observations very difficult, as there is no resolution to distinguish between models) or too large (trying to separate individual narrow lines, while for the stellar work the different broadening mechanisms render such very large resolutions unnecessary in many cases), or are not sensitive enough in the blue part of the spectrum (360-500 nm).

We need a spectrograph, highly sensitive both in the blue and red part of the spectrum, with a large multiplexing capability and the optimal resolution to separate stellar lines while collecting large numbers of photons. Table 23, Table 24 and Table 25 make a comparison of

existing and projected spectrographs, and compares them with SIDE. It is clear that the combination properties of SIDE place it in a very favorable position.

2.8.4 Science cases

2.8.4.1 MOS observing mode

The Shape of the IMF

Observations in recent years have allowed major advances in the understanding of the IMF. For stars with masses above the solar mass, the IMF seems to be similar to the original Salpeter (1955) power law up to very large masses (Massey et al., 2003). However, the IMF (in number of stars per unit logarithmic mass interval) flattens below one solar mass and declines in the substellar regime. This means that the IMF in logarithmic units is a peaked function, with a broad maximum at a few tenths of a solar mass (Scalo 1986; Kroupa 2001, 2002). This form of the IMF strongly suggests that Nature has a preference for stars with mass of this order. The amount of mass that goes into stars in each logarithmic mass interval also peaks at ~0.5 $M_{\odot}$, according to the approximation suggested by Kroupa (2002). Determinations of the IMF tend to find very similar results in many different star-forming environments. No clear dependence has been found on any plausibly relevant astrophysical parameter, such as metallicity.

In view of this, some authors have speculated that this characteristic mass is determined by basic physical properties of the cloud collapse process that leads to star formation. Larson (2005) has advanced a possible physical reason for the existence of this preferred mass. If this interpretation is correct, there should be little dependence of the IMF on metallicity, but higher cloud temperature in starburst regions may significantly shift the peak mass to higher values. A deficiency in low mass stars (with respect to the standard IMF) in starburst regions would have strong implications for our understanding of the origin of stellar populations.

Even though we cannot resolve the low mass component of starburst regions, we can test this idea by looking at moderately massive open clusters within the reach of GRANTECAN. The extensively studied Orion Nebula Cluster has only ~10^3 $M_{\odot}$ and thus does not really qualify as "massive". Among possible candidates, we note NGC 2244 in the Local Arm and the h Persei cluster in the Perseus Arm. At a distance of 2.1 kpc, h Persei has an estimated mass >3500 $M_{\odot}$ in stars more massive than the Sun (Slesnick et al. 2002). For a standard IMF, this implies close to 4000 $M_{\odot}$ in stars less massive than the Sun (and therefore 8000 such stars). Stars with ~0.5$M_{\odot}$, with expected spectral types in the K5--M0 range, will have magnitudes around V~21. Photometric studies may trace this low-mass population and determine the maximum of the IMF, but confusion with foreground M-type dwarfs will certainly be an issue.

Intermediate-resolution spectroscopy with SIDE of a few hundred photometric candidates will allow the identification of actual members via the detection of the LiI 6707Å line, which is only present in young stars. Relatively low resolution (R~ 3000) and moderate SNR (~60) will be enough to separate cluster members and obtain a significant statistical inference of how many photometric candidates are actually cluster members.

The Population of Substellar Objects

SIDE also presents various advantages to study brown dwarfs and planets. First of all, these cool objects are brighter in the wavelength interval 0.7-2.5 micron than in the optical, and SIDE will be able to obtain nearly simultaneous spectra at both visible and near-infrared wavelengths up to 1.7 micron. The spectral resolution of R=2000 (optical), 2800 (NIR) and 5000 (both optical and near-infrared) is sufficient for the analysis of the objects' physical properties, like surface temperature, gravity, and metal content because there are many sensitive atomic and molecular features (sodium, potasium, FeH, methane, water vapour, ammonia) that can be used for the diagnostics.

Furthermore, the MOS facility of SIDE will lead to obtain spectra of many substellar objects in one single shot when studying "concentrated" populations as for example, stellar clusters and young star-forming regions. Although other projects will obviously benefit from the SIDE MOS facility, this is quite relevant in the case of substellar objects because of their intrinsic low-luminosity nature. Long exposures are expected even in large-diameter telescopes. Therefore, plenty of time can be saved using the MOS mode for the spectroscopic study of the brown dwarf and planetary populations of young clusters. These studies are of critical importance to determine an accurate initial mass function and whether there is a minimum mass cut-off for the formation of substellar objects in isolation.

Massive Stars in Nearby Galaxies

Metallicity plays a key role in the physics of the Universe, particularly in the structure and evolution of stars and galaxies. However, it varies largely with spatial location and time. Processes in the early Universe took place in a low metallicity environment (Pettini 2004) and even in the local Universe there are systems like I Zw 18 with very low metal content (Skillman & Kennicutt 1993). To understand our Universe we therefore have to know the dependence of the relevant physical processes with metallicity. Yet, our knowledge of this dependence is rather limited in many cases.

Massive stars are central objects to the chemical and dynamical evolution of galaxies. In the course of their evolution they contaminate their surrounding medium through their stellar winds. This contamination depends on the composition of these stellar winds, that changes with evolution when the star moves away from ZAMS passing through the stages of supergiant, LBV, RSG and WR star (depending on the initial stellar mass and subsequent evolution). Even the nature of the compact object after the SN explosion will depend on the stellar wind, as it will modify the relation between the initial and final masses (Woosley, Heger & Weaver 2002). It is clearly of primary importance to know the behaviour of the stellar winds with metallicity.

The theory of radiatively driven winds is presently the standard theory to explain the winds of massive stars. Its prediction that the mass loss rate scales with Z^{α}, with α roughly 0.7-0.8 (Vink et al., 2001; Kudritzki & Puls 2000; Mokiem et al., 2007) has been adopted as a standard result, widely applied to problems of stellar evolution and thus incorporated into models of galactic chemical evolution (Maeder & Meynet, 2001; Carigi et al., 2005; Chiappini, Matteucci & Meynet, 2003). Confirmation of this prediction and of the extension of the theory towards very low metallicities (Kudritzki 2002) is one of the most important open questions in the field of massive stars.

Taking advantage of the high luminosities of massive blue stars, that allow us to obtain their spectra even at large distances, there have been a number of spectroscopic programs aimed at massive stars in galaxies of the Local Group (LG) and beyond using 4 and 10m-class telescopes (Keck, VLT, WHT). The major one, the FLAMES Survey of Massive Stars (PI S.J. Smartt) has systematically investigated the metallicity effects in a large number of massive OB stars in the Galaxy and the Magellanic Clouds (Evans et al. 2005; Mokiem et al. 2006; Mokiem et al., 2007). First results indicate an agreement with the theory of radiatively driven winds at high luminosities (log $L/L_{\odot} > 5.2$), but at lower luminosities the SMC stars have wind momenta lower than predicted (Bouret et al. 2003; Mokiem et al., 2006). While the effect may also be present in some Galactic stars (see the analysis of 10 Lac by Martins et al. 2004), it seems to be more generalized for SMC stars. The reason of this apparent breakdown of the theory is unknown, and whether it has a metallicity dependent threshold luminosity (thus initiating the wind at higher luminosities for lower metallicities) is an open question.

However, even the SMC however has a relatively high metallicity as compared to many other extragalactic systems. Therefore, we need to extend our results to lower metallicities. Fortunately, the Local Group offers systems of very low metallicity, like IC1613, Sex A or Leo A. But to analyze a large number of low metallicity stars in these galaxies we need a multiobject spectrgraph with blue sensitivity (because most stellar parameters and abundances are determined from the 400-700 nm regions) at R≥ 5000 (because the low metallicity decreases the contrast). This spectrograph has then to be attached to a 10m telescope and should be able to obtain the spectrum of a V= 20 star in 8-9 hours. With the simultaneous observation of about 100 stars per run we would be able to completely characterize the massive stellar contents of a Local Group galaxy (except the large spirals M31 and M33) in just 2-3 observing runs, covering the behaviour of stellar physics in more than a decade of metallicity.

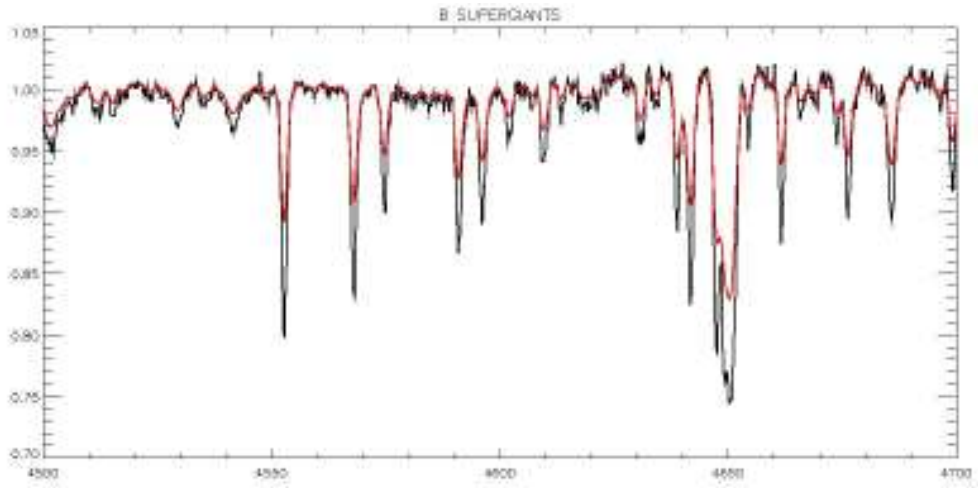

Figure 39: The spectrum of a B supergiant degraded from R= 10000 to R= 5000. We can see that many important spectral features begin to overlap. Note that when decreasing the resolution, the contrast of the spectral lines decreases as well, which is a very important effect at low metallicities.

Additionally, M31 and M33 are the nearest spiral galaxies, and thus offer an excellent laboratory for the study of galactic structure and for comparison with the Milky Way. In spite of this, no systematic studies of their stellar population have been carried out. The most extensive study in M33 (Urbaneja et al., 2005) contains only 11 stars.

Conveniently oriented nearly face-on and with low reddening, M33 is the obvious choice for investigating the properties of late-type spiral galaxies and their young stellar population. Like many spiral galaxies M33 seems to sustain a radial abundance gradient, previously quantified from oxygen abundances in B supergiants (-0.16±0.01 dex/kpc) and H II regions (Monteverde et al. 2000; Vilchez et al. 1988). The recent investigation on B supergiants in M33 by Urbaneja et al. (2005) which covered a larger spatial extent than previous works, revealed a shallower gradient of -0.052±0.018 dex/kpc with a variation in oxygen abundance from above solar in the center to SMC's at about 7.5 kpc. This result could also be interpreted using a bimodal distribution, yet the interpretations hinge on measurements for the two stars furthest from the galaxy center. The scatter, uncertainties and poor statistics involved in this work do not cancel out the presence of either a radial or bimodal distribution. While the range of metallicities found in B-supergiants agrees well with beat Cepheids (Beaulieu et al., 2006) and the gradient agrees with RGB photometry studies (Tiede at al., 2004), recent work by Crockett et al. (2006) in H II regions yields a lower value for the latter, -0.011±0.012 dex/kpc, indicating a discrepancy between results from H II regions and stars. Nevertheless the studies of Urbaneja et al. and Crockett et al., while being the most detailed to date, analyze only 11 and 13 randomly
distributed objects. This number of targets is insufficient to draw any hard conclusions on the metallicity distribution of M33. Even less stellar studies have been performed in M31. A spectrograph like SIDE, with the same conditions as outlined in the previous paragraph (of blue sensitivity, throughput and resolution), would allow us not only to trace the radial abundance gradient of many species in M33, but to get for the first time a detailed 2D abundance pattern map of two spiral galaxies to compare with theories of galatic structure and evolution (Chiappini et al., 2003; Renda et al., 2005).

Dynamical Studies of ULXs

ULXs (Ultraluminous X-ray Sources) are extragalactic X-ray point sources with X-ray luminosities in the range $L_x \sim 10^{39}$-10^{41} ergs/s, well in excess of the Eddington limit for a stellar-mass BH. They have been discovered over the last decade and tend to be found in galaxies with a high star-formation rate like the Antennae or the Cartwheel. The nature of their compact accretors is one of the big open questions in current astrophysics. Proposed scenarios are super-Eddington and beamed collimated accretion over stellar-mass BHs (King et al.2001) or accretion over IMBHs (intermediate-mass BHs) of 10^2-10^4 $M_\odot$(King & Dehnen 2005). The existence of IMBHs represents an exciting possibility: they may be remnants of collapse in the early universe or result from the collapse of dense stellar clusters and are expected to play a key role in the formation of supermassive BHs in galactic nuclei.. As a matter of fact, the variability and spectra of ULXs point to accreting binaries and there are several cases where periodicities have been reported, although no single dynamical evidence has been yet presented. Possible optical counterparts have been presented in several papers and, in some cases, they turned to be background AGNs (López-Corredoira & Gutiérrez 2006). However, in other cases the observed optical colours and spectra are consistent with OB stars (e.g. NGC 3031 X-11: Liu, Bregman & Seitzer 2002; NGC 5204: Liu, Bregman & Seitzer 2004; NGC 1313 X-2: Mucciarelli et al. 2005) and furthermore,

orbital X-ray modulation has been detected (NGC 3379: Fabbiano et al. 2006). SIDE brings in an excellent opportunity to derive dynamical masses of ULXs with brightest optical counterparts and settle the debate as to whether they contain IMBHs.

Since they tend to be hosted in star-forming regions they are usually contaminated by nebulosity and/or nearby young stars so small size fibers of about 1" are preferred. Only a handful of optical counterparts have been identified and their typical magnitudes are V~23, consistent with OB stars at a few Mpcs (e.g. ULX-1 in M101, X-11 in M81, X-2 in NGC 1313, X-1 in NGC 5204). At such distances, 1" corresponds to a physical scale of ~20 pcs. Although the targets are pretty faint, the estimated orbital periods (for assumed ~20 $M_{\odot}$ companions) are several days so long integrations (without significant velocity smearing) are feasible. The brightest of all, M33 X-7, has shown regular X-ray eclipses and photometric modulation (akin of an ellipsoidal modulation) with a period of 3.45 days. The optical counterpart is a V~19 star, with colours corresponding to a O6III but no dynamical constraints yet (Pietsch et al. 2006, Shporer et al. 2007).

Follow-up of VSOP

There are more than 38,000 known variable stars listed in the latest edition of the General Catalog of Variable Stars (GCVS; Kholopov et al. 1998). Almost 4,000 of these have no spectral type assigned and nearly 2,000 are listed with an uncertain variability type, often because of lack of spectroscopic characterisation. The rate of inclusion of new variables is currently around 500 per year; actually 1,700 between the Namelists 77 (Kazarovets et al. 2003) and 78 (Kazarovets et al. 2006). The true number of new variables is higher though, and this incompleteness of the GCVS will likely increase in the coming decade due to the large surveys that will be performed with both ground-based and space-based telescopes like GAIA. About half of the newly identified GCVS variables have unknown variability type and most of them have no published spectral type. Moreover, many (even "firm") variables have disagreeing designations between different authors and even between different catalogs, e.g. there are frequent disagreements between the SIMBAD database and GCVS. In addition, binarity is rarely detectable unquestionably by photometric data alone. Finally, many designations are taken at face value without questioning the reliability. This unreliability is a major obstruction to many individual studies, and would often require only one "snapshot" spectrum to achieve a major improvement. Of course, single shot spectra would not always be able to reveal binarity or transient phenomena. Even a high-quality light curve analysis can result in wrong conclusions about the nature of an object without spectroscopic confirmation. Therefore, the need for snapshot spectra is clear, and the vast collection of poorly studied variable stars contains many errors in terms of variability type designation, which may in many cases "cover up" some potentially interesting physical phenomena under a wrong and seemingly dull label. Motivated by the situation outlined above, the goals of VSOP are: 1. To obtain the first spectroscopy of all unstudied variable stars, revising spectral and variability types. 2. To process, publish, and make the data available as automatically as possible, facilitating additional science. 3. To generate serendipitous discoveries that will fuel future research. In addition, due to its beginnings as a proposal for an observatory project, VSOP has been designed with a view to both science and observatory efficiency. SIDE is therefore an instrument with which an spectroscopic follow-up survey of GAIA faint variables and other variable stars will be possible. Variable stars with V down to 20 mag and no GAIA spectroscopy will be followed-up in this survey.

2.8.4.2 mIFU observing mode (single or multiobject)

A supergiants in nearby galaxies

A supergiants are the visually brightest stars, reaching Mv ≈ -10, thanks to their large temperatures and radii. Therefore they can be observed at large distances, and spectra of intermediate resolution (10000-20000) can be obtained even beyond the Local Group (Przybilla et al., 2006). This is a relatively short phase (see Maeder & Meynet, 2000) during which the star exhibits a large range of atomic lines in its spectrum, from alpha elements to ion group and s-process elements, etc. Their relative abundance are very dependent on the details of their evolution, in particular to the number and extension of the blue loops of massive stars. They are then an ideal laboratory to test the predictions of stellar evolutionary models in many different galaxies and therefore metallicities and environments and can be used even as distance indicators once we completely understand the physics of their atmospheres. Although their number is scarce (because of the short lifetimes), we expect a large number of them in a entire galaxy (f.e., Castro-Rodiguez et al. find nearly 50 such objects in their preliminary study of NGC 55, a spiral galaxy 2 Mpc away). The difficulty in analysing these stars comes from their narrow lines and crowded spectra, caused by their low rotational velocities and atmospheric densities. Therefore, resolutions from 10000 to 20000 are needed.

Assuming a Mv = -8, A supergiants at 1Mpc (the outskirsts of the Local Group, M31, M33) can be observed at m_v= 17 and at 10 Mpc (already in the Virgo cluster) at m_v= 22. Present rough estimates for SIDE indicate that at R= 15000, the spectrum of a B= 21.7 star can be obtained with a SNR= 5 per pixel in 1 hr, for a seeing of 0.7, quite common in the ORM. Adopting (B-V)=0 and 3 pixels per resolution element, we see that the spectrum of a normal A supergiant in M33 or M31 can be obtained in only 2 hours at a resolution of R= 15000. Even if more than one exposure is needed to cover all the desired lines, it is clear that a multiobject spectrograph of moderate multiplexure factor can cover a large fraction of the A supergiant population in the Local Group galaxies. A supergiants in the Virgo cluster, with their brightest objects having m_v around 21, could be observed in three nights at SNR= 70 and R= 10000, which still allows for quantitative spectroscopy. With a number of IFUs all over the FOV, we could observe individual stars at intermediate resolution in a representative sample of Virgo cluster galaxies, which SIDE would allow to try for the first time.

Luminous Blue Variables in nearby galaxies

Luminous Blue Variables (or LBVs) constitute a short and critical phase in the massive star evolution. During this phase, the star reaches such high luminosities that it sometimes crosses the Humphreys-Davidson limit (or the Eddington limit, from a theoretical point of view). The star becomes unstable, and it is thought to suffer strong outbursts before recovering stability. η Car is an excellent example in our Galaxy.

During the LBV phase, the star is assumed to lose a large fraction of its mass. However, the integrated mass-loss rate, critical for the models prediction of the subsequent stellar evolution, is unknown. Therefore, we don't know the mass with which the star enters its later stages, and in particular its final fate as NS or BH. The analysis of their atmospheric parameters and abundances is expected to give us some clues about this critical phase also at different metallicities. However, only a few such stars are known in the Local Group (Massey, 2003) and their spectra, with strong P-Cygni profiles, are very difficult to analyze.

However advances in model atmospheres during the last decade (see Herrero & Najarro, 2007) have made possible to quantitatively analyze their spectra (f.e., Hillier et al., 2001). Therefore they are a perfect target for SIDE, as the conditions of their observations are very similar to those of A supergiants.

2.8.4.3 SIFU observing mode

Weighing Compact objects in XRBs

Resolving the rotational broadening Vsini of the optical companion in quiescent XRBs provides a direct determination of the binary mass ratio q (Gies & Bolton 1986) which is essential for a determination of the compact object mass. But this experiment is technically challenging as typical values of V sin i are 40-100 km/s, so intermediate spectral resolution (R ~ 10000) in the Hα region is needed. Given the faintness of these objects (V≥18), large telescopes are also required even for the brightest XRTs. Intermediate resolution (R ~ 10000) is also needed to resolve the sharp CIII/NIII components from the Bowen blend at ~4640 Å and trace the orbital motion of the X-ray heated companions in the population of persistent XRBs. Low resolution optical spectroscopy (R~2000) of new XRB candidates, selected from IPHAS (based on their strong Hα emission combined with appropriate diagnostic diagrams) will also be required. The galactic density of XRBs is very low and we do not expect to be affected by crowding. However, atmospheric dispersion is indeed an issue given our wide wavelength range and hence these projects aim for SIFU mode.

Abundance anomalies in the companion stars to XRBs

Companion stars in X-ray binaries have survived a supernova explosion and hence they are likely to be contaminated by nucleosynthesis products of the ejecta and the progenitor star. Therefore, the study of abundance anomalies in their atmospheres can be used to set further constraints on supernova models. This new approach was applied, for the first time to the XRT J1655-40 (Israelian et al.). The data showed a clear excess of OI (8446 and the triplet at 7771-5) and other α-elements (e.g. Mg, Si, Ti) relative to F6III-IV template stars. Spectral analysis using LTE model atmospheres showed that the α-elements are overabundant by a factor ~6-10, and, since they cannot be synthesized in the core of the ~ 2.3 $M_{\odot}$ companion, they must come from the ejecta of the supernova which formed the BH. Similar analysis was performed with optical spectra of the companions to the NS and BH binaries Cen X-4 and A0620-00 (González-Hernández et al. 2004, 2005). The comparison of the observed abundances with predictions of SN models enables to constrain the SN mass cut , and they are found to be in excellent agreement with the dynamical masses of the compact remnants.

High-resolution spectra in the 3800--4900 Å region can be also very useful. It is only in this region where we can check the abundances of r-process elements (ThII 4019 and 4086Å, EuII 4129 Å and 4205 Å) which are produced in Type II SN. The relative abundances of α-, r- and Fe-group elements can be compared with the theoretical yields for nucleosynthesis in Type II SN. These yields are a very sensitive function of the mass of the progenitor and therefore by comparison with theoretical predictions we can establish their masses for the first time. In the case of a large overabundance of r-elements one can even attempt to use abundances of those which are radioactive (Th, U) to constrain the time of the Supernova explosion. Detailed abundance analysis require high spectral resolution at R~15000.

2.8.5 Target number density and optimal number of fibers

- *Shape of IMF in massive star environments*: target number density expected to be rather high. It will decrease as we move out of the cluster core, which, in the example of h Persei is 10-12 arcmins across. 250-300 fibers needed. It is difficult to estimate how tightly packed stars will be at R~21 so fiber size is preferred to be small.

- *Massive stars in nearby galaxies*: tend to be grouped in OB assciations and close to regions of recent star formation. These however extend over large regions in the galaxies. In a FOV of 20 arcmin diameter, however, we expect hundreds of targets. To maximize the number of targets and avoid confusion a small fiber size is preferred.

- *Dynamical Studies of ULXs*: tend to be located in star-forming regions with severe crowding and nebulosity. To avoid target confusion (assuming nominal La Palma seeing) small size fibers of ≤ 1" are preferred.

- *XRBs (dynamical studies and abundance of companions):*XRBs are pointlike sources in typically uncrowded fields so fiber size is not an issue.

- *Follow-up of VSOP:* Being our targets stars of our Galaxy, the density will be higher in the Galactic plane. Preferred fiber size=1.0". No contamination from other sources is expected.

2.8.6 Justification of the spectral resolution and wavelength coverage

- *Shape of IMF in massive star environments*: R ~3000 in the Hα region needed to detect the LiI 6707 line.

- *Characterization of the substellar population*: R=2000-5000 (optical) and R=2800-5000 (NIR) is necessary to determine stellar parameters (temperature, gravity, metallicity).

- *Massive stars in nearby galaxies*: R= 5000-20000 is needed, particularly in low metallicity environments.

- *Dynamical Studies of ULXs*: R=2000 is recommended given the faint typical magnitudes (V~23) of the currently known counterparts.

- *Weighing Compact objects in XRBs:*R=5000-10000 in the Hα region needed to resolve Vsin i, and also in the ~4600 Å region to resolve the CIII/NIII fluorescent components from the Bowen blend. A double-arm spectrograph, optimized in the red and blue regions seems essential.

- *Abundance anomalies in the companion stars to XRBs:* R~15000 is required for detailed abundance analysis throughout the optical spectrum, from ~3800 Å (r-

process elements) up to ~8500 Å (OI lines). A double-arm spectrograph, optimized in the red and blue regions seems essential.

- *Follow-up of VSOP*: Optical range. V down to the limit magnitude of Gaia, i.e. V~20. Only those objects without Gaia spectroscopy will be target objects. Other variable stars will also be targets of this survey.

2.8.7 References

Beaulieu, J.P. et al., 2006, ApJ, 653, L101
Bouret, J.C. et al. 2003, ApJ, 595, 1182
Carigi, L. et al., 2005, ApJ, 623, 213
Casares 2007 in Proceedings of IAU Symposium 238: "Black Holes: From Stars to Galaxies -Across the Range of Masses", in press (astro-ph/0612312)
Casares et al. 2006, MNRAS 373 1235
Chiappini, C., Matteucci, F. & Meynet, G., 2003, A&A, 410, 257
Chiappini, C., Romano, D. & Matteucci, F. 2003, MNRAS, 339, 63
Cornelisse et al. 2007 MNRAS 375 1463
Crockett, N.R. et al., 2006, ApJ, 637, 741
Drew, J.E. et al., 2005, MNRAS, 362, 753
Evans, C.J. et al. 2005, A\&A, 437, 467
Fabbiano G. et al. 2006 ApJ 650 879
Gieren, W. et al., 2004, AJ 128, 1167
Gies & Bolton 1986 ApJ 304 371
González-Hernández et al. 2004 ApJ 609 988
González-Hernández et al. 2005 ApJ 630 495
Herrero, A. & Najarro, F., 2005, in Proceedings of the workshop on Resolved Stellar Populations, Cozumel, 2005, D. Valls-Gabaud & M. Chavez eds., ASP, en prensa
Hillier, D.J. et al., 2001, ApJ 553, 837
Hynes et al. 2003 ApJ 583, L95
Israelian et al.1999 Nature 401 1421
Kazarovets, E. V., Kireeva, N. N., Samus, N. N., & Durlevich, O. V. 2003, Informational Bulletin on Variable Stars, 5422, 1
Kholopov, P. N., Samus, N. N., Frolov, M. S., et al. 1998, in Combined General Catalogue of Variable Stars, 4.1 Ed (II/214A). (1998)
King A.R. et al. 2001 ApJ 552 L109
King A.R. & Dehnen W. 2005 MNRAS 357 275
Kroupa P., 2001, MNRAS, 322, 231
Kroupa P., 2002, Science, 295, 8276
Kudritzki, R.P., 2002, ApJ, 577, 389
Kudritzki, R.P. & Puls, J. 2000, ARA&A 38, 613
Larson, R.B. 2005, MNRAS 359, 211
Liu J-F., Bregman J.N. & Seitzer P. 2002 ApJ 580 L31
Liu J-F., Bregman J.N. & Seitzer P. 2004 ApJ 602 249
López-Corredoira M. & Gutiérrez C.M. 2006 A&A 454 77
Martins, F. et al., 2004, A&A, 420, 1087
Maeder, A. & Meynet, G., 2000, ARAA 38, 143
Maeder, A. & Meynet, G., 2001, A&A, 373, 555
Magrini, L. et al., 2002, A&A 386, 869
Massey, P., 2003, ARAA 41, 15

Massey, P. et al., 2006, AJ 131, 2478
Mayor & Queloz, 1995, Nature, 378, 355
Mokiem, M.R. et al., 2006, A&A, 456, 1131
Mokiem, M.R. et al., 2007, A&A, in press
Monteverde, M.I., Herrero, A. & Lennon, D.J., 2000, ApJ, 545, 813
Muñoz-Darias et al. 2005 ApJ 635 502
Mucciarelli, P. et al., 2005, ApJ, 633, L101
Nakajima et al. 1995, Nature, 378, 463
Pettini, M., 2004, XIII Canary Islands Winter School of Astrophysics, C. Esteban et al., eds., CUP, p. 257
Pietsch W. et al. 2006 ApJ 646 420
Przybilla, N., Butler, K., Becker, S.R. & kudritzki, K.P., 2006, A&A 445, 1099
Rebolo et al. 1995, Nature, 377, 129
Renda, A., Kawata, D., Fenner, Y. & Gibson, B.K. 2005, MNRAS, 356, 1071
Salpeter E. E., 1955, ApJ, 121, 161
Scalo J. M., 1986, Fundam. Cosmic Phys., 11, 1
Shporer A. et al. 2007 A&A 462 1091
Skillman, E.D. & Kennicutt, R.C., 1993, ApJ 411, 655
Slesnick, C.L., et al. 2002, ApJ, 576, 880
Steeghs & Casares 2002 ApJ 568 273
Strutskie, M.F. et al., 1997, ASSL Vol. 210 : The Impact of Large Scale Near IR Surveys
Tiede, G.P., Sarajedini, A. & Barker, M.K., 2004, AJ, 128, 224
Urbaneja, M.A., Herrero, A., Kudritzki, R.P. et al., 2005, ApJ, 635, 311
Vilchez, J.M., Pagel, B.E.J., Diaz, A.I., Terlevich, E. & Edmunds, M.G., 1988, MNRAS, 235, 633
Vink, J. S., de Koter, A., Lamers, H. J. G. L. M., 2001, A&A 369, 574
Woosley, S.E., Heger, A. & Weaver, T.A., 2002, Rev. Mod. Phys. 74, 1015

3 SIDE TECHNICAL STUDY

3.1 SIDE performance requirements

3.1.1 Aperture selection

3.1.1.1 Choice of Science Aperture

The choice of the science aperture affects all the downstream decisions about the optical design of the instrument down to the detector píxel scale. For SIDE at GTC, it is assumed that a microlens will re-image a spot on the focal plane (of approx.1200μm) to an optical fiber (with a core of approx. 200μm). In this document, "Science Aperture" refers to the spot size in the focal plane before any re-imaging.

This study recommends a science aperture of 1.5 arcsec. This choice is dependent upon the assumed seeing (0.8''), assumed lack of an atmospheric dispersion corrector (ADC), and the angular size of objects. A science aperture of 1.5 arcsec results in an efficiency within 80% of optimum for any reasonable deviations in these input parameters in the sky-noise limit (65% of optimum in the Poisson limit for bright sources). It also allows for a survey mode that could cover 15,000 square degrees with efficiency within a factor of 2 of optimal over the full wavelength range of 0.35-1.7 micron.

There are several competing factors that affect the choice of the science aperture:

- **Seeing:** This is the most obvious factor, since the optimal science aperture will scale exactly as the seeing for point sources. A further study should consider the seeing distribution at GTC, once that telescope is in operation. Similarly, the seeing as a function of wavelength should also be considered. Figure 40 shows the total energy enclosed in a MOS fiber as a function of the seeing, for science aperture diameters of 1", 1.2", 1.5" and 2.0", assuming a Moffat PSF for a point source.

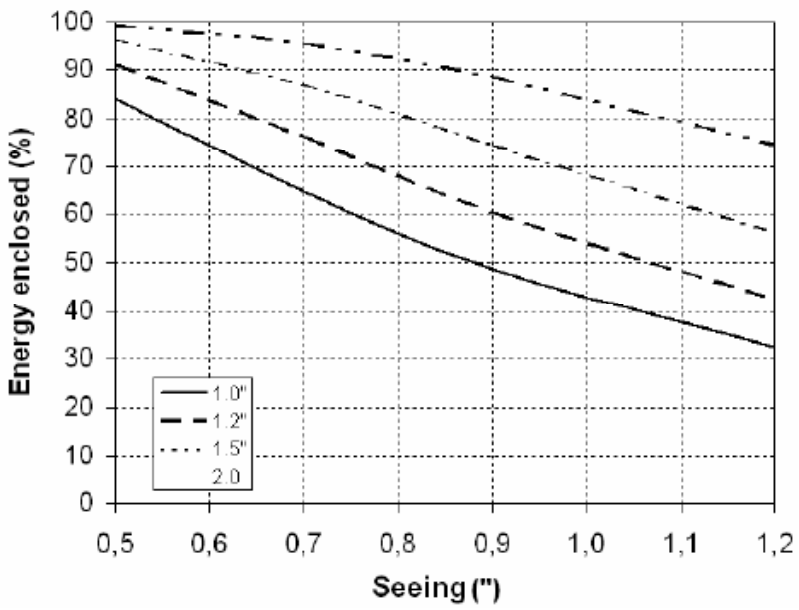

Figure 40: Energy enclosed in an aperture as a function of seeing for different science aperture diameters.

- **Object vs. Sky Brightness:** Very bright objects are most efficiently observed in very large apertures, since the noise can be dominated by Poisson statistics rather than sky noise. The SIDE instrument is probably more interested in observing faint objects in the sky-noise limit. As will be shown below, the optimal science aperture for faint objects is an acceptable choice for bright objects as well.

- **Object Size:** We will consider point sources (stars and QSOs), and galaxies at interesting redshifts. Figure 41 shows the energy enclosed in a MOS aperture diameter of 1" and 1.5" for typical galaxies at high redshift as a function of seeing. Disk and spheroid Sérsic light profiles with n=1 and n=4 have been convolved with the seeing Moffat PSF. We have considered galaxies of typical sizes at high-z of 0.5 and 1.0 arcsec effective radius respectively (Barden et al. 2005, McIntosh et al. 2005).

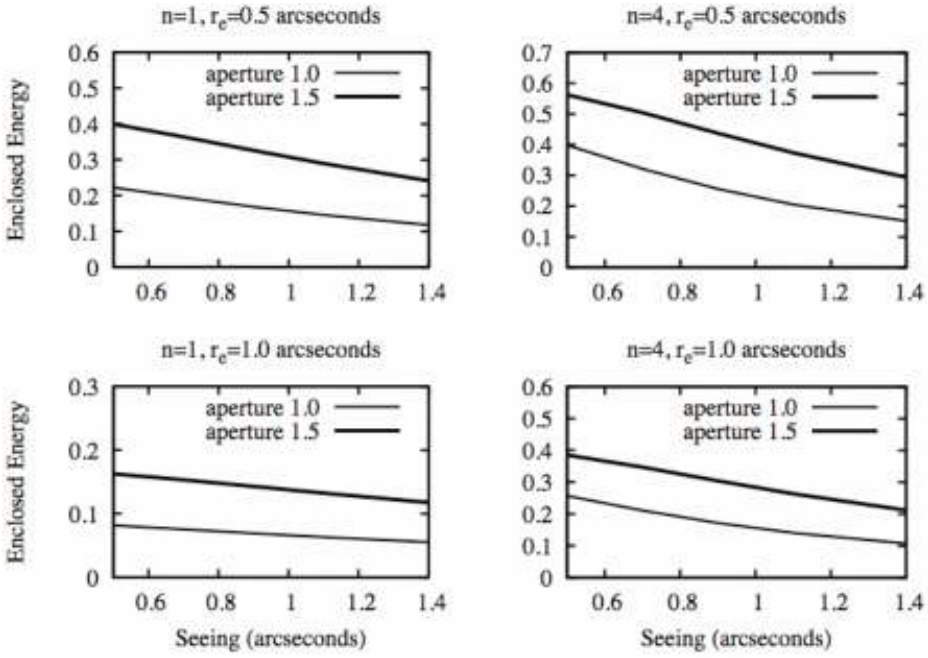

Figure 41: Energy enclosed in a MOS aperture of 1" and 1.5" as a function of seeing for typical high-z disk and spheriod galaxies.

- **Atmospheric Refraction:** This is a big consideration, since refraction can introduce very large errors, and it is now known that an ADC will not be possible for SIDE. Good efficiency for large wavelength coverage is considered a strength of SIDE, and this document considers what would be possible with or without an ADC.

- **Fiber Positioning Errors:** These errors will be assumed to be negligible compared to the seeing. Errors can result from (1) astrometry errors in the input catalogs, (2) imperfect knowledge of the focal plane, or (3) errors in the fiber placement. Input target catalogs can be made that have typical errors < 0.1 arcsec, especially given the UCAC astrometric catalog that is nearly complete in the Northern sky. SDSS makes use of this catalog, and achieves an astrometric accuracy of 0.04 arcsec (RMS). Imperfect knowledge of the focal plane is an issue for some large telescopes, such as Subaru. Subaru spectroscopy requires pre-imaging with the same instrument since the focal plane distortions are not well-mapped. However, the DEIMOS spectrograph at Keck-II has well-measured distortions, and can successfully target to high positional accuracy from catalog coordinates. Finally, errors in fiber placement should be very small (< 0.05 arcsec). The SDSS fibers are placed to an accuracy of 15μm (RMS) across a 62 cm FOV, which would correspond to 0.02 arcsec on the GTC focal plane. In Figure 42, we show the light losses at the entrance of the MOS aperture as a function of position error for object fibers of 1'' and 1.5'' for different seeing values.

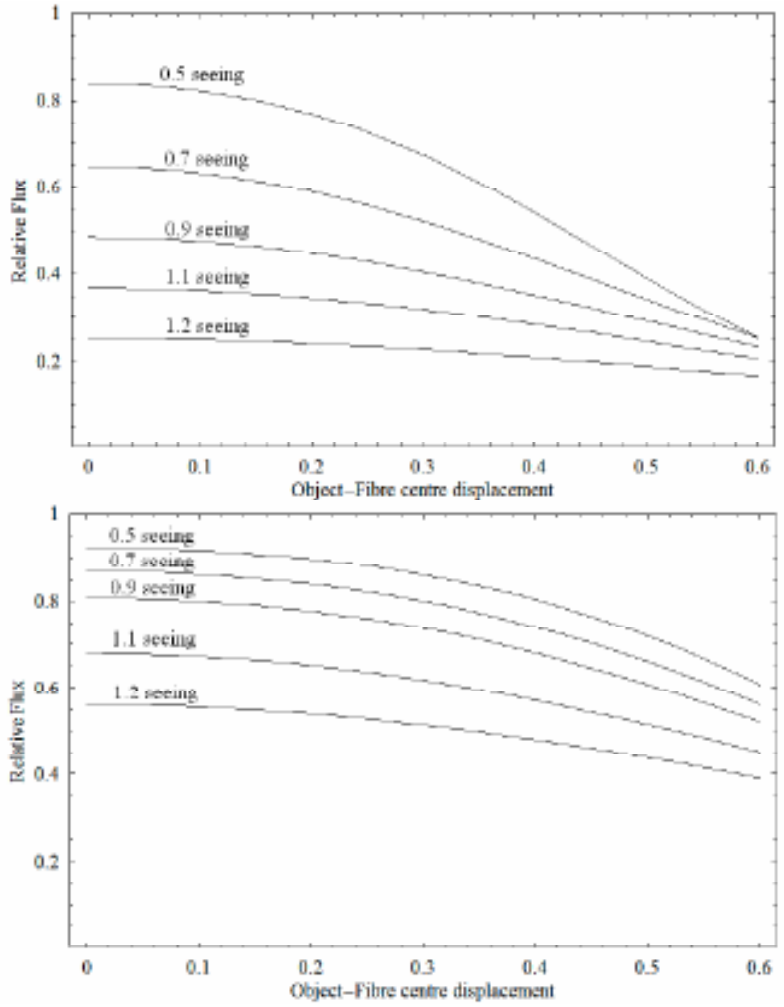

Figure 42: Light losses at the entrance of the MOS aperture as a function of position error for object fibers of 1'' (top panel) and 1.5'' (bottom panel) for different seeing values.

- **Read Noise:** The read noise has been ignored in this study. This was a significant consideration for the Howell (1989) study of aperture photometry. The GTC is a large enough telescope and detectors are sufficiently good that this should rarely be an issue. The only regimes where it could matter are for faint objects observed at high resolution and in the near-IR given the larger read noise of IR detectors.

3.1.1.2 Scientific metric

An appropriate metric is the $(S/N)^2$ collected in a given exposure time. Since the quantity $(S/N)^2$ increases linearly with time, one can fairly trade one for the other: an instrument that delivers twice the $(S/N)^2$ need integrate only half as long.

Consider the simple example of bright objects that are Poisson-noise limited. The signal increases linearly with either the fraction of the light collected or exposure time. The noise

increases as the square root. Therefore, $(S/N)^2$ increases linearly with integration time. This same scaling of $(S/N)^2$ with time is true in the sky-noise limited case.

3.1.1.3 Point sources (analytic)

The optimal aperture diameter can be computed analytically for the case of point sources, in the absence of atmospheric refraction, pointing errors, or read noise.

For the limit of objects much brighter than the sky, the optimal aperture is infinitely large. The $(S/N)^2$ metric scales linearly with the fraction of the PSF enclosed in the aperture. For a Gaussian PSF, this scaling is:

$$(S/N)^2 \propto 1 - e^{-0.5R^2/\sigma^2}$$

where R is the radius of the aperture, and the Gaussian can be described with either σ or the full width half-max (FWHM):

$$g(r) = \frac{1}{2\pi\sigma^2} e^{-0.5r^2/\sigma^2}$$

$$FWHM = 2\sqrt{\ln 2}\sigma = 2.35482\sigma$$

For the case of a 1.2 arcsec diameter aperture and 0.8 arcsec seeing, 79% of the light is enclosed in the aperture. That means that one need observe 1/0.79=1.27 times as long as if one had an infinitely large aperture.

For the limit of objects fainter than the sky, the optimal aperture size is a trade-off between the increased signal from a larger aperture with the increased sky noise from that larger aperture. Ignoring units, the S/N is expressed by:

$$(S/N)^2 = \frac{\int_0^R g(r) 2\pi r dr}{\sqrt{\pi R^2 s}}$$

where s is the sky flux per unit area and R is the aperture radius. The maximization of S/N as a function of R reduces to a root-finding of:

$$-\frac{1}{R^2} + \left(\frac{1}{R^2} + \frac{1}{\sigma^2}\right) e^{-R^2/2\sigma^2} = 0$$

The answer is R=1.5852010σ, or

$$D = 1.3463458 \cdot FWHM$$

We plot the $(S/N)^2$ metric for the Poisson-limited case (”bright star”) and the sky-limited case (“faint star”) in Figure 43. The first panel shows the results for the analytic cases, with no offset of the star position from the center of the aperture. The optimum is D=1.077 arcsec for the sky-limited case in 0.8 arcsec seeing. That same diameter choice is 71.5% as efficient as an infinitely large diameter for bright stars.

A more accurate description of the PSF for point sources is the Moffat profile, which includes power-law wings from atmospheric scattering. Because these wings are large relative to the core, the optization of aperture sizes is changed very little. For simplicity, here we adopt a Gaussian description for point sources.

3.1.1.4 Extended sources (galaxies)

SIDE at GTC would be most effective for galaxy studies if optimized for objects with a source density exceeding the aperture density of approx. 4/arcmin^2. The minimum photometric depth to reach this surface density is $i_{AB} < 23$ mag. That is the depth of the SDSS co-adds for weak lensing, with a median redshift of $<z>=0.5$. The typical size of these galaxies are $r_h=3h^{-1}$kpc for ellipticals and $r_e=3h^{-1}$kpc for spirals, corresponding to an angular size of 0.7 arcsec for concordance cosmology.

Samples of galaxies that could fill the GTC aperture density at z=1 would be elliptical galaxies with $r_h=3h^{-1}$kpc and spiral galaxies with $r_e=3h^{-1}$kpc. This corresponds to an angular half-light radius (θ_h) of 0.53 arcsec (see Table 17). These profiles are described by:

$$\sum(r)=\frac{1}{7.22\pi r_h^2}\exp\left[-7.67\left[\left(\frac{r}{r_h}\right)^{1/4}-1\right]\right] \text{ (ellipticals)}$$

$$\sum(r)=\frac{\sqrt{2}}{\pi r_e^2}\exp\left[-1.68r/r_e\right] \text{ (spirals)}$$

Both of the above profiles are normalized such that $\int_0^\infty \sum(r) 2\pi r dr = 1$.

redshift	θ_h ($3h^{-1}$kpc)	θ_h ($7h^{-1}$kpc)
0.1	2.32	5.42
0.2	1.30	3.03
0.3	0.96	2.24
0.4	0.80	1.86
0.5	0.70	1.64
0.6	0.64	1.49
0.7	0.60	1.40
0.8	0.57	1.33
0.9	0.55	1.28
1.0	0.53	1.25
2.0	0.51	1.19
3.0	0.56	1.30
4.0	0.62	1.40

Table 17: Angular size of galaxies in a concordance cosmology with Ω_m=0.3 and Ω_Λ=0.7. Typical (L_*) galaxies have a half-light radius of $3h^{-1}$kpc, and LRGs have a half-light radius of $7h^{-1}$kpc. Note that the minimum angular size is reached at z=1.60.

The intrinsically largest galaxies are luminous red galaxies (LRGs) that are well-described by de Vaucouleur profiles with a half-light radius of $7h^{-1}$kpc. The surface density of such objects would reach approx. 250 per square degree integrated from z=0 to z=1.0, so would only fill a few per cent of the GTC apertures. These objects at z=1 are included on the plots. They argue for slightly larger aperture diameters, but are not an interesting set of objects for this optimization exercise because of their low surface density.

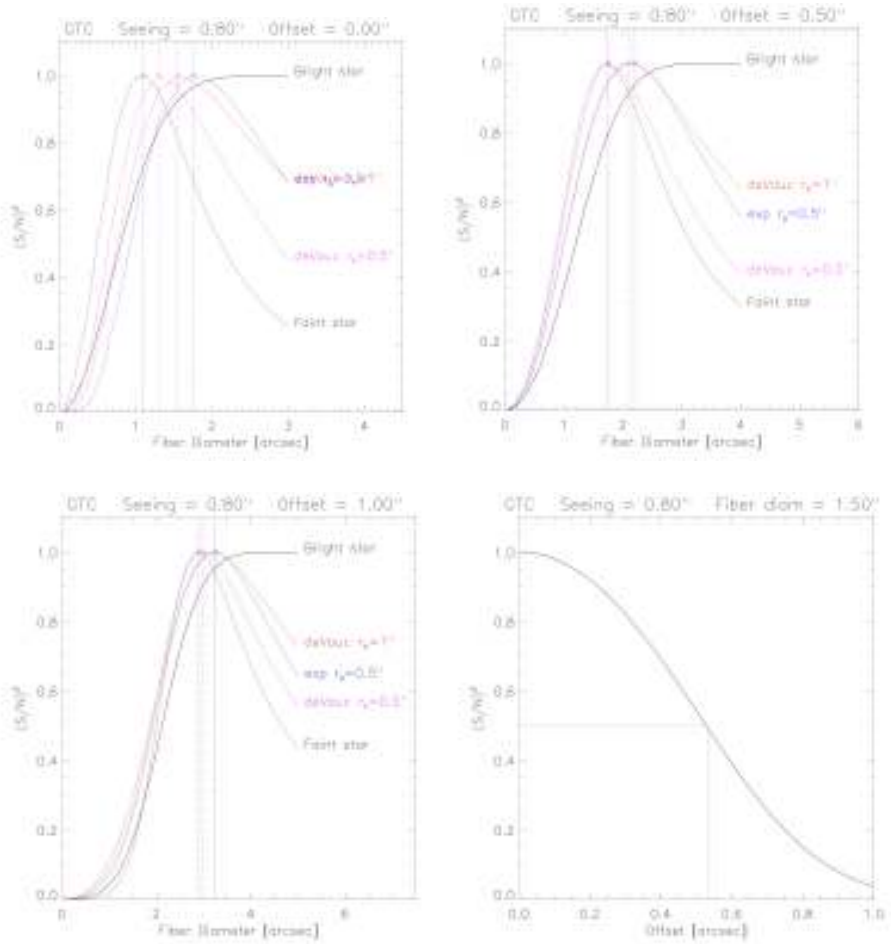

Figure 43: The required observing time scales with $(S/N)^2$ in either the sky-noise or Poisson-noise limited cases. The first 3 panels plot this $(S/N)^2$ metric versus aperture diameter for stellar sources in the Poisson limit ("bright") and the sky-noise limit ("faint"), and various galaxy profiles in the sky-noise limit. Each curve is normalized to a maximum value of 1, and each panel explores a different aperture centroiding offset. The last panel plots the $(S/N)^2$ metric as a function of offset for stellar sources in the sky-noise limit. If atmospheric refraction were to cause an offset of 0.53 arcsec at some wavelengths, one would be forced to integrate twice as long to achieve the same $(S/N)^2$ at those wavelengths.

The optimal aperture diameters are 1.30 arcsec and 1.55 arcsec for typical elliptical and spiral galaxies at z=1, as compared to the diameter of 1.08 arcsec for point sources (see Figure 43).

3.1.1.5 IFUs

Integral field units (IFUs) would quickly lose their usefulness if under-sampled. For example, it is mathematically impossible to centroid an object in an undersampled image. In the limit of extreme undersampling, that centroiding error approaches 0.5 pix.

For well-sampled images, that centroiding can (at least mathematically) approach zero error in the limit of infinite S/N. Sampling theory demands at least two pixels across each FWHM to Nyquist sample a Gaussian beam. For an assumed seeing of 0.7 arcsec with SIDE, this demands an IFU sampling of < 0.35 arcsec.

Well-sampled images also have the nice property of allowing deconvolution of the image for even higher resolution, when S/N is high. For an IFU, where there may be gaps between the fibers, one can also reconstruct a flux-conserving image. The idea of reconstructing a well-sampled image from dithered, undersampled images works reasonably well for HST/ACS where the PSF is unchanging; that technique is unlikely to be successful (even in principle) for a ground-based instrument with a highly time-variable PSF. A recent article that discusses the sampling theorem is Bernstein (2002).

A problem with the single-core and IFU fibers feeding the same SIDE spectrographs would be that the desired fiber sizes would be so different: 1.5'' vs. 0.35''. Designing for a pixel scale for the IFU fibers would oversample the single-core fibers by a factor of 4 in both wavelength and spatially. That both wastes detector real estate, and introduces a lot of read noise (see discussion on the spectrograph design sections).

3.1.1.6 Atmospheric refraction

3.1.1.6.1 General

The atmospheric refraction is significant for the GTC on La Palma, and an introduction of the topic is given here, while a more detailed discussion is found in Section 3.1.2. A complete general discussion on atmospheric refraction can be found in Filippenko (1982).

3.1.1.6.2 Conditions on the Roque de los Muchachos

Taking into account the GTC documentation (*see AD: ESP/STMA/0017-L*), the telescope is located at 2267.83 m of altitude (17º53'25.10" W of longitude and 28º45'20.15" N of latitude). The temperature range (measured 2 m above ground level) for nominal operation will be -2º to +19º C. The whole temperature range (measured 2 m above ground level) for operation will be -6º to +30º C. The nominal range of temperature variation (absolute value) at the GTC site during the night is given in Table 18:

Time	Variation range
15 minutes	0ºC-0.9ºC
1 hour	0ºC-1.8ºC
2 hour	0ºC-2.4ºC

Table 18. Temperature variation at GTC.

The relative humidity range for nominal operation will be 2% to 87%. The maximum relative humidity in which the GTC can operate will be 90% (or the value corresponding to a lower relative humidity if condensation is produced on the GTC). The atmospheric pressure range for nominal operation will be 770 to 790 mbar. These data result in a refraction of ±0.5 arcsec over the full wavelength range of 0.35-1.7 micron at a zenith distance of 25 degree (see Figure 44).

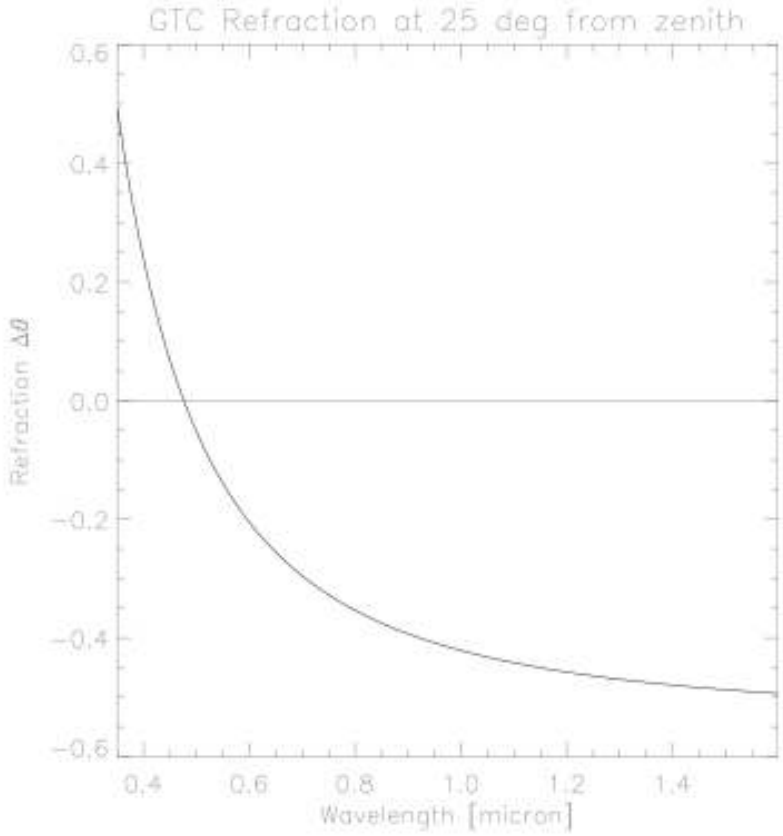

Figure 44: Atmospheric refraction observed at GTC at a distance of 25 degree from zenith. The differential refraction is set to zero at 0.476 μ.

With no ADC to correct for differential atmospheric refraction, keeping the refraction offsets to <0.5 arcsec require observing near transit and within 25 degree of δ=28.75 (the latitude of La Palma). This declination range contains 37% of the full sky, or 15,000 square degrees. Any GTC/SIDE survey projects would presumably be in this footprint. See Section 3.1.2 for more details.

This choice of 0.5 arcsec as an acceptable refraction offset is the point at which the bluest and reddest parts of the spectrum will be collecting $(S/N)^2$ at half the rate as the $\lambda = 0.476$ micron part of the spectrum (see last panel in Figure 43). Full wavelength coverage is not efficient at larger zenith distances. Observing at declinations $\delta < 4$ degree or $\delta > 54$ degree or at large H.A. would demand that the observer choose the wavelengths that are well-observed (and place the aperture where that color light is predicted to be).

3.1.1.6.3 Impact of the atmospheric dispersion

Taking into account the environment conditions on the Roque de los Muchachos and the spectral coverage of the SIDE spectrographs (0.4-1.7 microns), the impact of the atmospheric refraction is shown in **Figure 45** as a function of Zenith Distance.

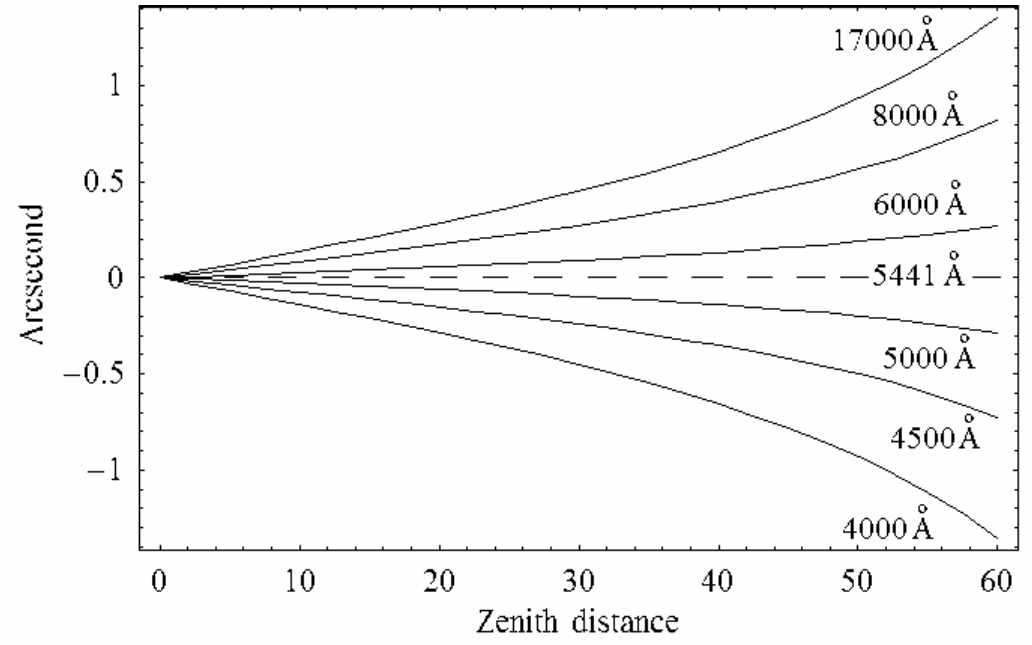

Figure 45. Differential atmospheric refraction as a function of zenith distance relative to 5441 Å.

3.1.2 The effect of atmospheric dispersion on SIDE observing capabilities

The effects of atmospheric dispersion, which have been introduced in the previous sections, are now analysed in order to quantify their influence on the observing capabilities of SIDE. For a better understanding of the topic, atmospheric dispersion is splitted into two components:

1) A monochromatic light path is deviated from straight line by the atmosphere.
2) Different wavelengths are deviated differently by the atmosphere.

Both effects are dependent on the angle of incidence between the light and the atmospheric layers which cover the Earth. In practice, we can look at the two effects as functions of the zenith distance (ZD) of the object observed.

3.1.2.1 Monochromatic effect

The monochromatic effect is usually corrected by a Telescope Control System (TCS) through guiding by means of a guide star. Of course, this is done at a specific wavelength and at a specific location over the Field Of View (FOV). These are the steps the TCS goes through for pointing to an object: 1) catalogue coordinates are roughly corrected for atmospheric dispersion at the given ZD, 2) the object is acquired and the telescope is kept pointing at a position relative to where the guide star actually appears at the selected wavelength, after its light has been refracted through the atmosphere. Thus, for most instruments, monochromatic refraction is overcome by using a guide star, but SIDE has such a wide Field Of View (FOV) that the refraction correction applied to the center of the FOV is no longer valid for the objects close to the upper and lower borders (where upper and lower mean towards the Zenith or opposite to it). At the start of the observation, the software of the fiber positioner can take off this effect, which can be modelled for that moment in time, but, during long exposures, the ZD gradually changes and the initial position of the science apertures is no longer correct; as time goes by, more and more light is lost from the fibers close to the upper and lower borders of the FOV.

Unless a real-time positioner is used (as the LBNL fiber positioner), this problem can be overcome only by stopping the observation and starting a new positioning cycle, which is an unacceptable waste of time. All the calculations we make are for a distance of 8 arcmins from the center of the FOV (10 arcmins would be the border itself).

3.1.2.2 Chromatic effect

The chromatic effect can be satisfactorily corrected by an Atmospheric Dispersion Corrector (ADC), made of two doublets of prisms which rotate according to the actual ZD. In the absence of an ADC, this chromatic splitting effectively limits the observable sky at the telescope, because, with increasing Zenith Distance, two different wavelengths would separate more and more and, in the end, one would fall off the science apertures. Without an ADC, the whole FOV suffers this effect, although the part of the field closer to the Zenith is less affected, while the opposite border is the most affected. This phenomenon is more severe when the wavelengths considered are widely spaced apart. By splitting the whole spectral range of SIDE (0.365μ - 1.7μ) into three appropriate intervals, it is possible to make the

displacement between two limiting wavelengths the same for the three ranges. Moreover, we assume that the guiding is always done at a wavelength such that it stays in the middle between the relative shift of the blue and red ends. This means that the blue and the red ends will shift equally (with opposite directions) from the guide star wavelength.

The three triplets of wavelengths (blue end, guide, red end) which satisfy the above requirements are (0.365μ 0.3969μ 0.44μ), (0.44μ 0.5037μ 0.61μ), (0.586μ 0.78μ 1.7μ) and these will be used hereafter.

It is important to quantify the two effects of Atmospheric Dispersion and to estimate the amount of time available for observing before the light losses become significant. We try to resume here the observing capabilities of SIDE in a practical and understandable way, taking into account monochromatic and chromatic dispersion through the Earth's atmosphere. We do it both in terms of accessible declinations on the sky and of time available for observations.

We calculated the atmospheric dispersion (given the mean Dry Air Atmospheric Pressure, mean Vapour Pressure, mean Temperature and Site Altitude for GTC at the Roque de Los Muchachos and given the wavelength) according to Stone (1996).

3.1.2.3 Focal plane distribution of light

Figure 46 shows the two combined effects of Atmospheric Dispersion on the distribution of light across the FOV at three different Zenith Distances (30, 50 and 70 degrees). This is done for one of the spectral ranges given before. The behaviour is the same for all three spectral ranges and also the guiding wavelength remains centerd at any Zenith Distances. We can see that the Monochromatic and Chromatic effects combination causes a reddening of the sources at the top of the FOV, and a blueing at the bottom, apart from the obvious loss of energy. The science aperture is taken here as 1.5" as specified in 3.1.1.

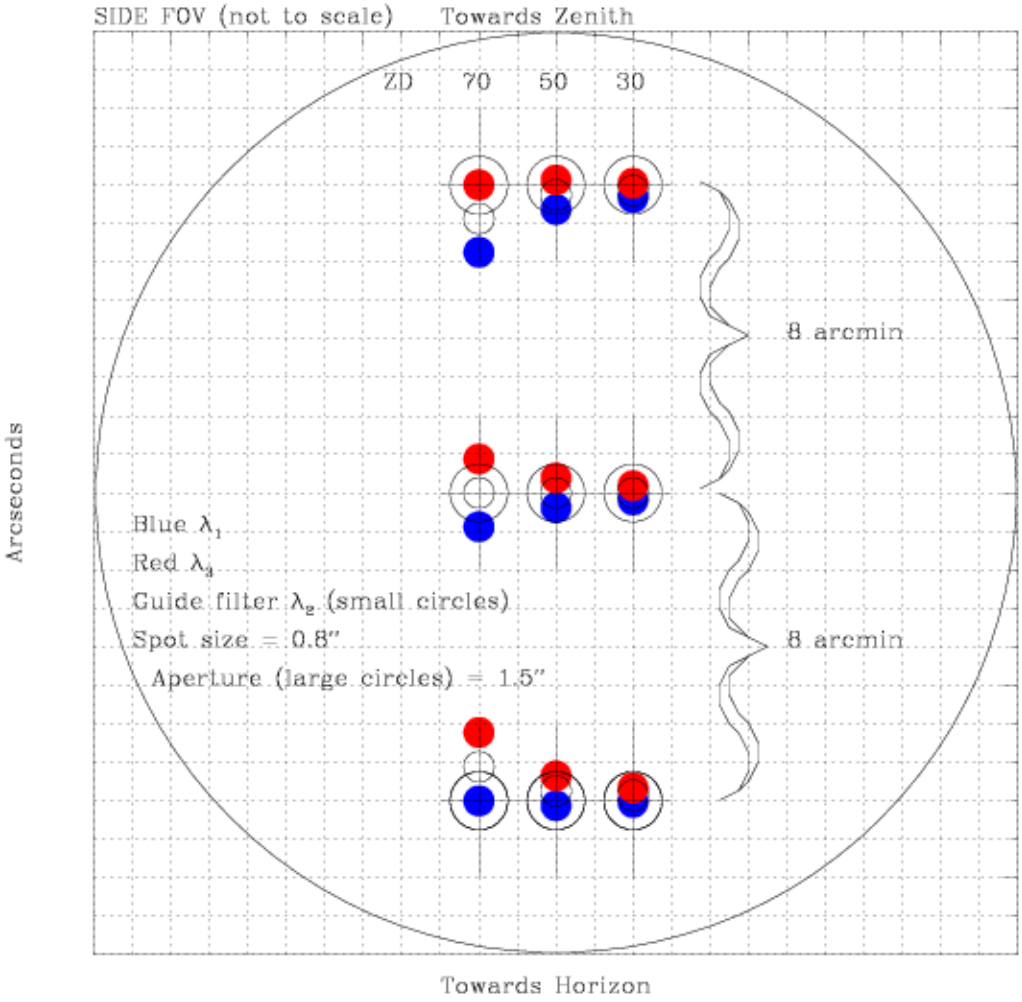

Figure 46 Distribution of light across SIDE FOV at 30, 50 and 70 degrees from Zenith. The scale in arcseconds refers to each of the three groups of spots, and NOT to the distance between the groups, for which arcmins are to be used instead. $\lambda_1,\lambda_2,\lambda_3$ are Blue, Guide (central) and Red wavelengths respectively. The plot is valid for any one triplet of spectral range as given in Section 3.1.2.2.

3.1.2.4 Monochromatic effect results

Two curves are shown in Figure 47; let's concentrate on the monochromatic curve (the lower one), taken at lambda = 0.8μ. Only this wavelength is shown here because the behaviour is very similar for any other wavelength of interest for us.

This curve shows the resulting dispersion at 8 arcmin from the center of the FOV as a function of ZD (airmass is also shown on the X axis for clarity). We can see that up to ZD = 77 deg. (arimass ~2.3) the relative displacement at 8 arcmin from the center of the FOV stays below 0.5".

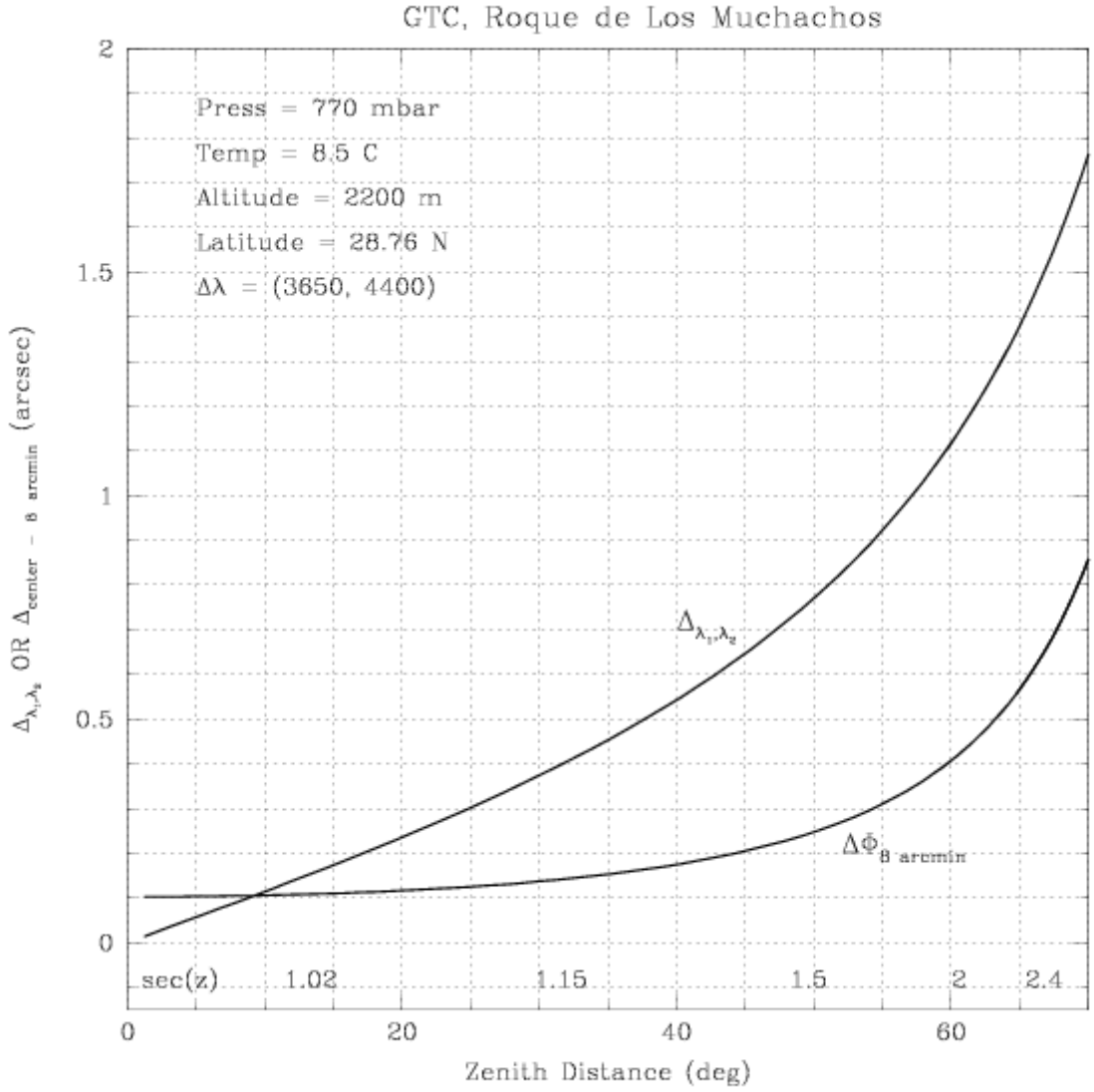

Figure 47: Atmospheric dispersion due to a shifted position (8 arcmin) from the center of the field ($\Delta\Phi$ at 0.8μ) and due to different wavelengths ($\Delta\lambda_1,\lambda_2$). The spectral range considered can be any of the three specified in section 3.1.2.2, although this plot was made for (0.365μ 0.44μ).

The upper curve of Figure 47 will be discussed later.

By using Figure 48, we can estimate the time available for observing with a very conservative 0.2" relative displacement of the sources at 8 arcmin from the FOV center, ***in case our spectral range was restricted to a single wavelength***. This plot is for 0.8μ, but considering other wavelengths makes just a few minutes of difference in time. This available time is declination-dependent, because not only the instantaneous position (ZD) of an object matters, but also how it will move from that position as time goes by. For declination +10, if we start with a field to the East at ZD = 33.5, we can observe it for about 4^h40^m before the

relative displacement at 8 arcmin reaches 0.2". Of course, if we start at the same ZD, but with the field to the West (thus setting), we only have 45 min left before hitting the 0.2" limit.

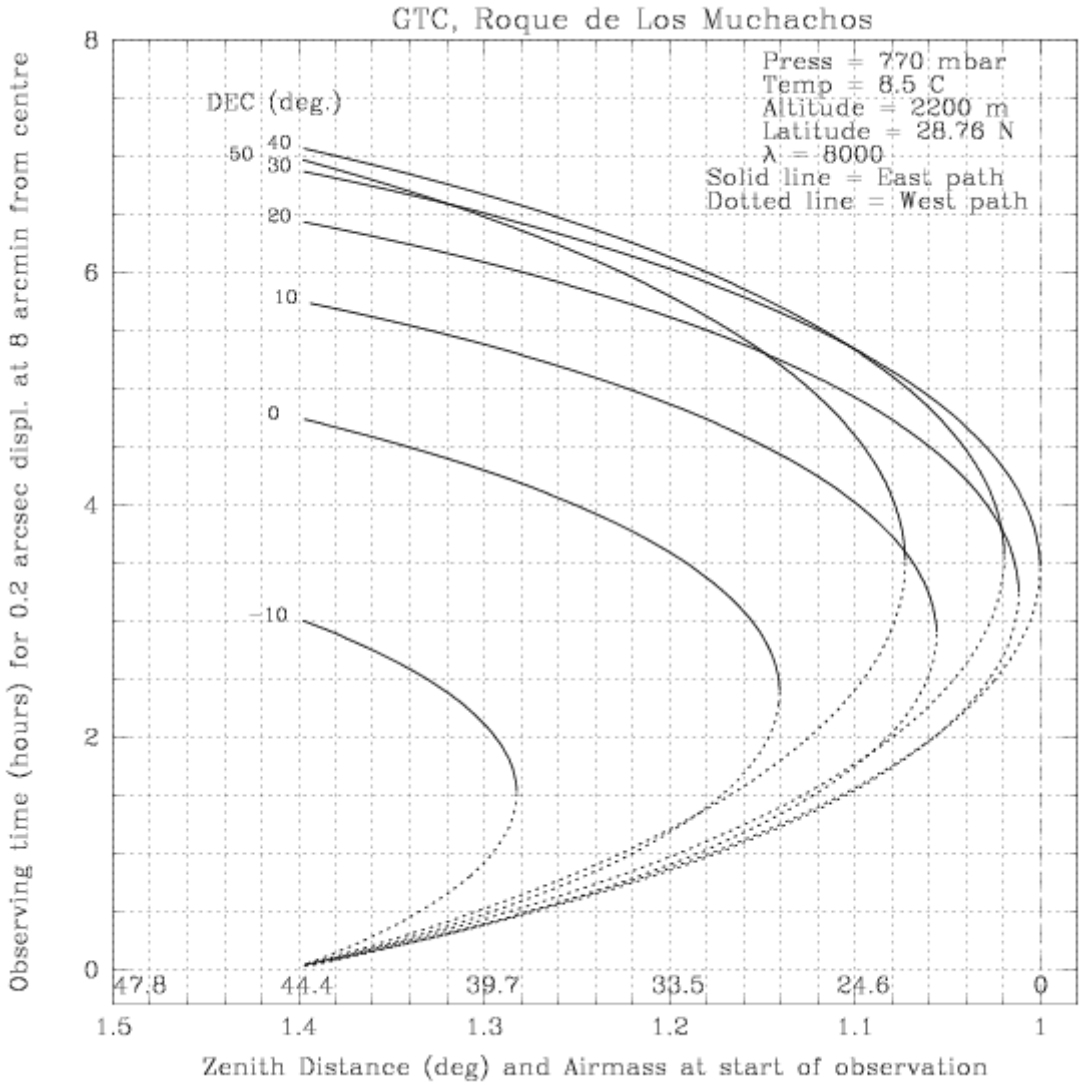

Figure 48: Time available to observe a field before the shift of a single wavelength due to atmospheric dispersion at 8 arcmin from the center reaches 0.2". The figure is done for $\lambda = 0.8\mu$, but other wavelengths exhibit only a few minutes difference.

3.1.2.5 Chromatic and global effects results

Normally we are observing over a spectral range, not at a single wavelength, so we want to know the maximum displacement of our wavelength range extremes due to atmospheric dispersion as a function of Zenith Distance. This is shown on Figure 47, as the upper curve of the plot.

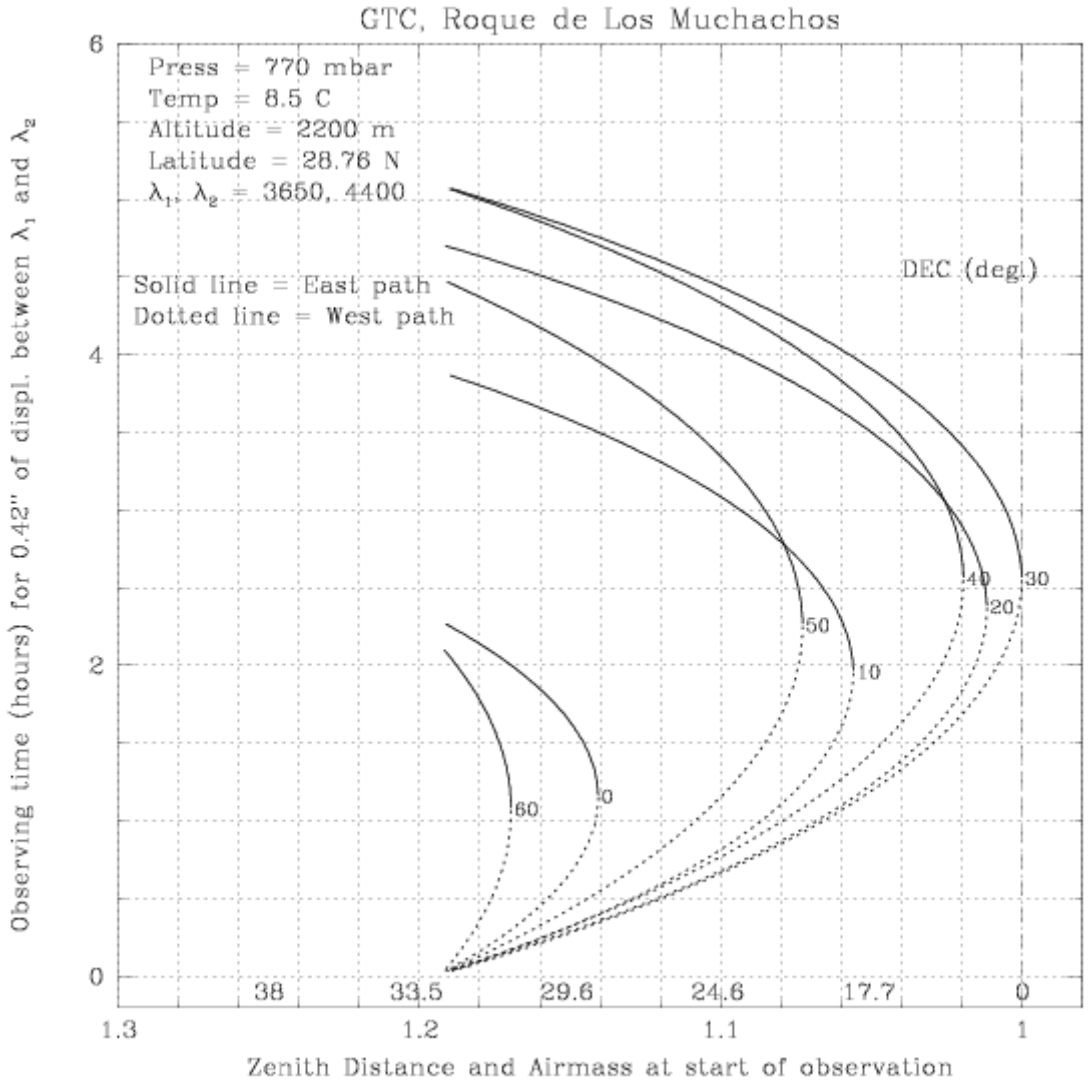

Figure 49: Time available to observe a field at the center of the FOV before the shift due to atmospheric dispersion over the range $\lambda_1 = 0.365\mu$, $\lambda_2 = 0.44\mu$ reaches 0.42".

Figure 49 shows the observing time available for each declination due to the chromatic effect alone. Here we set our limit of displacement between lambdas to 0.42", which still gives 80% of the energy in a science aperture of 1.4" (see Rabaza, 2007). ***Note that such plot is valid only for the horizontal central part of the FOV, where the differential effect of the large FOV is not present***. Declinations above +10 deg allow at least 4 hours of observation, provided that the scheduling is well planned.

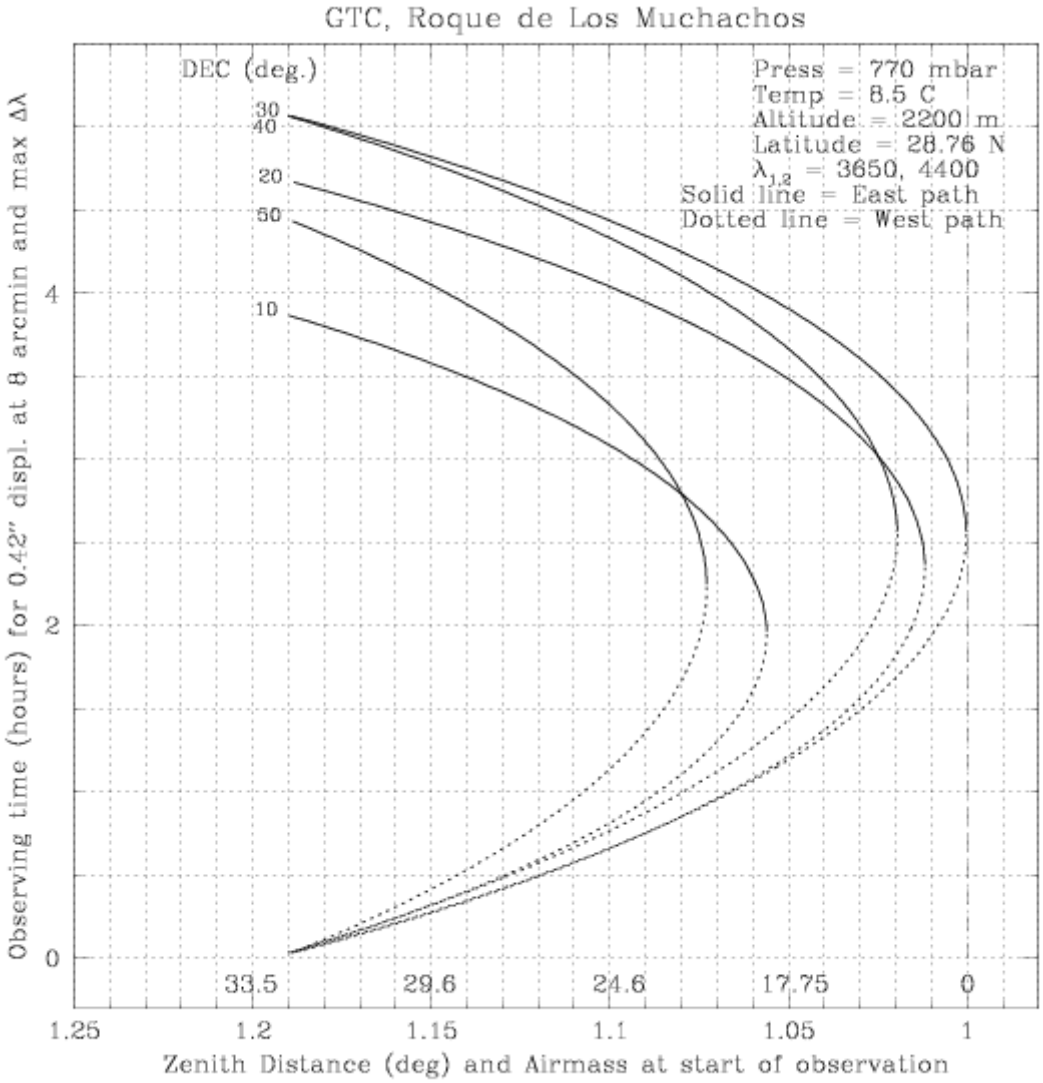

Figure 50: Time available to observe a field over the range $\lambda_1 = 0.365\mu$, $\lambda_2 = 0.44\mu$ and at 8 arcmins from the center of the field, before the centroid of some wavelength gets shifted by 0.42".

Finally, Figure 50 shows the worst case of the chromatic and monochromatic effects superimposed, ***which only happens close to the upper and lower borders of the FOV*** (at 8 arcmin from the center). If we want to keep the whole range 0.365μ-0.44μ (or the equivalent ones) within 0.42" ***at a position close to the upper or lower border of the FOV***, we can still

observe for 4 hours or more, but only at declinations from +10 to +50; for other declinations we need narrower ranges or a reconfiguration of the fibers halfway through the observation, unless the Fiber Positioner can track atmospheric dispersion in real time (as LBNL fiber positioner).

3.1.2.6 References

Barden et al. 2005, ApJ, 635, 959
Bernstein, G. 2002, *Advanced Exposure-Time Calculations: Undersampling, Dithering, Cosmic Rays, Astrometry, and Ellipticities*, PASP, 114, 98
Howell, S. 1989, *Two-Dimensional Aperture Photometry: Signal-to-Noise Ratio of Point-Source Observations and Optimal Data-Extraction Techniques*, PASP, 101, 616
Filippenko, A. 1982, *The importance of atmospheric differential refraction in spectrophotometry*, PASP, 94, 715
McIntosh et al. 2005, ApJ, 632, 191
Stone R. C., 1996, *An accurate method for computing Atmospheric Refraction*, PASP n. 108, 1051-1058
Rabaza, O. February 2007, *Impact of the Atmospheric Refraction at SIDE*, SIDE Tech Report Optic-01

3.1.3 Resume of science goals and science requirements

Table 19 shows a resume of the science goals devised from Chapter 2.

Section	Mode	FOV	Sky sampling	# of units	R	VIS-NIR simultaneity
Energetic phenomena	SIFU	30”	0.5”	-	4k	-
Energetic phenomena	MiniIFU	3”*3”	0.4”	20	3k-5k	Yes
First objects & IGM	MOS	-	1.2” -1.5”	500-1000	1k-5k	-
First objects & IGM	MiniIFU	4”*4”	1.2” -1.5”	30-50	1k-5k	-
Galaxy evolution	MOS	20’-41’ diameter	1.5”	300-600	1k-4k	Yes
Galaxy evolution	MiniIFU	3”*3”	0.3”-0.4”	10-20	-	-
Galaxy evolution	SIFU	15”x15”	0.3”	-	-	-
Galac.struc.& local group	MOS	20’ diameter	1.2”-1.5”	-	Many	Yes
Galac.struc.& local group	MiniIFU	10”-20”	0.25”	-	Many	Yes
Galac.struc.& local group	SIFU	20”	0.25”	-	Many	Yes
LSS & cosm. Parameters	MOS	20’ diameter	0.5”	1000	1k-2k	Yes
LSS & cosm. parameters	SIFU	10”-20”	0.5”	-	-	Yes
Solar system	SIFU	30”	1”	-	Any	-
Stellar physics	MOS	20’ diameter	1”	-	3k	Yes
Stellar physics	MiniIFU	30”	1”	-	15k	-
Stellar physics	SIFU	30”	1”	-	10k-15k	-

Table 19 Resume of the scientific goals taken from the Scientific Justification chapter.

After a detailed analysis of the scientific cases of Chapter 2, a summary of the requirements for SIDE which best fit the science can be drawn. Such resume of SIDE science requirements is given in Table 20.

Type	Common User Instrument
Focal station	Nasmyth & Folded Cass
Field of View (MOS)	20’ diameter
Field of View (SIFU)	30”x 30”
Field of View (Mini-IFUs)	3”x 3”
Science aperture (MOS)	1.5”
Fiber aperture (MOS, SIFU, mIFU)	0.5”
N. of MOS units	1000
N. of mIFUs	30
Spectral range	350-1700 nm
Simultaneity VIS-NIR	Yes
Spectral resolutions	1000 < R < 30000
Simultaneous spectral range	4000 Å at R=1500 in VIS&NIR 2000 Å at R=5000 in VIS&NIR 500 Å at R=15000 in VIS
N. of exposures for entire range	1 for VIS + 1 for NIR @ R=1500 3 for VIS + 3 for NIR @ R=4000 10 for VIS @ R=15000
Observing mode	Nod & Read
Limiting magnitudes goal[1] (VIS, NIR)	

	R	J
R=1500	22.7	20.1
R=4000	22.1	19.5
R=15000	21.2	-

Robot positioning time	< 5’
Robot positioning accuracy	<0.1”
Fiber cross talk	0.1%
Detector quantum efficiency	CCD >60% @ 400 nm; >80% @ 900 nm NIR array; >80% @ λ>900 nm
Detector cut-offs (response curve)	1.7 μ IR array

Table 20: SIDE scientific requirements

(1) Point source limiting magnitudes for 1hr integration, S/N=5 per pixel along the dispersion axis, 0.7” seeing.

3.1.4 Instrument sensitivity

The following discussion on the instrument sensitivity follows the concept of instrument found in Section 1.1.2.
In Table 21 we give an estimation of the expected SIDE limiting magnitudes in several spectral bands in the visible and near-IR for different spectral resolutions. Results are for one hour integration on a point source, S/N=5 per píxel along the dispersión axis for 0.7 arcsec seeing. The object spectral shape has been assumed to be flat. Typical sky background fluxes for La Palma have also been taken into account.

	B	R	I	J	H
R=1500	23.5	22.7	22.0	20.1	19.7
R=4000	22.8	22.1	21.4	19.5	19.1
R=15000	21.7	21.2	20.6	-	-

Table 21: SIDE limiting magnitudes

We must note here that this is a rough estimation and it must be considered as tentative. There are a number of assumptions included in the computation of the limiting magnitudes, such that the total instrument efficiency (telescope plus the entire instrument: WFC, microlenses and fibers, spectrograph and detector performance). A better estimation of the instrument efficiency will be obtained at the end of the conceptual design phase.

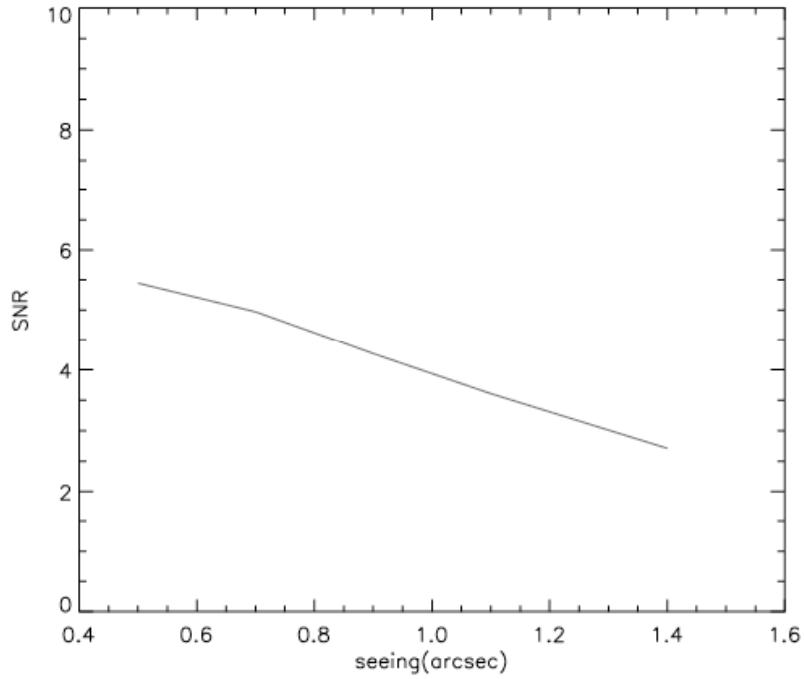

Figure 51: R-band Signal-to-Noise ratio as a function of seeing (see text)

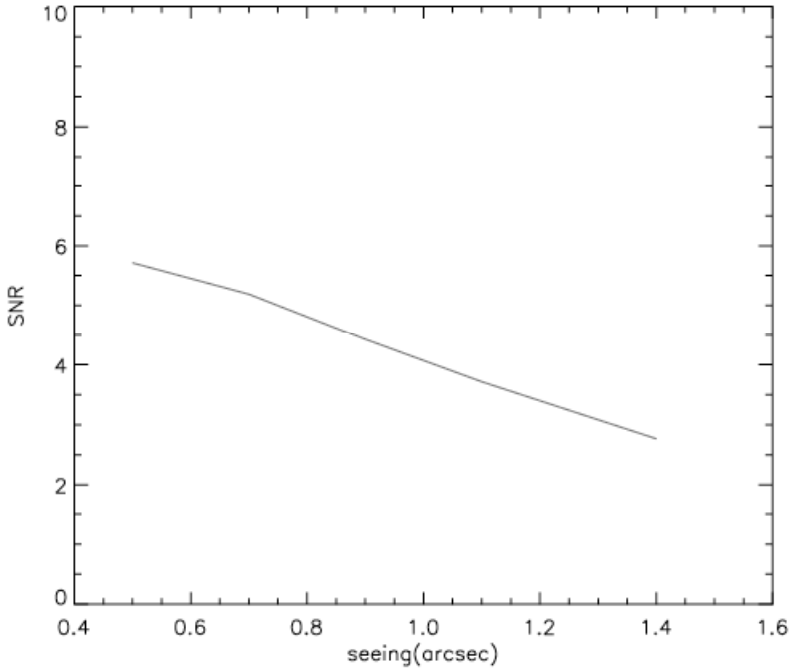

Figure 52: J-band Signal-to-Noise ratio as a function of seeing (see text)

In Figures Figure 51 and Figure 52 we plot the SNR in the R- and J-band as a function of seeing respectively, adopting the same parameters given above. A MOS aperture of 1.5 arcsec has been considered and a Moffat PSF was adopted in our calculations.

Table 22 shows Vega magnitudes for a range of typical halo stars and typical z=1 galaxies. S/N values are determined per pixel along the dispersion axis, assuming point sources in 1hr integration and 0.7" seeing. In Figure 53 we show the SED templates for the the stars and the z = 1 galaxies.

The conclusion is that simultaneous observations of a general object mix are optimized for the I-band. Roughly similar S/N ratios across the whole range from B to H can not be obtained for any object category. F and G stars as well as blue z=1 galaxies are better detected in the optical range B to I than in the NIR. However, M stars and red galaxies are best detected in I to H. For z=1 galaxies the critical features are expected in the I-band with an extension reaching across z and J (i.e. O-II to Ha across 370-660 nm restframe).

Object	B (WFI)	R (WFI)	I (WFI)	J (UKIDSS)	H (UKIDSS)
F0V	21.92	21.48	21.25	21.14	21.01
G0V	22.46	21.68	21.25	20.99	20.74
K0V	22.82	21.77	21.25	20.83	20.42
M0V	24.21	22.35	21.25	20.31	19.70
M5V	26.19	23.66	21.25	19.53	18.77

Object	S/N B	S/N R	S/N I	S/N J	S/N H
F0V	21.40	15.33	10	1.94	1.52
G0V	13.09	12.77	10	2.23	1.93
K0V	9.39	11.79	10	2.57	2.61
M0V	2.62	6.94	10	4.16	5.02
M5V	0.43	2.09	10	8.50	11.75

Galaxy z=1	B (WFI)	R (WFI)	I (WFI)	J (UKIDSS)	H (UKIDSS)
Very blue	22.68	22.13	21.25	20.69	20.26
Blue	23.06	22.39	21.25	20.61	20.10
Mod blue	23.81	22.73	21.25	20.32	19.67
Mod red	24.10	22.86	21.25	20.14	19.40
Red	24.45	22.98	21.25	19.89	19.05
Very red	25.34	23.25	21.25	19.53	18.53

Galaxy z=1	S/N B	S/N R	S/N I	S/N J	S/N H
Very blue	10.65	8.45	10	2.93	3.00
Blue	7.52	6.68	10	3.15	3.47
Mod blue	3.78	4.90	10	4.11	5.18
Mod red	2.89	4.34	10	4.87	6.59
Red	2.10	3.87	10	6.09	9.16
Very red	0.93	3.04	10	8.50	14.65

Table 22 Magnitudes and expected S/N values per pixel along the dispersion axis for a range of typical halo stars and typical z = 1 galaxies.

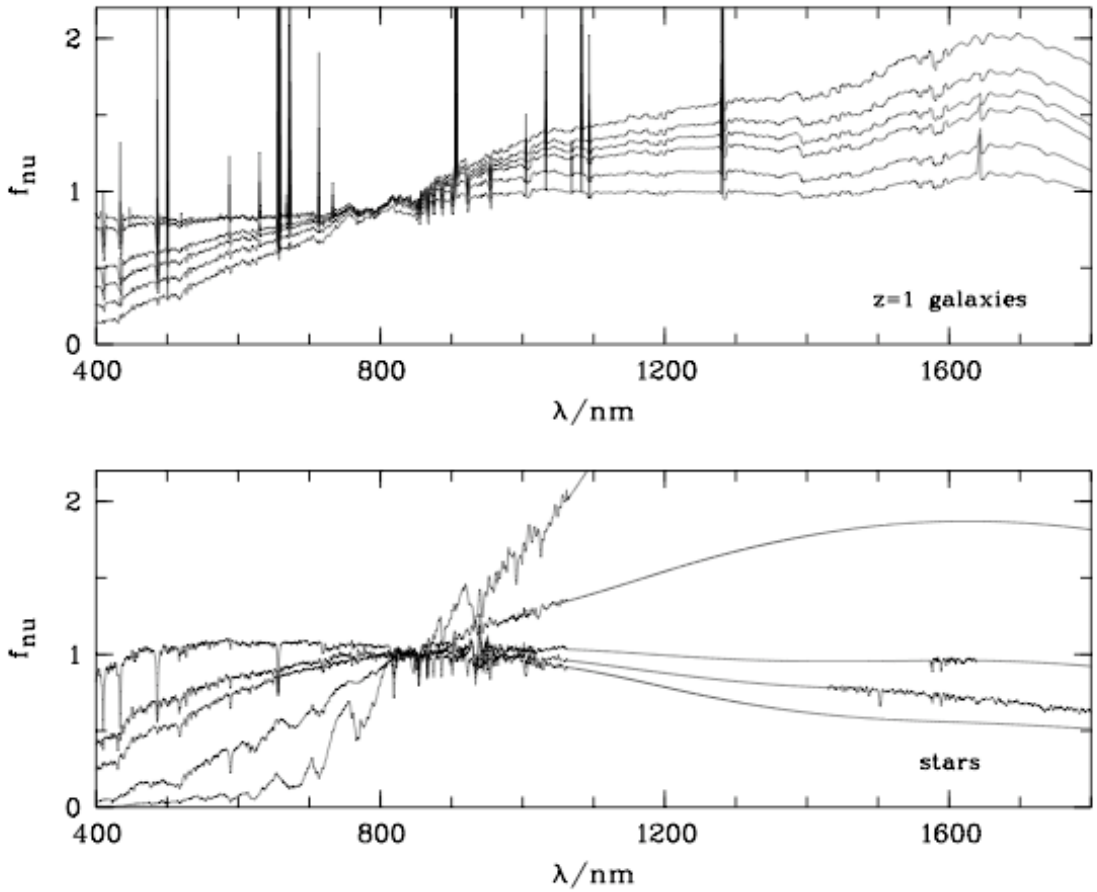

Figure 53 SED templates assumed for our set of stars and z = 1 galaxies.

3.1.5 SIDE as compared to other instruments

The following tables show an interesting comparison between SIDE and other existing or planned instruments in world 10 m class telescopes. Table 23 concerns the MOS mode, and Table 24 and Table 25 concern the Integral Field Spectroscopy modes (i.e. SIFU and mIFU modes).

We also compare the main characteristics of SIDE with OSIRIS and EMIR (Table 26, all of them GTC instruments). SIDE has the additional and unique observing mode of "simultaneity", which means that both the optical and the near-IR wavelength range can be observed at the same time.

As it can be seen in Table 26, in the optical wavelength range SIDE will have 10 times higher resolution that OSIRIS. The most remarkable characteristic of SIDE is its multiplexity. SIDE can observe, simultaneously in the VIS and NIR, up to 1000 targets in one shot, which is a factor 50 faster that both OSIRIS and EMIR. In addition SIDE has a

Super Integral Field Unit (SIFU) that can cover a field of ~30" x 30" with 2500 fibers, and 30 mini-IFUS. Both modes are not available in either OSIRIS or EMIR.

Telescope	**Apert. (m)**	**Instrument**	**Slit/fiber**	**IFU**	**Resolution (λ/Δλ)**	**Spectral Range (nm)**	**f.o.v (sq.deg)**	**N_{obj}**	**η[1]**
Keck	10	DEIMOS	slit	no	1700-4800	410-1000	0.023	100	1.0
VLT	8.2	VIMOS	slit	yes	180-2500	370-1000	0.062	750	1.87
SUBARU	8.3	FMOS	fiber	no	1500-3000	900-1800	0.2	400	0.32
SUBARU	8.3	WFMOS	fiber	no	1000-30000	390-1000	1.77	3000	0.27
GTC	10.4	SIDE	fiber	yes	1500-30000	350-1700	0.09	1000	2.76

Table 23 Comparison with other instruments (MOS mode).

[1] Survey efficiency relative to DEIMOS, defined as $(Apert)^2 N_{obj} / FOV$

Telescope	Aper. (m)	Instrument	Nr. Slices, fibers or lenses	Spati. Samp. Slice/Lense/Fiber (arcsec)	FOV	λ range (μm)	R=λ/Δλ
VLT	8.2	SINFONI/ SPIFFI(AO)	32	0.25, 0.1 or 0.025	8"x8"	1-2.5	1500 to 4000
GEMINI S	8.1	GNIRS-IFU (with AO??)	21 or 26	0.15 or 0.04	3.5"x4.8"	0.9-2.5 (5.5?)	1700-5900
GEMINI N	8.1	NIFS (AO)	29	0.1	3.0"x3.0"	0.9-2.4	4990-6040
VLT	8.2	VIMOS-IFU	6400	0.33 or 0.67	54"x54"	0.36-1.0	180-3100
VLT	8.2	GIRAFE/ FLAMES	300 (15x20 or 300)	IFU mode (0.52) ARGUS 0.52 or 0.3	15 x 2"x3" 11.5"x7.3"	0.37-0.9	11000-39000
GEMINI N AND S	8.1	GMOS	1000 (obj) 500 (sky)	0.2	5.7"x3.5" (obj) 5"x3.5" (sky)	0.1-1.1	640-4400
SUBARU	8.2	Kyoto-3DII	37x37	0.093	3.4"x3.4"	0.4-0.9	~1200
KECK	10	OSIRIS(AO)	3000??	0.02,0.035,0.05,0.1	4.8"x6.4"	1-2.5	~3500
GTC	10.4	SIDE SIFU	2500	0.5	30"x30" 3"x3" 1.5"x1.5"	0.35-1.7	1500-30000

Table 24. Comparison with other instruments (SIFU and mIFU modes). Color Code: **Image slicers**, **Fibers coupled to lenses**, **Lenslet arrays**. White text: working in the visible, Black text: working in the visible and NIR.

Telescope	Aper. (m)	Instrument	Nr slices, fibers or lenses	Spati. Samp. slice/lense/fiber (arcsec)	Maximum FOV	λ range (μm)	R=λ/Δλ
GTC	10.4	FRIDA	18	0.036 or 0.060	1.2"x2.2"	0.9-2.5	500, 5000, 3000
VLT	8.2	KMOS	24 IFUs 14 slices/IFU	0.2	24 x 2.8"x2.8"	1-2.45	3400-3800
VLT	8.2	MUSE (AO)	24 IFUs 12 Slices/IFU?	0.025 or 0.2	1'x1'	0.46-0.93	2000-4000
Various	~8	SWIFT	44	0.1 or 0.15	6.6"x13.6"	I/Z 0.65-1.0	3500-8500
JWST	6.5	NIRSpec	30	0.1	3"x3"	0.6-5	100, 1000, 2700
JWST	6.5	MIRI	4 IFUs? ~10 Slices/IFU	0.27 to 0.76 Depending on channel	3"x3.9" to 6.7"x7.7" depnding on channel	5-27	2400-3700
HET	9.2	VIRUS	132 IFUs 247/IFU	1	145x2.8"x2.8"	0.34-0.57	5000 opt to NIR
LBT	2x8.4	LUCIFER (2 inst.)	682	0.025 or 0.25	???????	NIR	?
GTC	10.4	SIDE	2500	0.5	30"x30" 3"x3" 1.5"x1.5"	0.35-1.7	1500-30000

Table 25. Comparison with other instruments (SIFU and mIFU modes). Color Code: **Image slicers**, **Fibers coupled to lenses**, **Lenslet arrays**. White text: working in the visible, Black text: working in the visible and NIR.

Instrument	Spectral range	F.O.V. arcminutes	Spectral resolution	MOS number of targets	SIFU
SIDE	0.35-1.7 μm	20’ (diameter)	1500 < R < 30,000	1000	30”x30”
OSIRIS	0.365-1.05I	8’ (diameter)	500-1500-2500	20	No
EMIR	0.9-2.5	6’ x 4’	4000	20	No

Table 26 Comparison of SIDE with OSIRIS and EMIR.

3.2 Instrument Logistics and interface with the telescope

3.2.1 Telescope Characteristics applicable to SIDE

See AD: PUB/TELE/0031-L (1.A), DR/GTC/001 (1.H)

3.2.1.1 Mass and inertia

Some mass and inertia characteristics of GTC are shown in Table 27.

Telescope Mass (kg)		**Inertia Values (kg x m^2)**
• Primary mirror segments and drives	23,540	Tube: Ixx = 5.4 x 10^8 Iyy = 6 x 10^8 Izz = 4.5 x 10^8
• Cassegrain assembly	4,600	
• Folded Cassegrain and counterweight system	8,000	
• Secondary mirror or prime focus	2,000	Vertical tube + mount: Ixx = 1.56 x 10^7 Iyy = 2.15 x 10^7 Izz = 1.30 x 10^7
• Spider + secondary mirror support structure	4,300	
• Upper tube	28,300	
• Lower tube	9,900	Horizontal tube + mount: Ixx = 1.56 x 107 Iyy = 2 x 107 Izz = 1.45 x 107
• Primary mirror cell	12,400	
• Elevation ring and trunnions	41,700	
• Drive discs	10,200	
• Tertiary mirror tower and drives (including M3 baffle)	2,400	
Total tube mass	**147,240**	
• Structure of the mount	76,000	
• Rotating floor	35,000	
• Nasmyth platforms	14,800	
• Nasmyth instruments and rotators	20,000	
Total mount mass	145,800	
Total telescope mass	**293,000**	

Table 27. Telescope mass and inertia.

According to Table 27, Nasmyth Instruments and Rotators are estimated to weight 20,000 kg which means 10,000 kg for EMIR platform (Nasmyth "B" Platform) and 10,000 kg for SIDE platform (Nasmyth "A" Platform).

This 10,000 kg for the Nasmyth "A" Platform must be distributed among the following items:

- A&G System (1,100 kg)
- AO (1,691 kg)
- FRIDA
- SIDE (FPR + Spectrographs + Spectrograph room)
- Electronics
- Etc.

3.2.1.2 Nasmyth Rotator (NR)

The NR is a large flange to which scientific instruments (7,500 kg maximum) and the A&G System (1,100 kg) are attached. The flange is mounted on a bearing driven by a drive unit to allow rotation of the instruments and A&G system around the Nasmyth optical axis, following rotation of the celestial field. The rotator is the mechanical element placed between the Nasmyth instruments (rotating) and the telescope (fixed). In the GTC concept, the A&G arms are located inside the rotator.

The NR comprises: one tape encoder system, a single row cross-rolled bearing with external gear, drivers and brushless motors, one rotator adapter, one support structure, one cable wrap, limit switches and limit shock absorbers.

The support structure, which is welded, supports the NR bearing, the elevation encoder heads, the NR encoder heads, and the NR motor housing. Its bending eigenfrequencies are higher than 15 Hz considering the worst mass distribution over the NR structure.

3.2.1.3 Telescope rotating floor

The rotating floor is a flat, 18-m diameter floor that isolates the telescope chamber from the auxiliary chambers and permits the transit of maintenance vehicles.

This floor must be taken into account as a possible place for additional chambers of SIDE.

3.2.2 Summary of Nasmyth A Platform limitations and requirements

3.2.2.1 Instrument mass

SIDE weigth limits are as follow:

- To Nasmyth Rotator < 2400 kg
- To Nasmyth Platform < 7500 kg

Total mass limit on platform is 10,000 kg and it must be distributed as explained in 3.2.1.1.

3.2.2.2 Platform physical limits

- Limited size of the platform (see *DR/GTC/001*).
- There are two pillars which might interfere with displacement of parts.
- The robot (FPR) must stay vertical.
- The AO bench will stay in front of the NR flange, at a small distance from it.
- It would difficult to move the Pre-optics if it were placed inside the Nasmyth tube.
- Not much space is left on the platform for Electronics, Spectrographs etc. because of AO and FRIDA.
- The A&G ring and arms impose further limitations to space.

3.2.2.3 Summary of available space and requirements for the FPR + dedicated flange

- CoG of SIDE rotating part: -1115 mm < z < +385 mm
- Mass of SIDE rotating part: < 2400 kg
- Mass moment of inertia with respect to the rotating axis of SIDE rotating part: < 15000 kg·m^2
- Unbalanced moment of SIDE rotating part: < 1100 N·m
- Space from A&G arm to focal plane: 390 mm
- Distance from NR attachment flange to focal plane: 385 mm
- Inner aperture of A&G ring: 992 mm (diameter)
- Distance from optical Axis to floor: 2000 mm
- A&G connector blocks rotate with NR and in Figure 63 (red & blue boxes) are at park position.
- Don't invade A&G connector blocks:
    - Inner radius: 1314 mm
    - Outer radius: 1650 mm
- Space needed for Field Corrector: ≅ 200mm
- AO bench could be moved, at least, 1.2 m away from the NR flange.
- GTC M2 mirror can be moved ±1 mm → ±100 mm at focal plane. If GTC A&G has to be used, the maximum focal plane movement allowed is ± 40 mm.
- The Field Corrector is difficult to remove from the Nasmyth tube, but it can't be left there because AO will use all space up to the A&G arms.
- There is no space underneath the AO bench for the FPR.

Figure 54 represents the envelope available for the FPR + dedicated flange (dashed line) and connectors and electronic racks (solid line).

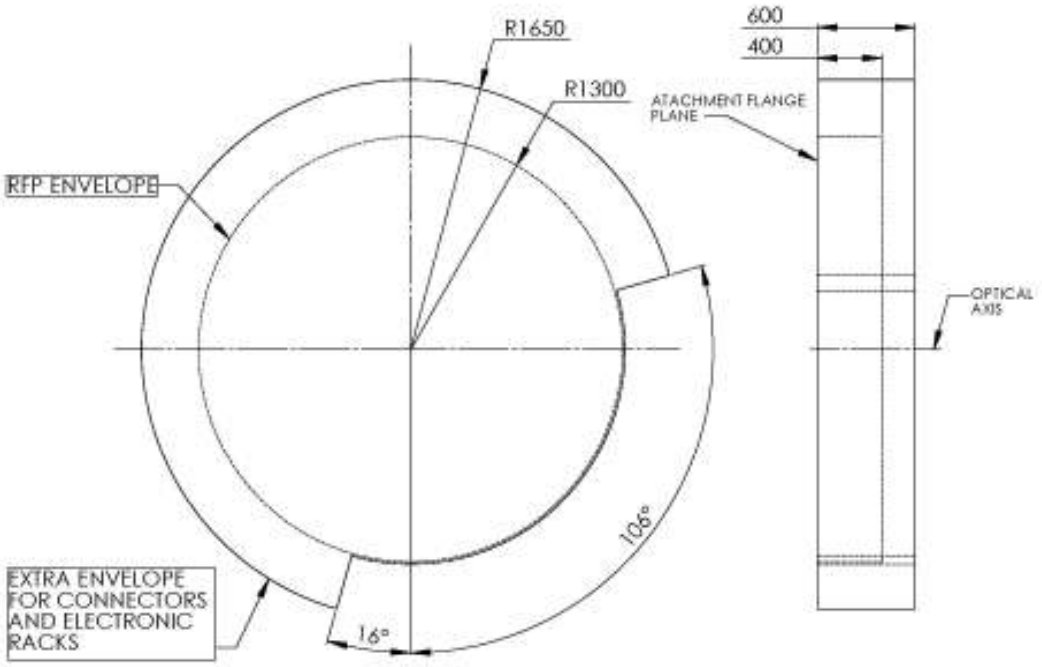

Figure 54. Envelope for the FPR + dedicated flange (dashed) and connectors and electronic racks (solid).

3.2.3 Mechanical Design

3.2.3.1 SIDE subsystems

From the point of view of its interface with the rest of the telescope, SIDE can be broken down into several subsystems:

- A dedicated flange to be attached to the NR interface.
- The FPR.
- The carrier and LCU.
- The Spectrograph room.

SIDE will be placed in the Nasmyth A Focal Station of GTC, sharing this Nasmyth platform with other instruments. For this reason, it must be possible to remove SIDE from the NR to leave place to the other instruments. The dedicated flange simplifies the instrument attaching/detaching from the NR. This operations shall be possible within 45 minutes if done with no air-supply or electrical hand tools.

As the NR interface has the following characteristics:

- 36xM20 at Ø2520
- 6 pins Ø50mm (holes Ø52mm)

– centering flange 2430H7g6 (maximum play = 0.319; minimum play = 0.034mm)

it looks clear that a direct attachment (without the dedicated flange) of the FRP to the NR would result in much more than 45 minutes for the attaching/detaching operations.

3.2.3.2 SIDE configuration during operation

Before the observations, the carrier will place the FPR into the dedicated flange which, at the same time, will be attached to the NR.

During SIDE observations, the carrier with the LCU will return to the carrier parking position. Table 28 shows a resume of this situation.

	SIDE during operation
Attached to NR	Dedicated flange + FPR
On and under Nasmyth Platform	Carrier with LCU + Spectrographs room

Table 28. SIDE configuration during operation.

3.2.3.3 SIDE configuration when it is not in operation

When SIDE finishes the observations, the carrier will detach the FPR from the dedicated flange. The right (when looking at the NR from the platform) area of the Nasmyth platform shall allow the movement of the carrier designed for this purpose over some rails.

The attachment of the dedicated flange to the NR will be permanent. This means that it will not be removed even when other instruments are making their observations. For this reason, the dedicated flange shall leave enough free space for other instruments to make their observations. Table 29 shows a resume of this situation.

	SIDE when it is not in operation
Attached to NR	Dedicated flange
On and under Nasmyth Platform	FPR + Carrier with LCU + Spectrographs room

Table 29. SIDE configuration when it is not in operation.

3.2.3.4 LCU location

See AD: DCI/STMA/0017-R (1.G), DCI/STMA/0018-R (1.G)

The local control system will be implemented in a LCU that should be placed on the carrier. If the rotating conductions provided by GTC are not enough for the instrument needs, the instrument shall incorporate its own cabling rotator.

3.2.3.5 Mechanical interface of the carrier

See AD: DR/GTC/001 (1.H)

To facilitate the operations of detaching the FPR from the dedicated flange in the NR and leave room to the AO, a carrier shall be implemented. The interface area will be located on the NP, shall meet the constraints defined in drawing *DR/GTC/001* and shall meet the values defined in 3.2.3.13.4. The definitive interface areas and fixation points shall be defined by an interface document provided by IAA-CSIC agreed with GTC.

3.2.3.6 Mechanical interface in stowage configuration

See AD: DR/GTC/001 (1.H)

When the system is not mounted in the dedicated flange into the NR, a carrier shall be foreseen to allow an easy removing from NR to the stowage position. The whole of optical fibers and cables shall be properly routed to avoid any stress or damage during transport for stowage. The stowage position in NP is shown in Figure 55.

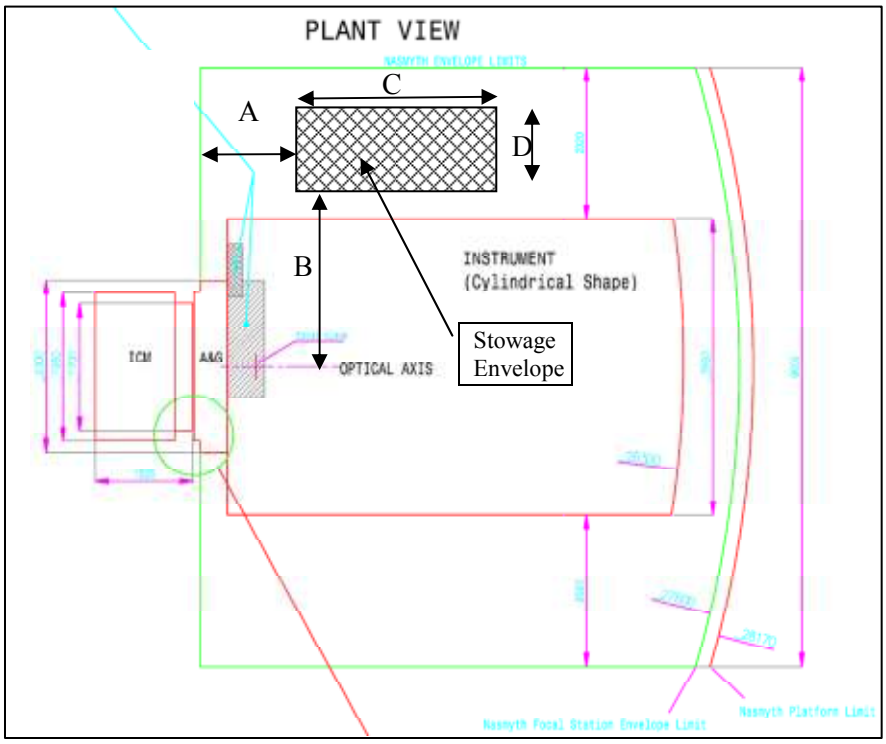

Figure 55 FPR stowage position on the Nasmyth Platform.

3.2.3.7 Envelope of the FPR System

See AD: DCI/STMA/0017-R (1.G), DCI/STMA/0018-R (1.G), DR/GTC/001 (1.H)

In Figure 63 it can be seen the envelope to access to the connection panel and A&G box conductions in the NR.

In accordance with that figure, the maximum envelope that the dedicated flange + FPR shall occupy is a cylinder of 1300 mm radius. The height of that cylinder is defined by the distance that the AO bench and FRIDA instrument can be moved away from the NR flange: 1200 mm.

The axis of the cylinder shall coincide with the optical axis defined in *DR/GTC/001* and one of its flat surfaces (the dedicated flange's surface that goes attached to the NR flange) coincident with the attachment flange of the NR as defined in *DR/GTC/001* and in *DCI/STMA/0017-R*.

The rear part of the robot might be another small cylinder in axis with the main cylinder (see Figure 56), that permits rolling or coiling of the cables (connecting FPR and LCU) and the optical fibers bundle (connecting FPR and Spectrographs room) for the de rotation function, better than use the big 4 metre diameter existing wheel in the NR.

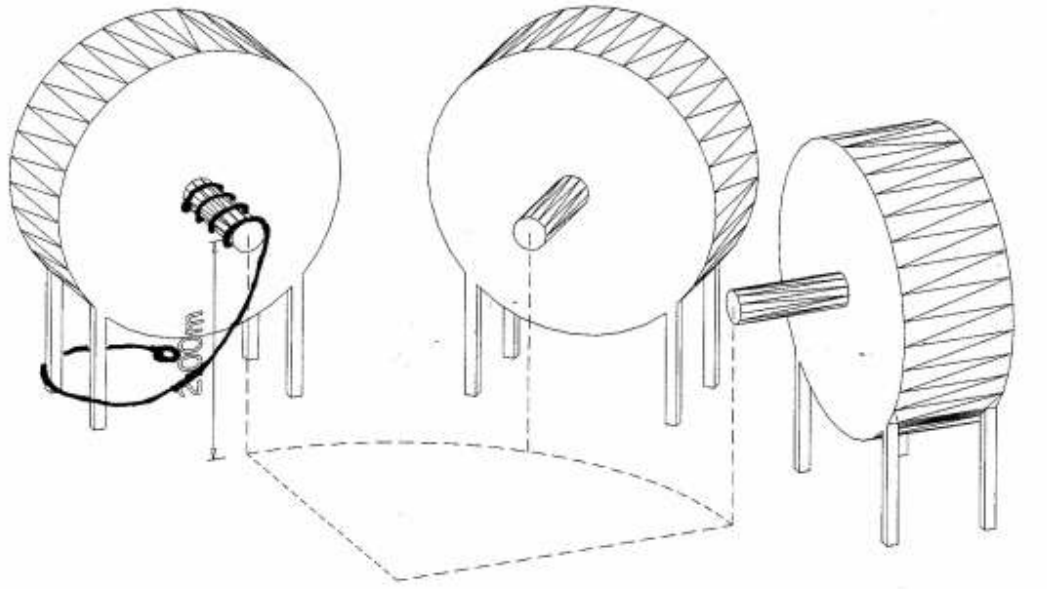

Figure 56. Rolling or coiling of the optical fibers bundle (connecting FPR and Spectrographs room).

A second cylinder of 1650 mm radius and 600 mm high, avoiding the volume occupied by the connection panel and A&G box conductions in the NR (see Figure 63), should be booked for connectors for the electronics arms, electronic racks and accessibility for maintenance. The axis of this second cylinder also coincides with the optical axis defined in *DR/GTC/001* and one of its flat surfaces is coincident with the attachment flange of the NR as defined in *DR/GTC/001* and in *DCI/STMA/0017-R*. The Visual System is foreseen to be located behind the Focal Plane.

3.2.3.8 Nasmyth Platform coordinate system

See AD: DCI/STMA/0017-R (1.G), RPT/STMA/0075-R (2.A)

Each focal station in GTC has its own coordinate system. All the measurements of each station are referred to their own coordinate system. For the definition of Nasmyth A coordinate system see the document *RPT/STMA/0075-R*. As a summary of that document, see next paragraphs and figure.

The Cartesian coordinate system for the Nasmyth Focal Station, (x_{nf}, y_{nf}, z_{nf}) –subindex nf standing for Nasmyth Focal Station–, shown in Figure 57, moves with the Nasmyth focus as the telescope rotates in azimuth.

- Origin O_{nf} : Is at the Nasmyth focus of the telescope, which lies on the telescope elevation axis, D_f meters (7.4 m) from its intersection with the azimuth axis (the floor of the Nasmyth platform lies D_{nh} meters (2 m) beneath the elevation axis).
- xnf-axis: Perpendicular to the nominal gravity vector and to the elevation axis. Its positive sense is defined so that the three axes constitute a right-handed coordinate system.
- ynf-axis: Its positive sense points to the zenith (anti-parallel to nominal gravity vector).
- znf-axis: Coincides with the optical axis (elevation axis) and points towards the tertiary mirror (opposite to the light beam sense).

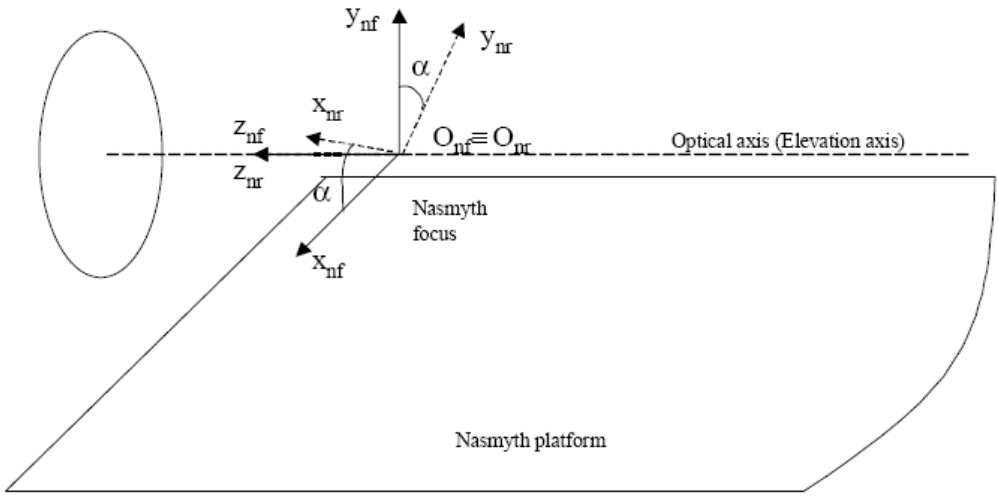

Figure 57. Nasmyth Focal Station and Nasmyth rotator coordinate systems.

3.2.3.9 Interface control between A&G CORE and SIDE

See AD: ESP/OPTI/0029-L (3.A), RPT/OPTI/0093-L (3.A)

The total mass of the A&G is 1100 kg.

The general configuration of the A&G (Acquisition and Guiding System) core (see Figure 58) is based on two probe arms which are moved independently in the field. The probe arms have a flat mirror (the 'probe mirror') at their end which can be positioned everywhere in the field and which can also be completely withdrawn. The arms contain optical instruments which are fed by the flat mirror.

It shall be possible to position both guide arm probes anywhere within a field of view of diameter 992 mm centered on the center of the field of view available at the Nasmyth focus. It shall also be possible to completely withdraw all components to avoid shadowing of the same area.

Thus, SIDE will receive the light through a maximum unvignetted diameter of 992 mm.

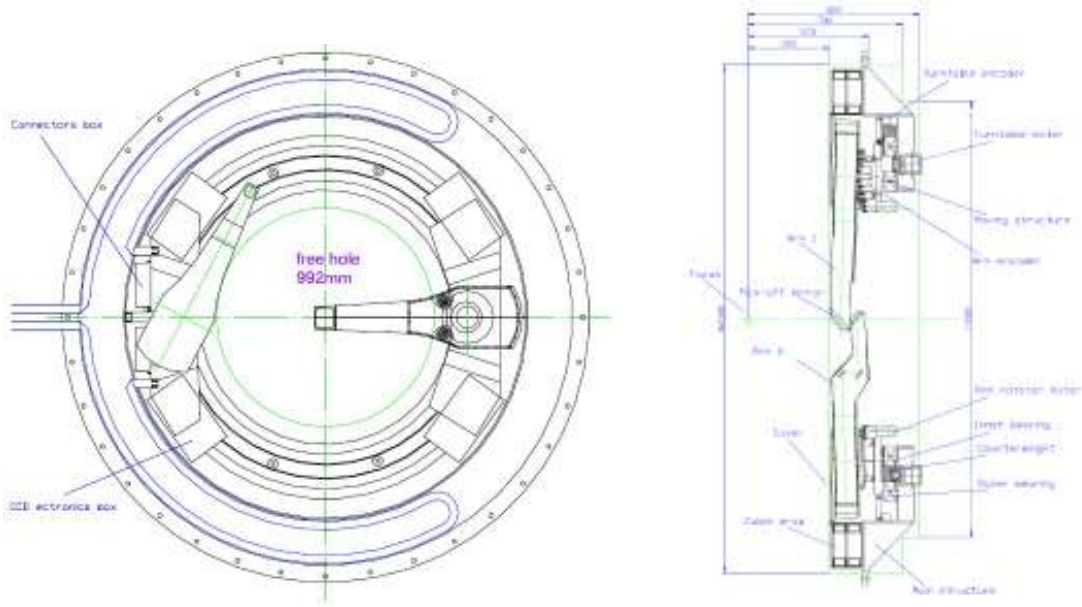

Figure 58. A&G CORE Front and Lateral Views.

3.2.3.10 Interface control between "AO system + FRIDA" and SIDE

See AD: RPT/OPTI/0244 –R (1.B)

The AO system will be located on the GTC Nasmyth A platform, and mounted on it by means of a structure which supports a commercial optical bench on which the wavefront corrector system and wavefront sensor will be placed.

The location of the AO system on the Nasmyth platform is shown in Figure 59 and Figure 60. The AO bench will have to be moved in order to leave space for the SIDE FPR. The AO bench could be monted on a trolley and moved up to 1200 mm away from the NR flange (see

3.2.3.7). FRIDA will also be installed at the Nasmyth A platform, right behind the AO System. It could also be moved 1200 mm away from the NR flange as the AO System does.

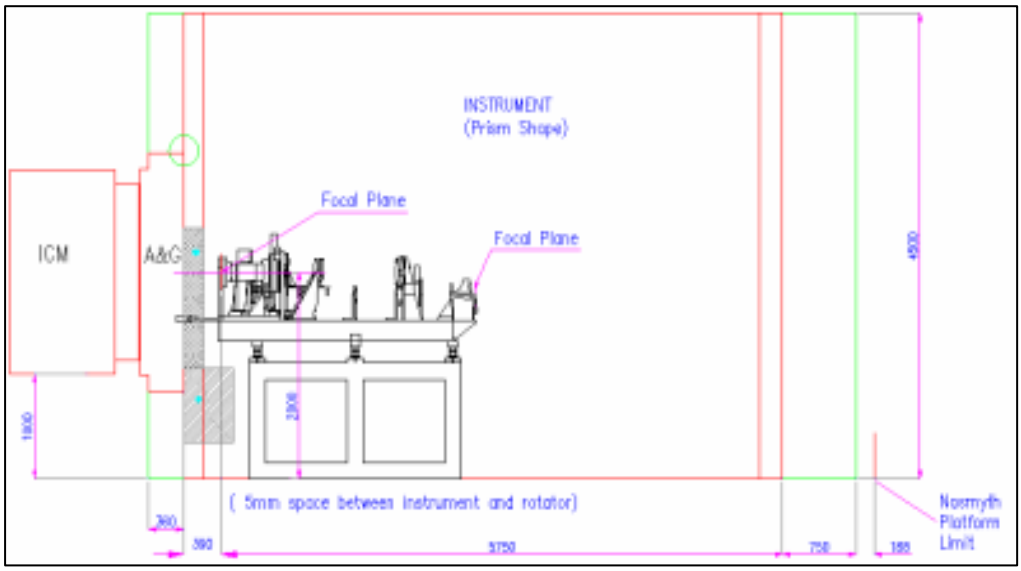

Figure 59. AO Front view

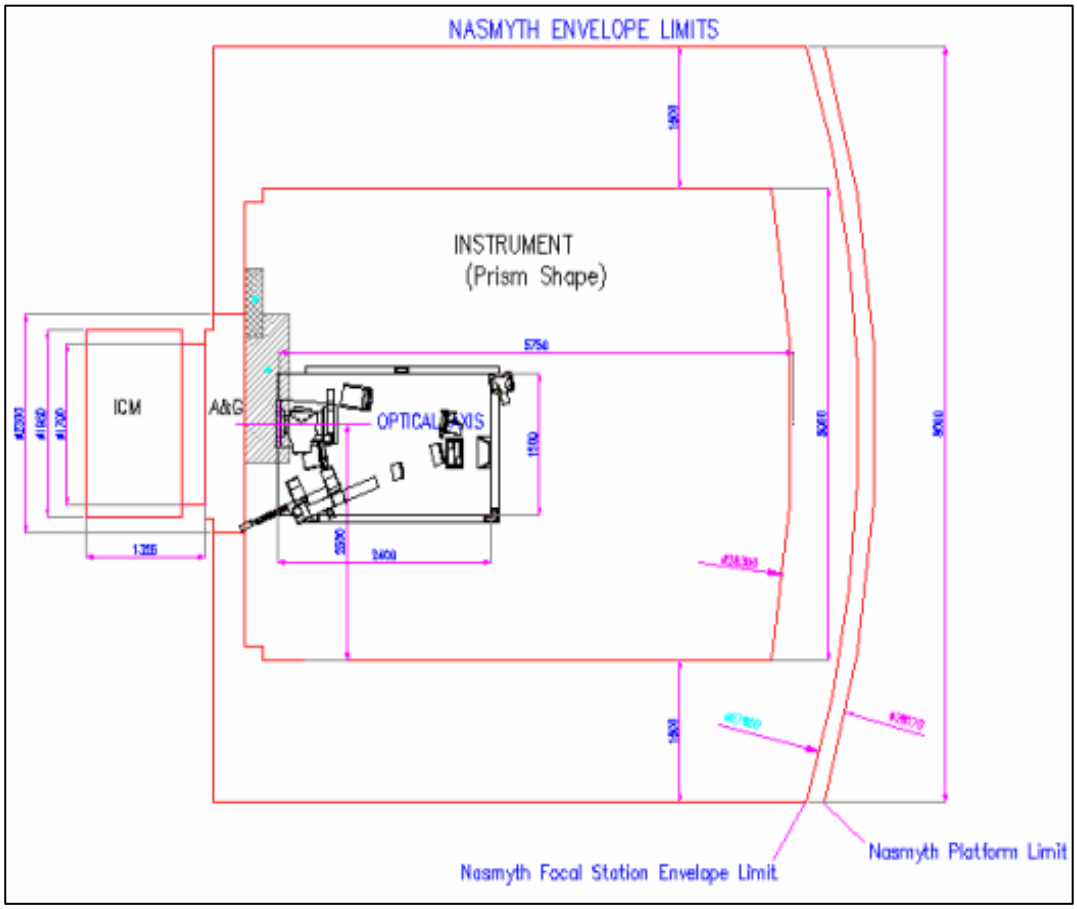

Figure 60. AO Plant view

3.2.3.11 Interface control between NR and SIDE

See AD: *DCI/STMA/0017-R (1.G), DCI/STMA/0018-R (1.G)*

Simplifying, it can be said that SIDE has two items: one item is the part of the instrument completely attached to the rotator and the other item is laying on and under the Nasmyth platform. The physical connection between the rotating and non-rotating parts of the instrument will be through optical fibers (between FPR and Spectrographs room) and cables (between LCU and FPR), and both parts can be considered independent one from each other from the point of view of the structure.

The envelope constraints for the rotating part are as in drawing: *DR/GTC/001 (Sheet 2/2)* and for the non-rotating part are as in drawing: *DR/GTC/001 (Sheet 1/2)*.

The rotating part is subjected to the requirements contained in document *DCI/STMA/0017-R* and the non-rotating part is subjected to the requirements contained in document *DCI/STMA/0018-R*.

Figure 61 shows the elements that interface with the FPR:

1. A&G Envelope
2. Nasmyth rotator flange
3. Nasmyth FPR instrument flange
4. WFC envelope
5. Nasmyth connectors envelope

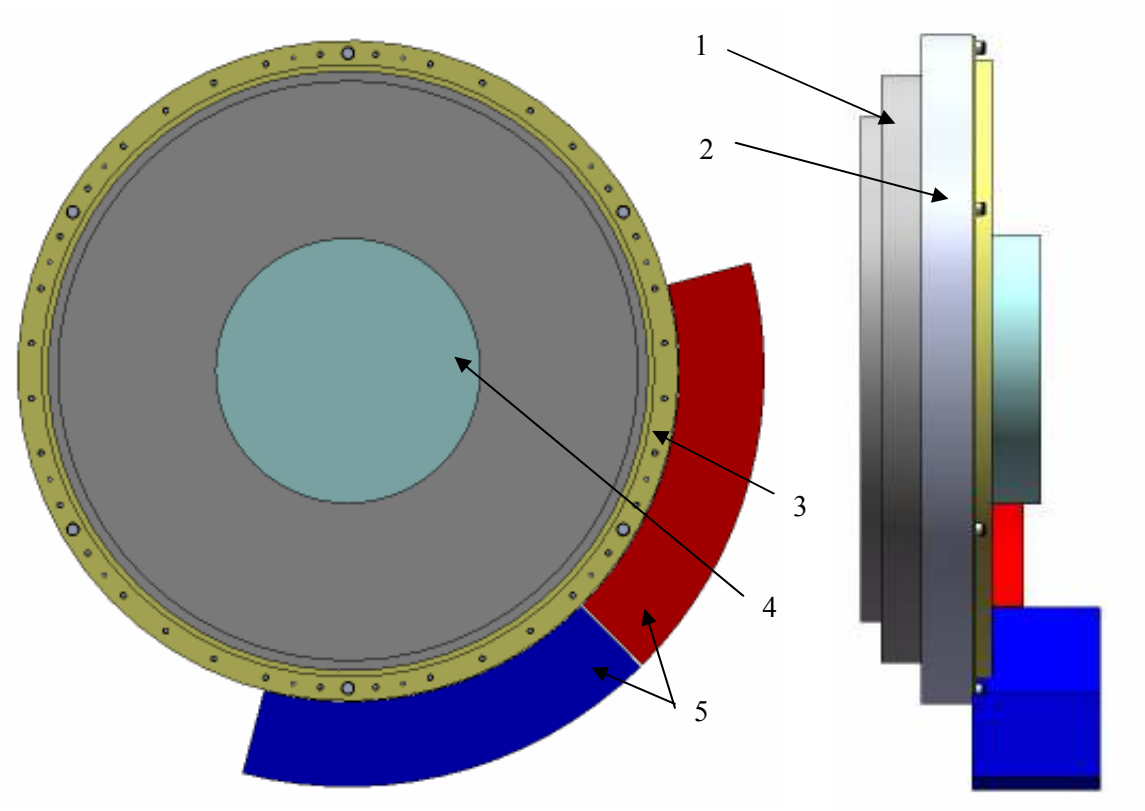

Figure 61. I/F flange to attach Robot Side.

3.2.3.12 Requirements for the rotating part

See AD: DCI/STMA/0017-R (1.G), ESP/STMA/0017-L (1.M), DR/GTC/001 (1.H), DR/I-IN-TL-001/001 (1.C)

3.2.3.12.1 Temperature of reference

The temperature of reference for all the dimensions and tolerances, unless otherwise specified, shall be 8.5º C.

3.2.3.12.2 Dimensional envelopes

3.2.3.12.2.1 Envelope for Nasmyth rotator

The NR envelope is as shown in drawings *DR/GTC/001 (Sheet 1/2 and 2/2)*.

This envelope includes the instrument rotator, cable wrap and rotator supporting structure.

3.2.3.12.2.2 Envelope for the rotating part of the instrument

The envelope of the rotating parts of SIDE shall be as shown in drawing *DR/GTC/001 (Sheet 2/2)*.

3.2.3.12.3 Loads on the Nasmyth rotator due to the instrument

3.2.3.12.3.1 Range of mass to be directly rotated

The science instrument mass to be directly rotated shall be in the range from 0 to 2400 Kg.

3.2.3.12.4 Other physical requirements

3.2.3.12.4.1 CoG of the rotating part of SIDE

The z coordinate of the Center of Gravity of the rotating part of SIDE shall be able to be located within the range of coordinates z = +385 mm to z = -1115 mm.

3.2.3.12.4.2 Mass moment of inertia around z-axis

The mass moment of inertia with respect to the rotating axis of SIDE (axis z in the Nasmyth coordinate system) attached to the rotator shall be less than or equal to 15000 $kg \cdot m^2$.

3.2.3.12.4.3 Unbalanced forces

The NR is able to rotate an unbalanced science instrument with a net moment up to 1100 N·m (see section *5.2.11.7* of document *ESP/STMA/0017-L*).

3.2.3.12.5 Attachment of SIDE to the Nasmyth Rotator

3.2.3.12.5.1 Attachment concept

The mechanical interface between the rotator and the rotating part of SIDE shall consist of a flat circular hollow flange (see Figure 62 and *DR/I-IN-TL-001/001*).

The Active Optics (AcO) functionality will maintain the Nasmyth focal plane both in position and shape with respect to this attachment flange, within the allocated errors with respect to the nominal situation.

The reference for assembling the instrument in the rotator shall be the attachment flange, when the rotator is in its parking position (see 3.2.3.14).

3.2.3.12.5.2 Attachment area

The attachment flange dimensions are as shown in drawing *DR/I-IN-TL-001/001*.

3.2.3.12.5.3 Attachment flange plane location

The attachment flange plane is parallel to the XY plane located at z = +385 mm (see drawings *DR/GTC/001 (Sheet 1/2 and 2/2)*).

3.2.3.12.5.4 Attachment points location

The attachment points are located in the attachment flange as shown in *DR/I-IN-TL-001/001*.

3.2.3.12.5.5 Local stiffness

The attachment flange is able to bear the maximum mass attached to it in 6 points equally spaced, while the requirements of dynamic behaviour and gravitational deformations are met.

3.2.3.12.5.6 Centering

3.2.3.12.5.6.1 Centering concept

There is a cylindrical centering flange, normal to the attachment flange, in order to center the instrument on the attachment flange (see Figure 62).

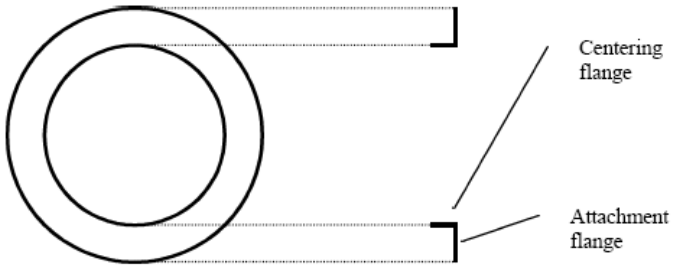

Figure 62. Schematic drawing of the attachment and centering flanges. Frontal and lateral views.

3.2.3.12.5.6.2 Centering diameter

The centering diameter is as shown in drawing *DR/I-IN-TL-001/001*.

3.2.3.12.5.7 Tolerances

3.2.3.12.5.7.1 Non-specified tolerances

All those non-specified tolerances shall be according to ISO 2768-fH-(E).

3.2.3.12.5.7.2 Assumptions

For all the tolerances it shall be assumed that:

• the telescope tube points to the zenith

• only the A&G is mounted in the rotator (not SIDE)

• the required values are maximum values in the whole rotation range

3.2.3.12.5.7.3 Concentricity tolerance of the real attachment flange axis with respect to the real elevation axis

The concentricity tolerance of the *real attachment flange axis* with respect to the *real elevation axis* is 0.5 mm (**TBC**).

3.2.3.12.5.7.4 Parallelism tolerance of the real attachment flange axis with respect to the real elevation axis

The parallelism tolerance of the *real attachment flange axis* with respect to the *real elevation axis* is 0.1 mrad (**TBC**).

3.2.3.12.5.7.5 Concentricity tolerance of the rotation axis with respect to the real attachment flange axis

The concentricity tolerance of the rotation axis with respect to the *real attachment flange axis* is 0.5 mm (**TBC**).

3.2.3.12.5.7.6 Parallelism tolerance of the rotation axis with respect to the real attachment flange axis

The parallelism tolerance of the rotation axis with respect to the *real attachment flange axis* is 0.050 mrad.

3.2.3.12.5.7.7 Tolerance of the diameter of the centering flange

The tolerance of the diameter of the centering flange is g6H7 according to ISO standards (**TBC**) (see 3.2.1).

3.2.3.12.5.7.8 Tolerance of the position of the attachment points

The tolerance of the position of the attachment points with respect to their nominal position as defined in 3.2.3.12.5.4 is 0.5 mm.

3.2.3.12.5.7.9 Tolerance of the distance between the real tube axis and the attachment flange

The tolerance of the distance between the real tube axis and the center of the attachment flange (the crossing point between the real attachment flange axis and the plane containing the rotator attachment flange) shall be ±1 mm.

3.2.3.12.5.8 Physical properties of the attachment flange

3.2.3.12.5.8.1 Flange Flatness

3.2.3.12.5.8.1.1 Nasmyth rotator attachment flange flatness

The Nasmyth rotator attachment flange flatness is better than 0.040 mm.

3.2.3.12.5.8.1.2 SIDE attachment flange flatness

The instrument attachment flange flatness shall be better than 0.040 mm.

3.2.3.12.5.8.2 Flange roughness

3.2.3.12.5.8.2.1 Nasmyth rotator attachment flange roughness

The Nasmyth rotator flange roughness is Ra 1.6 microns or better (ISO 1302).

3.2.3.12.5.8.2.2 SIDE attachment flange roughness

The instrument flange roughness shall be Ra 1.6 microns or better (ISO 1302).

3.2.3.12.5.8.3 Differential thermal expansion

In order to avoid the effects of the differential thermal expansion, SIDE attachment flange shall have a CTE similar to the rotator attachment flange CTE.

3.2.3.12.5.9 Gravitational deformations of the attachment flange

Motions of the attachment flange due to gravitational deformations, when SIDE and A&G are mounted in the rotator, are:

- Motion in the X-Y plane: < 0.5 mm
- Rotation around X axis: between -45 arcsec and +30 arcsec
- Rotation around Y axis: < 10 arcsec

Those motions are maximum values in the whole rotation range and in the whole telescope elevation and azimuth range.

In order to meet the requirement for rotation around X axis, the rotator is mounted in the telescope structure in such a way as when the rotator only supports the A&G, the attachment flange rotation around X axis is –45 arcsec. In this way, the attachment flange rotation around X axis, as a function of the science instrument rotating mass and assuming the A&G is mounted in the rotator, follows the values given in Table 30:

Items of SIDE mounted to the NR	**Attachment flange rotation around X axis**
Dedicated flange	≥ -45 arcsec
Dedicated flange + FPR	≤ +30 arcsec

Table 30. Attachment flange rotation around X axis.

3.2.3.12.5.10 Mounting and detaching

3.2.3.12.5.10.1 Mounting pins

In order to facilitate the attachment of the instrument to the NR, the NR attachment flange has 6 mounting pins as shown in drawing *DR/I-IN-TL-001/001*.

3.2.3.12.5.10.2 Mounting holes

In order to facilitate the attachment of the dedicated flange of SIDE to the NR, the instrument flange shall have 6 through mounting holes as shown in drawing *DR/I-IN-TL-001/001*.

3.2.3.12.5.10.3 Extracting recesses

It is not necessary to detach SIDE's dedicated flange from the NR at any time (see 3.2.3.3). However, in case it is necessary to do it and in order to facilitate the dedicated flange detachment from the NR, the NR attachment flange has 12 extracting recesses as shown in drawing *DR/I-IN-TL-001/001*.

3.2.3.12.5.10.4 Extracting bolts

In order to facilitate SIDE's dedicated flange detachment from the NR, the instrument shall have 12 extracting bolts as shown in drawing *DR/I-IN-TL-001/001*.

3.2.3.12.6 Positioning of the FPR into the dedicated flange

Te carrier shall place the FPR into the dedicated flange with a radial tolerance of ≅0.5mm (**TBC**). This error shall be compensated by M2 or by the SIDE acquisition & guiding system.

3.2.3.12.7 Nasmyth cable wrap concept

The Nasmyth cable wrap is an integral part of the NR. The cable wrap rotates the cabling needed, if any, by the rotating part of SIDE and the A&G at the same position, velocity and acceleration than the rotating part of SIDE and A&G.

3.2.3.12.8 Conductions connection

The rotating part of SIDE and A&G box conductions (cables and hoses) can go from the rotating instrument cabling outputs to a connection panel fixed to the rotating part of the NR. SIDE design shall guarantee the access to this panel for plugging and unplugging purpose while its rotating part is mounted on the rotator. Therefore, SIDE shall not invade the volume specified in Figure 63.

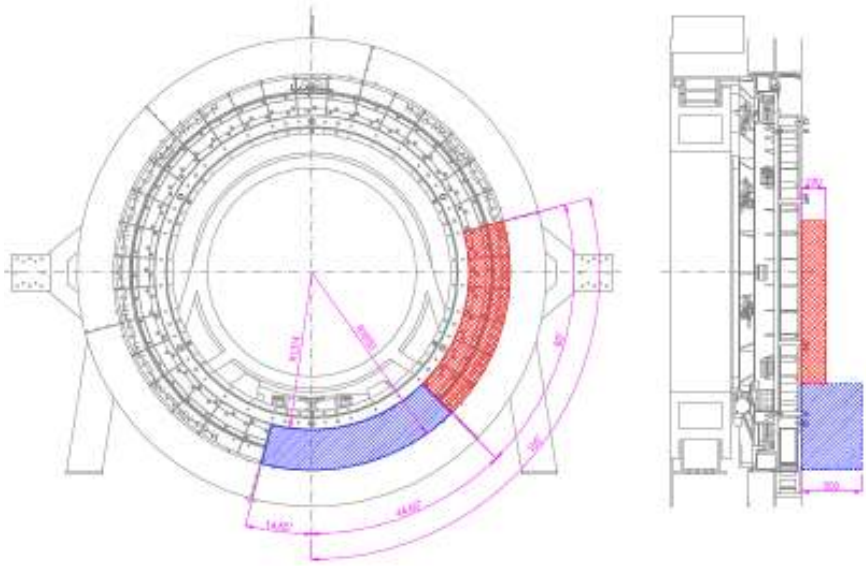

Figure 63. Envelope to access to the connection panel and A&G box conductions in the NR.

If the rotating conductions provided by GTC are not enough for the instrument needs, the instrument shall incorporate its own cabling rotator.

3.2.3.13 Requirements for the non-rotating part

See AD: DCI/STMA/0018-R (1.G), DR/GTC/001 (1.H), DCI/STMA/0021-R (1.C)

3.2.3.13.1 Temperature of reference

The temperature of reference for all the dimensions and tolerances, unless otherwise specified, shall be 8.5º C (the same as in 3.2.3.12.1).

3.2.3.13.2 Dimensional envelope

The dimensional envelope for SIDE at the Nasmyth platform shall be as presented in drawings *DR/GTC/001 (Sheet 1/2 and 2/2)*.

3.2.3.13.3 Loads on the Nasmyth Platforms

3.2.3.13.3.1 Fixed (non-rotating) mass of SIDE

The maximum mass of the fixed part of SIDE shall be 7500 kg.

3.2.3.13.3.2 Distributed loads

The Nasmyth platform is able to support a distributed load of 1500 kg/m2 in any place inside the instrumentation envelope (DR/GTC/001 (Sheets 1/2 and 2/2)).

3.2.3.13.3.3 Punctual loads

The Nasmyth platform resistant areas (see 3.2.3.13.4.3) are able to support punctual loads up to 2000 kg.

3.2.3.13.4 Attachment of the fixed (non-rotating) part of SIDE to the Nasmyth Platform

3.2.3.13.4.1 Attachment concept

The fixed part of SIDE shall be supported by the Nasmyth platform.

The Active Optics (AcO) functionality maintains the Nasmyth focal plane both in position and shape with respect to the NR attachment flange, within the allocated errors with respect to the nominal situation (see 3.2.3.12.5.1).

The reference for assembling the instrument in the Nasmyth focal station shall be the Nasmyth rotator attachment flange, when the rotator is in the parking position (see 3.2.3.12.5.1).

3.2.3.13.4.2 Attachment area

The fixed part of SIDE shall be able to be located anywhere inside the instrumentation envelope at the Nasmyth platform.

3.2.3.13.4.3 Attachment points location

The attachment points shall be located in resistant areas (see 3.2.3.13.3.3). The distance between two adjacent attachment points shall be as a maximum 1500 mm in x-axis and 1500 mm in z-axis as shown in drawing *DR/TL-MN-NP/001*.

3.2.3.13.4.4 Tolerance of the position of the attachment points

The tolerance of the position of the attachment points with respect to their nominal position as defined in 3.2.3.13.4.3 shall be 0.5 mm.

3.2.3.13.4.5 Gravitational deformations of the attachment points

Motions of the attachment points due to gravitational deformations, when the science instrument is mounted on the platform, shall be:

- Motion along X axis: **TBD** μm
- Motion along Y axis: **TBD** μm
- Motion along Z axis: **TBD** μm
- Rotation around X axis: **TBD** μrad
- Rotation around Y axis: **TBD** μrad
- Rotation around Z axis: **TBD** μrad

Those motions are maximum values in the whole telescope azimuth and elevation range.

3.2.3.13.4.6 Attachment point dimensions

Each attachment point shall be as shown in drawing *DR/TL-MN-NP/001*.

3.2.3.13.5 Local eigenfrequencies of the Nasmyth Platforms

The lowest local eigenfrequency at each Nasmyth platform shall be at least 13.64 Hz.

3.2.3.13.6 Handling

It shall be taken into account that due to other science instruments handling (installation and removal) the central area of the Nasmyth platform shall allow the movement of the carts designed for this purpose over the rails (see drawing *DR/TL-MN-NP/001*). See the interface document *DCI/STMA/0021-R*.

3.2.3.13.7 Conductions connection

See 3.2.3.12.8.

3.2.3.13.8 LCU location guideline

See 3.2.3.4.

3.2.3.14 Nasmyth Rotator Parking Position

See AD: DCI/STMA/0017-R (1.G)

To compensate for the rotation of the celestial field during observations, the telescope control system continuously controls the position angle of the rotator, rotating the instrument and the A&G attached to it with an accuracy of 6.5 arcsec rms. To protect the instrument cable wrap systems, the Nasmyth rotator is equipped with proximity, safety limits, and shock absorbers, which prevent movement beyond preset angles (± 324º).

The parking position of the NR is at the center of the rotation range.

The optical fibers and cables of SIDE must be long enough to permit the rotation of the rotating part of the instrument (dedicated flange + FPR) when it is attached to the NR.

3.2.3.15 Cables and optical fibers bundle wrap concept

In Figure 64 it is shown the optical fibers wrap concept.

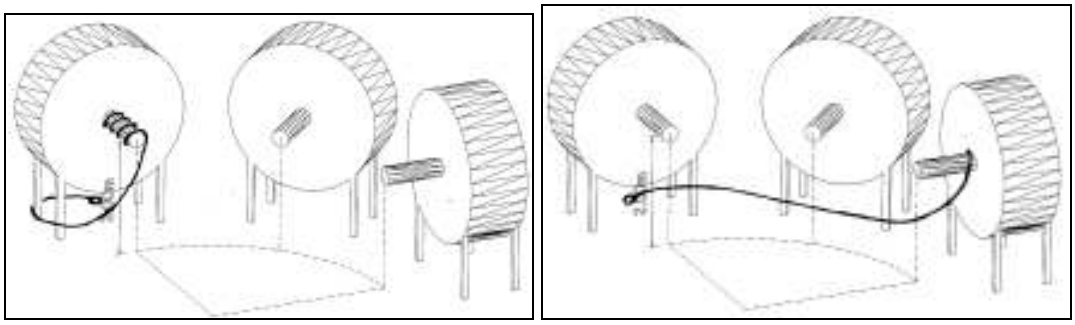

Figure 64. Optical fibers during observations (left) and in parking position (right).

The small cylinder (in the rear part of the robot) in axis with the main cylinder (see Figure 64), permits rolling or coiling the cables (connecting FPR and LCU) and the optical fibers bundle (connecting FPR and Spectrographs room) for the de rotation function, better than use the big 4 metre diameter existing wheel in the NR (see 3.2.3.7).

3.2.3.16 Nasmyth Rotator Zero Reference

See AD: DCI/STMA/0017-R (1.G)

When the NR is at its parking position one of the mounting pins shall be at the maximum y coordinate. This must be taken into account for attaching the dedicated flange of SIDE to the NR since the reference for assembling the instrument in the Nasmyth focal station shall be the NR attachment flange, when the rotator is in the parking position.

3.2.4 The Spectrograph room

3.2.4.1 System description

Notice that the requirements for the room have changed lately as the number of spectrographs has increased (See Figure 69). The following analysis will need a major revision and new parameters for the Spectrographs Room will have to be defined in the following phases. This part is left here as an indication of what will need to be done.

The function of the SIDE Spectrograph room is to support the spectrographs in a position below the Nasmyth A platform, but close enough in order to keep the length of the fibers as short as possible. The required internal dimensions of the room are foreseen to be

8 x 3.5 x 2.5 m (W x D x H). The Spectrograph room shall maintain the spectrograph at a constant temperature and controlled humidity.

The Spectrograph shall avoid the entrance of light from the telescope chamber, shall not have any light emitter device and shall be black painted in the inner side.

The system has been splitted according to the product tree shown in Figure 65.

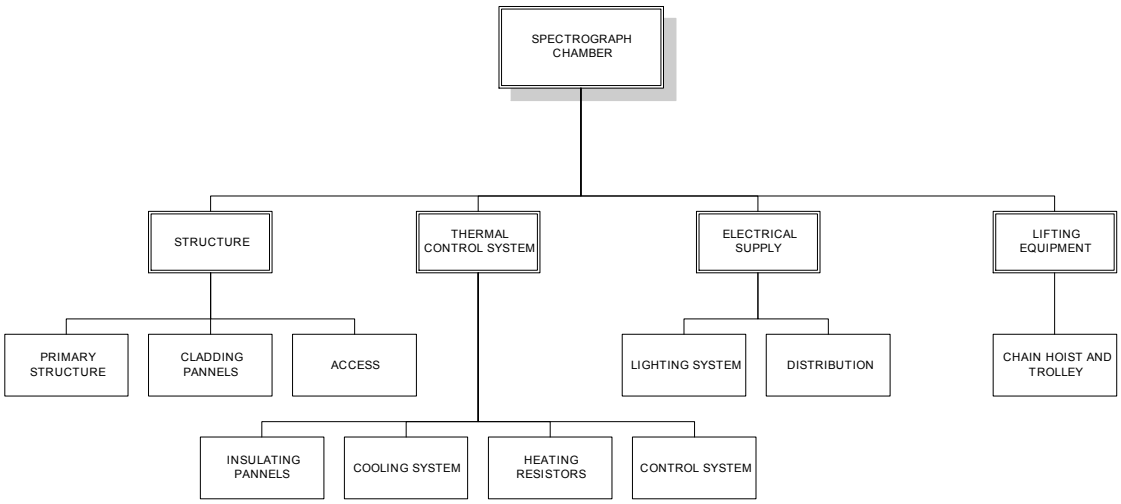

Figure 65 SIDE Spectrograph room Product Tree.

After exploring a few possible locations for the Spectrograph room, the best appears to be below the Nasmyth Platform, at a height of 4 m from the azimuth floor and at a distance of 7 m from the azimuth axis, out of the telescope structure. This is shown in Figure 66.

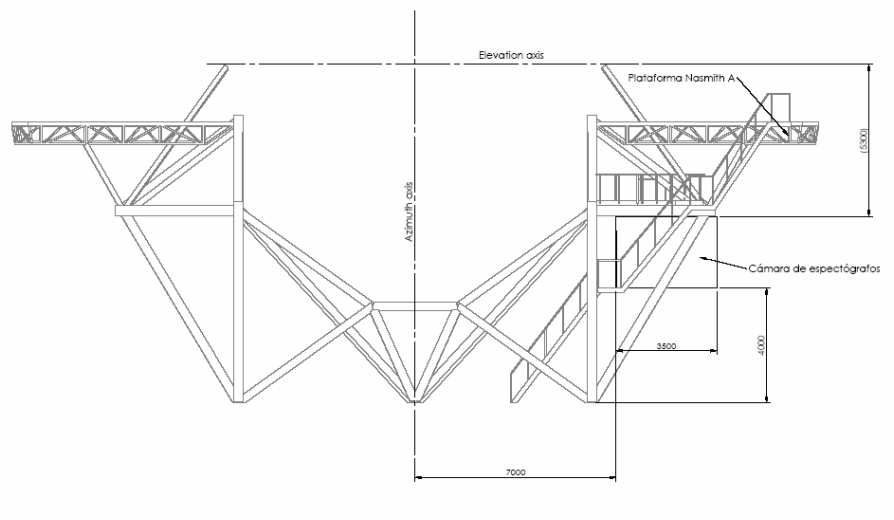

Figure 66 SIDE Spectrograph room location layout.

The main drawback of the other locations was the interference with telescope dome components (enclosure catwalks), the reduced available height and the difficulty in placing a standard lifting equipment

Figure 67 and Figure 68 show a view of the spectrograph room integrated onto the GTC structure. Following the recent baseline for the number of spectrographs, an example of a possible spectrograph distribution is shown in Figure 69.

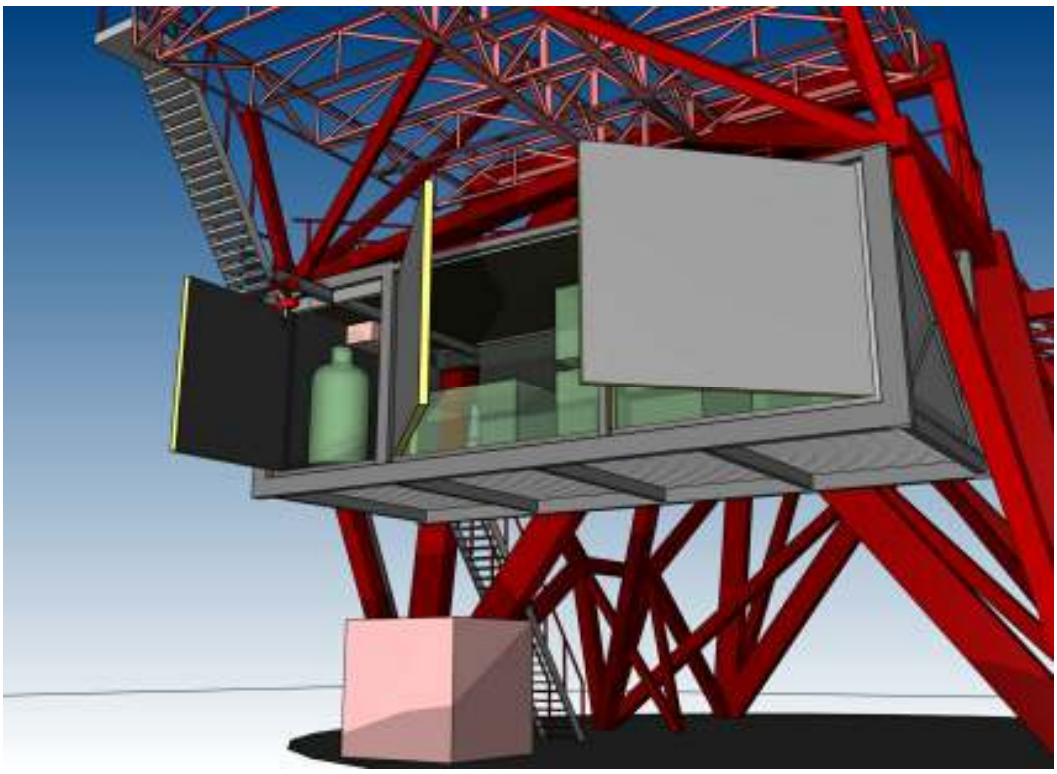

Figure 67 SIDE Spectrograph room Layout.

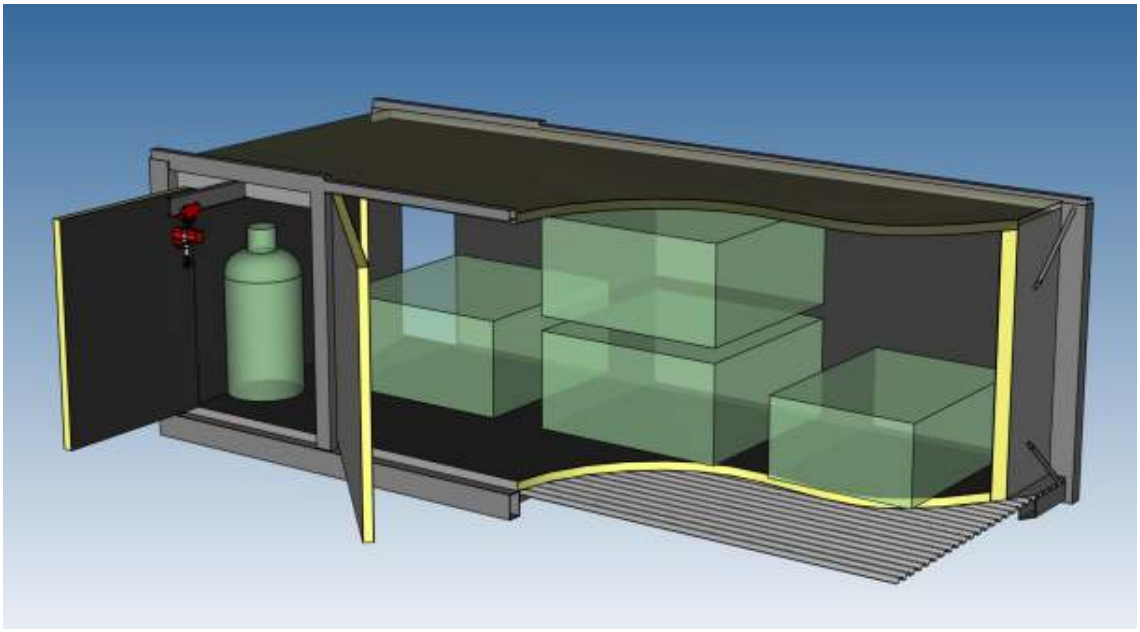

Figure 68 SIDE Spectrograph room Layout

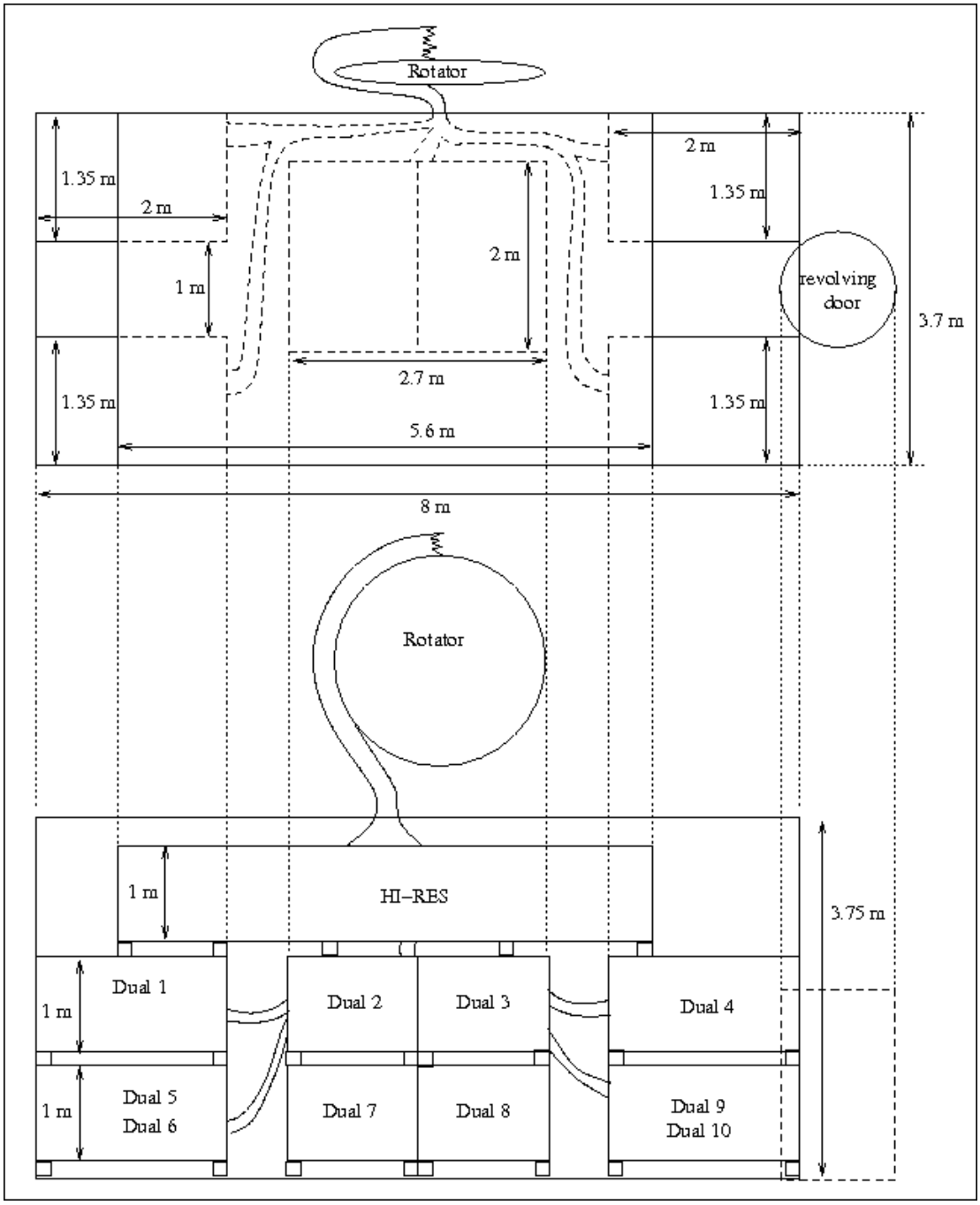

Figure 69 Top and side view of a possible distribution of the spectrographs in the room.

In the following chapter the requirements for each of the systems are summarized, the proposed solution is presented and the main interfaces with the GTC identified.

3.2.4.2 Structure

3.2.4.2.1 Requirements

The structure shall support the spectrographs in the position proposed in Section 3.2.4.1. The structure must withstand the existing loads,

- weight of the equipment: estimated as 3000 kg for the spectrographs, 500 kg for maintenance staff and 100 kg for the nitrogen cylinder.
- wind loads when the telescope is in operation
- others:
    - The vibration induced by external equipment (i.e. cooling system fans) and persons performing maintenance operation must be limited.
    - No particular requirement is stated regarding the dynamic behaviuour and natural frequencies.

The Spectrograph room must have the following accesses,

- entrance door on the inner side of the chamber, close to the staircase in order to facilitate the access for persons
- a large access for big loads on the outer side of the chamber
- an optional trap door for lifting the nitrogen cylinder

3.2.4.2.2 Description

The proposed structure consists of two frames hanged from the nodes of the telescope azimuth structure below the Nasmyth "A" Platform. The two frames are braced to each other by means of four tension rods and connected by means of several purlins.

In order to support the chain hoist an additional IPE profile supported on two frames has been considered.

The structure has been dimensioned in order to withstand a distributed load of 150 kg/m^2 (totalizing 4200 kg), with a limited deflection of L/750 (about 11mm).

The first natural frequencies of the system are,

- 3.5 Hz in vertical direction
- 8.5 Hz in vertical direction

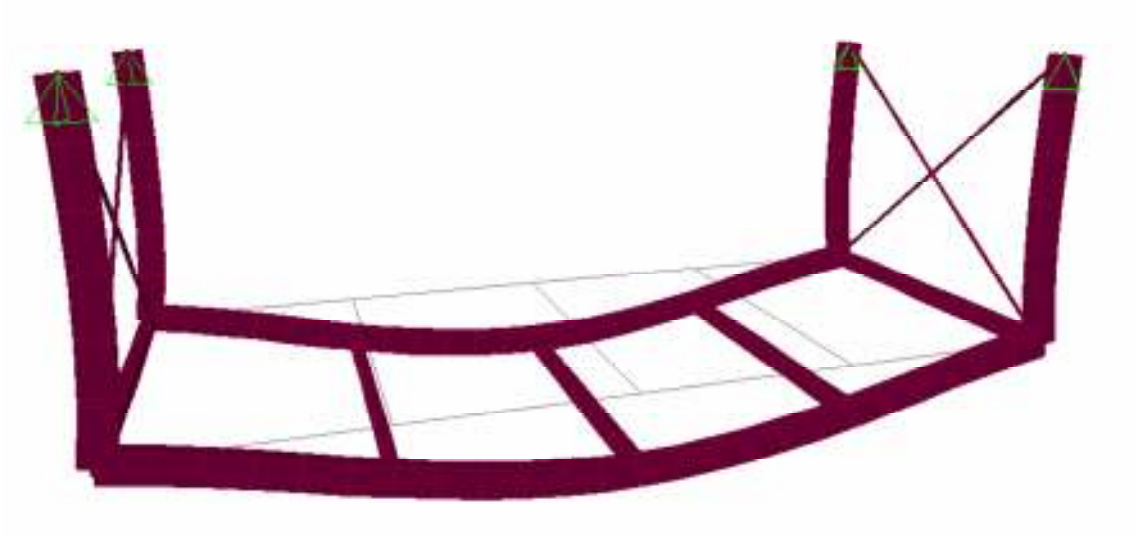

Figure 70. Deflection shape

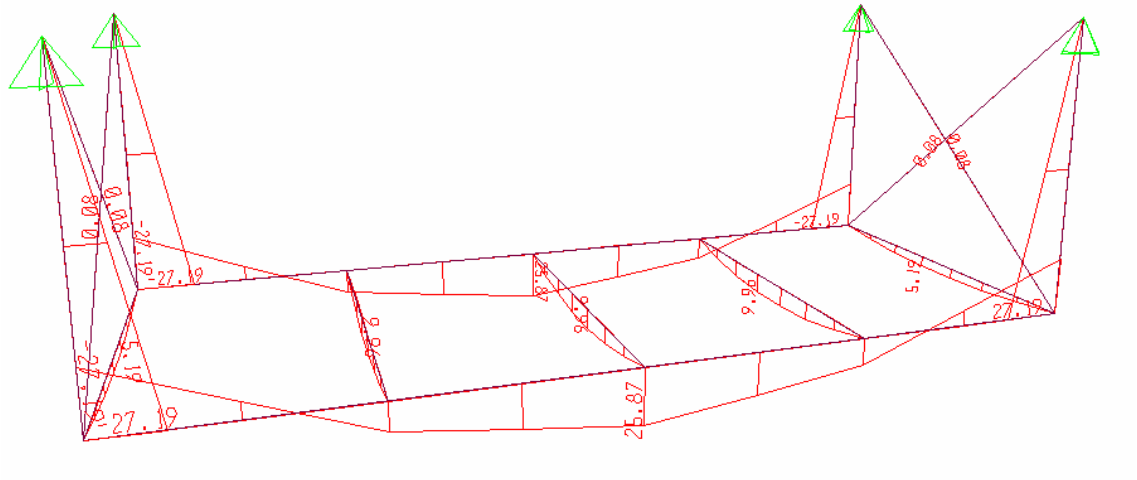

Figure 71. Bending moments diagram

The estimated weight of the primary structure designed according to the above commented criteria is about 2000 kg. The Bending moments and Deflection shape of the structure are shown in Figure 70 and Figure 71).

The weight of the steel structure can be subjected to a further optimization by,

- considering an intermediate support attached to the telescope structure or resting on the observing floor.

- adjusting the stiffness criteria as function of the requirements of the spectrographs.
- adjusting the weight of the considered equipment.

The cladding will consist on a deck plate on the ground and light cladding panels on walls and roof. The thermal insulation will depend on the insulating panels considered in the Thermal Control System.

3.2.4.2.3 Interfaces

1. Interface with the GTC Telescope Structure. The most suitable way of connecting the structure to the GTC azimuth structure nodes shall be analyzed and the static/dynamic requirements of the GTC azimuth structure shall be revised.

3.2.4.3 Thermal control system

3.2.4.3.1 Requirements

The Thermal Control System shall maintain the Spectrograph room temperature at the constant temperature of 8.5 ºC ± 1 ºC, despite the temperature of the telescope chamber which is subjected a variable range of temperatures.

The Spectrograph room shall be thermally insulated to avoid heat transfer between the two controlled chambers.

Appart from the heat loads transferred from the telescope chamber (which can be positive of negative), the following heat loads per spectrograph arm must be considered,

- CCDs proximity electronics: 6 W (permanent)

- Gratings motors: 60 W

- Pseudo-slit motors: 60 W

- Camera motors: 60 W

- CCDs Shutters motors: 60 W (permanent)

A total heat generation of 250 W per spectrograph arm can be estimated. Considering two low resolution spectrographs (with two arms, one for IR and one for visible) and one high resolution spectrograph, a total heat generation of 1500W can be estimated.

The relative humidity in the chamber shall be below 50%, and a humidity controlling device must be provided in order to avoid too low values.

3.2.4.3.2 Solution description

The Thermal Control System will be composed by,

- the insulation panels, for minimizing the heat transferred from/to the telescope chamber
- a cooling system, for compensating for the heat transferred from the telescope chamber and the internal heat generation
- a heating resistors battery, for compensating for the heat transferred to the telescope chamber
- a control system to control the operation of the above mentioned system to achieve the reference temperature

For the cooling system heat removal two alternatives are possible,

- interface this system with the GTC Nasmyth Platform A glycol water system
- consider a new external chiller and route new conductions through the cable wrap

The first option, consider the GTC Nasmyth Platform A glycol water system, is preferred as baseline solution because of the inherent simplicity and lower cost. The cooling system would be composed of,

- Condenser unit, (located out of the Spectrograph room) will be interfaced with the GTC glycol water system on one end, and with the evaporator inside the Spectrograph room in the other end.
- Evaporator unit, (located inside the Spectrograph room) will be connected to the condenser unit.

The condenser unit, outside the chamber, shall be encapsulated in order to remove the heat generated by the compressor. The proposed location for this component is the azimuth floor.

The estimated power consumption of the thermal control system is about 1500kW.

3.2.4.3.3 Interfaces

- Interface with the GTC Nasmyth "A" Platform glycol water system. The estimated consumption is about 350 l/h with a temperature rise of 10 ºC (TBC).

3.2.4.4 Electrical supply

3.2.4.4.1 Requirements

The Electrical Supply system shall provide lighting for the Spectrograph room and electric power to all the consumers identified in the system.

3.2.4.4.2 Description

In order to provide an appropriate lighting for working in the telescope chamber a distributed power of 20 W/m^2 is considered, which is about 600 W total lighting power.

A cabinet for the distribution of power to the following consumers is considered,

- Lighting 600 W
- Cooling System 1500 W
- Heating Resistor 1000 W
- Thermal Control 300 W
- Chain Hoists 100 W

The total installed power is about 3500 W and the maximum required power when in operation is about 2500 W.

3.2.4.4.3 Interfaces

- Interface with the GTC Nasmyth "A" Platform electrical system

3.2.4.5 Lifting equipment

3.2.4.5.1 Requirements

As no maintenance operation will be possible with the enclosure cranes (the chamber is placed below the Nasmyth Platform) an independent lifting system is required.

The lifting system capacity shall be at least 600 kg and shall be able to move the load in the whole chamber area.

3.2.4.5.2 Description

The proposed solution is an electrical chain hoist supported by a manual trolley mounted on IPE steel profile which continues out of the chamber, close to the location of the nitrogen cylinder.

The capacity of the selected systems is 1000 kg. An example is shown in Figure 72

Figure 72. 1000 kg electrical chain hoist mounted on a manual trolley.

In following stages of the project the logistics of assembly and maintenance of the spectrographs should be analyzed in details to determine the need for additional handling equipment.

3.2.4.6 Costs

Table 31 summarizes the budget for the different subsystems involved in the SIDE spectrograph chamber.

Structure	**24,000€**
Primary Structure	12,000€
Cladding	6,000€
Doors	6,000€
Thermal Control System	**35,000€**
Electrical Supply	**6,000€**
Lifting Equipment	**3,000€**
Professional Services	**25,000€**
Contingency (20%)	**19,000€**
TOTAL	**112,000€**

Table 31. SIDE Spectrograph room estimated costs

3.3 The Wide Field Corrector

3.3.1 Summary

A very wide field of view on a classical Ritchey-Chrétien 10.4-meter telescope requires a large corrector. Our study of alternative designs for the GTC telescope shows that we have not many options due to the Nasmyth focus envelope constraints, i.e., from the A&G box to the Nasmyth focal plane we have 390 mm free and the total aperture is 1000 mm in diameter as we can see in Figure 73. (*see AD: RPT/OPTI/0093-L, NTE/CCIA/0411-R*). Investigation of a number of possible designs led to the selection of the two lens corrector described below.

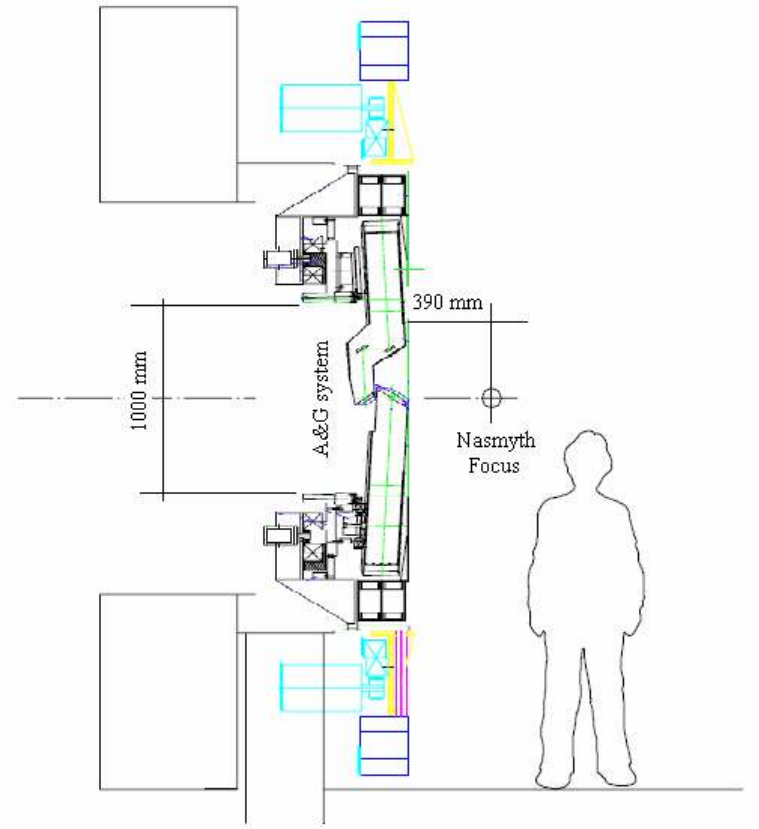

Figure 73. Space available for the Wide Field Corrector at the Nasmyth focus of GTC.

The WFC must serve the following purposes:

- Depending on the fiber positioner, it will be necessary to reduce the field curvature of the telescope focal plane. At present, the Nasmyth focal plane has a curvature radius of 1792.969 mm (*see AD: ESP/STMA/0017-L*).
- Concentrate the light spot so that no energy falls off the fibers.
- Achieve to keep maximum uniformity of the distribution of light all over the field of view.

- Achieve to keep the light perpendicular to the focal plane of the telescope.

3.3.2 Telescope without Wide Field Corrector

This section will demonstrate the necessity of a field corrector. Figure 74 shows the telescope encircled energy and Figure 75 shows the focal plane distribution of the energy in a field of view of 20 arcminutes in diameter.

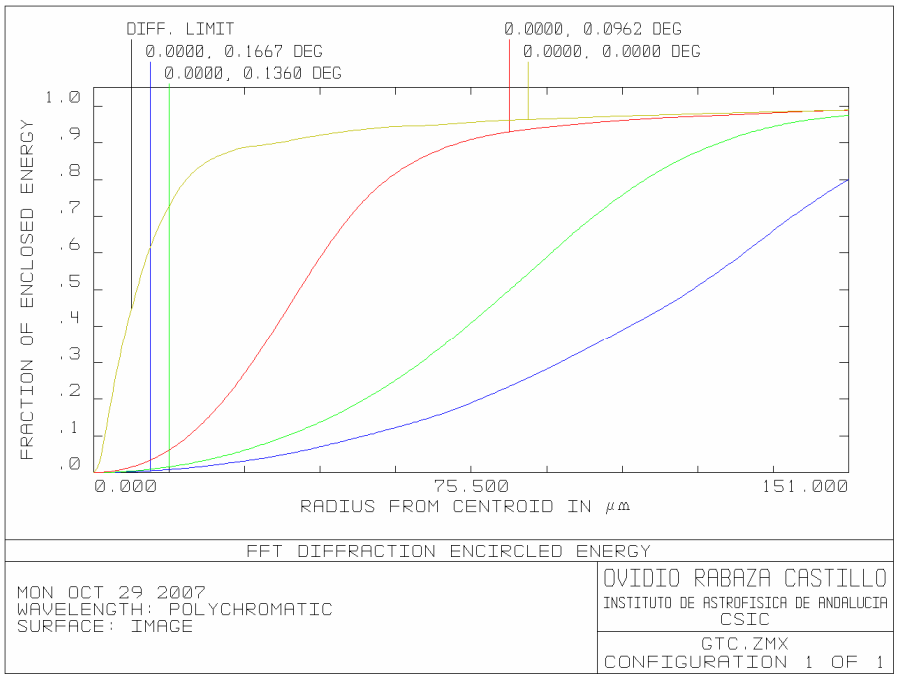

Figure 74. Diffraction encircled energy for 20 arcminutes diagonal field of view in the GTC focal plane.

It is clear that the encircled energy varies a lot from the center to the border of the field of view. Table 32 shows the 80% encircled energy for fields of 0', 11.544', 16.32' and 20':

Field (arcminutes)	80% Encircled energy (arcseconds)
0.0000	0.045 (diffraction limit)
11.544	0.142
16.320	0.267
20.000	0.366

Table 32. Relation between observing field and 80% encircled energy for the GTC telescope without wide field corrector.

We can deduce that the image degradation at the field border is eight times worse than in the center of the field.

It would appear from Figure 75 that the telescope achieves to concentrate the light into a microlens sky aperture (1.5 arcseconds) without any WFC, but, due to the atmospheric seeing (even if we don't take into account the atmospheric chromatic effect or atmospheric

refraction), this is actually impossible. For example, if 80% of the encircled energy in a field of 20 arcminutes is 0.366 arcseconds, then the maximum atmospheric seeing which allows that 80% of the energy enters the fibers is 1.45 arcseconds. If we take into account also the atmospheric dispersion, depending on the observing zenith distance, the maximum atmospheric seeing value is smaller. A WFC compensates this degradation effect.

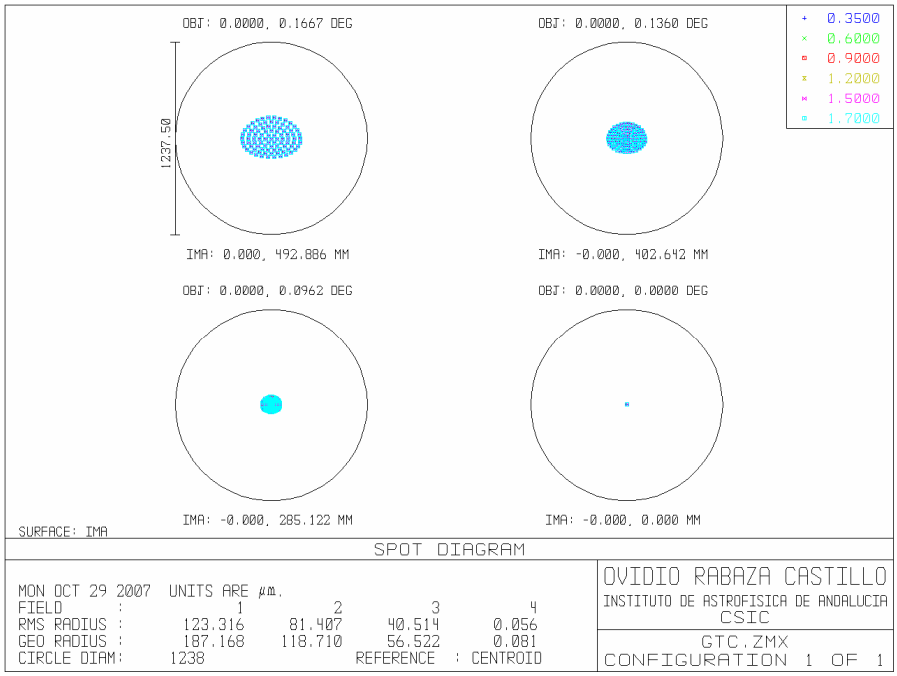

Figure 75. Spot diagram for 20 arcminutes diagonal field of view in the GTC focal plane. Circles are 1.5 arcseconds, equivalent to a microlens aperture.

3.3.3 Optical Design

The baseline of the corrector is similar to the FLAMES WFC (see Pasquini et al. 2002) (see Figure 76) and has an unvignetted field of view 20 arcminute in diameter, although the WFC support will probably reduce it to some extent. The spectral coverage is 0.35 - 1.7 microns and the optical beam is perpendicular to the focal plane all over the FOV. A parameter to be defined for the Fiber Positioner is the allowed focal plane curvature radius. For example, the LBNL robot has very relaxed requirements about the focal plane curvature radius. However, the UFL and IAA robot concepts need a minimum curvature radius of about 7500 mm. Another restriction, common to the three robot concepts, is that the light must be perpendicular to the focal plane.

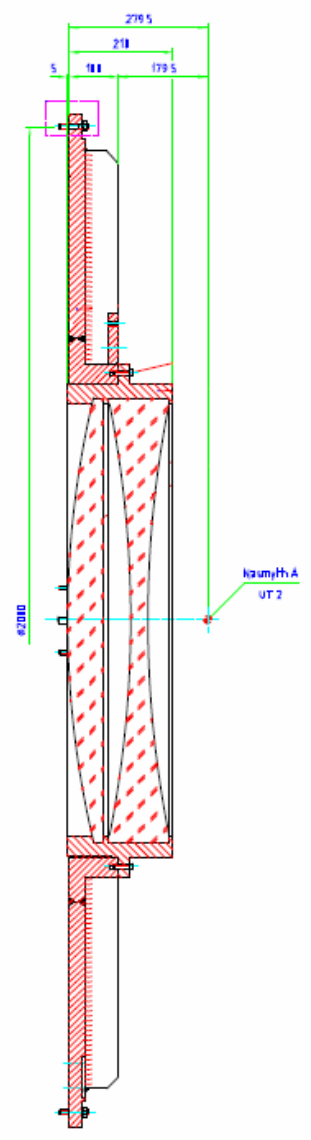

Figure 76. Wide Field Corrector of the FLAMES Spectrograph at the VLT.

3.3.3.1 WFC for the LBNL fiber positioner

The LBNL fiber positioner (see section 3.5) doesn't impose strict requirements about the focal plane curvature radius, but the light beam must be perpendicular to the focal plane. Moreover there is an important envelope constraint: along the optical axis we have only 390 mm free for the WFC. Figure 77 shows the "two-lenses" WFC optical design. Both lenses are of the same material N-FK5 (SCHOTT) and it has a good ratio Diameter/Width (less than 10), but the size is challenging as the maximum diameter is 986.451 mm. The focal plane curvature radius is 3574 mm and the light beam is perpendicular to the focal plane.

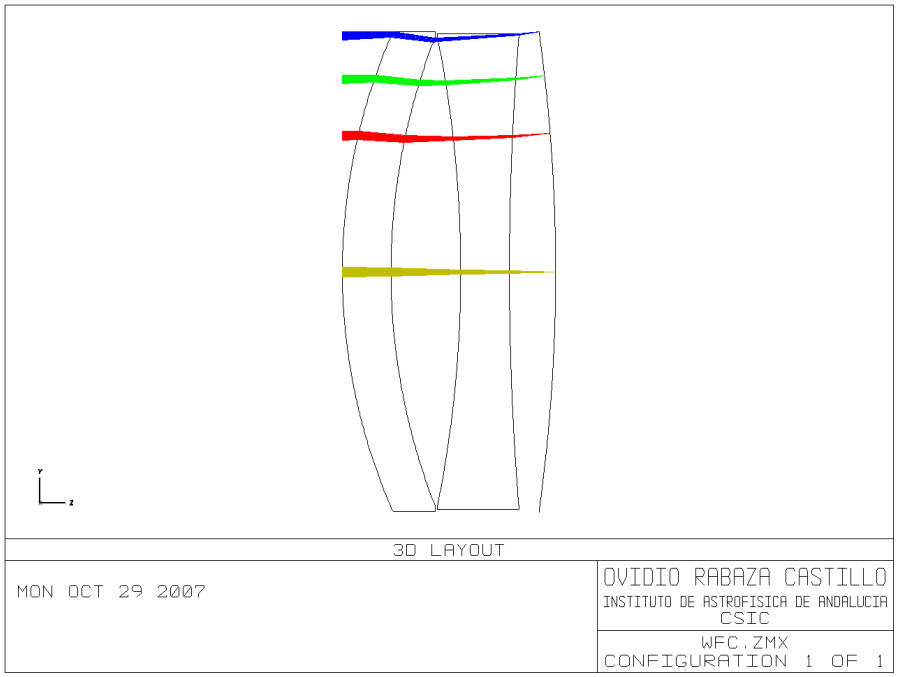

Figure 77. WFC Optical design for the LBNL fibers positioner.

Figure 78 shows the encircled energy of the telescope + WFC and it is clear that the energy distribution is more homogenous.

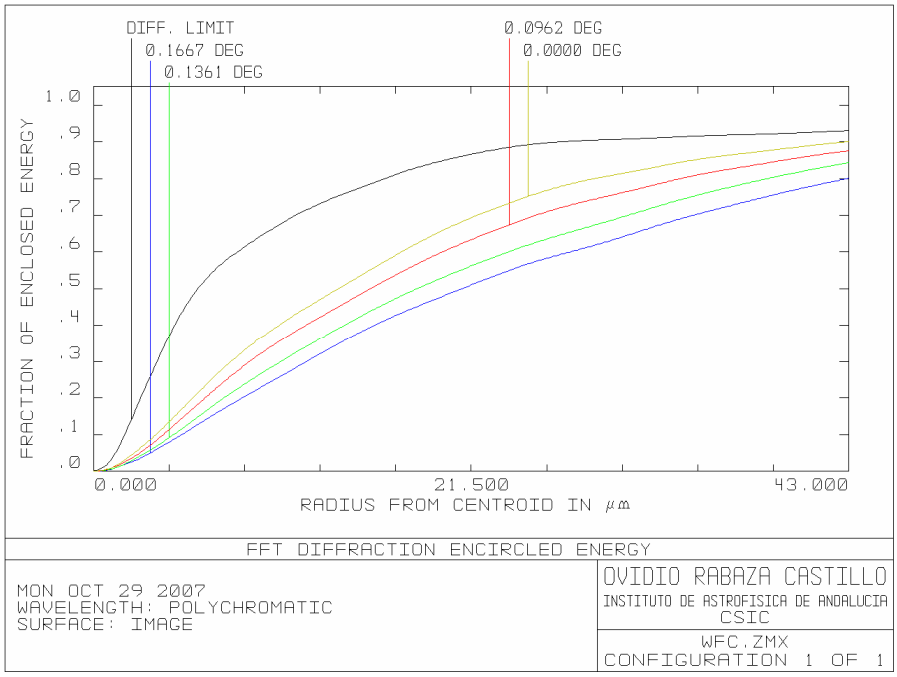

Figure 78. Diffraction encircled energy for 20 arcminutes diagonal field of view in the GTC+WFC focal plane.

Figure 79 shows the spot diagrams with respect to 1.5 arcseconds apertures (circles).

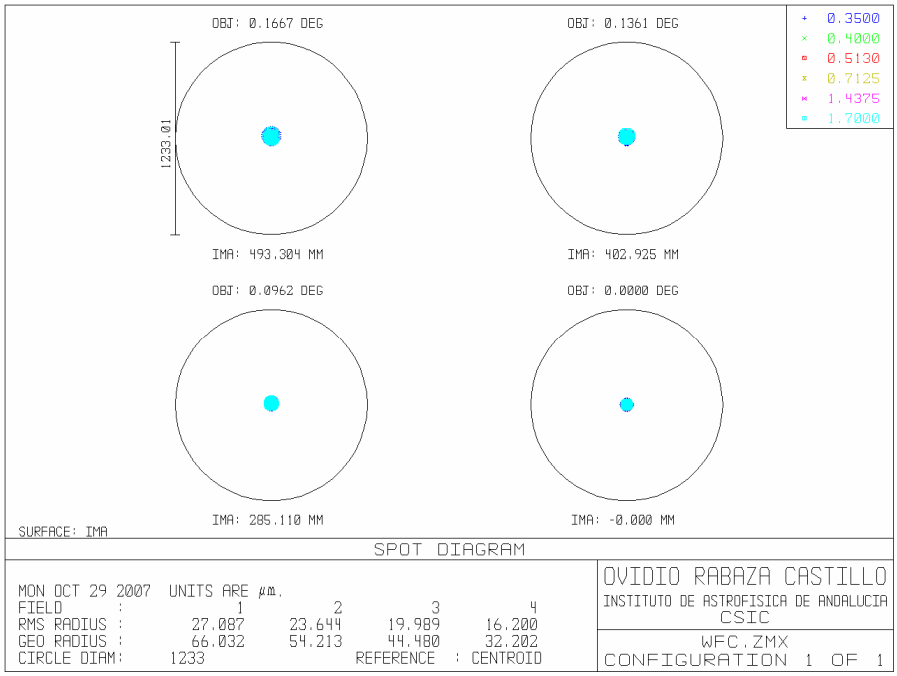

Figure 79. Spot diagram for 20 arcminutes diagonal field of view in the GTC+WFC focal plane.

This WFC the 80% of energy is enclosed as maximum in 0.1 arcseconds (≈ 86 microns) in all FOV.

3.3.3.2 WFC for the IAA and UFL fibers positioners

The IAA and UFL fibers positioners (see section 3.5) impose several restrictions about the focal plane curvature radius, perpendicularity of the light beam in the focal plane and the distance between the last WFC surface and the focal plane. The focal plane curvature radius can't be smaller than 7500 mm, the light beam must be perpendicular to the focal plane and the distance between the last WFC surface and the focal plane must be at least 90 mm. Taking into account that we have only 390 mm free for the wide field corrector, it is devised the design shown in Figure 80, a "two-lenses" WFC which satisfies these requirements. Both lenses are of N-LAK12 and N-KZFS11 materials (SCHOTT) and the ratio Diameter/Width is less than 10.52 for the first lens and 19.6 for the second lens. The maximum diameter is 986.33 millimeters.

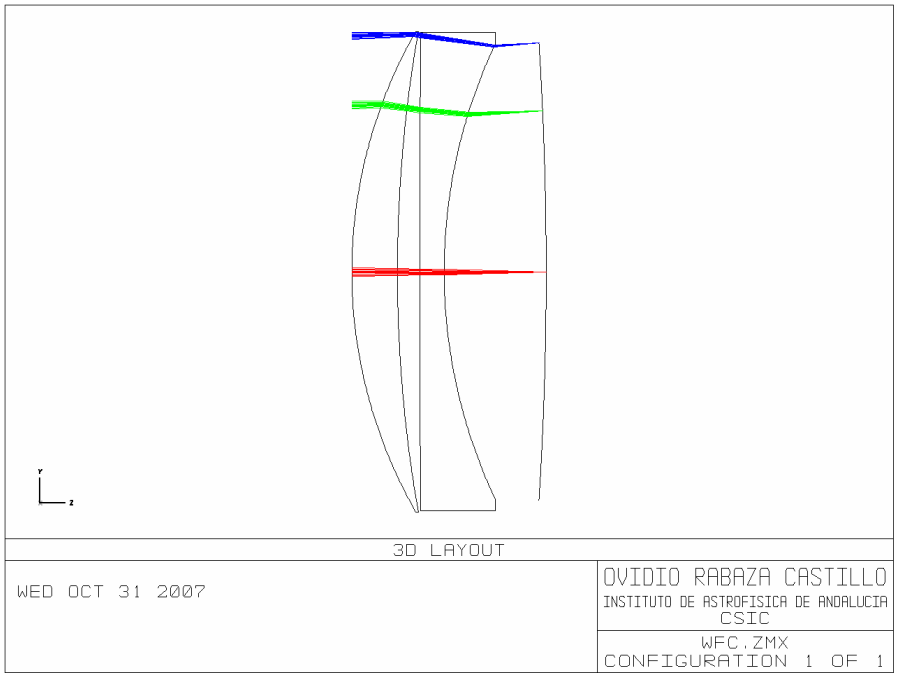

Figure 80. WFC Optical design for the IAA and UFL fibers positioner.

Figure 81 shows the encircled energy of the telescope + WFC. Qualitatively, the energy distribution is less homogenous than in the previous design and the real values of the energy are also far from the diffraction limit.

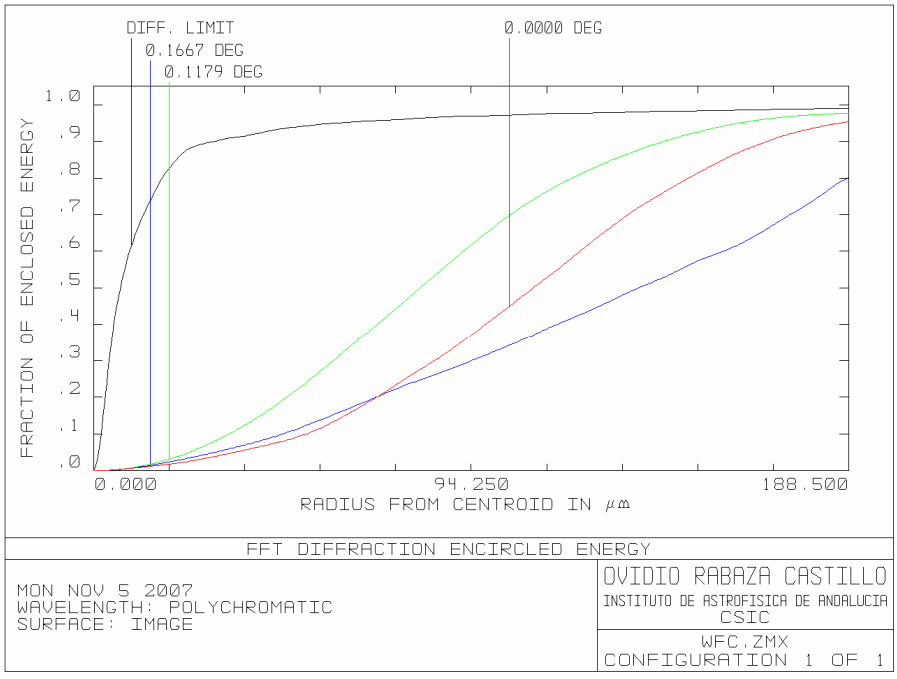

Figure 81. Diffraction limit encircled energy for 20 arcminutes diagonal field of view in the GTC+WFC focal plane.

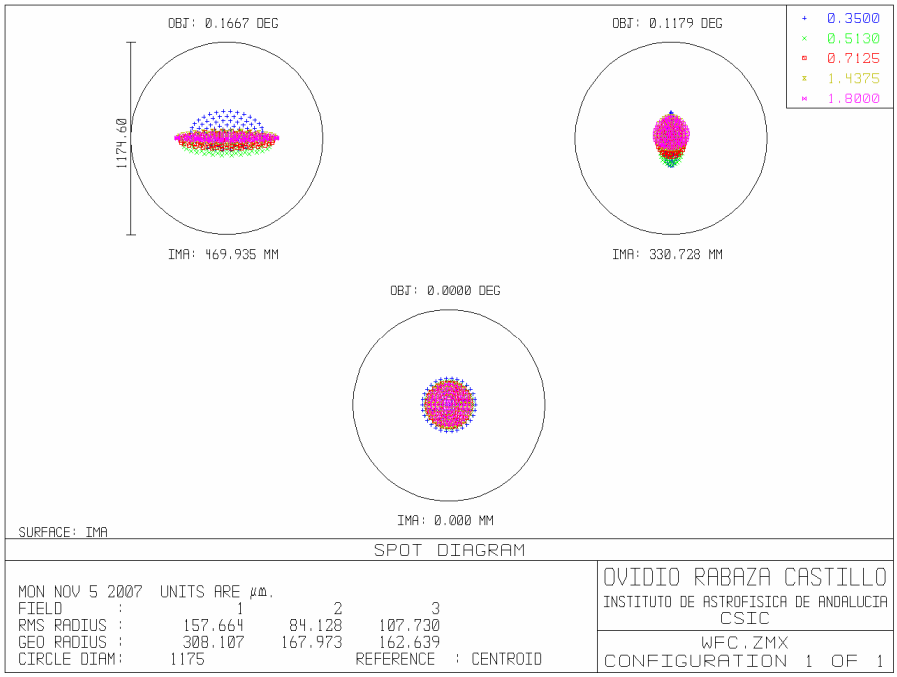

Figure 82. Spot diagram for 20 arcminutes diagonal field of view in the GTC+WFC focal plane.

Figure 82 shows the energy distribution in the focal plane. The non homogenous distribution is due to the limits imposed by the mechanical constraints of the robot positioner philosophy.

3.3.4 Mounting structure

The corrector will be mounted on a mechanical structure which will serve both to attach it to the Nasmyth ring and to hold the Fiber Positioner in place during observations. Once observations are finished, the whole system can be removed quickly to leave room for another instrument. Taking into account that this wide field corrector is similar to the FLAMES one, we will probably use the same philosophy in the mounting structure. In Figure 83 we can see the quartered drawing of the mounting structure of the FLAMES corrector at the VLT (see Pasquini et al. 2002).

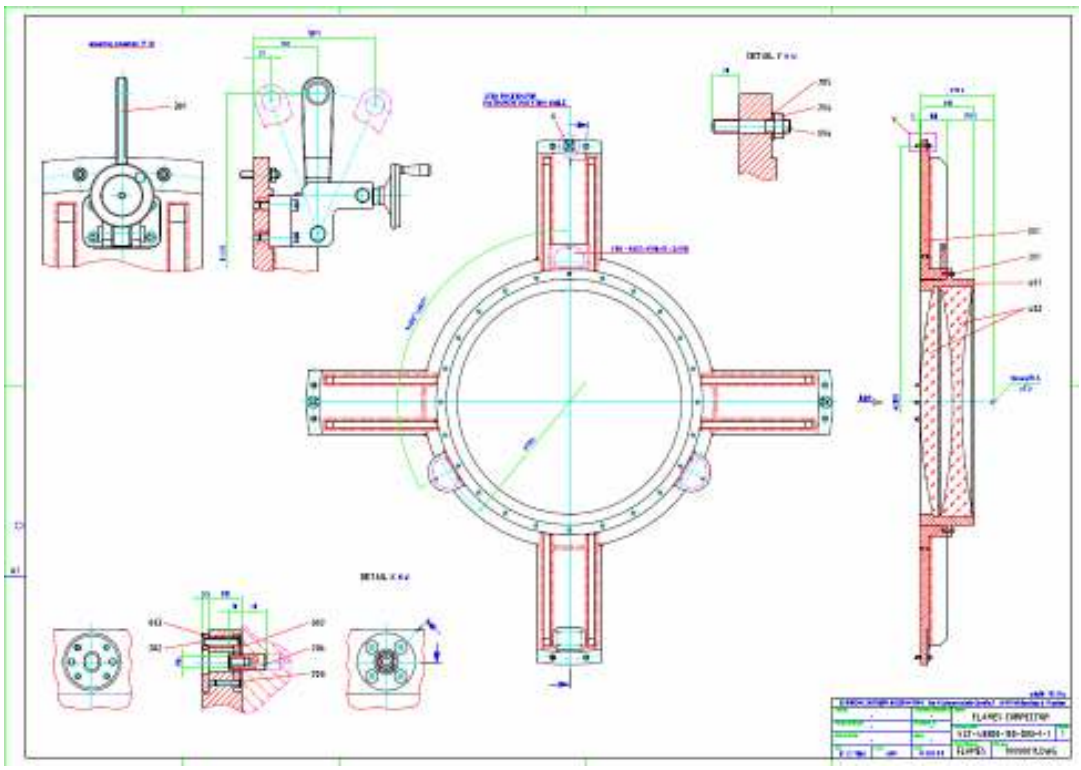

Figure 83. Quartered drawing of the mounting structure of the FLAMES corrector at the VLT.

3.3.5 WFC for the Folded Cassegrain focal station

In case the Folded Cassegrain focus is used for SIDE, a WFC for this focal station would be necessary too. In this case, the FOV is about a half of the Nasmyth FOV, so the WFC is far less challenging and a good curvature radius of the focal plane is easier to achieve because of the reduced size. The space available here (500 mm) is actually more than at the Nasmyth focus. Such a WFC would basically be a scaled-down version of the one just presented, with lighter support structure and more room to place the device, therefore we don't foresee any particular difficulty for it.

3.3.6 Costs

The cost of the WFC for FLAMES was about 165,000 euros including the mounting structure and the glasses manufactured by a Chinese company to standards corresponding to BK7. Taking into account the dimensions of the WFC of FLAMES (800mm of diameter) and the date of manufacture, we can estimate that the cost for the SIDE WFC (for the LBNL fiber positioner) should not exceed 300,000 euros, including the mounting structure. Obviously, the cost would be higher if the IAA or UFL fiber positioners were used at Nasmyth instead of the LBNL fiber positioner. The cost of a WFC for the Folded Cassegrain focus should not exceed 150,000 euros.

3.3.7 References

Pasquini, L., Avila, G., Blecha, A. et al. 2002, Installation and commissioning of FLAMES, the VLT multifiber Facility, The Messenger n. 110

3.4 The Atmospheric Dispersion Corrector

3.4.1 Summary

As it is shown in sections 3.1.1.6, 3.1.1.6.3 and 3.1.2, atmospheric dispersion is a significant issue for spectroscopy with optical fibers. The use of an ADC would almost completely solve the problem of the chromatic atmospheric dispersion effect (See section 3.1.2). Unfortunately, mainly because of space constraints, ***SIDE cannot have an ADC at Nasmyth***. The following sections are devoted to show the reasons for this.

The Folded Cass focus of GTC might host an ADC; on the other hand, atmospheric dispersion can be successfully software-corrected for IFUs or mIFU bundles, which would be used at Folded Cass. This means that ***an ADC at Folded Cass is not necessary***.

3.4.2 Optical design.

For the optical design of the ADC, two options are commonly used. We analyze both of them below.

3.4.2.1 First option: two doublets of prisms

In order to counter-balance the atmospheric dispersion, the straightforward idea is to use a prism. However, a simple prism would deviate the light away from the optical axis. So one uses an Amici prism, i.e., two prisms cemented together such that they appear like an optical element with parallel external surfaces. The two prisms have the same angle but different refraction indices, so that light of an intermediate wavelength is not deviated, while longer and shorter wavelengths are deviated to compensate the atmospheric dispersion. In order to be able to tune the device for different atmospheric dispersions (i.e., airmasses), one splits the job between two such doublets, each giving half of the required dispersion (see Figure 84). If we wanted to correct only a limited range of zenith distances, one double prism could be enough.

The two doublets must be free to rotate independently, so when they are in opposite orientations they give null dispersion, while they give maximum dispersion when their orientation is the same. An optical fluid can be used to fill the space between the two discs.

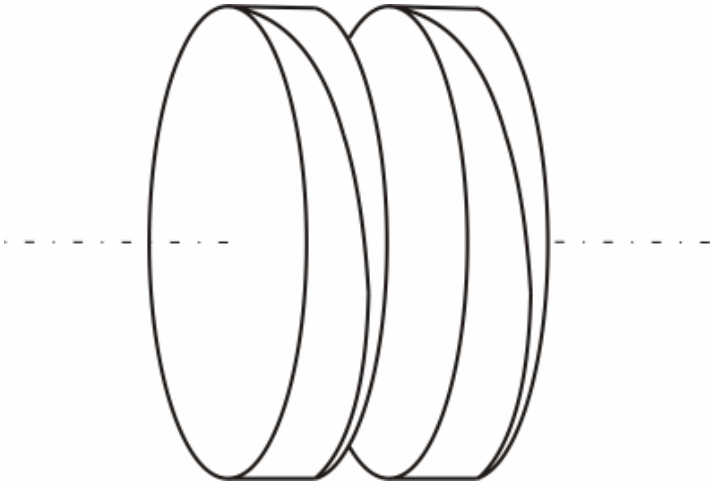

Figure 84. Atmospheric dispersion corrector of two doublets of prisms.

In a converging beam, such a device gives both plane-parallel aberrations and prismatic aberrations. The prismatic aberrations can be reduced by choosing special glasses, and by putting the ADC as far away from the focal plane as possible. Of course, one must choose glasses with good transmission up to the near-UV.

Such achromatized ADC of plane-surfaced Amici prisms could probably be used at a focal ratio of up to f/8 (see Wynne 1993). See Figure 85.

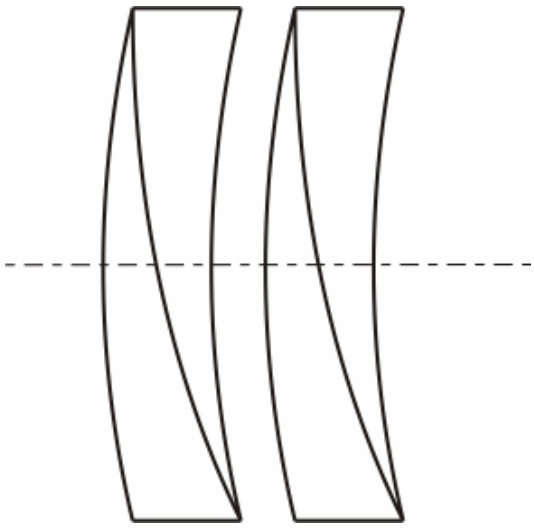

Figure 85. Wynne's ADC.

Beside the very high cost of such a device for SIDE, the thickness of the prisms, the distance between them and the size of the support for such larce diameter optics would surely require at least 200 mm. The free distance from the A&G box to the telescope focal plane telescope is 390 mm. The optical system of the WFC has a width of 290 mm approximately, moreover, taking into account than we will need a minimum of 90 mm to manipulate the fibers at focal plane (in case of failure), there are only 10 mm left for the ADC.

3.4.2.2 Second option: Linear ADC

The linear ADC consists of two small angle wedges with opposite orientation. Following the change in z, the front wedge is moved towards the pupil. The design is particular well suited for an altazimuth telescope, since only translation along the optical axis of one wedge with respect to the other will be needed. The needed range of translation depends on the full wavelength range to be covered and of the wedge angle. The larger the wedge angle the smaller will be the range of translation, but the larger will be the aberrations and their chromatic variations introduced by the device. For zenith pointing, the wedges will be close together and the main aberrations will be defocus and spherical aberration.

Moving away from zenith, the rotational symmetry is broken resulting in additional field astigmatism and field coma. Apart from this, there will be a wavelength dependent residual tilt within the compensated band (so-called secondary spectrum), which is the main culprit for restricting the corrected bandwidth. Secondary spectrum is minimized choosing a wedge material with a dispersion well matched to the atmospheric dispersion. The choice of wedge angle is a question of having a manageable translation range without being limited by aberrations. In the Figure 86 there is an example ADC design proposed for Becker for two of the ESO 8 m telescope (see Becker 1996).

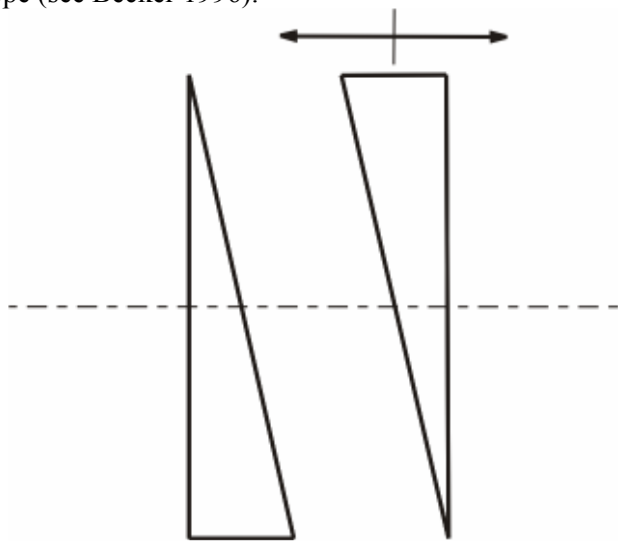

Figure 86. The linear ADC design proposed for the Euro50.

Again, the size of this device is well beyond the 10 mm available.

Consequently, ***we have not enough room to place an ADC at Nasmyth***, i.e., there is no ADC device (including glasses, mechanics and engine) that will fit in the limited available space *(Harland Epps, internal communication 10/5/2007).*

3.4.3 ADC for the Folded Cassegrain focal station

An ADC at Folded Cassegrain would be much easier, because of the reduced size and the larger space to the focal plane (see 3.3.5), but here the atmospheric dispersion would not be so critical because only the SIFU and the MiniIFUs would use this focal station, and both modes can software-correct the data to compensate for atmospheric dispersion. Experience with other instruments shows that post-corrections to the data satisfactorily solve the problem, therefore ***an ADC is not necessary for the Folded Cassegrain focus***.

3.4.4 References

Wynne, C.G., 1993, MNRAS, 262, 741-748.
Becker, T., 1996, Proc. SPIE, 2871, 1135-1143.

3.5 The fiber positioner

3.5.1 Introduction

A fundamental part of SIDE is obviously the fiber positioning system, which should take care of placing the fibers according to the field to observe. The SIDE Fiber Positioner should be capable of handling several button types: the single fibers of the MOS mode (or MOS-IFUs), the mIFU bundles and the auto guider buttons for the TV camera. It should also support the option of a central hole for placing the SIFU bundle, this one at a fixed position.

The number of buttons for the MOS mode is about 1000, in the 20' field of view of the Nasmyth A focus.

3.5.2 Environmental conditions

3.5.2.1 Location and focal plane

The Fiber Positioner would be placed at the GTC Nasmyth A focus so that the fibers lie on the focal plane surface over a field of view 20 arcmins in diameter; this corresponds to 990mm. The space here is limited by the back of the autoguider arms and the focal plane itself.

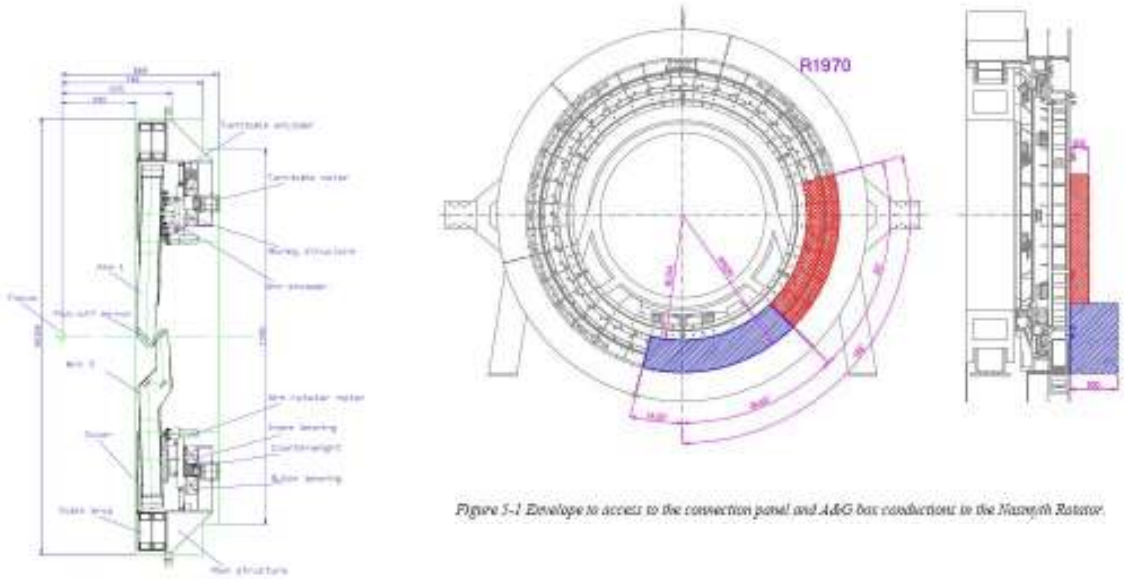

Figure 87. Dimensions at Nasmyth focus.

The distance from the rear of the auto guider arms to the focal plane is 390mm. It is also mandatory not to invade the red and blue volumes showed in Figure 87, and be constrained to a inner radius of 1314mm and outer radius of 1650mm.

The diameter of the free central hole of the auto guider is 992mm.

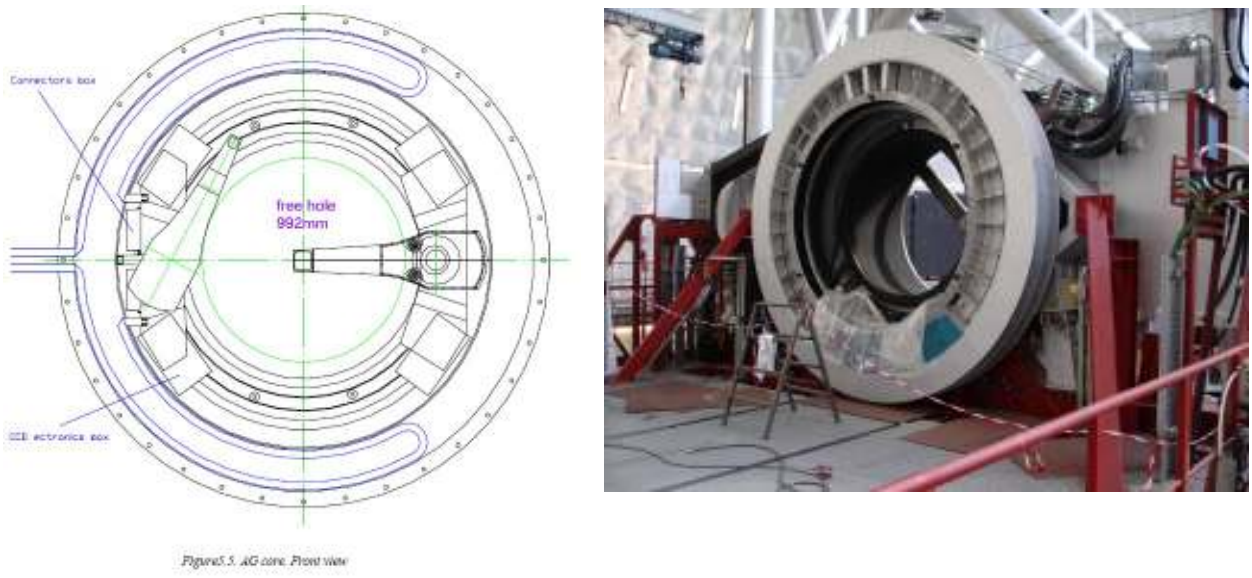

Figure 88. A&G box and its envelope.

The distance from the platform to the optical axis is 1970mm.

The optical parameters of GTC are f/17, with a scale 825µm/arcsec. The uncorrected focal plane is curved with a curvature radius of 1792.97mm. An optical system to correct aberrations and flatten the focal plane must be used (i.e., the WFC). Some curvature of the corrected focal plane is a requirement that the robot must accept.

3.5.2.2 Sky sampling, fibers dimension, fiber position accuracy

The sky sampling is determined by the scientific input, depending on the object to observe, but in general a small sky sampling implies some energy losses, and a large sky sampling implies bad sky subtraction. Atmospheric dispersion, telescope diameter, limiting magnitude, etc. are taken into account to determine the optimum sky sampling and fiber dimension (see Donnelly et al. 1989; see Brodie et al. 1988).

The positioning accuracy of the robot must be optimized and care must be taken of all the possible errors so as to achieve a fiber/button position which gives the maximum signal to noise for the object. Among these errors we have: astrometry, aberration, parallax, proper motion, coordinates conversion, fiber mounting, etc. (see Newman 2002).

The typical fiber position accuracy, as a requirement, should be 0.1”, which corresponds to 80 micron or ± 40 micron RMS at the focal plane.

3.5.2.3 Observing modes

The SIDE spectrograph can work in three different modes: MOS, mIFU and SIFU. There will be about 1000 MOS units, plus ~27 mIFU units with approximately 3”x3” FOV each. There will be also another type of units used to transport the light of a reference guide star to a TV camera.

The hole for the SIFU could be located in the center of the Nasmyth focal plane, and in this case this area would be inaccessible for the MOS units. Another possibility, explained elsewhere, is to place the SIFU in the folded Cassegrain focus, which has the advantage of being always available with a simple Tertiary swap. (see Section 3.7.11).

3.5.2.4 Robot position accuracy

We require the ability of the robot to place the fibers in the field even if the field curvature radius is small, e.g. 7000mm. For radial arms robot concepts, this means that the gripper should accept an extra distance in Z axis (of the order of 18mm) to add to the button height. Also it must compensate the descending position with the real descended position. A good and simple idea is to place in each arm (e.g. in the case of radial concepts) a double micro mirror that allows the star to be seen (as well as the correspondent fiber) at same time in a TV visualization camera (gripper open in the center), transporting the image of several arms over a single TV, that permits working in close loop. Hectospec implements this facility (see http://www.cfa.harvard.edu/mmti/hectospec.html).

3.5.2.5 Environment summary

- Diameter of the field behind the GTC A&G = 990mm or 20'.
- Distance between the rear part of GTC A&G and focal plane = 390mm
- Distance between the WFC and the Focal Plane ≈ 90mm.
- Maximum circular contour of the robot (to avoid contact with the GTC A&G Electronic Box) 1300mm.
- Number of units: ≈ 1000 for MOS mode, ≈ 27 mIFU units, ≈ 18 TV autoguider buttons.

3.5.3 The Fiber Positioner Robot requirements

3.5.3.1 Introduction

As it will be clarified in later sections, we are evaluating three possible concepts for the FPR, but all of them must fulfil a common set of requirements. These common requirements are listed in this section, along with useful information on interfaces and working conditions.

3.5.3.2 Item Functional Description

The FPR would be a robotic system capable to position a large number of optical end fibers (buttons) over a focal plate. The diameter of the focal plate is approximately the diameter field of view of the GTC Telescope, 990 mm. This system shall work in atmospheric conditions and in vertical position and while the rotator is rotating at a speed of 3 deg/sec (TBC).

The FPR System shall comprise a rigid mechanical structure, the Fiber Positioning Device, the Focal Plate, the Dust and Security Covers, the Carrier, the Local Control Unit (LCU), the Wide Field Corrector (WFC), the Engineering Mode Control Software and the rolling fibers systems.

The mechanical structure could be connected to the NP by means of the circular central hole existing under the rotator and could travel over a carrier to a storage position. The structure has the function of physically support the Fiber Positioning Device (FPD), the Focal Plate (FP) with the fiber buttons parking and reels, the Dust and Security Covers (DSC), the Local Control Unit (LCU) and the Wave Front Corrector (WFC). This structure shall be connected by a sure cable chain to other parts of SIDE and to the platform hole.

The Fiber Positioning Device will position the buttons on the focal plate in determined locations with a high level of accuracy and repeatability. The stiffness of these units shall be sufficient to minimise the effects transmitted to the kinematics by the gravity loads.

The Focal Plane is a curved surface composed by three different parts:

1. The Field of View is a circular concave area with a diameter of 990 mm where buttons will be located for observations. The concave radius shall be between 3000 and 8000mm.

2. The possible inner hole for the SIFU, aprox. 22mm diameter, shall be foreseen in the center of the filed of view.

3. The area reserved to the interface between the FP and the output to the “rear rotating part of the robot”.

The Dust and Security Covers are elements that protect from human injury during the normal operation of the Fiber Positioner, and also protect the mechanics and electronic elements from sand and dust.

The Wide Filed Corrector (see Figure 89) is the optical system in charge of adapting the light direction perpendicular to the Focal Plane concave area. This system shall always remain mounted in the FPR, providing an enclosure environment for Focal Plate and all of their parts. The WFC might be retracted to access to the physical FP i.e. to repair broken fibers etc.

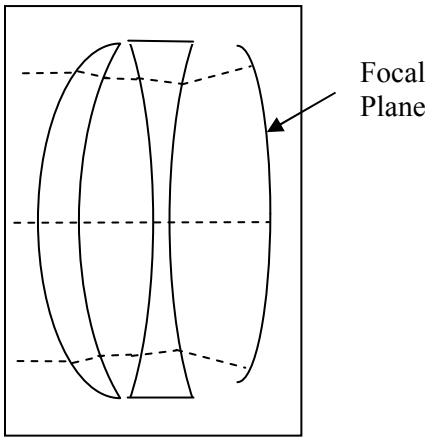

Figure 89: Wide Filed Corrector Schematic view.

3.5.3.3 Major Component List

A simplified diagram of the major components covered by this Technical Specification is shown below.

3.5.3.4 Requirements

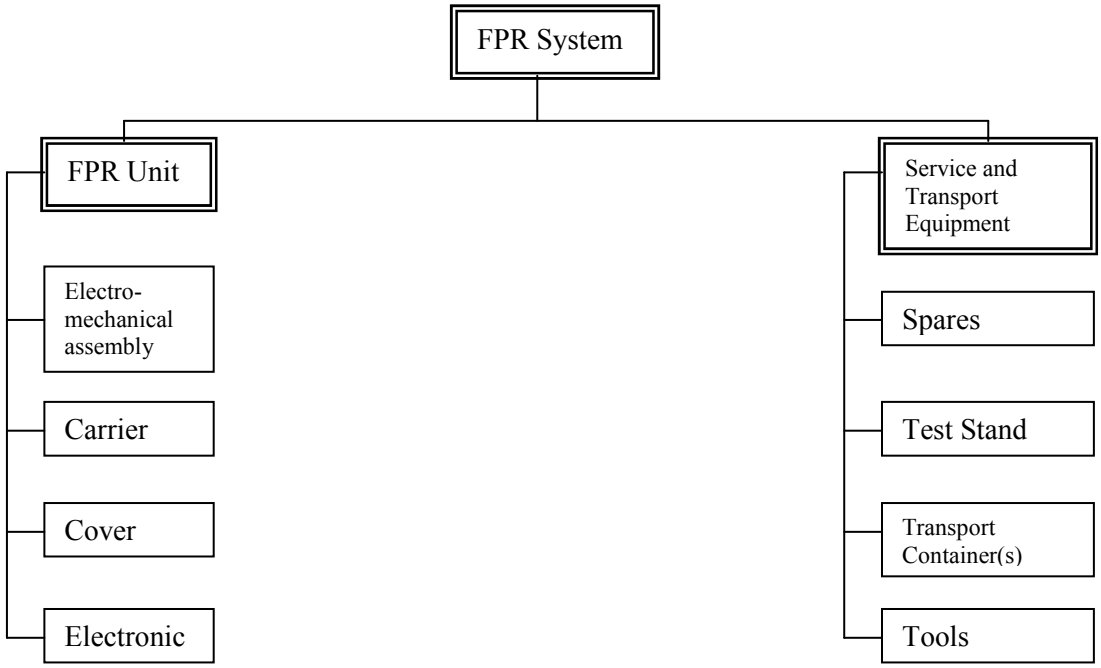

3.5.3.4.1 General

The FPR System shall be integrated on the Nasmyth A platform. Therefore the definitions of the CoG's and locations of the FPR System items shall be referred to the Nasmyth Focal Station Coordinate System (NFCS, see Ubierna 2007).

3.5.3.4.2 Mechanical Interface

In the definition of the mechanical interfaces four systems will be considered: the FPR, the LCU, the Visualization System and the carrier.

3.5.3.4.3 Temperature of reference

The temperature of reference for all the dimensions and tolerances, unless otherwise specified, shall be 8.5º C.

3.5.3.4.4 Mechanical interface of the FPR to Nasmyth Rotator

The FPR shall be attached to the attachment flange of the Nasmyth Rotator. The attachment flange shape and dimensions shall be as shown in drawing AD DR/I-IN-TL-001/001 and detailed in Ubierna 2007.

The mechanical interface between the rotator and FPR shall consist of a flat circular hollow flange (see AD DR/I-IN-TL-001/001). The FPR functionality shall maintain the Nasmyth

focal plane both in position and shape with respect to this attachment flange, within the allocated errors with respect to the nominal situation.

The reference for assembling the instrument in the rotator shall be the attachment flange, when the rotator is in its parking position (see Mounting and detaching).

- **Attachment area**: The attachment flange dimensions shall be as shown in AD DR/I-IN-TL-001/001.
- **Attachment flange plane location:** The attachment flange plane shall be parallel to the XY plane located at z = +385 mm (see drawings DR/GTC/001 (Sheet 1/2 and 2/2)).
- **Attachment points location:** The attachment points shall be located in the attachment flange as shown in AD DR/I-IN-TL-001/001.
- **Local stiffness:** The attachment flange shall be able to bear the maximum mass attached to it in 6 points equally spaced, while the requirements of dynamic behaviour and gravitational deformations are met.
- **Centring:** There shall be a cylindrical centring flange, normal to the attachment flange, in order to center the instrument on the attachment flange (see Figure 90).

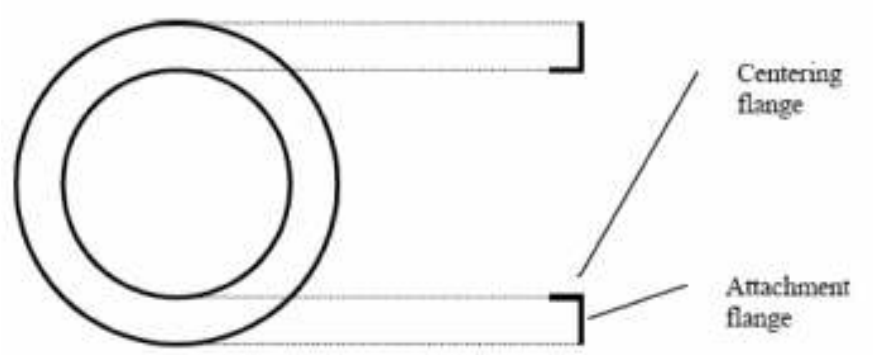

Figure 90: Schematic drawing of the attachment and centring flanges. Frontal and lateral views.

- **Centring diameter:** The centring diameter shall be as shown in drawing in AD DR/I-IN-TL-001/001.

Tolerances

- **Non-specified tolerances:** All those non-specified tolerances shall be according to ISO 2768-fH-(E).
- **Assumptions:** For all the tolerances it shall be assumed that:
    - The telescope tube points to the zenith.
    - Only the A&G is mounted in the rotator (not the science instrument)
    - The required values are maximum values in the whole rotation range.

- **Concentricity tolerance of the real attachment flange axis with respect to the real elevation axis:** The concentricity tolerance of the real attachment flange axis1 with respect to the real elevation axis shall be 0.5 mm (TBC).
- **Parallelism tolerance of the real attachment flange axis with respect to the real elevation axis:** The parallelism tolerance of the real attachment flange axis with respect to the real elevation axis shall be 0.1 mrad (TBC).
- **Concentricity tolerance of the rotation axis with respect to the real attachment flange axis:** The concentricity tolerance of the rotation axis with respect to the real attachment flange axis shall be 0.5 mm (TBC).
- **Parallelism tolerance of the rotation axis with respect to the real attachment flange axis:** The parallelism tolerance of the rotation axis with respect to the real attachment flange axis shall be 0.050 mrad.
- **Tolerance of the diameter of the centring flange:** The tolerance of the diameter of the centring flange shall be g6H7 according to ISO standards (TBC).
- **Tolerance of the position of the attachment points**: The tolerance of the position of the attachment points with respect to their nominal position as defined in 'Attachment points location' shall be 0.5 mm.
- **Tolerance of the distance between the real tube axis and the attachment flange:** The tolerance of the distance between the real tube axis and the center of the attachment flange (the crossing point between the real attachment flange axis and the plane containing the rotator attachment flange) shall be ±1 mm.

Physical properties of the attachment flange

- **Nasmyth rotator attachment flange flatness:** The Nasmyth rotator attachment flange flatness shall be better than 0.040 mm.
- **Instrument attachment flange flatness:** The instrument attachment flange flatness shall be better than 0.040 mm.
- **Nasmyth rotator attachment flange roughness:** The Nasmyth rotator flange roughness shall be Ra 1.6 microns or better (ISO 1302).
- **Instrument attachment flange roughness:** The instrument flange roughness shall be Ra 1.6 microns or better (ISO 1302).
- **Differential thermal expansion:** In order to avoid the effects of the differential thermal expansion, both the rotator attachment flange and the instrument attachment flange shall have a CTE of similar value.

Gravitational deformations

- **Gravitational deformations of the attachment flange:** Motions of the attachment flange due to gravitational deformations, when the science instrument and A&G are mounted in the rotator, shall be:
    - Motion in the X-Y plane: < 0.5 mm
    - Rotation around X axis: between -45 arcsec and +30 arcsec
    - Rotation around Y axis: < 10 arcsec.

Those motions are maximum values in the whole rotation range and in the whole telescope elevation and azimuth range.

In order to meet the requirement for rotation around X axis, the rotator shall be mounted in the telescope structure in such a way as when the rotator only supports the A&G, the attachment flange rotation around X axis is –45 arcsec. In this way, the attachment flange rotation around X axis, as a function of the science instrument rotating mass and assuming the A&G is mounted in the rotator, shall follow the values given in next table:

Science instrument rotating mass	Attachment flange rotation around X axis
0 Kg	≥ -45 arcsec
2400 Kg	≤ +30 arcsec

Table 33.- Mass and rotation around X axis

Mounting and detaching

- **Mounting pins:** In order to facilitate the attachment of the instrument to the Nasmyth rotator, the Nasmyth rotator attachment flange shall have 6 mounting pins as shown in AD DR/I-IN-TL-001/001.
- **Mounting holes:** In order to facilitate the attachment of the instrument to the Nasmyth rotator, the instrument flange shall have 6 through mounting holes as shown in AD DR/I-IN-TL-001/001.
- **Extracting recesses:** In order to facilitate the instrument detachment from the Nasmyth rotator, the Nasmyth rotator attachment flange shall have 12 extracting recesses as shown in AD DR/I-IN-TL-001/001.
- **Extracting bolts:** In order to facilitate the instrument detachment from the Nasmyth rotator, the instrument shall have 12 extracting bolts as shown in AD DR/I-IN-TL-001/001.

3.5.3.4.5 Mechanical interface of the LCU

The mechanical interface of the LCU shall meet the requirements defined in paragraph 5.1.8 of AD DCI/STMA/0017-R and chapter 5.1.8 of AD DCI/STMA/0018-R.

If these requirements could not be met, the LCU shall be located as near as possible of the electronic racks of the SIDE Spectrographs.

3.5.3.4.6 Mechanical interface of the Visualization System

TBD.

3.5.3.4.7 Mechanical interface of the carrier.

To facilitate the operations of detaching the FPR from the rotator of Nasmyth and leave room to the AO a carrier shall be implemented. The interface area will be located on the NP, shall met the constraints defined in drawing of AD DR/GTC/001 and shall met the values defined in chapter 5.1.4 of AD DCI/STMA/0018-R. The definitive interface areas and fixation points shall be defined by an interface document provided by the Instituto de Astrofísica de Andalucía (IAA-CSIC) agreed with GTC.

3.5.3.4.8 Mechanical interface in stowage configuration.

When the system is not mounted in the NR, a carrier shall be foreseen to allow an easy removing from NR to the stowage position. The whole of optical fibers and cables shall be properly routed to avoid any stress or damage during transport for stowage. The stowage position in NP is shown in the Figure 91.

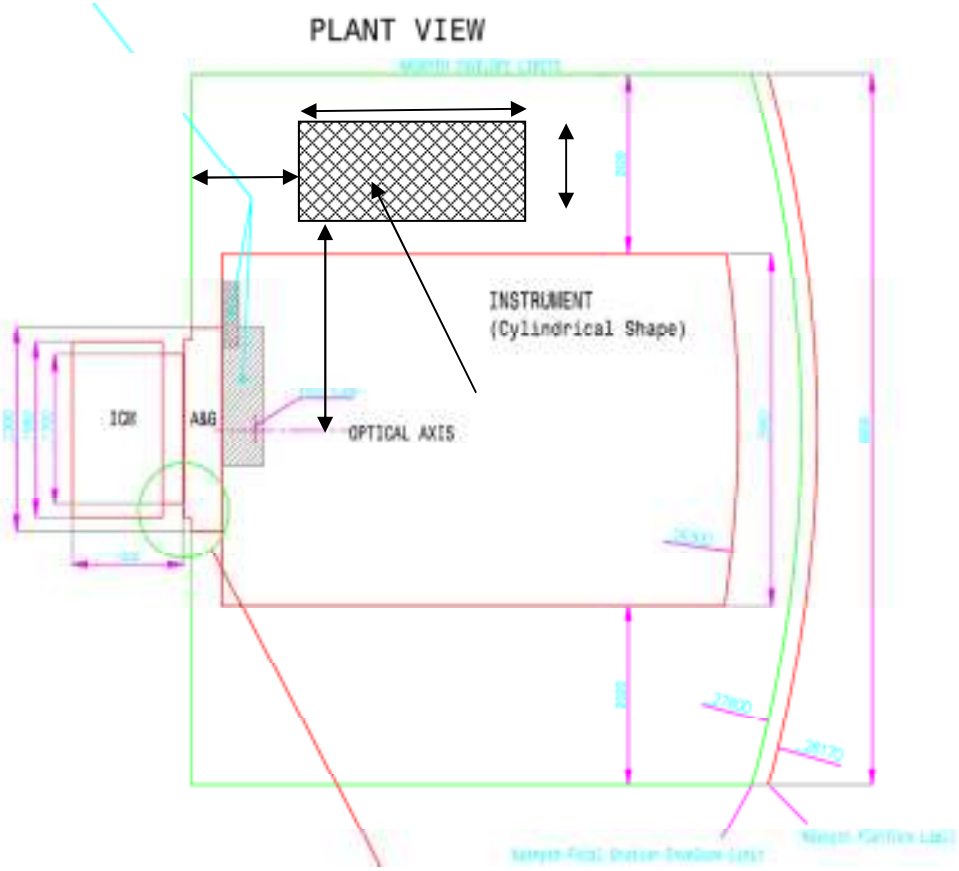

Figure 91: Stowage position and envelope

The dimensions shown in the previous figure are defined in Table 34.

Stowage Position Dimensions (mm)	Stowage Envelope Dimensions (mm)
A= TBD mm	C= TBD mm
B= TBD mm	D= TBD mm

Table 34.- Position and Stowage Dimensions

3.5.3.4.9 Envelope of the FPR System

The maximum envelope that the FPR shall occupy is a cylinder of 1300mm radius and 1200mm high (RD04). The axis of the cylinder shall coincide with the optical axis defined in AD DR/GTC/001 and one of its flat surfaces coincident with the attachment flange of the Nasmyth rotator as defined in AD DR/GTC/001 and in AD DCI/STMA/0017-R. The rear part of the robot might be another small cylinder in axis with the main cylinder, that permits rolling or coiling of the electrical and optical bundles for the de rotation function, better than use the big 4 metre diameter existing wheel (see Figure 92).

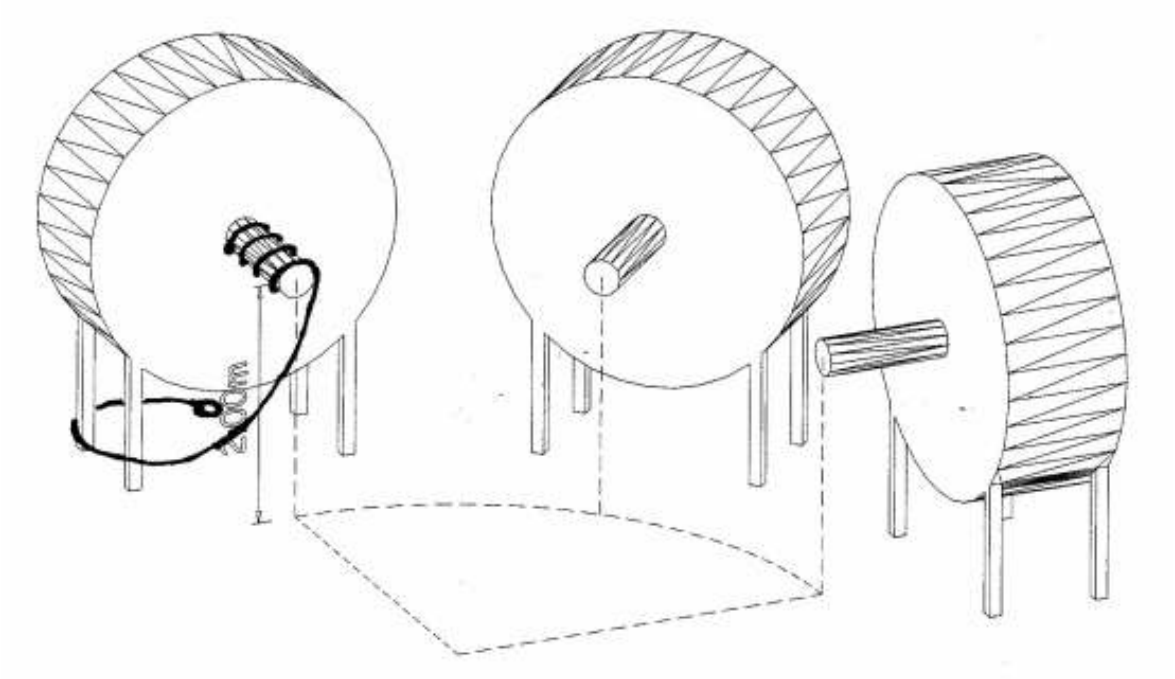

Figure 92: Rolling or coiling of the electrical and optical bundles option

A second cylinder of 1650 mm radius and 600 mm high, avoiding the volume occupied by the connection panel and A&G box conductions in the Nasmyth rotator (as shown in AD DCI/STMA/0017-R), should be booked for connectors for the electronics arms, electronic racks and accessibility for maintenance. The axis of this second cylinder also coincides with the optical axis defined in AD DR/GTC/001 and one of its flat surfaces is coincident with the attachment flange of the Nasmyth rotator as defined in AD DR/GTC/001 and in AD DCI/STMA/0017-R. The Visual System is foreseen to be located behind the Focal Plane.

3.5.3.4.10 Envelope of the LCU.

TBD.

3.5.3.4.11 Envelope of the Carrier.

The maximal dimensions of the carrier shall not exceed the volume defined in drawing AD DR/GTC/001 once installed in its final location.

3.5.3.5 Electrical interface between the FPR System LCU and the SIDE Spectrograph.

TBD.

3.5.4 The IAA-CSIC fiber positioner

The IAA-CSIC fiber positioner device would be an evolution of existing robotic systems, such as Hydra, Hectospec, 6dF or AutoFib-2, that were developed for other telescopes. This concept is now considered not convenient for the project, so this section only gives a brief description of it and a list of disadvantages which motivate the selection of other concepts instead.

3.5.4.1 Functional description

The IAA-CSIC fiber positioner consist of a radial arm robotic system capable to position a large number of optical end fibers (buttons) over a focal plate. The diameter of the focal plate is approximately the diameter field of view of the GTC Telescope, 990 mm. This system works in atmospheric conditions and in vertical position and while the rotator is rotating at a speed of 3 deg/sec (TBC).

The FPR System is composed by a rigid mechanical structure, the Fiber Positioning Device (FPD), the toothed crown system, the Focal Plate (FP), the Dust and Security Covers (DSC), the Carrier, the Local Control Unit (LCU), the Wide Field Corrector (WFC), the Engineering Mode Control Software and the rolling fibers systems.

Figure 93 shows a front view of FPR without the WFC, the Base Support and Flanges. Thus, it is visible the FPD, the toothed crown system and the FP.

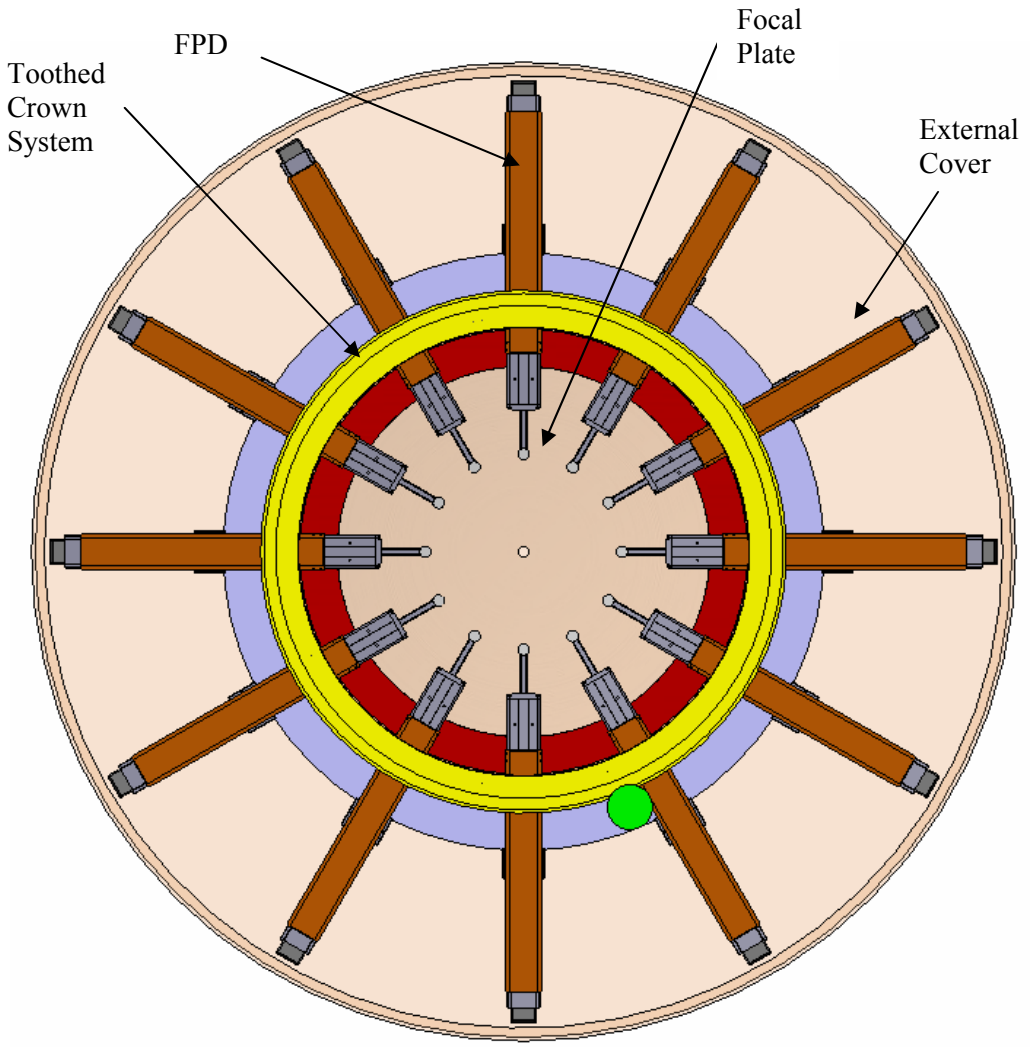

Figure 93. FPR Front View.

The design is performed to allow placing all the buttons in the selected location by the grippers located at the end of the arms. To achieve this, a design with FPD radially located and a Toothed Crown System is implemented. The FPD performs lineal movement in radial direction thanks to a Guide Actuator. On the other hand, The Toothed Crown System allows angular rotation to all the FPD. Thus, all the concavity FOV is swept.

The mechanical structure is connected to the NR by means of the NR attachment flange and could travel over a carrier to a storage position. The structure has the function of physically support the FPD, the FP with the fiber buttons parking and reels, the DSC, the LCU and the WFC. This structure is connected by a cable chain to other parts of SIDE through a hole in the platform.

The Dust and Security Covers are elements that protect from human injury during the normal operation of the Fiber Positioner, and also protect the mechanics and electronic elements from sand and dust.

The Wide Filed Corrector is the optical system in charge of adapting the light direction perpendicular to the Focal Plane concave area. This system shall always remain mounted on the FPR, providing an enclosure environment for Focal Plate and all of their parts. The WFC might be retracted to access to the physical FP i.e. to repair broken fibers etc.

The Fiber Positioning Device is designed to position a minimum of 1000 buttons (MOS buttons + mIFU buttons + calibration buttons) on the focal plate.

It is planned to place a SIFU unit in the central position of the plate.

Each of the FPD shall be capable to position each one of these buttons with a minimal accuracy and repeatability of ±40 μm RMS.

The maximal period of time needed to configure the buttons in the FOV shall not exceed 15 minutes and twice as much if the previous field shall be totally cleared. An optimal value of configuration time shall be about 10 minutes.

3.5.4.2 Design disadvantages

The IAA concept is now considered less convenient than the other concepts, both at Nasmyth or Folded Cassegrain. The details of its disadvantages are given in Section 3.5.8. For this reason no further details are given here on this concept.

3.5.5 UFL concept Fiber Positioner

3.5.5.1 Introduction

As its name implies, the primary function of the SIDE fiber positioner subsystem is to move the optical fiber ends to their desired location in the telescope focal plane. Key performance drivers for this subsystem include: positional accuracy, position repeatability, time for positioning, subsystem autonomy, subsystem reliability.

In this section, we consider a concept for the SIDE fiber positioner subsystem employing a set of simple robotic arms operating in parallel. This particular concept is closely based on designs for cryogenic multi-object spectroscopy pickoff positioners developed at the University of Florida for proposed next-generation Gemini and Thirty Meter Telescope instruments. In the sections below, an overview of the system is given, as well as some key performance parameters.

In summary, if provided of a gripper, this 20-arm concept can reliably position 1000 fibers in the GTC focal plane with an average time of ~11-12 minutes and an accuracy of <0.1-arcsec. If used without gripper for mIFU positioning, it could very quickly position ~25 mIFUs on the GTC Folded Cass focal plane with the same accuracy (<0.1-arcsec).

3.5.5.2 Positioner Overview

The primary function of the fiber positioner mechanism is to place fiber ends in the SIDE focal plane field-of-view so they can properly relay light to the SIDE spectrograph modules. In this concept for the SIDE positioner, this is accomplished using a number (up to ~20) of independently-controlled/actuated arms. Each arm operates in a sector ("slice of pie") of the field of regard, just above the GTC input focal plane.

Figure 94 shows a solid model view of the MOS probe mechanism for IRMOS, on which the SIDE design is based. The primary structural component of the mechanism is a top plate, to which all probe arm and motor components are mounted. The plate has a central cutout allowing light in the converging beam from GTC to fill a (quasi-)unvignetted 20-arcmin-diameter region at the focal plane. We assume that the "home position" of the optical fibers is a ring just outside the focal plane circle. We also assume that the fibers magnetically attach to a plate "below" this plate. The 20 positioner arms each patrol an 18-degree "slice of pie" region just above ("upstream" of) this focal plane. (Note that this assembly will probably be "side-looking" for SIDE).

In operation, the arm will move to the edge of the field of view, directly over an unemployed fiber. A solenoid-actuated mechanism will be "fired", causing an electromagnetic "grabber" extend down over the magnetic fiber end. Once the solenoid is fired, the electromagnetic is activated to connect to the fiber end, and the solenoid is released allowing the spring loading to return the "grabber" to its "up" position and lift the fiber off the magnetic plate. The positioner will then move to the desired location for the fiber target. The solenoid will be fired to replace the fiber down on its magnetic attachment plate, and the electromagnet will be de-activated to release the grasp. The solenoid is then released, retracting the grabber above the fiber plane. The arm is then ready to move another fiber. (Thanks to Justo Sánchez,

Ovidio Rabaza, and Marcos Ubierna for suggesting the magnetic grabber approach!). If used for mIFUs, each mIFU fiber bundle would be permanently attached to the end of its own positioning arm. In operation, the positioner would just move to the desired location for the mIFU target.

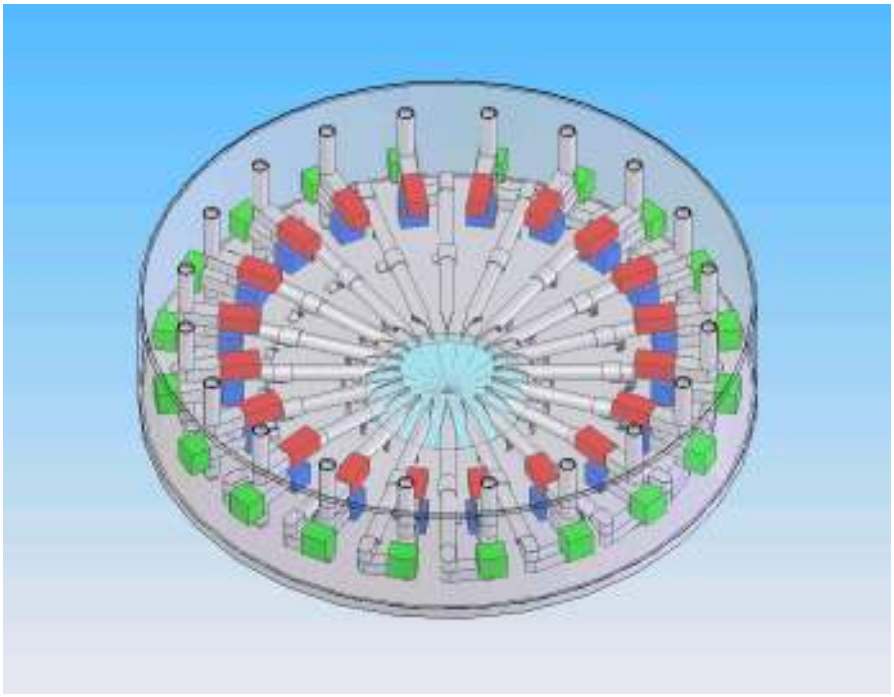

Figure 94. View of the MOS probe mechanism with 20 probe arms.

We provide a more detailed view of the articulated portion of the probe arms in Figure 95.

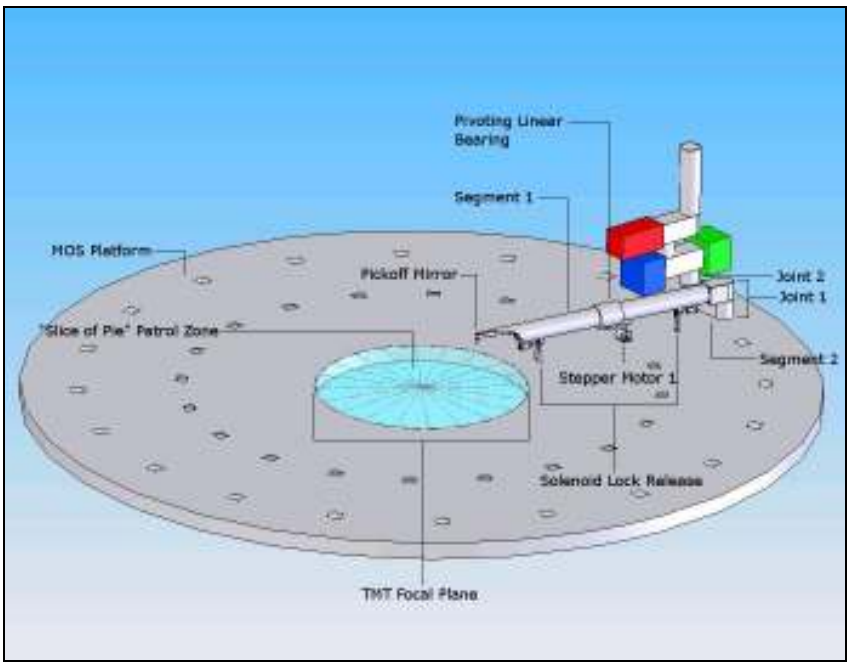

Figure 95 Close-up view of a MOS probe arm with its actuators and motors.

Each of the arm joints contains a rotary bearing, allowing the upper segment to rotate freely with respect to the lower segment (or with respect to the baseplate in Joint 2). Segment 1 rides on a linear bearing, which in turn sits on a rotary bearing attached to Actuator #2. Joint 1 also sits on a rotary bearing attached to Actuator #1.

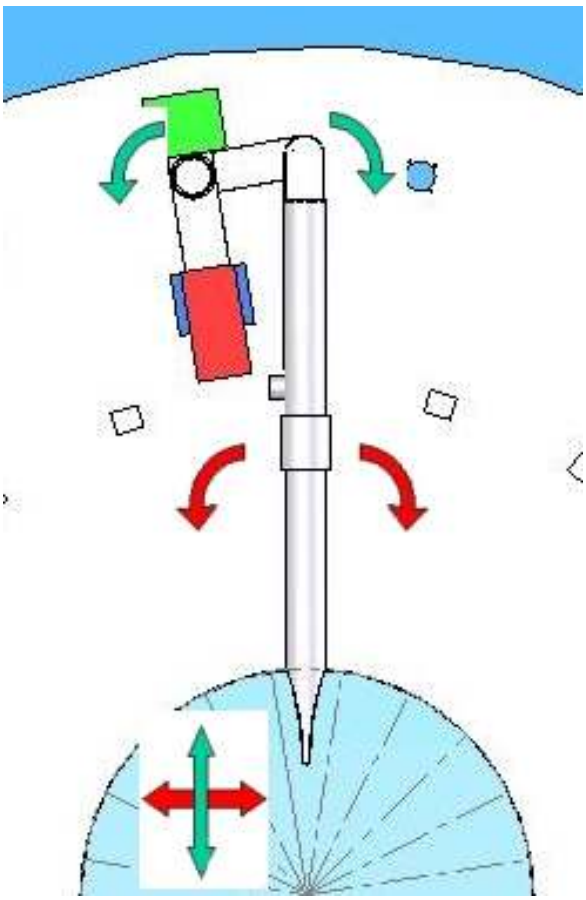

Figure 96 Schematic of MOS probe with relationship between actuator and probe tip motion

Each arm will be positioned via two stepper-motor-driven actuators. Figure 96 shows the relationship between rotation of the actuators and the motion of the positioner arm. Red arrows show the rotation of Actuator #1 and the corresponding motion of the arm tip, where the gripper is located. Blue-green arrows show the rotation of Actuator #2 and the corresponding motion of the arm tip, provided with a magnetic gripper or directly supporting a mIFU bundle. As can be seen, Actuator #2 primarily controls motion in the radial direction, while Actuator #1 primarily controls motion perpendicular to this, creating an approximation of "R-θ" motion control. Actuator #2 is driven by a stepper motor mounted below the baseplate, with a spur gear coupling to a single-lead worm drive engaged with a gear on the motor actuator underside. Actuator #1 is driven by another stepper motor with a single-lead worm drive engaged with a gear on the actuator underside. In order to accurately place the probe tip, software control will need to coordinate simultaneous motions of the two motors, with step counts carried out in a ratio which depends on the distance between the actuator points and the arm length.

3.5.5.3 Arm Homing and Positioning Accuracy

Each actuator will have a limit switch that is tripped at the "home" or "datum" location of its motion range. In this position the arm is fully retracted to just outside the edge of the GTC

field of view and at the angular center of its "slice of pie." From "home," the two stepper motors operate in synchronization with a constant ratio of step rates to position the probe. For instance, if the final position requires 600 steps for Actuator 1 and 400 steps for Actuator 2, the motors will be pulsed with a steady 3:2 ratio to this final step count. This synchronization is necessary to keep the arm from swinging into neighboring "slices of pie" and potentially colliding with other probes. We will use 2-axis synchronized controllers in order to ensure this coordination.

The positioning accuracy required for the positioner is ~0.1-arcsec (~80 μm projected on the GTC focal plane), which means that targets are within ~10% of the individual fiber field (assuming ~1-arcsec fibers to match seeing and target size). This implies a mechanical positioning accuracy also of 80 μm, and thus a position resolution of ±40 μm.

The ratio of range (600 arcsec) to resolution (0.05-arcsec) gives a total of 12000 steps required to achieve this goal (note that in practice, repeatability is typically <<1 step). With 100 steps per motor revolution, 120 motor revolutions will provide the full range of motion required. The full travel range of the probe is 180º of actuator rotation, so the gearing will need to have 240 revolutions of the single-lead worm per revolution of the actuator gear, which is reasonably similar to previous mechanisms of this type. Thus, straightforward gearing of the mechanism should provide the required range and resolution for the MOS probe.

One issue which has been raised during the Feasibility Study for SIDE is the positioning error on the probe tip introduced by "play" in the sliding bearing for the long segment of the positioner arm. When the arm is at maximal radial extension (i.e. to field center), the claim is that for a typical standard bearing, pivoting about the bearing could introduce an error as large as 100 μm in the probe tip position. First of all, we should note that this corresponds to an error on the sky of only ~0.12-arcsec and that even this only occurs at the worst case location in the field of view, combining to produce a virtually negligible scientific impact, and thus does not seem like a serious issue at the Feasibility Phase. Secondly, we point out that it is fairly easy to introduce custom bearings at relatively low cost which have reduced angular "play". Since the estimated error is already only marginally noticeable (if at all), even a slight reduction in "play-induced" positioning error should render it completely negligible. In addition, we know of at least two alternate bearing schemes which would dramatically reduce the "play" should further analysis indicate this is important – one involving dual sliding bearings separated by an axial distance, the other involving a modified arm cross-section to diamond-shaped with quadruple rolling-cylinder bearings. These are both commercially available options which would reduce the play by factors of several (at least). However, consideration of these options is well beyond the scope of this Feasibility Study – the initial design presented here already meets most reasonable scientific performance standards and (as shown) can be improved upon in a straightforward manner should those requirements be tightened.

3.5.5.4 Timing Performance

These motors are typically driven at ~1000 steps/second, to give a full range travel time of 12-seconds. Allowing for ~3 seconds to "grasp" a fiber and an additional ~3 seconds to release it, the maximum "round trip" travel time for positioning a fiber from the field edge to field center and then returning the arm for the next fiber is 30 seconds. For a quasi-random arrangement of targets in the field of view, the mean target location is at a radial distance of

2/3 of the maximum radius. In that case, the average travel time is 4 seconds each way, and combining with grasp/release time, the average "round trip" time for fiber placement is 14 seconds.

For N_{fib} fibers and N_{arm} arms, the total time to position fibers from their home position to target locations is given by

$T_{pos} = 14 * N_{fib}/N_{arm}$

For $N_{fib} = 1000$ fibers and $N_{arm} = 20$ (as shown above), then the total time for configuration is 700 seconds – just over 11 minutes. This then creates the possibility of efficient "on the fly" repositioning of SIDE fiber setups during the night's observations.

3.5.5.5 Arm Collision Avoidance and Fault Recovery

Another critical aspect of the MOS or mIFU bundles positioning design is collision avoidance, especially after a recovery from fault (i.e. power failure). For bundle positioning, a simulation software has been developed for the arm positions, including a "zone of avoidance" of 1.0 mm. Before probes are moved, such a simulation will be run to ensure that controlled motion of the arm does not result in an inter-arm collision. The synchronization of the two actuators ensures that the gripper motion is a straight line from the start point to its destination. Thus as long as the simulation shows that the final positions of the fibers do not enter the zone of avoidance, no collisions can occur.

3.5.5.6 Position Arm Size Analysis

Figure 97 and Figure 98 show the configuration on an individual probe arm, and give the parameters used in subsequent analysis. We note here that the IRMOS patrol radius of 320 mm is an identical match to that we envision for SIDE (300-mm radius of the FOV plus ~20-mm additional radius for the fiber "park" position).

However, the GTC Folded Cass focal station designs currently available show an upper limit of 1150-mm diameter, which would imply a significant constraint on the mIFU positioning as shown in subsection 3.5.5.6.2 below.

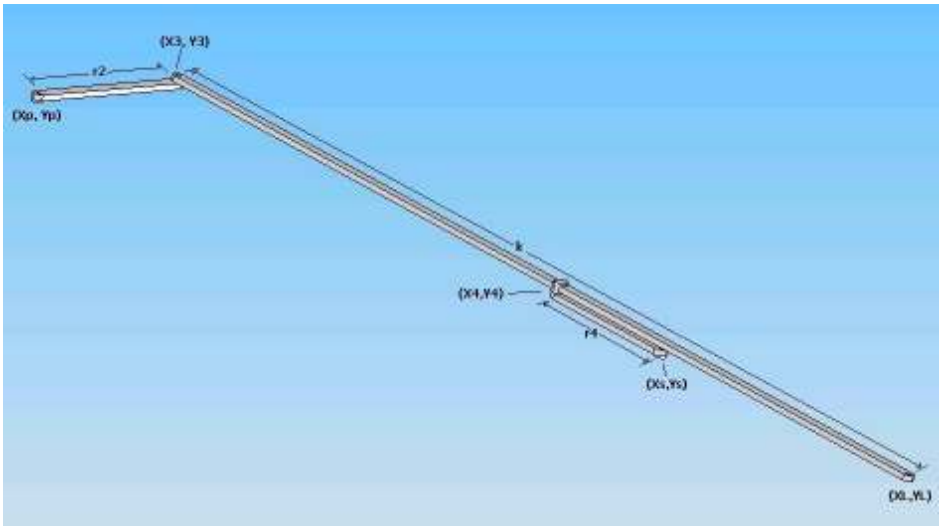

Figure 97 Configuration of Individual Probe Arm

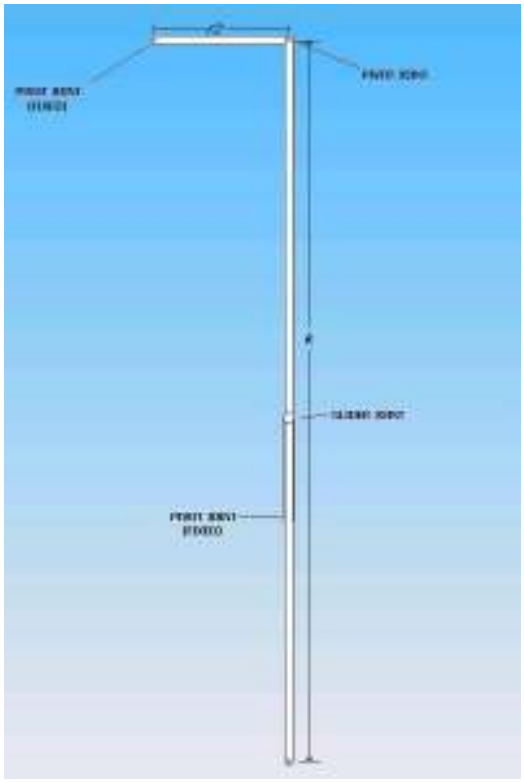

Figure 98 Top View of Probe Arm

3.5.5.6.1 Basic Size Parameters/Analysis

Figure 99 shows a kinematic model of the positioner arm as a four-bar slider-crank mechanism.

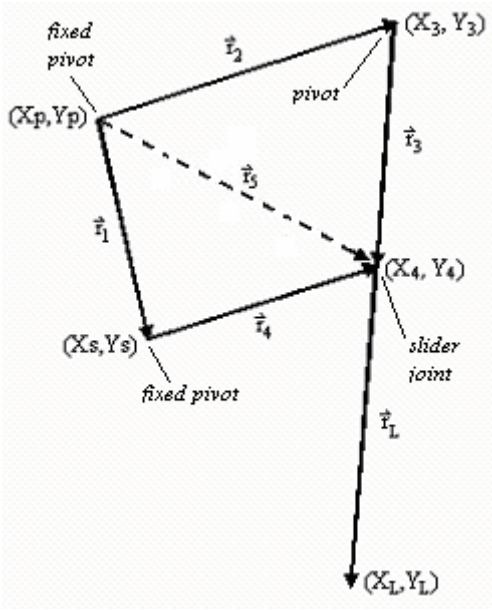

Figure 99 Kinematic Model of Positioner Arm

From Figure 99, the follow relationships can be determined:

$$\mathbf{r_1} + \mathbf{r_4} = \mathbf{r_5} \qquad \mathbf{r_2} + \mathbf{r_3} = \mathbf{r_5} \qquad \mathbf{k} = \mathbf{r_L} + \mathbf{r_4} \qquad k = r_L + r_4 \qquad \mathbf{r_L} \parallel \mathbf{r_3}$$

$$r_1 = \sqrt{(x_S - x_P)^2 + (y_S - y_p)^2} \qquad \theta_1 = \tan^{-1}\left(\frac{y_s - y_p}{x_s - x_p}\right)$$

$$r_5 = \sqrt{(x_S - x_P + r_4\cos\theta_4)^2 + (y_S - y_p + r_4\sin\theta_4)^2}$$

$$\theta_5 = \tan^{-1}\left(\frac{y_S - y_p + r_4\sin\theta_4}{x_S - x_p + r_4\cos\theta_4}\right)$$

$$r_3 = \sqrt{(x_S - x_P + r_4\cos\theta_4 - r_2\cos\theta_2)^2 + (y_S - y_p + r_4\sin\theta_4 - r_2\sin\theta_2)^2}$$

$$\theta_3 = \tan^{-1}\left(\frac{y_S - y_p + r_4\sin\theta_4 - r_2\sin\theta_2}{x_S - x_p + r_4\cos\theta_4 - r_2\cos\theta_2}\right)$$

The points (x_p, y_p) and (x_s, y_s) will be defined by other design considerations. Therefore, we can define the remaining point in Figure 97 as:

$$(x_3, y_3) = (x_p + r_2 \cos\theta_2, y_p + r_2 \sin\theta_2)$$

$$(x_4, y_4) = (x_p + r_2 \cos\theta_2 + r_3 \cos\theta_3, y_p + r_2 \sin\theta_2 + r_3 \sin\theta_3)$$

$$(x_L, y_L) = (x_p + r_2 \cos\theta_2 + k \cos\theta_3, y_p + r_2 \sin\theta_2 + k \sin\theta_3)$$

The radius of the positioner subsystem, R_T, can be determined using trigonometry. Figure 100 is a sketch of a slice of pie in the SIDE positioner. Below are the calculations to determine R_T.

$$\theta_P = \frac{2\pi}{n}, \qquad \text{where } n = \#\ of\ probe\ arms$$

$$R = 320mm$$

$$\sin\left(\theta_P/2\right) = \frac{x}{R} \quad \Rightarrow \quad x = R\sin\left(\theta_P/2\right)$$

$$\boxed{R' = r_2 \Big/ \tan\left(\theta_P/2\right)}$$

$$R' - L = \frac{x}{\tan\left(\theta_P/2\right)} = \frac{R\sin\left(\theta_P/2\right)}{\tan\left(\theta_P/2\right)} = R\cos\left(\theta_P/2\right) \quad \Rightarrow \quad L = R' - R\cos\left(\theta_P/2\right)$$

$$\tan\left(\alpha/2\right) = \frac{x}{L} = \frac{x}{R' - R\cos\left(\theta_P/2\right)} \quad \Rightarrow \quad \alpha = 2\tan^{-1}\left[\frac{x}{R' - R\cos\left(\theta_P/2\right)}\right]$$

$$k = R' - R/2$$

$$\boxed{R_T = R' + \frac{R}{2}}$$

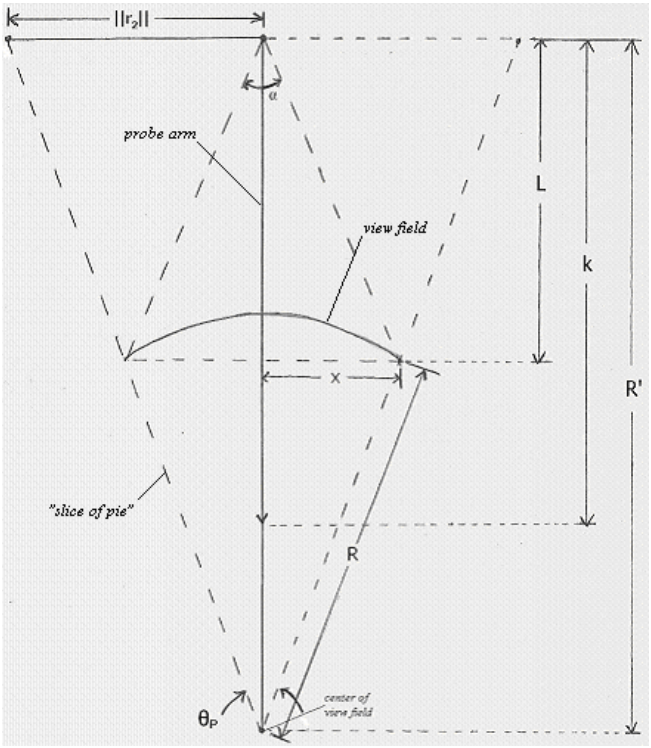

Figure 100 Sketch of Probe Arm and Slice of Pie

Since R, the radius of the view field, is fixed, R_T is a function of r_2 and θ_P. θ_P is defined by the number of probe arms. Therefore, in order to determine R_T, r_2 must be defined. Figure 101 shows the range of motion of r_2 as a function of R and θ_2.

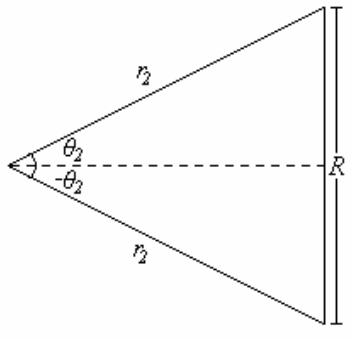

Figure 101 Range of Motion of r_2

$$\sin\theta_2 = \frac{R/2}{r_2} \;\Rightarrow\; r_2 = \frac{R}{2\sin\theta_2}$$

$$0 \le \theta_2 \le \pi/2$$

Therefore, by varying the limits of θ_2, the size of r_2 will change. For example, when $\theta_2 = \pi/2$, R_{Tmin} *(20 arms) = 1170.20*mm.

A MATLAB m-file called *robust4bar* was created to plot the four-bar slider-crank model of the probe arm for various parameters, as calculated above, and positions.

3.5.5.6.2 Field of View versus Number of Probes

As shown above, for 20 probe arms and a 300-mm radial field of view, we get a mechanism minimum radius of 1170-mm. At the Folded Cass station, this could be a problem as it is potentially larger than the available space as found on the GTC documents. However, the exact space envelope at Folded Cass is still an open issue for the GTC Project. Preliminary communications from the Project Office (J. Castro) indicate that diameters of ~1510-mm should definitely be possible, and larger diameters may be feasible.

Thus, we can use the above analysis to derive the maximum field of view covered for a given number of probe arms and assuming that the total system diameter cannot exceed 1510-mm as:

$D_{FOV} \le 3020 \text{ mm}/[\cot(\pi/N_{probe})+1]$

Or, in arcminutes,

$D_{FOV} \le 61.0 \text{ arcmin}/[\cot(\pi/N_{probe})+1]$

This then yields the results shown in Table 35**.**

Number of Probes	FOV Diameter (arcmin)
14	19.8 (full field)
16	17.8
18	16.2
20	14.9
25	12.4
27 (nominal number)	11.7

Table 35 Number of Probes versus Patrol Field Diameter

Concerning mIFU positioning, we can see that, for a reasonable number of mIFU, we can patrol the entire available GTC Folded Cass FOV, and for numbers approaching the nominal value of 27 mIFUs we can still patrol the majority of the areal FOV. If the GTC Folded Cass envelope constraints are relaxed, this situation will only improve.

3.5.5.7 Costs

Table 36 shows the estimated costs in Euros for the UFL fiber positioner.

External hardware	180,000
Labor (incl. fabrication)	450,000
Miscell. (travel, shipping, insurance etc.)	90,000
Total	**720,000**

Table 36 Cost estimation for the UFL fiber positioner.

3.5.6 LBNL Fiber Positioner

3.5.6.1 Introduction

The LBNL fiber positioner design for the GTC/SIDE is a very different design than the other robotic positioners being considered. The LBNL design divides the focal plane into ~1000 hex cells. Each fiber is individually-actuated within one hex cell. The fiber motion extends slightly beyond its hex cell, such that there is no spot on the focal plane that cannot be reached by at least one fiber.

The downside of the LBNL design is that the fibers cannot be densely packed in any one part of the focal plane. For example, one could not pack all of the fibers into 1/4 of the focal plane if there were a compact cluster of targets, or even follow the large-scale structure of clustering for galaxies. This limitation can be mitigated by a clever set of offset pointings, made possible by the fast reconfiguration time (discussed later).

The upside of the LBNL design is that the reconfiguration time is extremely fast. The entire focal plane can be reconfigured in under 20 sec. The local precision need be only 1 part in 1000 for each actuator to achieve 30 micron precision, which is possible running open loop. There is also an inherent robustness to this design: any mechanical failures would compromise only 1 MOS science unit.

3.5.6.2 Mechanical design

The focal plane is defined by a 2-inch thick aluminum block machined to the exact shape of the focal surface. The active focal plane is 99.35 cm to cover the 20' field, but the block would extend beyond that by several cm for mounting purposes. 1003 circular holes are drilled into this block with a center-to-center separation of 2.92 cm. Each of the 1003 fiber actuators is plugged into one of these holes from the backside. The astrometric surface is defined by 3 ball bearings (per actuator) on the backside of the block. Grooves in the actuator casings contact the bearings, forming a proper kinematic mount. Embedded magnetic retention aids in locating the actuators, and 3-bolt fasteners secure them.

Each fiber actuator is mechanically independent of every other. The fiber is moved in a 2-dimensional plane, since the focal surface is approximated as flat within the footprint of one fiber. There are two MicroMo 8mm motors that control the two degrees of freedom. There is a geared, linear rack on the top of the actuator that moves the fiber radially from the center. This rack is driven by a MicroMo motor pointed up to the center of the small 3-gear assembly. This entire top assembly (in blue) is moved rotationally by the second MicroMo motor. This motor points downward to a small gear on the bottom of the assembly. That gear drives against a large gear that is fixed to the actuator outer casing (in green). The fiber reach is 1.686 cm from its center position,

The fiber (in red) is mounted in the end of the rack in a bushing. The details of the MOS fibers and their associated lenses can be found in Section 3.7.12. A serious consideration for any fiber-fed spectrograph is that the light is only telecentric at the center of the field, and will in general deviate by several degrees at the edge of the field. The LBNL design does allow for the light to approach the focal plane at an angle, with the reducing lens mounted on

each fiber compensating. Since each fiber is local to its position in the focal plane, the correct lens can be manufactured for each fiber. The fiber + lens assembly does need to be prevented from rotating with the azimuthal gear. This is achieved by holding the fiber in a flexible hyperdermic tubing that is fixed on the backside of the actuator. The fiber + lens then rotates within the bushing in the rack on the top end, and maintains its position rotationally relative to the sky.

The actuators are run in open loop with a positional accuracy of ±30 μm (corresponding to ±0.04 arcsec on the focal plane). An initial position reference is supplied by an index switch of two gold-plated pins in a crossbar configuration. One pin (actually a wire) has flexibility so that the switches can slightly over-travel and not change the zero-point by over-stressing the crossbars. The rotational movements are supported by ball bearings ranging in size from 3 mm to 28 mm diameter. An electronics assembly sits on the back side of each actuator. See Figure 102, Figure 103, Figure 104, Figure 105 and Figure 106 for the details and description.

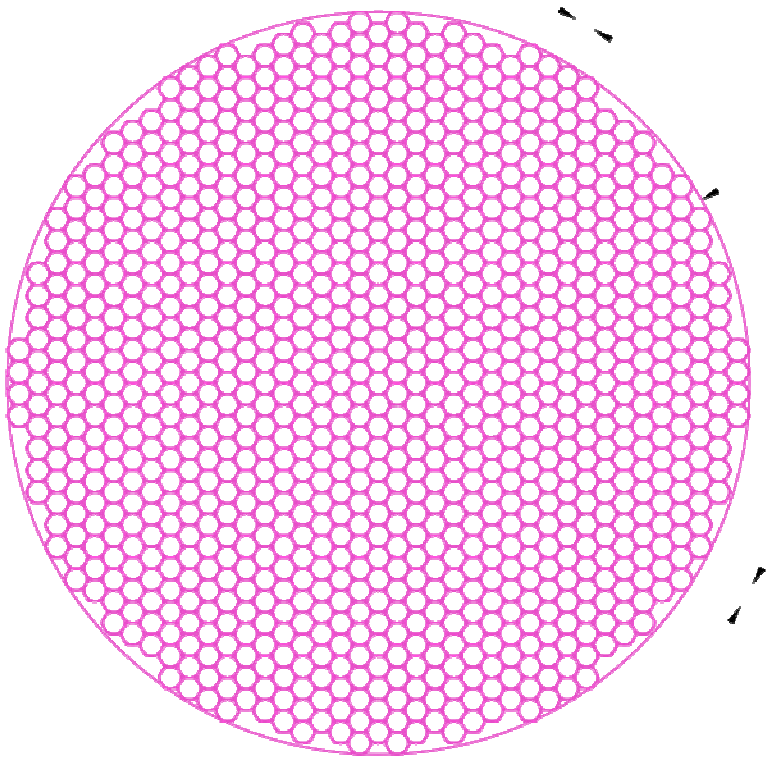

Figure 102. Focal plane divided into 1003 hex cells, with a center-to-center spacing of 2.92 cm. An LBNL fiber actuator with one fiber is mounted in each cell. The fibers can reach beyond the hex cell, such that every position on the focal plane is accessible by at least one fiber.

Figure 103. Top-view of several LBNL fiber actuators. The fiber itself is shown in red. Radial motion of the fiber is controlled by the rack-and-pinion.

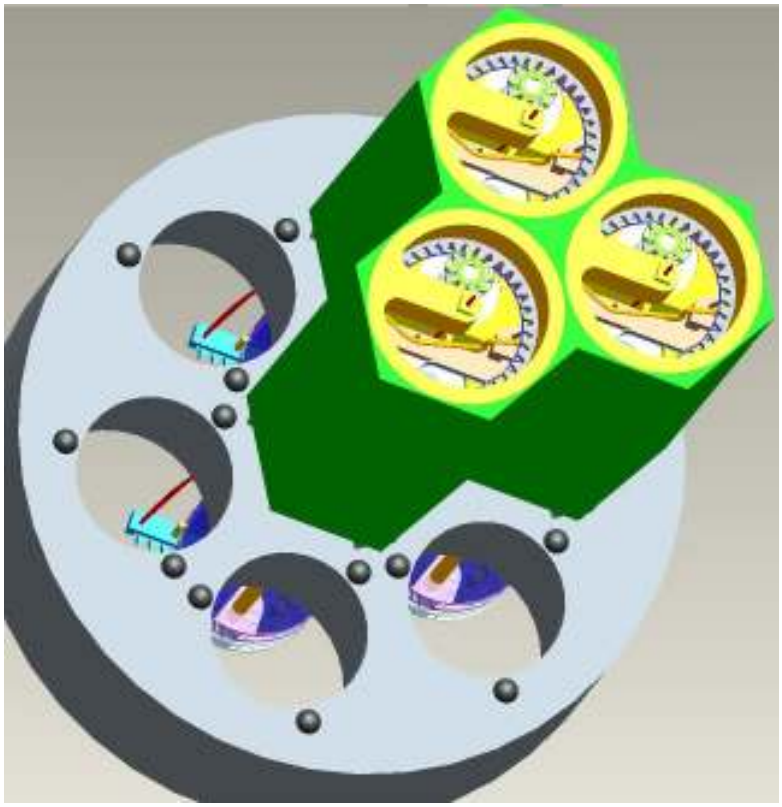

Figure 104. Bottom view of several LBNL fiber actuators. Azimuthal motion is controlled by turning the small gear against the large (grey) gear that is fixed to the stationary (green) casing.

Figure 105. Disassembled LBNL actuator of the 1.92 cm hex size. The SIDE/GTC actuator would be somewhat larger, with a 2.92 cm hex size.

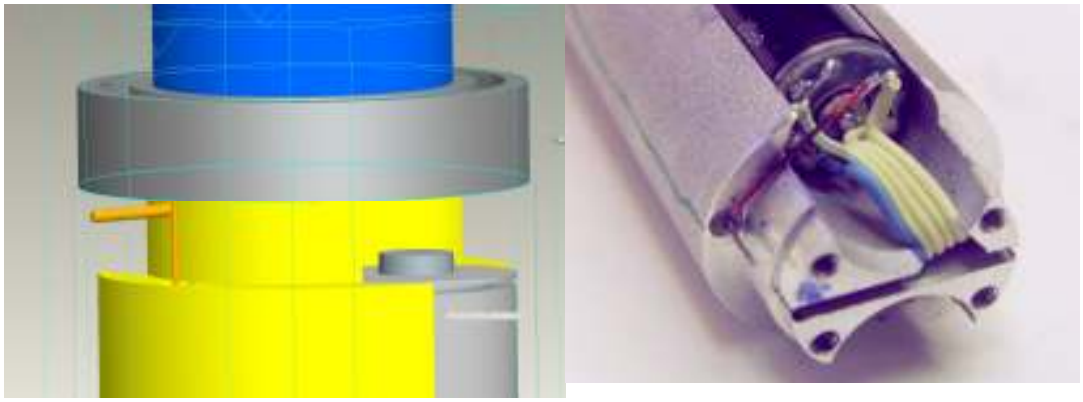

Figure 106. Rotational index switch in the conceptual drawing (left), and wiring in the prototype unit (right).

3.5.6.3 Electronics and control design

The LBNL fiber system is an array of 1000 actuators, each containing two stepper motors that are driven by identical driver/controller PC board modules residing in each actuator.

Each pair of modules is connected to a multi-conductor cable that delivers both power for the motors and communications for the motor-controllers.

These cables parallel the fiber-optic cable paths from the actuators to the 50 fiber termination blocks for all 1000 fibers. Each fiber termination block also has an attached electrical termination block that combines all the conductors for each group into a multi-conductor cable.

Each multi-conductor cable contains the electrical signals for the actuators in that fiber group and goes to the Module Interface Unit. This unit accepts the signals for all 50 groups and multiplexes the serial communications of the whole array of 2000 motors and acts as a pass-through for power from a separate commercial supply

The serial communication hardware enables the motor controllers, which have an address range of 32, to be mapped to a host address space of 2048 devices. RS422 protocol is used between the actuators and the Motor Interface Unit and RS232 is used to the host computer. All motor controllers talk only if addressed by the host.

The job of communications is left up to a dedicated host computer whose function is to efficiently distribute new positions to each of the 2000 motors and to perform housekeeping tasks for the actuator array. Because the motors perform more than one move per repositioning, the motor controllers execute a generic on-chip program whose parameters are adjusted for each move by the host, thus allowing the host to load multiple moves to actuators without waiting for those moves to complete. Embedded routines in the controller non-volatile memory offload command and monitoring from the host.

To avoid excessive power dissipation, motor controllers turn off the power to the motors during non-motion periods. A special control scheme assures that when motors are switched off, they are at a magnetic pole position so they will not jump to a nearby magnetic pole, thereby losing their position. See Figure 107 for details.

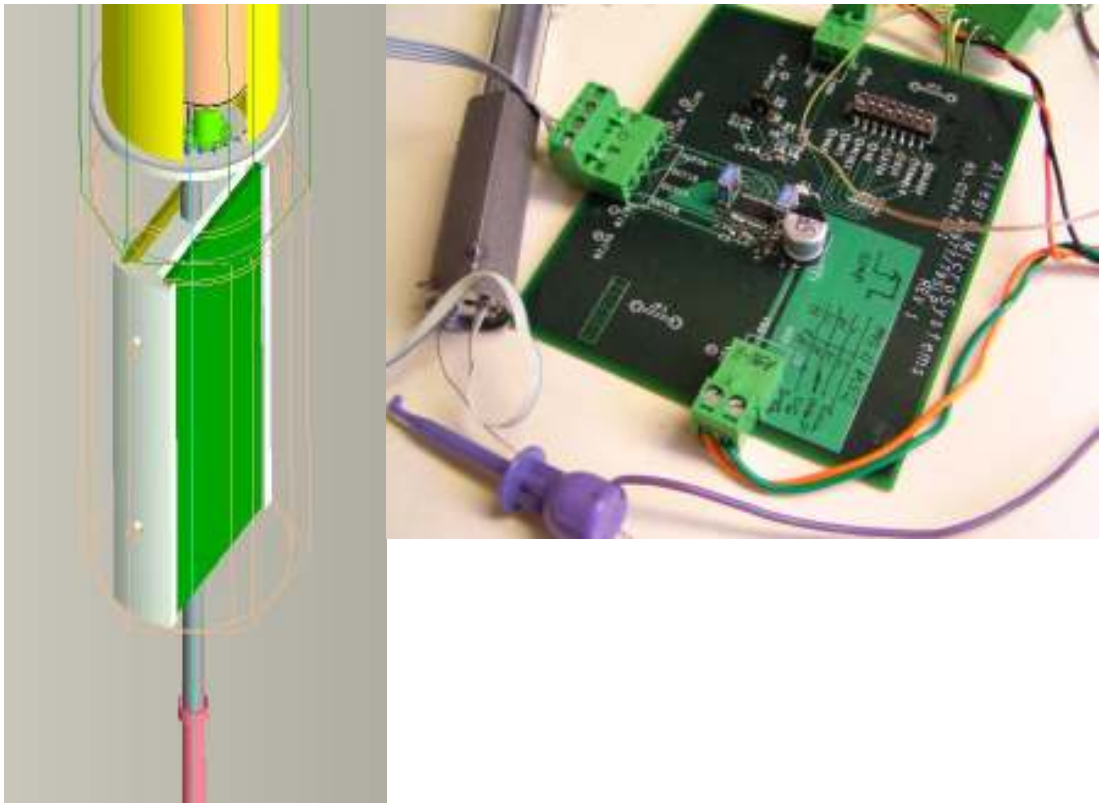

Figure 107. Conceptual drawing of the miniaturized electronics control package at the back of the actuator (left), and the current bread-boarded electronics (right).

3.5.6.4 Survey modes

The conceptual design of the LBNL fiber actuators differs from the other robot positioners primarily in that each fiber has a limited patrol radius. This does argue for one to approach certain survey modes differently with the LBNL positioners.

For most modern wide-field surveys, the targets are fairly uniform on the sky. Because of this, a design where the fibers each patrol a small area is a suitable solution. Note that all fiber positioners have the limitation that the fibers are mounted in ferrules that cannot approach closer than approximately 3 mm -- this is the “fiber collision” problem.

We have considered several survey modes for the GTC/SIDE with the LBNL or robotic fiber positioners. In all cases, we consider a patch of sky to be covered that is signficantly larger than the GTC/SIDE field of view. Specifically, we have performed simulations using a 2°×2° patch of sky (46 times larger than the GTC/SIDE field). The most clustered case would be the brightest galaxies, at r≈21 mag to achieve the requisite target density. The least clustered case would be more distant galaxies or Milky Way stars, both of which are approximated by random density fields.

The first question for a survey is whether ***completeness*** is important. This was a driver for the SDSS-I galaxy survey, but not for the supplementary science programs (such as the Milky Way programs). For reference, the SDSS main galaxy survey was 93% complete, with the incompleteness primarily from fiber collisions. The SIDE/GTC fibers sample the sky 126X more densely than SDSS-I, at 11,500 targets per square degree. A completely naive use of the LBNL fiber positioners would result in a completeness of only 44% for the most clustered case (galaxies at r≈21) and 64% for the least clustered case. The unassigned fibers could be used for sky fibers and fainter targets. For a magnitude-limited galaxy survey, that would require observing 0.3-0.4 mag fainter to make use of those fibers.

The very fast reconfiguration time (< 20 sec) for the LBNL fiber positioners has made us re-think the way to perform a large-area survey. The SDSS plug-plate system or robotic positioners (such as 2dF) are sufficiently slow that a given patch of sky is visited exactly once for a total exposure time of 1+ hour. All these surveys then arrange circular tiles on the sky in a compatct hex pattern where 18% of the sky is in tile-to-tile overlaps. This amounts to a survey inefficiency of 18%, and an incompleteness dominated by fiber collisions.

The LBNL fiber positioners in survey mode would split each exposure into sub-exposures, where the tile position is moved a fraction of the field size. For example, one could offset the telescope by 1/3 of the 20 arcmin field size in right ascension for each sub-exposure and by $1/3\sqrt{2}$ of the field size in declination. Any target would then be visible in 9 exposures, and assigned to a different fiber in each of those exposures. A strategy like this can be used to achieve very high completeness, and even recover objects otherwise lost to fiber collisions by alternating between observing each of a pair of close neighbors. The observing **efficiency** is between 44% (nearby galaxies) and 64% (distant galaxies), as compared to 82% for a traditional fiber robot. However, the **completeness** would be even better than for a robot positioner, with virtually every target observed in at least 3 sub-exposures (for the example above). And once sky fibers are considered, the differences in survey efficiency become smaller. If there are supplementary, piggy-back programs (such as the Milky Way program in SDSS-I), then all fibers are fully-utilized regardless.

The individually-actuated fibers have a number of other advantages: In survey mode, one could assign fibers more often to the fainter objects than to brighter objects, thus achieving more uniform S/N for all targets. Very bright calibration stars could be observed simultaneous to faint targets by driving fibers quickly across those stars. Atmospheric dispersion corrections could be corrected dynamically, with the proper corrections for the wavelengths of interest for each object.

3.5.6.5 Performance and guiding

The basic performance of the LBNL fiber actuator system would easily meet the specifications for the GTC/SIDE instrument. The positioning accuracy of the fibers would be ±30 μm. The reconfiguration time for all the fibers would be less than 20 sec, which is shorter than the read-out times of the CCDs. There is some power dissipation in the focal plane from the motors, but this appears as only a 15 W heat source since the motors are powered up for only brief periods of time and the heat escapes from the motor assemblies slowly. If deemed necessary, a glycol loop or air cooling could be used to remove this heat.

Guiding at the GTC/SIDE can be handled in several different ways. It is desirable to have the guiding elements as close as possible to the fibers on the focal plane. The solution for SDSS

was to use 11 coherent fiber bundles that image fields of 7 arcsec diameter onto a CCD guide camera. These fibers are positioned exactly like the science fibers, guaranteeing that there is no positional offset between the science and guide fibers. These fibers easily overconstrain the problem of tracking the telescope central position, scale and rotation. GTC/SIDE could employ similar guide fibers. An enhancement would be to offset several of these guide fibers tangent to the focal plane. By solving for the FWHM of stars in fibers that are both in and out of focus, one can dynamically track the telescope focus throughout a spectroscopic exposure ***independent of seeing***. The SDSS Telescope employs such a trick with tangentially-offset CCDs in its imaging array to maintain focus, but did not do so for spectroscopy.

The fiber positions will be updated several times during an exposure to **dynamically track atmospheric dispersion**. This is especially important for the SIDE instrument, which lacks an atmospheric dispersion corrector. The telescope guider removes the first-order offset of object positions from atmospheric refraction. However, without an ADC, the refraction errors accumulate in a quadrupolar offset pattern across the 20-arcmin field during an observation (see Section 3.4). Updating the fiber positions every few minutes prevents these errors from accumulating.

Another mitigation technique for the lack of an ADC is to position the fibers at the wavelength of interest for each object. For example, if there are both z=3 QSOs and z=1 red galaxies in the same field, the QSO fibers would be positioned to be centered at the 5000 Å light (for the LyA forest) and the galaxy fibers would be centered at 1 micron. By dynamically tracking a chosen wavelength for each object, there would effectively be no ADC losses for at least the most interesting wavelength range for each object.

3.5.6.6 Costs

Table 37 shows the estimated cost for the LBNL fiber positioner.

Mechanical	
motors	$ 242.00
gears	$ 51.50
bearings	$ 136.24
mechanical parts	$ 126.58
assembly & test	$ 50.00
	$ 606.32
Electronic	
printed wiring boards	$ 4.43
passive components	$ 6.10
active components	$ 30.18
assembly & test	$ 3.00
	$ 43.71

Table 37. LBNL fiber actuator cost breakdown (in bulk).

The LBNL fiber positioner is being funded by a Laboratory Directed Research and Development (LDRD) grant at the Lawrence Berkeley National Laboratory, with David Schlegel as the principal investigator. This work began in October 2006, and is expected to be funded for a total of three years.

The initial prototype of the LBNL fiber positioner is for a 1.92 cm module with positional tolerances of ±20 μm. The mechanical assembly of this prototype will be completed by December 2007. A testing apparatus will be completed by March 2008 for end-to-end tests of the positional accuracy. The initial costing estimates are US $650 for each actuator (in quantity), with the MicroMo motors accounting for nearly half that cost. A 1000-fiber system has been costed at US $800,000, including the base plate, power supplies, control computer, and assembly.

The GTC/SIDE positioner would rescale the module spacing to 2.92 cm, and dramatically loosen the tolerances to ±100 μm. The prototyping work for GTC/SIDE could be completed as part of the LDRD grant in 2008. The components of the system would be slightly less expensive, since the slightly larger gears would be less expensive. A more dramatic cost savings is possible if the precision MicroMo motors could be replaced with a lower-cost, less precise alternative.

It should be noted that the LBNL design is similar in concept to that of the LAMOST project at Xinglong Observing Station in China (see Figure 108). Professors Xing Xiao and Zhai Chao (University of Science and Technology of China) have built individually-actuated fibers using the same MicroMo motors driving two rotational stages (rather than r-Θ). The full LAMOST project will have 4000 such actuators with a center-to-center spacing of 2.56 cm. The LAMOST project saw first light using 123 fibers on June 18, 2007 (see http://www.lamost.org/en/). The LBNL design is believed to be somewhat simpler and more robust.

LBNL will begin work with the Spanish company Added Value Solutions (AVS) to finalize the fiber actuator design specific to the GTC, and to produce 20 actuators for a small-scale SIDE instrument prototype. Since AVS built the GTC image rotator, they are well-suited to design the actuator mountings to the GTC focal plane. This focal plane has a sizeable curvature of 5 cm. The fibers, power cables, and electronics cables must be managed in the context of the image rotator. The first LBNL fiber actuators have a center-to-center spacing of 1.92 cm, whereas the SIDE instrument will require 2.92 cm spacing. This demands a modest re-design of the actuator, although in general the components become less expensive when scaled up in size. Construction of 20 actuators by AVS should validate our cost model for the 1000-fiber system, where the biggest uncertanties are in the assembly and testing costs.

Figure 108. LAMOST fiber actuator on the bench for testing at Lawrence Berkeley Lab. The concept is very similar to the LBNL fiber actuator.

3.5.7 Fiber Positioner software

A fundamental component of SIDE will be the software to control the fiber positioner.

This will strongly depend on the fiber positioner concept selected in the end, but in general it will have to optimize the number of covered targets while avoiding MOS unit collisions.

With the LBNL fiber positioner, the software will have to track the differential atmospheric dispersion (due to the large FOV) in real time, and possibly control a focus real-time correction as well, apart from the MOS units positioning.

For the UFL fiber positioner at Folded Cass, the software will have to manage the mIFUs, again avoid collisions and control the positioning.

3.5.8 Fiber Positioner comparison

After the description of the three concepts available to us for the FPR for SIDE, we need to compare them and evaluate the advantages and disadvantages of each.

The possible robot concepts considered for SIDE are explained in sections 3.5.4, 3.5.5 and 3.5.6. Here we list the advantages and disadvantages of each robot concept for the two possible focal stations where they could be placed.

3.5.8.1.1 LNBL concept

Advantages

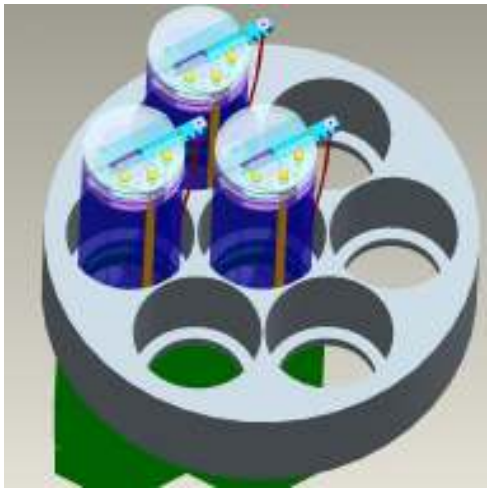

- More relaxed WFC because the focal plane can adopt a curved surface and the different actuator are tailored for its positions. In Nasmyth or folded-Cass.
- Faster positioning time, all actuators are working simultaneously.
- Possible correction in real time of the atmospheric refraction effect, that permits more observing time.
- Fibers are not stressed by the robot.
- Possibility to track the focus (TBC)
- Low cost robot.

Disadvantages

- Not ideal when the field is not homogeneous.

3.5.8.1.2 UFL concept

Advantages

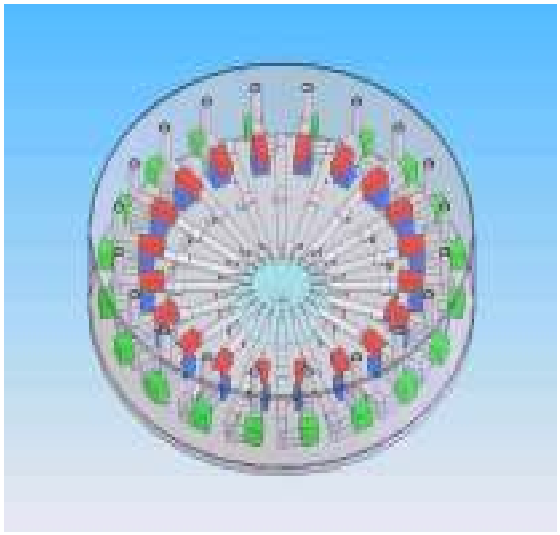

- Quasi independent movement of each arm, in its patrol area. Possible overlapping of an area for two or more nearest arms.
- Possible correction in real time of the atmospheric refraction effect, that permits much more observing time (if used without gripper).
- This concept is currently being used in a cryogenic IR environment, so under severe conditions.

Disadvantages

- Grippers and fiber buttons not simple for wide distances
- Long repositioning time.
- Needs a more complex WFC because it needs a flatter focal plane.
- Longer and more stressed fibers because of the rolling fiber system.

3.5.8.1.3 IAA concept

Advantages.

- Very robust robot. Limited numbers of motors.
- Possibility of close loop operation.

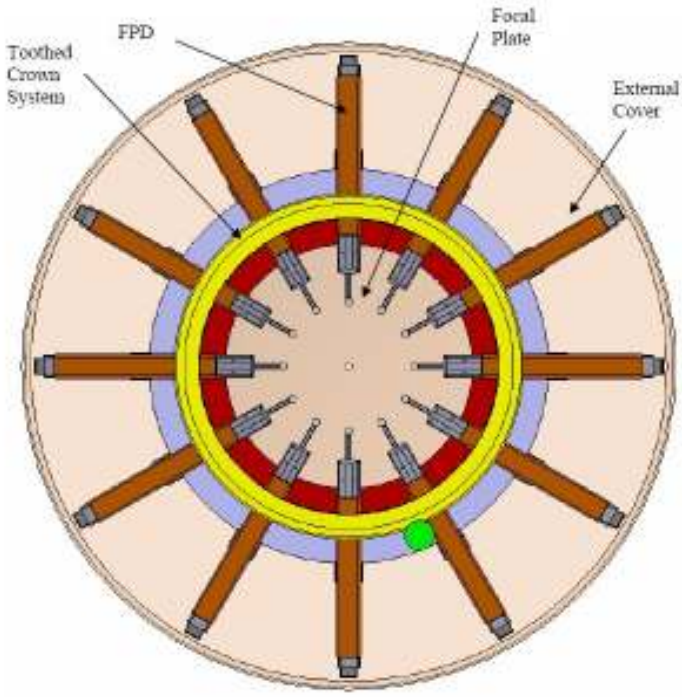

Disadvantages.

- The movement of the arms is not rotationally independent; some synchronism must be included in the software design.
- Very long repositioning time.
- Needs a more complex WFC because it needs a more flat field plane.
- Longer and more stressed fibers because of the rolling fiber system.
- Needs a complicated gripper system.

Following the idea that two telescope focal stations can be used for SIDE (Nasmyth and Folded-Cass) we now analyze how the three robot concept can adapt to each.

The analysis on the Nasmyth WFC (see section 3.3) shows that a device that yields a large curvature radius (≥7000 mm) is more difficult and more expensive to build, because of the limited space available. The only positioner which can work on a highly curved focal plane is the LBNL concept, which, as we can see in the advantage list above, has also other convenient features. The main disadvantage of the LBNL concept is the forced homogenous distribution of the apertures, which limits the survey mode efficiency, but (see section 3.5.6.4) the fast repositioning of the fibers partially compensates this and the overall efficiency is good. On the other hand, one of the main problems of the robots with radial arms is the gripper and all the related issues (FOV not flat, long distances from parking to working position, gravity flexure of the fiber cable, uncertainty in the magnet operation, crossing of fiber cable, which is a 3D problem, fiber retainer, software algorithms, etc). All of these problems aren't present in the LNBL concept, so that the best solution seems to use

the LBNL concept at the Nasmyth focus. If the gripper was suppressed, the radial concepts would gain in speed and simplicity, so they could be useful for positioning a reduced number of science units (same number as the robot arms), especially in a small FOV. Then, concerning the Folded-Cass focus, the IAA concept has the problem that the arms are not independent in the rotation direction, so the UFL concept is the best for positioning the mIFUs bundles at the Folded-Cass.

3.5.8.1.4 Combinations of observing modes at the telescope

We can consider the main parameters or characteristics or SIDE (FOV, WFC, ADC and A&G), and see how these match with the different robot concepts and the two focal stations:

A. MOS in Nasmyth with three concept: LBNL, UFL, IAA
B. SIFU in Nasmyth or SIFU in Folded-Cass
C. Mini IFU in Folded (8' to 10' FOV)
D.

Table 38 shows these parameters matched with the robot concepts. Red and blue colors are used for underlying the impossibility or the usefulness of a solution, respectively.

	Robot Conc.	MOS Nasmyth		SIFU Nasmyth	SIFU Folded-Cass		MiniIFU Folded-Cass
FOV	LBNL Nasm.	20' (1000 object) ≈		near 30" (≈ 2500 fib.)	near 30" ≈ (2500 fib.)		8' to 10' (9+18 MiniIFU)
	UFL &IAA Nasm.	20' (1000 object) ≈		near 30" (≈ 2500 fib.)	near 30" ≈ (2500 fib.)		×
WFC	LBNL Nas.	Easy		No need	No need		Easy
	UFL &IAA Nasm.	Not Easy		×	×		×
A&G	LBNL Nas.	7 bundles 7" each		7 bundles 7" each	Each arm with A.G. & Mini IFU		Each arm with A.G. & Mini IFU
	UFL &IAA Nasm.	A&G buttons		A&G buttons	Each arm with A.G. & Mini IFU		Each arm with A.G. & Mini IFU

Table 38 Observing modes versus selected parameters for the different robot concepts. A red color indicates an impossible condition. A blue color highlights a remarkable capability. X means that the option is forbidden.

To compare the three Robot concept isn't a question of technical parameters only (accuracy, speed, etc), but we need to convolve these with the whole instrument and telescope system to test the best solution which allows the scientific observations in optimal conditions. Table 39 addresses this issue.

	LBNL Nasmyth	UFL	UFL F-Cass *	IAA	IAA F-Cass *
Object # MOS/mIFU	≈1000/	1000/60	N.A./9+18	1000/60	N.A./9+18
Arms		20	9+18 (one per MiniIFU)	18	9+18 (one per MiniIFU)
Method	Hex-cell package	Slice of pie	Slice of pie	Parallel arms on a wheel	Parallel arms on a wheel
Positioning time	20sec.	11 minutes	20 sec.	15 minutes	20 sec.
Position accuracy	±30μ	<0.1" or ±40μ	<0.1" or ±40μ	±40μ	±40μ
Foc. plane geometry	Curved	Almost flat	Almost flat	Almost flat	Almost flat
Fiber replacem.	Easy (one to one)	Difficult	Easy	Difficult	Difficult
Exposing		Not possible	Auto (in case Folded 9+18		
Sky fields accuracy	Good,fast, homogen.	Dead time	Good, fast	Dead time	Not possible
Gripper MOS Nas	×	Needed	×	Needed	×
Gripper Folded 20/18	×	×	Not needed Exp.Ref.auto	×	Not possible
A & G system	7 bundles 7" each	Some A.G. bundles	×	Some A.G. bundles	×
A & G sys. F-Cass	×	×	Each arm with A.G. + mIFU	×	Not possible

Table 39 Robot concepts versus SIDE parameters. The 1st group of rows show general robot characteristic, the 2nd are capabilities or remarkable items, the 3th are the gripper needs, the 4th are A&G system issues. The red color indicates a lack of capability. The blue color indicates a remarkable capability. X means that the option is not applicable.

* with LBNL in Nasmyth

3.5.8.2 Conclusions

The problem to choose the best configuration is not easy and the various solutions presented above (and possibly more) must be studied in detail.

At the present status of the project, a good solution seems to place the LNBL robot in the Nasmyth focus and the SIFU and MiniIFU in the Folded Cassegrain. The UFL robot in Folded-Cass is then the best solution, but each arm should be equipped with a MiniIFU and an A&G bundle, to ensure both functions. A gripper is not necessary in Folded-Cass and this avoids difficulties and complications: each arm can be dedicated to a selected object or A&G star, and can move in real time to minimize the refraction atmospheric correction.

The overall advantages of this configuration for SIDE's robots are:

- Negligible repositioning time.
- Real time atmospheric refraction correction, at a fixed λ, or over an interval.
- Cost savings.

The disadvantages are:

- The FOV in Nasmyth is more suitable for homogeneous fields; other fields with variable density populations must be covered by mosaicing the observations.

3.5.9 References

Brodie, J.P., Lampton, M. and Bowyer, S. 1988, Astronomical Journal, 96, 2005-2010.
Donnelly, R.H., Brodie, J.P., Bixler, J.V. and Hailey, C.J. 1989, PASP, 101, 1046-1054.
Haynes R., McGrath, A., Brzeski, J. et al. 2006, Proc. SPIE, 6273, 62731V.
http://www.cfa.harvard.edu/mmti/hectospec.html
http://www.lamost.org/en/
Marcos Ubierna Gorricho, "SIDE Constraints in GTC Nasmyth A platform, Techincal note, March 2007
Newman, P.R. 2002, PASP, 114, issue 798, 918-928.

3.6 Microlenses

3.6.1 Telescope –fiber bundle coupling.

From the point of view of efficiency, the best coupling between a telescope focal plane and fibers is carried out through microlenses. These systems permit on one hand a greater efficiency in the sampling of the objects to observe (Table 40) but, above all, they permit fitting the focal ratio of the light entering the fiber. In that way, they minimize the effect of the Focal Ratio Degradation, FRD, controlling the cone of light at the entrance of the fiber.

Focal plane element	Energy enclosed
0.8” slit	76.1 %
0.5” slit	53.8 %
1.5” optical fiber	91.2 %
7 (0.5”) optical fibers in hexagonal arrangement	63.1 %
7 (0.5”) hexagonal microlens in hexagonal arrangement	91.3 %
9 (0.5”) square microlens in square arrangement	99.0 %

Table 40 Geometrical analysis of energy enclosed. Data obtained assuming a 0.8” seeing

The function of the microlenses is to get the light of a determined field in the focal plan of the telescope and inject this light in the fiber. The microlenses form an image of the pupil of the telescope on the fiber in such a way that the energy received by the telescope in that field is introduced in the fiber entirely.

It is well known that the focal ratio at the entrance of the fibers, due to the FRD, is degraded at the fiber output. On the other hand, it is necessary to feed the spectrographs with the appropriate focal ratio. So, putting microlenses at the fiber end, at the same time, will minimize the effect of the FRD and will feed the spectrograph adequately. The characteristics of these microlenses will be determined during the design of the spectrograph.

3.6.2 Microlenses types

The formats of the arrays of microlenses could be linear arrays, squares, hexagonal, polygonal etc. In our case, this relies on the type of sampling to carry out. For the MOS mode, a single microlens or a small array of 7 hexagonal microlenses are proposed. For the mini-IFU modes, an array of 36 or 37 microlenses seems appropriate. The SIFU mode will require a compact array (hexagonal or square) with hundreds of microlenses.

Figure 109 shows the three configurations that we could adopt:

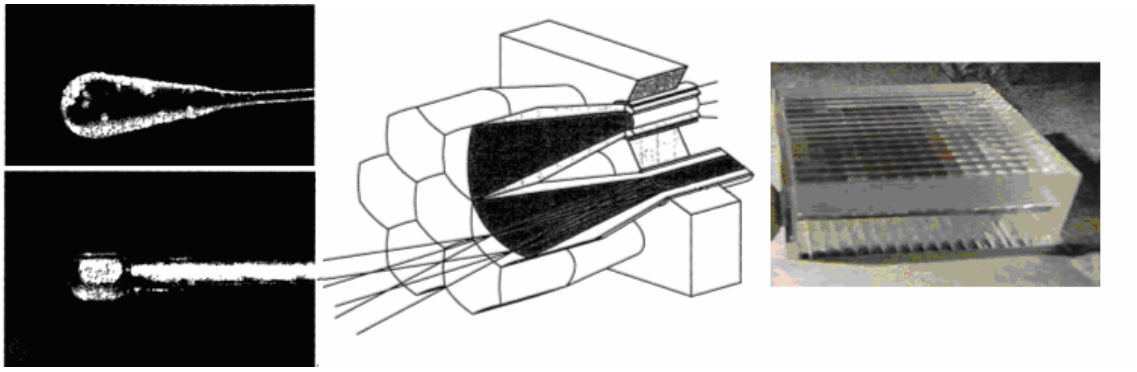

Figure 109 Some examples of microlens configuration: Single microlenses (left), small hexagonal array (center), and big square microlenses array (right). From Tecza & Thate, (1998).

3.6.3 Microlenses manufacturers

There is a great variety of companies dedicated to the fabrication of micro optic of great quality that can satisfy our necessities. We list some of these companies in Table 41.

Company Name	**Type of company**			
	Manufacturer Stock Items	**Manufacturer Custom Items**	**Distributor & Supplier**	**Design & Prototype**
SUSS MicroOptics		■	■	■
Micralyne		■	■	■
Axetris Microsystems		■		■
RPC Photonics Inc		■		■
MEMS Optical, Inc	■	■	■	■
HEPTAGON	■			■
AOA MICRO-OPTICS	■		■	■
CSEM		■		■
LIMO	■		■	■
MICROFAB TECHNOLOGIES,	■	■	■	■
O/E LAND INC	■	■		■

Table 41. Microlenses companies.

3.6.4 Costs

Microlenses costs are shown at the end of the next section (see Table 51).

3.7 The Fiber Link

3.7.1 Introduction

Multiobject and integral spectroscopy are required by the high level requirements of SIDE. This means that the use of optical fibers to link the telescope and the spectrograph are absolutely necessary. Others techniques as multislit spectroscopy or slicing mirrors have not the necessary versatility to implement both techniques simultaneously.

The fiber link has the following functions:

- Act as interface with the fiber positioner.
- Act as interface with the instrument rotator.
- Match the input aperture of the telescope in each fiber.
- Transfer the light to the spectrographs with
    - Appropriate level of transmission efficiency.
    - Minimal level of focal ratio degradation.
- Interface to the telescope structure.
- Must not hinder telescope motion and performance.
- Interface to the spectrograph room.
- Interface to the spectrographs.

When an optical fiber link between a telescope and a spectrograph is proposed, a set of parameters must be taken in account:

- Efficiency of telescope - fiber bundle coupling
- Efficiency of light transmission through the fiber
- Efficiency of fiber bundle – spectrograph coupling

In the following sections all that parameters will be analyzed in order to define the characteristics of SIDE fiber bundles.

3.7.2 Light transmission through the fiber. The optical fiber

Nowadays optical fibers, with remarkably high efficiency, are commercially available in a large variety of core sizes (typically 50-800 μm). However, in order to minimize the focal ratio degradation and avoid light losses, the fiber must be fed in a proper way, i.e. with its nominal f/number. Generally such f/number (typically between 3 and 7) does not match the typical f/number of modern telescope (generally between 8 and 15). A proper microlenses array must then be positioned at the telescope focal plane to change the f/number that enters the fiber bundle. This also may be necessary in the other fiber end to match the spectrograph focal ratio. Finally, the fiber transmission and the wavelength range are extremely important to maximize the light gathered by the telescope.

3.7.3 Transmission

Tacking into account the SIDE spectral range, from 350 to 1700 nm, broad band fibers will be the best selection for the instrument. Fibers like FBP from Polymicro Technologies or Optran WF from Ceramoptec presents an optimal behavior in the whole spectral range of interest.

In Figure 110 we can see the internal transmission plot of Polymicro's fiber with reference FBP200220240.

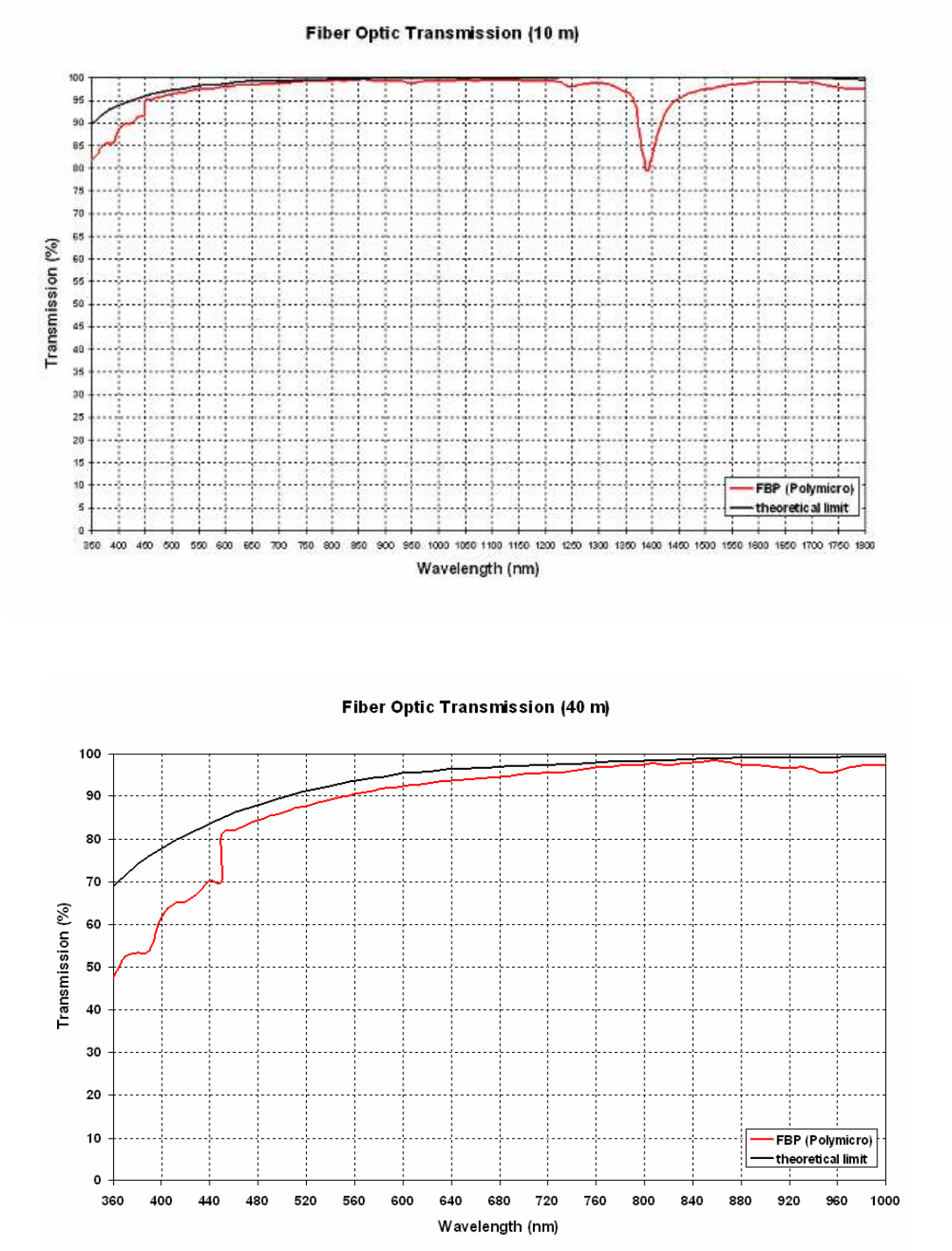

Figure 110 Transmission plots of the Polymicro's FBP fiber and Rayleigh theoretical limit for 10 meters (top) and 40 meters (bottom).

Note the effect of the fiber length on the performance, which is clear when comparing the two previous graphs. The 40 m fiber would be the consequence of placing the spectrographs far away from the focal station.

In the blue, the new broadband optical fiber performs close to the theoretical Rayleigh scattering limit for silica, having better than 80% transmission down to 350 nm (specification for length of 10 m).

3.7.4 Focal ratio degradation

The FRD is a fiber property widely studied in the last twenty years. Ideally, the light emerging from the fiber should be contained in a cone with angular extent equal to the focal ratio of the light illuminating the fiber at the entrance. However, that condition is met only for very fast focal ratios (Figure 111). At slow input focal ratios, the fiber will either decrease the resolving power and or the throughput efficiency of the spectrograph.

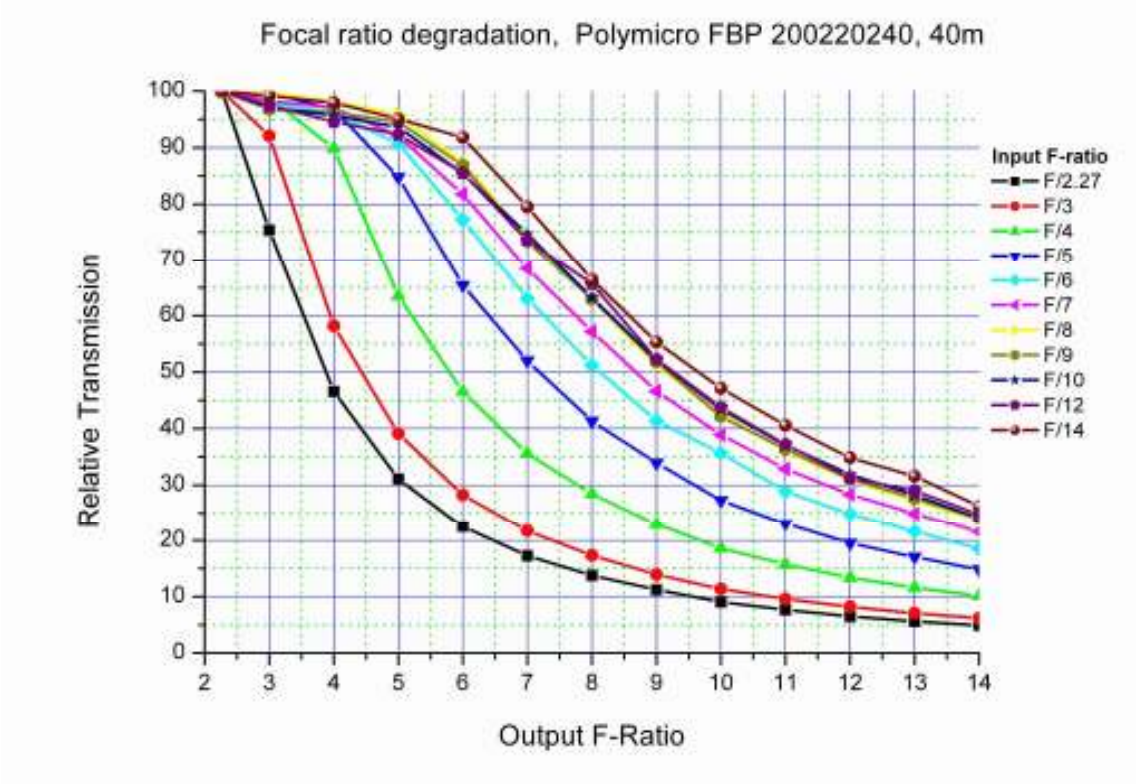

Figure 111 FRD measurements for a 40 m Polymicro FBP200220240 fiber. Fresnel losses are not included.

The amount of FRD produced by a fiber depends on several factors: the fiber-drawing process (how well the diameter was controlled), the fiber cabling (stress introduced by an outer jacket), the end termination (how good is the polishing at the end), and the fiber mounting (epoxy-induce stress levels). In other words, the FRD present in a fiber bundle depends on the fiber manufacture and the bundle manufacture, and both processes must be taking in account. A proof of this is obtained by comparing Figure 111 with Figure 112: the result is better for the 40 m fiber because of the better polish finish performed at the IAC laboratory. The quality of the polishing could even be further improved spending more time on the process.

We can find companies as Polymicro Technologies or Ceramoptec which can offer fibers of very high quality regarding the FRD conservation (core and cladding diameters, stress between layers and microcurves in the fibers are minimized), however Figure 113 shows Polymicro fiber bundles compared with a similar one manufactured at the IAC.

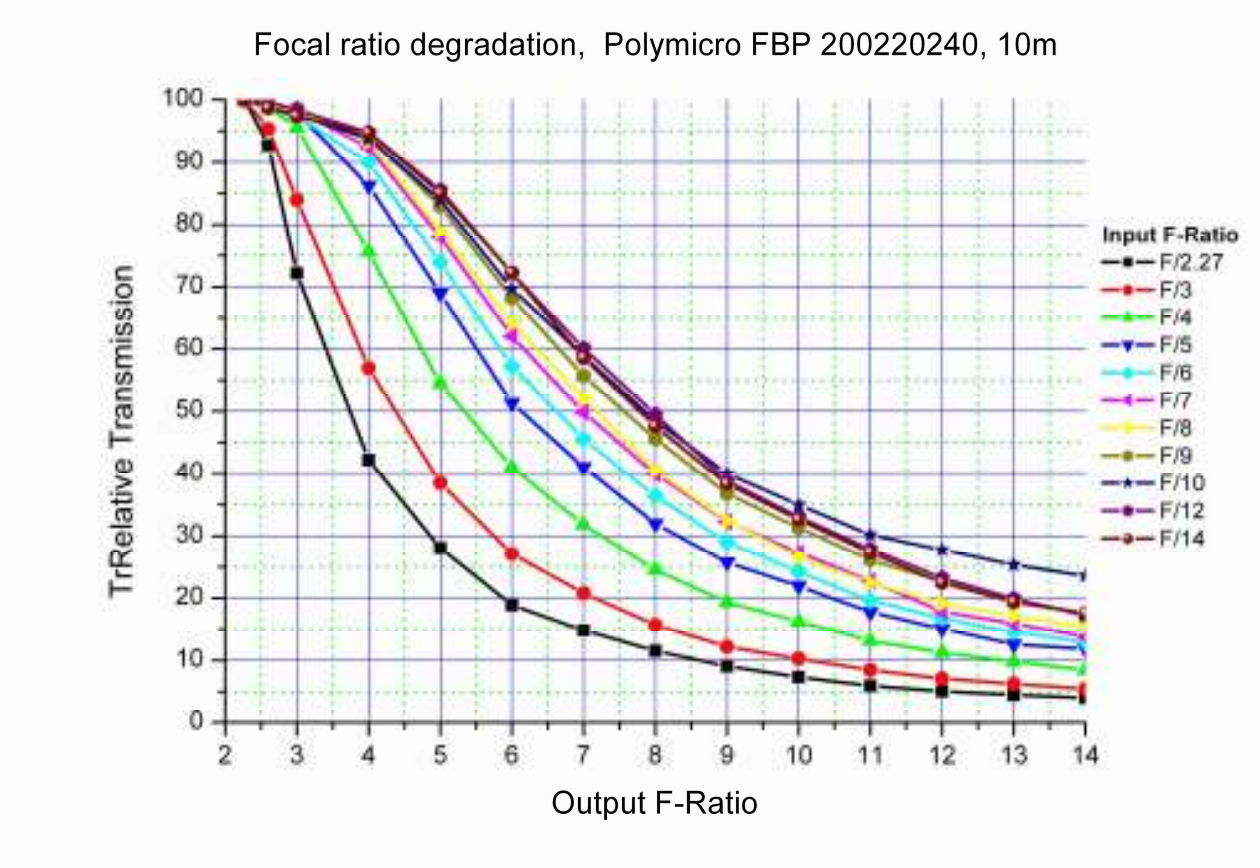

Figure 112 FRD measurements for a 10 m Polymicro FBP200220240 fiber. Fresnel losses are not included.

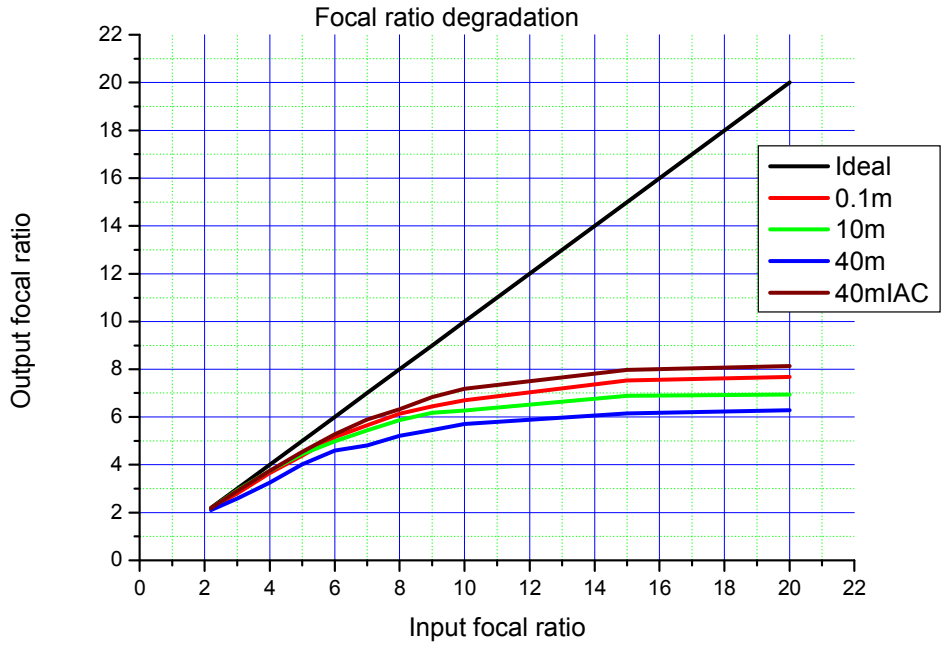

Figure 113 A plot representing the focal-ratio degradation of several fibers as measured in the IAC laboratory.

The Figure 113 is a plot of the FRD for several fibers of fused silica. The red, green and blue lines correspond to Polymicro broadband fibers with unknown quality of polishing and glue process. The brown line corresponds to a fiber polished at the IAC with a careful manufacturing process. This illustrates the need for a precise specification of the polishing and glue process in order to minimize the FRD. As can be seen in the figure, the optimum range for the focal ratio is between 2 and 4. The following list shows some of the important companies dedicated to the fiber production and manufacturers of fiber bundles.

- Polymicro Technologies, LLC
- CeramOptec Industries Inc
- Fiberguide Industries, Inc
- Fiberoptics Technology, Inc
- RoMack, Inc
- Fiberoptic Systems, Inc.
- FiberTech Optica Inc.
- SCHOTT North America, Inc.
- Fiberoptic Engineering Corp
- FiberTech GmbH

3.7.5 Fiber environment

The optical fiber cable is declared able to operate over temperature ranges of -65ºC to +300ºC and relative humidity of up to 95%, so it is suitable for astronomical applications.

3.7.6 Fiber length estimation

The length of the fibers from the fiber positioner to the spectrographs must be minimized to ensure the maximum light throughput. In this sense we need to study the possible routes from the positioner rear side to the pseudo-slit of the spectrographs.

3.7.6.1 Environment

Essential conditions:

A. The fiber bundles come out of the rear side of the fiber positioner, coiling around the cylindrical rear part for de-rotation.

B. The fiber bundles enter the spectrographs and end into several pseudo-slits. The pseudo-slits are close to one another.

C. The fiber positioners attached to the de-rotator must be able to rotate ±324º around the optical axis.

D. The Nasmyth fiber positioner (attached to the de-rotator when observing) must be moved to a lateral parking position by means of a trolley on circular rails installed on the platform, when other instruments are in use.

There are several possible bundle routes:

a) The Nasmyth focus has a double circular wheel guide around the de-rotator that has 4 m radius, in this case a rectangular hole in the floor of the platform can be used to pass the fiber bundles to the spectrographs room.

b) The other method of crossing the platform is by means of a circular hole, located near the bottom of the Nasmyth wheel guide.

c) We could cross the platform by means of a drilled hole in any other available place.

3.7.6.2 Possible solutions and fiber bundle lengths

In all three conditions mentioned above the fiber bundles must wind around the rear circular part of the positioner to permit de-rotation.

If we use the 1st possibility of the double circular guide, an extra length of fiber must be added.

The 2nd possibility of the circular hole in the floor below the de-rotator is better, from the point of view of the length of the fiber, but it implies the use of a chain in the floor to protect the fiber.

The best solution is the 3rd possibility guiding (by a chain) the fiber from the rear part of the positioner to the best position for the hole in the floor (nearest to the under floored pseudo-slit) to minimize the total length of the fiber. Taking into account:

The course of the trolley,

The relative position of the pseudo-slits under the floor,

The possible areas to drill the floor,

The forbidden ways for the chain at the floor level, etc.

3.7.6.3 Length estimations

We suppose that the rear part of the positioner is a cylinder on which the fiber bundles are rolled several times to permit the de-rotation.

The total length is obtained by adding subsections independently, in two different configurations. In the 2nd option, using the circular hole to cross the platform, we have:

A. case: when SIDE Nasmyth fiber positioner is observing

- Fiber length inside the robot ~2m
- Fiber length for 2.5 turn (> +/-324º) around a circumference of radius 15 cm (minimum curvature radius of the bundle) ~2.5m
- Fiber length from the Nasmyth axis to the floor ~2m
- Fiber length from the floor (at observing position) to the circular hole ~1m
- Fiber length under the floor to the pseudo slit (variable) but ~5m

Total A case (+10% margin): ~14 meters

B. case: when SIDE Nasmyth positioner is parked (not observing)

- Fiber length inside the robot ~2m
- Fiber length for 0.5 turn around a circumference of radius 15 cm (minimum curvature radius of the bundle) ~.5m
- Fiber length from the Nasmyth axis to the floor ~2m
- Fiber length from the floor to (at parking position) to the circular hole ~4m
- Fiber length under floor to the pseudo slit (variable) but ~5m

Total B case (+10% margin): ~15 meters

We suppose that in parking position there is only 0.5 turn around the rear cylinder of the positioner, because all the fiber is unwound.

In the case of the SIFU, the required length would be between 22 m and 25 m for the Folded Cassegrain location (see Section 3.7.11.2)

3.7.7 Fiber bundle – spectrograph coupling. Using microlens and pseudoslit arrangement.

In order to optimize the fiber bundle – spectrograph coupling, it is necessary to choose one of these two options:

a) fitting the spectrograph optical design to the output f/# of the fibers.

b) use microlenses at the fiber output in order to fit the f/# of the collimator.

In any case it is recommended to work with fast f/# (close to the fiber numerical aperture) on the fiber input because, in this way it is possible to have an appropriate f/# homogeneity in the fiber output and a uniform pupil for all the fibers.

It is interesting to have in mind that fibers destroy the information of the telescope central obscuration, then it is recommended to work with dioptric systems or catadioptric systems without (or minimal) central obscuration.

Finally, regarding the arrangements of the fibers on the pseudoslit, it is recommended that fibers seeing different objects should be separated on the pseudoslit at least a distance 0.85 times the fiber core diameter. In this way, the crosstalk between fibers is minimized.

3.7.8 The bundle configuration

SIDE will employ the technique of microlenses + fibers. Four different configurations of microlenses + fibers are considered.

- MOS-IFUs: fiber bundles of 7 fibers for the MOS mode with 1.5” total aperture and 0.5” per fiber.
- Mini-IFUs: fiber bundles of ~37 fibers for a spatial coverage of 3”x 3” with 0.5” per fiber.
- Mini-IFUs for Hi-Res VIS spectrograph: fiber bundles of ~37 fibers for a spatial coverage of 3”x 3” with 0.5” per fiber.
- SIFU, a single bundle of hundredths of fibers for large spatial coverage.

Figure 114 illustrates the distribution of the fiber bundles from the positionerS and SIFU to the spectrographs, according to the observation modes.

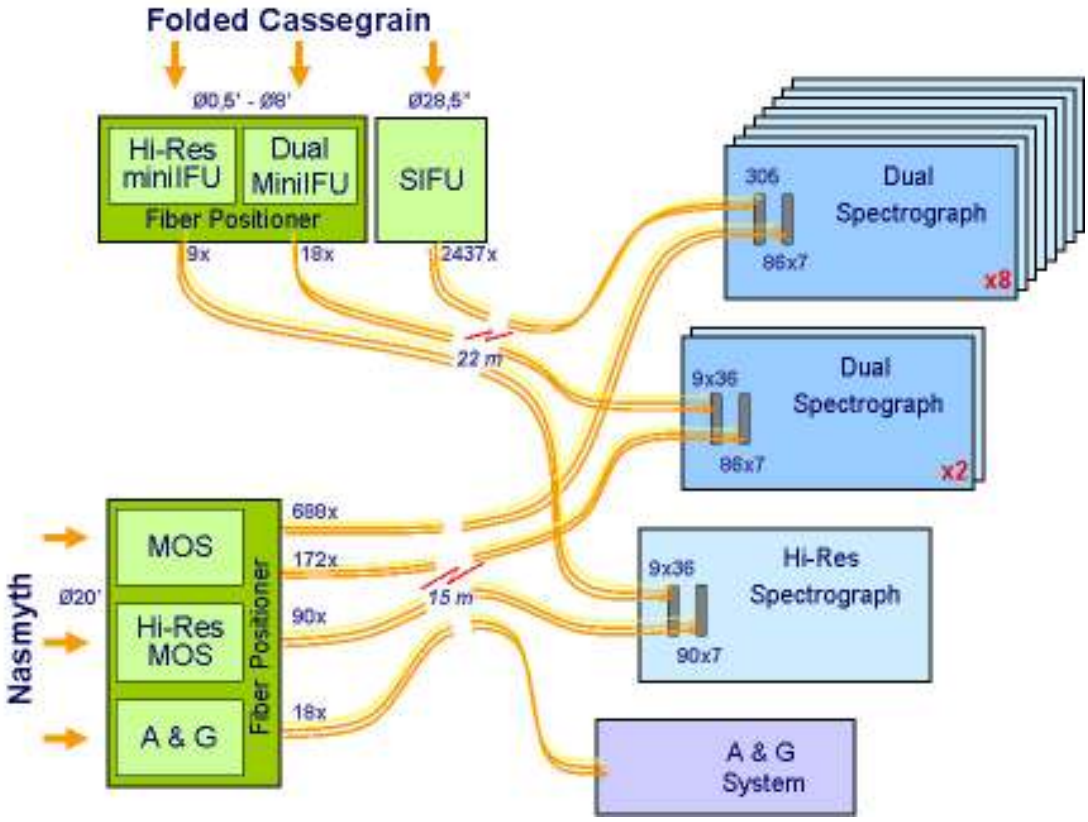

Figure 114 Distribution of the fiber bundles.

The geometry of the different fiber bundles for the SIFU, mini-IFU and the MOS-IFU modes can be square or hexagonal. The difference between both geometries is the number of fibers and the effective area of the sampling (see Figure 115). In the following tables, the size of the microlenses and their diameter is calculated for the two arrangements.

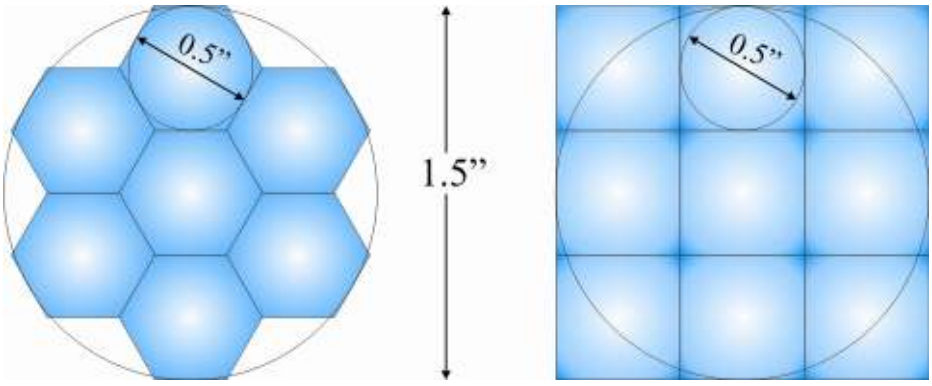

Figure 115 The classical microlenses arrays: hexagonal and square.

3.7.9 Design of the fiber bundle

For the design of the fiber bundles with micro lenses, first the required sampling has to be considered, which determines the size of the microlenses. Later, with the F numbers of the microlenses and the telescope, the size of the pupil can be calculated, which is then used to calculate the size of the fiber.

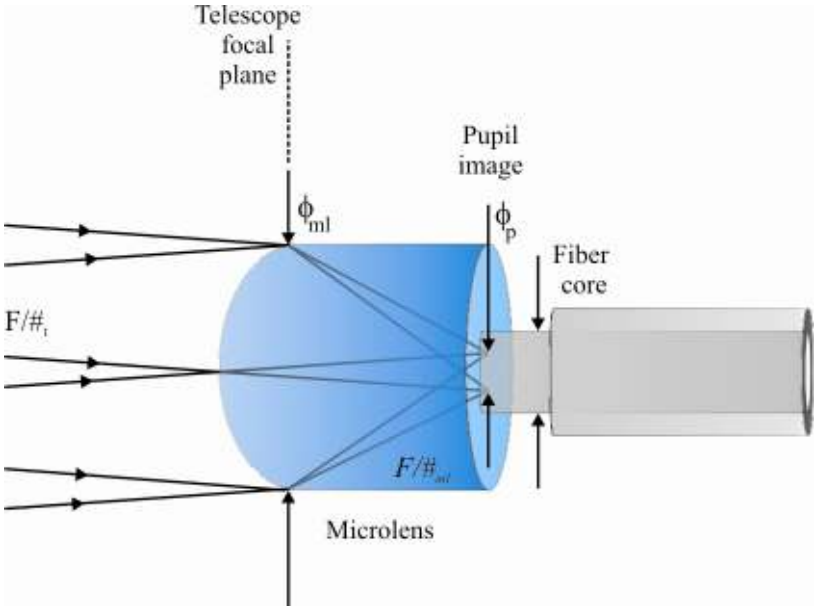

Figure 116 Entrance lens configuration.

In Figure 116 the microlens is placed in the focal plane of the telescope and it forms an image of the pupil of the telescope on the fiber in such a way that the energy received from the telescope in that area is all introduced in the fiber.

In order to fit the size of the pupil to the size of the fiber it must be

$$F/\#_t = \frac{f_{ml}}{\phi_p} \quad (1)$$

where

$F/\#_t$ it is the focal ratio of the telescope

ϕ_p Size of the pupil

f_{ml} EFL the microlens

The size of the pupil determines the diameter of the fiber. For practical reasons the size of the pupil can be equal or slightly smaller than the diameter of the fiber.

In addition we must fit the focal ratio at the entrance of the fiber in such a way that:

$$F/\#_f = F/\#_{ml} = \frac{f_{ml}}{\phi_{ml}} \quad (2)$$

where

$F/\#_f$ it is the input focal ratio of the fiber

$F/\#_{ml}$ it is the focal ratio of the microlens

ϕ_{ml} It is the diameter of the microlens

With the equation (1) and (2) it is possible to define all the necessary parameters for the design of the coupling of the telescope and the fiber bundle.

As it were mentioned previously the geometry of the IFUs can be square or hexagonal. The calculation for each fiber bundle is made considering these two geometries. Table 42 shows the basic characteristics of the union of the telescope with the fiber beam

ϕ Microlenses		Fiber F/# input	EFL Microlens μm	ϕ Pupil μm
Arcsec"	μm			
0.5	**412.1**	**10**	**4121**	**242.4**
0.5	412.1	9.5	3914.95	230.23
0.5	412.1	9	3708.9	218.2
0.5	412.1	8.5	3502.85	206.1
0.5	**412.1**	8	3296.8	193.9
0.5	412.1	7.5	3090.75	181.8
0.5	**412.1**	**7**	**2884.7**	**169.7**
0.5	412.1	6.5	2678.65	157.6
0.5	412.1	6	2472.6	145.5
0.5	412.1	5.5	2266.55	133.3
0.5	**412.1**	**5**	**2060.5**	**121.2**
0.5	412.1	4.5	1854.45	109.1
0.5	412.1	4	1648.4	96.9
0.5	412.1	3.5	1442.35	84.8
0.5	412.1	3	1236.3	72.7
0.5	412.1	2.5	1030.25	60.6

Table 42 Possible configurations of bundles as a function of the focal ratio at the entrance of the fiber.

3.7.10 Super-IFU mode

For the SIFU mode, the number of microlenses and fibers is approximately 2437, depending on the configuration, with a length of 15 – 25 m. The total number of fibers is distributed in 8 separate but identical spectrograph slits (see Figure 117). Two possible configurations of the SIFU are shown in Table 43.

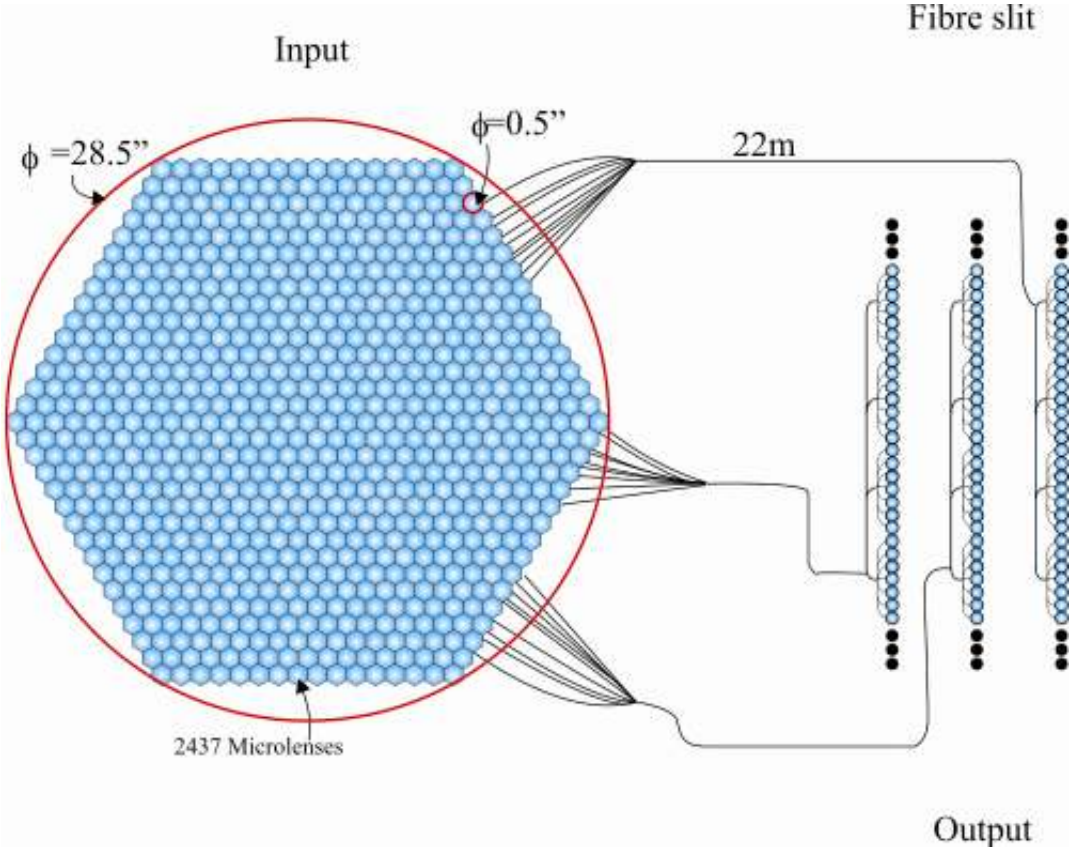

Figure 117 Fiber bundle in SIFU mode.

ϕ Microlenses		No Fibers		Fiber F/# input	EFL Microlens µm	ϕ Pupil µm
Arcsec”	µm	SIFU: square array Field 28.5”x28.5”	SIFU: hexagonal array Field ϕ=28.5”			
0.5	412.1	3249	2437	5	2060.5	121.2

Table 43 Possible configurations of the SIFU, without considering the effects of the FRD

3.7.11 The SIFU possible locations

3.7.11.1 SIFU at Nasmyth

The SIFU was originally planned for the Nasmyth focus, which means that it would be placed in the center of the focal plane. In this case it would require the central area of the focal plane to be forbidden for the other buttons.

With the SIFU at Nasmyth:

- The SIFU sits behind a WFC, which is planned to redirect the light perpendicular to the focal plane, so possible aberrations are minimized.
- A rotator is needed because, at certain position on the sky, the sky rotation at the external fibers of the SIFU would allow only 0.6 sec of integration.
- Both the SIDE auto guider system or the GTC A&G can be used. The precision would be better than 0.1" in both cases.
- The fiber bundle length estimation is 15 meters, with the bundle coiling around the rear robot cylinder. See technical note (fiber course from Robot to Spectrographs of SIDE).
- No ADC can be used, but corrections can be made to this respect via software.

3.7.11.2 SIFU at the folded Cassegrain

Another interesting possibility is to place the SIFU bundles in a folded Cassegrain focus; the biggest advantages are that it would be available all the time and a change to this focus from other instruments is very fast, because only the tertiary mirror has to be moved.

With the SIFU at Folded Cassegrain:

- No WFC nor ADC are mandatory for the SIFU, because the difference of energy between two fibers (a central one and another at 7.5" off center) is <2% if we don't use optics. The atmospheric dispersion effect could be corrected by software.
- On the other hand, an ADC could be installed at the Folded Cassegrain focus much more easily than at Nasmyth, as the beam size involved is minimal.
- A rotator is needed because, at certain position on the sky, the sky rotation at the external fibers of the SIFU would allow only 0.6 sec of integration.
- An auto guider is necessary for this focal station. This facility could be provided by GTC at the folded Cassegrain the same way as the A&G for Nasmyth (TBC).
- The precision of the auto guider in folded Cassegrain must be 0.1" (like A&G of GTC for Nasmyth), even when observing close to the meridian.
- The best focus is the folded Cassgrain nearest to the Nasmyth A platform. The fiber length estimation is about 22 to 25 meters.

3.7.12 MOS mode

In the MOS mode, we have around 950 units (860 units for the Dual VIS-NIRSpectrographs and 90 units for the Hi-Res Spectrograph) with a cable length of 15 m. Each one covers 1.5" field of view with microlenses. These units can have seven or nine fibers, (Figure 118). The total number of fibers and their characteristics are shown in Table 44 and Table 45.

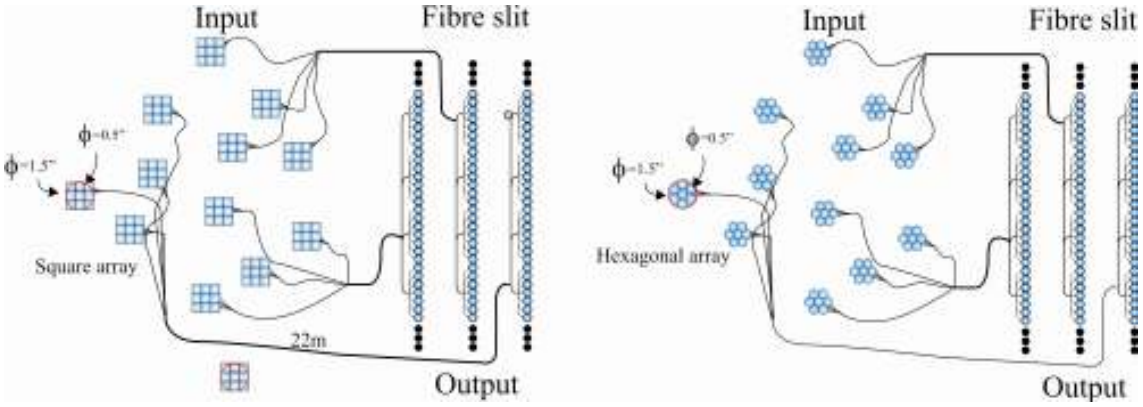

Figure 118 Fiber bundles in MOS mode using MOS-IFUs, in a square and hexagonal configuration.

ϕ Microlenses		**No Fibers**		**F/# input fiber**	**EFL Microlens µm**	***ϕ Pupil µm***
Arcsec"	**µm**	Mini IFU: square array Field 1.5"x1.5"	Mini IFU: hexagonal array Field ϕ=15"			
0.5	412.1	860x9	860x7	5	2060.5	*121.2*

Table 44 Characteristics of the fiber bundles for a square MOS-IFU.

ϕ Microlenses		**No Fibers**		**F/# input fiber**	**EFL Microlens µm**	***ϕ Pupil µm***
Arcsec"	**µm**	Mini IFU: square array Field 1.5"x1.5"	Mini IFU: hexagonal array Field ϕ=15"			
0.5	412.1	90x9	90x7	7	2884.7	*169.7*

Table 45 Characteristics of the fiber bundles for a hexagonal MOS-IFU.

3.7.13 Mini-IFUs for the Dual VIS-NIR Spectrographs

In this mode the fiber bundle consists of 18 mIFUs of 36 or 37 fibers that cover a field of 3"x3" arcsec, and with a length of 22 -25 m. The total number of fibers is distributed in the slits of two Dual VIS-NIR spectrograph (Figure 119). Their characteristics are shown in the Table 46.

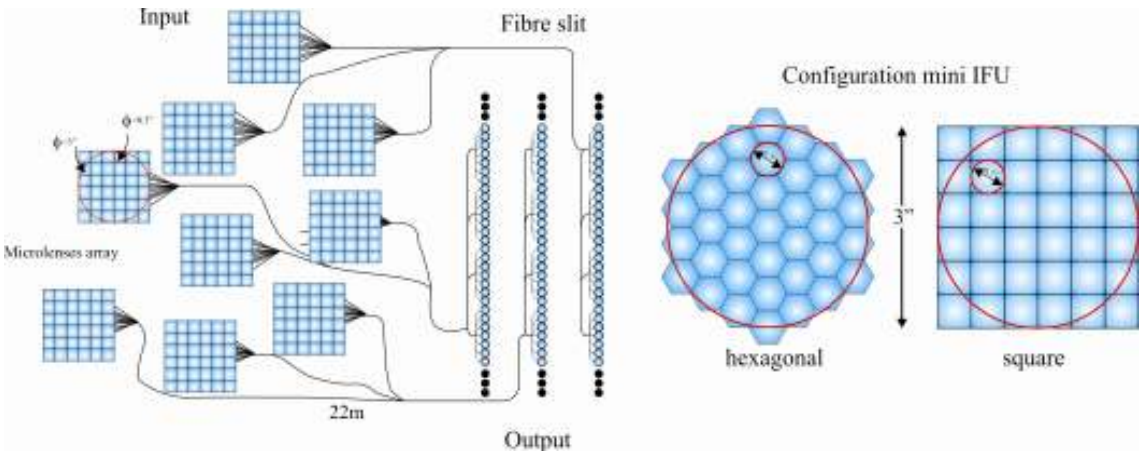

Figure 119 Fiber bundles for the mIFUs feeding the Dual VIS-NIR spectrograph.

ϕ Microlenses		No Fibers		F/# input fiber	EFL Microlens µm	*ϕ Pupil µm*
Arcsec"	µm	Mini IFU: square array Field 3"x3"	Mini IFU: hexagonal array Field ϕ=3..0"			
0.5	412.1	18x36	18x37	7	2884.7	169.7

Table 46 Possible configurations of the fiber bundle in Mini-IFU mode.

3.7.14 Mini-IFUs for the Hi-Res VIS spectrograph

In this mode the fiber bundle consists of 9 mIFUs of 36 or 37 fibers which cover a field of 3"x3" arcsec. The fibers are similar to the previous ones and feed the Hi-Res VIS spectrograph (Figure 120). Their characteristics are shown in the Table 47.

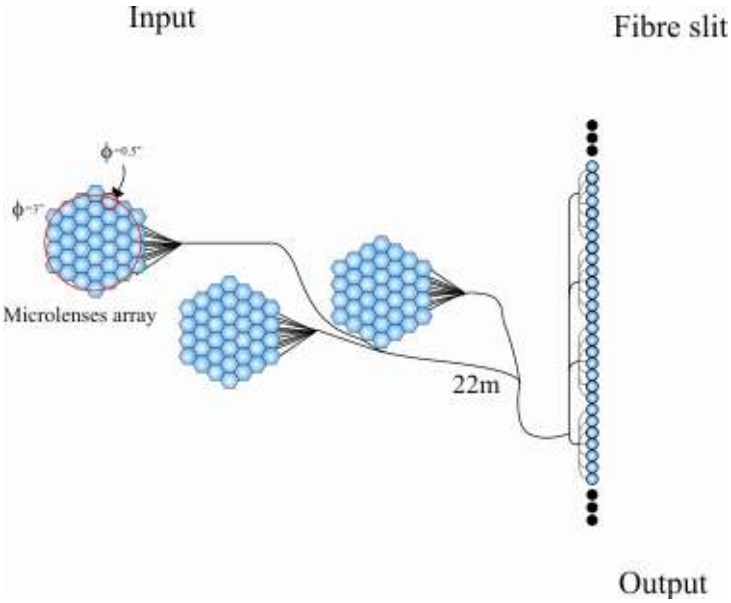

Figure 120 Fiber bundles mIFUs for the Hi-Res VIS spectrograph.

ϕ Microlenses		**No Fibers**		**F/# input fiber**	**EFL Microlens μm**	***ϕ Pupil μm***
Arcsec"	**μm**	Mini IFU: square array Field 3"x3"	Mini IFU: hexagonal array Field ϕ=3"			
0.5	412.1	9x36	9x37	7	2884.7	169.7

Table 47 Possible configurations of the fiber bundles mIFUs for high resolution .

3.7.15 Conclusions

According to the values obtained for each fiber bundle, Table 48 shows the characteristics of the fiber bundles of SIDE for the different modes of observation.

SIFU							
ϕ Microlenses		**No Fibers**		**F/# input fiber**	**EFL Microlens μm**	**ϕ Fiber μm**	*Size slit (Nod & Read mode) mm*
Arcsec"	**μm**	SIFU: square array Field 28.5"x28.8"	SIFU: hexagonal array Field ϕ=28.5"				
0.5	412.1	3249	2437	5	2060.5	120	
MOS							
ϕ Microlenses		**No Fibers**		**F/# input fiber**	**EFL Microlens μm**	**ϕ Fiber μm**	*Size slit (Nod & Read mode) mm*
Arcsec"	**μm**	Mini IFU: square array Field 1.5"x1.5"	Mini IFU: hexagonal array Field ϕ=15"				
0.5	412.1	860x9	860x7	5	2060.5	120	
0.5	412.1	90x9	90x7	7	2884.7	180	
Mini IFU Dual							
ϕ Microlenses		**No Fibers**		**F/# input fiber**	**EFL Microlens μm**	**ϕ Fiber μm**	*Size slit (Nod & Read mode) mm*
Arcsec"	**μm**	Mini IFU: square array Field 3"x3"	Mini IFU: hexagonal array Field ϕ=3"				
0.5	412.1	18x36	18x37	7	2884.7	180	
Mini IFUs HiRes							
ϕ Microlenses		**No Fibers**		**F/# input fiber**	**EFL Microlens μm**	**ϕ Fiber μm**	*Size slit (Nod & Read mode) mm*
Arcsec"	**μm**	Mini IFU: square array Field 3"x3"	Mini IFU: hexagonal array Field ϕ=3"				
0.5	412.1	9x36	9x37	7	2884.7	180	

Table 48 Characteristics of the fiber bundles of SIDE.

The values of Table 48 permit us to affirm that the design and manufacture of the fiber bundles for SIDE are feasible fulfilling the parameters required by the scientific program.

3.7.16 Efficiency.

The theoretical efficiency of a SIDE fiber bundle is shown in Table 49. AR coating is assumed in the microlens and alignment errors are considered as losses in the interface microlens – optical fiber. The internal transmission of the fiber is a mean over the spectral range of interest.

Element/Intefase	Transmission
Microlens Input face	0.98
Microlens Internal transmission	0.99
Interface microlens – optical fiber	0.96
Fiber internal transmission (15m)	0.94
Interface optical fiber – microlens	0.96
Microlens Internal transmission	0.99
Microlens Input face	0.98
TOTAL	0.81

Table 49 Bundle total efficiency

3.7.17 Costs

Fiber costs can be calculated as shown in Table 50:

Observing Mode	**Fibers per bundle**	**Number of Bundles**	**Bundle length (m)**	**Total length (Km)**	**Price per meter ($)**	***Price***
MOS IFU	7	950	15	99.8	3	*299400€*
mIFU Dual	36	18	22	14.3	3	*42900€*
mIFU Hi-Res	36	9	22	7.13	3	*21390€*
SIFU	2437	1	22	53.6	3	*160800€*
TOTAL				*174.83*		*524490€*

Table 50 Details of the fibers cost.

The total cost for the fibers is thus estimated to be around 540 K € for a total of 180 km length, considering the MOS, mIFU and SIFU modes.

Microlenses costs can be calculated as shown in Table 51:

Observing Mode	**Number of Bundles**	**Number of Microlenses**	**Cost of the first Micro arrays**	**Cost of the second Micro arrays (each one)**	***Price***
MOS IFU	950	950	10000€	1000€	*959000€*
mIFU Dual	18	18	10000€	1000€	*27000€*
mIFU Hi-Res	9	9	10000€	1000€	*18000€*
SIFU	1	1	10000€	1000€	*10000€*
TOTAL		*978*			*1022000€*

Table 51 Details of the microlenses cost.

The total cost for the microlenses is thus estimated to be around 1.00M € for a total of about 978 arrays of microlenses, considering the MOS, mIFU and SIFU modes.

The total Cost of the bundles is shown in Table 52.

Observing Mode	**Fibers**	**Microlenses**	**Manufacturing**	***Price***
MOS IFU	299400€	959000€	2,516,800 €	*3,775,200 €*
mIFU Dual	42900€	27000€	139,800 €	*209,700 €*
mIFU Hi-Res	21390€	18000€	78,780 €	*118,170 €*
SIFU	160800€	10000€	341,600 €	*512,400 €*
TOTAL	*524490€*	*1022000€*	*3092980 €*	*4639470 €*

Table 52 Details of the bundles cost.

Under "Manufacturing" cost, coatings, mechanical parts, adhesives, and other items are considered.

The total cost of SIDE bundles and microlenses is estimated in 4.7 M €

3.7.18 References

Bacon, R., Adam, G., Baranne, A., Courtes, G., Dubet, D., Dubois, J.P., Emsellem, E., Ferruit, P., Georgelin, Y., Monnet, G., Pecontal, E., Rousset, A., & Say, F. 1995 A&A Suppl. 113, 347B.
Bacon, R., Copin, Y., Monnet, G., Miller, B. W., Allington-Smith, J. R., Bureau, M., Carollo, C. M., Davies, R. L., Emsellem, E., Kuntschner, H., Peletier, R. F., Verolme, E. K., & de Zeeuw, P. T. 2001, MNRAS, 326, 23
Content, R., 1997, SPIE Vol. 2871, 1295
Content, R., 1998, SPIE Vol. 3356, 122
Krabbe, A., Thatte, N., Kroker, H. & Tacconi-Garman, L. 1997, SPIE Vol. 2871, 1179.
Priéto, E., Le Fèvre, O., Saïsse M., Voët C., Bonneville C., 2000, SPIE, Vol. 4008, 510, Very wide integral field unit of VIRMOS for the VLT: design and performances.
Ren, D. & Allington 2002, PASP, 1140, 866
Tecza, M., Thatte N., ASP Conference series, Vol. 152, 1988

3.8 The pseudoslits

3.8.1 General

Based on the development of other instruments and considering the number of fiber bundles (SIFU, MOS and mini-IFU) which feed 2 different kind of spectrographs (Dual VIS-NIR Spectrographs and Hi-Res Spectrograph), we need to design two specific pseudo slits. Although the pseudo slits will be different they will follow the same basic principle. Fiber slit technology is well developed and has been used on numerous fiber spectrographs such as 2dF, FLAMES, VIRUS, Hectospec an PMAS, where a number of small flat-ended slitlets containing a few fibers are mounted side by side to make up a large curved slit unit as we can see in Figure 121, Figure 122 and Figure 123.

Figure 121: Diagram of the slit fiber unit for AAOmega. The slitlets are shown alternating brown and pink for clarity. Each slitlets contains 10 fibers, which are fed away from the slit along the channels shown behind. The slitlet is polished flat and arranged to form a curved pseudo-slit. From Haynes et al 2004.

Figure 122: The pseudo-slit output of the IFU bundles of VIRUS. The fibers are arrayed on a precision grooved plate that sets the spacing and angle between fibers. The fibers are arrayed perpendicular to the back surface of a cylindrical lens bonded to the convex surface of the plate. From de Hill el at 2006.

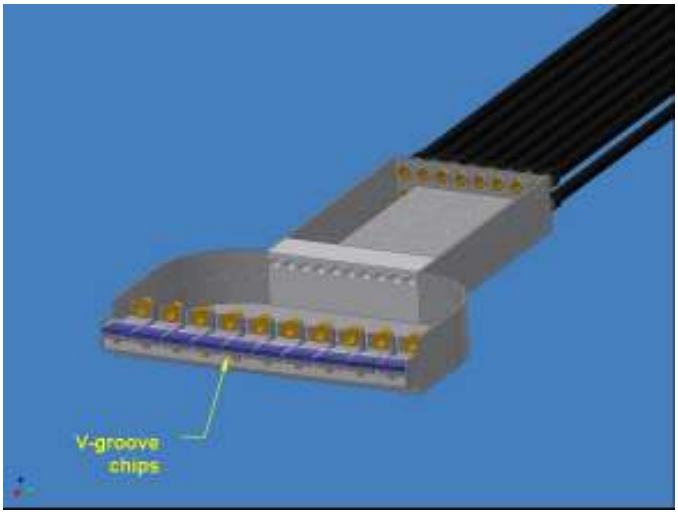

Figure 123: The design for the FMOS slit unit . Pseudo–slit of fibers formatted as linear arrays. The lid has been removed in this drawing, and for clarity the fibers are not shown.

We plan to follow this same line for the development of the pseudo-slit for SIDE. The details for the pseudoslits of the Dual VIS-NIR and Hi-Res spectrographs can be found in Section 3.10.

3.8.2 References

Haynes et al. (2004), SPIE Proceedings, Astronomical Telescopes and Instrumentation 2004, Vol. 5494-74.
Hill. Gary et al. Proceedings of the SPIE, Volume 6269, pp. 62692J (2006).

3.9 Pseudoslit configurations

3.9.1 Introduction

We study the pseudoslit configuration for the three observing modes, MOS, SIFU and mIFU, according to the current instrument concept, and the physical implementation on the different spectrographs, taking into account that each spectrograph can be fed with two adjacent and parallel pseudoslits. The numbers given here will have to be fine-tuned, as well as the Collimators F numbers, in order to optimize the instrument efficiency, during the design phases of the project. The aim here is just to show a possible solution for the configuration of SIDE´s pseudoslits and fibers.

3.9.2 Fiber election and optical parameters

Section 3.1.1 shows that 1.5" of total sky sampling in MOS is the most appropriate for the scientific cases and that 0.5" per fiber of sky sampling can be adopted in SIFU, Mini IFU and in the 7-fiber hexagonal package of each MOS science unit.

For all the observing modes we use a reducer micro-lens in front of each optical fiber (See sections 3.6).

The Optical parameters of the telescope (focal number and scale) and the possible fiber diameters determine the design of a collimator–camera for the spectrographs.

The adopted fiber diameter for the Dual VIS-NIRspectrograph is about 120 μ of core at f/5 of input, and this core projects onto ≈4.8 pixels in the VIS arms and onto ≈2.4 pixels in the IR arm.

For the Hi-Res spectrograph the fibers would be 170 μ of core at f/7. The size of the projection of the core onto the chip depends on the wavelength. Here we take the blue-most case, which is the less favorable concerning cross-talk. Any other wavelength will yield better (lower) cross-talk values than this. At the blue-most end, the 170 μ of the core project onto ≈3.8 pixels.

The fiber manufacturers recommend a cladding of about 10% of the core and a buffer of about 15% of the core. This means a core + cladding + buffer total diameter of ≈150 μ for the Dual VIS-NIRspectrograph and about 170μ for the Hi-Res spectrograph.

3.9.3 Chip parameters

Section 3.11 shows a collection of the nowadays available CCD's. For SIDE, the adopted CCD here has 4096x4096 pixels of 15 μ. The IR array has 2048x2048 pixels of 18 μ.

3.9.4 Observing modes, Pseudoslits, Spectrograph diagrams.

The starting point is to have the MOS mode in the Nasmyth platform, with a total of 950 science units of 7 fibers each, but divided it in two sections: about 90% of the MOS units going to the DUAL VIS-NIRspectrographs and about 10% of the MOS units going to the HiRes spectrograph. Thus, the Nasmyth FOV would be divided into two circular segments, one containing the Dual VIS-NIRand the other containing the Hi-Res MOS units.

The SIFU unit is planned to be placed in the Folded Cassegrain focus, centered in the FOV, made of 28 hexagonal layers plus a central fiber. All of its 2437 fibers would feed the DUAL VIS-NIRspectrograph. Leaving out the sky fibers (mounted on one or more separated bundles on the focal plane), the SIFU FOV final diameter would be some 28.5".

The MiniIFUs, of 6x6 fibers each, are planned to be placed in the Folded Cassegrain, but ≈9 of them feeding the HiRes spectrograph and ≈18 feeding the DUAL VIS-NIRspectrograph.

3.9.5 Pseudoslit configuration

To configure the fibers at the pseudoslits we need to find a way to reduce the cross-talk to an acceptable value for each mode, which is then studied independently:

- MOS: in this case the 7 fibers are considered like a unique source of light. Then, at the pseudoslit, the 7 fibers of a MOS unit are stuck together and cross-talk within the fibers of the same unit is unimportant, while unit-to-unit cross-talk is avoided with 1 dead fiber between each 7 fibers packet. See Figure 124.
- SIFU: in this case the information of each fiber should be independent from the others, thus 1 dead fiber must be used between SIFU fibers. Also, 1 extra dead fiber (so a total of two interline fibers) must be placed between different SIFU lines of the hexagonal distribution, so as to separate well parts of the field which are completely independent. See Figure 125.
- Mini IFU: this case is similar to the SIFU, so we need one dead fiber between active fibers and an extra dead fiber (so a total of two inter unit fibers) between the MiniIFU units at the pseudoslit. See Figure 126.

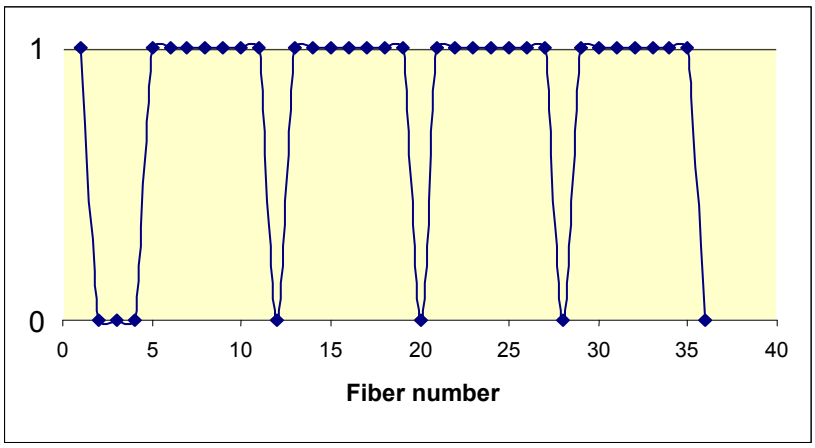

Figure 124 MOS units diagram. The zero level corresponds to the dead fibers, the 1 level corresponds to the live fibers. The first fiber to the left is a spectral reference, then 4 units are shown, separated by one dead fiber.

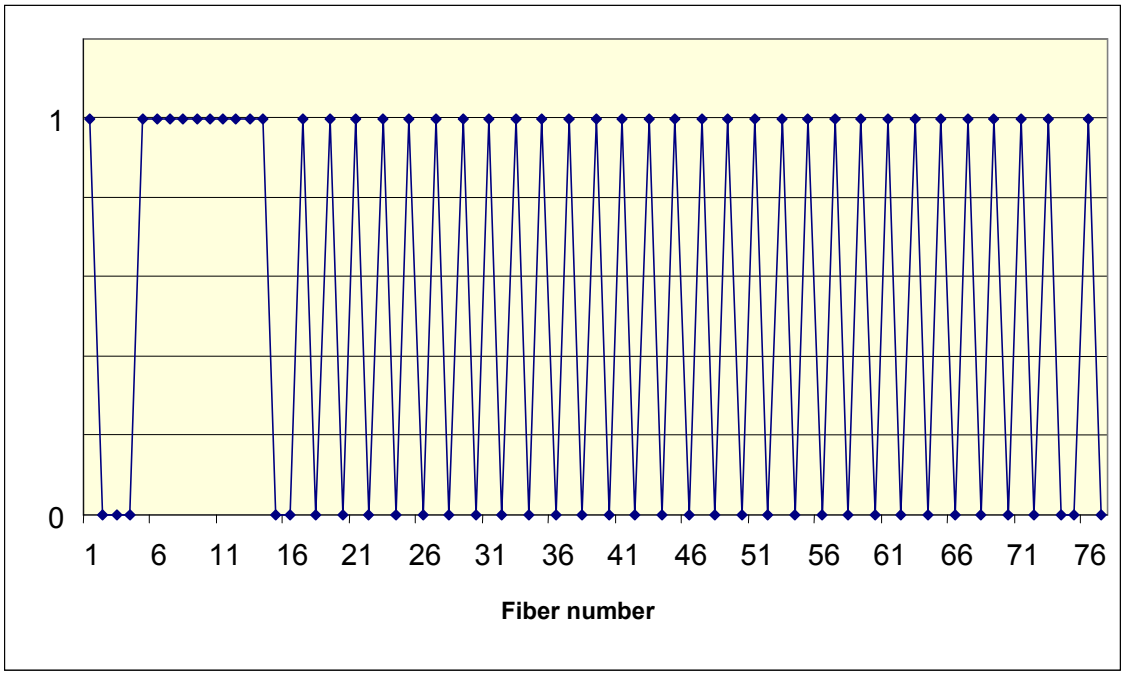

Figure 125 SIFU unit diagram. The zero level corresponds to the dead fibers, the 1 level corresponds to the live fibers. The first fiber to the left is a spectral reference, and the next live fibers are 10 Sky fibers, followed by the set of 29 live-dead fibers of the first SIFU hexagon line. The second line starts after two more dead fibers.

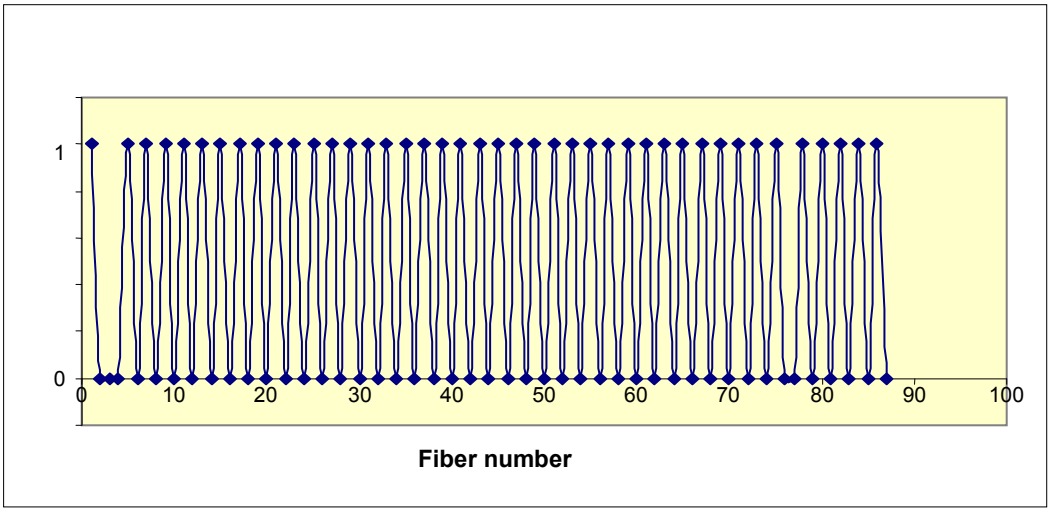

Figure 126 MiniIFU unit diagram. The zero level corresponds to the dead fibers, the 1 level corresponds to the live fibers. The first fiber to the left is a spectral reference. After two more dead fibers it follows a set of 36 live-dead pairs, which form the first MiniIFU. After two more dead fibers a new MiniIFU begins.

3.9.6 Lateral fibers for spectral reference

To have a spectral reference in each image we propose to place two reference fibers at the beginning and at the end of the pseudoslit, carrying arc-lamp light onto the CCD. This is useful because it tells us about how the entire spectrograph acts over a fiber light at different wavelengths. The two reference fibers are separated from the rest by 1 or 2 dead fiber for each (left and right).

3.9.7 Sky fibers

The configuration of sky fibers in SIFU mode must take into account the following points:

1) The sky fibers must not be far from the SIFU on the focal plane, say 1.5' to 2'.
2) Some sky fibers must be present in all the pseudoslits of the SIFU (because they feed different spectrographs) in order to allow good sky subtraction.
3) The sky fibers must be placed in packets homogeneously distributed along the pseudoslit, in order to obtain good sky subtraction all along the pseudoslit and in any of the spectrograph (see GMOS webpage).

In order to fulfill these points, we reserve 5 groups of 10 fibers homogeneously distributed along the pseudoslit, separated by 2 dead fibers from the near-most SIFU fiber, but with no dead fibers between them. As it can be seen from Table 53, Table 54 and Table 55, the real required number of spectrographs is less than the integer number (necessarily) adopted, so we can use the extra space available at the pseudoslits for sky fibers, which we estimate to be of the order of a few hundreds in total, or as dead fibers evenly distributed along the pseudoslit, if we want to diminish cross-talk further. More extra fibers for sky or dead spaces will probably come also from the distribution of the SIFU rows: it may be considered more convenient to complete a row with extra fibers than starting a new pseudoslit with just a few fibers of a SIFU row, although the total science fiber number would diminish.

In MOS mode, the sky can be obtained simply through some units not used for science, homogeneously distributed in the FOV. In MiniIFU mode too we can use some MiniIFUs for sky subtraction. In both cases, the fraction of sky fibers will be a choice of the observer.

3.9.8 Dead fibers spacing, cross-talk

When the fibers are placed on the pseudoslit with small center to center distance, a cross-talk takes place among them. Depending on the observing mode, this cross-talk must be minimized by spacing two consecutive live fibers with dead fibers. Also, dead fibers must be used as a mark on the spectra when a special circumstance occurs, like a change of line in SIFU or a change of unit in MOS and MiniIFU.

We calculated the Cross-talk between fibers by a 10 and a 25 degree polynomial extracted from Sanchez (2006). The results are given in Table 53, Table 54 and Table 55, for each observing mode.

Here the cross talk is modeled in two ways: first it is considered an aperture of '1 FWHM' centered on the peak signal of the fiber, to recover the flux, and then an aperture of '3 FWHM', the same way as before. The first is a lower limit, with reduced cross-talk, and the second gives the maximum energy recovered, but with higher cross-talk.

The real cross-talk foreseen for the SIDE fibers is somewhere between the "1 FWHM" and the "3 FWHM"result, and is very dependent on the optics, fiber quality, etc.

This is compatible with the experience of the astronomers that has reduced SIFU data in other spectrograph like MPFS@6m, PMAS@Calar-Alto, GMOS@Gemini,VIMOS@VLT, Giraffe@VLT)

3.9.9 Detailed results

Table 53, Table 54 and Table 55 show the results of our pseudoslit analysis. Note that some very small values (< 0.1%) of cross-talk do not make much sense because the polynomials are used to their limit. The main point of such values is that the cross-talk is very low.

	Units	SIFU	MOS unit	MiniIFU unit
Fiber core	μ	120	120	120
Core + clad + buffer	μ	150	150	150
Projection of the core (FWHM)	pixel	4,7234	4,7234	4,7234
Size of CCD	pixel	4096	4096	4096
Live fibers between dead fibers	#	1	7	36
N. of fiber between lines or units	#	2	1	2
Spectral reference fibers	#	1	1	1
Dead fibers around spectral reference fibers	#	3	3	3
Number of fibers in each Sky packet	#	10	0	0
Dead fibers around sky fibers packets	#	2	0	0
Groups of Sky-dead fibers in the pseudoslit	#	5	0	0
Total number of science resolved units	#	2437	860	18
Effective number of science pixels of CCD	pixel	3686.1	4049.2	4049.2
(fiber center to fiber center) / fiber diameter for side to side fibers (Niquist criteria: ratio ≥ 2.5)	ratio	2.48		2.48
Cross-talk fib.core to fib.core 1FWHM (3FWHM)	**%**	**0.36 (0.08)**	**4.80 (38.82)**	**0.36 (0.08)**
Cr.-talk fib.core to fib.core interline 1FWHM (3FWHM)	**%**	**0.10 (0.09)**	**0.36 (0.08)**	**0.10 (0.09)**
Cross-talk fib.c.to ERL fib. 1FWHM (3FWHM)	**%**	**0.08 (-0.04)**	**0.08 (-0.04)**	**0.08 (-0.04)**
N. of science resolved units per CCD	**#**	**307.61**	**86.44**	**9.34**
Pseudoslit length	mm	103.73	103.73	103.73
Total N. of spectrographs	**#**	**7.92**	**9.95**	**1.93**

Table 53 Results for the pseudoslit parameters of the Dual VIS arm.

	Units	SIFU	MOS unit	MiniIFU unit
Fiber core	μ	120	120	120
Core + clad + buffer	μ	150	150	150
Projection of the core (FWHM)	pixel	2.3617	2.3617	2.3617
Size of detector	pixel	2048	2048	2048
Live fibers between dead fibers	#	1	7	36
N. of fiber between lines or units	#	2	1	2
Spectral reference fibers	#	1	1	1
Dead fibers around spectral reference fibers	#	3	3	3
Number of fibers in each Sky packet	#	10	0	0
Dead fibers around sky fibers packets	#	2	0	0
Groups of Sky-dead fibers in the pseudoslit	#	5	0	0
Total number of science resolved units	#	2437	860	18
Effective number of science pixels of detector	pixel	1843.1	2024.6	2024.6
(fiber center to fiber center) / fiber diameter for side to side fibers (Niquist criteria: ratio ≥ 2.5)	ratio	2.48		
Cross-talk fib.core to fib.core 1FWHM (3FWHM)	**%**	**0.36 (0.08)**	**4.80 (38.82)**	**0.36 (0.08)**
Cr.-talk fib.core to fib.core interline 1FWHM (3FWHM)	**%**	**0.10 (0.09)**	**0.36 (0.08)**	**0.10 (0.09)**
N. of science resolved units per detector	**#**	**307.61**	**86.44**	**9.34**
Pseudoslit length	mm	103.73	103.73	103.73
Total N. of spectrographs	**#**	**7.92**	**9.95**	**1.93**

Table 54 Results for the pseudoslit parameters for the Dual IR arm.

	Units	MOS unit	MiniIFU unit
Fiber core	μ	170	170
Core + clad + buffer	μ	200	200
Projection of the core (FWHM)	pixel	3.8	3.8
Size of the CCD	pixel	4096	4096
Live fibers between dead fibers	#	7	36
N. of fiber between lines or units	#	1	2
Spectral reference fibers	#	1	1
Dead fibers around spectral reference fibers	#	3	3
Total number of science resolved units	#	90	9
Effective number of science pixels of CCD	pixel	3285.2	3285.2
(fiber center to fiber center) / fiber diameter for side to side fibers (Niquist criteria: ratio ≥ 2.5)	ratio	1.40	2.35
Cross-talk fib.core to fib.core 1FWHM (3FWHM)	**%**	**4.80 (38.82)**	**0.47 (0.50)**
Cr.-talk fib.core to fib.core interline 1FWHM (3 FWHM)	**%**	**0.47 (0.50)**	**0.10 (0.09)**
N. of science resolved elements per CCD	**#**	**86.44**	**9.34**
Pseudoslit length	mm	146.97	146.97
Total N. of spectrographs	**#**	**0.98**	**0.91**

Table 55 Results for the pseudoslit parameters for the Hi-Res spectrograph.

Table 56 shows a short resume of the fiber-to-spectrograph distribution.

	SIFU to DUAL	MOS to DUAL	MOS to HiRes	MiniIFU to DUAL	MiniIFU to HiRes
Number of science units	1 (2437 fibers for Ø=28.5")	860 (7 fiber each)	90 (7 fiber each)	18 (36 fiber each)	9 (36 fiber each)
Units per spectrograph	1/8 (~305 fibers)	86	90	9	9
N. of spectrographs, integer (real)	8 (7.92)	10 (9.95)	1 (0.98)	2 (1.93)	1 (0.91)

Table 56. Resume of the fiber-to-spectrograph distribution

We plan to construct double pseudoslits for all the spectrographs, and distribute the different observing modes so that only one side of each double pseudoslit is used at a time. This way, by simply covering the unused focal station, we block any light to one side of the used pseudoslits, and thus we can avoid diffuse light contamination.

In all cases, it is critical that the two halves of the pseudoslits are placed as close as possible one to the other and also we need to seal light-tight the input to the pseudoslit not in use in each moment.

The double pseudoslits must be as narrow as possible to reduce their vignetting effect. This has been quantified to be not much higher than a single pseudoslit (See Section 3.10.1.3.2) The effect of each pseudoslit being slightly off-center has been studied and seems negligible (See Section 3.10.1.3.2).

In the HiRes spectrograph we need one pseudoslit for MOS-HiRes and one pseudoslit for the MiniIFU-HiRes. The number of DUAL VIS-NIRspectrographs is driven by the MOS-IFUs number: we need 10 pseudoslits for the MOS-DUAL units. The other side of these 10 pseudoslits would be shared between the SIFU fibers (8 pseudoslits) and the 18 MiniIFU (2 pseudoslits), which makes 10 double pseudoslits in total. Due to the availability of 8 pseudoslits for the SIFU, we could push its fiber number up to 2611. In the end, not all of them would be available for science, because some would be used for the Sky. If we scale down from 2611 fibers to the next hexagonal configuration, we get 2437 science fibers and a 28.5" working diameter.

In order to seal the input light to the Nasmyth or Folded Cassegrain focus, a big cover at the input of these focuses could be used. The rear part of these covers, painted white, could provide a Flat Field and spectral calibration screen to each focal station.

A diagram for the Dual VIS-NIR and HiRes spectrographs is shown in Figure 127.

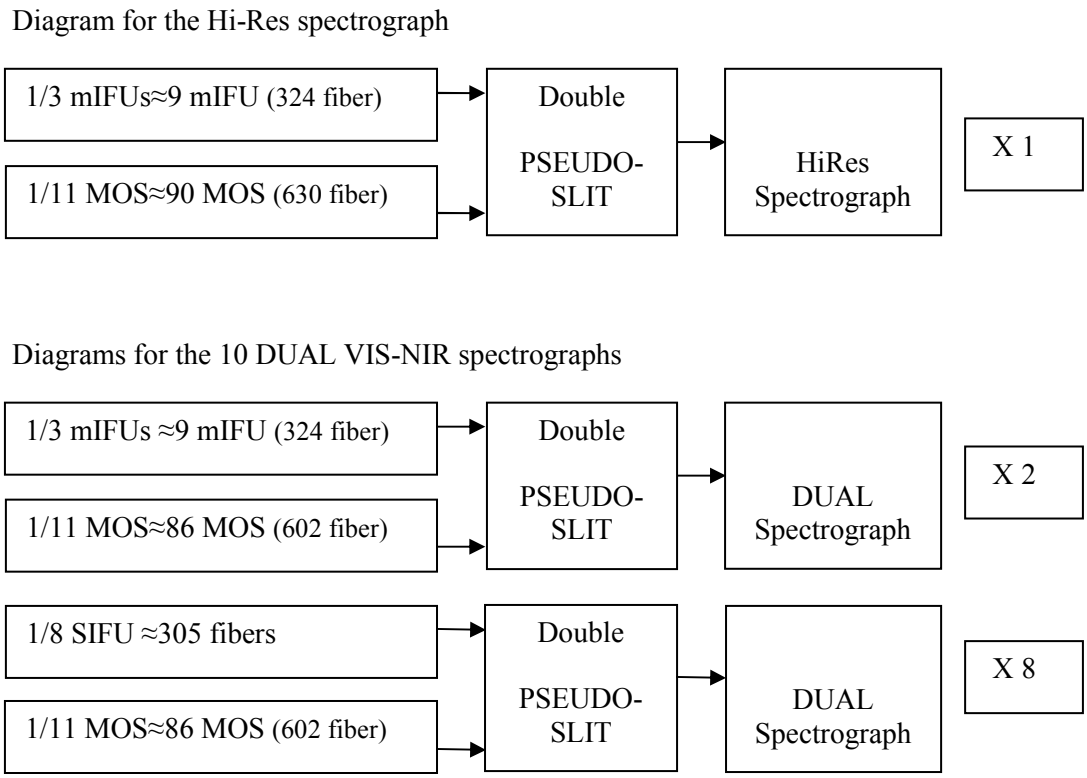

Figure 127 Distribution of the fibers according to the different observing modes.

3.9.10 Conclusions.

1. The double pseudoslit is a way to reduce the number of spectrographs, although these are more difficult to build. It seems optically feasible.
2. The large number of DUAL VIS-NIR spectrographs is motivated by the MOS requirements that force to 950 MosIFUs of 7 fibers each. The inter-fiber space within the same MosIFU is reduced to zero (i.e. only the cladding + buffer).
3. For all the spectrographs, the Flat Field and Spectral calibration can be done by illuminating the rear part of a cover placed at the corresponding focus. This will be explained in more detail in Section 3.13.
4. The problem of the diffuse light inside the SIDE spectrograph can be minimized by leaving extra distance (dead fibers) between separated blocks of fibers, a technique frequently used with success.
5. Sky fibers for all the modes must be studied in more detail during the next phases of the project.

3.9.11 References.

The GMOS webpage: Integral Field Units:

http://www.gemini.edu/sciops/instruments/gmos/gmosIndex.html

Sanchez S. F., 2006, "Techniques for reducing fiber-fed and integral-field spectroscopy data: An implementation on R3D", Astronomische Nachrichten, Vol. 327, I. 9, p. 850.

3.10 The SIDE Spectrographs

3.10.1 The Dual VIS-NIR Spectrograph

3.10.1.1 Summary

We present in this section the dual VIS-NIR spectrograph baseline for SIDE. The Table 57 shows a summary of the scientific requirements:

Science requirements				
	Visible Beam		NIR Beam	
Spectral Resolution	1500	4000	1500	5000
Wavelength Ranges	0.40-0.95 μm		0.95-1.7 μm	
Number of Simultaneous Targets in MOS mode	~1000			
Observing modes	FOV			
MOS at Nasmyth	20’ diameter			
SIFU at F-Cass	28.5’’ x 28.5’’ (0.5’’ per fiber)			
mIFU at F-Cass	10’ diameter (27 single mIFU of 3’’ x 3’’, 0.5’’ per fiber)			

Table 57. The SIDE Dual VIS-NIR spectrograph main science requirements.

Some additional implementation assumptions relevant to the SIDE Dual VIS-NIR spectrograph design are detailed in Table 58.

	Visible Beam	NIR Beam
Detector Format	4096 × 4096	2048 × 2048
Pixel Size	15 μm	18 μm, 20 μm
Fiber Diameter at Slit	120 μm	
Fiber Output Focal Ratio	f/5	

Table 58. Fiber and detector parameters for the SIDE Dual VIS-NIR spectrograph design.

3.10.1.2 Dual VIS-NIR Spectrograph Concept Overview

The initial optical requirements are to cover the spectral range from 400[1] nm to 1700 nm with 4 exposures at R=4000 for the VIS arm and 3 exposures for the NIR arm (from 950 nm to 1700 nm) and almost the entire spectral range from 525 nm to 1700 nm in one single exposure at lower resolution R=1500. A FOV of 20' diameter at MOS mode and 0.5' x 0.5' at SIFU mode is required. Also, a good number of mIFUs can be deployed in the 10' FOV at Folded-Cass. This section discuss the optical parameters of the spectrograph for the MOS mode because is more restrictive than the SIFU or mIFU mode.

The spectrograph baseline is similar to the Sloan Digital Sky Survey Spectrograph (see Figure 128) with a mirror collimator (reverse Schmidt camera) and two arms separated by a dichroic. The BLUE arm cover the spectral range from 390 nm to 600 nm and the RED arm will cover the spectral range from 600 nm to 910 nm.

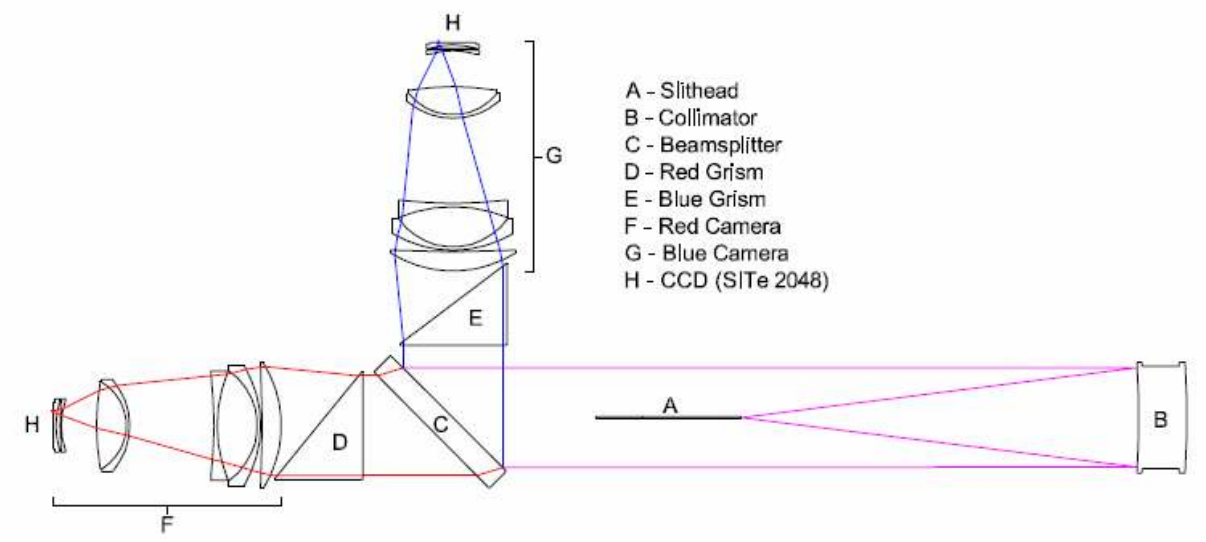

Figure 128. Sloan Sky Digital Survey Spectrograph

The Figure 129 and Figure 130 shows the optical layout of the SIDE Dual VIS-NIR spectrographs. A curved slithead positions the fibers on a radius concentric with the spherical collimating mirror, which transforms the f/5 output from the fibers to a 100 mm diameter collimated beam. The 45 degree dichroic beamsplitter reflects the VIS portion of the bandpass ($\lambda < 950$ nm) and transmits the NIR wavelengths ($\lambda > 950$ nm). Immediately after the beamsplitter in each channel is the grating wheels that contain grism and vrism (VPH+PRISM). The dispersed light exits the gratings (grisms and vrisms) and enters all-refractive, six-element, f/1.75 geometrical (f/1.35 underfilled) NIR camera and f/2.92 geometrical (f/2.3 underfilled) VIS camera. The NIR camera contains a single 2k2k CCD

[1] The main reason for setting this limit is that the optical glasses needed to accomplish color correction absorb strongly below 400 nm. The extreme derivatives of index with wavelength below 400 nm further cripple the optical design and strongly dominate the outcome of any feasibility study. Others reasons are the atmosphere transmission: 50% at 365 nm and the poor fibers efficiency about 70% below 400 nm for 10 meters.

with 18 μm pixels and the VIS camera contains a single 4k4k CCD with 15 μm pixels. The NIR camera demagnification from f/5 to f/1.75 produces fibers images that are just 2.33 pixels in diameter separated by ~ 3 pixels center-to-center. The VIS camera demagnification from f/5 to f/2.92 produces fibers images that are just 4.7 pixels in diameter separated by ~ 6 pixels center-to-center.

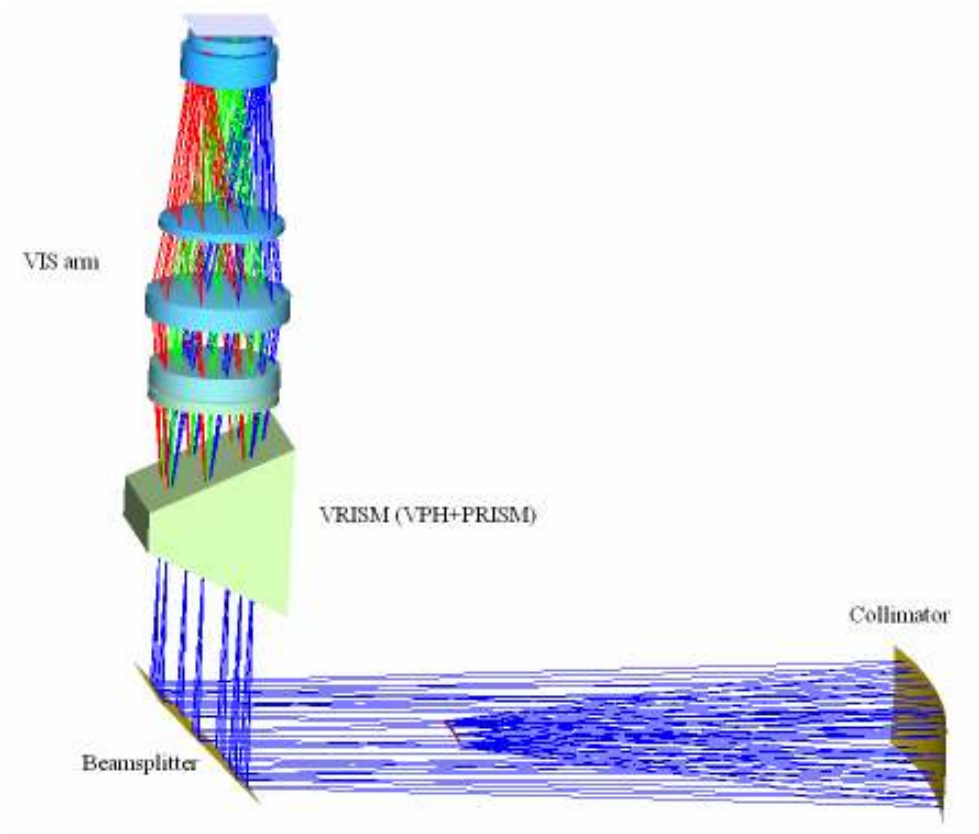

Figure 129. SIDE Dual Spectrograph, VIS arm.

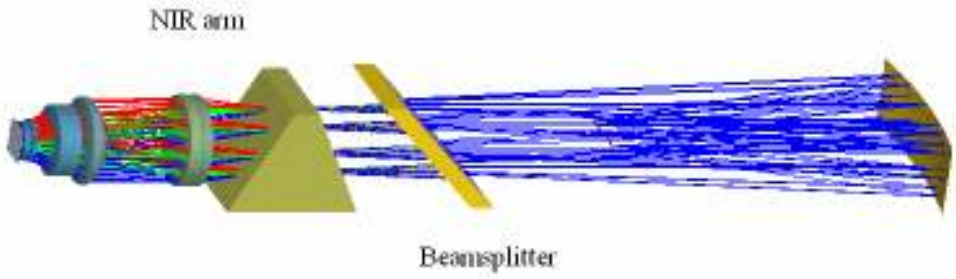

Figure 130. SIDE Dual Spectrograph, NIR arm.

3.10.1.2.1 Quantitative Basis for Spectrograph Parameter Selection

The fundamental parameters that define the characteristics of SIDE Dual VIS-NIR spectrograph are summarized in Table 59.

Telescope Diameter (mm)		10000[1]
Aperture per Single Fibers (arcseconds)		0.5
Anamorphic Factor		1
Beam Diameter (mm)		100
Detector ½ height (mm)	**VIS**	30.72
	NIR	18.432
Collimator Field Radius (degrees)		6º
Resolution	**VIS**	1500, 3400, 3650 and 4000
	NIR	1500, 4000 and 5000
Central Wavelength (µm)	**VIS**	0.56, 0.74, 0.46, 0.57, 0.69, 0.85
	NIR	1.33, 1.10, 1.24, 1.58

Table 59. Minimum parameters needed that define the characteristics of the SIDE spectrograph.

Since it was clear that fiber inputs to the collimators would be aligned along pseudo-slits, perpendicular to dispersion, and some space would be required between the fibers for cladding, etc., we chose to assign one "dark space" of equal width to each fiber so as to form imaginary "units" along each of the pseudo-slits. In practice, the number of fibers that can be accommodated along each pseudo-slit will depend on the details of their construction, cladding, and the amount of dead space provided between object spectra. Those details must be established in a subsequent study but the number of units are the total amount of pseudo-slit length available for the purpose in a convenient way. Our initial calculations led quickly to two results, which were fundamental to all of the numerical work that followed:

1. The telescope imaging scale (determined by its focal length) can be modified prior to the collimators with no appreciable impact on the optics that follow, provided the aberrations introduced by doing so are negligible. For example, the 20.0-arcmin field corrector could modify the scale. It could also be modified by using individual microlenses or microlenslet arrays as inputs to the fibers that couple the telescope f.o.v. to the collimators. We assumed that such fore-optics would in fact be used, such that we could safely define a new scale without designing the fore-optics ahead of time. As an initial approximation we chose a scale of 242.65 microns/arcsec, which provides an f/5 input to the fibers.

[1] Due to the hexagonal shape of the GTC primary, a diameter of 10 m (instead of 10.4 m) is used for optical calculations.

2. It did not appear possible to design spectrographs for SIDE that could accept the stipulated 1.5-arcsec input fiber size without adopting collimated beam diameters that would be prohibitive in cost and instrument volume. Thus, some form of image slicing would be required. We chose to proceed on the assumption that the fiber input for each astronomical object in the f.o.v. would be a "hex-pack" (see Figure 131) containing one central 0.5-arcsec diameter fiber, surrounded by 6 additional 0.5-arcsec diameter fibers to form a symmetric hexagonal shape. We assumed that these hex-packs would be custom-designed and manufactured for maximum packing factor, such that the equivalent circular diameter would be about 1.5 arcsec, with each 0.5-arcsec fiber core being about 120.0 microns in diameter.

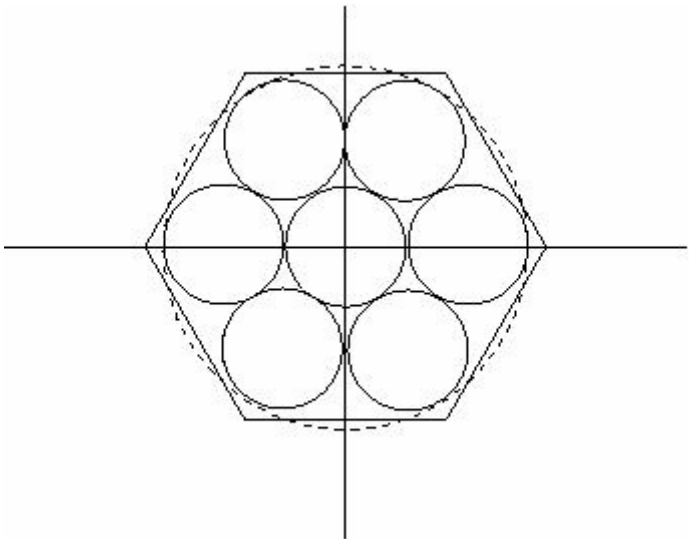

Figure 131. Hex-pack unit configuration for MOS mode.

An interesting consequence of the 1st point listed above is the fact that the sizes, geometries and designs for the dispersing elements and the cameras do not depend at all on the *choice of scale* at the fiber input end. Thus, if that choice should need to be modified after those designs are completed, no work will have been lost and no harm will have been done.

3.10.1.2.2 Parameters Selected for the SIDE Dual NIR arm.

A (2048 x 2048 by 20-micron) Raytheon array was initially specified as the detector. It was assumed that dispersion would be provided with grisms or VPH gratings. If so, the central anamorphic factor would be 1.0 with a range of about +/- 0.05 at the red/blue ends of the spectra. A collimated beam diameter of 100.0 mm was adopted as a compromise that would be affordable to build, would provide adequate resolution and would not dilute the pixel sampling at the detector to an unacceptably low level. A collimator field radius of 6.0 degrees was selected as a compromise that would provide an adequate total pseudo-slit length but would not cause the camera's required field radius to become excessive and would also not dilute the pixel sampling at the detector unacceptably.

The pixel sampling is 4.72 pixels/arcsec (2.36 pixels/pseudo-slit-width) in the dispersion direction, which is quite coarse but may just barely be acceptable.

These parameters, led to a required camera focal length of 194.9 mm and a field radius of 8.5 degrees, which covers the corners of the array. The dispersion values required to accommodate central wavelengths in the (1.3 to 1.5)-micron range, with resolution in the R= (1500 to 5000) range, appear to be attainable with practical grisms and VPHs. The selection criteria will include transparency, and especially *availability* in the large sizes required. An attempt will be made to minimize the prism angles to the extent possible.

The grism/VPH entry face(s) will have to be roughly 112 mm wide, such that their depth(s) along the optical axis could reach roughly 200 mm. If the nominal collimator exit pupil is placed at the mid-point, the camera's entrance aperture vertex would have to be located at least 110 mm beyond that plane. Conservatively, We adopted an entrance pupil distance of 130.0 mm for the preliminary NIR camera design. That allows some extra room for mounting hardware, and it led to an predesign estimate for the camera's entrance aperture diameter of about 146 mm (f/1.33, underfilled).

As we will see below will be possible to reduce the entrance pupil distance would lead to cameras that were smaller, optically slower and somewhat easier to design and build.

An alternative (2048 x 2048 by 18-micron) Hawaii-2RG array may be a more realistic choice for the detector. With all of the other parameter choices listed above remaining the same, led to a required camera focal length of 175.4 mm. Since all of optics ahead of the camera must remain the same, the aforementioned 146-mm entrance aperture diameter results in an even faster, harder to design (f/1.20, underfilled) NIR camera.

3.10.1.2.3 Parameters Selected for the SIDE Dual VIS arm.

A (4096 x 4096 by 15-micron) LBNL CCD or equivalent array has been specified as the detector. The 100.0-mm collimated beam diameter, grisms or VPH gratings with a central anamorphic factor of 1.0 and a 6.0-degree collimator field radius were assumed for the VIS optics for the same reasons mentioned above in Section 3.10.1.2.2 for the NIR optics. The resulting pixel sampling of 4.72 pixels/pseudo-slit-width in the dispersion direction is generous. Note that since the same collimator will be used for both the NIR and VIS spectra *simultaneously*, with the beams being split by a dichroic mirror placed ahead of the dispersing elements, it is not practical to increase the VIS collimator field radius. These parameters led to a required camera focal length of 292.3 mm and a field radius of 8.5 degrees, which covers the corners of the array. The dispersion values required to accommodate central wavelengths in the (0.5 to 0.85) micron range, with resolution in the R= (1,500 to 4000) range, appear to be attainable with practical grisms and VPHs. Thus, the conclusions about entrance pupil distance for the VIS camera are the same as for the NIR camera(s) described above in Section 3.10.1.2.2. The estimated 146-mm entrance pupil diameter results in a somewhat slower (f/2.00, underfilled) VIS camera.

3.10.1.3 Optical Design

In the following sections we will show each optical element of the SIDE Dual VIS-NIR Spectrograph taking into account the initials parameters established above.

3.10.1.3.1 Slithead

Light enters the spectrograph through fibers, which terminate at the slithead. For the purposes of this study, we have assumed 120 μm diameter fibers with an f/5 output cone. The

fibers are stacked vertically to form a long slit and are placed on a radius whose center of curvature coincides with that of the collimator. Additionally, the fibers are aimed in a fanlike pattern outward from the center curvature toward the collimator, so that the central (gut) ray from each fibers strikes the collimator normal to the surface. Thus, the slithead is at the focus of a one-dimensional Schmidt collimator. See Section 3.10.1.4.1 for more details on the slithead design. The SIDE Dual VIS-NIR slit will be 105 mm in length.

3.10.1.3.2 Slithead with double fiber row

As mentioned in Section 3.9.9, the Dual VIS-NIR pseudoslits should be formed by two parallel rows of fibers, as close as possible to minimize both the de-centering and the occultation. We present here some preliminary results on the consequences of this setup.

We assume that, due to the double fiber row, the thickness of our slithead will be increased from 4 mm up to 8 mm, and the distance of the center of each row of fibers from the slit middle position is 3 mm (de-centering is therefore 3 mm).

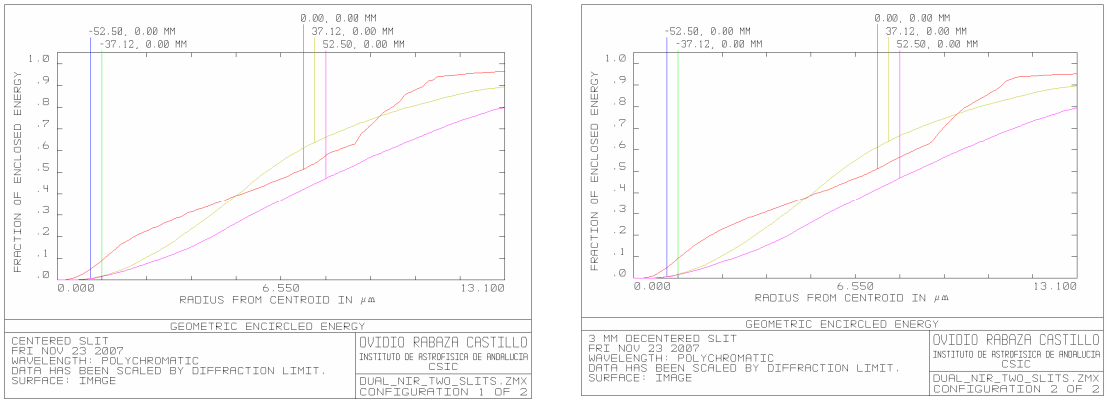

Figure 132 Comparison of the spot encircled energy with centered fibers (left) and 3 mm de-centered fibers (right). The different lines refer to the center of the slit, to ± 37 mm from the center and to ± 52 mm from the center, along the slit.

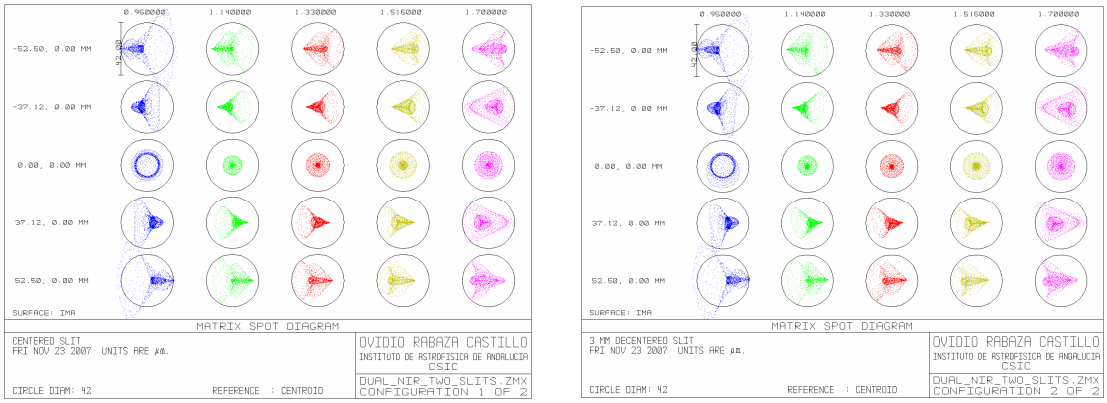

Figure 133 Comparison of the spot diagram for a centered slit (left) and 3 mm de-centered slit.

We can compare the two situations (centered and 3 mm off center slit) in Figure 132 and Figure 133. The difference appears to be negligible. Notice that this exercise has been done with the IR camera, with which we found the most evident difference. The same graphics done on the VIS camera hardly exhibit any difference at all.

Concerning occultation due to the wider double slit, we compared a 4 mm thick slit and an 8 mm thick slit *with 3 mm de-centered fibers,* in Figure 134.

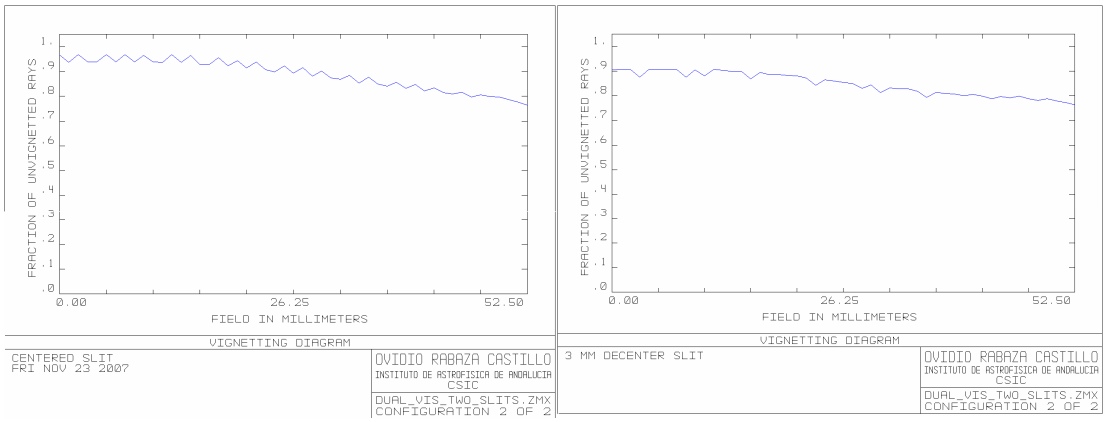

Figure 134 Comparison of the occultation caused by a 4 mm thick slithead (left) and an 8 mm thick slithead (right) *with de-centered fibers*.

Here we can see some 5% difference in the center of the slit, and nearly no difference away from the center.

We don't have the final size and de-centering of our double pseudoslits, but ***we can expect a minimal impact on the spectrograph efficiency due to the double pseudoslits***.

3.10.1.3.3 Collimator

The collimators for SIDE will be quite simple and effective. The SIDE Dual VIS-NIR collimator is assumed to work at f/5 such that it requires a 500.0-mm focal length to produce the adopted 100.0-mm beam diameter. The only optical element needed is a spherical mirror whose radius is twice the focal length, or 1000.0 mm. As we saw in the Section 3.10.1.3.1 the fiber "ends," where light exits, must be placed along a circular arc whose radius is 500.0-mm, with a center point that is also located at the mirror's center of curvature. This geometry will produce a 100.0-mm diameter exit pupil, on a plane perpendicular to the optical axis that passes through the mirror's center of curvature. Thus, in effect, we can think of the collimator as a "correctorless" Schmidt camera working in reverse, whose f.o.v. is confined the plane of the fiber fan (Slithead).

By symmetry, it is apparent that the only aberration present will be spherical aberration, which is independent of field angle. The only optical requirement is that the spherical aberration produces a "spot size" that is small and negligible compared with the diameter of each individual fiber. A Zemax model along these lines was formulated for the SIDE Dual VIS-NIR collimator so as to calculate the aberration spot size by direct ray tracing. The model was illuminated in parallel light, through its "exit" pupil, like a normal Schmidt camera. The resulting spots (on the curved slithead surface) are shown in Figure 135 for

several field angles (on axis, 1, 2, 3, 4, 5 and 6) of the full 6.0-degree field radius. The total aberration blur spot is very small as compared with the 120.0-micron diameter fiber shown as a circumscribed circle. Thus, the SIDE Dual VIS-NIR collimator described here is fully adequate for the purpose.

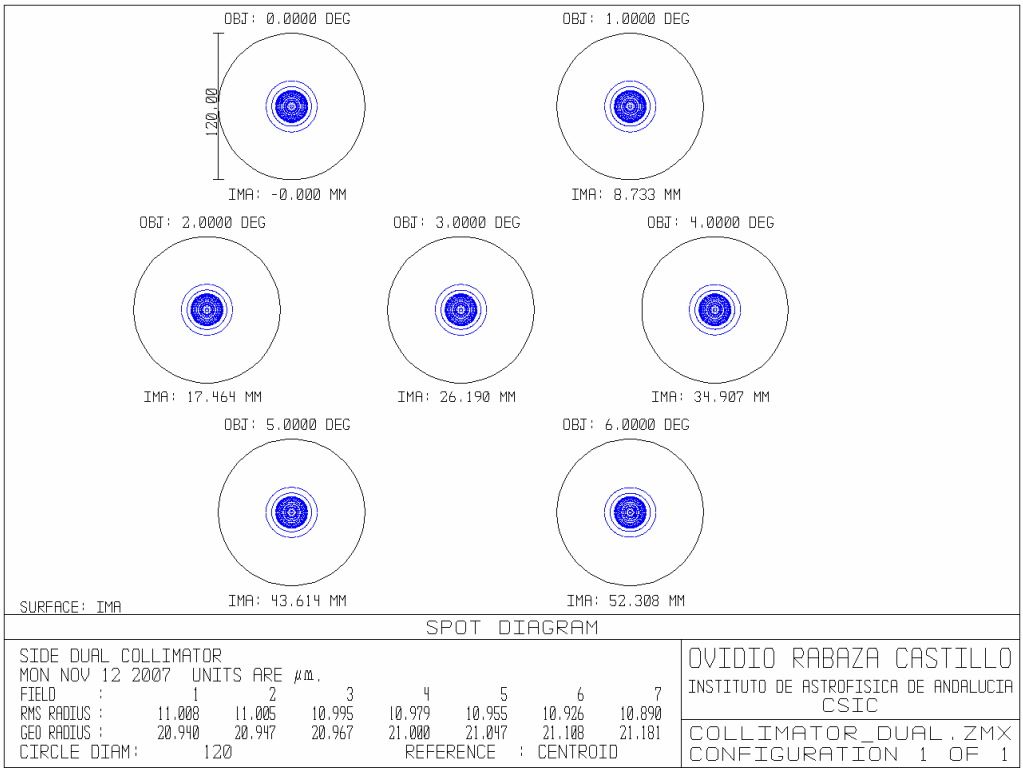

Figure 135. Qualitative measured of the collimator spherical aberration for several field angles.

The mirror itself is fabricated from a rectangular Hextek borosilicate blank, 100 mm wide, 310 mm tall, and 60 mm thick (see Figure 136). The planar blank is slumped by Hextek's gas-fusion process to near-net radius and then ground and polished to the final radius of 1000 mm. The collimator is the largest optic in the spectrograph and drives the overall height of the optical bench.

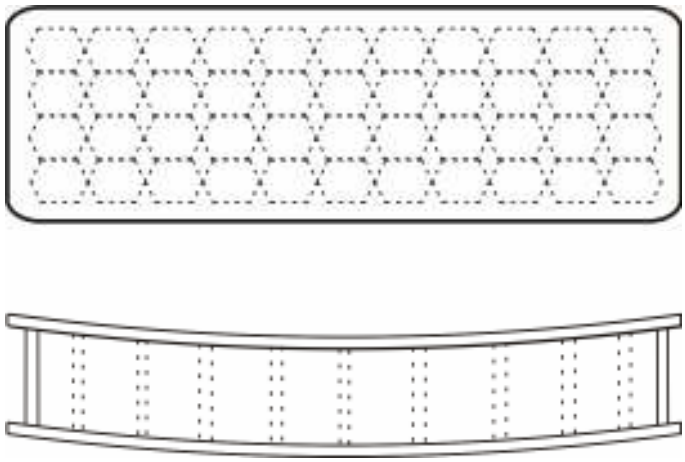

Figure 136. Drawing of the Hextek collimator mirror.

The collimator mount provides tip/tilt and focus adjustment (see Section 3.10.1.4.3). An initial focus adjustment can compensate for surface radius variation from nominal, allowing for less critical fabrication tolerances on the mirror and optomechanics. The Hartmann shutter (see Section 3.10.1.4.4) allows shifts in the collimator focus to be measured rapidly. Tip/tilt adjustment allows the collimator to be precisely coaligned to the cameras, or at least to an average of the two camera axes. Thus, the center fibers can be positioned at the center of the detector in the spatial direction, and the central wavelength can be positioned at the center of the detector in the spectral direction.

The collimator forms a pupil at the center of curvature of the mirror, and this is where the gratings are located in each channel in order to minimize their required size.

3.10.1.3.3.1 Things to take into account during the next phase

Due to the fibers Focal Ratio Degradation will be necessary reconsider the collimator f/number. The Figure 137 show that the transmission energy in our case when the f/input is 5 will be estimated in the 85% (energy loss of the 15%) for a f/5 collimator, nevertheless if the f/input to fibers is 4 the transmission energy measured is 90% (energy loss of the 10%) for a f/4 collimator, but if we decrease the f/number of the collimator then the spherical aberrations are increased. In the next phase we will take a final decision.

It must also be taken into account that, depending on the scientific program, some order-blocking filters will be needed for the Dual VIS-NIR spectrograph. These could be easily located in the space between the dichroic and the grating.

An interesting possibility for lowering the costs of the large gratings would be to use gratings with a smaller angle, much cheaper than the one adopted here, and work with a folded beam. The fact that the instrument is restricted to spectroscopy (i.e. no imaging) means that the aberrations involved could be accepted.

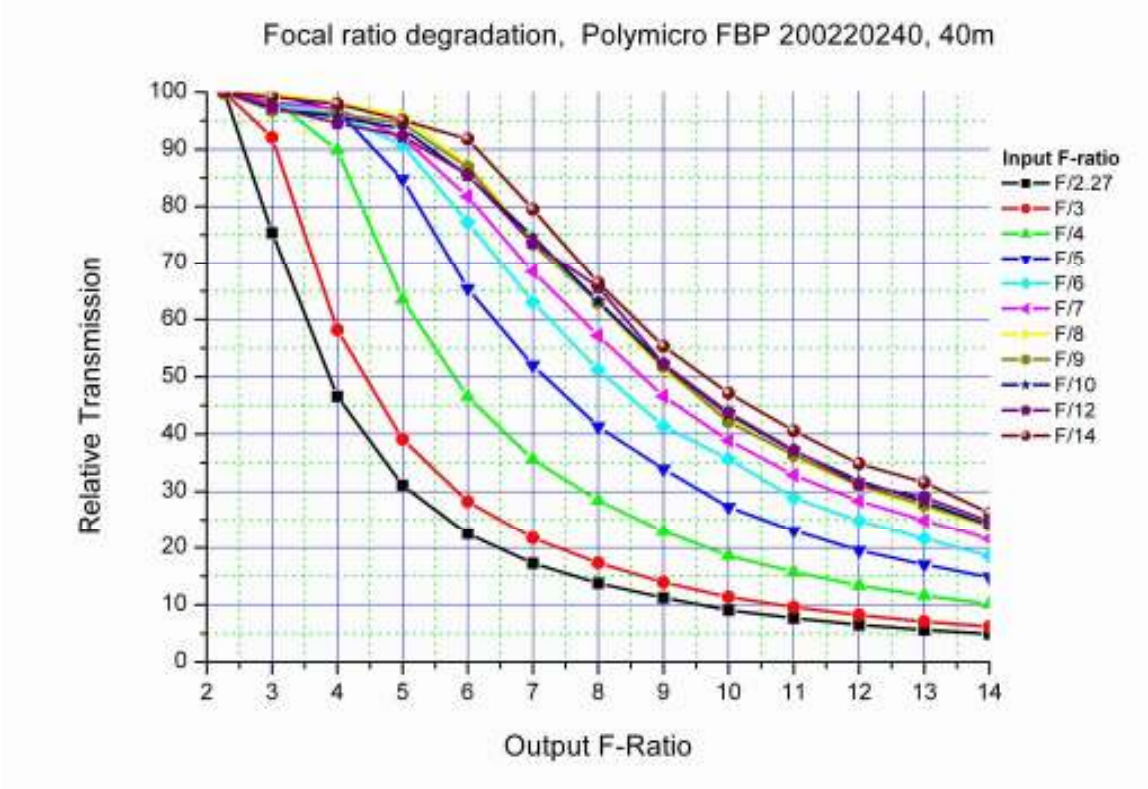

Figure 137. Focal ratio degradation of the fibers Polymicro FBP for several F/input.

3.10.1.3.4 Beamsplitter

A dichroic beamsplitter divides the incident collimated beam, reflecting the VIS wavelengths portion of the bandpass ($\lambda < 950$ nm) and transmitting NIR wavelengths ($\lambda > 950$ nm). It is fabricated from fused silica, 160 x 160 x 35 mm, with the dichroic coating applied to the incident surface. The coating will reflect the VIS light very efficiently ($R > 99\%$) and transmit the red light somewhat less efficiently ($T > 92\%$ average, including the reflection loss at the exit surface, which has a high performance broadband antireflection coating). The 10%–90% zone at the crossover wavelength is approximately 50 nm wide.

3.10.1.3.5 Gratings

The main issues that are requested to be covered in this section are the grating feasibility concept, the grating efficiency and the confirmation of manufacturers to supply the elements.

As a main conclusion, the proposed VPH and grism option is conceptually a feasible option that should perform as required regarding the resolution (grism gratings pending to be selected). No manufacture difficulties are expected with the current parameters. Minor recommendations are given in order to close the concept and for the following phases.

Nevertheless a second VPH solution is given in order to be considered as it seems to improve the manufacturability of the units improving the cost/performance ratio and the transmission performance.

The current SIDE concept contains two different cameras and dispersive elements. The F/5 collimator supply a 100 mm beam that is splitted at the dichroic. We can see in Figure 138 and Figure 139 an optical layout of the SIDE Dual VIS-NIR working in resolution 1500 and resolution 4000. For change of resolution we will use two grating wheels (see Section 3.10.1.4.5). In principle to cover all the spectral range from 0.4 μm to 1.7 μm we will use a total of 10 disperser elements (3 grisms and 7 VPHs), although, depending of the spectral ranges of interest maybe the number of disperser elements will be less.

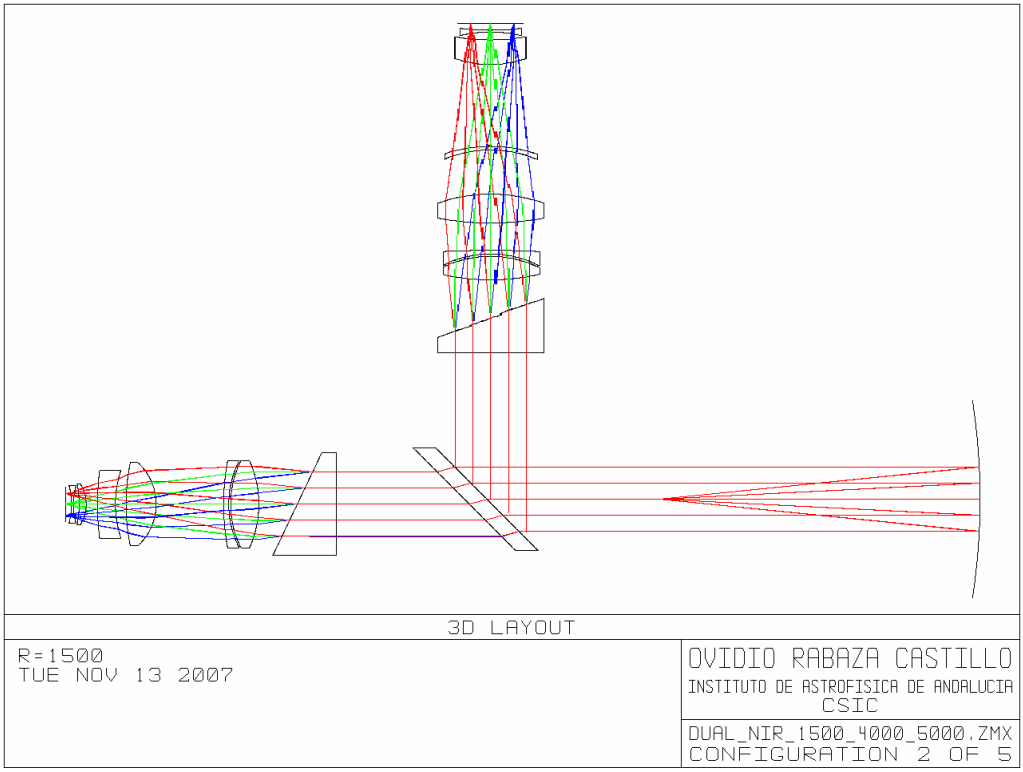

Figure 138. Optical layout of SIDE Dual VIS-NIR Spectrograph at resolution 1500.

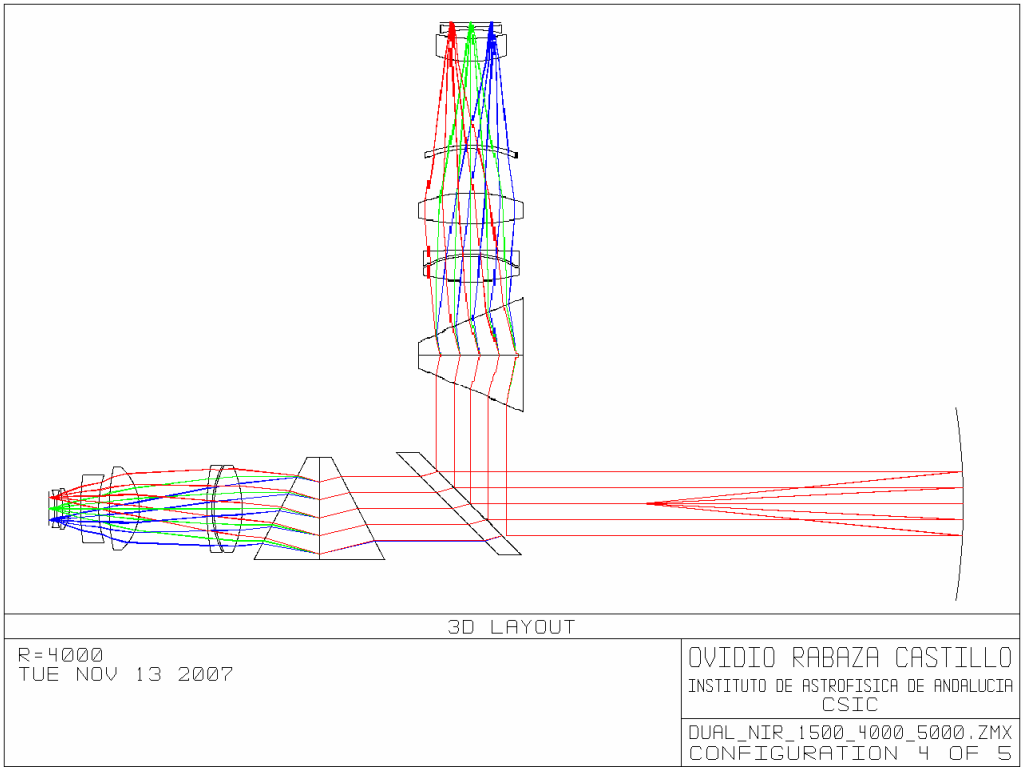

Figure 139. Optical layout of SIDE Dual VIS-NIR Spectrograph at resolution 4000.

Low resolution dispersers are considered to be transmission gratings mounted on a prism as shown in Figure 140 while mid resolution gratings are based on a volume phase hologram as shown in Figure 141. In both cases the beam is maintained in axis with the aid of high index prisms.

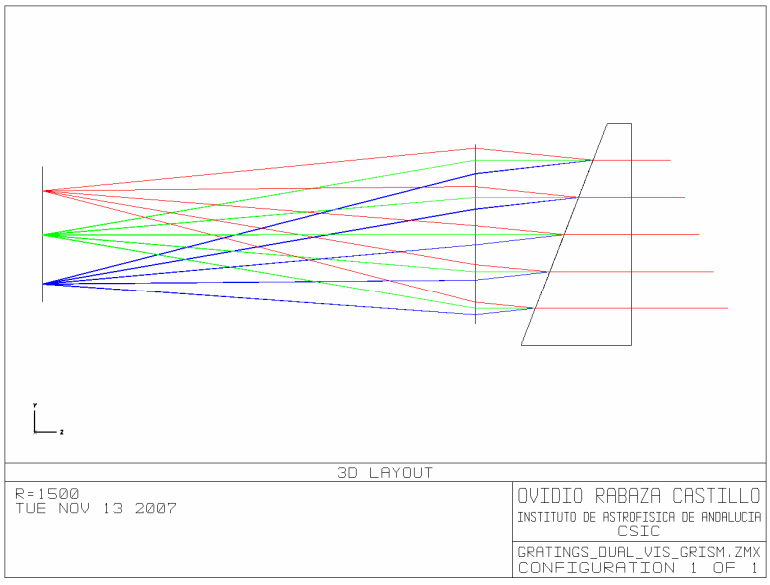

Figure 140. Grism layout concept.

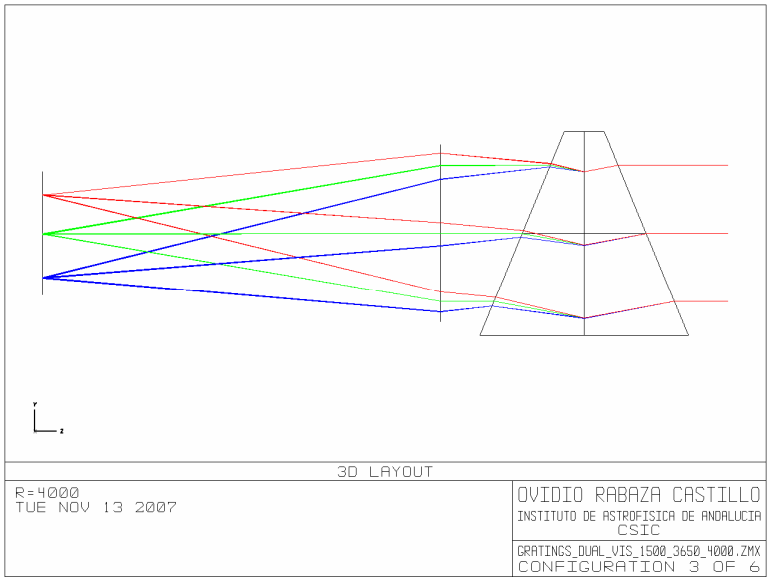

Figure 141. VPH layout concept.

A summary of some main parameters of the gratings has been done in order to evaluate potencial difficulties in the design, and is shown in Table 60 and Table 61. The columns contain the following information; extreme wavelength range for each disperser, transmission for the wavelengths considering the material absorption (which can be the largest contribution with the grating efficiency), the grating lines/mm, the material of the prisms as well as some dimensional parameters and finally the approximate incidence angle of the beam relative to the grating normal. All the parameters are within obtainable values. Only the grism number of lines has to be adapted to the existing gratings in the catalogue.

VIS DISPERSIVE UNITS								
	Wavelength Range (μm)	Transmittance[1]	Lines/mm	Material	Prisms bottom thickness (mm)	Prism top thickness (mm)	Apex angle (degree)	AOI on grating
R1500 Grism	0.40-0.70	78/99	558	NLASF41	75	15	22.0	22.0
R1500 Grism	0.52-0.95	83/98	435	NLASF46	73	16	21.2	21.2
R3400 VPH	0.40-0.52	60/94	1480	NLASF41	80	14	22.0	10.5
R4000 VPH	0.51-0.63	58/92	1420	NLASF46	80	10	25.0	12.1
R4000 VPH	0.61-0.76	90/96	1184	NLASF46	80	9	25.7	12.4
R3650 VPH	0.75-0.95	96/98	906	NLASF46	80	11	24.6	11.8

Table 60. Main parameters for the VIS dispersive elements.

NIR DISPERSIVE UNITS								
	Wavelength Range (μm)	Transmittance[2]	Lines/mm	Material	Prisms bottom thickness (mm)	Prism top thickness (mm)	Apex angle (degree)	AOI on grating
R1500 Grism	0.95-1.7	99/90	236	SF14	90	20	25.5	25.5
R4000 VPH	0.95-1.17	96/96	802	NLASF46	94	16	27.4	13.2
R4000 VPH	1.11-1.37	96/92	687	NLASF46	94	16	27.4	13.1
R5000 VPH	1.44-1.7	92/79	633	NLASF46	101	8.5	32.16	15.54

Table 61. Main parameters for the NIR dispersive elements.

[1] We have considered the absorption in the prism.

[2] We have considered the absorption in the prism.

Table 62 and Table 63 show the spectral parameters of the Dual VIS-NIR spectrograph Visible and NIR arms.

Resolution	Central Wavelength (Angstrom)	Spectral Width (Angstrom)	Dispersion (Angstrom/pix)	Pixels/Resolution element	Detector Format
1500	5600	3200	0.78	≈ 4.8	4096x4096 @ 15 μm /pix
1500	7400	4200	1	≈ 4.8	4096x4096 @ 15 μm /pix
3400	4600	1200	0.3	≈ 4.8	4096x4096 @ 15 μm /pix
4000	5700	1200	0.3	≈ 4.8	4096x4096 @ 15 μm /pix
4000	6900	1400	0.34	≈ 4.8	4096x4096 @ 15 μm /pix
3650	8500	2000	0.5	≈ 4.8	4096x4096 @ 15 μm /pix

Table 62 Spectral parameters of the visible arm of the Dual VIS-NIR spectrograph.

Resolution	Central Wavelength (Angstrom)	Spectral Width (Angstrom)	Dispersion (Angstrom/pix)	Pixels/Resolution element	Detector Format
1500	13000	7500	3.7	≈ 2.4	2048x2048 @ 18 μm /pix
4000	11000	2500	1.22	≈ 2.4	2048x2048 @ 18 μm /pix
4000	12400	2700	1.3	≈ 2.4	2048x2048 @ 18 μm /pix
5000	15700	2600	1.3	≈ 2.4	2048x2048 @ 18 μm /pix

Table 63 Spectral parameters for the NIR arm of the Dual VIS-NIR spectrograph.

3.10.1.3.5.1 Required Update Consideration

The size of the elements (blanks and gratings) has not margin for mounting. This implies an increase of the sizes of the prisms and gratings will be unavoidable to avoid vignetting. Nevertheless, the current sizes regarding gratings and blanks allow having room enough for this minor increase that has not been evaluated.

3.10.1.3.5.2 Blanks (Grisms)

For the cost estimation, we have taken into account that two prisms can be obtained from the same blank in order to save material.

No problems are detected for the sizes and materials. For the following phase we suggest working on the material selection (the current selection is a good one considering the index of the glass) to improve the transmission at short wavelengths in the NLASF41 case and try to use same materials of prisms dimensions to save engineering and manufacturing cost.

3.10.1.3.5.3 The Prisms (Grisms)

No difficulties are seen in their manufacture. We advise that some grating manufacturers do not accept to place the grating directly on the prisms because of the required tooling for the process. In that case the grating could have to be mounted on a flat window that has to be cemented on the prism afterwards as shown in Figure 142.

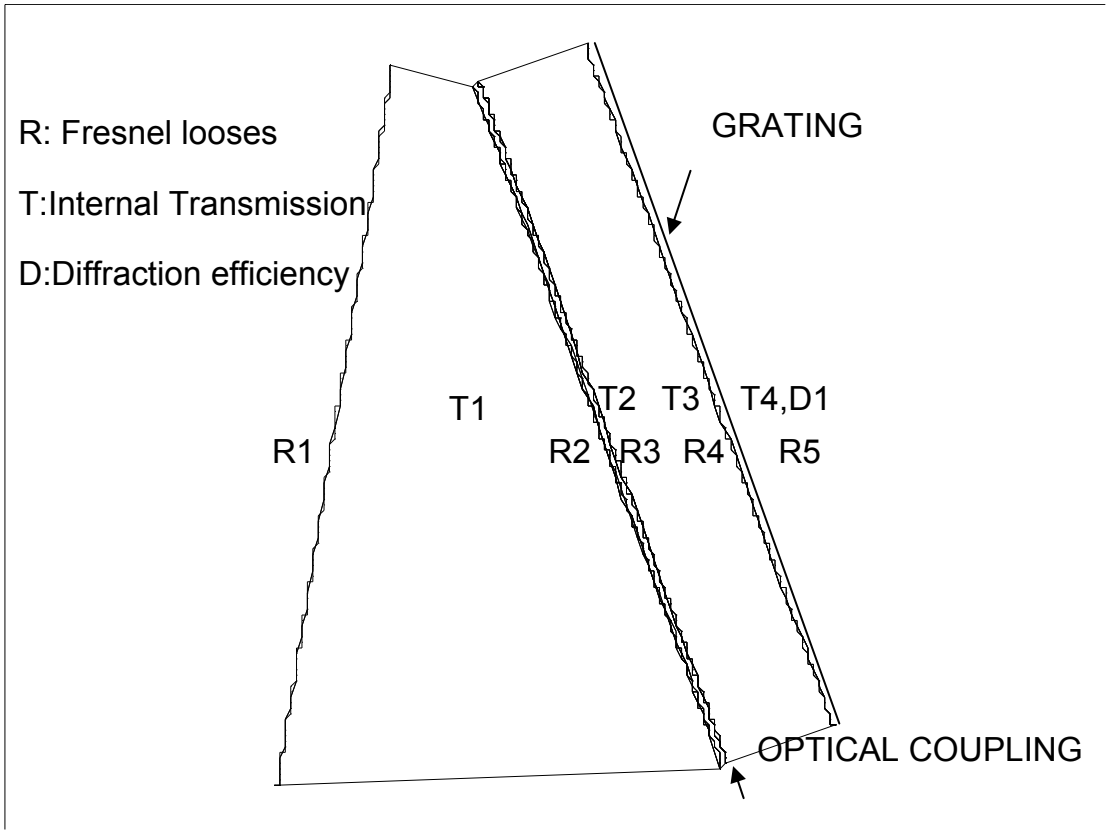

Figure 142. A Grism assembly with the parameters to evaluate the complete efficiency.

3.10.1.3.5.4 Grating Selection (Grisms)

The proposed gratings to obtain R1500 have 558, 432 and 236 lines per mm. A final selection of the master to be used in the replica will have to consider the footprint size of the ruled area of the grating and the blaze angle to improve the efficiency.

The Richardson catalogue has different gratings, large enough and at different blaze angles for 600, 500 and 245 lines/mm that seems to be blazed at the correct angles for the transmission operation. There is also a different epoxy resins options that can be used to optimize the final performance. A new design will be required according to the availability of the gratings. Yvon Jobin (see appendix) is another grating source that can be considered.

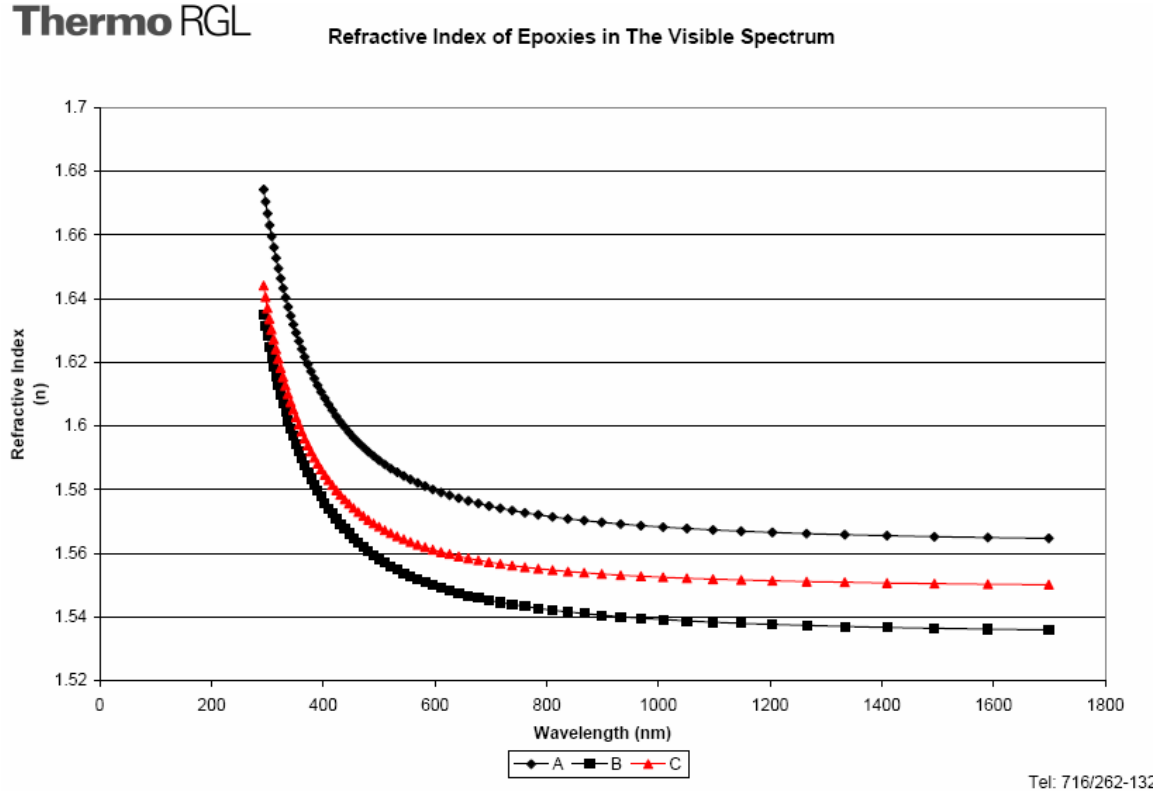

Figure 143. Refractive index for the epoxies used in the replicas. These can be used to optimize the blaze wavelength or minimize coupling looses with the substrate.

3.10.1.3.5.5 Grating Efficiency (Grisms)

In Figure 143 the absolute peak efficiency for several gratings from Richardson is given when the gratings are used in transmission. This can be used as guideline of what can be expected for the grating efficiency. In our case we would be taking about peak efficiency around 65%. The final performance will also consider Fresnel losses and the material absorptions.

Spectra-Physics
Lasers & Photonics
Richardson Gratings
705 St Paul Street
Rochester, New York 14605 USA

phone: (585) 262-1331 • fax: (585)454-1568
e-mail: gratingsales@spectra-physics.com
http://www.spectra-physics.com/gratings

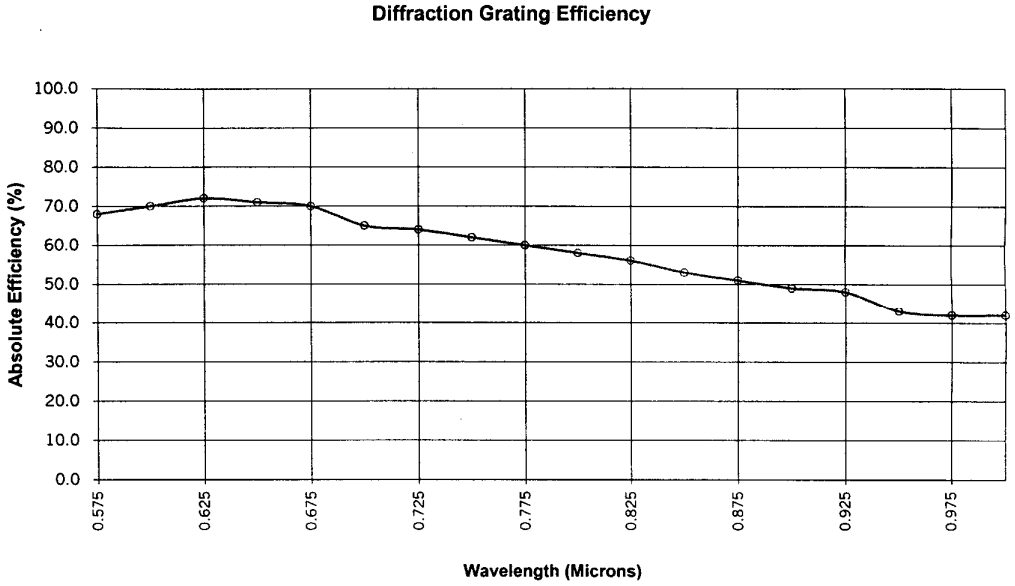

Serial Number: 900-27-1-503
Catalog Number: 54999SP07-77R
G/mm: 300
Blaze Angle (deg.): 17.457 Degrees
Polarization: Unpolarized

Grating Type: Ruled
Coating: Transmission
Test Date: 7/25/03
Operator: BS
Order Number: 19967024

Figure 144. Real measurement on a transmission grating (grism) for Elmer as reported from the manufacturer without the prism.

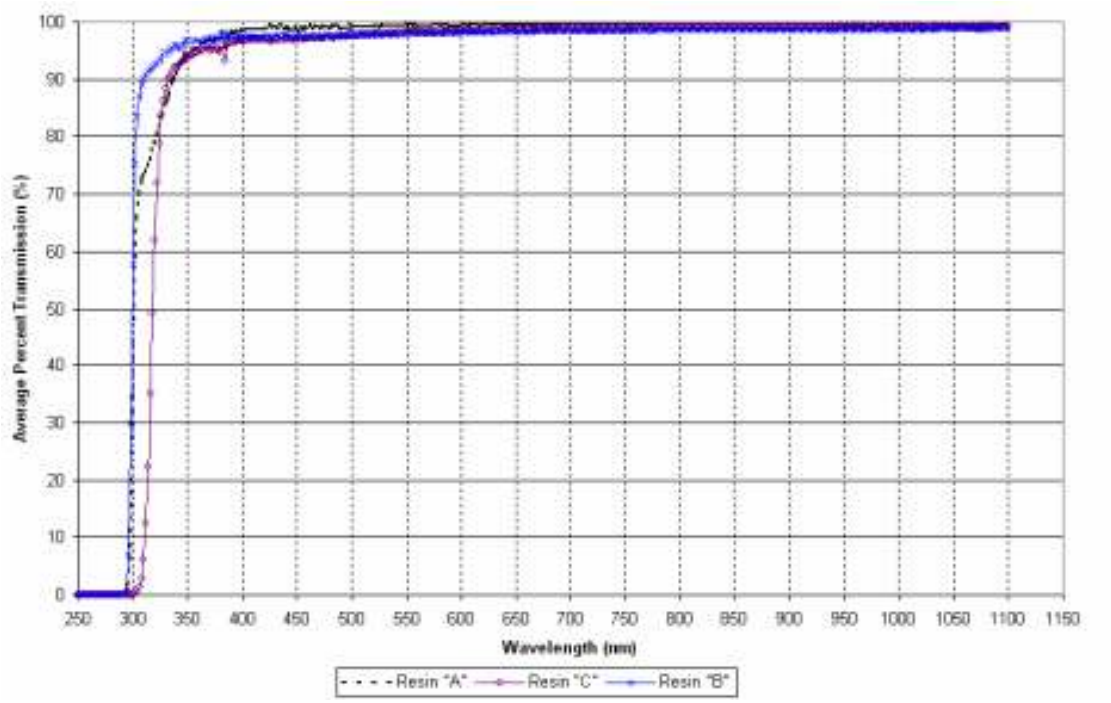

Figure 145. Epoxy transmission curves as given by ThermoRGL. These epoxies are used to make the replica of the master. A confirmation about the use at 1.7 microns has to be done to guarantee that no absorptions are in this wavelength range.

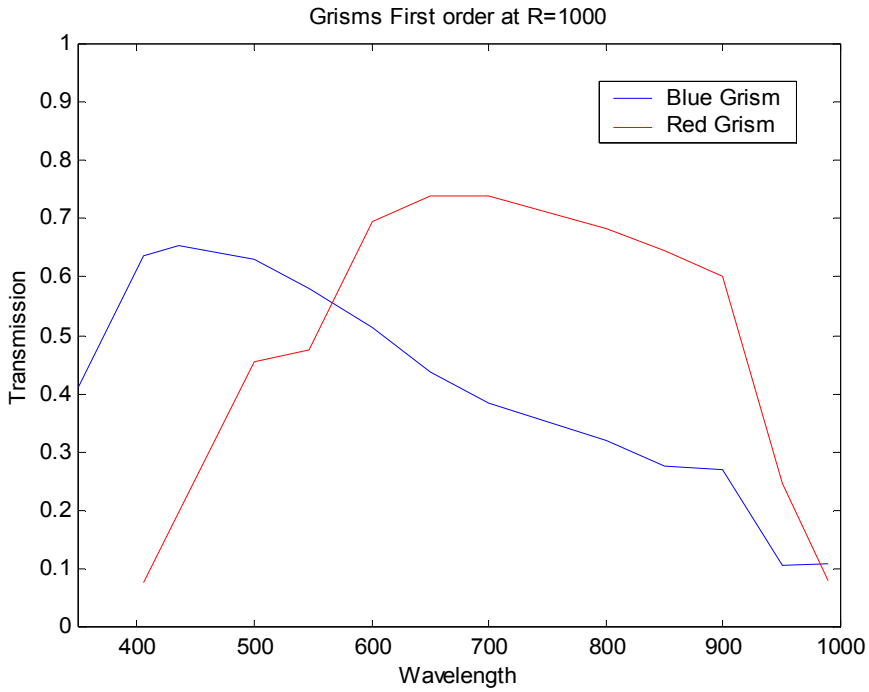

Figure 146. Complete performance for Elmer grisms. The peak efficiency is around 75% .

3.10.1.3.5.6 Blanks (VPHs)

We considered for the cost estimation that two prisms can be obtained form the same blank in order to save material.

No problems are detected for the sizes and materials. For the following phase we suggest to work on the material selection to improve the transmission at short wavelengths in the NLASF41 case.

A second recommendation is to try to use same materials of prisms (savings on blanks and coatings), same dimensions (savings on drawings and a gain in the reliability of the final item) that overall impacts on the engineering and manufacturing cost.

3.10.1.3.5.7 Grating Selection (VPHs)

No difficulties are expected regarding the number of lines required or the size (VPHs over 400 mm in diameter are currently delivered and considered within standard manufacture capabilities). The current clear apertures could be around 150mm in diameter that is well within the manufacturing capabilities.

3.10.1.3.5.8 Grating Efficiency (VPHs)

The grating efficiency depends on several manufacturing parameters that are maintained as an in-house process. Peak efficiency is dependent on the Dn value that is graved in the gelatin, while the lobe efficiency is dependent on the gelatin thickness.

It is a standard rule to use the minimum thickness regarding the gelatin to increase the lobe efficiency, then the *Dn* is adjusted to obtain the maximum efficiency with in the setup geometry (that is giving the lines/mm).

The Kolgenic analytical model allows us to determine the parameters for the peak efficiency to get an approximate response. The dependence of the efficiency is not directly related with wavelength but with the out of Littrow angle.

Considering that we place the blaze wavelength in the center of the detector we have two cases:

In the NIR camera, the marginal wavelengths (at the edges of the detector) are seen an angle of arctan(30.7/175) of ±10º.

In the VIS camera, the marginal wavelengths are seen at an angle of arctan(30.7/293) of ±6º.

So the first consideration is that the VIS camera will display a better performance that the NIR one.

Peaks efficiency (regarding diffraction at Littrow) are proven (Elmer case) to be over 95% while the degradation at the edges for this instrument (with a ±4º FOV) drops between 10% and 15%.

In Figure 147 it is shown a manufacturer grating model for the expected results. It can be said that in the average the efficiency drop is between 10% and 15% at ±4º for the different gratings.

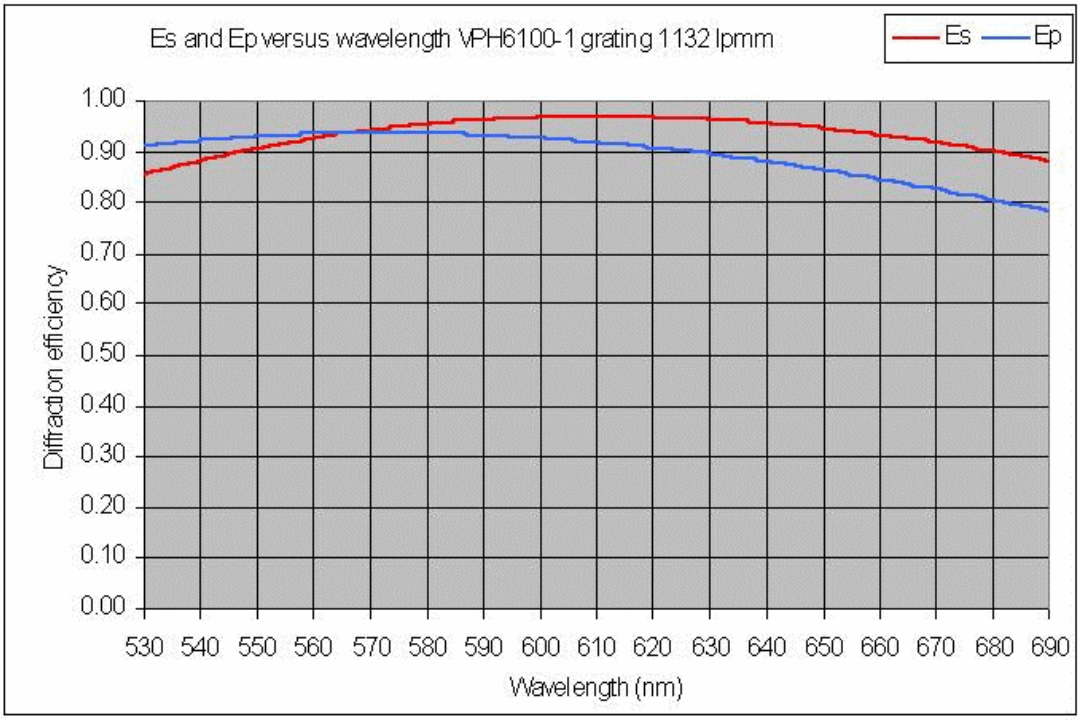

Figure 147. VPH example of the expected design as modeled for an R=2500 grating.

Extrapolation to larger angles involves a higher degradation. A first and rude model for the 6º VIS camera is shown in Figure 148. We can consider a loss of efficiency between 20% and 25% relative to that of the peak. It is to be remembered that these values can be considered the top efficiency of the surface gratings in transmission.

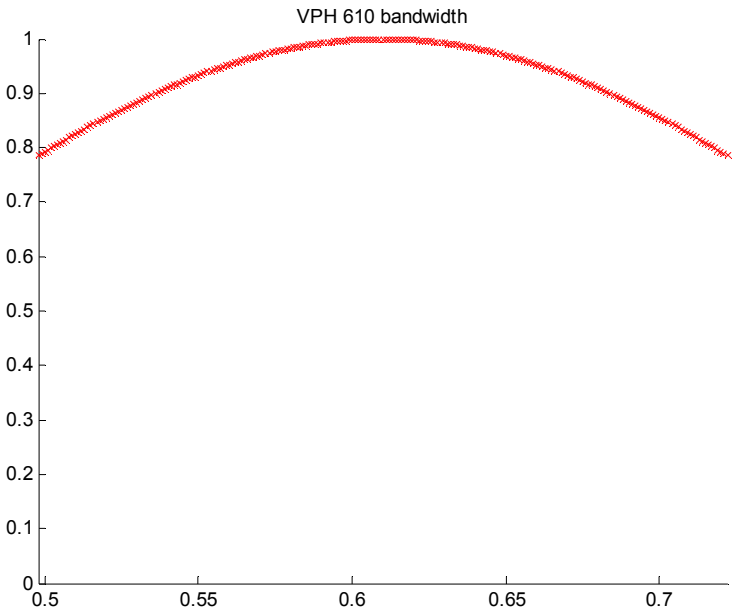

Figure 148. Kolgenic model and Gaussian fit for the lobes.

In the case of the NIR camera values will be probably dropping up to 40% at the edge of the detector. A detailed model requires a specific analysis from the manufacturer or the designer to account for a more reliable value. As an example of what should we expect for an equivalent design in Figure 149.

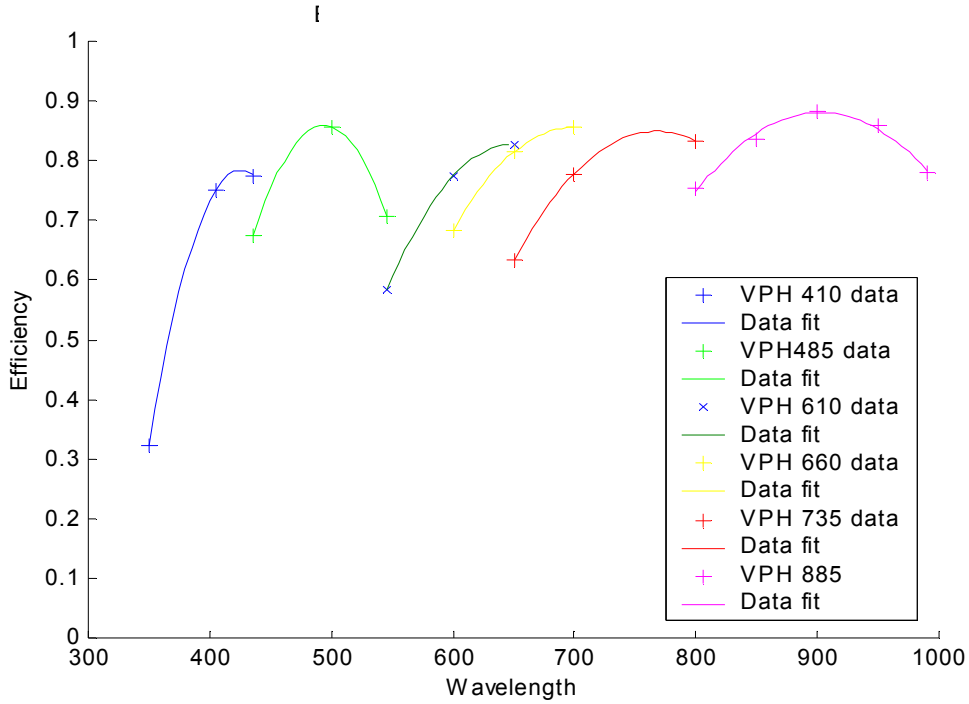

Figure 149. As built measured data for complete VPH units from ELMER at R=2500.

As SIDE expands the wavelength range to the NIR we show the absorption of a gelatin film as those used for the VPHs.

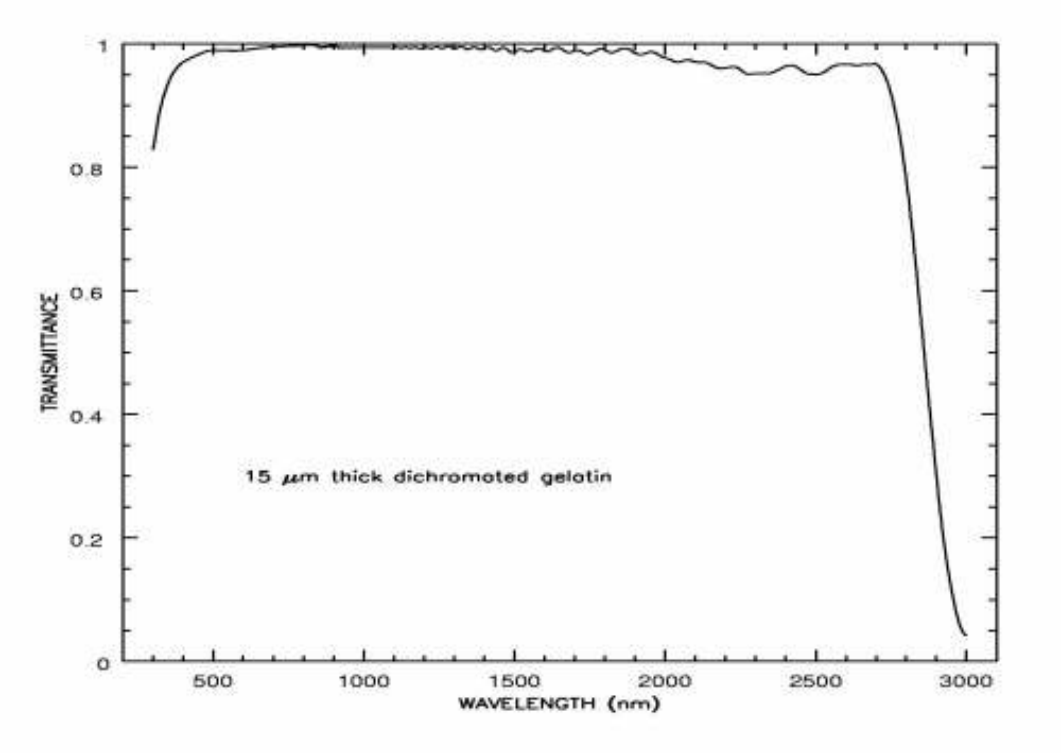

Figure 150. Transmission profile for the dichromate gelatin.

3.10.1.3.5.9 Possible Alternatives

In the next phase we will explore the following options:

- The suppression of grisms (surface gratings) accordingly with the proven and superior performance of the VPHs that also allow to select precise manufacturing parameters.

- This would allow using very small apex prisms with lower indexes of refraction (better transmittance in the blue) at a fraction of cost of the current material.

- A very large improvement would be also possible at the edges of the spectrum regarding transmission due to the material change as well as a lower specification level regarding surface quality. So this would be a tremendous gain regarding cost and a gain in performance. The weight of the units and the envelope would be also lowered.

3.10.1.3.6 Cameras

The SIDE Dual VIS-NIR spectrograph cameras were designs for the prof. Harland W. Epps (University of California, Santa Cruz). There are three cameras design, one of these cameras is for the VIS arm and two of these are for the NIR arm, one for use a 2k×2k@20 μm detector and the another camera for use it in a 2k×2k@18 μm.

3.10.1.3.6.1 Selection of Infrared Optical Materials and their Characteristic Properties

The design of high-performance optics for the traditional (1.0 to 2.4)-micron chromatic range is strongly curtailed by the limited selection of suitable optical materials. (See: Epps, H.W., and Elston, R., SPIE Vol. 4841, pp. 1280-1294, August 2002.). However limiting the long-wavelength cut-off for the design to 1.70 microns makes it practical to consider a number of standard optical glasses, which would otherwise have been excluded due to strong absorption beyond 1.8 microns.

The Ohara catalogue was reviewed in order to select available optical glasses which exhibit an internal transmission of 0.994 or greater at a wavelength of 1.40 microns, for a 10.0-mm thickness.

Traditional infrared materials from the aforementioned SPIE reference are included, such as BaF2, CaF2, LiF, Infrared Fused Quartz (called FQTZ), etc. It can be seen that the uniquely small dispersive power of Barium Fluoride (BaF2) makes it extremely attractive as the provider of substantial positive power in a fast, high-performance camera. However its well known hygroscopic tendency (some 100 times worse than CaF2) and its extreme softness (which makes it difficult to polish and to coat) conspire to make it a poor choice for use in SIDE.

For convenience of intercomparison, the data are all given at "room temperature" (T= +25.0 C for the optical glasses; T= +20.0 C for the traditional infrared materials). The preliminary optical designs reported here were also done at room temperature as the detailed temperature distribution through the camera(s) has not yet been specified. Generic refractive indices were used for the various optical materials. The corrections to proper temperature(s) will all be at the level of typical "melt-sheet" corrections. They can be done when the selected designs are updated prior to construction.

One notes also that the camera designs presented make no distinction between "air" and "vacuum." This approximation is safe as refractive index corrections at that small level can also be made at construction design time or even ignored entirely as they always result only in a very small wavelength-independent focus shift, even in optical systems which are much faster optically than the cameras needed for SIDE.

3.10.1.3.6.2 A 6-Element All-Spherical f/1.33 NIR Camera Lens Design for a 20.0-micron Detector.

Given a 194.9-mm focal length specification, with a 100.0-mm diameter collimated beam, an entrance pupil distance of 130.0 mm, a maximum field radius of 8.5 degrees needed to cover

the detector to its corners with (as yet unspecified) grisms and VPH gratings whose anamorphic factors could become appreciable away from the central wavelengths, H. W. Epps anticipated that the camera's first lens element could become as large as 146 mm in diameter. Thus, the camera's optical speed could be as fast as f/1.33 (underfilled), which implies a formidable design task over the (0.95 to 1.70)-micron chromatic range. However lateral color can be neglected, which is helpful. H. W. Epps selected a (100 by 107)-mm elliptical entrance pupil and a 130-mm entrance pupil distance and he started the design from several near-ir cameras (with somewhat different parameters) that he had previously designed for the PFIS project on SALT and for the MOSFIRE project on Keck 1. This enabled to explore element configurations and glass distributions quickly and select the most promising models for further development. H. W. Epps used precisely parallel light to illuminate the camera so as to avoid any interaction between the camera's aberrations and those of any particular collimator and grism and VPH grating combination.

As the camera configuration developed, it became apparent that the best solution forms were those in which a closely-spaced [CaF2 + Glass #1] doublet was followed by a loosely-spaced [CaF2 + Glass #2] doublet and a pair of free-standing singlets near the detector, serving primarily as a compound field flattener. A systematic study was made of the available moderate-to-high dispersion optical glasses so as to seek candidate combinations that would provide the best *axial* color correction with excellent internal transmission also. It was found that S-LAM66 accomplished both of those goals quite well when used as the 2nd and 6th (last) lens elements.

It proved possible to thicken the 4th lens element while maintaining a substantial distance between it and the singlets near the detector. Thus, it becomes a good candidate to be used as the vacuum window. This will provide maximum isolation of the sensitive NIR detector, enabling it to be cooled and well shielded from unwanted background radiation. Additional glass exchange calculations led to the conclusions that Infrared Fused Quartz would be the best material for the 4th lens, while Ohara S-FPL51X is preferred for the 5th (positive meniscus) lens and S-LAM66 is confirmed as being best for the 6th (bi-concave) lens.

When illuminated in perfectly parallel light from the entrance pupil, as described above, this 6-element all-spherical camera shows residual aberrations with an rms image diameter of 16.6 +/- 2.3 microns (0.83 +/- 0.12 pixels) averaged over field angles and wavelengths within the (0.95 to 1.70)-micron passband *without refocus*. 3rd-order barrel distortion is some 0.28% at the edge of the full field (the corners of the detector). Thus, the image quality is excellent.

A scaled drawing of this camera is shown in Figure 151 parallel light rays, represented by the chief ray and the marginal rays for an 8.5-degree field angle, radiate from the entrance pupil on the left, moving toward the right. The rays pass through the lens elements and converge to focus at the flat detector array on the right. The total length from the entrance pupil to the detector is 447.05 mm. The length of the camera itself, from the first lens vertex to the detector is 317.05 mm, which is substantially more than the camera's 194.9-mm focal length. This difference is typical in camera designs of this type and it cannot easily be avoided.

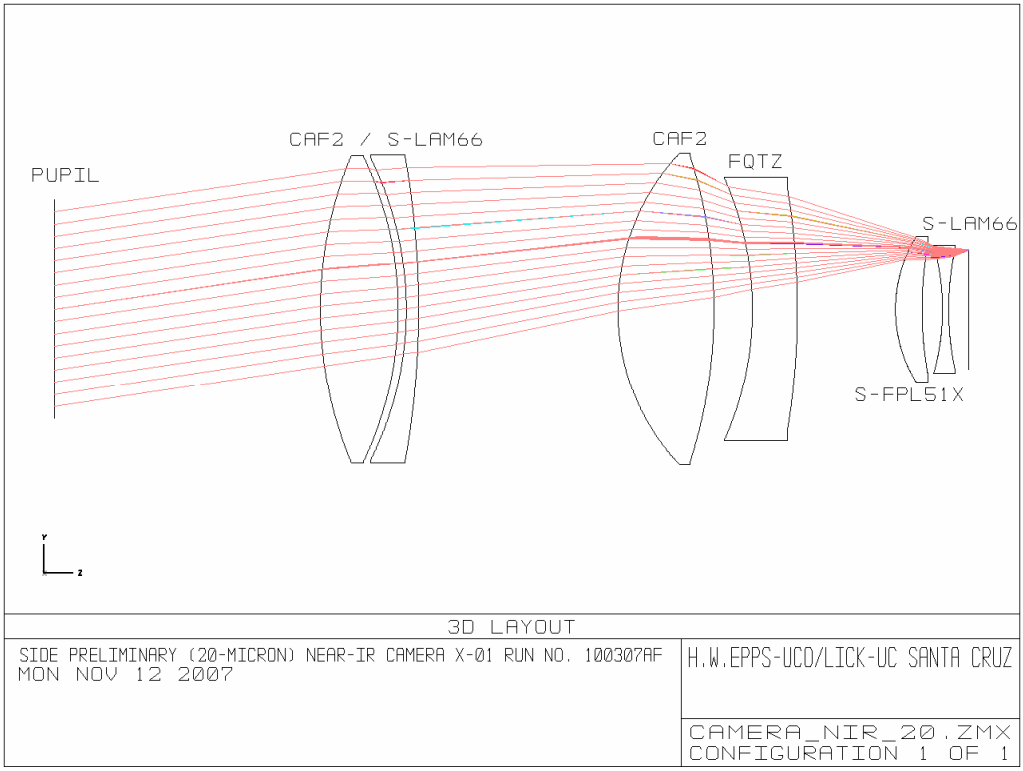

Figure 151. SIDE NIR Camera optical design for a 2k×2k @ 20 μm detector.

The lens apertures shown are minimum clear apertures. In practice, the lens elements would be made larger in diameter so as to allow sufficient material for mounting purposes, for beveling and for convenience of optical figuring and coating.

The entrance pupil distance needed taking into account the gratings design will be as maximum 60 mm instead of the 130 mm designed by H. W. Epps, then the camera's first lens element could become as large as 130 mm in diameter and the final camera's optical speed only will be as fast as f/1.5 (underfilled).

3.10.1.3.6.3 A 6-Element All-Spherical f/1.20 NIR Camera Lens Design for a 18.0-micron Detector.

The 175.4-mm focal length specification required for this camera, together with all of the other parameters given for the (f/1.33, underfilled) camera in Section 3.10.1.3.6.2 above, leads to an even more difficult (f/1.20, underfilled) challenge! H.W. Epps started the design from the f/1.33 model and quickly determined that the axial color correction, required to maintain parfocality with wavelength, represented the pivotal issue in the design. He repeated some of his glass exchange experiments with the moderate-to-high dispersion optical glasses and tried to redistribute the positive and negative optical power among the individual lens elements but
he found very little that was helpful along those lines. Basically, the faster camera simply causes all of the various curvature and thickness issues to become more extreme. The residual axial color (as a fraction of focal length) remains roughly the same as in the prior

(f/1.33) model but the faster (f/1.20) f/ratio in this model causes an increase in the rms image diameters. The smaller 18.0-micron pixels make matters even worse.

H.W. Epps experimented with the addition of another lens element and also with the use of an aspheric surface. These modifications tended to produce designs with somewhat less severe geometry and slightly better image quality but the improvements did not appear to justify the added complexity (and anticipated large construction cost differential). Thus, he did not pursue them further.

It proved possible to retain the relative geometry of the 4th, 5th and 6th lens elements such that the (very thick) 4th lens element is still a good candidate to be used as the vacuum window. As with the f/1.33 camera for the 20.0-micron detector, doing so will provide maximum isolation of the sensitive NIR detector, enabling it to be cooled and well shielded from unwanted background radiation.

When illuminated in perfectly parallel light from the entrance pupil, as described above, this 6-element all-spherical camera shows residual aberrations with an rms image diameter of 19.1 +/- 3.2 microns (1.06 +/- 0.18 pixels) averaged over field angles and wavelengths within the (0.95 to 1.73)-micron passband *without refocus*. 3rd-order barrel distortion is some 0.55% at the edge of the full field (the corners of the detector). Thus, the image quality is quite good.

A scaled drawing of this camera is shown in Figure 152 parallel light rays, represented by the chief ray and the marginal rays for an 8.5-degree field angle, radiate from the entrance pupil on the left, moving toward the right. The rays pass through the lens elements and converge to focus at the flat detector array on the right. The total length from the entrance pupil to the detector is 431.45 mm. The length of the camera itself, from the first lens vertex to the detector is 301.45 mm, which is substantially more than the camera's 175.4-mm focal length. This difference is typical in camera designs of this type and it cannot easily be avoided.

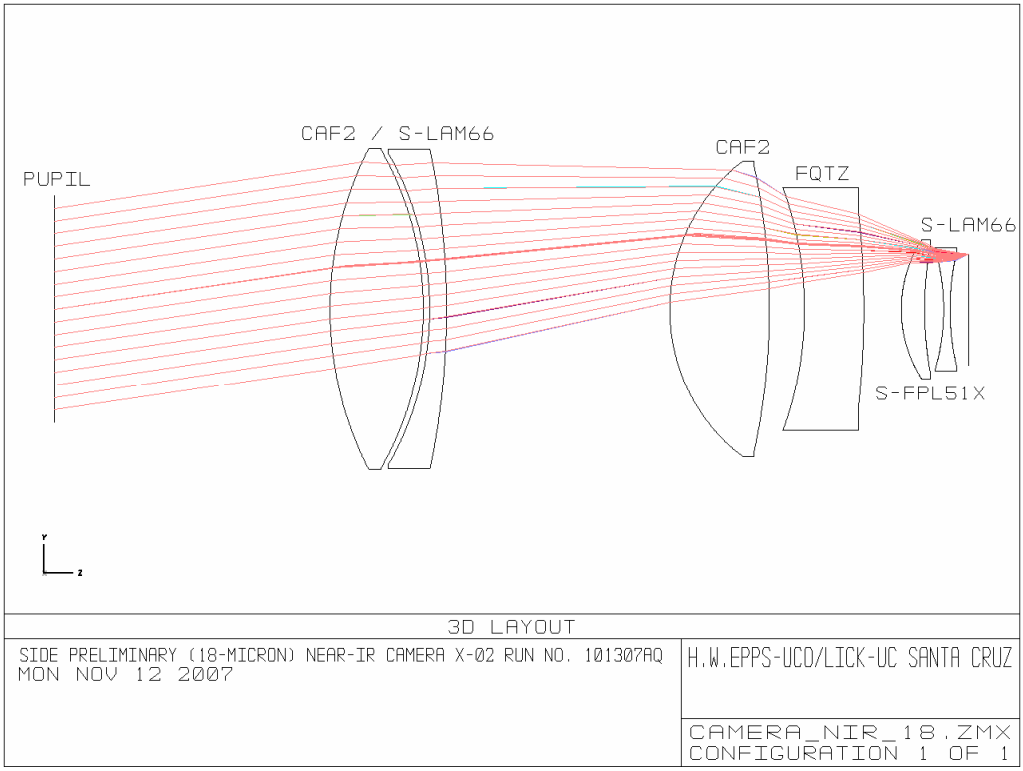

Figure 152. SIDE NIR Camera optical design for a 2k×2k @ 18 μm detector.

The lens apertures shown are minimum clear apertures. In practice, the lens elements would be made larger in diameter so as to allow sufficient material for mounting purposes, for beveling and for convenience of optical figuring and coating.

The entrance pupil distance needed taking into account the gratings design will be as maximum 60 mm instead of the 130 mm designed by H. W. Epps, then the camera's first lens element could become as large as 130 mm in diameter and the final camera's optical speed only will be as fast as f/1.35 (underfilled).

3.10.1.3.6.4 A 6-Element All-Spherical f/2.0 VIS Camera Lens Design for a 15.0-micron Detector.

The 292.3-mm focal length specification required for this camera, together with all of the other parameters given for the NIR cameras, leads to a slower (f/2.00, underfilled) geometry. However the extreme (0.39 to 0.95)-micron spectral range makes the axial color correction even harder to achieve than in either of the NIR cameras. The choice of materials is key and that choice is made all the more complicated by reason of the larger number of suitable materials available in this spectral range.

H.W. Epps used the 194.9-mm NIR camera as the starting point and retained CaF2 as the obvious best choice to produce the large positive power provided by lens #1 and lens #3. He left the materials for lens #5 and lens #6 as they were, since their function is primarily to flatten the field, by providing large curvatures near the focal plane where their effects on the axial color are not extreme. Thus, the initial design effort was to assess the color correction

interplay between the two doublets, by manipulating the choices of materials for lens #2 and lens #4. This is a somewhat "tricky" process as the interplay between two different dispersion curves can easily lead to false conclusions regarding the "best" glass combination. Trial and error is not a viable approach as there are simply too many possible combinations to investigate.

It became obvious that the color correction needed to be distributed more evenly than had been the case in the NIR designs. For that purpose, H.W. Epps chose lower-index, lower-dispersion glasses for lens #2 and found that Ohara S-LAL7 appeared to be good compromise, by reason of its excellent transmission in the near-uv as compared with other glasses with comparable indices and dispersive properties.

As the 2nd doublet assumed more of the color correcting responsibility, it became clear that the interaction improved steadily as the group was allowed to evolve into a free-standing quartet. Doing so enabled lens #4 to become more effective by getting thinner, while at the same time, lens #5 improved the system by becoming thicker. In this approach, lens #5 becomes identified as the best candidate to be used as the vacuum window.

Additional glass exchange calculations identified Ohara @PBL26Y as the best choice for lens #4. This is a special "i-line" glass with enhanced UV transmission all the way down to the i-line at 0.365 microns. Additional calculations showed that S-FPL51Y and @PBM2Y made an excellent combination for lens #5 and lens #6. These are also Ohara "i-line" glasses with excellent UV transmission.

H.W. Epps found that by adding a 7th lens element, he could improve the image quality somewhat but the improvement did not appear to justify the added complexity (and anticipated large construction cost differential). Thus, he did not pursue it further. He didn't try an aspheric surface in the VIS camera because he thought that doing so would not improve the image quality enough to warrant the extra cost. Axial color, not severe geometry, is the main residual aberration in the VIS camera and that problem is rarely helped by adding an aspheric surface.

When illuminated in perfectly parallel light from the entrance pupil, as described above, this 6-element all-spherical camera shows residual aberrations with an rms image diameter of 14.5 +/- 4.2 microns (0.97 +/- 0.28 pixels) averaged over field angles and wavelengths within the (0.39 to 0.95)-micron passband *without refocus*. 3rd-order barrel distortion is some 0.13% at the edge of the full field (the corners of the detector). Thus, the image quality is comparable (in pixels) to that in the 175.4-mm NIR camera although somewhat more variable. It appears to be acceptable.

A scaled drawing of this camera is shown in Figure 153 parallel light rays, represented by the chief ray and the marginal rays for an 8.5-degree field angle, radiate from the entrance pupil on the left, moving toward the right. The rays pass through the lens elements and converge to focus at the flat detector array on the right. The total length from the entrance pupil to the detector is 539.35 mm. The length of the camera itself, from the first lens vertex to the detector is 409.35 mm, which is substantially more than the camera's 292.3-mm focal length. This difference is typical in camera designs of this type and it cannot easily be avoided.

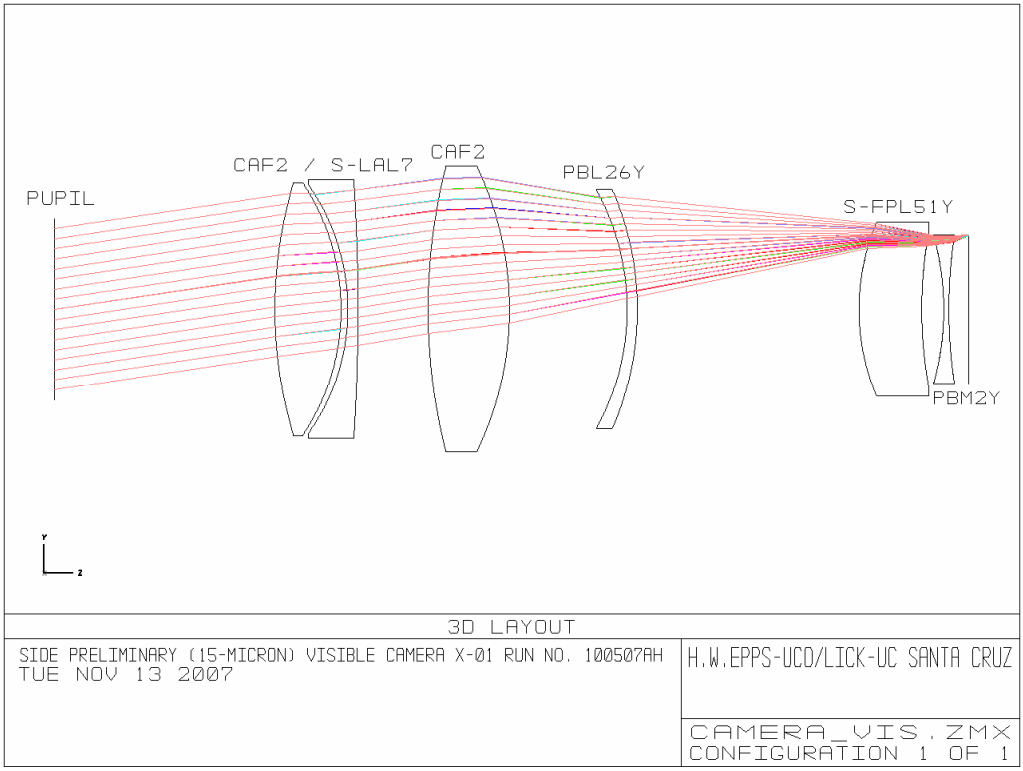

Figure 153. SIDE vis Camera optical design for a 4k×4k @ 15 μm detector.

The lens apertures shown are minimum clear apertures. In practice, the lens elements would be made larger in diameter so as to allow sufficient material for mounting purposes, for beveling and for convenience of optical figuring and coating.

The entrance pupil distance needed taking into account the gratings design will be as maximum 60 mm instead of the 130 mm designed by H. W. Epps, then the camera's first lens element could become as large as 127.3 mm in diameter and the final camera's optical speed only will be as fast as f/2.3 (underfilled).

3.10.1.3.6.5 Detail Optical Performance of the Preliminary NIR and VIS Camera designs

It is commonly agreed that if images are more-or-less "round", without extreme bumps, wiggles or tails, and they are more-or-less "smooth", without rings and voids, then they will be pixel-sampling limited if about 80% or more of the energy is included within a (2-pixel x 2-pixel) Nyquist sampling box and 95% or more of the energy is included within a (3-pixel x 3-pixel) sampling box (both centered on the image centroid). If the images were Gaussian in shape, 80% of the energy would be contained within 1.27 rms image diameters and 95% would be contained within 1.72 rms image diameters. The corresponding criteria for quasi Gaussian images to be pixel-sampling limited is that *(roughly speaking)*, they should have rms diameters in the (1.6 to 1.7) pixel range (or smaller). This criterion is no substitute for detailed modulation transfer calculations but it is probably more than adequate for the purpose of examining preliminary optical designs such as those presented in this Feasibilty Study.

A (100 by 107)-mm entrance pupil at an entrance-pupil distance of 130.0 mm was used for the calculations and the cameras were illuminated in perfectly parallel light. It should be noticed that this illumination pattern actually "overdrives" the cameras in the sense that the bluer wavelengths will have smaller anamorphic factors. It can be seen that the worst-case images for the 194.9-mm focal length (20-micron) camera have rms diameters of only about 1.00 pixels. The distribution of rms image diameters for the optically faster 175.4-mm focal length (18-micron) camera are somewhat larger and more variable but the worst-case rms image diameter is only 1.31 pixels (at the extreme blue wavelength, in the very corner of the detector). Thus, it appears fair to conclude that both of these preliminary NIR camera designs are strongly pixel-sampling limited. Their imaging characteristics appear to be excellent for the intended purpose.

The illumination pattern was the same as described above for the NIR cameras and the same comment about "overdriving" the camera applies here as well. It can be seen that the worst case images for the 292.3-mm focal length (15-micron) VIS camera have rms diameters that are somewhat larger than those in the NIR cameras, mostly due to the longer focal length and the smaller pixel size. However the worst-case rms image diameter is only 1.60 pixels (at the extreme blue wavelength, in the very corner of the detector). Thus, it appears fair to conclude that the VIS camera design is also strongly pixel-sampling limited. Its imaging characteristics appear to be excellent for the intended purpose.

The expected optical performance of these cameras is further illustrated with *polychromatic* spot diagrams, in Figure 154 for the 20-micron NIR camera, Figure 155 for the 18-micron NIR camera and Figure 156 for the VIS camera. All of these spot diagrams were calculated with the illumination patterns described above. The spots for the NIR cameras and for the VIS camera are enclosed in (3-pixel x 3-pixel) sampling boxes.

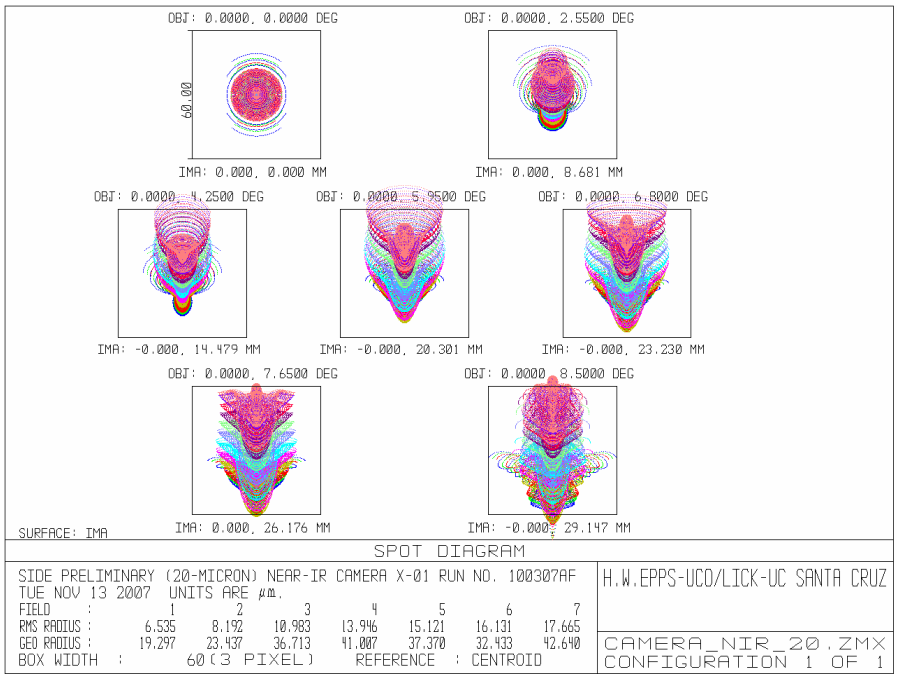

Figure 154. Spot diagram for the NIR camera (2k×2k @ 20 μm detector).

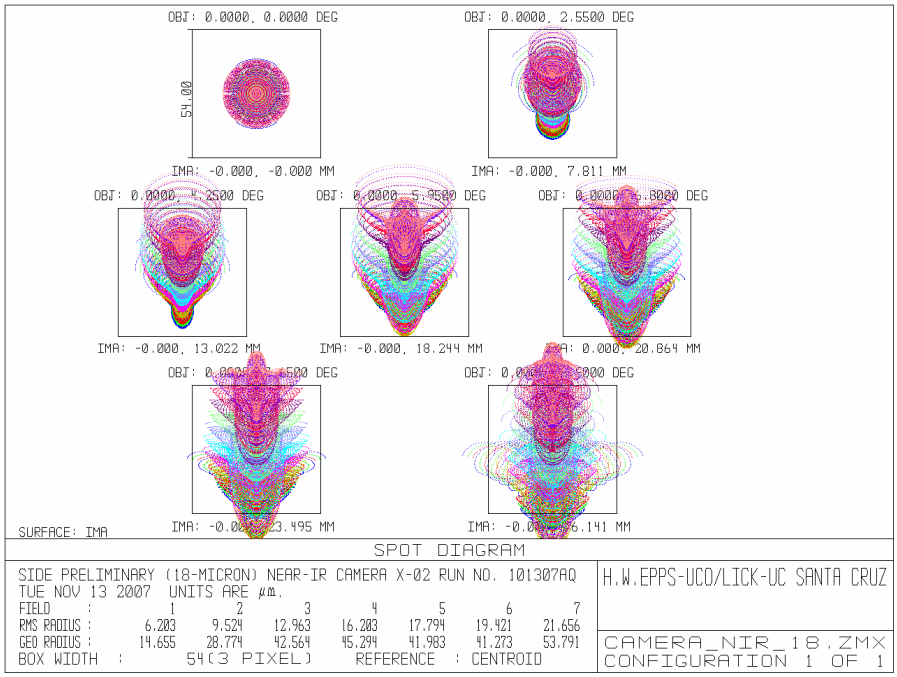

Figure 155. Spot diagram for the NIR camera (2k×2k @ 18 µm detector).

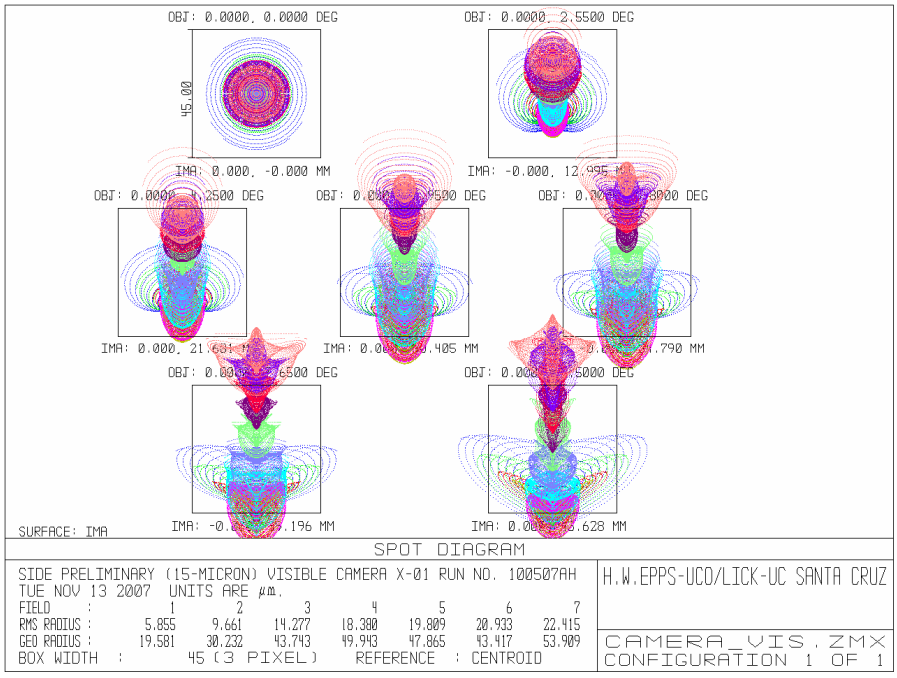

Figure 156. Spots diagram for the VIS camera.

These spot diagrams must be interpreted carefully because the *vertical* image smear is due to *lateral color*, which is *irrelevant* in cameras that will never be used for direct imaging! Thus, the viewer must compress the spots vertically in his/her mind to assess them in a way that is

more nearly appropriate to their intended use as spectroscopic-only cameras. The subjective point to be made is that indeed, virtually all of the energy will be included within the (3-pixel x 3-pixel) sampling boxes, such that the cameras will certainly be pixel-sampling limited in practice.

3.10.1.3.7 Image Quality

Spot diagrams for the VIS and NIR channels, including all the optical elements, are shown in Figure 157 and Figure 158 the spots are shown within a 70 µm diameter circle and 42 µm, representing the imaged fiber diameter on the VIS and NIR detectors.

Each diagram covers the full respective bandpass of the channel, and field points covering the full length of the respective slits.

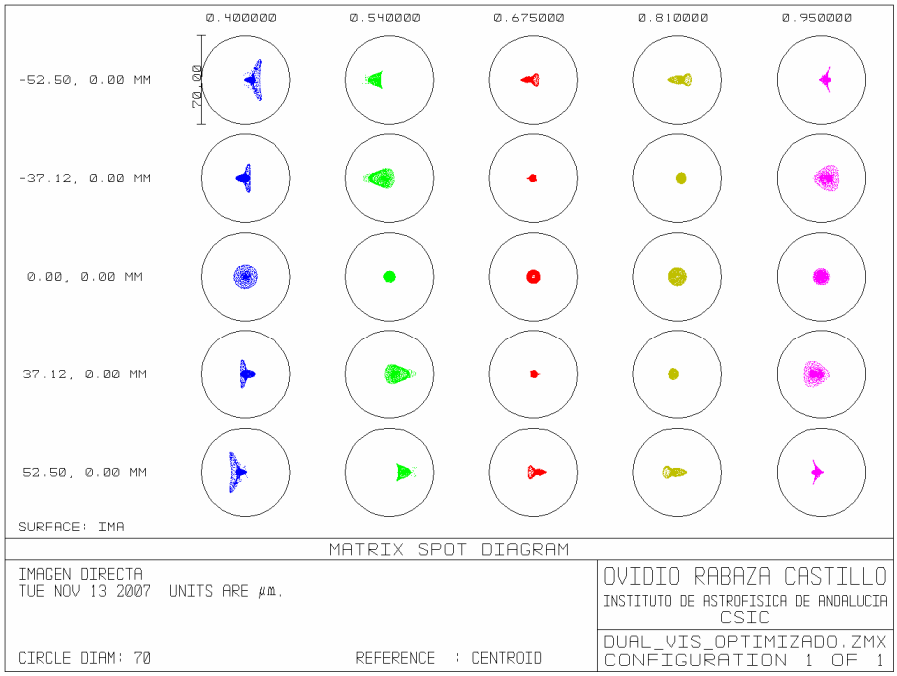

Figure 157. Spots diagrams for the VIS channel, including all the optical elements.

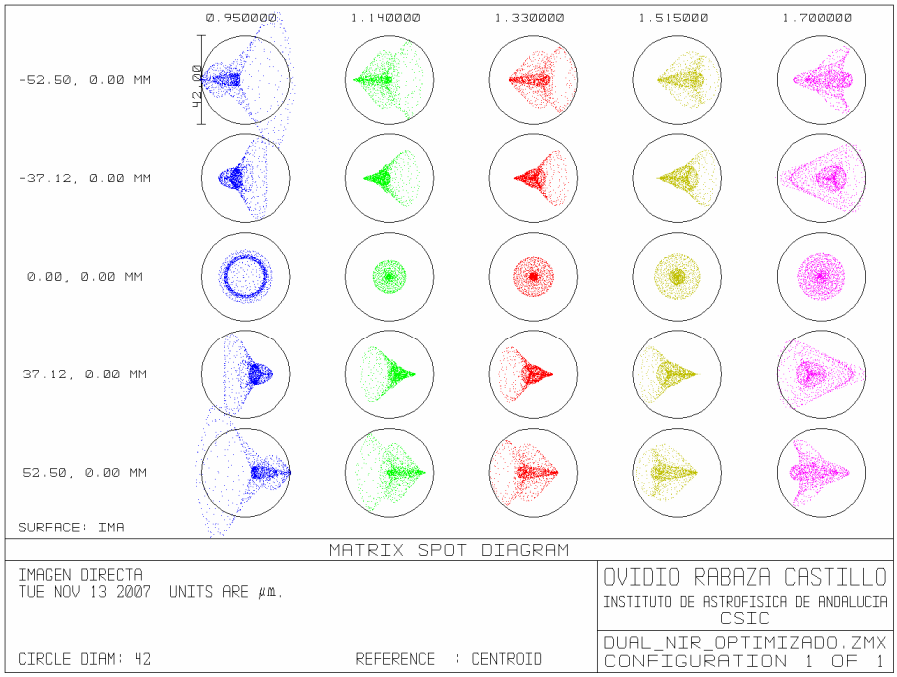

Figure 158. Spots diagrams for the NIR channel, including all the optical elements.

3.10.1.4 Mechanical Design

The Mechanical Design of the Dual VIS-NIR Spectrograph is driven by the double-arm optical layout. This design is based upon SDSS design. As its own name indicates (*VIS-NIR Spectrograph*), one of the big differences, compared to the SDSS design (see Figure 128), is that the two arms does not correspond to *VIS blue* and *VIS red* arms but to *VIS* (see Figure 129) and *NIR* (see Figure 130) arms. This feature implies a wider spectral range, which, together with resolution changes, make it necessary to use two *gratings wheels* which interchange the gratings with the required positioning precision.

The thermal analysis performed in Section 3.10.1.5.4 recommends, in order to maintain the instrumental thermal photon noise below the estimated minimum sky signal, a temperature of 240K, which needs to be applied to the whole spectrograph main elements including the VIS arm. Apart from taking this temperature into account for selecting mechanisms, motors, etc. that work properly at this operating conditions (e.g. gears fabricated in DuPont Vespel SP3, for self-lubrication, etc.), we must note that the Thermal Control System shall maintain the spectrograph room temperature at the constant temperature of 281.5K ± 1K (8.5ºC ± 1ºC). Thus, a thermal insulation of the Dual Spectrograph respect to the spectrograph room is needed in order to keep this 41.5K ± 1K temperature difference (and, at the same time, protect the optics from dust). The thermal enclosure can be the same for the 10 Dual spectrographs with all of them inside a small room at 240K, which will save insulating foam and also some space in walls thickness compared to individual spectrograph insulation (Vicente Sánchez, private communication).

This cooling must not create condensation of water vapor on the elements, for which we can actuate in three different ways, which will be studied during a later phase:

1. Vacuum chamber
2. Nitrogen atmosphere
3. Dry air atmosphere

Each system has its own advantages and disadvantages, as wall foam thickness if no vacuum is used, rigidity of the enclosure for supporting vacuum, cooling system etc.. All this will have to be taken into account during the design phases. For example at FMOS, dry chilled air generated outside the enclosure by a chiller and circulated inside the spectrograph (Tosh et al. 2004) but then, the air should be dry enough to avoid condensation.

An automatic LN_2 distribution system will be used for feeding VIS and NIR arms detectors.

SIDE Dual VIS-NIR Spectrograph Layout is shown in Figure 159.

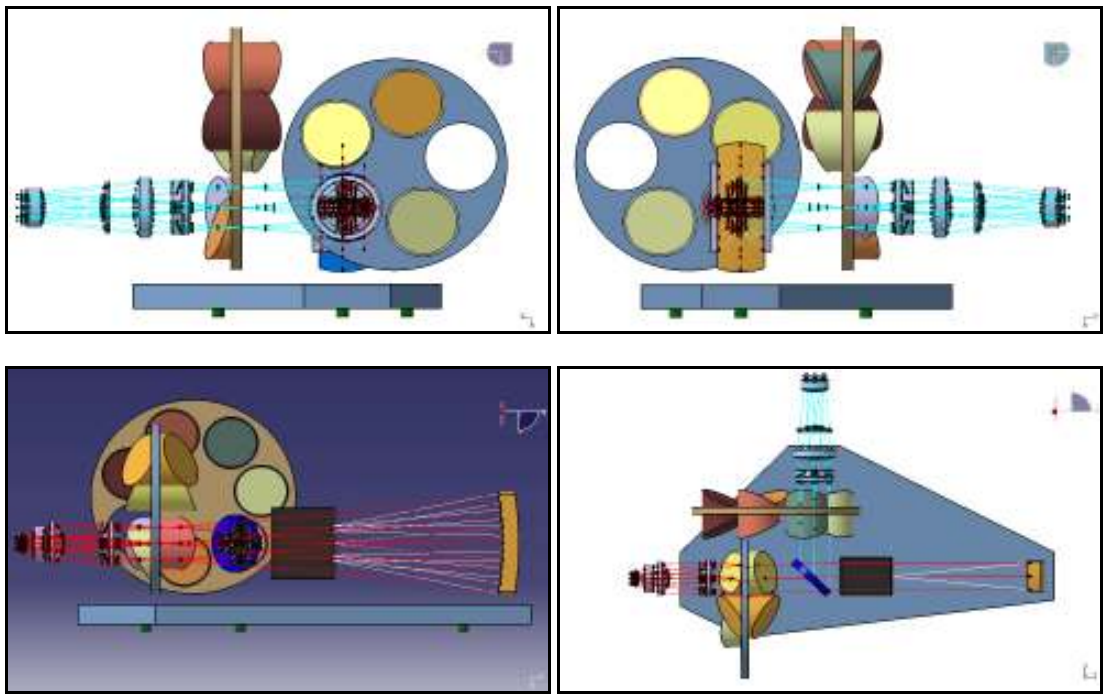

Figure 159 SIDE Dual VIS-NIR Spectrograph Strawman layout: left view (up-left), right view (up-right), front view (down-left) and plant view (down-right). Red rays show optical path for NIR arm. Blue rays show optical path for VIS arm.

The length of the Dual Spectrograph is determined by the NIR arm. Taking into account that the layout in Figure 159 is about 1,500 mm long and that some extra length must be added to this value (because of the NIR CCD dewar, which is attached right behind the field flattener lenses of the camera, and the collimator's mount are not included in the figure) in order to obtain the total length of the Dual Spectrograph, we can set an upper limit of less than 2,000 mm for this value. Again, the layout in Figure 159 is about 1,150 mm wide so, including the VIS CCD dewar and giving some extra space between the NIR gratings wheel and the Spectrograph's envelope, the maximum width of the Dual Spectrograph will be about 1,500

mm or at least it will have a protrusion of that size. Finally, we envision a height for this Spectrograph of about 1,000 mm.

All the above gives a total size of the instrument in length, width, and height of ≈ 2,000 mm x 1,500 mm x 1,000 mm, respectively. However, due to the restricted available width of the spectrograph room (8,000 mm) we must say that the spectrographs don't just occupy a rectangular area but an approximately t-shaped area (with the VIS arm CCD as a lateral appendix) in a plant view of the spectrograph room.

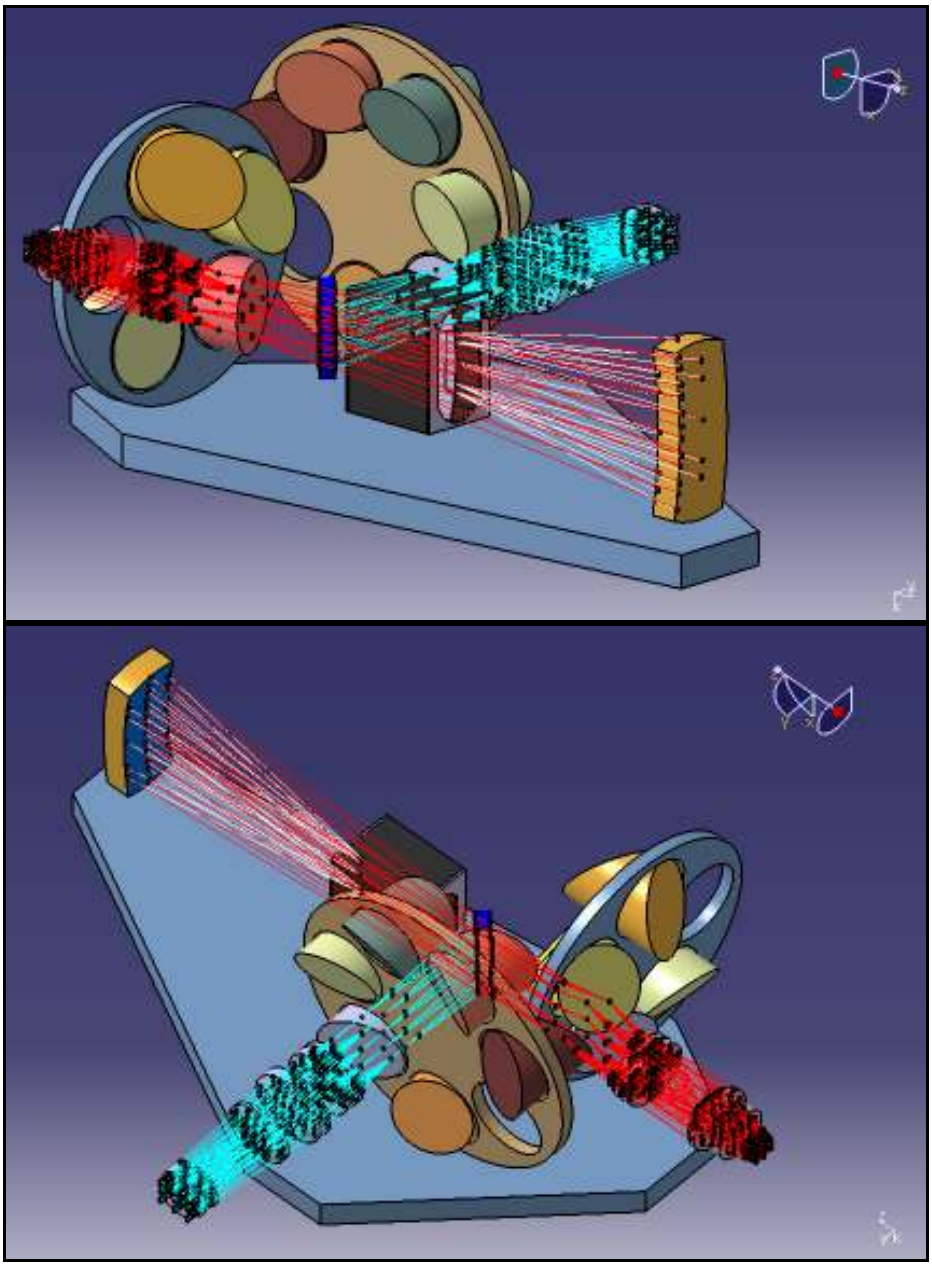

Figure 160 SIDE Dual VIS-NIR Spectrograph 3D Strawman layout: Slithead, Collimator, Beamsplitter, Gratings and Gratings Wheels, Cameras and Optical Bench Base. Red rays show optical path for NIR arm. Blue rays show optical path for VIS arm.

3.10.1.4.1 Optical Bench

All the optical elements will be mounted and aligned on the optical bench. Wherever possible, adjustments will be eliminated in favor of precision machined interfaces that provide accuracy and repeatability while reducing the number of mechanisms as much as possible.

The optical bench must support the spectrograph optics and optomechanics that will operate at 240K. For this reason, its contraction relative to the spectrograph room (at 281.5K ± 1K), as its cools down (to 240K), must be permitted by its support legs, which fix the optical bench to the spectrograph room and, at the same time, act as thermal insulation between the room and the instrument.

As first option, the optical bench base will be a honeycomb aluminum plate of about 60 mm thick lightened a 40% in weight, which results in a base of about 65 kg. Heavier and more expensive, but with near-zero CTE, Invar-surfaced optical bench bases will also be considered. Finite Elements Models must be carried out to analyze the rigidity of this base and of the rest of the optical bench but this values are given as a first approximation.

Also, more commercial but still highly customized optical tables can be acquired from companies as Newport, which design and manufacture equipment to stiffen optical work surfaces and isolate the system from vibration effects, and has a vast experience in optical tables and related vibration isolation products, in case we need anti-vibration feet chosen to match the vibration characteristics of the instrument as a whole.

3.10.1.4.2 Slithead

Fiber slit technology is well developed and has been used on numerous fiber spectrographs as 2dF, FLAMES, Hectospec and PMAS, where a number of small flat-ended slitlets containing a few fibers are mounted side by side to make up a large curved slit unit. There should be little generic risk associated with these units. Using slitlets instead of large monolithic slits presents the main advantages of easier machining and cheaper fiber replacement in case of fiber breakage.

SIDE slithead design is similar to the SDSS one (see Figure 161). The main difference is that our vertical plate, were the slitlets are mounted, will have two pseudoslits (double pseudoslit) mounted on it, and feeding the collimator. The double pseudoslit is a way to reduce the number of spectrographs. Although it is more difficult to build, it seems optically feasible in terms of vignetting and image quality deterioration due to off-center fibers.

Fibers come from the Nasmyth Platform and, after entering the spectrograph room, they are conducted through the external enclosure of the spectrograph to its slithead, curving the fibers gently so they don't get stressed in their housing: the vertical central plate of the pseudoslits. The fibers terminate along the curved edge of this plate, the radius of curvature being half the radius of the collimator. The axis of each fiber is normal to the collimator surface in front of it.

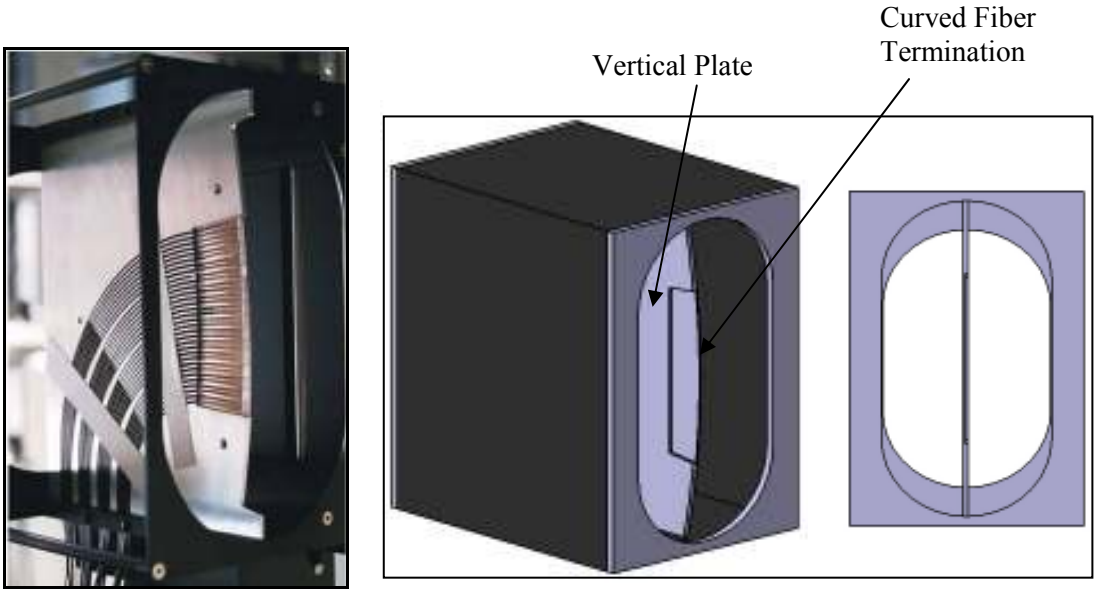

Figure 161 SDSS slithead showing the fiber strain relief (left). SIDE slithead assembly (right).

The different observing modes (MOS-IFU, mIFU and SIFU) are distributed to the spectrographs so that only one side of each double pseudoslit is used at a time. It is critical that the two halves of the pseudoslit are placed as close as possible one to the other. The double pseudoslit must be as narrow as possible to reduce its vignetting effect. This has been quantified to be not much higher than a single pseudoslit. The effect of each pseudoslit being slightly off-center has been studied and seems negligible in terms of image quality.

Dead fibers are used to reduce croos talk wherever necessary. Live fiber-dead fiber distribution depends on the observing modes implemented in the Dual spectrographs (see Section 3.9).

Independently of the different distributions, each Dual spectrograph will have a pseudoslit length of almost 105 mm (see Section 3.9.9).

The vertical plate spans from the top to the bottom of the slithead and vignettes a small portion of the beam. It provides strain relief for the fibers and the curved leading edge serves as a gage for mounting the fibers on the correct arc.

The slithead will be positioned on the optical bench with a kinematic mount (three tooling balls engaging a cone, a v-groove and a plane). The kinematic mount guarantees repeatable placement of the slithead in the spectrograph. While not strictly necessary for SIDE, this kinematic mount is robust, economical, and desirable should the unit have to be removed to repair a damaged fiber.

The slithead box shape is adapted so the beam coming from the collimator passes through two holes of same width but different height (the first one is bigger than the second one) so both of them fit the size of the beam minimizing the stray light and background (see Figure 159 and Figure 161).

3.10.1.4.3 Collimator

The collimator is a honeycomb lightweight mirror fabricated from a rectangular Hextek borosilicate blank with approximately the next dimensions: 100 mm wide, 310 mm tall, and 60 mm thick. See Figure 162.

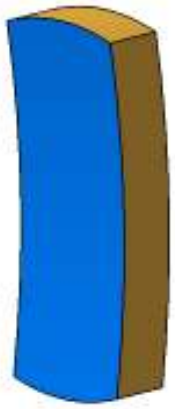

Figure 162 Collimator dimensions (100 x 310 x 60 mm) at SIDE Dual VIS-NIR spectrograph.

As the rest of the optical elements, the collimator will be permanently at 240K so it will only need one-time focus adjustments that will be performed at room temperature and verified through some cool down cycles to check that the spectrograph is correctly aligned at operation temperature.

In the rear part of the mirror, three micrometer screws fixed to the mounting structure define the axial position of the collimator. They also give a passive (manual) control in tip, tilt (for spatial and spectral adjustments) and focus. One of these mounting points will be coplanar with the slit at all times and its movement is allowed in the vertical direction through a linear slide to allow differential contraction of the mirror and its mounting structure without stressing the collimator. This contraction is permitted at each of the other two mounting points through a linear slide and a rotary bearing providing self alignment.

In the vertical direction, this tall collimator can be *simply supported* at the lower side on a flat rigid plate[1] with flexures (supporting the mirror at its front and rear sides) that have sufficient compliance to adapt themselves to the shape of the mirror to avoid stressing it. The rigid plate is suspended from two points on the collimator mounting structure. These two points are adjustable to allow control over the vertical position of the mirror.

Other possible solution for the vertical support is a membrane flexure (see Figure 163) at the very center of the back surface of the collimator that constrains it vertically but permits tip, tilt and focus adjustments. The fixed edge of the membrane flexure would be attached to the collimator mounting structure. The movable inner part of the membrane flexure should be attached to the collimator in a way that not introduce significant stress into it due to thermal differential contractions.

[1] The surfaces of the supporting plate and the lower side of the collimator must fit together. Thus, a flat-bottomed collimator should be requested (instead of a spherical-bottomed one as in Figure 162).

Figure 163 Membrane flexure used at SDSS for vertical support of the collimator.

Also, following the philosophy of eliminating the maximum possible adjustments in favor of precision machined interfaces that provide accuracy and repeatability but reducing the number of mechanisms as much as possible, the whole collimator could be supported by a kinematic mount with the corresponding three shims for adjusting the position of the collimator.

In the next stage of the project, this solutions will be studied in deeper detail. Finite Element Analysis will help to decide which is the most appropriate one.

3.10.1.4.4 Hartmann Shutter / Doors

If needed, a Hartmann test device should be provided, for quick focus determination. With this test, the out-of-focus condition is quantified via software with the detectors and the axial position of the collimator can be corrected.

At present, foreseen potential locations and mechanisms types for this component are:

- Two doors just in front of the collimator.
- Two sliding shutters downstream of the slithead, which could also be used for controlling the exposure time of the detector (CCD) at the VIS arm (see 3.10.1.4.8). Each of the two shutters may be deployed individually to perform the Hartmann test.

3.10.1.4.5 Dichroic

TBD. The mount of this optical element will not present major difficulties compared to the rest of the optomechanics of the spectrograph.

3.10.1.4.6 Order blocking filters

The optomechanics of the order blocking filters is TBD as this elements have not been defined yet. These filters will be located between dichroic and gratings.

3.10.1.4.7 Gratings Wheels

We need several gratings in each arm for changing the resolution. In principle, to cover all the spectral range from 0.4 μm to 1.7 μm we will use a total of 10 disperser elements (3 grisms and 7 VPHs), although, depending of the spectral ranges of interest maybe the number of disperser elements will be less. These gratings will be mounted onto two wheels, one for the NIR arm and one for the VIS arm (see). Each wheel will have an empty position so we finally have a 5 positions wheel at the NIR arm and a 7 positions wheel at the VIS arm.

The wheels will have a steel core mounted on preloaded bearings, backlash-free toothing and gears and a flexure-type retaining system for giving the positioning precision required for the gratings. The wheels will be mounted onto the optical bench base.

When the final decision is made on the gratings shape and size, their mounts will be designed accordingly. The size and thickness of the wheels will be set with the help of Finite Elements Models. Figure 163 shows 25 mm thick gratings wheels:

- VIS wheel: 7 (6 gratings +1) positions; 600 mm diameter
- NIR wheel: 5 (4 gratings +1) positions; 523 mm diameter

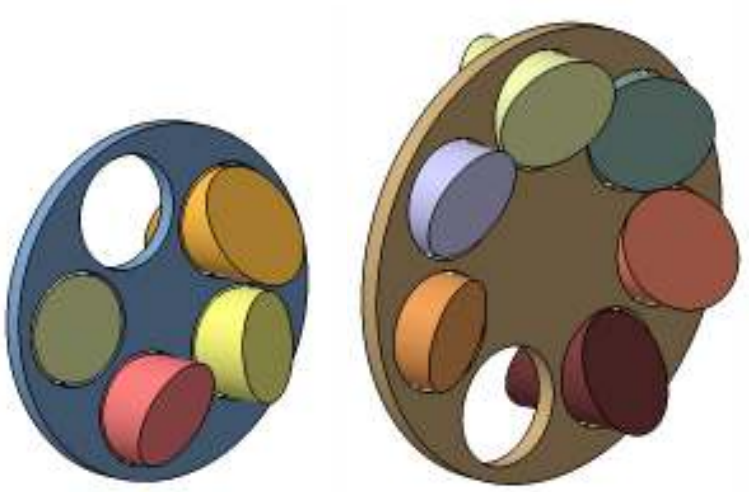

Figure 164 Strawman layout of the NIR (left) and VIS (right) gratings wheels.

3.10.1.4.8 VIS arm Shutter

The VIS arm requires a shutter for controlling the exposure time of the CCD.

A sliding shutter type mechanism has been foreseen. At the moment, two potential locations have been considered:

- At the rear of the slithead (see 3.10.1.4.4).
- Right before the camera or between two barrels of the camera.

The sliding shutter must be light-sealed around the edges to prevent light leaks. The door(s) slide(s) in the slots of a picture-frame guide, which has a cut-out matched to the beam profile.

3.10.1.4.9 Camera Optomechanics

Both cameras must have a focusing mechanism to match the gratings selected for a specific observing program.

The mechanisms required can be purchased from companies such as Owis.

3.10.1.4.10 References

Tosh, I. et al. 2004, "The current status of the UK-FMOS spectrograph", Proc. SPIE, 5492, 1362-1370.
http://www.newport.com/Optical-Tables-and-Vibration-Control/137658/1033/catalog.aspx
http://idg.pha.jhu.edu/optomech.html
http://www.jhu.edu/~sdss/Spectrographs/Drawings/index.html
http://www.owis-staufen.com/index_en.html

3.10.1.5 Thermal analysis for the Dual VIS-NIR spectrograph

Using RAL's experience from a similar study on the FMOS spectrograph, an optical model of the instrument, based on the specifications and documents already supplied by IAA[1], is developed. Additionally, the model includes a representative camera along with predicted detector performance in-band and out-of-band beyond 1.7 μm. With dedicated Zemax and ASAP models, investigations are channeled towards the effect on noise and background levels as a function of possible instrument and sub-assembly operating temperatures. The different sections below report on the general approach and obtained results alongside drawn initial recommendations.

3.10.1.5.1 Radiometric Considerations Based on Detector and General Environment Properties

The baseline concept for the SIDE IR arm relies on a 2kx2k 18 μm pixel pitch MCT IR focal plane array (FPA) as detector. Properties of typical recent MCT IR FPAs from Rockwell (HAWAI 2RG type array) and Raytheon (VIRGO type array) have been investigated and reported in Brown (2007). Here, we take as baseline the Rockwell one as it presents best in-band QE performances. The in-band QE performances, reaching ~90% flat in J and H bands without AR coating are displayed in Figure 165 below.

For typical expected thermal background source with temperature between 100K and 300K, the radiant emission will increase exponentially with wavelength (Wien region) and therefore largest radiance can be expected out-of-band (oob) beyond the nominal 1.7 μm cut-off in the notorious K band. To account for the oob contribution and its associated detection efficiency by the array, the oob QE data are fitted with an exponential model.

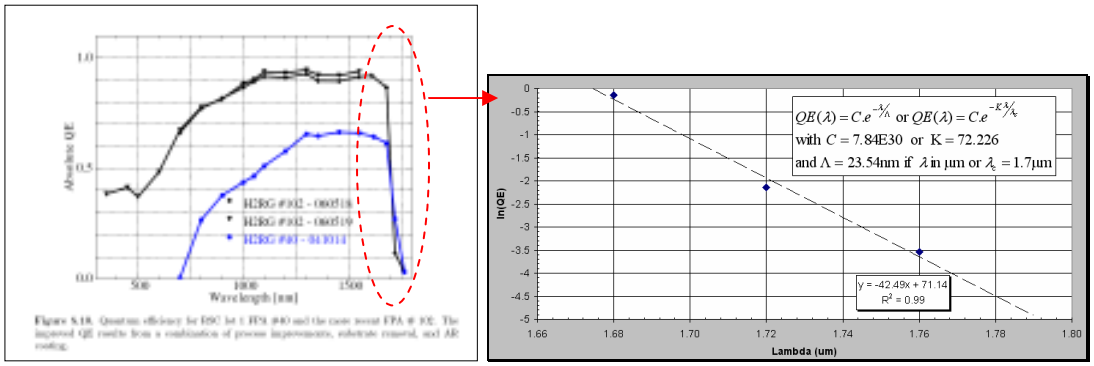

Figure 165. Measured QE on recent HAWAI 2RG type IR FPA from RD1 (left), and exponential model fit of the QE spectral variations beyond the 1.7 μm cut-off (right).

[1] This analysis is based on the initially received conceptual drawing and values. A supplementary Zemax file of the IR arm optical design received later is not used here as the models and analysis were already underway, but the difference in camera design would not have significant impact on the overall stray radiometric estimated levels, which are more dependent on geometry of extra elements such as baffle, enclosure, dichroics, etc. The thermal stray sources, in-field or out-of-field, ahead of the slit (i.e. at fiber input) are not considered here, although the in-field ones are expected to be comparatively very low (low surface emissivity, dispersed spectrum like the sky source as they are inside the FoV). The out-of-field case is briefly investigated in Annex E.

Note that the shortwave oob is irrelevant because completely negligible in terms of thermal stray for the expected range of temperature and therefore is not discussed further in this report.

In a general surrounding environment of effective emissivity ε at temperature T, the total detected signal, in W per pixel, can be expressed as:

$$s_{total} = \varepsilon.A_{pixel}.\Omega.\int QE(\lambda).L_{BB}(T,\lambda).d\lambda \text{ with } L_{BB}(T,\lambda) = \frac{2.h.c^2}{\lambda^5.(e^{hc/\lambda kT}-1)} \approx \frac{2h.c^2}{\lambda^5}.e^{-hc/\lambda kT}$$

assuming no or very low spectral dependence of the source emissivity. It can be splitted into in-band and out-of-band contribution as:

$$s_{total} = s_{in-band} + s_{obb} = \varepsilon.A_{pixel}.\Omega.\left(QE_{in-band}.\int_{\lambda} L_{BB}(T,\lambda).d\lambda + \int_{\lambda>\lambda_c} QE_{oob}(\lambda)L_{BB}(T,\lambda).d\lambda\right)$$

where the in-band QE is taken as per above data (see Figure 165) as spectrally flat and the spectral variations of oob QE beyond cut-off wavelength λ_c=1.7 µm is given by the exponential model above. For a given pixel, it is interesting to look at the ratio of the in-band to oob signal, displayed below.

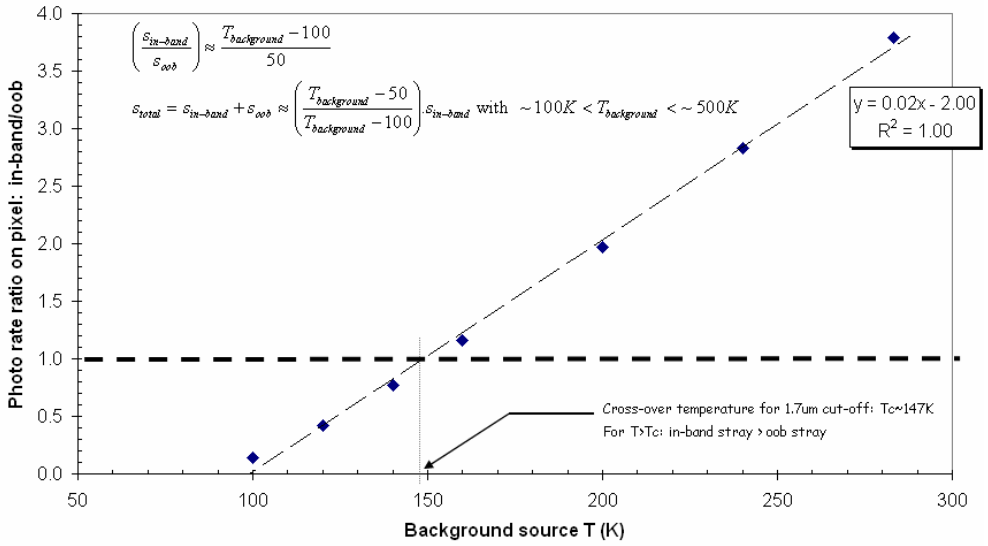

Figure 166. Ratio stray in-band over oob signals for element at different typical temperatures for a given FPA pixel.

Only for T< ~150K the oob part dominates (ratio < 1) but the exponential dependence of the source radiance on its temperature is such that the absolute value of the oob signal for T<150K is negligible so this is not relevant. For T>150K, the ratio remains >1 and increase linearly, reaching a level at ambient temperature such that the oob contribution is only ~20% of the total signal. This figure will vary with sharper or less sharp detector spectral response cut-off response. The linear fit to the ratio - valid in the range 100K to ~500K so well within the range of expected spectrograph elements temperatures -, then re-written in term of total signal, provides an easy empirical relation, with simple dependence on the source

temperature, linking the total detected radiant stray signal to the in-band one. The latter one is easier to evaluate due to flat in-band QE here and existing analytic expression to Planck integral in the Wien region. The fit on the ratio implicitly contains the FPA QE cut-off sharpness.

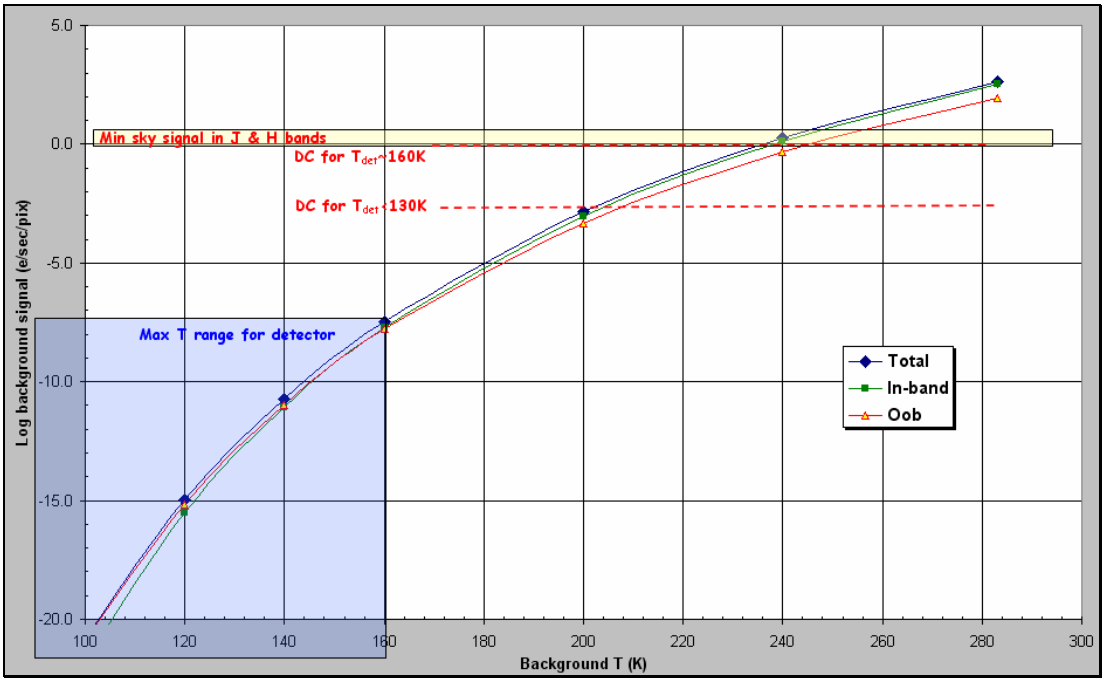

Figure 167. thermal stray signal variations, in log scale, with background temperature; additionally dark currents levels for different detector temperature and minimal in-band sky signal are also displayed.

In Figure 167 above, the log scale variation of the stray signal and discussed-above sub-contributors vs background temperature is given in the worst-case scenario i.e. isothermal source with $\varepsilon=1$ and $\Omega=\pi$. In practice, such value can be reached if for example the SIDE IR arm geometry is sufficiently closed and compact like a cavity in front of the FPA.

To put the values in context, comparison is made with dark current (DC) values for different detector temperatures. These, reproduced below, are also from RD1 for the same IR FPA as discussed above. The temperature variation follows well the theoretical exponential model with gap linked to the λ_c above ~130K with approximately a factor x10 increase per 10K. Below 130K, the DC remains fairly stuck to a floor level around a few 10^{-3} e/sec/pix.

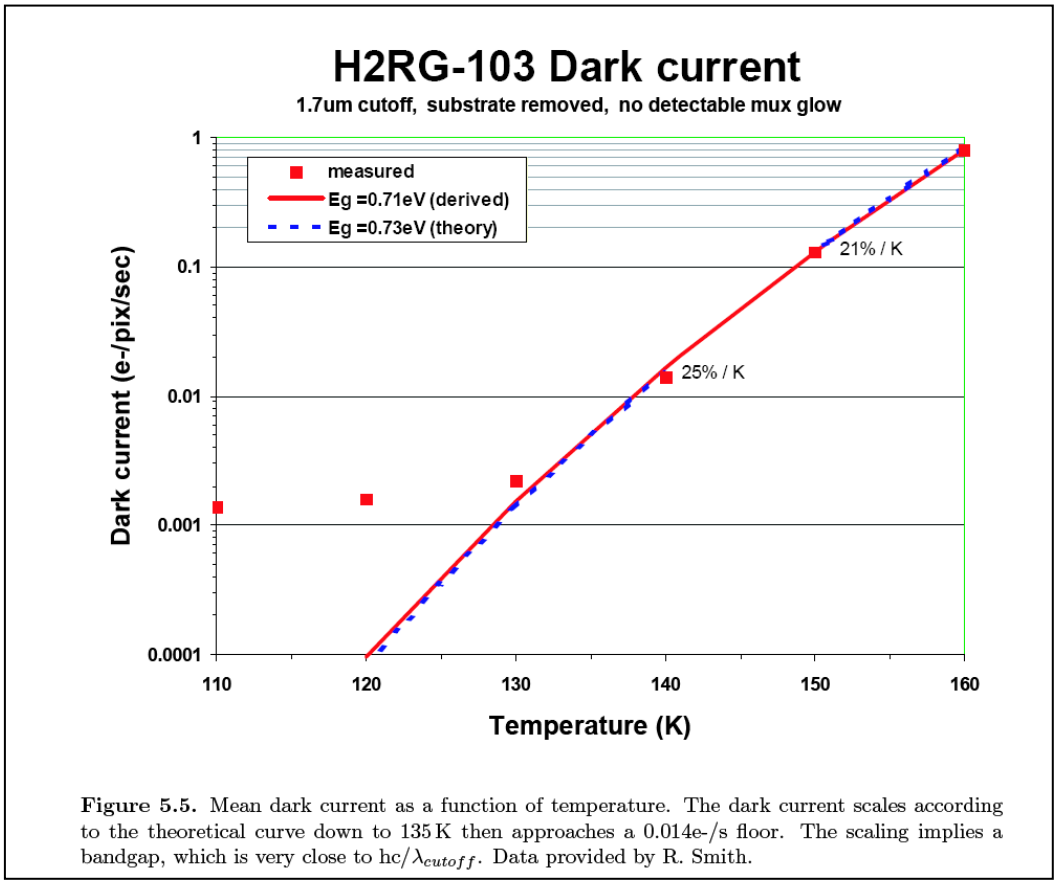

Figure 5.5. Mean dark current as a function of temperature. The dark current scales according to the theoretical curve down to 135 K then approaches a 0.014e-/s floor. The scaling implies a bandgap, which is very close to hc/λ_{cutoff}. Data provided by R. Smith.

Figure 168. Dark current variation with detector temperature from recent HAWAI 2RG type IR FPA (from RD1).

In Figure 167 is also reported some range estimates for the minimum sky level signal: they are taken from Eikenberry (2007), see details in Annex C which also contains the value for the FMOS case. The latter ones appear lower but FMOS is more complex (more elements) and includes a hardware-based OH-suppression so transmission may be lower on top of the difference linked to the different respective observatory location. Also depending on the spectral resolution mode, the minimum sky signal, between 0.95 and 1.7 μm, is here taken as between 0.66 and 8e/sec/pix so (log) average around 2.3e/sec/pix.

From these, we can already draw a few preliminary conclusions:

- It does not look interesting to have a FPA at 160K or warmer as in that case the DC will be of same order as the minimum sky signal and to minimise impact on science it is desirable to minimise the total instrumental photon noise (sum of the DC and detected instrument stray background);

- One can notice that if the SIDE IR arm assumed-closed cavity is maintained at the same temperature as the detector for any detector temperature <160K, the thermal background is negligible;

- Considering that there is no improvement in the DC by cooling the detector below to 130K or below, it is then unnecessary to maintain the SIDE IR arm cavity at temperature lower than 200K;

- So preferred operating temperature for the FPA is around 140-150K with associated DC level in the range of 0.02 to 0.2e/sec/pix i.e. 1 to 2 orders of magnitude lower than minimum expected sky level;

- It is then desirable to try to achieve similar level for the stray thermal background signal: from Figure 167, it would mean that the required spectrograph background temperature to be in the region of 230-240K max; this is in-line with the conclusions of negligible loss of science sensitivity across the full spectral band for -40degC derived in RD2; for $T_{background}$>250K, the dominant photon noise contributor is the thermal background and at ambient spectrograph condition, the sky level become even very small i.e. a few orders of magnitude, below it;

- Note that the presence of a blocking optical filter does not appear necessary: it can improve the sharpness of the detector cut-off (already quite sharp) without bringing itself new direct in-field emission but only if it is itself at a temperature close to the FPA one therefore in close physical proximity and the in-band contribution to total thermal stray is already dominant so that the oob hardly requires further reduction by extra element.

To improve on this first order approach, the next section is devoted to a more detailed modelling of the stray thermal background based on the modelled conceptual optical layout of the SIDE IR arm spectrograph with added basic representative enclosing elements at different temperatures.

3.10.1.5.2 Bottom-up approach based on spectrograph conceptual design

3.10.1.5.2.1 Optical model

A series of Zemax models have been developed in order to provide basic optical designs of the different modes for the SIDE IR arm, so as to provide representative geometry and dispersing capability when compared to the nominal baseline spectrograph concept.

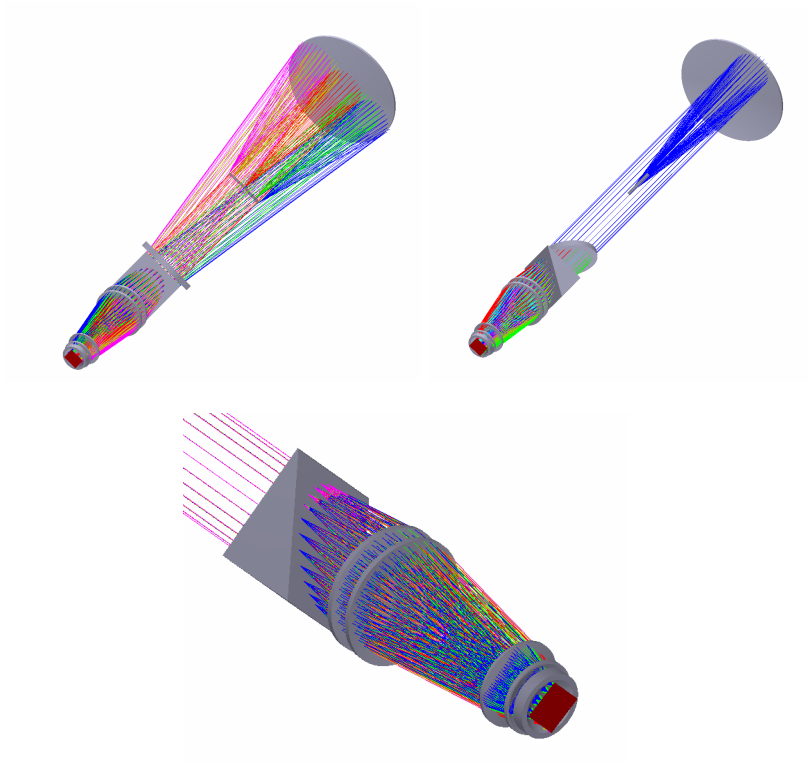

Figure 169. 3D view of the Zemax model optical layout of SIDE IR arm in lower resolution/full band mode. Upper left: global view, rays colored by fields. Upper right: after 90deg axial rotation, rays are now colored by wavelengths. Bottom: zoom on the grism and camera lens elements up to FPA.

- **Front elements (pre-grism):**

The slit for the fiber input to spectrograph is taken as 105mm in height and taken as following a curved shape of ROC=500mm. This forms the entrance object surface of the spectrograph. Fibers are taken as radiating in a solid angle given by NA=0.1 as per the provided "*col_dual.zmx*" file. A ROC=1m spherical mirror (~310mm diameter) is then used as collimator, delivering a pupil (not flat, but taken as location of stop) of diameter ~100mm at ~1m. Note that if with circular aperture, the collimator is widely under-illuminated on the lateral sides (typically only ~105mm out-of the ~310mm diameter are used in the transverse direction) and that all fields are vignetted by the slit and its support (not described) as the collimator is here on-axis, although this makes the whole spectrograph more compact than in the FMOS off-axis case.

To split the VIS and IR arms, a dichroic at 45deg incidence is used. Due to large tilt (which is not good for polarisation), and its position ahead of the pupil plane (left for the grism), its clear aperture diameter has to be ~150mm so here a minimum ratio of 1:10 is applied to define its thickness i.e. 15mm. Assuming the dichroic coating is applied to the front surface, the dichroic substrate is chosen to be a broadband IR transmissive glass such as fused silica. Optimisation towards lower dispersion NIR glass can be eventually

thought. Note that the substrate optical thickness-induced lateral shift is taken into account when positioning the next components

- **Grism(s):**

The groove densities and the baseline grism materials as given in the concept description note have been kept. For all IR sub-bands, the respective grism is used at order m=+1. Potential deviation between the not given refractive indices of the grism material and the ones actually used in the Zemax models is compensated by adjusting slightly the grism apex angle in order to recover zero angular deviation at band central wavelength for each mode/band; as seen in summary table below, this is limited to ~10arcmin differences max in every case.

Band / mode	0.947-1.731 / R=1500	0.95-1.18 / R=4000	1.1-1.369 / R=4000	0.95-1.18 / R=4000
Central wavelength	1.33 μm	1.065 μm	1.236 μm	1.535 μm
Grism material	Fused Silica	SF58	LASF35	LASF35
Groove density	210 lines/mm	600 lines/mm	550 lines/mm	441 lines/mm
Nominal apex angle	38.71322deg	46.812deg	43.857deg	43.993deg
Used apex angle	38.54deg	46.64deg	43.704deg	43.84deg

Table 64. Summary of the gratings initially selected.

Note that some clearance (a few cm typically) before and after the grism have been voluntary implemented to account for the fact that the mode/band change may be performed via rotating wheel (in which the grisms are mounted at different positions for example).

- **Back elements (post-grating):**

It is assumed that the focusing camera has to be common to all modes and is based on refractive elements for compactness, and therefore needs to be intrinsically broadband. A design based on all-silica spherical lens camera is used, based on 2 separate lens groups. This follows the approach of FMOS camera, although here at preliminary stage, it is seen as more practical to use a single standard well-known glass such as fused silica when the temperature of the different elements is not known or varied parametrically for the need of the analysis.

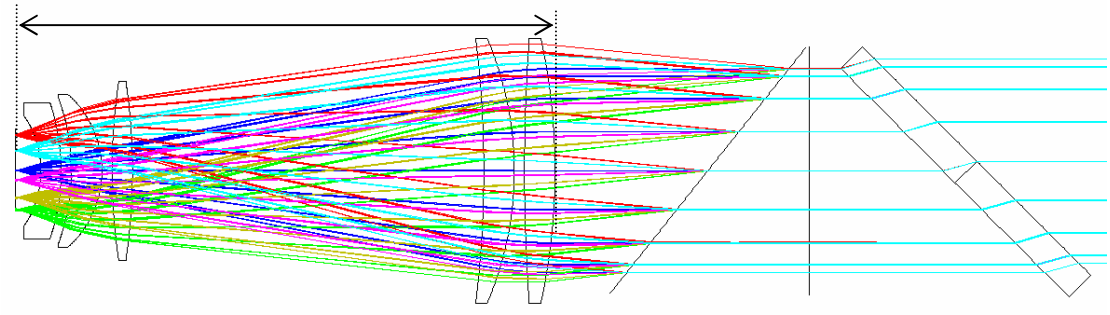

Figure 170. Side view of the multi-wavelength optical paths after the VIS/IR separator dichroic.

It is not optimised for image quality but meant to provide representative general focusing and imaging capabilities under the following constraints: in the spatial direction it has to cope with +/-6deg FOV from the slit length. For baseline FPA with 36.86mm side length (from 2kx2k & 18 µm pixel), the focal length needs to be ~175mm for a ~100mm pupil diameter (so ~f/1.75 camera). In the spectral direction, the grism dispersion is made such that in the respective bands/modes the spectral spread is +/-6deg as well, to match the square FPA.

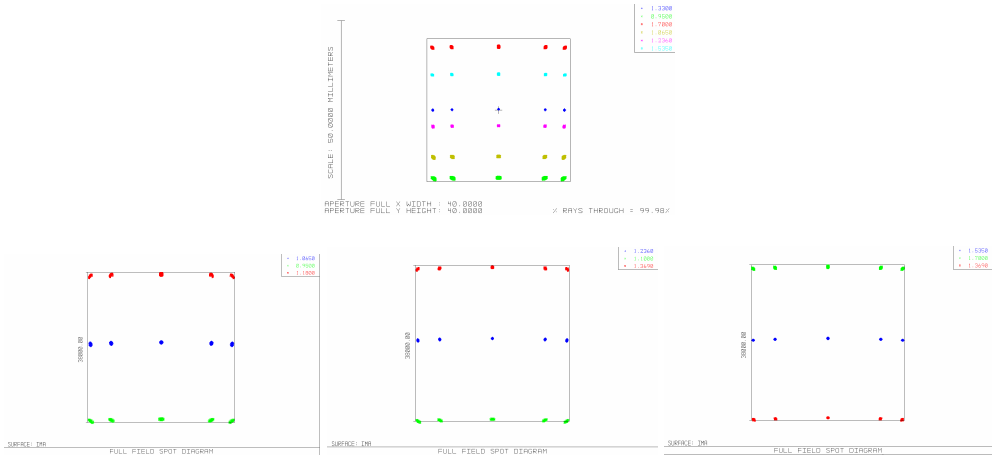

Figure 171. Illustration of the focal plane geometric imaging performances of the design in the Zemax models for full field size (slit full length) and respective spectral bands. Top: full IR band. Bottom: from left to right, the Y, J and H band cases respectively.

3.10.1.5.2.2 Straylight model

Translated from the Zemax models discussed above, an ASAP model of the SIDE IR arm is then built. In addition to the baseline sequential optical model, basic realistic elements standing for baffles or enclosure surrounding optics have been included. For the purpose of the thermal analysis, 8 separate zones (from A to H) have been identified and are schematically displayed below.

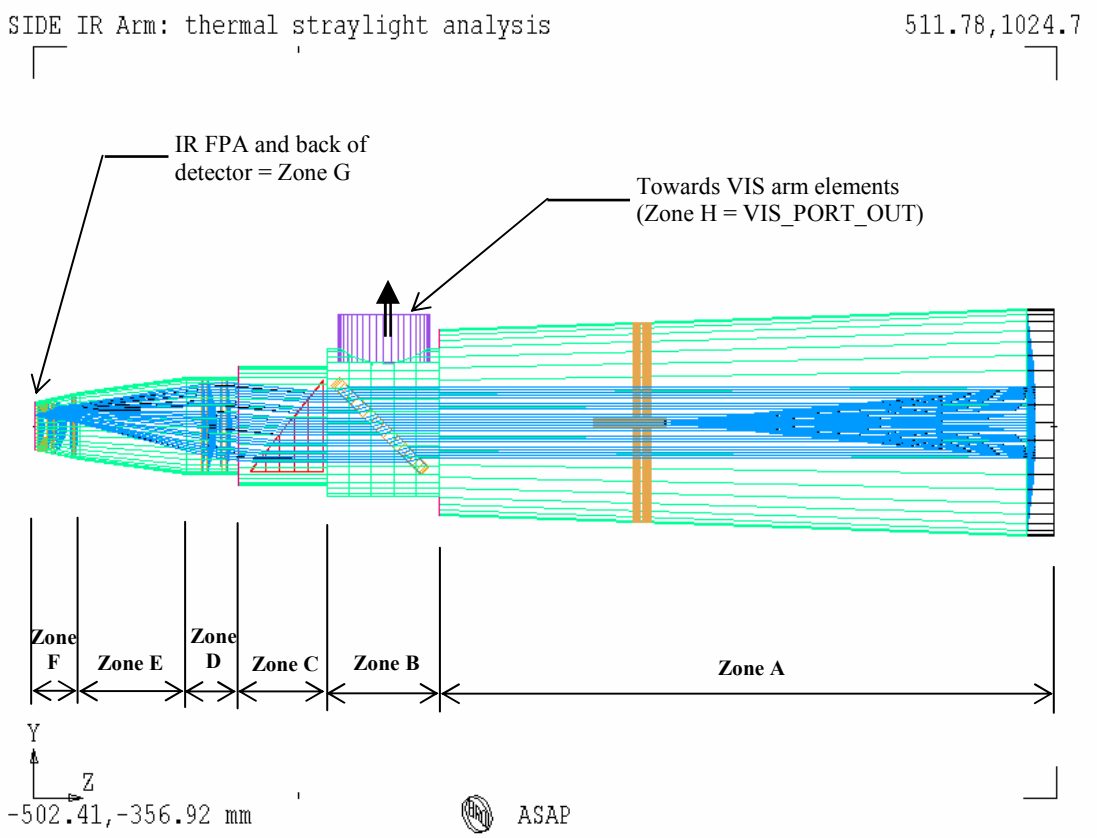

Figure 172. Side view for the ASAP model including the optics from the Zemax optical model and additional surface features standing for basic mechanical elements in proximity of the spectrograph optical elements.

In more details:

- Zone A contains the collimating mirror and the entrance slit. The slit has been expanded into a structure with a real volume for the fiber holder and general attachment to surrounding enclosure, with minimum vignetting so orthogonal to the slit length direction;
- Zone B is at the separation VIS/IR channels with the dichroic with a dedicated lateral tubular cur-out and enclosure representing the optical port interface to the VIS arm and ended with a surface defining zone H;
- Zone C is for the grism; zone D, E and F are defined by the location of the camera optical elements (i.e. respectively front, middle and back ones) with associated circular mount/baffle around;
- Zone G is for the detector and its support plate; this is separate because expected to be the coldest part of the IR arm in any case.

Verification of the translation into ASAP is done by checking location of optical components and verifying that similar focal plane spot diagrams are obtained at different in-band

wavelengths and field positions in forward raytrace mode. The ASAP model is then used in general non-sequential approach (specific Monte-Carlo mode) starting isotropically from the detector (hence "backward" raytrace) in order to retrieve the View Factors (VF), from the FPA, of the different opto-mechanical elements of the spectrograph represented by surfaces in different zones of the model.

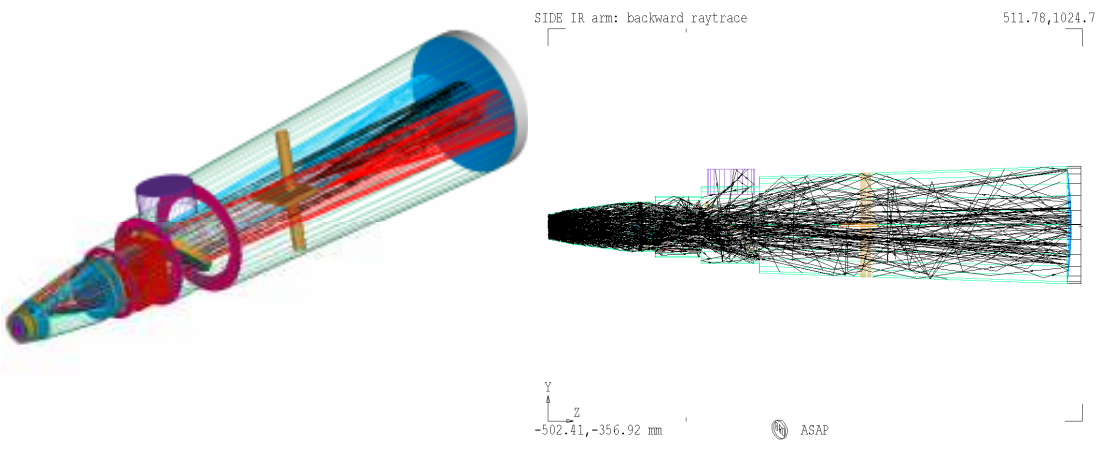

Figure 173. 3D view of the SIDE IR arm ASAP model with forward raytrace from 3 field positions at the slit (left) and side view with backward raytrace (partial; only <0.1% of rays are actually shown) from the detector (right)

Different surface properties have been implemented1: average in-band reflection coefficient at normal incidence of 97% for the collimating mirror, 5% for the dichroic, and 1% per lens surface or other AR coated in-field glass elements (e.g. dichroic back surface). The grism has a baseline 70% in-band efficiency in the m=+1 main order and the remaining is spread equally between the nearby orders (0 and +2). Supplementary angular spreading at optical elements surface is taken into account by a Total Integrated Scatter (TIS) of 0.5% for each surface typical of standard clean, low micro-roughness/good polish optical surface at these wavelengths. The lens edge surfaces are assumed to be in contact with mount and are described in the same way as all the inner surface of the enclosure sections with a 50% reflective surface with large Lambertian value of 50% as they as likely to be coarse finish (i.e. rough wrt any in-band wavelength) and therefore need to be modelled as diffusing metal surface. Previous tests with the FMOS model (see Ferlet 2003) with fully reflective and fully absorbing inner enclosure surfaces indicated that the worst case is not for the black case. This is due to the closed geometry and multiple internal reflections can cause an apparent increase of the enclosure effective emissivity. In practice, it is also not always desirable to blacken large surface area with special paint that can outgas if used under the necessary vacuum for cold or cryogenic environment. The spectral variations of these surface properties is not known precisely but assumed low and therefore neglected here. Note that multiple (ghost) reflections between dominantly transmissive component surfaces is also taken into account.

[1] Values used in the model here follows from values used in other instruments such as VLT-KMOS and VISTA IRCAM.

Sets of simulations test runs have been performed. First with lower number of rays (N~2.10^5 typically), but at different wavelengths, to assess the possible spectral variations of the VFs. And then, at a fixed wavelength, test of stability of the resulting VFs when the number of source rays was varied as a check of the simulation statistical uncertainty (approximately expected to vary in ~$1/\sqrt{N}$). Detailed output results can be found in Annex D. Good stability (very low standard deviations for all VFs) has been found for N equal to a few 10^6 typically so final run is done with N_o=5.10^6. From 0.95 µm to 1.7 µm, the 12 surfaces or elements the most contributing potentially (i.e. with highest VFs, total representing 90%) are all the same and in the same order with relative 1σ variation around 1-2% max typically. Expectedly, the grating part of the grism appears to have the strongest spectral dependence (due to trapping by TIR, grating structure resonance at specific incidence,…) but around an average VF level of ~1% so impact is very limited. Interestingly, the efficiency of the path towards the zone H, i.e. VIS arm, is also strongly varying relatively a lot with in-band wavelength around and average level of VF~1.5%. But it turns out for this particular element that lowest VF level are obtained for shortest wavelength which are not contributing to thermal background (exponential decrease of the radiance with λ in the Wien region for a given temperature) and that these spectral relative variations get reduced once the ray statistics is increased. As a bottom line, a single model Monte-Carlo run at central in-band wavelength and with No initial is found sufficiently representative to derive an accurate baseline of view factors distribution towards the different elements of the spectrograph for its different modes.

3.10.1.5.2.3 Results

The thermal background signal per pixel at detector from the different surface elements of emissivity ε_i at respective temperature T_i is then retrieved via:

$$s_{total} = \sum_i \varepsilon_i . A_{pixel} . \Omega_i . \int QE(\lambda) . L_{BB}(T_i, \lambda) . d\lambda$$

Using the link between VF and solid angle, i.e. Ω_i=π.VF_i, and the found relation between total and in-band radiance discussed in section 3.10.1.5.1, we can re-write it into:

$$s_{total} = \frac{A_{pixel} . \pi . QE_{in-band}}{\left(\frac{hc}{<\lambda>} \right)} \sum_i \varepsilon_i . VF_i . K(T_i) . \int_{\Delta\lambda} L_{BB}(T_i, \lambda) . d\lambda$$

where $K(T_i)$=(T_i-50)/(T_i-100) from section 3.10.1.5.1 and Δλ is defined by the minimum IR in-band wavelength of 0.95 µm to the cut-off λ_c=1.7 µm. Also a final normalisation by $hc/<\lambda>$ is used for the conversion of flux in W into signal in e/sec, $<\lambda>$ being the average in-band wavelength.

Distribution of view factors is obtained from the results of the backward raytrace in the straylight model. Distribution of the element surface emissivity is taken for consistency from the applied surface properties in the same model (see section 3.10.1.5.2.2). The details of the stray signal level retrieval is then given below for different cases. Each case is based on different temperature distribution for the spectrograph elements. The thermo-mechanical design not being known, the different temperature are simply attached to spectrograph zones

as defined in the straylight model rather than on a per surface element basis like the VF_i or ε_i. On top of the breakdown of the total instrumental thermal background signal retrieval, comparison is made with minimum sky signal and detector DC for a set detector temperature of T_{det}=140K following discussion in section 3.10.1.5.1. An equivalent effective emissivity is also given by ratio of the reconstructed thermal signal detected radiance over the radiance of a single blackbody at the highest implemented temperature for each case. Finally indicative estimates of the total read noise for different, assumed typical, exposure times[1].

- **CASE 1:** The VIS arm is at ambient temperature (taken as 10degC), the IR arm is mostly at 240K with a realistic gradient across the different element of the camera, reaching 140K for the FPA at IR spectrograph camera focal plane (see Table 65).

Final results: CASE 1

Zone	Element	VF	Eps	VFxEps	Sum(VF.Eps)	T	Empirical coef from in-band to total	L(T) integrated	L(T)*coef*Sum(VF*Eps)	Fraction of the total
H	VIS_PORT_OUT	1.53%	1	0.015328	*0.015328*	283.2	*1.2729*	5.442E-08	*1.06E-09*	*97.0%*
G	FPA.ARRAY	10.15%	1	0.101479	*0.123952*	140	*2.2500*	1.327E-21	*3.70E-22*	*0.0000%*
	DET_BACK	4.49%	0.5	0.022473						
F	SECTION_F	14.64%	0.5	0.073211	*0.166606*	160	*1.8333*	2.938E-18	*8.97E-19*	*0.0000%*
	LENS_5.EDGE	14.52%	0.5	0.072597						
	LENS_5.BACK_PLANE	6.79%	0.05	0.003396						
	LENS_4.EDGE	2.53%	0.5	0.01264						
	LENS_4.BACK_PLANE	1.67%	0.05	0.000835						
	LENS_3.EDGE	0.79%	0.5	0.003926						
	LENS_4.FRONT	0.03%	0.005	1.52E-06						
E	SECTION_E	14.17%	0.5	0.070857	*0.070857*	200	*1.5000*	1.475E-13	*1.57E-14*	*0.0014%*
D	SECTION_D	3.95%	0.5	0.019755	*0.021887*	200	*1.5000*	1.475E-13	*4.84E-15*	*0.0004%*
	LENS_2.EDGE	0.32%	0.5	0.001598						
	LENS_1.EDGE	0.11%	0.5	0.000534						
C	SECTION_C	3.11%	0.5	0.015526	*0.028532*	240	*1.3571*	2.086E-10	*8.08E-12*	*0.7%*
	GRISM.BOTTOM	1.15%	0.5	0.005756						
	GRISM.GRATING	0.91%	0.1	0.000908						
	GRISM.LEFT_SIDE	0.54%	0.5	0.002692						
	GRISM.RIGHT_SIDE	0.54%	0.5	0.002678						
	EDGE_C_D	0.19%	0.5	0.000973						
B	SECTION_B	3.54%	0.5	0.01771	*0.031530*	240	*1.3571*	2.086E-10	*8.93E-12*	*0.8%*
	EDGE_B_C	1.13%	0.5	0.005673						
	DICHROIC.EDGE	0.91%	0.5	0.004539						
	VIS_PORT_TUBE	0.72%	0.5	0.003608						
A	SECTION_A	9.52%	0.5	0.047615	*0.056326*	240	*1.3571*	2.086E-10	*1.59E-11*	*1.5%*
	EDGE_A_B	0.70%	0.5	0.003479						
	SLIT_SUPPORT	0.57%	0.5	0.002872						
	SLIT_WALL	0.42%	0.5	0.002117						
	SLIT_BACK	0.05%	0.5	0.000244						

Highest T:	283.2	K
In-band and oob max detected radiance:	6.31E-08	W/m2.sr
Effective emissivity for whole IR arm spectrograph:	1.7%	

Typical exposure time (sec)	Photon only read noise per pixel (e)
3	5.3
30	16.6
300	52.5

Total:	1.09E-09	W/m2.sr
Final thermal background signal	6.89	e/sec/pix
compared with dark current:	0.02	e/sec/pix
for T_det=	140	K
compared with min sky estimates (non suppressed OH lines):	2.29	e/sec/pix
Total photon noise:	9.20	e/sec/pix
of which	***75.0%***	***is from instru background***

Table 65. Case 1 results.

The total background is ~3x higher than the average minimum sky signal estimate so well dominant, detector DC relatively negligible. The major contribution comes from the ambient VIS arm even if the VF is low. Its effective emissivity is taken as 1 as it is assumed to form a closed isothermal cavity.

- **CASE 2:** Same as Case 1 but this time the VIS arm is assumed thermalised at the same temperature T=240K as the IR arm (See Table 66).

[1] Limited to 300sec because with the pixel average well depth of 3.10^5e and in-band OH-lines signal level reaching ~10^3photons/sec/pixel, this will be approximately the saturation level per pixel. The given total read noise is photon-based only, i.e. extra contribution from 1/f noise and/or residual from the reading/sampling techniques are not accounted for here.

Final results: CASE 2

Zone	Element	VF	Eps	VFxEps	Sum(VF.Eps)	T	Empirical coef from in band to total	L(T) integrated	L(T)*coef*Sum(VF*Eps)	Fraction of the total
H	VIS_PORT_OUT	1.53%	1	0.015328	*0.015328*	240	*1.3571*	2.086E-10	*4.34E-12*	*11.6%*
G	FPA.ARRAY	10.15%	1	0.101479	*0.123952*	140	*2.2500*	1.327E-21	*3.70E-22*	*0.0000%*
	DET_BACK	4.49%	0.5	0.022473						
F	SECTION_F	14.64%	0.5	0.073211	*0.166606*	160	*1.8333*	2.938E-18	*8.97E-19*	*0.0000%*
	LENS_5.EDGE	14.52%	0.5	0.072597						
	LENS_5.BACK_PLANE	6.79%	0.05	0.003396						
	LENS_4.EDGE	2.53%	0.5	0.01264						
	LENS_4.BACK_PLANE	1.67%	0.05	0.000835						
	LENS_3.EDGE	0.79%	0.5	0.003926						
	LENS_4.FRONT	0.03%	0.005	1.52E-06						
E	SECTION_E	14.17%	0.5	0.070857	*0.070857*	200	*1.5000*	1.475E-13	*1.57E-14*	*0.0420%*
D	SECTION_D	3.95%	0.5	0.019755	*0.021887*	200	*1.5000*	1.475E-13	*4.84E-15*	*0.0130%*
	LENS_2.EDGE	0.32%	0.5	0.001598						
	LENS_1.EDGE	0.11%	0.5	0.000534						
C	SECTION_C	3.11%	0.5	0.015526	*0.028532*	240	*1.3571*	2.086E-10	*8.08E-12*	***21.6%***
	GRISM.BOTTOM	1.15%	0.5	0.005756						
	GRISM.GRATING	0.91%	0.1	0.000908						
	GRISM.LEFT_SIDE	0.54%	0.5	0.002692						
	GRISM.RIGHT_SIDE	0.54%	0.5	0.002678						
	EDGE_C_D	0.19%	0.5	0.000973						
B	SECTION_B	3.54%	0.5	0.01771	*0.031530*	240	*1.3571*	2.086E-10	*8.93E-12*	***23.9%***
	EDGE_B_C	1.13%	0.5	0.005673						
	DICHROIC.EDGE	0.91%	0.5	0.004539						
	VIS_PORT_TUBE	0.72%	0.5	0.003608						
A	SECTION_A	9.52%	0.5	0.047615	*0.056326*	240	*1.3571*	2.086E-10	*1.59E-11*	***42.7%***
	EDGE_A_B	0.70%	0.5	0.003479						
	SLIT_SUPPORT	0.57%	0.5	0.002872						
	SLIT_WALL	0.42%	0.5	0.002117						
	SLIT_BACK	0.05%	0.5	0.000244						

Highest T:	240	K
In-band and oob max detected radiance:	2.58E-10	W/m2.sr
Effective emissivity for whole IR arm spectrograph:	14.5%	

Typical exposure time (sec)	Photon only read noise per pixel (e)
3	2.8
30	8.7
300	27.6

Total:	3.73E-11	W/m2.sr
Final thermal background signal	0.23	e/sec/pix
compared with dark current:	0.02	e/sec/pix
for T_det=	140	K
compared with min sky estimates (non suppressed OH lines):	2.29	e/sec/pix
Total photon noise:	2.54	e/sec/pix
of which	***9.3%***	***is from instru background***

Table 66. Case 2 results.

The thermal background signal is now at the level of a 150K detector DC and below the minimum sky signal. The effective emissivity of ~14.5% for a 240K source background temperature reference shows that in practice a reduction compared to the worst-case scenario stray signal discussed in section 3.10.1.5.1 can be obtained, providing further margin. But the overall price to pay is the overall IR front elements including grism and all VIS arm elements to a colder than ambient temperature of ~-33degC (within general vacuum enclosure to avoid any condensation).

- **CASE 3:** Same as Case 2 but this time the VIS arm is assumed thermalised at the same ambient temperature of 10degC as the IR arm. The front elements of the IR arm camera forms the interface between ambient and the start of the necessary cryogenic conditions required by the focal plane detector (See Table 67).

Final results: CASE 3

Zone	Element	VF	Eps	VFxEps	Sum(VF.Eps)	T	Empirical coef from in-band to total	L(T) integrated	L(T)*coef*Sum(VF*Eps)	Fraction of the total
H	VIS_PORT_OUT	1.53%	1	0.015328	*0.015328*	283.2	*1.2729*	5.442E-08	*1.06E-09*	*11.6%*
G	FPA.ARRAY	10.15%	1	0.101479	*0.123952*	140	*2.2500*	1.327E-21	*3.70E-22*	*0.0000%*
	DET_BACK	4.49%	0.5	0.022473						
F	SECTION_F	14.64%	0.5	0.073211	*0.166606*	160	*1.8333*	2.938E-18	*8.97E-19*	*0.0000%*
	LENS_5.EDGE	14.52%	0.5	0.072597						
	LENS_5.BACK_PLANE	6.79%	0.05	0.003396						
	LENS_4.EDGE	2.53%	0.5	0.01264						
	LENS_4.BACK_PLANE	1.67%	0.05	0.000835						
	LENS_3.EDGE	0.79%	0.5	0.003926						
	LENS_4.FRONT	0.03%	0.005	1.52E-06						
E	SECTION_E	14.17%	0.5	0.070857	*0.070857*	200	*1.5000*	1.475E-13	*1.57E-14*	*0.0002%*
D	SECTION_D	3.95%	0.5	0.019755	*0.021887*	240	*1.3571*	2.086E-10	*6.20E-12*	*0.068%*
	LENS_2.EDGE	0.32%	0.5	0.001598						
	LENS_1.EDGE	0.11%	0.5	0.000534						
C	SECTION_C	3.11%	0.5	0.015526	*0.028532*	283.2	*1.2729*	5.442E-08	*1.98E-09*	***21.6%***
	GRISM.BOTTOM	1.15%	0.5	0.005756						
	GRISM.GRATING	0.91%	0.1	0.000908						
	GRISM.LEFT_SIDE	0.54%	0.5	0.002692						
	GRISM.RIGHT_SIDE	0.54%	0.5	0.002678						
	EDGE_C_D	0.19%	0.5	0.000973						
B	SECTION_B	3.54%	0.5	0.01771	*0.031530*	283.2	*1.2729*	5.442E-08	*2.18E-09*	***23.9%***
	EDGE_B_C	1.13%	0.5	0.005673						
	DICHROIC.EDGE	0.91%	0.5	0.004539						
	VIS_PORT_TUBE	0.72%	0.5	0.003608						
A	SECTION_A	9.52%	0.5	0.047615	*0.056326*	283.2	*1.2729*	5.442E-08	*3.90E-09*	***42.7%***
	EDGE_A_B	0.70%	0.5	0.003479						
	SLIT_SUPPORT	0.57%	0.5	0.002872						
	SLIT_WALL	0.42%	0.5	0.002117						
	SLIT_BACK	0.05%	0.5	0.000244						

Highest T:	283.2	K
In-band and oob max detected radiance:	6.28E-08	W/m2.sr
Effective emissivity for whole IR arm spectrograph:	14.5%	

Typical exposure time (sec)	Photon only read noise per pixel (e)
3	13.4
30	42.3
300	133.6

Total:	9.13E-09	W/m2.sr
Final thermal background signal	57.21	e/sec/pix
compared with dark current:	0.025	e/sec/pix
for T_det=	140	K
compared with min sky estimates (non suppressed OH lines):	2.28	e/sec/pix
Total photon noise:	59.52	e/sec/pix
of which	***96.1%***	***is from instru background***

Table 67. Case 3 results.

This is expectedly completely dominated by the thermal stray background signal (although ~6x lower than the worst-case first order approach in section 3.10.1.5.1 thanks to large value VFs towards local out-of-field potentially cold elements around the detector), with nearly one order of magnitude larger than for the case 1 where only the VIS arm is assumed at ambient. The common front elements (slit, collimator and dichroic support and surrounding enclosure) are now the dominant sources, in front of the VIS arm seen under low VF efficiency. Note the ~10% view factor for the cold FPA[1]: in the case of an ambient spectrograph with cold detector, this would potentially lead to a narcissus effect.

- **CASE 4:** Same as Case 2 with VIS and IR arm at 240K but with stricter thermal control and/or higher cold-to-cryo interface so that even the IR grism zone is already assumed at temperature lower than 240K (See Table 68).

[1] Higher than the in-field VF~7.5% (to be further modulated by the slit to FPA throughput) from fiber output signal at slit in the f/1.75 camera beam so the detector ultimately "sees" more from himself than from fiber at slit.

Final results: CASE 4

Zone	Element	VF	Eps	VFxEps	Sum(VF.Eps)	T	Empirical coef from in-band to total	L(T) integrated	L(T)*coef*Sum(VF*Eps)	Fraction of the total
H	VIS_PORT_OUT	1.53%	1	0.015328	*0.015328*	**240**	*1.3571*	2.086E-10	*4.34E-12*	*14.8%*
G	FPA.ARRAY	10.15%	1	0.101479	*0.123952*	**140**	*2.2500*	1.327E-21	*3.70E-22*	*0.0000%*
	DET_BACK	4.49%	0.5	0.022473						
F	SECTION_F	14.64%	0.5	0.073211	*0.166606*	**160**	*1.8333*	2.938E-18	*8.97E-19*	*0.0000%*
	LENS_5.EDGE	14.52%	0.5	0.072597						
	LENS_5.BACK_PLANE	6.79%	0.05	0.003396						
	LENS_4.EDGE	2.53%	0.5	0.01264						
	LENS_4.BACK_PLANE	1.67%	0.05	0.000835						
	LENS_3.EDGE	0.79%	0.5	0.003926						
	LENS_4.FRONT	0.03%	0.005	1.52E-06						
E	SECTION_E	14.17%	0.5	0.070857	*0.070857*	**160**	*1.8333*	2.938E-18	*3.82E-19*	*0.0000%*
D	SECTION_D	3.95%	0.5	0.019755	*0.021887*	**200**	*1.5000*	1.475E-13	*4.84E-15*	*0.017%*
	LENS_2.EDGE	0.32%	0.5	0.001598						
	LENS_1.EDGE	0.11%	0.5	0.000534						
C	SECTION_C	3.11%	0.5	0.015526	*0.028532*	**200**	*1.5000*	1.475E-13	*6.31E-15*	*0.022%*
	GRISM.BOTTOM	1.15%	0.5	0.005756						
	GRISM.GRATING	0.91%	0.1	0.000908						
	GRISM.LEFT_SIDE	0.54%	0.5	0.002692						
	GRISM.RIGHT_SIDE	0.54%	0.5	0.002678						
	EDGE_C_D	0.19%	0.5	0.000973						
B	SECTION_B	3.54%	0.5	0.01771	*0.031530*	**240**	*1.3571*	2.086E-10	*8.93E-12*	***30.5%***
	EDGE_B_C	1.13%	0.5	0.005673						
	DICHROIC.EDGE	0.91%	0.5	0.004539						
	VIS_PORT_TUBE	0.72%	0.5	0.003608						
A	SECTION_A	9.52%	0.5	0.047615	*0.056326*	**240**	*1.3571*	2.086E-10	*1.59E-11*	***54.6%***
	EDGE_A_B	0.70%	0.5	0.003479						
	SLIT_SUPPORT	0.57%	0.5	0.002872						
	SLIT_WALL	0.42%	0.5	0.002117						
	SLIT_BACK	0.05%	0.5	0.000244						

Highest T:	240	K
In-band and oob max detected radiance:	2.58E-10	W/m2.sr
Effective emissivity for whole IR arm spectrograph:	11.3%	

Typical exposure time (sec)	Photon only read noise per pixel (e)
3	2.7
30	8.6
300	27.3

Total:	2.92E-11	W/m2.sr
Final thermal background signal	0.18	e/sec/pix
compared with dark current:	0.02	e/sec/pix
for T_det=	140	K
compared with min sky estimates (non suppressed OH lines):	2.29	e/sec/pix
Total photon noise:	2.49	e/sec/pix
of which	***7.4%***	***is from instru background***

Table 68. Case 4 results.

The dominant sources remains the front common elements at the highest temperature of 240K here. This is only marginally better than the case 2 in terms of thermal stray signal level: no major gain in forcing the grism zone to be a bit colder than the front elements.

- **CASE 5:** Same as Case 2 and 4 with VIS and IR arm at 240K but with more relaxed thermal control and/or lower (i.e. closer to detector) cold-to-cryo interface so that even the IR camera front lens elements and camera inter-element zone is at the nominal 240K temperature (See Table 69).

Final results: CASE 5

Zone	Element	VF	Eps	VFxEps	Sum(VF.Eps)	T	Empirical coef from in-band to total	L(T) integrated	L(T)*coef*Sum(VF*Eps)	Fraction of the total
H	VIS_PORT_OUT	1.53%	1	0.015328	*0.015328*	240	*1.3571*	2.086E-10	*4.34E-12*	*6.8%*
G	FPA.ARRAY	10.15%	1	0.101479	*0.123952*	140	*2.2500*	1.327E-21	*3.70E-22*	*0.0000%*
	DET_BACK	4.49%	0.5	0.022473						
F	SECTION_F	14.64%	0.5	0.073211	*0.166606*	200	*1.5000*	1.475E-13	*3.69E-14*	*0.06%*
	LENS_5.EDGE	14.52%	0.5	0.072597						
	LENS_5.BACK_PLANE	6.79%	0.05	0.003396						
	LENS_4.EDGE	2.53%	0.5	0.01264						
	LENS_4.BACK_PLANE	1.67%	0.05	0.000835						
	LENS_3.EDGE	0.79%	0.5	0.003926						
	LENS_4.FRONT	0.03%	0.005	1.52E-06						
E	SECTION_E	14.17%	0.5	0.070857	*0.070857*	240	*1.3571*	2.086E-10	*2.01E-11*	***31.5%***
D	SECTION_D	3.95%	0.5	0.019755	*0.021887*	240	*1.3571*	2.086E-10	*6.20E-12*	*9.7%*
	LENS_2.EDGE	0.32%	0.5	0.001598						
	LENS_1.EDGE	0.11%	0.5	0.000534						
C	SECTION_C	3.11%	0.5	0.015526	*0.028532*	240	*1.3571*	2.086E-10	*8.08E-12*	*12.7%*
	GRISM.BOTTOM	1.15%	0.5	0.005756						
	GRISM.GRATING	0.91%	0.1	0.000908						
	GRISM.LEFT_SIDE	0.54%	0.5	0.002692						
	GRISM.RIGHT_SIDE	0.54%	0.5	0.002678						
	EDGE_C_D	0.19%	0.5	0.000973						
B	SECTION_B	3.54%	0.5	0.01771	*0.031530*	240	*1.3571*	2.086E-10	*8.93E-12*	*14.0%*
	EDGE_B_C	1.13%	0.5	0.005673						
	DICHROIC.EDGE	0.91%	0.5	0.004539						
	VIS_PORT_TUBE	0.72%	0.5	0.003608						
A	SECTION_A	9.52%	0.5	0.047615	*0.056326*	240	*1.3571*	2.086E-10	*1.59E-11*	***25.1%***
	EDGE_A_B	0.70%	0.5	0.003479						
	SLIT_SUPPORT	0.57%	0.5	0.002872						
	SLIT_WALL	0.42%	0.5	0.002117						
	SLIT_BACK	0.05%	0.5	0.000244						

Highest T: 240 K
In-band and oob max detected radiance: 2.58E-10 W/m2.sr
Effective emissivity for whole IR arm spectrograph: 24.7%

Typical exposure time (sec)	Photon only read noise per pixel (e)
3	2.8
30	9.0
300	28.5

Total: 6.36E-11 W/m2.sr
Final thermal background signal 0.40 e/sec/pix
compared with dark current: 0.02 e/sec/pix
for T_det= 140 K
compared with min sky estimates (non suppressed OH lines): 2.29 e/sec/pix
Total photon noise: 2.70 e/sec/pix
of which ***14.8%*** ***is from instru background***

Table 69. Case 5 results.

An affordable factor ~x2 increase in stray thermal background signal compared to case 2, but still lower than minimum sky signal. This noticeable increase is indicative of a high sensitivity towards the in-field and out-of-field elements close to the detector which should be maintained as much as possible at a low temperature as well. This is also seen in the fractional contributions: the central elements (camera central and front elements) and grism zone become here the dominant sources.

3.10.1.5.3 Extension to the SPECIAL case of a 1.4 µm CUT-OFF IR DETECTOR

Consequences of the option to restrict the science IR band of the spectrograph up to 1.4 µm instead of 1.7 µm (i.e. dropping the H band portion) considered in the sections above is now briefly discussed.

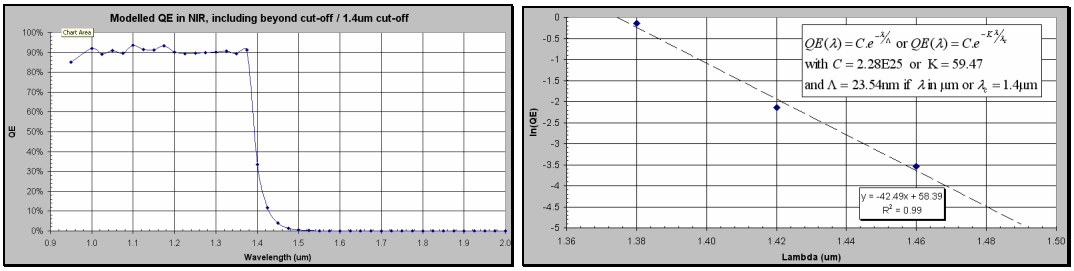

Figure 174. modelled IR FPA QE with 1.4 µm cut-off (left) with same cut-off sharpness, via similar exponential oob spectral response as in the 1.7 µm case (right)

By extrapolation from section 3.10.1.5.1, the QE spectral variations of an IR FPA with 1.4 μm cut-off are modelled via the same in-band values and similar steepness of decrease oob (again via an exponential model). Following the same procedure, the ratio between in-band and oob is computed. This time the cross-over background temperature beyond which the in-band stray flux dominates, is around ~213K. The effectiveness of the (assumed) same cut-off spectral sharpness as in the 1.7 μm case is less as the ratio only reach ~2 at ambient. Under this assumption, it appears that the empirical dependence of T_c can be taken as $\sim\lambda_c^{-2}$.

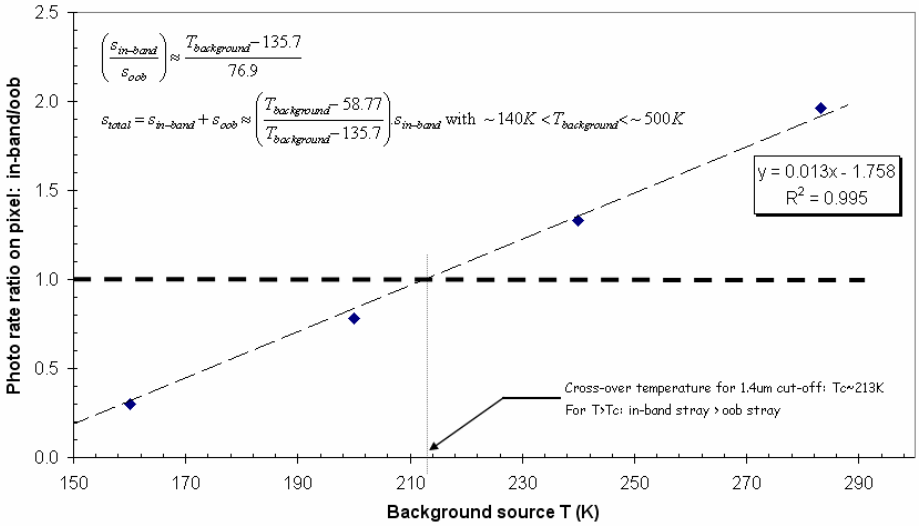

Figure 175. Same as Figure 166 but for the case of 1.4 μm cut-off detector.

For a high emissivity closed cavity/enclosure-like source at temperature filling the angular solid angle of any FPA pixel, the total background thermal signal level is plotted in Figure 176 below. Again comparison with detector DC is made. Here a shorter wavelength cut-off means larger detector energy gap (~0.886eV at 1.4 μm) and using the theoretical dependence of the DC on the detector temperature and the energy gap, a scaling of the 1.7 μm cut-off DC values is made via:

$$\frac{DC(\lambda_c = 1.4um)}{DC(\lambda_c = 1.7um)} = e^{-\left(\frac{E_g(\lambda_c=1.4um) - E_g(\lambda_c=1.7um)}{2kT}\right)}$$

in order to obtain the 1.4 μm DC values ones, reported in the graph below. We can already notice that a detector at 200K and an entire spectrograph left at ambient generate photon noise level of same order of magnitude as the minimum in-band sky signal.

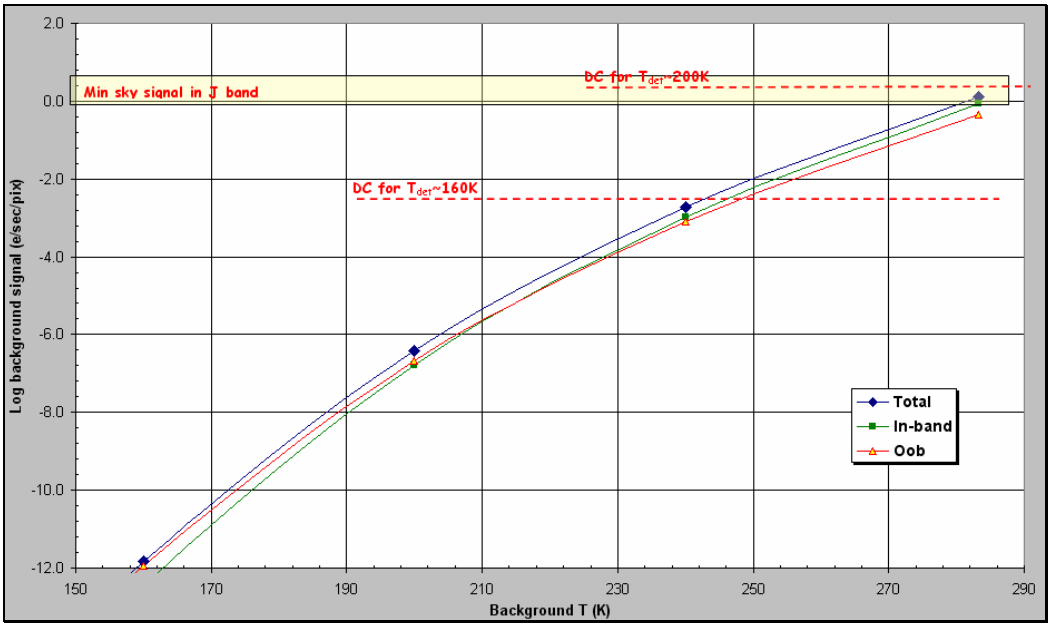

Figure 176. Same as Figure 167 but for the case of 1.4 µm cut-off detector.

A more precise estimation based on the same approach as developed in Section 3.10.1.5.2 is made and results are summarised in Table 70.

Final results: CASE 3bis (1.4um cut-off case)

Zone	Element	VF	Eps	VFxEps	Sum(VF.Eps)	T	Empirical coef from in-band to total	L(T) integrated	L(T)*coef*Sum(VF*Eps)	Fraction of the total
H	VIS_PORT_OUT	1.53%	1	0.015328	*0.015328*	283.2	*1.5216*	1.577E-10	*3.68E-12*	*11.6%*
G	FPA.ARRAY	10.15%	1	0.101479	*0.123952*	180	*2.7366*	1.494E-17	*5.07E-18*	*0.0000%*
	DET_BACK	4.49%	0.5	0.022473						
F	SECTION_F	14.64%	0.5	0.073211	*0.166606*	200	*2.1964*	2.988E-17	*1.09E-17*	*0.0000%*
	LENS_5.EDGE	14.52%	0.5	0.072597						
	LENS_5.BACK_PLANE	6.79%	0.05	0.003396						
	LENS_4.EDGE	2.53%	0.5	0.01264						
	LENS_4.BACK_PLANE	1.67%	0.05	0.000835						
	LENS_3.EDGE	0.79%	0.5	0.003926						
	LENS_4.FRONT	0.03%	0.005	1.52E-06						
E	SECTION_E	14.17%	0.5	0.070857	*0.070857*	200	*2.1964*	2.988E-17	*4.65E-18*	*0.0000%*
D	SECTION_D	3.95%	0.5	0.019755	*0.021887*	240	*1.7376*	1.913E-13	*7.27E-15*	*0.023%*
	LENS_2.EDGE	0.32%	0.5	0.001598						
	LENS_1.EDGE	0.11%	0.5	0.000534						
C	SECTION_C	3.11%	0.5	0.015526	*0.028532*	283.2	*1.5216*	1.577E-10	*6.85E-12*	*21.7%*
	GRISM.BOTTOM	1.15%	0.5	0.005756						
	GRISM.GRATING	0.91%	0.1	0.000908						
	GRISM.LEFT_SIDE	0.54%	0.5	0.002692						
	GRISM.RIGHT_SIDE	0.54%	0.5	0.002678						
	EDGE_C_D	0.19%	0.5	0.000973						
B	SECTION_B	3.54%	0.5	0.01771	*0.031530*	283.2	*1.5216*	1.577E-10	*7.56E-12*	***23.9%***
	EDGE_B_C	1.13%	0.5	0.005673						
	DICHROIC.EDGE	0.91%	0.5	0.004539						
	VIS_PORT_TUBE	0.72%	0.5	0.003608						
A	SECTION_A	9.52%	0.5	0.047615	*0.056326*	283.2	*1.5216*	1.577E-10	*1.35E-11*	***42.8%***
	EDGE_A_B	0.70%	0.5	0.003479						
	SLIT_SUPPORT	0.57%	0.5	0.002872						
	SLIT_WALL	0.42%	0.5	0.002117						
	SLIT_BACK	0.05%	0.5	0.000244						

Highest T: 283.2 K
In-band and oob max detected radiance: 2.19E-10 W/m2.sr
Effective emissivity for whole IR arm spectrograph: 14.4%

Typical exposure time (sec)	Photon only read noise per pixel (e)
3	2.8
30	8.9
300	28.2

Total: 3.16E-11 W/m2.sr
Final thermal background signal 0.20 e/sec/pix
compared with dark current: 0.150 e/sec/pix
for T_det (1.4um cut-off)= 180 K
compared with min sky estimates (non suppressed OH lines): 2.30 e/sec/pix
Total photon noise: 2.65 e/sec/pix
of which 7.5% *is from instru background*

Table 70. Case 3 bis results.

The case is similar to the previously discussed Case 3 with an ambient (10degC) spectrograph (VIS and IR arms) and FPA at 180K for a baseline DC value around ~0.15e/sec/pix with a typical gradient across the camera between spectrograph front elements and detector at focal plane.

The elements with largest contribution are the common front element enclosures which could be even tuned slightly (rough polish) to maintain a good inner surface reflectivity/low emissivity. The resulting thermal background signal is of the same order as the DC of a 180K 1.4 μm cut-off detector and the combined effect of both is still several times lower than the minimum sky signal. Note that optical filtering (with cut-off at 1.4 μm) would only slightly improve (reduced by ~25%) the thermal background and would be effective only if filter is at T_{filter}<200K, which would mean located in the as part of the back or central elements of the camera in this configuration with a 180K FPA.

Effectively this ambient 1.4 μm cut-off spectrograph configuration gives same performance level as a spectrograph at 240K with ~145K 1.7 μm IR detector cut-off (see Case 2 in section 3.3) but with reduced scientific spectral coverage (up to J band only).

3.10.1.5.4 Summary and Recommendations

An analysis of the thermal background signal levels for the SIDE IR spectrograph arm has been performed.

First based on a first-order general radiometric model modulated by detector properties taken from recent characterisation of real IR FPA devices. Then, through optical modelling of the SIDE IR arm conceptual design elements with added basic representative baffling and surrounding enclosures, a more detailed approach to thermal stray signal level retrieval is made based on the relative distribution of VF towards the different elements of the spectrograph, obtained by Monte-Carlo-based backward raytrace radiative transfer method.

Different temperature distributions for the spectrograph elements are then applied and associated background signal results are compared in these different cases alongside with detector DC and minimum sky signal. Equivalent effective emissivity at a fixed single highest temperature are derived in each case.

The main conclusions and recommendations derived from this study are:

- An operating detector temperature in the range of 140-150K typically: colder is technically more demanding with no real performance gain (DC floor threshold); warmer and the DC will dominate over the minimum sky signal level;

- No optical filtering for out-of-band rejection is found necessary: the improvement in out-of-band rejection will be overall marginal as oob already is a small contributor and would actually be effective only if filter is not much warmer than detector itself;

- To maintain the instrumental thermal photon noise (sum of the DC and thermal background stray) below the estimated minimum sky signal, a temperature of 240K appears adequate for the whole spectrograph main elements including the VIS arm. The steady state spatial gradient at interface between the 140-150K detector and the

240K spectrograph would be established over the camera elements and is acceptable as long as central and back camera elements are maintained at not too stringent intermediate temperatures (typically around 200K or lower);

- A best performance spectrograph with very small/negligible instrumental thermal noise (typically a few 10^{-2}e/sec/pix) compared to in-band minimum sky level would require a FPA at 140K or lower and the entire spectrograph (IR and VIS arms) at around -60degC or lower. But then the dispersed in-band spectrum of the picked out-of-field thermal (potentially fluctuating) emission of the observatory would become dominant, particularly in a lower resolution (R~1000-2000) mode;

- An ambient spectrograph (10degC) would completely dominate the photon noise with its thermal background emission. A 240K IR arm with an ambient VIS arm would still be dominant and therefore damaging for overall spectrograph sensitivity. If the VIS arm needs to be maintained at ambient, then a possible solution is to trade a few % throughput reduction in the VIS arm by adding an "extended hot mirror"[1] at VIS arm interface, typically between main dichroic and VIS grism. This would drop the effective emissivity, in the IR bands, of the ambient VIS arm by approximately one order of magnitude (with limited increase of the IR arm elements VF at low overall contribution when at 240K), just enough to end up with an instrumental thermal photon noise of the order or slightly below the minimum sky noise, limiting therefore the overall system performance degradation.

All the above applies for the main case of a 1.7 μm IR detector cut-off. For the case of a 1.4 μm cut-off detector, an ambient (10degC) spectrograph feeding a FPA at ~180K would be acceptable because delivering an instrumental thermal photon noise still several times lower than the minimum sky signal level. It is also possible to operate up to the J band only with a 1.7 μm cut-off IR FPA and adding a 1.4 μm cut-off filter in the camera at intermediate temperature (philosophy similar to the FMOS design, see RD3) but to maintain a low DC the 1.7 μm cut-off IR FPA would still have to be operated in the 140-150K max range.

3.10.1.5.5 References

M.G. Brown, "*Development of NIR detectors and science requirements for SNAP*", PhD thesis - University of Michigan (2007)

S.S. Eikenberry, "*Thermal emissivity of Infrared Arm*", SIDE System Design Note v1.0 (19/05/2007)

M. Ferlet, "*UK-FMOS: straylight analysis of the spectrograph+camera design*", UK-FMOS Technical Report issue 0.4 (28/02/2003)

[1] As commonly called in off-the-shelf catalogue item list; reflecting NIR, transmitting VIS and therefore acting as the opposite of the spectrograph main separating baselined dichroic.

3.10.1.6 Costs

3.10.1.6.1 Collimator

The total cost for ten spectrograph copies is estimated at 67,500 € and it is thought to be reliable at the +/- 10 % level. This amounts to a cost of 6,750 € per Dual VIS-NIR Spectrograph (for each of the 10 copies).

3.10.1.6.1.1 Blanks: 750 € per Dual VIS-NIR Spectrograph

The cost of a "Hextek" collimator mirror blank with dimensions 100 mm × 310 mm and curvature radius is 750 €.

3.10.1.6.1.2 Polishing and Coatings : 6,000 € per Dual VIS-NIR Spectrograph

The cost of polish and coatings run is 6,000 € per collimator mirror.

3.10.1.6.2 Dichroic Beamsplitter

The total cost for ten copies is estimated at 11,000 € and it is thought to be reliable at the +/- 10 % level. This amounts to a cost of 1,100 € per Dual VIS-NIR Spectrograph (for each of the 10 copies).

3.10.1.6.3 Gratings

The total cost for ten copies is estimated at 2,166,000 € and it is thought to be reliable at the +/- 10% level. This amounts to a cost of 216,600 € per Dual VIS-NIR Spectrograph (for each of the 10 copies).

3.10.1.6.3.1 Materials: 58,500 € per Dual VIS-NIR Spectrograph

BLANK SUPPLY: Two prisms per block (It is recommended to have a spare unit per material)					
	Mechanized BLANKS: thickness × diameter, index homogeneity report. Melt index.				
	Size	Material	Price/unit	units	Price
VIS-1500-I	100×150×150	N-LAF41	5000	1	5000
VIS-1500-II	100×150×150	N-LAF46	5000	1	5000
VIS-3400 (2)	115×150×150	N-LAF41	5800	1	5800
VIS-4000-I (2)	115×150×150	N-LAF46	5800	1	5800
VIS-4000-II(2)	115×150×150	N-LAF46	5800	1	5800
VIS-3650 (2)	115×150×150	N-LAF46	5800	1	5800
NIR-1500	115×150×150	SF14	5800	1	5800
NIR-4000-I(2)	120×150×150	N-LAF46	6500	1	6500
NIR-4000-I(2)	120×150×150	N-LAF46	6500	1	6500
NIR-5000	120×150×150	N-LAF46	6500	1	6500

Table 71. Blanks cost.

3.10.1.6.3.2 Manufacture: 102,000 € per Dual VIS-NIR Spectrograph

PRISM MANUFACTURE: Polishing & coating					
	Size	Material	Price/unit	units	Price
VIS-1500-I	100×150×150	N-LAF41	6000	1	6000
VIS-1500-II	100×150×150	N-LAF46	6000	1	6000
VIS-3400 (2)	115×150×150	N-LAF41	6000	2	12000
VIS-4000-I (2)	115×150×150	N-LAF46	6000	2	12000
VIS-4000-II(2)	115×150×150	N-LAF46	6000	2	12000
VIS-3650 (2)	115×150×150	N-LAF46	6000	2	12000
NIR-1500	115×150×150	SF14	6000	1	6000
NIR-4000-I(2)	115×150×150	N-LAF46	6000	2	12000
NIR-4000-I(2)	115×150×150	N-LAF46	6000	2	12000
NIR-5000	115×150×150	N-LAF46	6000	2	12000

Table 72. Cost of the prism manufacture.

3.10.1.6.3.3 Blanks: 6,600 € per Dual VIS-NIR Spectrograph

WINDOWS BLANKS (TBC)					
	Size	Material	Price/unit	units	Price
For VPHs	20×150×150	N-BK7	600	8	4800
For Grisms	20×150×150	N-BK7	600	3	1800

Table 73. Cost of the windows blanks.

3.10.1.6.3.4 Surface Gratings Replica: 18,000 € per Dual VIS-NIR Spectrograph

SURFACE GRATING REPLICA				
	Ruled area	Price/unit	units	Price
VIS-1500-I	165x150	6000	1	6000
VIS-1500-II	160x150	6000	1	6000
NIR-1500	160x150	6000	1	6000

Table 74. Cost of the grisms surface grating replica.

3.10.1.6.3.5 VPH Gratings: 31,500 € per Dual VIS-NIR Spectrograph

VPH GRATING				
	Diameter	Price/unit	units	Price
VIS-3400	F=140mm	4500	1	4500
VIS-4000	F=140mm	4500	1	4500
VIS-4000	F=140mm	4500	1	4500
VIS-3650	F=140mm	4500	1	4500
NIR-4000	F=140mm	4500	1	4500
NIR-4000	F=140mm	4500	1	4500
NIR-5000	F=140mm	4500	1	4500

Table 75. Cost of the VPH gratings.

3.10.1.6.4 VIS-NIR Cameras

Estimates have been made for the various costs involved in producing and delivering the 120 (one hundred twenty) high-precision AR coated lens elements that will be needed to build 10 copies each of the VIS and NIR cameras for the SIDE spectrograph(s). These estimates are based upon real SIDE specific quotes for most of the optical materials, on closely related recent quotes for the production of similar-sized optics for the MOSFIRE cryogenic near-ir spectrograph for Keck 1, and the like.

The total cost is estimated at 1,612,421 € and it is thought to be reliable at the +/- 10% level. This amounts to a cost of 80,621 € per camera for each of the 10 VIS and 10 NIR cameras.

3.10.1.6.4.1 Materials: 666,706 €

For the purposes of this feasibility study, it is assumed that materials will be purchased in California, USA and transported as necessary for subsequent purposes, although that is not necessarily the way it will happen in practice. However comparable costs will occur, no matter where the material is purchased. Here below are the identified individual contributions to the sub-total amount listed for this section.

1. CaF2 lens blanks, 11 (eleven) each of the 4 (four) required blank sizes (480,150 €). The "extra" set mitigates loss of production time in the event of breakage (usually required by

manufacturer). Additional spare CaF2 blanks, if needed, could be ordered later without disrupting the optical design as the refractive indices are generic.

2. Fused Quartz (Infrasil 302) lens blanks, 11 (eleven) of the single required blank size (24,357 €). Price is from a Heraeus Quartz America Inc. quote (03/08/06), scaled by volume with a 10% inflation factor included.

3. Ohara lens blanks, 14 (fourteen) each of the 7 (seven) required blank sizes (95,630 €). The "extra" sets mitigate optical design disruption in the event of breakage as additional blanks of the same melt and anneal would not be available later.

4. Extra 5th-place "line readings" (refractive index measurements) for 6 (six) Ohara glass types (2,084 €). CaF2 witness samples for coating, 70 (seventy) finished windows for estimated 30 to 35 coating runs (4,750 €). Price from Edmund Optics on-line catalog, Part No. NT47-683.

5. Fused Silica (OK substitute) witness samples for Infrasil 302 coating, 20 (twenty) finished windows for estimated 10 to 12 coating runs (1,200 €). Price from Melles Griot on line catalog, Part No. 02 WLQ 006.

6. Ohara glass witness sample blanks 20 (twenty) each of 5 (five) glass types and 40 (forty) of glass type S-LAM66 for estimated 10 to 12 coating runs for each of 7 (seven) lens types (2,590 €).

7. Pyrex or equivalent lens blanks for 24 test-plate pairs (3,714 €). Price by rough estimate of 72 € per blank on average, with 4 (four) spares.

8. California state sales tax on materials at 8.50 percent (52,231 €).

3.10.1.6.4.2 Labor: 945,715 €

For the purposes of this feasibility study, it is assumed that polishing and coating will be done in the USA by a recognized provider of precision scientific optics, such as Coastal Optical Systems, Inc. (COSI) and its subcontractors. Here below are the identified individual contributions to the sub-total amount listed for this section.

1. Polish and certify 24 (twenty four) high-precision large-diameter test-plate pairs (120,000 €). Price determined by averaging over comparable-sized test plate pairs that have been made over the past several years at COSI, Tucson Optical Research Corporation (TORC), etc.

2. Polish 140 (one hundred forty) witness sample blanks on both sides (20,000 €). Price determined by averaging over COSI quote of July 2007, with an estimated 10% quantity discount applied.

3. Polish 120 (one hundred twenty) lens elements of 12 (twelve) different types and provide suitable quality assurance (QA) documentation (497,144 €). Price determined by averaging over COSI quote of July 2007, with an estimated 10% quantity discount applied.

4. AR coat 120 (one hundred twenty) lens elements of 12 (twelve) different types on both sides with high efficiency broad passband multi-layer dielectric AR coatings and provide QA documentation based on witness sample residual reflection measurements (308,571 €). Price determined by averaging over COSI quote of July 2007, with an estimated 10% quantity discount applied.

3.10.1.6.5 Mechanics costs

The overall cost for the mechanics has to be studied in detail during the next phase of the project depending on the final optomechanics and related mechanical subsystems chosen (cooling system, etc). For the 10 spectrographs, this cost is estimated roughly at 3,700,000 €.

3.10.1.6.6 Conclusion

The total costs of the Dual VIS-NIR spectrograph/s is shown in Table 76.

Item	Price/unit or per Spectrograph	Total price for ten spectrographs
Collimator	6,750 €	67,500 €
Beamsplitter	1,100 €	11,000 €
Gratings	216,600 €	2,166,000 €
Camera VIS	80,621 €	806,210 €
Camera NIR	80,621 €	806,210 €
Mechanics	370,000 €	3,700,000 €
Entire Spectrograph	**755,692 €**	**7,556,920 €**

Table 76. SIDE Dual VIS-NIR total cost.

3.10.2 The Hi-Res VIS Spectrograph

3.10.2.1 Introduction

Within the context of SIDE instrument, the spectrograph that will provide moderate resolutions from 7900 to 29000, has been designated as the Hi-Res VIS spectrograph. In this section we present preliminary optical designs, developed by Harland Epps, for collimator and camera optics for such spectrograph . We provide quantitative image analyses and polychromatic spot diagram evaluations for them.

We assume fiber bundles containing 7 closely packed 0.5-arcsec fibers, illuminated at the telescope focus by microlenslet arrays such that their output into the collimator can be specified to f/7.0. The 7 fibers from each unit will be placed side-by-side, as close as possible to one another, to form a pseudo-slit (for each object) that is 0.5-arcsec wide along the dispersion direction and ~ 4.5 arcsec tall considering a fibre core of 170 micron and a buffer diameter of 200 micron.

A 4096 x 4096 by 15 micron Fairchild CCD486 or equivalent array has been considered as a detector. The required R = (7,900 to 29,000) resolution could be attained with a collimated beam diameter of about 300 mm. We adopted that value and assumed that the dispersion would be provided by a large reflection grating, working in 1st interior order. Assuming a spectrograph collimator-to-camera angle of Q = 40.0 degrees, and a grating with 1,400 grooves/mm, the anamorphic factors are (1.223, 1.445 and 1.848) for central wavelengths of (0.37, 0.60, and 0.85)-micron, respectively. A collimator field radius of 2.0 degrees was adopted such that the number of objects to observe in MOS mode is the same as in the Dual VIS-NIR spectrograph. The pixel sampling along the dispersion direction becomes (3.87, 3.28 and 2.56) pixels/pseudo-slit-width for the 3 aforementioned central wavelength set ups, respectively. The sampling is perhaps somewhat coarse for the red-most set ups. However those tend to produce the highest resolution so some degree of compensation occurs, which may prove to be acceptable.

These parameters, led to a required camera focal length of about 880.0 mm and a camera field radius of about 2.85 degrees, which covers the corners of the array. The dispersion values required to accommodate central wavelengths in the (0.37 to 0.85)-micron range, with resolution in the R = (7,900 to 29,000) range, appear to be attainable with a single 1st-order reflection grating as described above but it will require a (310 x 600)-mm grating so as to accommodate the 0.85-micron central wavelength set up without vignetting at the ends of the grating. That grating will surely have to be made as a mosaic.

The Q = 40.0-degree spectrograph angle, together with the grating angle of Theta= 59.29 degrees for the most extreme (0.85-micron) central wavelength set up, led to a conservative estimate of about 700.0 mm for the camera's entrance pupil distance and a predesign estimate for the Hi-Res camera's entrance aperture diameter of about 630 mm (f/1.40, underfilled) in order to accept the (300 x 555)-mm elliptical pupils produced by the 0.85-micron set up, without vignetting. Refracting cameras of those dimensions and spectral characteristics are not feasible so a catadioptric camera of the style used in the Keck 1 HIRES spectrograph will be required (e.g. Epps, H.W. and Vogt, S.V. 1993).

3.10.2.2 Collimator optical design

The collimator is quite simple and effective. The only optical element needed is a spherical mirror whose radius is twice the focal length. The pseudo-slit must be made in the form of a thin "fan," whose individual fibers point toward the mirror with their individual axes all pointing back such that they intersect an optical axis at the mirror's center of curvature. The optical axis is selected such that the fan of fibers is bilaterally symmetric. The fiber "ends," where light exits, must be placed along a circular arc, with a center point that is also located at the mirror's center of curvature. Thus, in effect, we can think of the collimator as a "correctorless" Schmidt camera working in reverse, whose f.o.v. is confined the plane of the fiber fan (pseudo-slit).

The collimator f-ratio that best accomplished the spot diameter required was f/7, with a focal length of 2100.0 mm and a spherical mirror radius of 4200.0 mm (Figure 114). By symmetry, it is apparent that the only aberration present will be spherical aberration, which is independent of field angle. The only optical requirement is that the spherical aberration produces a "spot size" that is small and negligible compared with the diameter of each individual fiber.

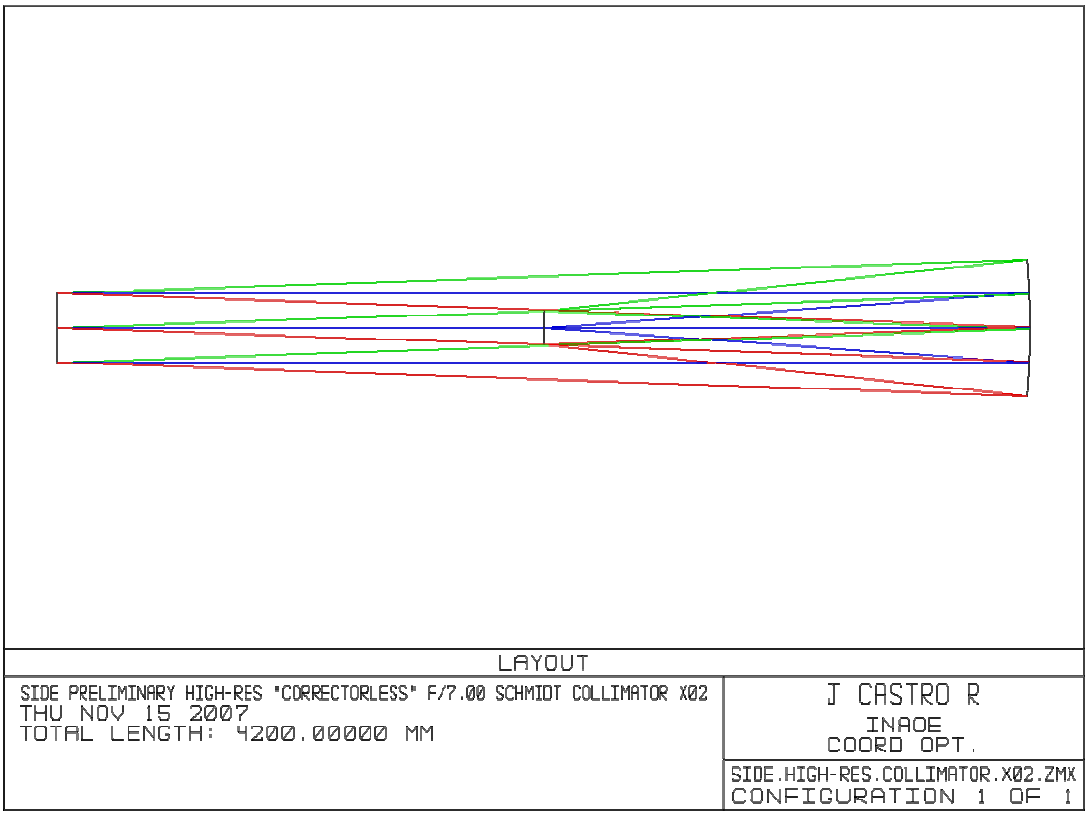

Figure 177 High resolution "correctless" Schmidt collimator.

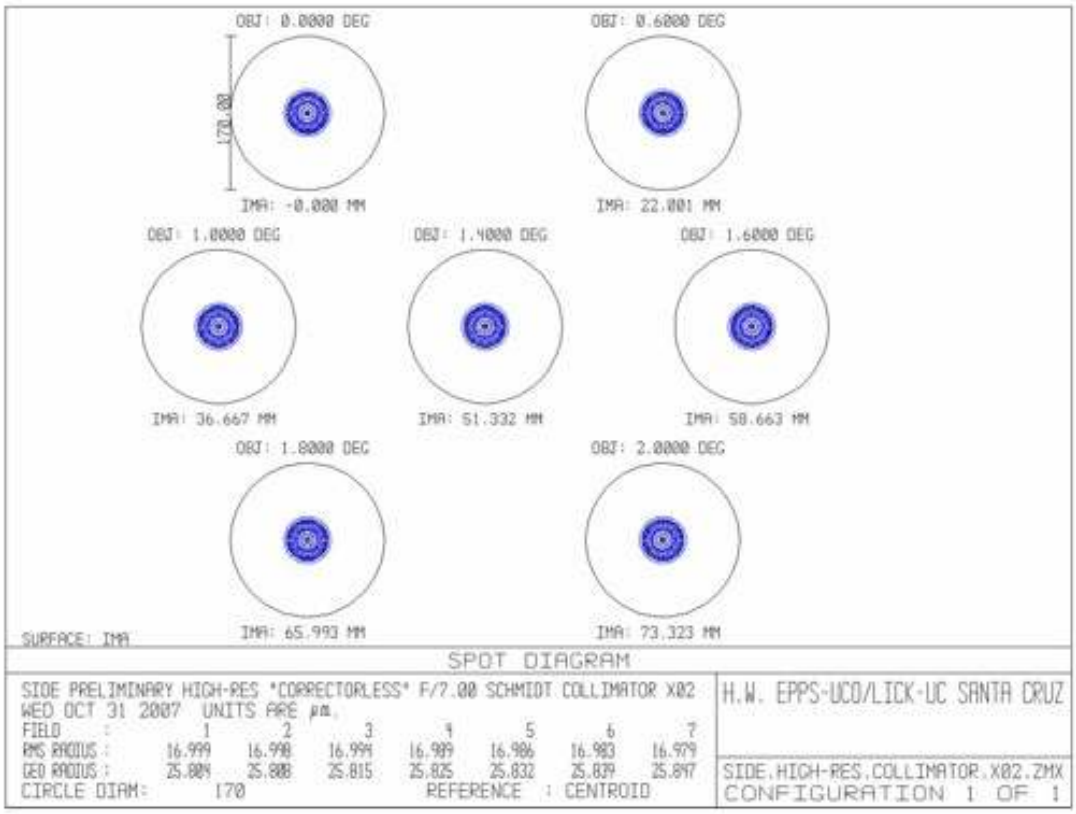

Figure 178 High resolution correctless Schmidt collimator spot diagram. For a field radius of 2 degrees the spot size is 26 microns. The circles correspond to 170 microns fiber diameter.

The resulting spots, shown in Figure 178, confirm that the total aberration blur spot is very small as compared with the 170.0-micron diameter fiber shown as a circumscribed circle. Thus, the f/7.00 Hi-Res collimator described here is fully adequate for the purpose.

3.10.2.3 Grating optical design

The optical characteristics of the reflection grating are: a ruling of 1400 lines/mm, Blaze Wavelength of 0.51 microns and Blaze angle of 22.3282º. In order to cover all the spectral range, the grating tilt will be tunable and will span 23.3º, from 36º to 59.3º of angle from the collimator. The advantage of such setup is the use of one single grating without the need of refocusing. On the other hand, the grating is a difficult and expensive optical part. However, the success of similar instruments, like HIRES, and the fact that we contacted the company Bach Research, which ruled a larger grating for the instrument SOFIA, suggest that it should be posible to build the grating for the Hi-Res spectrograph.

3.10.2.4 Camera. A Catadioptric All-Spherical f/1.4 Hi-Res Camera

A design for a 15.0-micron detector was developed. The 880.0-mm focal length, 700.0-mm entrance pupil distance, anticipated 630.0-mm entrance aperture diameter and 2.85-degree field radius make this camera roughly comparable in size but somewhat easier to design than the so-called "super-camera," which H. Epps designed for the HIRES spectrograph on Keck 1. A catadioptric camera of this style makes use of a closely-spaced optically neutral pair of positive and negative all-spherical lenses located somewhat ahead of the center of curvature of a concave spherical mirror, which provides about 90% of the total optical power in the system. That is followed by an all-spherical positive meniscus field flattener lens near focus, which usually contributes about 10% of the positive power. All of the lens elements are customarily made of the same optical material, usually Fused Silica if the system is to operate in the uv/visible spectral range.

The optimization of a camera of this type is straight forward and need not be discussed here. A main issue is to be sure that the thicknesses of the positive and negative lenses are large enough to provide sufficient stiffness. The field flattener meniscus always has a tendency to become overly thick, which tends to increase its diameter unnecessarily. It should be constrained to be as thin as possible, consistent with adequate imaging performance and with the dual purpose of serving as the vacuum window.

The field flattener causes a central obstruction, which is one of the main drawbacks of a camera of this type. The vignetting is typically in the (10% to 40%) range, depending on the collimator pupil diameter, the expected anamorphic factors and the detector/Dewar package geometry. Obstruction and scattering caused by the Dewar support hardware can be problematic as well. In the case of SIDE, H. Epps was able to limit the vignetting to about 30% for the bluemost set ups, down to about 21% for the redmost set ups. In practice, it may be possible to reduce the vignetting by careful non circular "shaping" of the field flattener that is consistent with the square shape of the detector.

When illuminated in perfectly parallel light from a slightly oversized (310 x 573.5)-mm elliptical entrance pupil, located 700.0 mm ahead of the first lens vertex, this camera shows residual aberrations with an rms image diameter of only 9.3 +/- 2.0 microns (0.62 +/- 0.13 pixels) averaged over field angles and wavelengths within the (0.345 to 0.875)-micron passband *without refocus*. 3rd-order pincushion distortion is some 1.84% at the edge of the full field (the corners of the detector), which is noticeable but probably acceptable. The image quality is outstanding.

A scaled drawing of this camera is shown in Figure 179. The 0.85-micron set up with an anamorphic factor of 1.848 is illustrated. Parallel light rays, represented by the chief ray and the marginal rays for a 2.85-degree field angle, radiate from the entrance pupil on the left, moving toward the right. The rays pass through the large positive and negative lens elements and proceed to the spherical mirror on the right. They are reflected back toward the left, passing through a plane (the obstruction, where vignetting has occurred), then continue through the thick field flattener meniscus and come to focus on the flat detector array. The total length from the entrance pupil to the spherical mirror is 3674.33 mm. The length of the camera itself, from the first lens vertex to the mirror is 2974.33 mm, which is about 1.57 times larger than would be expected in a Schmidt camera. This difference is typical in HIRES-style camera designs and it cannot easily be avoided.

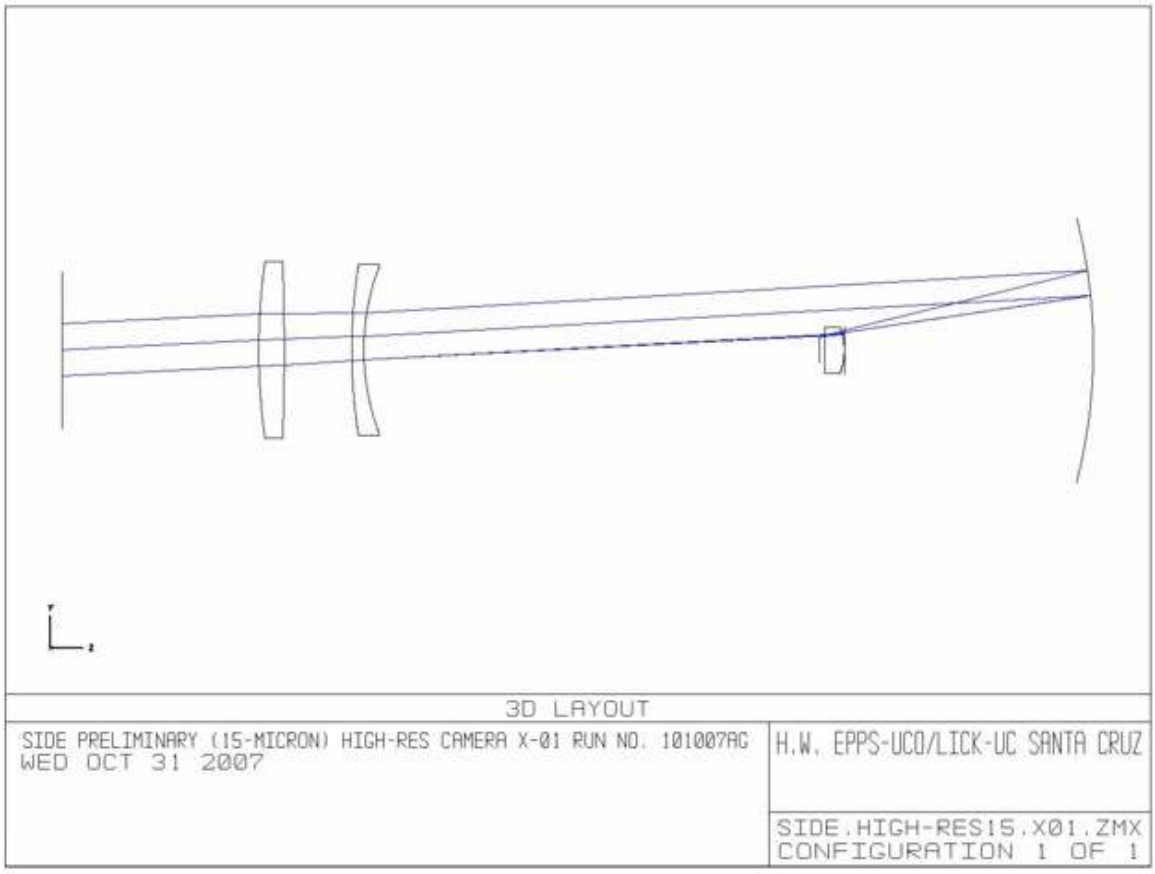

Figure 179 SIDE preliminary high resolution camera**.**

The view shown in Figure 179 is repeated in Figure 180 but more rays are included, such that the vignetting is clearly evident. Figure 180 shows those rays as they arrive on the first lens surface.

Figure **181** shows the rays arriving on the spherical mirror after having been vignetted by the field flattener obstruction.

The lens and mirror apertures shown are minimum clear apertures. In practice, the lens elements would be made larger in diameter so as to allow sufficient material for mounting purposes, for bevelling and for convenience of optical figuring and coating.

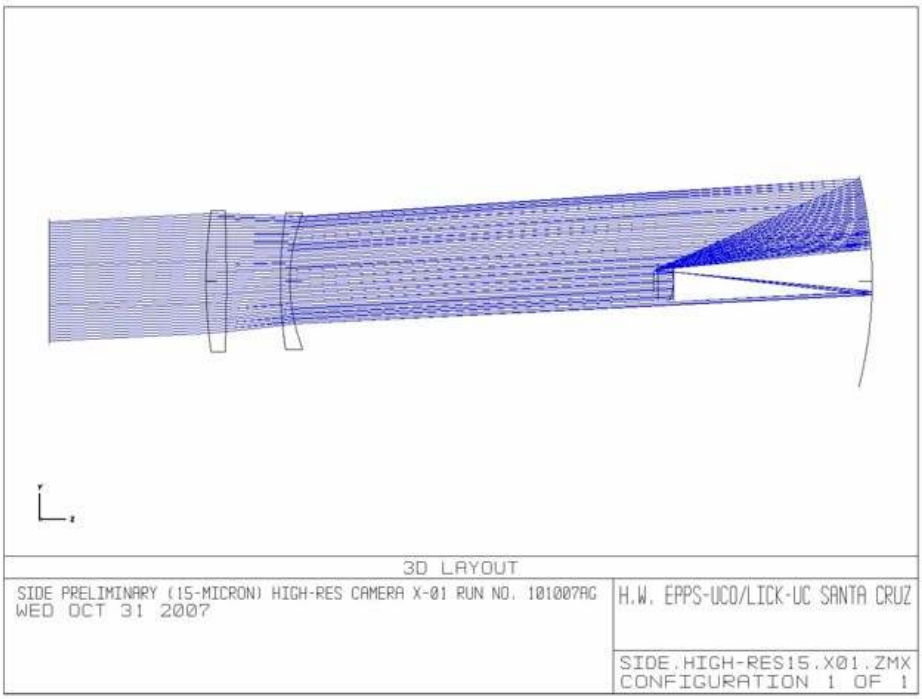

Figure 180 Same as Figure 179 but with more rays to indicate the vignetting.

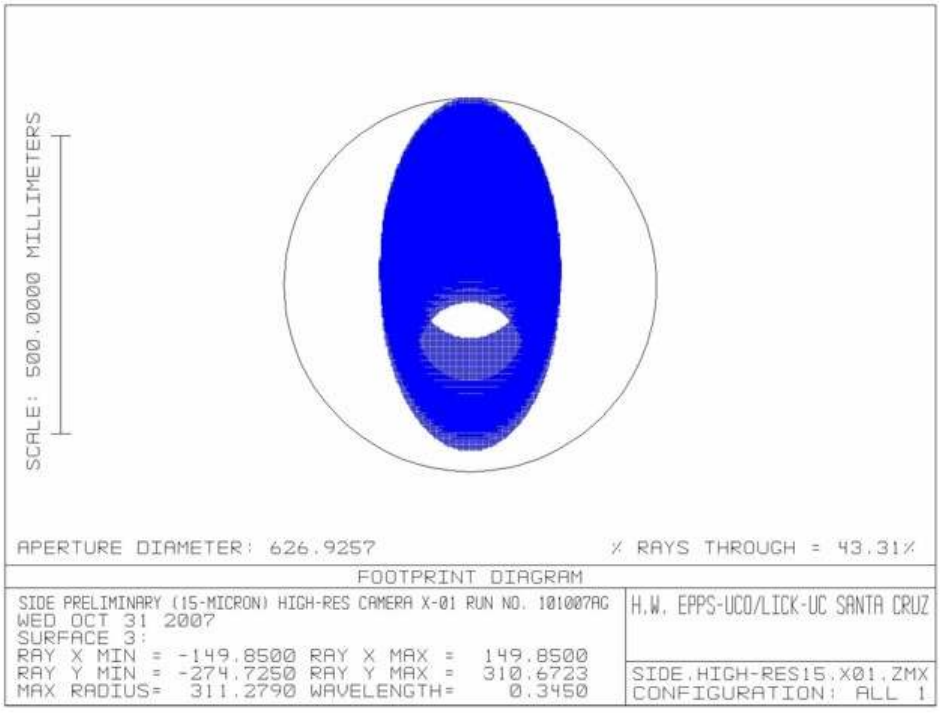

Figure 181 Rays arriving on the spherical mirror after having been vignetted by the field flattener obstruction.

3.10.2.5 Detailed Optical Performance of the Hi-Res camera designs

It is commonly agreed that if images are more-or-less "round", without extreme bumps, wiggles or tails, and they are more-or-less "smooth", without rings and voids, then they will be pixel-sampling limited if about 80% or more of the energy is included within a (2-pixel x 2-pixel) Nyquist sampling box and 95% or more of the energy is included within a (3-pixel x 3-pixel) sampling box (both centered on the image centroid). If the images were Gaussian in shape, 80% of the energy would be contained within 1.27 rms image diameters and 95% would be contained within 1.72 rms image diameters. The corresponding criteria for quasi-Gaussian images to be pixel-sampling limited is that (roughly speaking), they should have rms diameters in the (1.6 to 1.7) pixel range (or smaller). This criterion is no substitute for detailed modulation transfer calculations but it is probably more than adequate for the purpose of examining preliminary optical designs.

Monochromatic image analysis for the Hi-Res camera includes rms image diameters in pixel units over the full spectral range without refocus. A (310 by 573.5)-mm entrance pupil at an entrance-pupil distance of 700.0 mm was used for the calculations and the camera was illuminated in perfectly parallel light. This illumination pattern strongly overdrives the camera in that the entrance pupil will never be quite that large, even for the most extreme red wavelengths. However it can be seen that all of the images for this 880.0-mm focal length (15-micron) camera have rms diameters less than about 0.9 pixels. Thus it is quite clear that the HIGH-RES camera will be very strongly pixel-sampling limited. Its imaging characteristics appear to be outstanding.

The expected optical performance of this camera is further illustrated with polychromatic spot diagrams in Figure 182 for the Hi-Res camera. The spots are enclosed in (2-pixel x 2-pixel) Nyquist sampling boxes.

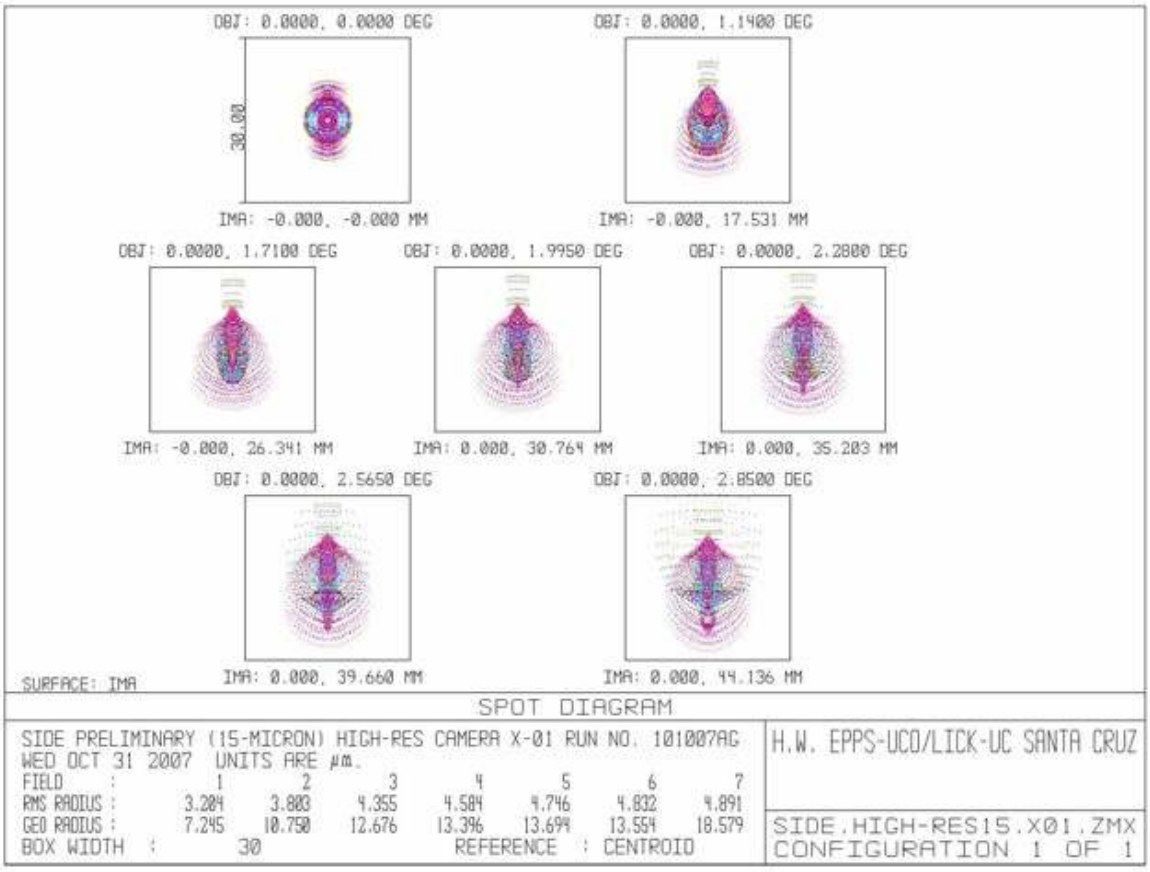

Figure 182 Spot diagram of SIDE high resolution camera.

These spot diagrams must be interpreted carefully because the vertical image smear is due to lateral color, which is irrelevant in cameras that will never be used for direct imaging! Thus, the viewer must compress the spots vertically in his/her mind to assess them in a way that is more nearly appropriate to their intended use as spectroscopic-only cameras. The subjective point to be made is that indeed, virtually all of the energy will be included within the (3-pixel x 3-pixel) sampling boxes, such that the cameras will certainly be pixel-sampling limited in practice.

3.10.2.6 The complete optical system

Figure 183 shows a layout of the preliminary Hi-Res VIS spectrograph design. We conclude that image slicing, by use of fiber coupling with units containing 7 fibers, makes it possible to achieve spectral resolution and wavelength coverage mandated by the science goals for SIDE, with collimated beam sizes that are buildable and affordable.

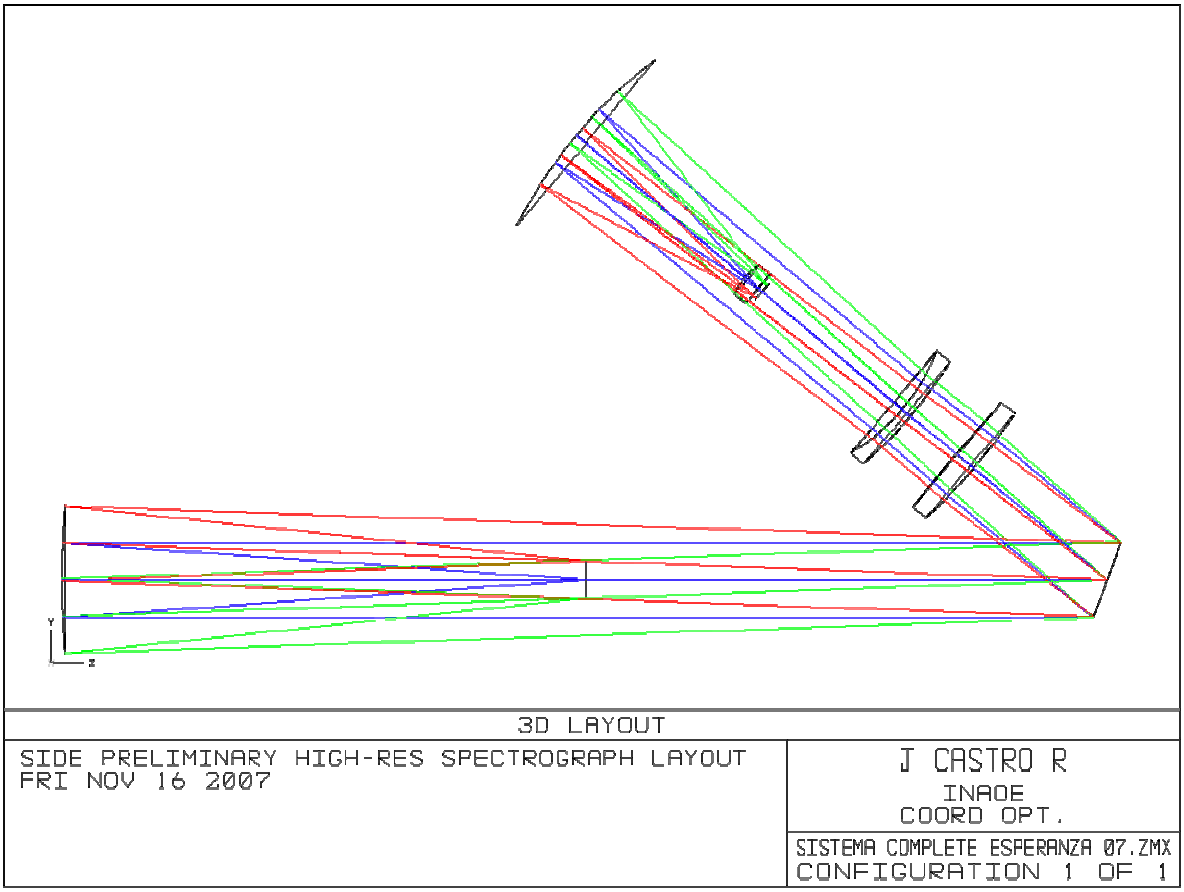

Figure 183 SIDE preliminary Hi-Res VIS spectrograph layout.

The different resolutions will be achieved by changing the grating angular position. As an example, Table 77 presents the parameters for three resolutions.

Resolution	Central Wavelength (μm)	Spectral Range (μm)	Spectral Width (Angstrom)	Dispersion (Angstrom/pixel)	Pixels/Resolution element	Detector Format
8000	0.37	[0.35 – 0.40]	500	0.1	4.7	4096x4096 @ 15 μm/pix
15000	0.60	[0.57 – 0.62]	500	0.09	4.7	4096x4096 @ 15 μm/pix
29000	0.85	[0.83 – 0.87]	500	0.06	4.7	4096x4096 @ 15 μm/pix

Table 77 Hi-Res VIS spectrograph resolutions for fibres with an aperture of 1.5 arc sec using a grating of 1400 gr/mm with λ_B = 0.6 micron. In this MOS mode, 96 objects could be observed simultaneously (Rabaza 2007).

It has proved possible to design single-spherical-mirror collimator for Hi-Res application. The Hi-Res collimator will operate at f/7.00 and the input imaging scale from the telescope will be 340.0 micron/arcsec. The required input f/ratios will be achieved by the use of

microlenslets or microlenslet arrays to down size the GTC's native 825.0 microns/arcsec imaging scale.

The preliminary optical designs have been done with generic dispersion coefficients for the optical materials at "room temperature." High precision (a few parts in the 5th decimal place) indices of refraction and derivatives with temperature for the actual lens blanks will have to be provided so as to attain the image quality described here for the preliminary designs.

It has proved possible to design a preliminary catadioptric all-spherical camera for the Hi-Res application. The design accommodates the most extreme anamorphic factor expected for the redmost set up of a (310 x 600)-mm 1st-order reflection grating. The image quality of this camera is strongly pixel-sampling limited.

The Hi-Res camera will require the use of order-separating filters for some science applications. These filters should be placed in parallel light, at an angle to the optical axis, so as to avoid ghost images. The Hi-Res filter will be quite large and may push the state-of the-art.

It is assumed that high-efficiency antireflection (AR) coatings will be used on all exposed optical (transmission) surfaces. This will be essential in order to maximize throughput and to avoid potential ghost images and ghost pupils by back reflection (off of the detector in particular). An attempt has been made to mitigate such unwanted ghosts by careful choice of lens-element radii during the design process although at some residual level they cannot be avoided. This issue should be revisited more carefully as a preconstruction optical design for SIDE is developed.

3.10.2.7 Preliminary optomechanical concept

The functional specifications and the final optical configuration will drive the mechanical design of the instrument, therefore at this stage we present the thinking behind the optomechanical design. The Hi-Res VIS spectrograph will be a stationary one, mounted on a optical bench in an insulated but unheated room underneath the Nasmyth platform. To reduce thermal bowing, the optical bench will be designed with an aluminium honeycomb core and Invar facesheets. The optics will be mounted in a fixed orientation with their optical axes pararell to the bench surface. As a worst-case-analysis, temperature changes as large as 40°C (-20 to 20°C) are considered here. Since the spectrograph is not subject to varying gravitacional loads, the major design challenge will be to minimize thermal distortions and to maximize the mount stiffness while controlling the mass. The only moving part is the grating that would be mounted on a rotary motorized stage with an encoder to ensure realibility in the grating angular position.

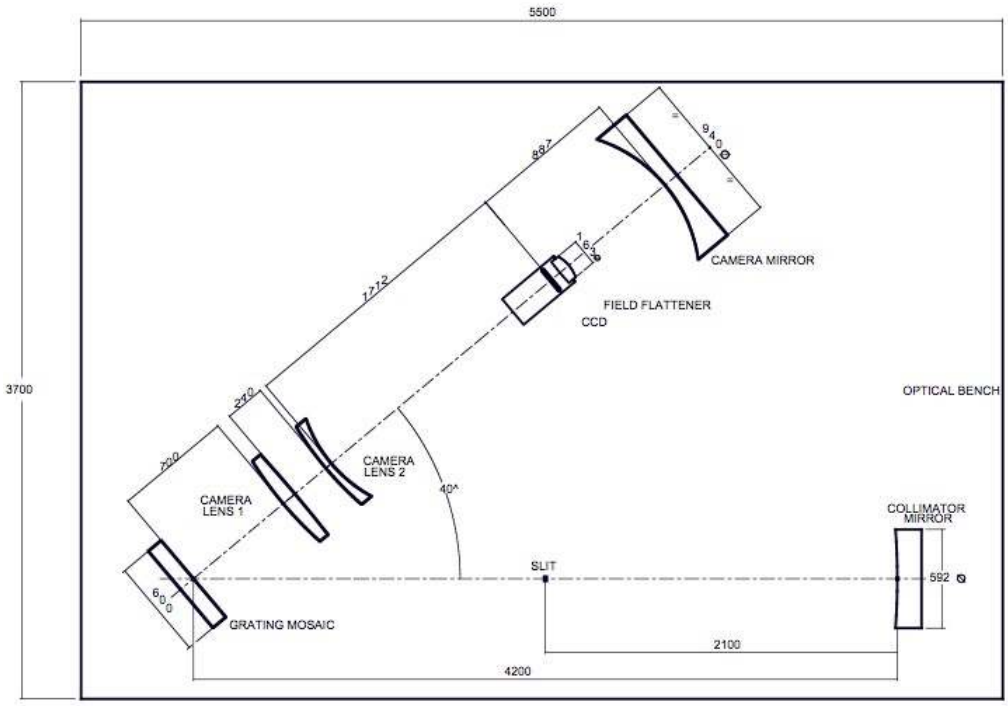

Figure 184 A view of the Hi-Res VIS spectrograph on the optical bench.

For our analysis we consider Harland W. Epps preliminary optical design dimensions, the collimator and camera mirrors diameters are 590 mm and 940 mm respectively, while the fused silica camera lenses diameters are 627, 608 and 163 mm, respectively. The grating will be 300 x 600 mm. Figure 184 shows a view of the spectrograph optics as it would look on a optical bench. The distances between the components are also included to illustrate the dimensions of the spectrograph and the 3700 mm x 5600 mm optical bench required.

There are several mountings techniques for lenses and mirrors. Studies of the deformed optical surfaces predicted by finite element models will determine the best option. Nevertheless from previous experience is very likely that the tangencial support will be adequate for most surfaces (Langarica, et al. 2006). Following the experience of the bench spectrograph Hectospec for the converted MMT (Fata et al. 1999), that has fused silica lenses and zerodur mirrors, we analyzed the possibility of developing a similar concept for the optical mounts.

The most challening mount is that of the largest compoment of the system i.e. the 940 mm diameter camera mirror- that very likely during the optics optimization process will increase its size. Therefore for the preliminary analysis we concentrate in this mount. The mirror mount has three components: tangential flexures, a support structure and an athermal interface to accomodate the CTE mismatch between a steel support and the Invar optical bench.

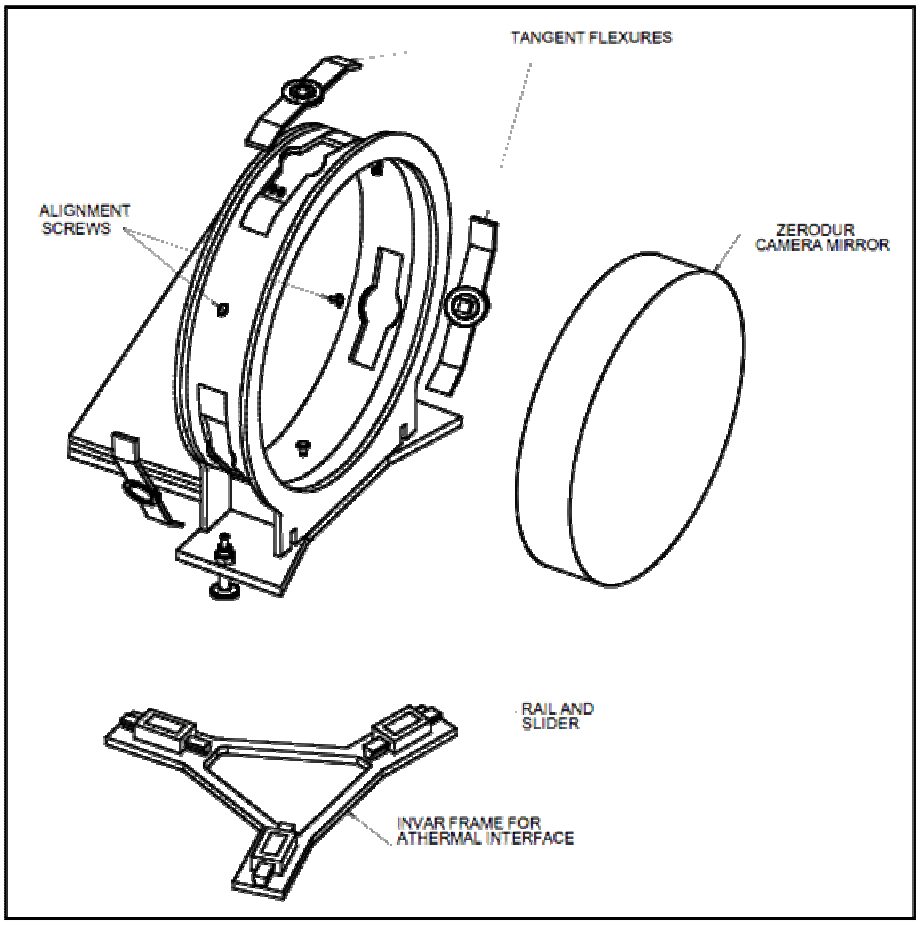

Figure 185 A schematic view of the mirror mount based on Hectospec mirrors mounts concept.

The flexures need to be designed to provide stiffness in the axial and tangential directions and to be compliant in the other four degrees of freedom. They must accomodate radial differential expansion between the steel mount and the Zerodur mirror without introducing excessive stress. The athermal interface uses three linear slides between the base plate of the optical mounts and the Y-shaped Invar plate that is bolted to the bench. The slides are located so that each carries one-third of the mounts weight.

We developed a model of the mirror mount shown in Figure 185. For the model we consider a 940 mm diameter zerodur mirror with a 117.5 mm central thickness and a radius of curvature of 896 mm. The mass of the mirror is 174.5 kg and the mass of the unit formed by the mirror and the mount is 218 kg. The model is presented in Figure 187, Figure 188, Figure 189 and Figure 190. In Figure 186 the mirror mount is shown in different positions to illustrate its components. Using finite element techniques we calculated the stresses and displacements from gravitacional load for the camera mirror mount unit. The results, obtained without any optimization and shown in Figure 187, illustrate that in this case the maximun displacement is 5.7 micron.

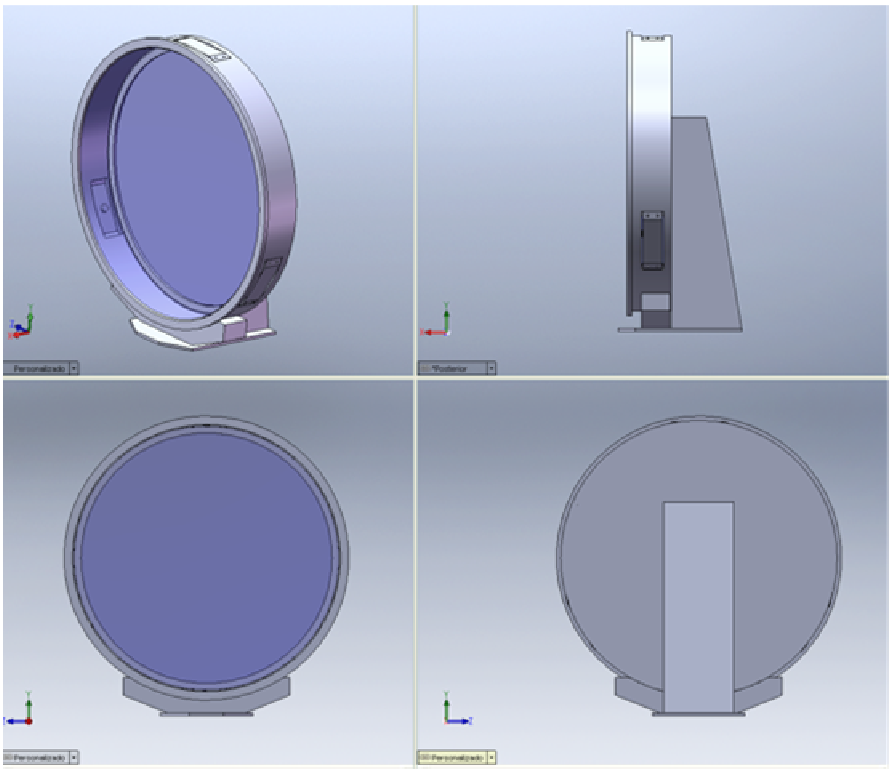

Figure 186 Model of the 940 mm diameter mirror mount of the Hi-Res VIS spectrograph.

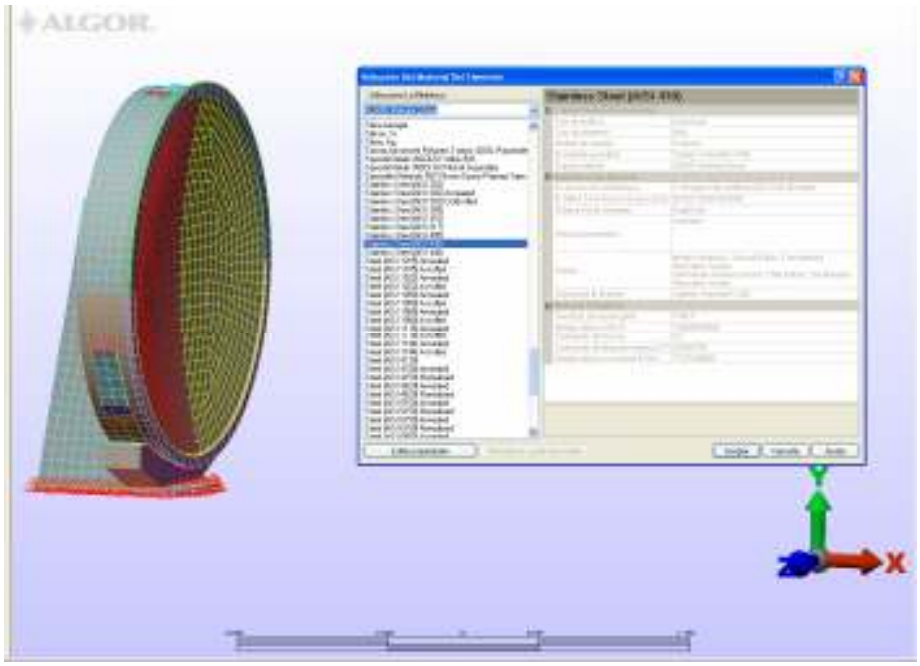

Figure 187 The material used for the finite element analysis was AISI 430.

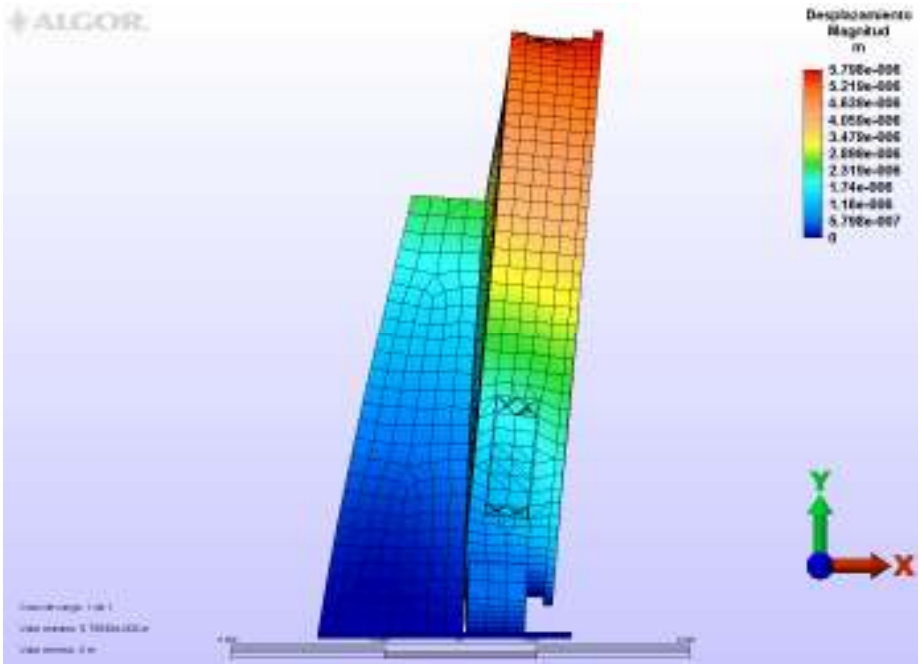

Figure 188 Finite elements analysis of stiffness under gravity load of the 940 mm diameter zerodur mirror in a steel mount. The mirror mass is 174.5 kg and the mass of the unit formed by the mirror and the mount is 218 kg.

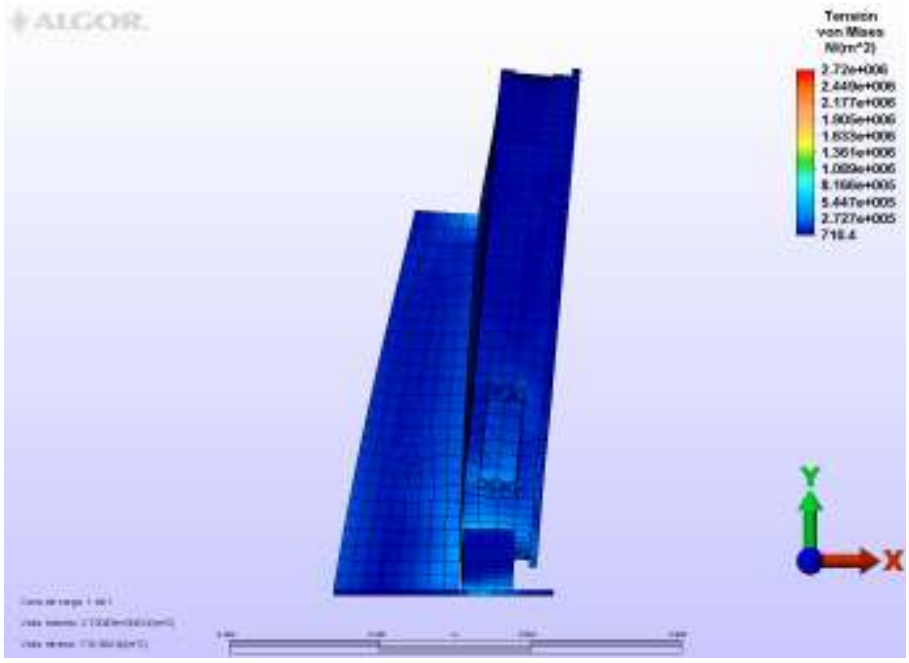

Figure 189 Stresses under Von Mises criteria show that we have a robust model that can be optimized for the weight–stiffness relation.

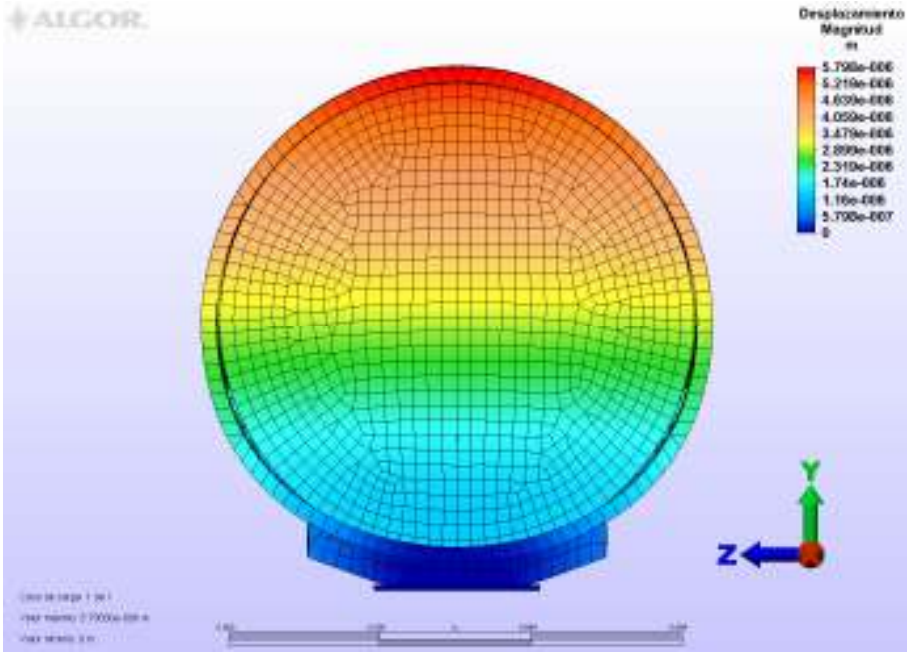

Figure 190 Displacements of the 940 mm diameter mirror under gravity load.

For assembly, the mirror opening would be facing up such as the mirror is lowered into the mount until its back surface rests on three axial screws adjacent to the flexures locations. The three radial screws function would be to align the mirror with respect to the support. Once the mirror is properly aligned with respect to the cell, the flexures would be attached by bolting the ends of the flexure to the support structure. The mirror assemblies would be aligned in the spectograph by some mechanism below the athermal interface or on top of a rail and slider.

In the cases of the camera lenses, the grating and the order-separating filters, the mounts would also be made from the same material as the mirrors mounts so that the optics will be decentered equally with respect to the bench as the temperature changes. The stresses and the deflections in all the optical and structural components resulting from gravitational and thermal loads need to be calculated using finite element techniques, as shown in Figure 188 to Figure 190 for the gravity load. As a reference in the case of Hectospec, the lens and mirror deformations due to gravity and to 40 °C temperature changes were predicted by finite elements analysis and fitted with Zernike polynomials. The Zernike fits of the deformed surfaces were ray traced and the deformations showed a negligible effect on image quality. As Hectospect optics, ranging in size between 200 mm and 800 mm, are similar to SIDE Hi-Res VIS optics dimensions we are confident in achieving the same level of accuracy.

We have developed a model for the mount of the largest and heaviest optical element, the 940 mm diameter camera mirror. The preliminary results of the finite elements analysis *without any optimization* show that our model is robust and feasible. Therefore we conclude that it is possible and affordable to design the cells and mounts for all the optical components of the Hi-Res VIS bench spectrograph.

3.10.2.8 Costs

Table 78 shows the estimated cost in Euros for the Hi-Res spectrograph.

Camera + Collimator	2,680,069
Collimator masters	800,000
Grating (estimated)	660,000
Filters (estimated)	300,000
Total optics	**4,440,069**
Mechanics (materials + machining)	**1,751,500**
Overall total	**6,191,569**

Table 78 Cost breakdown for the Hi-Res spectrograph.

3.10.2.9 References

Epps, H.W., and Vogt, S.V., 1993 Applied Optics, Vol **32**, No. 31, pp. 6270-6279.

Langarica, R., Carrasco, E., Ortíz, M., Pérez, C. & Páez, G. et al. 2006, INAOE Technical Report RTO 573. *Design, construction and test of Frodospec red arm optics.*

Fata, F. and Fabricant, D.G. 1999, Proceedings SPIE, **3355**, pp. 275-283. *Mounting large lenses in wide-field instruments for the converted MMT.*

3.11 The Detectors system

A starting point to work about the Detectors System is the Table 79. It summarizes the main SIDE requirements already known and also those to be defined:

Requirement	Optical CCD	IR array
N. of detectors: **Science** **Engineering** **Multiplexers (IR)** **Spares**	1x(4kx4k) per spectrograph TBD TBD TBD	1x(2kx2k) per spectrograph TBD TBD TBD
Format **Gap** **Flatness**	4kx4k monolithic N/A TBD	2kx2k N/A TBD
Pixel size	15 micron	18 micron
Working wavelength range	350-950 nm	950-1.700 nm
Quantum efficiency	>60% @ 400 nm >80% @ 900 nm	>80% @ λ>900 nm
Readout noise	<6-8 e^- (rms)	<20 e^- (rms)
Readout speed (frames/s)	TBD	TBD
Dynamic range (well depth and linearity)	~200 ke^- <1% up to 90% full well	~200 ke^- 2-4% from 10-80% full well
Dark current	2-3 e^-/pixel/hour	<1 e-/s/pixel
Working temperature	-90/-100 ºC	70/80 K
Cosmetics (number of defect allowed)	TBD	TBD
Fringing or other spurious effects	No fringing	No fringing
Mounting alignment requirements (mechanics)	TBD	TBD

Table 79. SIDE detectors requirements

In the first part of this section, as a result of a market analysis of astronomical detectors, we will show the visible and infrared detectors that we think are more suitable for SIDE.

The controllers market is analyzed separately in the next part of the section.

During the market analysis we have seen that there are several possibilities to cover the required spectral range 0,35-1,7 nm from the detectors point of view. Apart from the classic two arms spectrograph which requires a detector for each arm, we could use a SWIR array

without the sapphire substrate in just one arm spectrograph, as the response of this kind of devices seems to be rather good over the whole spectrum (excepting, perhaps, in the blue range < 500 nm). Nevertheless, the present optical design and the maximization of the sensitivity of the system over the whole spectral range narrow the detector alternatives.

3.11.1 Visible detectors

The main specifications of the available detectors suitable for SIDE are given below. These figures of merit must be understood as commercial specifications, not as requirements of SIDE. In some cases, there is the possibility to customize some performances –as the pixel size, or some special coating– under request, if the option to be elected demands them.

(a) E2V Technologies (UK) – Model CCD44-82 and Model CCD231-84

- **Features**:
  i. 2K x 4K pixels for 44-82 model and 4K x 4K for 231-84 model
  ii. Pixel size: 15 microns
  iii. Back illuminated (high QE, see Figure 192)
  iv. Readout Noise (RON) < 2.5 electrons rms @ 20 KHz
- **Advantages**:
  i. Widely used (most common and popular large-format CCD)
  ii. Very low noise.
  iii. Easy camera integration. For example, with Spectral Instruments.
  iv. GTC to E2V company fluid relation.
  v. Wide experience at the IAC-GTC facilities. It is the CCD of OSIRIS (mosaic x2) and ELMER (x1) GTC instruments.
  vi. New development: CCD44-82 back illuminated red optimized (30-55% @ 900nm). Other customized developments available under request.
- **Note**:
  i. 4K x 4K format is a very recent development but as it inherits all the characteristics of the 2K x 4K format we do not expect any problems by the time these detectors will be needed by SIDE.

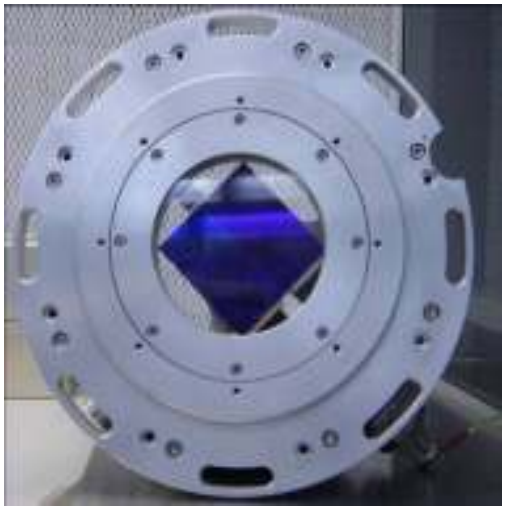

Figure 191 2x (2Kx4K) CCD44-82 mosaic in the OSIRIS-IAC-GTC cryostat

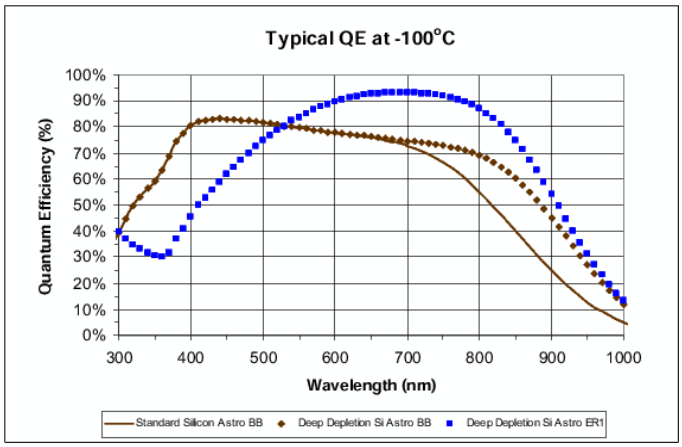

Figure 192 E2V CCD44-82 quantum efficiency plot.

(b) LBNL CCD (Lawrence Berkeley National Laboratory)

- **Features**:
  i. 2K x 4K and 4K x 4K pixels format
  ii. Pixel size: 15 microns
  iii. Back illuminated (high QE, see Figure 194)
  iv. Readout Noise (RON) ~ 7 e^- rms @ 250 KHz, ~ 4 e^- rms @ 100 KHz
- **Advantages**:
  i. Very high RED quantum efficiency
  ii. Price can be low if included in DES production batch.
  iii. Fluid contact with IFAE and LBNL.
  iv. No fringing.
- **Notes**:
  i. As in the previous case, 4K x 4K format is a very recent development but as it inherits all the characteristics of the smaller formats we do not expect major problems.
  ii. Customized product, not fully commercially available.

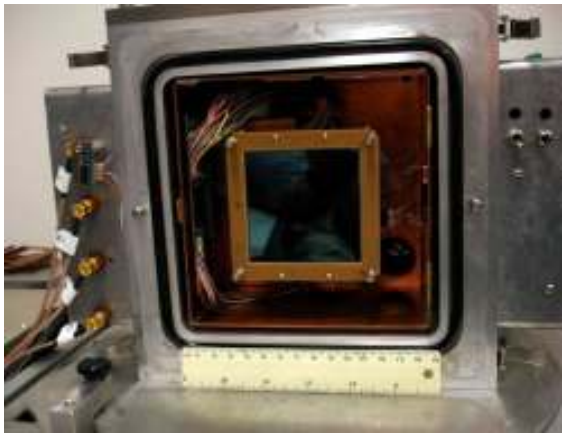

Figure 193. LBNL 4K x 4K under tests

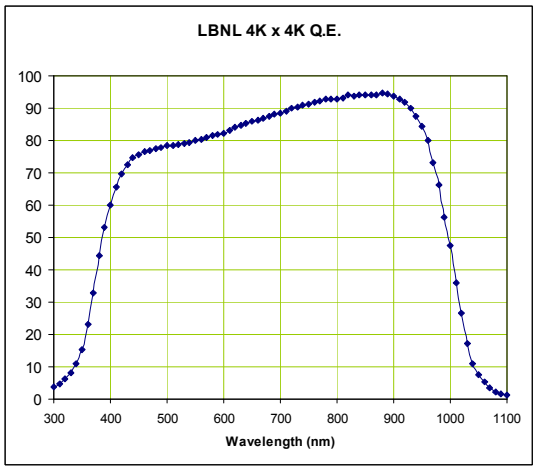

Figure 194. LBNL 4K x4K quantum efficiency plot

Other CCDs were considered during this study, for instance, the 4kx4k Fairchild CCD486 and STA 0500A, but the abovementioned match better the SIDE requirements.

In conclusion, for the Dual VIS-NIR spectrograph we consider that LBNL CCD is probably the best choice due to its good quantum efficiency in the red and its lack of fringing. For the Hi-Res Spectrograph, were a higher response in the blue spectrum is required, the E2V CCD seems more appropriate.

3.11.2 IR Arrays

All of these devices are based on the CMOS technology instead of the CCD one. There are two main manufacturers (Teledyne –formerly Rockwell- and Raytheon), and their products are very customizable. A new series of devices based on InGaAs were also considered, but it seems not possible to get one of these new cheap chips to fulfill the SIDE SWIR requirements.

(a) Raytheon VIRGO 2K

- **Features**:
  i. 2K x 2K pixels (HgCdTe technology)
  ii. Pixel size: 20 microns
  iii. Spectral Range: 0.8 – 2.5 microns (tunable: available cutoff at 1.7 μm)
  iv. Readout Noise (RON) < 20 electrons rms @ 400 KHz
  v. QE (mean): ~80 %
- **Advantages**:
  i. Availability < 10 months.
- **Notes:**
  i. No ASIC available (see later Teledyne products for comparison).
  ii. Poor technical support.

Figure 195. Raytheon VIRGO 2K 3-side buttable

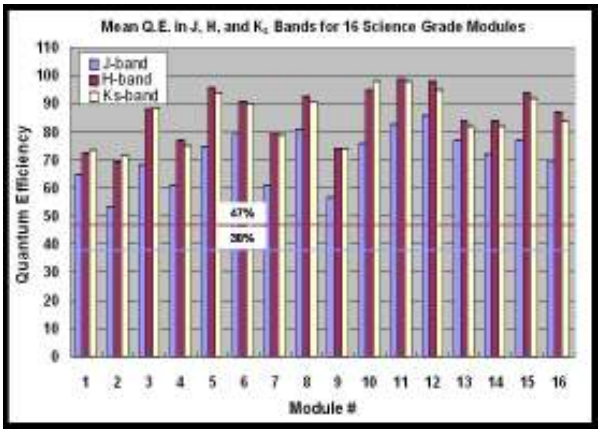

Figure 196. VIRGO 2K quantum efficiency plot for 16 VISTA arrays

(b) Teledyne (Rockwell) HAWAII 2 RG

- **Features**:
  i. 2K x 2K pixels
  ii. Pixel size: 18 microns (also HgCdTe)
  iii. Spectral Range: 0.8 – 2.5 microns (tunable, available cutoff at 1.7 μm)
  iv. Readout Noise (RON) < 15 electrons rms @ 100 KHz
  v. QE (mean): ~80% AR coated
- **Advantages**:
  i. Previous experience at IAC-GTC with this type of arrays (PACE-HAWAII 2 in EMIR, tested in IAC facilities).
  ii. ASIC (Application Specific Integrated Circuit) available: SIDECAR (very soon)
- **Note**:
  i. Very poor technical support.

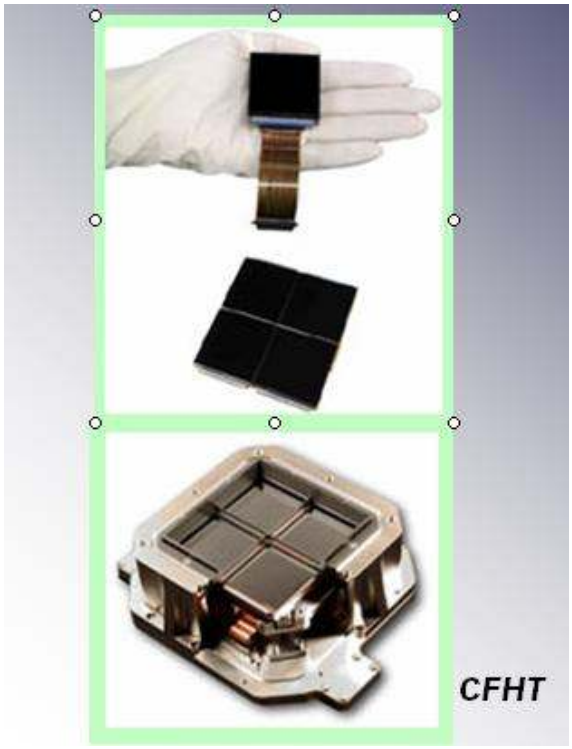

Figure 197. HAWAII 2 RG chips and mosaic (CFHT)

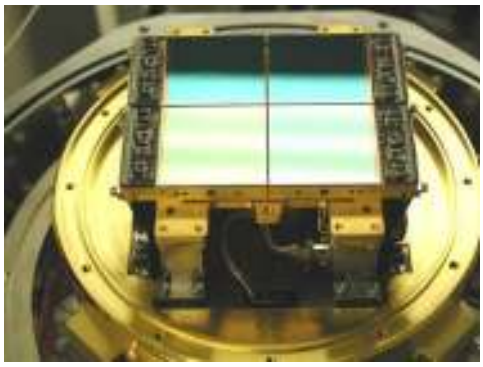

Figure 198. HAWAII 2 RG chips and mosaic (JWST)

Although both arrays (VIRGO and HAWAII) have fairly similar characteristics we consider that the previous experience on the HAWAII detectors by the IAC and the availability of an ASIC from the same manufacturer to make easier the process of read and command the detector, make the HAWAII option preferable.

3.11.3 Controller and cooling systems

There are two main questions related with the handling of the imaging devices: the control electronics –commonly known as "the controller"–, and the cooling system to operate the detectors properly. Regarding to this second matter, normally the working temperature is a trade-off between some requirements involved, such as readout noise, dark current or indeed quantum efficiency. But the mechanisms to carry out this procedure are well known, and the number and type of alternatives do not seem to be a major problem for SIDE, which only works up to 1.7 microns.

For the purpose of this document we have focused our attention on detector controllers commercially available. Given the large amount of controllers that will be needed by SIDE, the possibility of developing entirely a new control electronics have been considered. Nevertheless, the scope and risk of such development probably are in excess of those affordable for SIDE. This kind of development will be reexamine in the future if some synergies are found with other projects, groups and/or Grantecan, for instance, through the LISA initiative. LISA (Laboratory of Imaging Sensors for Astronomy) is a new facility, a

joint venture of Grantecan and IAC at Tenerife, with the objective of acquire, test, characterize and accept astronomical detectors for GTC. Also, its purpose is to adapt detector controllers to the GTC Control System software and hardware standards, to support viability studies for new instruments to be installed at the GTC and to prototype and test new developments in this wide area.

In the following paragraphs we show briefly the survey of current commercial controllers market:

(a) In the visible range (up to 1 micron, and only CCDs devices), the most confident company currently available is **Spectral Instruments (SI)**, from Tucson, USA. They offer the 600, 800, 900 and 1000 model series, including CCD formats of 2K x 4K, 4K x 4K, and mosaics. Spectral Instruments use a proprietary electronics with commercial arrays (as the E2V44-82 or the Fairchild CCD486 before mentioned), achieving a RON over the 3 electrons rms at minimum readout speed. To cool down the devices it is possible to adapt a TEC (Thermo Electric Cooling, commonly Peltier type) or the now famous and comfortable PolyCold-Cryotiger closed cycle cooler. The main advantages of the Spectral Instruments products are their plug & play electronics and the delivery of complete camera systems which means an off-the-self solution for controller, cryostat and cooling system in one shot. The IAC uses SI camera systems in the IAC80 and UES instruments. As disadvantages, SI currently do not admit custom changes in their series (for example, using lenses as windows) and the control is limited to Labview with Windows and Linux drivers. This means that the software has to be adapted to the GTC control system standards and perhaps it is a straightforward solution for the Hi-Res Spectrograph E2V CCD but not for the IR array nor the LBNL CCD, although this last has to be confirmed.

Figure 199. Some SI cameras

Figure 200. Large format (including shutter) SI camera

(b) Also in the visible range but extending their performances to the SWIR we find the widely spread **ARC controllers** (formerly SDSU –San Diego State University– or simply Leach (Bob) controllers). This company shows a slow but successful evolution in their series, from the Generation II ones (most simples, designed to handle common CCDs as the E2V ones), to Gen III (to perform complex operations, as coadding and multiple analog channels in the infrared), and the new Gen IV, which substitutes the classical DSP56000 series as the core of the controller by a

powerful Altera FPGA, allowing an easy C-programming instead of the complex assembler code. The main features of the ARC controllers are: (i) able to handle almost any type of CCD or SWIR array, (ii) flexible programming –but complex, and (iii) a custom configuration of cards. Parameters as readout noise are rather good (~3 electrons rms). Other advantages are the different hardware interfaces (PCI, VME –obsolete-, Sbus –also obsolete– or PMC) and software drivers (Linux, Windows, Labview, Solaris and VxWorks). These systems are well known by any astronomical institution (for example, IAC-GTC operates with ARC controllers the CAIN2, LIRIS, OSIRIS, EMIR and Elmer instruments). The disadvantages are also known: based on an old design, are big, no plug&play systems and need a long learning period. Besides, there is not an official technical support, with many different developments and variations from different institutions. Summarizing, it is considered an open system, very popular in the community and it is a practical solution for controlling all the CCDs and IR arrays of SIDE.

Figure 201. Typical ARC controller

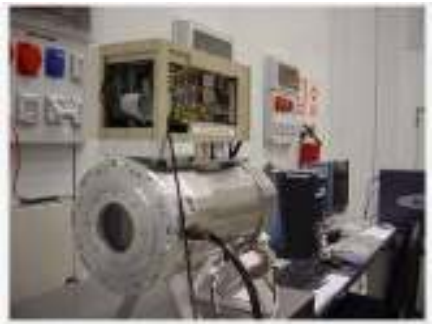

Figure 202. ARC controller mounted on the OSIRIS cryostat (with a couple of E2V-4482)

(c) Some detector manufacturers sometimes offer a devoted controller for some or their products. This is the case of **Teledyne-Rockwell**. The most interesting news from Rockwell is SIDECAR. SIDECAR is an ASIC (Application Specific Integrated Circuit) which provides all the clocks and bias voltages necessary to operate the array, performing 12 or 16 bit analog to digital conversion on-chip. SIDECAR is the acronym of System Image, Digitizing, Enhancing, Controlling and Retrieving. In some sense, chips as SIDECAR are the future in the handling of imaging arrays. By the moment, this Rockwell design is under testing, but it has been conceived to handle the HAWAII-2 RG multiplexers. Although this is not a solution for a common controller for all the detectors of SIDE, it could be the best solution for the IR detectors in the Dual VIS-NIR spectrograph.

(d) An entirely new detectors controller developed by the **NOAO is Monsoon**. Monsoon is able to handle almost any type of CCD or IR array, with –similarly to the ARC ones– a customizable configuration of cards. Monsoon incorporates, obviously, a modern solution, with a crate-based system (in Eurocard format) and a compact-PCI backplane but without its protocol. The advantages of Monsoon are mainly its large software framework and, maybe, its nature of "open system". This is sometimes good (as it happened with the old SDSU controllers), mainly if the cooperation with

the NOAO team works properly. It is remarkable the IFAE experience with Monsoon in the DES project. The main disadvantage is, as in the ARC case, the learning curve and the no plug&play nature of this system, with many configurable parameters and not optimized for the CCDs readout. It can be considered as a product in development, not a commercial controller. Its use in SIDE and the adaptation of its high level software to the GTC control system standards will require a considerable man power effort for the SIDE team.

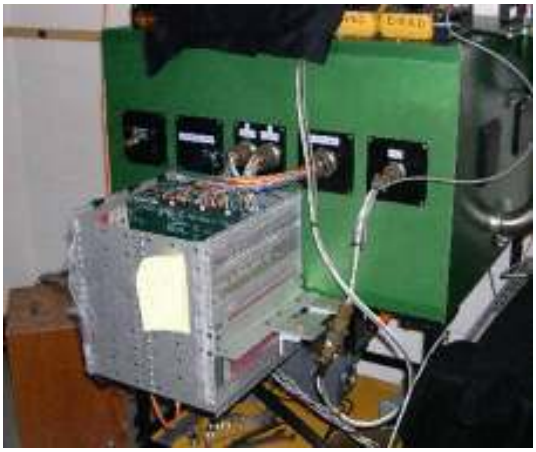

Figure 203. A Monsoon controller.

To finish the section on controllers, it its work to mention the possibility, to acquire a customized controller based on similar or existing commercial product for devoted cameras. For example, high performance camera manufacturers as Andor, SciMeasure, Dalsa or Teledyne-Rockwell in the infrared range have developed its own controllers. Other possibility is the availability of controllers developed by third institutions, as ESO. But these are currently remote options.

Regarding cooling systems, if they are not included with the entire camera (for example, Spectral Instruments), we can call to companies as Infrared Laboratories (Tucson, USA), SNLS (Grenoble, France), GL Scientific (Hawaii, USA) or others to get a classical liquid nitrogen cryostat, a TEC one if the working temperature is not very demanding, or a new Polycold-Cryotiger closed cycle cooling system, a special device with no vibration elements that is getting more and more success among the astronomical community. Although cooling a small cryostat nowadays is not a big issue, in the case of SIDE, due to its large number of cryostats, some practical problems may arise. One of them is the GTC directive of avoiding any vibration mechanism in the telescope platform which affects the use of powerful close cycle coolers and vacuum pumps. The other is the limited capacity of the compressed Helium lines provided by GTC to the focal stations.

To keep the detector temperature stable inside the cryostat, we propose the use of a commercial controller with a PID-based control, like the Lakeshore (USA) ones, which is almost a standard in the GTC instruments.

3.11.4 Proposed solutions

Along the previous sections, we have surveyed the current detectors market in the SIDE spectrum range: from 0.35 to 1.7 microns. At the beginning of this study, where the optical design was open, there were many possible options. Presently the concept of SIDE is converging towards a classical two arm (Vis & IR) spectrograph replicated 10 times plus one high resolution spectrograph. The requirements applying to every single spectrograph are not very demanding from the detector or electronics point of view, because the focal plane is not very large (a 4kx4k pixel detector is enough) and the modes of operation and detector characteristics are the usual ones, being the quantum efficiency at the wavelength of interest the main driver. Difficulties may appear in the control system to manage such number of detectors, controllers, mechanisms and so on, but they are somehow independent of the detector and controller solution that we may finally select for SIDE.

Summarizing the results of this study we propose the following solution:

(a) The Dual VIS-NIR spectrograph visible detector first choice is LBNL CCD 4kx4k. A good alternative is E2V CCD231-84. Also, a mosaic of two 2kx4k models of these detectors is an option.

(b) The Dual VIS-NIR spectrograph IR detector first choice is Teledyne Hawaii 2 RG. The Raytheon VIRGO is an alternative but its different pixel size (20 micron instead of 18 micron) may have an impact in the optical design.

(c) The Hi-Res spectrograph detector first choice is E2V CCD231-84 due to its better blue response. The LBNL CCD 4kx4k and both 2kx4k mosaics are also alternatives.

The best solution for the Hi-Res spectrograph camera is probably the Spectral Instruments one. They can serve the complete camera. Nevertheless, this is probably not viable for the Dual VIS-NIR spectrographs with the proposed detectors. To have a homogeneous solution, the best choice is the ARC controller with a commercial cryostat. ARC controllers can handle all these detectors.

An interesting alternative for the Hawaii 2 RG array is the use of the SIDECAR ASIC controller from the same manufacturer. If its availability and performances are confirmed in the next future, this will probably be the best choice for the IR detector controller, although its integration with the GTC control system will require some effort. Alternatives to the ARC controller for the visible detectors are the adaptation of Monsoon or the development of a brand new controller but a considerable man power will be needed.

3.11.5 Nod and Shuffle with SIDE ?

3.11.5.1 Introduction

With CCD detectors, the 'nod-and-shuffle' technique allows rapid alternate sampling of target and sky spectra, whilst avoiding the extra noise that would normally be associated with equally frequent detector reads. By taking almost contemporaneous pairs of target and sky spectra using the same detector pixels and optical path, sky subtraction residuals due to temporal or instrumental variations (including differences between optical fibers, where applicable) can be reduced almost to zero. This near Poisson limited performance is, however, achieved at the expense of onsource efficiency and multiplex (see below). It also requires being able to offset the telescope pointing every minute or so. For further details of the nod and shuffle technique, see Glazebrook & BlandHawthorn (2001). Additional references of interest include Abraham et al. (2004), where nod and shuffle performance is discussed in the context of faint object detection with GMOS multislit spectroscopy, and Roth et al. (2004), which presents some test results from nod and shuffle with the PMAS fiber IFU.
However, we believe that the background subtraction with sky fibers without the need of Nod&Shuffle will be satisfactory for SIDE, following the recent results by Bolton & Burles (2007) (astroph /0703312), which has shown the high quality of the B-spline sky subtraction for Magellan-IMACS and Gemini-GMOS fiber fed spectrographs.

3.11.5.2 Performance considerations (for a fiber spectrograph)

Table 80 shows some considerations on the performance of a fiber spectrograph.

	Classical	**Nod and shuffle**
Sky subtraction residuals	Sky subtraction residuals tend to be dominated by inaccuracies in correcting for the following (rather than by inherent noise): a) with dedicated sky fibers • Fiber efficiency variations. • Fiber PSF variations or wavelength misalignments. • Detector flat variations, including fringing. • Scattered light variations. b) when nodding to sky • Temporal variability of telluric emission lines. • Instrumental instabilities, typically due to flexure, in the properties affecting a).	Sky subtraction is limited mainly by the statistical noise inherent in the detection (which can still be large for bright sky lines), rather than residual artefacts.

	Classical	**Nod and shuffle**
Multiplex (or field of view)	The full CCD detector area can be used for recording N fiber spectra.	At least half of the CCD area must be used for storing offtarget background spectra, limiting the maximum n. of fibers to N/2.
Onsource efficiency	Where the background is sampled using dedicated sky fibers, the entire observing time can be spent on the target (efficiency ~100%); otherwise long exposures are taken alternately on/off target (~50%).	Half the integration time must be spent on sky. In addition, nodding between target and sky as often as once per minute leads to large settling overheads for pointing and guiding (GMOS efficiency ~42%).
Poisson noise from background	A background spectrum can be produced by averaging over multiple sky fibers, such that it does not add significant noise to target spectra when used for subtraction.	Each target spectrum is skysubtracted using a background spectrum from the same individual fiber. Thus the background noise level contributes twice to the result (once from the target spectrum and once from the sky).
Detector cosmetics	Usually a small fraction of detector pixels are defective.	Repetitive charge shuffling in two directions brings out some additional charge trap defects. Dark exposures can help identify these during processing.
Data reduction	Background subtraction requires careful flat fielding, wavelength calibration etc. beforehand; might take more work than is otherwise needed for scientific purposes.	Subtracting object and sky pairs gives accurate results immediately

Table 80: Performance considerations for a fiber spectrograph

Some of these factors are considered in detail by Allington-Smith & Content (1998). See also Bolton & Burles (2007).

3.11.5.3 Applicability to a specific instrument design

The benefit of nod and shuffle depends on key parameters derived from the scientific requirements, notably spectral resolution, expected target brightness, sensitivity and wavelength of interest. The few strongest sky lines (such as [O I] at 557 or 630nm) are bright enough that their associated Poisson noise is likely to drown out useful information in the relevant pixels, whether or not systematic residuals are a factor (ie. with or without N+S). More important are the multitude of weaker OH emission lines spanning red to infrared wavelengths. At low resolution, these lines can blend and dominate the background level in many of the spectral pixels, in which case accurate removal with nod and shuffle can be important for optimizing the final sensitivity. At moderate to high resolutions, line subtraction residuals are better localized and may be acceptable as long as the spectrum between OH lines is free from significant residuals after processing. What constitutes an acceptable level of contamination depends on the target brightness, of course, with inaccuracies in sky subtraction becoming much more evident as target counts (ADUs) approach the level of the background.

3.11.5.4 Experience with GMOS-S IFU and IMACS at Gemini

3.11.5.4.1 Nod and shuffle

The field-to-detector mapping of optical fibers in the GMOS-S IFU (unlike GMOSN) allows the unit to be configured for use with nod and shuffle. Few datasets have been taken in this configuration to date, but a quick reduction of system verification data taken in the red (500 900nm at R~3000) is consistent with the expectation of Poissonlimited sky subtraction, without obvious residuals. Roth et al. (2004) likewise demonstrate accurate sky subtraction using nod and shuffle with the PMAS fiber IFU. The important question is therefore what accuracy can be achieved using classical sky subtraction, for comparison.

3.11.5.4.2 Classical background subtraction with sky fibers.

To compare classical background subtraction performance, GMOS IFU data extending to a moderately red wavelength setting (400-700nm, R~3000) have been reduced using sky spectra from the separate background field. At this intermediate resolution (and in the absence of the strong fringing seen at longer wavelengths), background residuals are at most a few counts (or percent) when following a standard reduction process, except in the 557nm line, as long as flat fielding and wavelength calibration are performed carefully enough. In particular (although the effect must exist at some level), there is no evidence for large residuals due to differing fiber PSFs, as discussed by Allington-Smith & Content (1998). The author's feeling is that classical data reduction will likely be good enough for targets with spectra at a level of some tens of counts per exposure, but could become problematic at levels of only a few counts. These numbers are for 'pixels' of 0.2” × 0.045nm. Clearly, further experimentation on fainter data at longer wavelengths would be valuable. Since, however, the limiting performance of classical reduction can only be tested using best case data and careful processing, further work is constrained by the ready availability of appropriate datasets with optimal calibrations. However, Bolton & Burles (2007) have shown excellent results for Magellan-IMACS and Gemini-GMOS fiber IFUs by using their new B-spline technique for sky subtraction without the need of Nod&Shuffle (See).

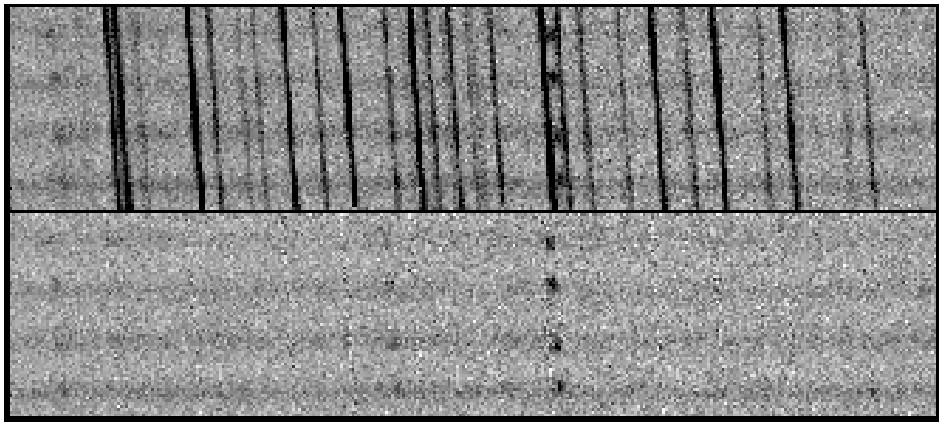

Figure 204 GMOS-N *i*-band sky subtraction for a single 900s exposure: before (above) and after (below). A total of 100 fiber spectra are displayed in each case, arranged vertically. Wavelength direction is horizontal, and covers approximately the same range as is shown in Figure 205.

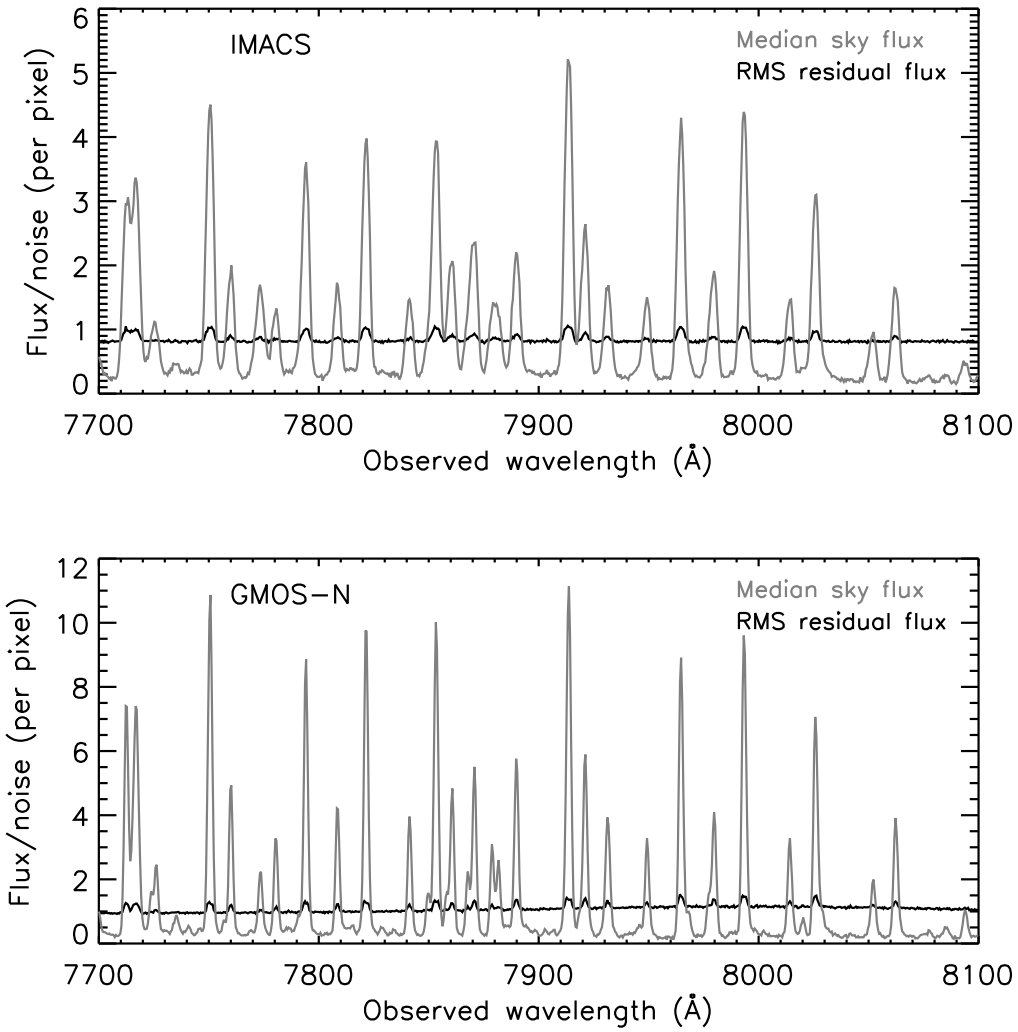

Figure 205 Wavelength-dependent IFU sky subtraction performance for IMACS (top) and GMOS (bottom) in an *i*-band wavelength range containing strong OH rotational transition lines. Shown in gray is the median across fibers of the ratio of sky counts to noise counts. The RMS across fibers of the ratio of sky-subtracted residual counts to noise counts is shown in black. When the noise is estimated correctly and the sky is subtracted perfectly, this second ratio will be 1. Pixel size is approximately 1.3 Å for IMACS and 0.9 Å for GMOS-N (including a binning factor of 2). Curves are computed for each exposure separately using all sky fibers; curves shown are a median across all individual exposures used in this paper. No adjustment is made for differing exposure times, airmasses, or moon phases between the individual exposures.

3.11.5.5 References

Abraham R.G., Glazebrook, K., McCarthy, P.J., Crampton, D., Murowinski, R., Jorgensen, I., Roth, K., Hook, I.M., Savaglio, S., Chen, H., Marzke, R.O. & Carlberg, R.G. (2004), AJ 127, p. 2455
AllingtonSmith, J.R. & Content, R. (1998), PASP 110, p. 1216
Bolton & Burles 2007, NJP, in press (astroph/0703312)
Glazebrook, K. & Bland Hawthorn, J. (2001), PASP 113, p. 197
Roth, M.M, Fechner, T., Becker, T. & Kelz. A. (2004), SPIE 5499, p. 387

3.11.6 Costs

Science grade large format CCDs cost about 100k €. NIR detectors 2kx2k will cost about 250k €. For the desired SIDE CCDs we are exploring the opportunity to get them through the DES collaboration which would significantly reduce the cost of each unit.

3.12 Acquisition and Guiding

3.12.1 Introduction

The A&G Unit must provide the following capabilities:

- Acquire the target field and align the telescope and instrument to the targets
- Provide closed-loop tracking of the target field with fast and slow guiding interfacing with the telescope.

3.12.2 Optical design

A schematic of the guiding system is shown in **Figure 206**. It comprises a guide fiber button connector supporting the output ends of the guide bundles, re-imaging optics, and a sensitive CCD camera.

A possible guide camera is the model ORCAIIBT from Hamamatsu Photonics. Extensive analysis selected this camera for the same role in FMOS-Echidna, and the requirements are essentially the same for SIDE.

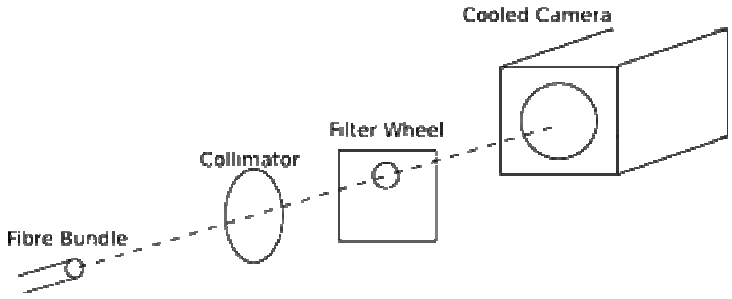

Figure 206 A schematic of the GFB re-imaging system.

It is necessary to use a filter wheel in order to minimize the effect of differential atmospheric refraction, that needs to be taken into account for proper acquisition and guide operation. In order to have the displacements due to differential refraction below the fiber size and at a given air mass, the number of filters between 350 and 1700 nm should vary (see Rabaza 2007).

3.12.2.1.1 Back-illumination for guide buttons

No back illumination is foreseen for this subsystem. The requirements for the positioning robot assert the correct allocation of the fiber bundle.

3.12.3 Mechanical design

3.12.3.1 Camera Systems

The Acquisition and Guiding system comprises two main functionalities that can share or not their camera systems. The acquisition will require the use of various acquisition objects and therefore the acquisition camera system is likely to require multiple cameras to achieve optimal field coverage or re-image the various objects onto one camera. The cameras used in these systems do not require in principle the sensitivity provided by a cooled detector, but some control over the exposure time may be necessary. The guide camera system requires high sensitivity, and therefore is likely to be a cooled camera. Both systems can in principle share the camera system differentiating their functionality at the software level.

There are several camera options that can be considered, largely depending on the camera interface.

Analogue cameras produce interlaced video at TV frame rate (25 or 30 frames per second). They usually have limited resolution (< 1 Megapixels) to maintain compatibility with television standards, and are essentially "dumb", with no control over exposure time or region of interest (ROI). Some cameras may have some switches or external digital inputs for automatic gain control, gamma correction and electronic shuttering.

Images from an analogue camera are acquired using a bus level analogue frame grabber, which is essentially synchronized to the camera video signal and performs analogue to digital conversion of the camera analogue data. Some frame grabbers may support windowing capability, and some frame grabbers can accept switchable input from multiple cameras. Long cable lengths are possible and fiber optic video cable extenders are available.

These cameras suffer from several sources of error - noise pickup and signal reflections in the cable and aliasing between frame grabber "pixels" and camera pixels (pixel jitter). These errors complicate the task of determining the centroids of the fibers in the field.

A better option seems to use digital cameras for all vision tasks, as for example is the case in a similar instrument WFMOS (see *WFMOS feasibility study report, 2005*). A digital camera contains an on-board analogue to digital converter, and sends digital data to the computer. These cameras are generally high resolution (up to 6 Mpixels), with programmable trade-offs between frame rate and resolution. The cameras usually have a number of programmable features, including exposure time, ROI, video format, frame rate etc. These cameras are available with a number of interfaces, including:

- Gigabit Ethernet - high bandwidth (1000 Mbits/second), peer to peer, 100m cable, no standard protocol for video.
- IEEE 1394 (Firewire) - high bandwidth (400 Mbits/second), peer to peer, 72m cable with hub, 200m with fiber optic interface, latching connectors, standardised protocols (DCAM/IIDC).
- USB2.0 - high bandwidth (480 Mbits/second), master to slave, limited cable length, non-industrial connectors, proprietary protocols.

- CameraLink - very high bandwidth (255 MBytes/second), point to point, 10m cable, fiber optic extenders available, requires CameraLink compatible frame grabber.
- Proprietary LVDS links - requires proprietary frame grabber.

A concept design phase will identify the most appropriate cameras and camera interfaces, but for the purposes of this study it is assumed that IEEE 1394 cameras will be used for the STRIP and acquisition functions, and either a CameraLink or IEEE 1394 camera will be used for the guiding function.

There are a number of manufacturers of Megapixel cameras with IEEE 1394 interfaces. Some of the cameras that have been identified as being suitable for the acquisition and guiding function are:

- PixeLINK PL-A780: This is a 6.6 Megapixel camera based on a 2210 x 3002, 3.5 µm2 pixel CMOS sensor (IBIS4-6600). It is assumed that the guide camera will need to be of a cooled type for minimal dark current and read noise and maximum full well and dynamic range.
- Hamamatsu ORCAII-BT-1024: This camera has a 1024 x 1024, 13µm2 pixel CCD (EEV47-10), is available with liquid cooling and has either an IEEE 1394 or a CameraLink interface.
- AAS2_AXT100: with a thermopile sensor and a resolution of 256 x 248 pixels. The point of this camera is that it has a spectral range of 0.7 to 1.4 µm.

The first camera option is the higher resolution camera with a CMOS sensor but it needs cooling system, as the Hamamatsu option. The other options are lower resolution but can be used to obtain the measures in the measuring spectral range of the spectrograph.

The size of the pixel is critical for the correct acquisition of the faintest objects selected for the A&G since the core of the optical fiber used for the guiding button is of 100µm with a focal ratio of f/4 and the spot diameter created in the sensor is proportional to the wavelength $d = f/\#\cdot\lambda$. This diameter will also define the signal to noise ratio in the sensor.

$$S/N = \frac{\sum f_{obj} \cdot t}{\sqrt{\sum \left(f_{obj} + f_{bg} + f_{dark}\right) \cdot t + Num_{pix} \cdot \sigma^2}}$$

where:

A.1. f_x is the flux for the object, the background, and the dark current of the sensor.
A.2. t is the time of exposition.
A.3. Num_{pix} is the number of pixels the image is spread over.
A.4. σ^2 is the detector read noise (e-).

Whether all fiber bundles are imaged onto a single or several cameras, the image acquisition and processing do not seem to create a performance issue. Nevertheless, the effects of camera

image acquisition and processing on the control computer would be investigated in the concept design. A fall back scenario is to offload some of the cameras (e.g. the acquisition and guiding cameras) to a second control computer.

3.12.3.2 The guiding system

The FOV for SIDE in the Nasmyth focus is foreseen to be of 990mm, using 1000 fibers, and the physical space of the focus is 1000 mm leaving only 10 mm for the guiding. Using the GTC guiding system will imply a vignetting effect on the instrument.

A similar guiding concept to that used in FMOS-Echidna is proposed for the SIDE instrument to correct telescope pointing throughout observations. A significant source of error for this type of fiber positioner is gravitational deflection of the Echidna spines as the telescope moves in zenith angle. If left uncorrected each of the fibers could gradually move away from the object under observation because of spine deflection. The proposed guide concept avoids this problem by using guide spines which have the same deflection characteristics as the science spines.

3.12.3.2.1 Overview

The guide system comprises some number (1-4) of guide buttons, each with at least 25 fibers occupying some of the available FOV. Each guide button contains a 25-fiber bundle of 100μm diameter core fibers (compared to the 200μm core science fibers). Given that each guide button is virtually identical to a science button (except for the nature of the fibers contained within them) the relative deflection is similar enough to use the guide buttons for guidance. With guide stars (R~16-18) located on a subset of the available guide buttons, the movement of the images on the guide fiber bundle can be used to track the telescope during observation, implicitly correcting for button deflection. The bundle of fibers travel from the core of the positioner assembly to the guide re-imaging system located alongside, on the instrument mounting plate

The following points were considered when commencing the design of the Guide Fiber Bundle re-imaging system:

- The guide fiber core diameter is 100μm. The input beam F/ratio is approximately F/4.
- The optimal CCD pixel size is ~TBD μm with 1:1 imaging if the guide fiber output is to be adequately sampled. The magnification must be scaled appropriately if the CCD pixel size of the selected guide camera differs from this value.
- To reduce the size of the re-imaging optics and CCD chip size (the latter is favourable but not essential) the slid connector should be as compact as possible.
- The button connector must allow for removal of a single guide fiber bundle, preferably without affecting the others. This allows for a quick module interchange if required.
- The bundle connector must house a minimum of 25 fibers. The light from each fiber must be successfully imaged onto the chip with adequate sampling.

Other issues:

- A filter wheel allowing the transmission of different wavelength band width is to be located in between the optical system and the CCD.
- As always the difficulty of manufacture, ease of assembly and cost should be considered at all times.
- Interface with the GTC (mechanical and software) for the guiding and WFS.

3.12.4 Performance

The SIDE instrument will require its own facility for target field acquisition and guiding. Table 81 lists the preliminary requirements for such a facility.

Requirement	Value	Comments
Number of acquisition probes	Minimum of 2 to define translation and rotation	Acquisition can be done with relatively bright stars, but needs a minimum of two.
Number of guide probes	Minimum of 3 to define translation and rotation	A minimum of two could do the job, but three are highly desired to help averaging out any astrometric errors
Magnitude limit for acquisition	TBD but probably V~18	To be set by sensitivity of detector, field of view for each probe, number of available probes, and stellar density.
Magnitude limit for guiding	TBD but probably V~18	To be set by number of guide probes, field coverage of guide probes, sensitivity of guide probes, and stellar density.
Positional Accuracy for acquisition	1 arc-second	Level to which the acquisition system must be able to determine telescope alignment. This will allow the guide probes to pick up their stars.
Guiding accuracy	TBD but probably about 0.1 arc-second	Level to which the guiding system must be able to hold the telescope in alignment with the field.

Table 81 Requirements for the Guiding System.

Acquisition and guiding can be done either by separate facilities or by the same system but with different software. The acquisition is carried out by imagers that acquire easily identifiable stars and then send commands to the telescope to center the target field accordingly. Once the acquisition system has centerd the telescope within about 1 arcsecond, the guiding system takes over.

Target acquisition can be achieved with a set number of fixed optical imagers located around the periphery of the telescope field of view. A cost effective solution is to utilize off-the-shelf CCD cameras.

The large collecting area of GTC makes the stellar density even at the galactic poles to be large enough not to drive the number of acquisition probes required. This number is a combination of the total field of view of the combined probes and their sensitivity. Table 82, taken from Allen's Astrophysical Quantities, gives a guideline to the stellar density as a function of magnitude. The final column gives an estimate of the photons detectable at the SIDE focus with a typical CCD/CMOS detector running at about 10 Hz.

V magnitude	Number stars per square degree at galactic poles	Number stars per square arc-minute at galactic poles	Minimum Field (sq arc-min) required to see 1 star	Approximate Counts (S/N) detected in 0.1 second exposure
15	180	0.05	20	6400 (50)
16	350	0.10	10	2500 (25)
17	600	0.17	6	1000 (10)
18	1000	0.28	4	400 (4)

Table 82 Stellar density as a function of magnitude.

Given that the acquisition and guiding will be done by fibers placed at the focal plane by the fiber positioner robot, in principle all the focal plane area is suitable for guiding objects. In practice, due to the fiber positioning configuration for a given field, some areas will not be available. Nevertheless, the stellar density for stars easily reached by the system guarantees the availability of suitable guiding objects.

3.12.5 Software design

All the A&G system software shall be developed on a Linux operating system with Intel architecture fully compatible with, and running, a VxWorks framework. The language used shall be ANSI ISO standard C/C++ in order to develop software while using the GTC standards. It is intended to follow all coding standards and use any libraries developed for the GTC A&G interface system, taking advantage of the SW architecture provided.

The aim of the algorithm is to (after accounting for refraction and dispersion effects, see below) adjust the telescope and rotator positions to ensure the Guide bundle images are centerd as well as possible.

Figure 207 is a simple flowchart style representation of the algorithm. The text which follows it, is a more detailed explanation of the algorithm.

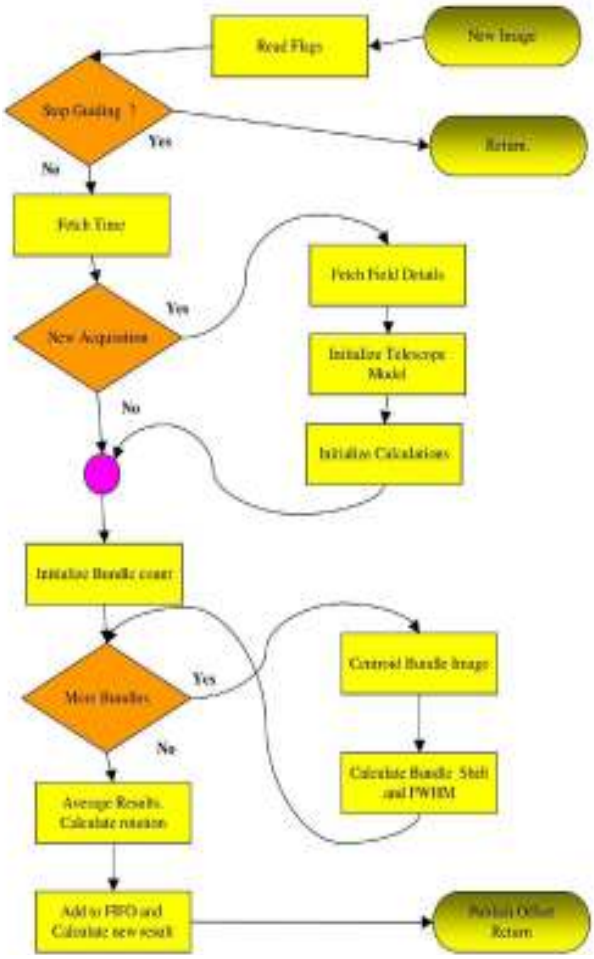

Figure 207 Example block diagram of the A&G algorithm.

3.12.5.1 Guider Image Offset Calculation Process.

The error in each Guide Bundle position is determined by finding a centroid for each Guide Bundle that has been assigned to a guide star. Only if a valid centroid is found will that guide bundle be used in the rest of the calculations.

This result needs to take into account any possible rotation due to the twist of the fiber bundle. It is then scaled to account for the number of microns per pixel. Next, refraction and dispersion effects (see below) are accounted for. The result is the movement of the Guide Bundle object image in microns on the field plate.

This result is then converted to an offset in Right Ascension and Declination using a matrix determined in the initialisation sequence. The average of each of these is the telescope position error.

3.12.5.2 Accounting for Refraction/Dispersion Effects

The impact of the change in object positions on the focal plane due to Refraction and Dispersion effects between the Guider wavelength and the spectrograph wavelengths is considered to be significant in some cases.

Consider an object that has a position on the focal surface of P_{gTc} at λ_g (guider wavelength) Angstroms at the central observation time. Assume its position at the spectrograph observing wavelength at the same time is given by P_{oTc} at λ_o (Observing Wavelength) Angstroms. If this object is a Guide object, the Guide Button will be positioned on the plate such that at the central observation time T_c, the Guide button central fiber aligns with P_{gTc}. The difference between these two positions is given by $\Delta T_c = P_{gTc} - P_{oTc}$.

For any given time T_n, let the positions of these objects on the focal surface be P_{gTn} and P_{oTn}. The difference is given by $\Delta T_n = P_{gTn} - P_{oTn}$. Thus at both wavelengths the object may have moved. Whilst the Guide bundles will only detect light at λ_g Angstroms, it is the light at λ_o Angstroms that we want to keep at the same relative position to the Guide Bundle center. Thus to keep this arrangement, we must allow the object at λ_g Angstroms to be off center by $\Delta T_c - \Delta T_n$.

To implement this the guider software will, for each Guide bundle, run the telescope optical model for the configuration time at both wavelengths. This is done during the field acquisition with the result saved.

Then when processing each image, the telescope optical model software is again run for each Guide Bundle and each wavelength, this time for the time the image was taken. $\Delta T_c - \Delta T_n$ and will be subtracted from the Guide bundle centroid, allowing the Guide bundle centroid to be off center by the required amount to keep the spectrograph wavelength aligned correctly.

3.12.5.3 Validation of the individual centroid result

The “Full Width Half Maximum” (FWHM) of a centroid result can be used to determine if the result is reasonable. Minimum and maximum values for FWHM will be specified. Additionally, a sensible result check is done to ensure the resulting offset is not too high.

3.12.5.4 Calculating Rotation

A formula that determines the rotation error, given the offsets in RA/Dec for each FACB is:

$$\Delta_{ROT} = \sum_{n}^{i=1} \frac{RA_i * (\Delta RA_i - \Delta RA_{avg}) - DEC_i * (\Delta DEC_i - \Delta DEC_{avg})}{RA_i^2 * DEC_i^2}$$

Where

Δ_{ROT}	=	Rotation Error
N	=	Number of bundles for which we have valid centroids.
RA_i	=	RA position of bundle i's object.
DEC_i	=	Declination position of bundle i's object.
ΔRA_i	=	Error in RA position of bundle i.
ΔDEC_i	=	Error in Dec position of bundle i.
ΔRA_{avg}	=	Average error in RA position of all bundles.
ΔRA_{avg}	=	Average error in RA position of all bundles.

Note that if we have only one valid guide bundle centroid, the rotation is zero. Also, if all bundles experience the same offset, the result is also zero. This is expected. The resulting rotation is validated against range errors.

3.12.6 Guiding system for the IAA or UFL positioner concepts

As seen in Section 3.5, these fiber positioners could be used with or without gripper. In the first case, some of the magnetic buttons carrying the fiber bundles should be provided with a coherent bundle able to image a star onto a camera. These bundles should be properly positioned on the FOV by the gripper, like the other science units, wherever a suitable guide star is found on the field. If no gripper is used and the fibers end is permanently mounted on an arm of the positioner, a few arms of the positioners will have to be dedicated to guiding, with special coherent bundles for that. The numbers (number of guiding bundles, FOV of each bundle) should be as specified in section 3.12.4.

3.12.7 Guiding system for the LBNL positioner concept

The LBNL fiber positioner is based on homogeneously distributed cylinders over the FOV; these cylinders provide the fine position of the units formed by the MOS fiber bundles and their microlenses.
The guiding system for this fiber positioner would be a set of dedicated, each carrying a special coherent bundle of fibers, therefore able to image a star onto a TV camera (See also 3.5.6.5). These guiding bundles could also be used to actively keep the telescope in focus, unless each cylinder has the capability of focussing individually.
The position of these guiding cylinder on the FOV will be studied in more detail in the next phase of the project, however there should be some radial variety, as having a guiding cylinder close to the center of the field and others closer to the border of the field, so that centering and rotational corrections can be obtained.
The number of guiding cylinders and the reachable field by each guiding bundle (more than 27” in diameter for the LBNL positioner cylinders) should be such that several guide stars can be available anywhere in the sky. These parameters should be as specified in section 3.12.4.

3.12.8 Costs

The costs of this subsystem is estimated to be about 100,000 euros.

3.12.9 Risks

None of the working packages in this section is considered to incur in any significant risk.

3.12.10 References

Rabaza, O. February 2007, *Impact of the Atmospheric Refraction at SIDE*, SIDE Tech Report Optic-01
WFMOS Feasibility Study v1, 03/2005
http://www.pixelink.com/
http://www.hamamatsu.com/
http://www.aas2.com/

3.13 The calibration unit

3.13.1 Introduction

All the optical system (Telescope, WFC, micro lens-fibers, optics, grating and detectors) that form the SIDE spectrographs must be calibrated in different ways to know the system transmission at all intensities and wavelengths of the spectrographs ranges.

The final percentage of transmission of the light coming from the sky to the detector is defined as the total optical transfer function of the system, and it depends on intensity and wavelength. To get this information, we should know the different transfer function of each subsystem and convolute them together: telescope, WFC, micro lens, optical fiber, collimator, disperser element, camera and detector, but this is not simple.

We discuss here the different calibrations we can make in order to characterize the whole system. Some will be automatically provided to the astronomer and others will be the astronomer responsibility.

3.13.2 Detector Flat Field

The flat field is used to know the pixel-to-pixel response of the detector to different light levels of a homogeneous monochromatic light.
The most probable situation is that the last optical element of the Camera is the cryostat window, which is a lens; then, the flat field mentioned before must be taken in a laboratory with a flat window in the cryostat. These tests are valid to know parameters like cosmetics, hot pixels, etc. and cannot be reproduced once the detector is mounted in the spectrograph. If a double pseudo-slit is used, such situation is very difficult to reproduce with homogeneous lamps in the laboratory.

3.13.3 Detector Flat Field (with spectrograph)

The closest calibration to a real detector flat field that we can have in SIDE is a detector entire flat field in lambda (at the spectral range selected in the disperser element). It is obtained by placing (at the pseudo slit position) a linear flat lamp, like a “classical long slit”, with a width corresponding to the fiber diameter. With this method all the pixels of the detector are illuminated (remember that, when a real pseudo slit of fibers is used, only the pixel correspondent to live fibers are illuminated). This way, the detector plus spectrograph flat field matrix is obtained.

3.13.4 Fiber position offsets on the pseudo-slits

Because the pseudo-slits are not perfect, we need to know the offset of the fibers with respect to one another, on each pseudo-slit, by locating the image of each single fiber on the CCD.
In order to do this we need a homogeneous light at the input of each pseudo-slit (MOS, SIFU, mIFU), **with the disperser element removed**. The image obtained is the proper pseudo slit re-imaged on the detector, on which we can measure each fiber x-y offset, and a defocusing. This way the matrix of fiber position error is obtained. See Sánchez (2006).

3.13.5 Fibers to detector transmission in light intensities

Because the fibers are not of homogeneous quality, we need to know the transmission of each fiber on each pseudo-slit, by studying the image of each single fiber on the CCD.

The method is to analyze the same images as before, but measuring the intensity of all the pixels of each fiber, independently from the x-y offset. The result is the fibers light transmission matrix, which, for each fiber, shows the response of the whole system.

3.13.6 SIDE Flat Field, GTC facility, focal station covers

In principle, GTC provides a special power lamps system or "Flat-Field box" to all the instruments. These are of quartz type, and illuminate a white screen in the dome, etc. **TBC**. A homogeneous light over the 20' FOV must be provided for calibrating the MOS fibers at Nasmyth, and the mIFUs and the SIFU at Folded Cassegrain. The mIFUs and SIFU case at Folded Cassegrain would be easier because they would be available at all times. The double pseudo-slit setup, introduced in Section 3.9.9, is a commonly used technique where multiple sources of light feed the spectrograph, activated one at a time. Each side of SIDE's double pseudo-slits comes from a different focal station, so it is easy to obscure one side of the pseudo-slit by covering the corresponding focus with a blind. Both blinds would be painted white inside (towards the fibers) and black outside. They could be thus illuminated with appropriate light according to the required calibration. The white blind surface can be considered Lambertian and each fiber or fiber bundle can be calibrated for transmission and position. This is valid for all the three observing modes.

This type of flat field is the most used by astronomers because all the system is taken into account (also the telescope) in one shot. Sky flats are possible too, but with special care concerning the Sun lines, and must be taken close to the Zenith, to ensure that the wide 20' field is not affected by light gradients.

With a flat field we obtain the response of the entire system to flat light. This image is then corrected with the "fiber position error" matrix, then the "fiber light transmission" matrix, and finally with the "detector Flat Field with spectrograph" matrix.

The result is the response of each pixel of each fiber and for each lambda through the whole system.

3.13.7 Reference spectral fibers on the pseudo slits

In order to have a good spectral reference in each spectrum of SIDE, some of the fibers in all the pseudo slits must came from a "spectral calibration box". This feature would be extremely useful in SIDE, because the position error of the slit (after a slit movement) can be removed by knowing the real spectral position of each lambda.

This procedure is independent of the flat field and spectral calibration of the fibers explained before.

The spectral reference fibers are interposed between the science fibers at the pseudo-slit in different possible configurations. Their mission is to provide a reference to the astronomer or the reduction software along the spectral direction. To work properly, the light at the input of

the reference spectral fibers must be at the same focal ratio as that of the telescope, and also the diameter must be the same as that of the fibers used in MOS, SIFU, and mIFUs.

The spectral box that feeds these fibers contains selectable spectral lamps covering all the range of the spectrographs. An electronic shutter controls the intensity of the light over these fibers, according to the corresponding exposure time.

Usual references lamps are: HgZnCd, Hydrogen, Deuterium, Helium, Nitrogen, Oxygen, Water (vapour), Carbon Dioxide, Carbonic (acid), Neon, Argon, Krypton (gas), Krypton (isotope 86), Xenon, Mercury, Chlorine, Iodine, Bromine, etc.

To detect if there is any flexure along the exposure, one method is to take reference spectral calibrations at the beginning and at the end of the exposure. If the thickness of the spectral line is bigger than usual, it means that some flexure has occurred (see Kelz et al, 2006). In the case of SIDE at Nasmyth, no flexures are expected.

3.13.8 Mechanical design

The reference spectral calibration box is a independent module containing the spectral lamps, which is interconnected by fibers to all the pseudo-slits. The light to the input of the fibers is at the same f/number as the telescope; a fast shutter serves to control the intensity.

3.13.9 Costs

The cost of this system is estimated to be about 50,000 euros.

3.13.10 References

Techniques for reducing fiber-fed and integral-field spectroscopy data, S.F. Sánchez – A.N. Vol 327, Issue 9, Page 850, 00/2006.
PMAS The Potsdam Multi-aperture spectrophotometer. Andreas Kelz et al. PASP118:129-145, January 2006

3.14 Control System

3.14.1 Description

The control system of SIDE comprises the hardware and software elements to control and command all the mechanisms and electronics devices of the instrument. Through the control system, the user will have access to the instrument and will be able to configure the observing modes and obtain the data.

The control system of SIDE will be fully integrated in the control system of GTC, that is, it will be implemented as a *Device Component* which is an element of the GTC software architecture, with a very precise definition and interfaces. Hardware and software will comply with the standards, regulations, requirements, constraints and guidelines of GTC.

Being integrated in the GTC control system, the user will benefit from a familiar environment, with standard graphical panels with information and common ways to command the instrument and get the images. For the development team, this integration maximizes the use of many hardware and software services and infrastructures already existing at GTC and it also facilitates the reuse of the components and the experience obtained in the development of other instruments.

Figure 208 shows the four layer model of the GTC control system software, where the SIDE software will be integrated. Also the dependencies of the different packages and services are shown (from GTC AD, ESP/CTRL/0132-R).

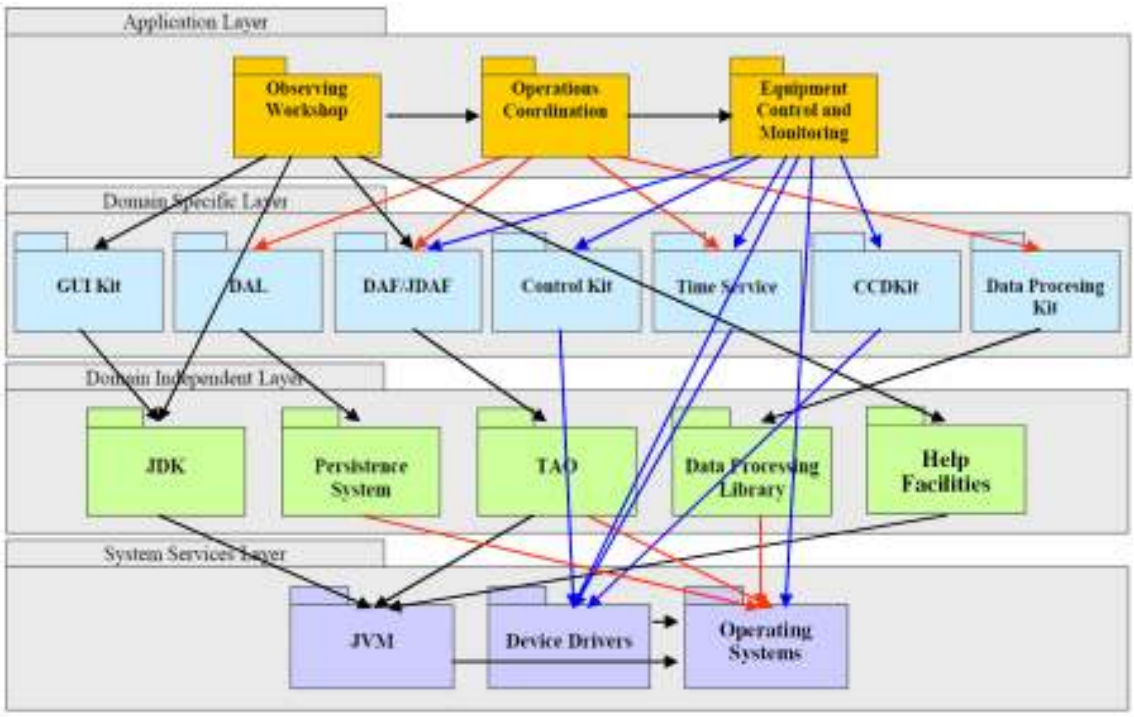

Figure 208 GTC Software model

Figure 209 shows the different packages that constitute the instrument control system software.

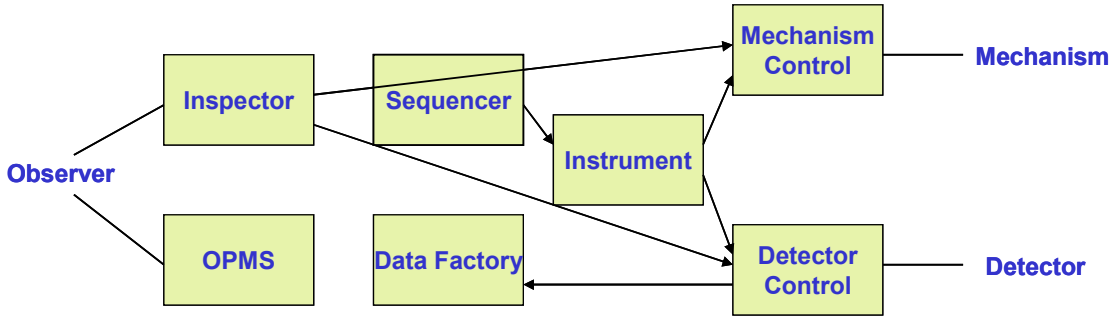

Figure 209 Instrument software packages according to the GTC software model

The *Observing Program Management System* is in charge of the preparation of the observations. This system will assist the user to prepare offline its observations and to enter, through graphical panels, the input parameters of the sequence of the observing run. The instrument simulator, described in other chapter of this document, is part of the OPMS.

The *Inspector* is the program that manages the instrument specific graphic user interface panels to control and monitoring the observation. The system provides default views for configuration, commands, monitoring, alarms and logging. The SIDE team will develop the specific panels that may be needed to be incorporated in the Inspector.

The *Sequencer* is the specific instrument processes, like the movements of a mechanism or the reading of an image, that are executed, in parallel or sequentially, in order to setup the instrument for observing and perform the observation. It consists in a temporal ordered list of high level commands. The sequencer is also in charge of coordinating the movement or the setup of the telescope for an observation.

SIDE will develop the specific sequencer commands to perform all the observation modes of the instrument.

The *Instrument* is a Device Component, according with the GTC model, which represents the instrument as a whole. Methods of this device will be invoked by the sequencer in order to setup the instrument and perform an observation.

The *Mechanisms Control System* consists of programs, running in a Local Control Unit (LCU) under VxWorks operating system, to control and monitor all the mechanism of the instrument. This system is described in more detail below.

The *Data Acquisition System, DAS,* is in charge of commanding the detectors, read the images, preprocess them, if necessary, and to transfer them to the data factory. It is also implemented in a LCU under VxWorks and is described below.

The *Data Factory* is composed of reduction templates and data processing filters for each observing mode. The SIDE team will develop the appropriate filters and templates to be

integrated in the GTC data factory. This software is described in more detail in other chapter of this document.

We will develop these packages making use of the tools and infrastructure that GTC offers to facilitate this work and an easy integration in its control system, that is, several specialized programming guides, a development kit and its centralized support system.

The SIDE control system hardware architecture deployment is shown in the next figure:

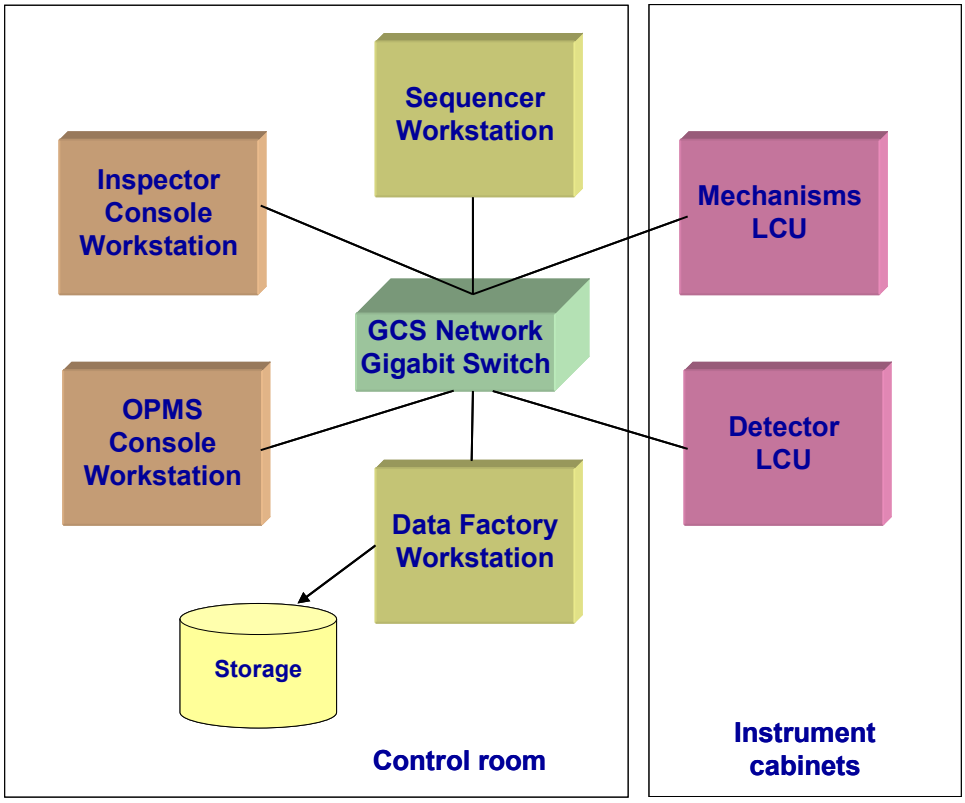

Figure 210 Control system deployment

The MCS and the DAS as well as the controllers and additional electronics are enclosed in cabinets near the instrument.

3.14.2 Data Acquisition System, DAS

The data acquisition system is responsible for commanding the detectors, read the images and send them to the Data Factory, according to the SIDE requirements and GTC standards and constraints.

The hardware architecture proposed for the DAS is shown in Figure 211:

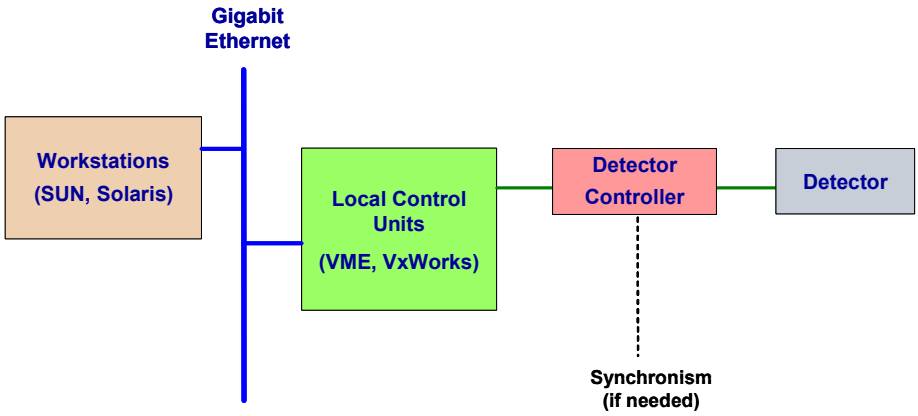

Figure 211 DAS architecture

Because the detectors in each spectrograph, in principle, may have different setup and exposure times the baseline concept assumes that each detector has its own controller and LCU. Each Dual VIS-NIR spectrograph will have then two detector controllers and two LCUs. An additional controller and LCU will be needed for the Hi-Res spectrograph.

The camera for acquisition and guiding will probably be an off-the-self CCD with a digital interface connected to the LCU. The images acquired by this camera will allow the user to confirm that the fiber positioner is working well and that the field to observe is properly oriented and acquired. This step has to be performed before reading the detector. Probably these images will also be used to guide the tracking of the telescope.

All the detector images will be sent to the GTC Data Factory and will be processed with the appropriate data pipeline filters, before archiving them. An Inspector panel will display a quick-look image to the user.

Figure 212 shows in more detail the DAS for a CCD.

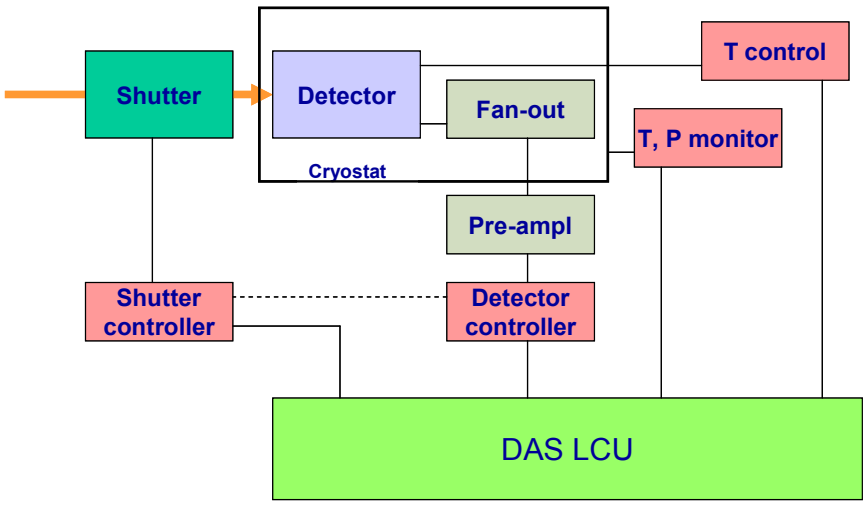

Figure 212 CCD Data Acquisition System block diagram

The dotted line in the figure is the synchronization signal that connects the detector controller with the shutter. In OSIRIS, this signal is also read by an I/O board in the LCU (not shown in the figure) to timestamp the operation of the shutter.

For the sake of clarity and physical proximity, the temperature, pressure and shutter controller are connected to the DAS LCU but they could also be connected to the MCS LCU, as it is the case for the rest of mechanisms.

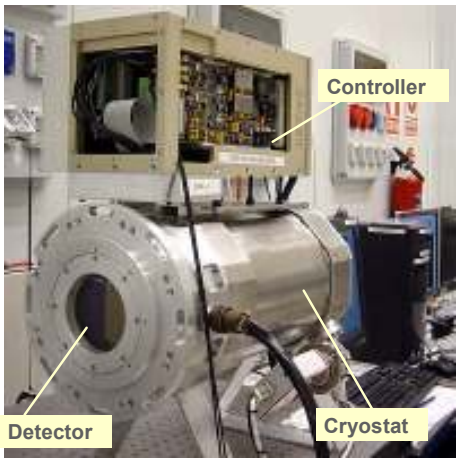

Figure 213 OSIRIS cryostat and detector controller

Figure 213 shows the cryostat with the 4kx4k mosaic and the detector controller of OSIRIS at the IAC premises.

From the software point of view, the DAS will be fully integrated into the GTC control system environment. It will be part of the "Equipment Control and Monitoring" package on the upper layer of the GTC software model shown in Figure 208. The DAS will be implemented as a Device, in the GTC model of components and its specific graphics panels

will be integrated in the Inspector. Alarms, events and status will be monitored with the corresponding GTC services and infrastructure.

The DAS will run in a LCU under the VxWorks operating system.

Apart from this high level software, when the final detector controller is selected we will determine if some lower level programming is necessary on this controller.

Given the large number of detectors, (see Figure 214) and the limited bandwidth of the present GTC gigabit Ethernet, we must study in more detail the data throughput in the LCUs and its transfer to the GTC Control System.

We must also investigate the benefits of operate the Dual VIS-NIR spectrographs by groups instead of individually. In the present concept there are two possible configurations for SIDE: Nasmyth and Folded-Cass. In the first one, the 10 Dual VIS-NIR spectrograph receive fibers from the positioner and they are operated with the same acquisition parameters (TBC). In the Folded-Cass configuration, 2 Dual VIS-NIR spectrograph receive the mini-IFU from the positioner and the remaining 8 receive the fibers from the SIFU. Presumably the 2 spectrographs with the mini-IFUs can be operated with the same parameters and the group of 8 as well. Operated by the same parameters means that all the CCD in one group share the same exposure setup and all the IR arrays in that group also have the same parameters. If the operation by groups is confirmed, we will probably be able to reduce significantly the DAS hardware, as several CCD will be controlled by only one controller and one LCU. And the same applies for the IR arrays.

During the development of the DAS, we will reuse as much as possible all the existing software (device drivers, classes and packages) already implemented in other GTC instruments, and we will maximize the transfer of knowledge from the groups that presently are developing the OSIRIS and EMIR DAS, in order to reduce the learning curve of the GTC Control System.

3.14.3 Mechanisms Control System, MCS.

The mechanisms control system is responsible for controlling, commanding and monitoring, all the instrument active mechanical devices and sensors.

We have identified the following subsystems with mechanisms to be controlled (Figure 214):

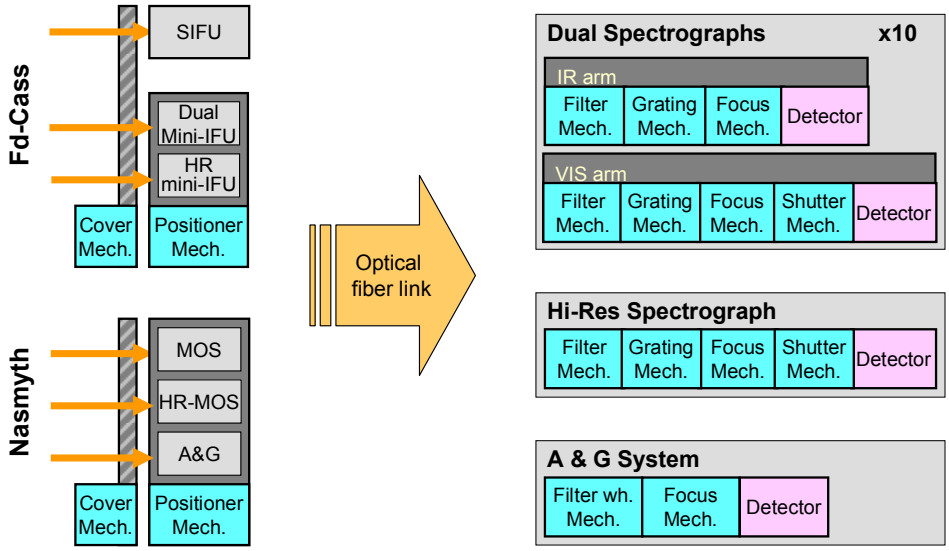

Figure 214 Diagram of the SIDE subsystems and mechanisms

Fiber Positioner Systems

These systems are in charge of positioning all the multi object spectrograph fibers, the mini integral field unit fibers and the acquisition and guiding fibers. The Nasmyth and folded Cassegrain stations have different concepts which are described in detail elsewhere in this document.

The concept proposed by UF for the folded Cassegrain station fiber positioner is based on 27 independently controlled arms that are responsible for positioning the 27 mini-IFU fiber buttons in its corresponding sector. Each arm is articulated and all the possible positions in each sector are reached by combining the movement of two motors.

The concept from LBNL to the Nasmyth focal station fiber positioner is quite different from the previous one. In this case each fiber button has its own positioning system which comprises a rotating plate with a linear positioner on it. The whole field of view is populated with these devices in a fixed regular pattern. This positioning mechanism is massively replicated, taken into account that there are thousands of fibers to be positioned.

The fiber positioner systems are the most complex systems to be controlled in SIDE. Apart from electric matters, like power dissipation or cabling, some of the key issues are the complex algorithms that have to be implemented to maximize the number of objects to

observe in each exposure run and, at the same time, dealing with the strategies to avoid possible collisions or forbidden areas during the positioning of the fibers.

Due to the complexity of the positioning algorithms and according to the software architecture of GTC, these algorithms should be executed in the OPMS, previously to any observation. In that way, the tasks to be performed by the controller of this mechanism should be simpler. Nevertheless rigorous checks should be performed online during the positioning of each fiber in order to preserve the integrity of the system.

Cover Mechanisms

The fiber cables from both focal stations arrive at the entrance of the spectrograph in such a way that each spectrograph sees two pseudo slits, one corresponding to the fibers of the Nasmyth station positioner and the other to the fibers from the folded Cassegrain positioner and SIFU. Both pseudo slits can not receive light at the same time because mirror M3 of GTC points to only one focal station in every moment. But nevertheless, the pseudo slit that is not in use should be covert to avoid any diffuse or indirect light enter the spectrograph while observing with the other pseudo slit. To do that, a cover mechanism has to be deployed in front of each focal station before the light coming from M3 hits the fibers. These mechanisms will probably consist of a rotating part with few positioning sensors.

Fiber Derotator

The fiber cables in both focal stations will require a derotator. The use of the GTC derotator is not recommended because it adds an excessive length to the fiber cables. In the present concept, a passive derotator is envisaged at the back of each positioner, minimizing in that way the path to the spectrographs room. Although passive, these derotating mechanisms will require some sensors to be monitored by the control system in order to stop the movement if stress limits are surpassed.

Spectrographs

Each spectrograph will have the following subsystems to be controlled.

- Filter positioner

One or more filter wheels will be needed in every Dual VIS-NIR spectrograph arm and in the Hi-Res VIS spectrograph. One motor and a number TBD of position sensors and switches per wheel will be controlled straightforwardly and easily with a commercial controller. The same design will be replicated in all the filter wheels.

- Dispersive element positioner

Every arm of the Dual VIS-NIR spectrographs will have a wheel to position the appropriate prism or grism in the light path. Although the mechanical tolerances and technical requirements will probably be different from those of the filter wheels, the same control design will be applied but, in this case, taken into account the new specifications (precision, resolution, power...) in the purchase of the motor and sensors.

The dispersive element of the Hi-Res VIS spectrograph may require a different mechanism due to the size of the gratings and the need to fine tuning every element around its nominal position (TBD). If one rotating turret does not fulfill all the requirements, a second rotating

mechanism should be implemented on top of the turret. In that case, the turret movement should be blocked mechanically at fixed positions and the fine tuning would be performed with a short range high precision rotating mechanism along the wavelength dispersion direction. From the control point of view, this mechanism is treated as a two independent axes mechanism.

- Focus positioner

A high precision translation unit with one motor and TBD sensors, will be controlled to adjust the best focus of the image on the detector. This mechanism compensates the minor displacements in the focus position that may appear when changing the observed spectral range or thermal conditions.

- Shutter

For the CCD in the visible spectrographs, a shutter mechanism, close to the detector, will give us a precise exposure time. The mechanism will probably be similar to that employed in OSIRIS. To guarantee the simultaneity of the opening and closing movements of the shutter with the detector exposure intervals, a dedicated synchronization signal will be provided between the detector controller and the shutter trigger. An I/O digital board, installed in the LCU, will timestamp the observation, reading this synchronization signal.

- Detector temperature control

The proper operational temperature of the detector will be maintained by a commercial temperature controller, probably a Lakeshore model, incorporating several temperature sensors and an output for a resistive heater, allowing a closed loop control.

- Temperature and pressure monitor

Other temperature sensors will be monitored with the same controller mentioned above, using free channels. If more sensors are needed, an additional dedicated controller from the same manufacturer will be use.

Similarly, the each detector cryostat pressure will be monitored using a commercial controller, probably from Edwards.

Acquisition and Guiding System

The acquisition and guiding bundles will be positioned with the fiber positioner system at the Nasmyth station, not requiring a special or dedicated mechanism. There will be no acquisition and guiding fibers at the folded Cassegrain station where the GTC A&G system will be used instead.

The A&G camera will need a filter wheel and a focusing mechanism similar to those proposed in the case of the spectrographs.

Auxiliary Systems

The main auxiliary system is the cryogenic infrastructure. Every CCD and IR array cryostat will need a vacuum and a cooling system. Although these cryostats have not yet been selected, presumably, we will need a centralized control system to read all the sensors and manage the actions to be taken by the vacuum and cooling systems during the operation of SIDE as well as during the periods of parking.

Other auxiliary systems are the parking mechanism of the Nasmyth positioner and the air conditioner of the spectrograph room. Probably these systems will have its own autonomous control system but during operation they will be monitored by the SIDE control system. Other systems that will not be integrated with SIDE control system are the handling and transport equipment and the specific subsystem or devices that will be needed for verification or calibration purposes during the development or integration phase of the project.

At the present stage, we have not decided the motors to use in these mechanisms neither the details of the sensors needed to control them, such as encoders, limit switches, home positioning devices, temperature and pressure sensors, etc. But we will try to use the experience gained in the development of the OSIRIS and EMIR mechanisms. We will be able to detail these items as soon as the requirements and specifications for these subsystems are determined.

The functionality of these devices will comply with the GTC limits regarding the operational atmospheric conditions.

The electronic architecture of the MCS will be deployed according to the GTC standards and requirements. The goal is to benefit form an extensive use of the experience of the previous instruments.

Figure 215 shows the proposed hardware architecture for controlling all the mechanisms:

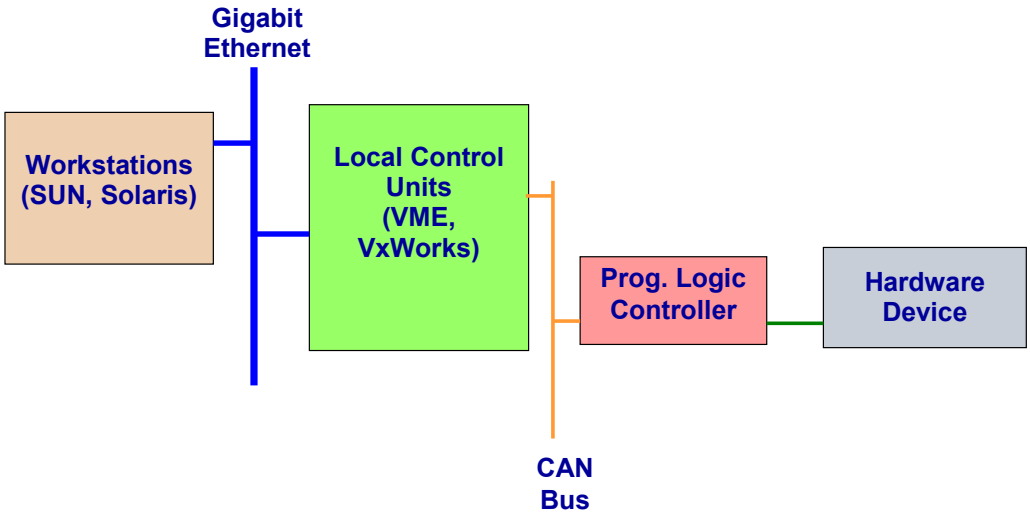

Figure 215 Mechanisms control architecture

The LCU will host the CPU board and a CAN bus card. The use of a general purpose Digital/Analogue I/O card is also foreseen to timestamp the shutter signal.

Each mechanism or group of similar mechanisms like, for example, the wheels in every VIS-NIR spectrograph, will be controlled via a programmable commercial controller that will interface to the driver, power, motor and sensors of each mechanism.

For those commercial controllers that may have only an interface RS-232 as input, the use of an interface module CAN/RS-232 is proposed.

In that way the mechanisms will all be accessed through the CAN bus and they will be commanded and monitored with off-the-shelf controllers that offer a high reliability, as they are robust systems and, very often, they are provided by the same motor or sensor manufacturer, assuring in that way a proven compatibility.

From the software point of view, the MCS will be fully integrated in the GTC control system environment. It will be part of the "Equipment Control and Monitoring" package, in the Application Layer of the GTC Control System software model (see Figure 208). Its specific graphics panels will be integrated in the Inspector and the alarms, events and status will be monitored with the GTC services and infrastructure.

Following the GTC standards, the MCS will be implemented in the LCU running the VxWorks operative system. The control of every mechanism within the MCS will be implemented as a *Device*, and all the mechanisms hardware will be accessed through the use of *Device Drivers*.

In addition to high level software, some low level programming will be needed to command the commercial controllers of the mechanisms. Usually this is done quite easily configuring the controllers with the tools and instructions given by the manufacturer.

As in the case of the DAS, during the development of the MCS, we will reuse all the existing common device drivers, classes and packages already implemented in the GTC software, and we will transfer the knowledge from the OSIRIS and EMIR groups to minimize the learning period of the GTC Control System.

3.14.4 Interfaces

SIDE functionality will require access to the calibration lamps system to calibrate the IR and VIS detectors and the spectral response. Also, SIDE will need to access the M2 positioning system in order to synchronize its movement for "nod and read". The fiber positioners at both focal stations will need from the telescope on-line information regarding the coordinates of both rotators.

The integration of the SIDE software within the GTC control system makes very easy the access to all the GTC subsystems and services without any additional interface. From the hardware point of view the use of several modules provided by GTC, like the standard module for interface to its communication system, MOC, also facilitates this task. For the rest of the electronic and electric interfaces, like connectors, cabling, etc, we will follow the GTC hardware standards.

3.14.5 Electronics Cabinets

All the electronics of SIDE will be enclosed in thermally isolated cabinets. These cabinets should be located close to the SIDE spectrographs room.

A tentative approach to a possible distribution inside a cabinet of the electronics for one Dual VIS-NIR spectrograph is shown in Figure 216. Taken into account that there are 10 Dual VIS-NIR spectrographs, a Hi-Res VIS spectrograph, two fiber positioner systems, two cover mechanisms one acquisition and guiding unit, plus other auxiliary systems, we can estimate that, the simple replication of that system, at least, will require 11 big cabinets. Such number of big cabinets, close to the spectrographs, will probably not fit in the available space.

During the earlier phases of the project this problem has to be addressed. Some improvement may come from the use of physically smaller electronics, controllers with larger number of channels, serialization of the commanding of mechanisms in order to have smaller power supplies, etc. In that sense, the operation by groups of the Dual VIS-NIR spectrographs may also play and important role in reducing the electronic hardware of the data acquisition system, as less detector controllers and LCUs should be needed.

Apart from these cabinets close to the spectrographs, some other electronics will be needed close to the detectors outside the cabinets and a medium size electronic cabinet should rotate attached to each fiber positioner. Following the GTC requirements, these components will also be thermally isolated.

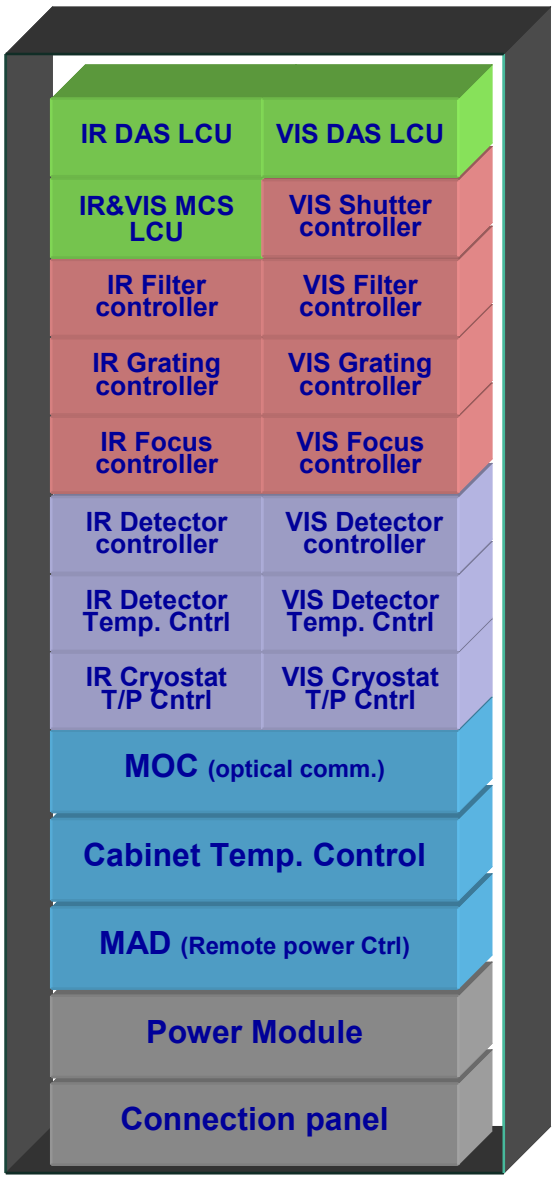

Figure 216 Possible distribution of the electronics of a Dual VIS-NIR spectrograph inside a cabinet (see text). In the lower part of the cabinet are indicated the standard GTC modules for communications, remote power control and cabinet temperature control.

3.14.6 Cost estimates

The approximate cost of the control system is shown in Table 83. Included elsewhere in this document are the costs of the detectors systems, the data pipeline and the acquisition and guiding systems.

LCUs (Rack, CPU, Gigabit, PMC & CAN Boards)	150.000 €
PCs & Workstations	14.000 €
Software (VxWorks)	30.000 €
Cables & Connectors	130.000 €
Cabinets	20.000 €
Consumables & Miscellanea	30.000 €
Total	374.000 €

Table 83 System control cost estimates.

Not included in this table are the costs of the specific sensors, motors, drivers, power supplies, controllers and electronic components needed to actuate, at low level, the different mechanisms. As shown in Figure 217 these subsystems will have an RS-232 or CAN interface to the control system.

With the exception of the fiber positioners, that will require an ad-hoc and complex electronic system, we expect that the rest of the mechanisms will be controlled with commercial components. There are several manufacturers who can provide complete off-the-self high precision translation or rotating mechanisms, which could be used to position all not cryogenic moving parts of the spectrographs. Possible cryogenic mechanisms will also have commercial electronics but will require cryogenics motors and sensors, and a specific mechanical design. The opto-mechanical design will determine the specifications for these mechanisms, with a direct impact on their cost. Typical prices are in the range of 2.000 – 6000 € per mechanism plus an additional 1.000 - 2.000 € for the controller. These controllers can also be mounted in racks.

From the previous figures, a rough estimation of the total cost of the electronics for controlling the mechanisms, including in many cases the mechanism itself, is 300.000 €. The cost of the fiber positioners electronics is not considered here.

3.15 The pipeline data reduction package

3.15.1 Introduction

This section describes the capabilities of the SIDE Data Factory Pipeline and the current status of its development. It also describes the common problems of the visible and near-infrared Multi Object and Integral Field Spectroscopy data reduction and how the SIDE pipeline shall afford them.

The SIDE Data Factory Pipeline (DFP) shall be composed with a set of robust software tools and algorithms optimized for handling and reducing VIS and nIR Multi Object and Integral Field Spectroscopy data. A complete set of tasks for step-by-step data reduction, with reduction recipes, and a fully automatic reduction mode shall be available. The DFP is embedded into the GTC Data Factory (DF) operations.

The main aim of this document is to summarize the capabilities of the SIDE DFP as well as to show the current status of its development.

3.15.2 DFP overview

The SIDE DFP is the part of GTC Data Factory dedicated to processing raw data acquired with SIDE. The SIDE DFP is a set of advanced REDUCTION RECIPES (which consist in a series of FILTERS, atomic operations in GTC terminology) for each observation template and Quality Assessment rules to be followed. It shall deliver reduced images as a final product to the GTC Operation Repository, by means of robust software tools and algorithms optimized for handling and reducing optical and nIR Integral Field Spectroscopy data. This set of filters will be executed by the GTC Data Factory in real time. Unlike other public general packages (such as IRAF, MIDAS, etc.), the DFP shall be developed and optimized for 3D spectroscopy work with SIDE. The SIDE DFP is being designed in an auto consistent way, tackling in a comprehensive way all the filters and reduction templates that SIDE operations will require.

The DFP will be accessed through the GTC "Inspector". This will create a common framework in which SIDE, and other instrument specialized software, could be executed. For each of the SIDE observing modes (MOS, mIFU, SIFU), there are associated data types, including calibration observations (darks, flats, etc.) and science frames. Once an observation is completed, the DFP will need to interact with the GTC Operation Repository, where the existing calibration frames and the results are stored. Later, the DFP shall provide the GTC Operation Repository with a final reduction of each set of observations in physical units and its associated error frames.

The DFP has to tackle several critical problems in order to reduce the VIS and near-IR raw data obtained by SIDE:

- More than 1000 simultaneous spectra can be achieved in the MOS and mIFU observing mode. Such quantity of data has to be handled properly.

- Spectrographs are generally designed to minimize the effects of cross-talk (contamination among neighbor fibers at the pseudoslit positions). However, there is always a trade-off between the number of fibers "packed" in the spectrograph, the size of the CCD and the width of the profiles, and the final cross-talk (see Sánchez 2006). Furthermore, the spectra are not perfectly aligned along the dispersion axis due to different effects as the configuration of the instrument, its setup, the instrument focus and any flexures effect. There are also differences in the fiber-to-fiber transmission due to different tensions, slight misalignments and intrinsic physical differences. All these effects will need to be taken into account in the data reduction.

- In near-IR spectroscopy, the time variation of the background limits the exposure time to scales around 900s. With longer exposures, the removal of the sky with low residuals cannot be guaranteed. To minimize the impact of the sky, the objects will be observed in different positions (for example, following an ABBA sequence).

- The user will need a reliable error estimation. Errors associated to each image shall be carefully tracked.

The SIDE DFP shall be coded following GTC Programming (see AD ESP/CTRL/0042-R) and Software Standards (see AD ESP/CTRL/0045-R), this is, ANSI-C++, with an object-oriented architecture. Each frame from the optical/nIR detector will be considered as an object of the class "Frame", which includes a 2-D "Array" for the frame itself and a second 2-D "Array" for variance data. Other objects related with the reduction process are: sets of Regions of Interest (ROI´s) which define special regions in the frame (such as the useful and effective regions of the detector, etc.) and a list of features for cosmetics defects and cosmic rays.

Currently, the DFP is not intended to be public, though this option is being taken into consideration.

3.15.3 Data flow of the DFP

Raw data in the detector is actually a convolution of the source astronomical signal plus the different contributions from each of the media the light travels through, i.e., the atmosphere, the telescope, the instrument and, finally, the detector itself. To uncover the scientific information contained in this noisy signal, a data reduction must be performed. This will depend on the type of data, e.g. those related to calibration purposes, such as darks and flat-fields, and those of science interest. The Reduction Process or Data Flow followed in the different cases can be graphically summarized in Figure 218.

The main steps to follow in the reduction of science frames provided by fiber-fed spectrographs are:

a) Dark correction and bias correction (this last only in the case of optical spectroscopy).

b) Flat-field division, in case SIDE is provided with a lamp to illuminate directly the detector and so the pixel response non-uniformity correction is possible.

c) Cosmic rays removal and cosmetic masking for the defects of the detector.

d) Sky emission subtraction, where different techniques are needed, depending on the observing wavelength (VIS or NIR).

e) Identification of the position of the spectra on the detector for each pixel along the dispersion axis.

f) Scattered light subtraction and extraction of each individual spectrum.

g) Distortion correction of the extracted spectra, and determination of the wavelength solution.

h) Correction of the differences in the fiber-to-fiber transmission if the lamp mentioned in step b) is not available.

i) Flux calibration.

For IFUs it is also required to reorder the spectra on their original location on the sky and correct for the differential atmospheric refraction.

The SIDE DFP will comprise a set of filters, which can be grouped into two types:

- Characterization Filters (CAF), which measure certain properties of a frame, without modifying it. This information will be stored for further use, so these filters do not correct any defect in frames.

- Correction Filters (COF), which take the information previously calculated by a CAF and correct frames for their effect.

For example, when Detect Cosmetic Defects use-case is executed, a special algorithm is used in order to find the location of cosmetic defects in a certain frame, but no interpolation is applied. If this is requested, the corresponding COF (Clean Frame) is run after the cosmetic defects have been detected. The philosophy of the proposed DFP is to delay as long as permitted the manipulation of frames, in order to maintain the original information as long as possible and avoid error correlation (see Cardiel et al. 2002).

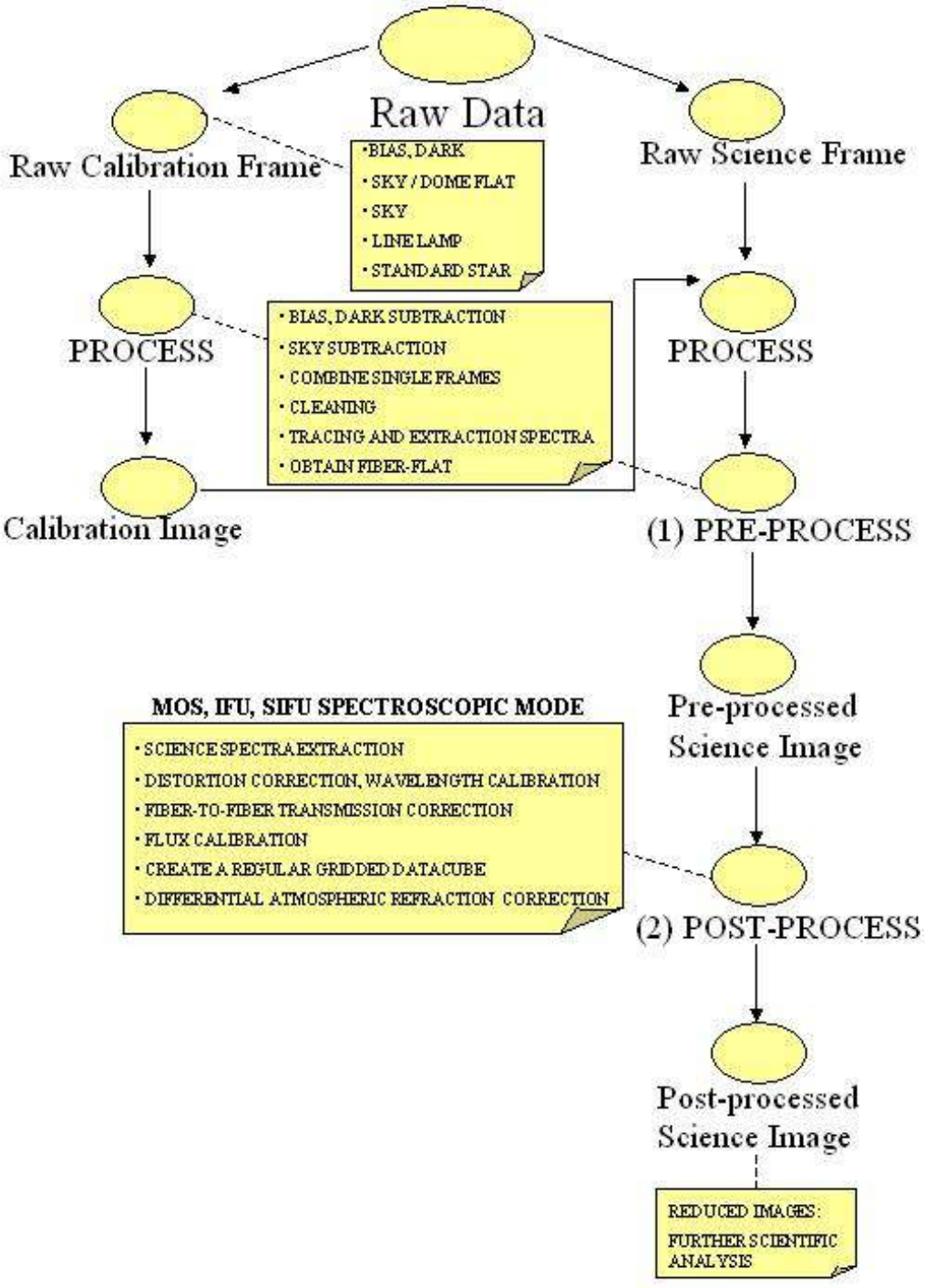

Figure 218 Data flow of the SIDE DFP.

3.15.4 Raw Calibration Frame Process

Calibration Frames can be cosmetic defect masks, bias, darks, flat-fields, dome or sky-flats, sky frames, line lamp frames or standard star frames. For the correct reduction of the 3D data we need to take into account the following calibration steps:

1. Dark subtraction, and bias subtraction (this last in case of optical spectroscopy).

2. Flat-field division, in order to correct for pixel response non-uniformity in the detector. This correction requires the capability of the instrument for direct illumination of the detector.

3. Cosmetic masking for defects in the detector, such as dead pixels, also with a two-dimensional interpolation if requested.

4. Cosmic rays removal, with a two-dimensional interpolation between neighbor adjacent pixels.

5. Sky subtraction. The high and time-changing contribution of the sky background in the near-IR makes this observing mode different from the optical one at this reduction step. For near-IR spectroscopy we need to subtract a near (in time) sky exposure for each fiber. In this case a nodding observing strategy is necessary. In optical observations we can use the Nod & Shuffle or Nod & Read observing modes or use an average sky exposure computed from a combination of the signal in several sky fibers, in this last case the sky subtraction is applied after step 8 in the reduction.

6. We need a well illuminated continuum exposure to find and trace the position of the spectra on the CCD. For IFUs that suffer some flexures, these exposures should be taken just before or after the science exposures and without moving the telescope from the position where the target has been observed.

7. Calibration arc-lamp observation is need in order to correct for intrinsic curvature of the spectrograph and for distortions due to the packing of the fibers in the pseudo-slit. These distortions must be corrected fiber-to-fiber before finding a common wavelength solution.

8. Correction of the differences in the fiber-to-fiber transmission. For this correction we need an exposure of a continuum, well-illuminated, and flat source like a dome or sky flat. We can use this exposure to determine the differences in the transmission fiber-to-fiber by comparing the flux spectra-to-spectra and deriving the so-called fiber-flat.

9. For the flux calibration we need the observations of a spectrophotometric standard star during the night to perform reliable absolute spectrophotometry. This absolute calibration with fiber-fed spectrographs is complex. In principle with SIDE it will be possible to obtain an absolute flux calibration since the flux losses in IFU-mode are solved with the coupling of lens-array to the fiber-bundle.

3.15.5 Raw Science Frame Process

Science frames, which correspond to astronomical objects of interest, suffer a longer process until the total reduction, which can be divided into two clear phases: Pre-Process and Post-Process.

3.15.5.1 Science Frame Pre-Process

In this phase the raw science frames are corrected with bias, dark and sky subtraction. If we have the total exposure time for the same target divided in several frames they must be combined. In this process of combination, the cosmic rays signal can be removed and the cosmetic masking for the defects of the detector can be done.

3.15.5.2 Science Frame Post-Process

After being pre-processed, a science frame needs further recipes to completely end its reduction.

1. When the extraction of the scientific spectra is performed (using the solution from item 6 in Section 3.15.4) we need to apply the distortion and dispersion correction (using the solution found in item 7 in Section 3.15.4).

2. The wavelength calibrated scientific frame is divided by the fiber-flat computed frame in case the detector can not be illuminated directly (flat-field).

3. The flux calibration is applied to the science frame.

Finally, and mainly for mIFU and SIFU observing modes, it is important to reorder the spectra to their original positions on the sky. It is necessary to have a position table which relate the spectra to their location on the sky. In this way it is possible to interpolate the data spatially and create a regular gridded datacube and reconstruct the image of the target at any wavelength. If the instrument SIDE finally is not going to be provided with an Atmospheric Dispersion Corrector (ADC) we need to perform a final spatial interpolation of the datacube to correct for the differential atmospheric refraction. To correct for this effect we can use the reduce datacube to trace the intensity peak of a reference object in the field-of-view along the spectral range and recentering it. Another option is to re-center the images using the theoretical offset given by the DAR formulae (see Filippenko, 1982).

3.15.6 Key features of the DFP

In the following lines we present an overview of the most important features that the SIDE DFP will include:

- The SIDE DFP shall be prepared to handle and propagate image errors throughout the reduction process, in order to check the quality of every image. The error images associated to each data image are generated just after reading out the raw frames, considering the readout noise and gain. Special care shall be taken in order to avoid error correlation, when moving the signal contained in a certain pixel a fractional amount of pixel.

- All the operations performed to any image shall be recorded in the GTC Operation Repository. Checks and quality control procedures shall be also included to provide the GTC Operation Repository with tools to estimate the quality of the data.

- The whole DFP, which is embedded into the GTC Data Factory, shall be coded under an object-oriented architecture. This point of view allows interpreting an observation as an "object", this is, an instance of a C++ class created for observations. This class will include the image (as a matrix), additional parameters including calibrations applied, and another matrix for the associated errors. The "methods" of this class (called "member functions" in C++) will be the different reduction operations to be performed in this image.

- The DFP will tackle each observing mode as an independent problem. In this sense, optimized solutions shall be implemented when necessary. However, whenever possible, already developed software shall be reused for different SIDE modes.

- The DFP is intended to be fully integrated into the GTC Control System, in special, into the GTC Data Factory. This means that this software will not be of public access, but will be used at GTC facilities.

- For most of the frames, the DFP is intended to work in an off-line regime. For certain situations (for example displaying or acquiring), a quick and simplified basic reduction will have to be carried out for performance considerations.

3.15.7 Current status

The UCM group has acquired great experience in the development of Reduction pipelines for astronomical instruments. The current work is concentrated into the DFP of the EMIR and FRIDA instruments for GTC.

Some of the basic filters that will be needed for the SIDE DFP are already available as result of the work done for the EMIR prototype (first release submitted to Grantecan during the February 2007) and FRIDA Preliminary Design Review. Moreover, the “know how” needed for the SIDE DFP is also available as result of different research projects using the PPAK and PMAS instruments at Calar Alto Observatory and INTEGRAL instrument at La Palma Observatory.

All the software developments are carried out using a SUNFIRE V250 software development station where GCS 1.5 (june 2007) is installed.

3.15.8 Costs

The estimated cost for this subsystem is about 50,000 euros.

3.15.9 References

Sánchez, S. F. Techniques for reducing fiber-fed and integral field spectroscopy data, Astronomische Nachrichten, 2006, vol. 327, Iss. 9, p. 850.

Cardiel, N.; Gorgas, J.; Gallego, J.; Serrano, Á. et al. Proper handling of random errors and distortions in astronomical data analysis, 2002, Proceedings of "Astronomical Telescopes and Instrumentation", SPIE, Hawaii.

Filippenko A.V. 1982, The Importance of Atmospheric Differential Refraction in Spectrophotometry, PASP, 94:715-721

4 PROJECT MANAGEMENT

4.1 Organization and structure

4.1.1 General definitions

System: The whole instrument can be divided into parts, with boundaries defined by operational issues. SIDE will have a Pre-Optics, a Fiber Positioner, the Fibers, the Spectrographs and the Software necessary to use them, Electronics units and Detectors. These can be qualified as the main Systems of SIDE. In practice, the boundary between one system and the other is that they need different skills to be planned and constructed, although, of course, they are tightly interrelated and there are common skills among them.

Subsystem: each system can be divided further into smaller parts; this is needed to be able to focus one's attention properly and analyze the details of the systems. For example the preoptics is formed by the Wide Field Corrector and the ADC (if applicable), as well as all the structure, supports etc. The Fiber Positioner has a structure, arms, grippers, etc.

Work Package: On a day-to-day basis, it is convenient to select the tasks to assign to a particular group somehow differently from the System or Subsystem classification. A Work Package is a set of tasks grouped such that it makes it easier to work for SIDE from a practical point of view. A whole system may be too big a job for a single group, as it could be a subsystem still. Moreover, several Systems/Subsystems may have common parts which are more efficiently done by a single group. It may be equally inconvenient to divide a System too much (communication becomes critical and errors risk arises) as to keep too many tasks for a single group (excessive work load and risk of delays on the schedule). Work Packages must be carefully selected to keep a group focused, self contained, with a realistic amount of work and efficient use of particular skills. As an example, the many mechanisms of SIDE will all need control systems, which need to be compatible to one another, but also be adapted to each different environment within the instrument. For example there will be mechanisms to focus the WFC, to move the arms of the Fiber Positioner, to move the pseudoslits, to move the optical elements within the spectrographs etc. All these must follow a standard, but also adapt to the different parts they apply to. This is a single Work Package.

4.1.2 Management structure

The SIDE management structure is shown in Figure 219.

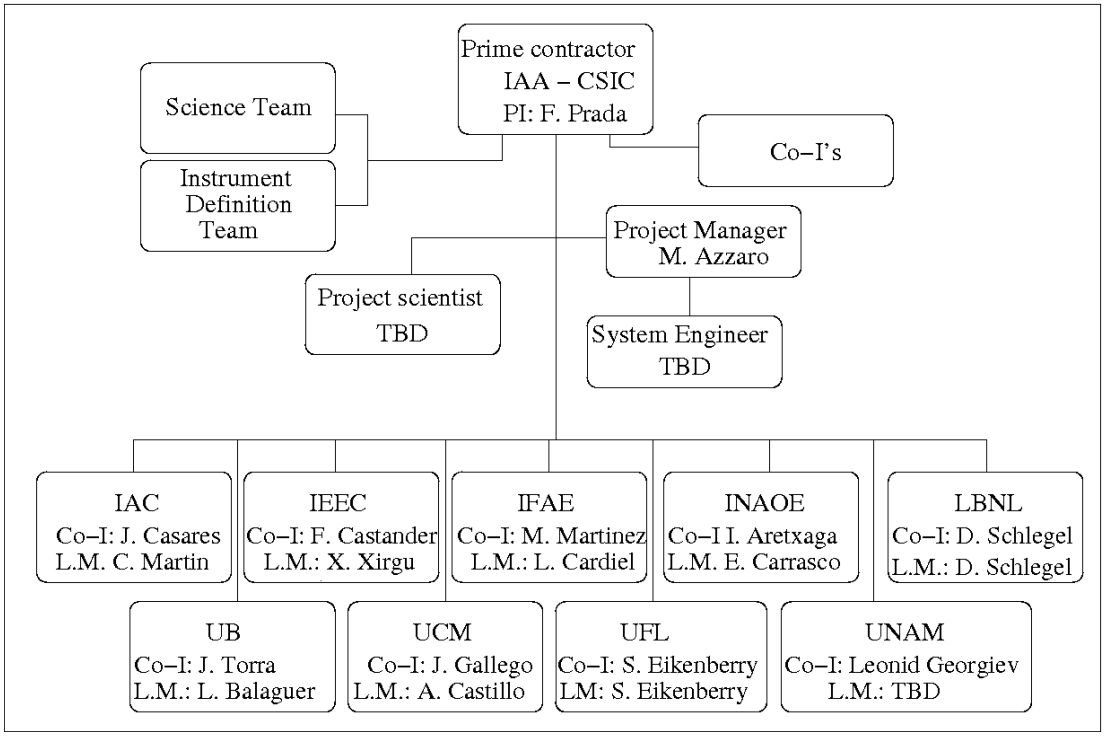

Figure 219. SIDE management structure.

The IAA-CSIC will be the Prime Contractor and will have a formal commitment with GTC, therefore the basic structure is simple and hierarchic. There are two consulting bodies directly depending on the SIDE PI: the Science Team and the Instrument Definition Team. All the Consortium members communicate with the PI directly through the corresponding Co-Is or through the Local Managers and the SIDE Project Manager (see Section 4.1.4.5for details on the Communication protocol). A system engineer is not crucial at this stage and will be hired in the future. There is a strong need for a Project Scientist and this post will have to be filled as soon as possible.

4.1.3 The Consortium

An international Consortium of institutions was formed on September 20th 2006. The following institutions committed themselves with a formal Letter of Intent for the phase of the Feasibility Study (see Annex **¡Error! No se encuentra el origen de la referencia.**) and their logos are shown in Figure 220:

- Instituto de Astrofísica de Andalucía (IAA-CSIC)
- Instituto de Astrofísica de Canarias
- Institut d'Estudis Espacials de Catalunya
- Institut de Física d'Altes Energies
- Instituto Nacional de Astrofísica de Óptica y Electrónica
- Universitat de Barcelona
- Universidad Nacional Autónoma de México
- Universidad Complutense de Madrid
- University of Florida
- Lawrence Berkeley National Laboratory

Figure 220: Logos of the Consortium members institutes

4.1.4 Consortium structure

4.1.4.1 Regular Members

A member of the SIDE consortium is any institution or group who participates to one or more Work Packages (WP) within the project.

A member in charge of one or more WP is also responsible of the relative documentation and, in case of having one or more complete subsystems included in the WP, is responsible of the AIV of that/those subsystems.

The WP of which the member is in charge are specified in the Letter of Intent (LoI) of that member.

The regular consortium member must have a Local Manager (LM) to keep communication with the SIDE Project Manager (PM), a Co-I as responsible scientist to lead that part of the work and a qualified team to develop and complete the tasks included in his WP. Contact details for the Co-I and LM must be available to the other members through the Web pages of the consortium.

The consortium member is financially involved in the project and his contribution will be specified in the MoU produced at the SIDE contract signature.

The consortium member is expected to fulfil the schedule for his WP and to regularly inform the SIDE PM about the progress and status of the work. Schedule constraints are specified by the SIDE PM.

The consortium member has the ability to sign contracts on his own (with companies or institutions), when this is required to complete the WP. Only the member himself is responsible of the consequent contractual duties, either financial, timelines etc. The SIDE PI and SIDE PM must be informed about such initiatives.

All these actions must be coordinated and authorized by the SIDE PM.

In general, the regular consortium member manages his own activities internally and communication with the prime contractor or with other members is done through the LM. The details of the internal work and activities do not concern anybody outside the member (Prime contractor or other members), being the LM the only communication channel visible from outside.

The regular consortium member must inform the SIDE PI (through the relative Co-I) and the SIDE PM (through the relative LM) on a regular basis about the activity on the WP, and about financial or contractual actions taking place during his tasks (not about the internal details of these, see previous point).

4.1.4.2 General structure

Each party of the Consortium has a Co-I and a PM, plus the technical staff, engineers, and possibly external industries.

- Letter of Intent

Each party must write down his own commitment and send it to the IAA-CSIC. This is a short letter which states clearly the activity that the institution will do within the WPs scheme, signed by the head of the institution/department. This commitment is at institutional level, i.e. it is an agreement between that institution (represented by the director) and the IAA-CSIC (represented by the IAA-CSIC director). Such commitment should be agreed internally by each institution and, once set, does not concern lower levels along the management tree of that institution.

There can be other ways of collaborating with SIDE apart from being member of the Consortium. The SIDE PI must approve other types of collaboration.

- **Co-I**. Co-I's are supposed to refer to the SIDE PI. They will deal with science or strategic issues, as a channel for the institution to the SIDE PI and the rest of the Co-I's. Co-I's mission is to follow operational questions on a day-to-day basis within the respective Institution. Co-I's report directly to the SIDE PI during the progress meetings held once every month.

- **PM (LM)**. LM's will report to the SIDE PM only. They will deal with technical and organization issues, being the official channel for the institution to transmit to the rest of the Consortium about the internal progress of the technical work. The technical work of an institution is "seen" from outside through the LM only. LM's must internally be always up to date with the status of the work, problems and risks, in terms of work volume and timing, and they must report all the information to the SIDE PM during the Progress Meetings held once a month. LM's must closely monitor the industries/manufacturers needed for the development of the assigned WP(s) and regularly report the status of their work to the SIDE PM.

- **ST**. The Science Team is a group of scientists, divided into different scientific areas, each of which has a coordinator member. The ST has an advisory function in selecting and focusing key science cases to pursuit through SIDE. The ST must help the PI defining the science that SIDE will perform. The ST members do not represent their institutions when acting as such.

- **IDT.** The Instrument Definition Team is a group of science/technical persons in charge of translating the scientific requirements which come from the ST into technical specifications for the instrument. The IDT has an advisory function and acts as an interface between the ST and the SIDE PM. Much interaction is expected between the ST and the IDT, specially during the initial phases of the project. The two groups have to work in parallel and constantly refine the instrument characteristics list. The IDT has to evaluate whether the ST requirements can be operationally achieved, find a way to achieve them and discuss the devised method with the engineers until the tasks are seen as feasible. In case of serious problems, the IDT reports back to the ST and discuss whether the problematic requirements can be relaxed or achieved in a different way.

- **INSTITUTIONS.** All the Consortium members are Institutions, represented before the Consortium by their Co-Is.

- **INDUSTRIES.** External industries will be needed during the project. There must be a follow up of their activity and they must report to the PM/LM of the Institution who engaged them (either through a contract or any kind of collaboration). There will be direct contact between the industries and the engineers of the Consortium, provided that the relative PM/LM is kept up to date about their activities. They must follow a quality control policy on their products and this must be transparent to the engaging Institution.

4.1.4.3 The Science Team

A Science Team (ST) was formed following the first SIDE meeting in Sevilla (September 20th, 2006) with the aim of defining scientific cases for SIDE. The ST is divided in seven groups by science areas and each has a coordinator. The ST structure is shown in Figure 221:

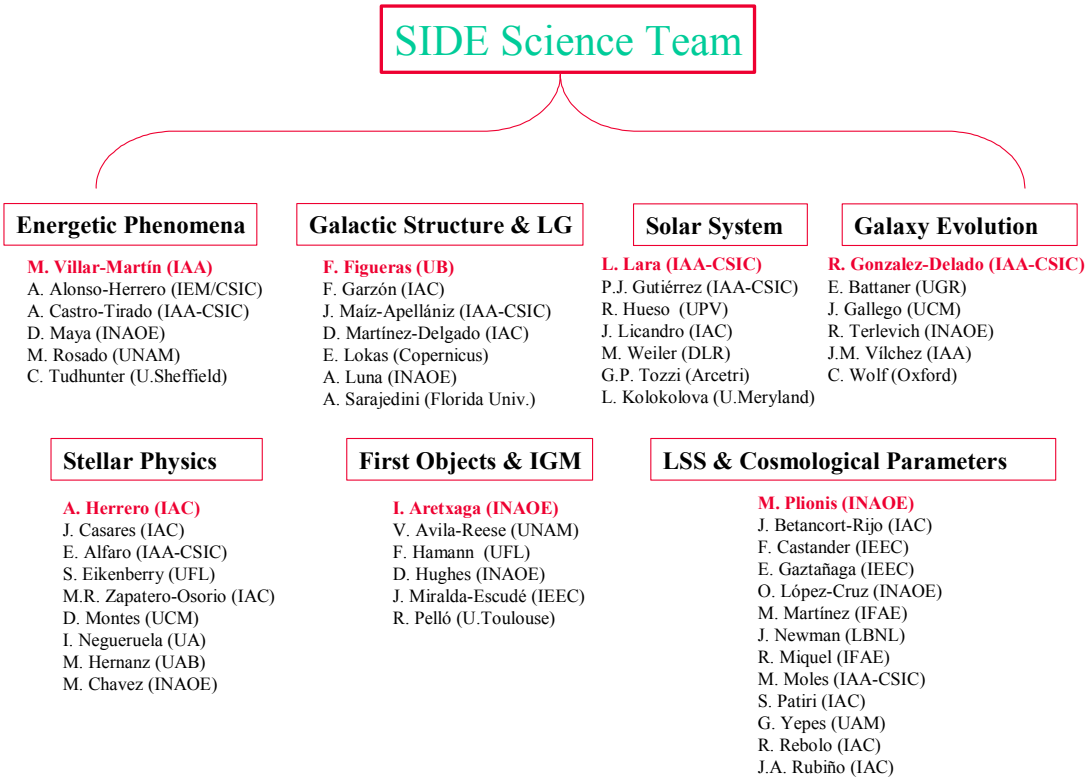

Figure 221: SIDE Science Team.

4.1.4.4 The Instrument Definition Team

An Instrument Definition Team (IDT) was formed following the kick-off meeting of September 20th, 2006 in Sevilla, with the aim of translating the scientific recommendations of the ST into engineering parameters for the SIDE instrument. The IDT is formed by 7 recognized instrumental specialists from various institutions (not necessarily tied to the SIDE Consortium). The IDT is as follows:

- E. Carrasco (INAOE)
- S. Eikenberry (U. Florida)
- A. Manchado (IAC)
- E. Mediavilla (IAC)
- J. Sánchez (IAA-CSIC)
- D. Schlegel (LBNL)
- J. Turner (Gemini)

4.1.4.5 Relationships amongst the various agents (Communication chart)

Whatever is not included here, is NOT an official channel within the Consortium and will not result in any effective actions within the Project.

PI with Co-Is: regular communication about:
- Consortium strategic issues
- WP issues
- Funding issues

PI with LMs: Only specific issues provided that the PM is informed.

PI with ST: regular communication about:
- Science cases to pursuit
- Scientific requirements
- Scientific requirements priority

PI with IDT: regular communication about:
- Instrument technical issues
- Scientific requirements priority

PI with Industries: Negotiations at contract signature.
- Occasional specific issues
- Occasional funding/payment issues

PM with Co-Is: occasional communication on specific issues provided that the PI is informed.

PM with LMs: regular communication about:
- Work progress in each WP
- Schedule status, coordination with others

- Risks recognition
- Non-conformities

PM with ST: No communication.

PM with IDT: Occasional communication during presential meetings or specific issues.

PM with Industries: Negotiations at contract signature.
Regular communication about:

- Work progress status
- Non-conformities

Co-Is with PI: regular communication about:

- Consortium strategic issues
- WP issues
- Funding issues

Co-Is with PM: occasional communication on specific issues provided that the PI is informed.

Co-Is with LMs: When not belonging to the same institution, no communication.

Co-Is with ST: frequent communication for specific points.

Co-Is with IDT: frequent communication for specific points.

Co-Is with Industries: When not hired by their institution, no communication.

LMs with PI: occasional communication on specific issues provided that the PM and the respective CoI are informed.

LMs with PM: regular communication about:

- Work progress in each WP
- Schedule status, coordination with others
- Risks recognition
- Non-conformities

LMs with LMs: Communication relative only to common tasks within a WP.

LMs with Co-Is: When not belonging to the same institution, no communication.

LMs with ST: No communication.

LMs with IDT: No communication.

LMs with Industries: When not hired by their institution, no communication.

ST with PI: regular communication about:

- Science cases to pursuit
- Scientific requirements
- Scientific requirements priority

ST with PM: No communication required.

ST with Co-Is: frequent communication for specific points.

ST with LMs: No communication.

ST with IDT: frequent communication for specific points.

ST with Institutions: No communication.

ST with Industries: No communication.

IDT with PI: regular communication about:

- Instrument technical issues
- Scientific requirements priority

IDT with PM: Occasional communication during presential meetings or specific issues.

IDT with Co-Is: frequent communication for specific points.

IDT with LMs: No communication.

IDT with ST: frequent communication for specific points.

IDT with Institutions: No communication.

IDT with Industries: Occasional communication during presential meetings or specific issues.

Industries with PI: Negotiations at contract signature:

- Occasional specific issues
- Occasional funding/payment issues

Industries with PM: Negotiations at contract signature.
Regular communication about:

- Work progress status
- Non-conformities

Industries with Co-Is: When not hired by their institution,
no communication.

Industries with LMs: When not hired by their institution, no communication.

Industries with ST: No communication.

Industries with IDT: Occasional communication during presential meetings or specific issues.

Industries with Institutions: Negotiations at contract signature.

4.1.4.6 Modifications within the Consortium

- Incorporation of a new member: Institution applies for membership. PI proposes to the Consortium. PI decides after discussion with the Co-Is.

- Members departure: A member wants to leave: PI + Consortium discuss about taking over the leaving member duties. If it is possible, departure is approved. No refunds can be claimed. Publications will report left member during one more year.

If there are serious reasons, like duties/tasks not fulfilled, unjustified or harmful delays, unjustified fund withdrawal etc.: PI decides to finish the partnership. No refunds can be claimed. Publications will not report the left member starting from the departure event.

- WP modification

Members can propose to expand their WP participation. This should be justified and supported by adequate resources. Withdrawal of resources from other WPs to support expansion must be studied with care. PI has the final decision.

Members can propose to diminish their WP participation. This should be justified by lack of funds or resources. This must be declared at least 6 months in advance to allow the hole to be filled.

4.1.4.7 Financial management

The PI is in charge of the financial decisions above a TBD amount. All the members are expected to seek funds on their own, through their funding agencies, or, for the Spanish members, by joining a funding request together with other members.

Any actions for fund procurement should be communicated to the SIDE PI and PM. In the case of Spanish institutions, any actions for fund procurement should be previously discussed with the SIDE PI.

There is a Contingency Budget available for emergencies (current funds are about TBD €). This is also managed by the PI and may be used by the members with a unexpected financial problem which may severely affect the Schedule or the Scope of the project.

A formal request must be issued, together with a full justification (what is going to be done with that money) and an explanation of why the emergency arose in the first place.

4.1.5 Responsibilities

The institution who committed for completing a Work Package is responsible for its completion before the IAA-CSIC, as well as for writing and maintaining the relative documentation.

4.1.6 Contracts arrangements

Contracts with external industries will be needed for the tasks which cannot be completed within the Consortium. Contracts will be signed between an Institution and the manufacturer and will only concern that institution (not the rest of the Consortium).

4.1.7 External parties

Various external industries have been involved in the Project already during the Feasibility Study phase: NTE, IDOM and AVS.

NTE helped with the Fiber Positioner study, with the input from the IAA-CSIC (J. Sánchez del Rio, M. Ubierna Gorricho) concerning the global requirement of the Fiber Positioner, and the input from the UFL (S. Eikenberry) and LBNL (D. Schlegel) concerning their respective robot concepts (see Section 3.5).

IDOM is in charge of the Spectrograph room to be mounted onto the GTC structure.

AVS is in charge of the study for the LBNL robot concept production.

Other companies have approached us showing a great interest for collaborating in the project, such as Sener, Lidax, Fractal etc.

The Rutherford Appleton Laboratory has performed the Dual IR arm thermal analysis.

The optical consultant Harland Epps has drawn a baseline for the SIDE spectrographs.

4.2 Work breakdown

4.2.1 Work Packages

A work packages distribution within the Consortium was organized during the first SIDE meeting of September 2006, and has remained basically the same since, apart from the inclusion of GTC in the Detectors work package. This seemed convenient because a new standard for detectors is being created by GTC, so it looks natural that SIDE detectors definition goes along with the new standard formation process and thus GTC is present in the detectors work package. The Work package distribution for the Feasibility Study phase is as shown in Table 84.

Project management	**IAA**
Fiber positioner	**IAA**, UFL, LBNL
Pre-Optics	**IAA**
AIV responsibility	**IAA**, IAC
Pipeline data reduction	**UCM**, UB
Observing software	**IAA**, UB
Detectors and Cryogenics (purchase, characterization, controllers, DAS)	**IAC**, IFAE, IEEC, GTC
Fibers (MOS, IFU), microlenses, connectors, pseudoslits	**IAC**, IAA
Guiding unit, TVs	**IEEC**, IAA
Calibration unit	**IAA**
Mechanism control, motors, low level software	**IAC**
High level software control	**IAC**, UB
Mechanics, mountings, supports, focal station logistics (racks etc.)	**IAA**

SPECTROGRAPHS	**IAA**
Spectrograph (Dual VIS-NIR)	**IAA**, UFL
Spectrograph (opt. Hi-Res)	**INAOE**, IAA, UFL

Table 84 Consortium Work Packages distribution for the Feasibility Study Phase (institutions in **BOLD** are responsible for the relative Working Package).

4.2.2 Documentation

4.2.2.1 General

During this phase the documentation available is linked on the Private Consortium web page of SIDE. The structure is: Technical Notes, documents from GTC, documents concerning other instruments, SIDE Power-Point presentations and, finally, several science papers which could be useful for the project. A version-control system is going to be implemented in the near future for the SIDE documentation, on the Server machine at IAA (Granada). The purchase of a specialized software for document generation + management is being evaluated at present.

4.2.2.2 Technical documentation

Most of the analysis done for the SIDE definition has been recorded in the form of Technical Notes linked at the SIDE Consortium web page. There are Technical Notes on the Fiber Positioner, on the fiber end buttons, on the impact of Atmospheric Dispersion and bad Astrometry on SIDE observations, on the optimum fiber size, on the Acquisition, Guiding and Calibration systems, on the mechanical envelopes, on the spectrograph baseline and on SIDE IR thermal emissivity.

4.2.2.3 On line documentation

A web page for SIDE has been created and is available at http://side.iaa.es. There is a private page (password protected) where all the current documentation can be found: GTC documents, Technical Notes, talks and presentations of key meetings, relevant publications etc. The Consortium mailing lists can also be found here.

4.2.2.4 Drawings

At this stage the only drawings within the SIDE documentation are those provided by GTC, concerning the Nasmyth A platform, envelopes and accessories, the platform structure, the Nasmyth rotator, the Telescope Mount assembly, the Telescope Mount Yoke,

4.3 SIDE prototype

4.3.1 Short term model: miniSIDE

SIDE will be a highly modular instrument, therefore it offers the possibility to build a prototype model (miniSIDE), performing the basic observing functions, well in advance of the commissioning of the whole instrument. It is our plan to pursuit the construction of a copy of the Dual VIS-NIR spectrograph, fed by some test units, in a couple of years time, and use this as a benchmark for analyzing the fiber positioner, optics and fiber-related problems. The expensive parts of this device would be completely recyclable for the real instrument.

The basic idea would be to build some 10 MOS IFUs and a SIFU of reduced size (together with a Sky bundle), and feed a Dual VIS-NIR spectrograph prototype, provided with the VIS arm only and with only two disperser elements. All the mechanisms (focusing of the spectrograph, etc.) can be manually actuated in order to simplify the device as much as possible. If the LBNL robot concept is finally used, 10 cylinders could be distributed across a reduced FOV, so that a WFC would not be necessary, and different positions on the focal plane could be tested. The MOS bundles could end into different types of configurations at the pseudoslit, so that several fiber set-ups can be tested concerning cross-talk, inter-fiber distance, alignment etc. In terms of science, the reduced SIFU will provide already unique 3D spectroscopy capabilities for the GTC with a FOV of ~10” diameter.

Such a prototype could be planned to be ready in 2 years time, in parallel with the conceptual and preliminary design phases, and would provide unvaluable information and experience at a reduced cost, while delivering competitive science quality data already.

4.4 Schedule

A provisional schedule for the whole project is provided in Figure 222. Many are the uncertainties at this early stage, so a number of fundamental dates are expected to change in the future.

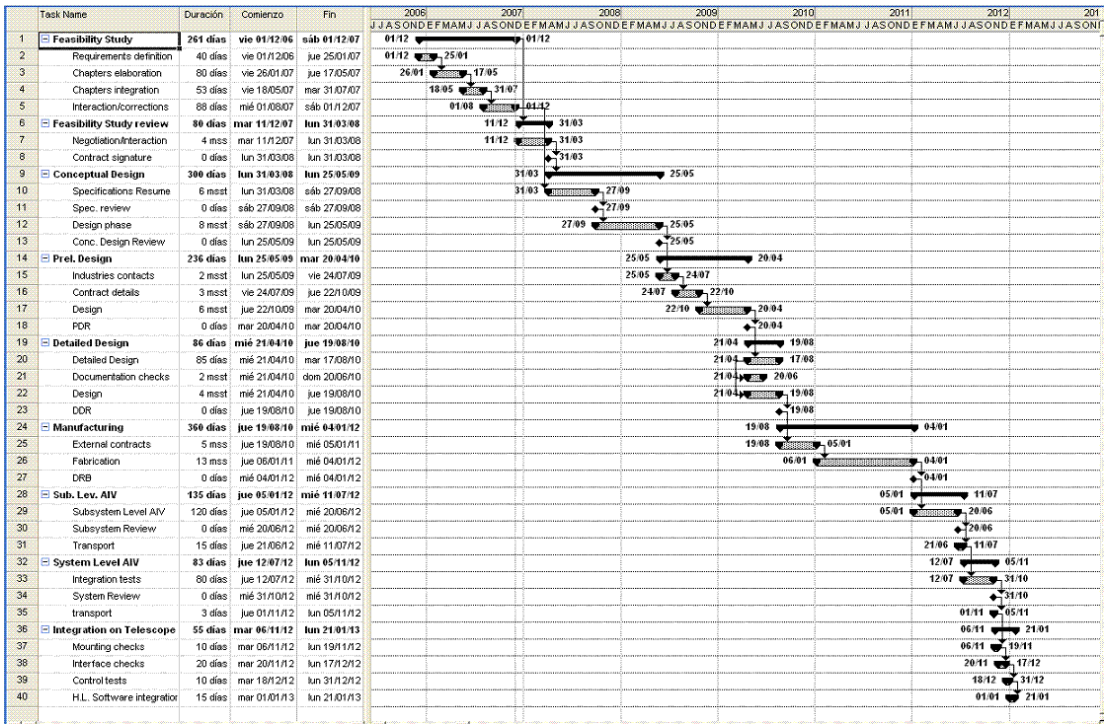

Figure 222: SIDE project schedule.

4.5 Risk management

4.5.1 Identification of risks

Risk forecast and identification is essential for the good progress of the project. In most cases, risks arise during the development of tasks and are difficult to foresee, thus close and constant monitoring is the only way to limit their effect. A number of common risks can be supposed as a general guideline and by extracting experience from similar projects. This section aims to give an overall estimation of possible risks and the planned way to manage and mitigate them.

4.5.2 Risk management plan

Constant monitoring is the key to limit the consequences of risks. The Project Manager needs constant contact and response from all the members in order to anticipate or, at least, recognize a risk as soon as possible. The same applies to the PI as for being in regular contact with the CoIs. Risks are identified, analyzed and assessed by the Project Manager and the Technical Staff involved and marked according to their importance (severity of their consequences). In case of severe cost impact or important delays, a decision on the risk mitigation will require the PI action.

4.5.2.1 General

A number of risks can be foreseen for the project even at this early stage; these are listed below. Such list is necessarily incomplete; risk assessment and abatement is an always ongoing process during the project development.

RISK	CONSEQUENCE	SOLUTION
Lack of funds.	Severe delay or project suspension.	Search other funding mechanisms
Personnel job uncertainty / limited personnel available.	Discontinuities and delays in task accomplishment.	Explore more stable contract schemes
Poor interface definition.	Components would not fit. Delays and cost increase.	Careful inspection of interface definition
WPs distributed across different Consortium members	Poor coordination, delays and cost increase.	Keep WP splitting to a minimum plus close monitoring of activities
Poor coordination among the Consortium members due to large Consortium.	Delays and management overload, cost increase.	Frequent monitoring/ communication

Cost increase (inflation, delays etc.)	Budget overcome	Contingency funds provision.

4.5.2.2 Science

RISK	CONSEQUENCE	SOLUTION
Science goals not well defined.	Instrument performance level not optimal.	Redefine goals with ST
Science goals too ambitious and too broad (i.e. "do-all" philosophy).	New or challenging technology required, delays and cost increase.	Reduce goals to a reasonable extent
Other instruments competition	Instrument is not competitive	Closely monitor other ongoing projects.

4.5.2.3 Optics

RISK	CONSEQUENCE	SOLUTION
Optics elements transport.	Damage during transport, delays and cost increase.	Reduce transportation needs.
Blanks take too long to be manufactured	Risk of extreme delays in case of breakage.	Order spares in advance.
Blank material not available.	Change to optics design, severe delays and extra-costs.	Check blanks availability in advance.
Fiber optics cable breakage.	Delays and cost increase.	Provide spares.
Spectrographs performance inadequate.	Poor performance and failure of science goals.	Careful optical and optomechanical design.
Inadequate spectral calibration system.	Lower quality data.	Careful optical and optomechanical design.

4.5.2.4 Electronics

RISK	CONSEQUENCE	SOLUTION
High heat production.	Instrument performance decrease, power load increase.	Careful estimation of heat production and good planning.
Too much space required.	Logistic affected, delays, conflict with other instruments.	Careful estimation of electronics and good planning. Keep contact with other instruments.
Too heavy.	Change in structures, delays.	Careful estimation of weights.

4.5.2.5 Mechanics

RISK	CONSEQUENCE	SOLUTION
Excessive weight.	Interface problems, change in structures, delays transport difficulty.	Careful estimation of weights.
Does not perform to specifications.	Delays and cost increase.	Good mechanical specifications.
Interface problems.	Delays and cost increase.	Good mechanical specifications.

4.5.2.6 Detectors

RISK	CONSEQUENCE	SOLUTION
Do not fulfill specifications.	Scientific effectivity reduced.	Check in advance with manufacturers.
Delay in delivery.	Delays.	Check in advance with manufacturers.

4.5.2.7 Software

RISK	CONSEQUENCE	SOLUTION
Poor definition of specifications.	Unsuitable software, delays and cost increase.	Integrate software people early in the instrument definition.

4.6 System engineering

4.6.1 General

During this phase of the project, the level of definition of the various subsystems and interfaces is not advanced enough for drawing a complete picture of how to integrate the whole system, therefore, at this point, little can be said about System Engineering, apart from underlining the importance of it in later phases, and the importance that the System Engineer will have at that point. The selection of a good System Engineer will be crucial for the project, and it will be a difficult task to find a qualified and experienced person. The next section deals with the functions and skills of the System Engineer.

4.6.2 System engineer functions

The role of the system engineer is always of great relevance but especially for large technical projects as SIDE, and particularly, when the project team members belong and work in different institutions, locations and countries.

In coordination with the Project Manager, the SIDE system engineer will assure that SIDE design meets the required performance applying a structured approach from design to verification through all the life cycle of the project.

Its main responsibility is to focus on:

-Specifications

-Product Tree

-Interfaces

-Technical error budgets

-Integration and verification

The system engineer is in charge of their correct definition and managing and documenting their changes, with the purpose of always controlling the real configuration and its traceability to the scientific requirements.

He performs this formal configuration control being responsible for the documentation at the system level, controlling the processes of approval and change of these documents and disseminating them to the rest of the project.

The technical error budget (optical, mechanical, thermal...) is an iterative process to allocate allowable tolerances between related subsystems in order to fulfill the top requirements. From the error budget analysis and the design constraints, the subsystem specifications are derived.

Following this iterative process, low level specifications maintain traceability from the top requirements, the design concept and the architecture evolve accordingly, a product tree is produced and the interfaces are defined.

Low level specifications regarding parts and components are generated by the responsible of each subsystem but the system engineer is in charge of supervising this process in order to guarantee that the fulfillment of the low level specifications assures that the top level specifications are satisfied.

The system engineer will also participate actively in the assembly, integration and verification phase (described elsewhere in this document) in order to assure that, during these processes, all the interfaces and specifications are correctly tested and validated, and that the appropriate documentation is produced.

In general, the system engineer will assist the project manager as the maximum responsible of the design, performing risk analysis and mitigation plans, evaluating trade-offs and taking technical decisions to assure a viable and balanced design.

4.7 AIV plan

4.7.1 General

The goal of the AIV process is to perform the assembly and integration of all SIDE components and subsystems, and ensure that the instrument fulfils the scientific requirements.

An instrument AIV plan will be developed to address the assembly and verification of all the subsystems, their integration in the instrument, and the final verification of SIDE as a whole. All the assembly, integration and verification/acceptance processes will be described in detail in the corresponding documents. Also, all the procedures, tests and results will be documented.

The assembly, integration and verification will consists of two phases: AIV at subsystem level and AIV at system level. Each subsystem has its own entity and specifications. The fulfillment of these specifications will be verified during the acceptance process, in house or at the manufacturer's premises, previously to their integration in SIDE.

With the exception of the cryostat of the detectors, SIDE is not foreseen to be a cryogenic instrument. Because of that, all the verification tests will probably be performed at room temperature. Only the detectors' cryostats will be tested first at room temperature and later at working temperature.

4.7.2 AIV procedure

In more detail, the AIV process will consists of:

- Verification and acceptance of components.

  Depending on the complexity of the components, different approaches will be followed. Some components will be tested during their integration process and other may require a complete acceptance plan.

- Assembly and integration of subsystems.

  From its components, the assemblies and subsystems are integrated. In complex subsystems some partial verification and tests can be done during the integration process.

- Verification of subsystems and assemblies.

  According to the global verification plan, the parameters to be verified will be specified and specific test and procedures will be detailed. Apart from simple test, like mass, dimensions, basic functionality, etc. some subsystems may require special setups and instrumentation to be verified. Optical performance, mechanical precision, repeatability, stability, etc. are among those. During the verification process, a number of complementary tests will be done in order to measure relevant parameters to the integration and setup of other subsystems.

- Assembly and integration of the System.

  As in previous phases, a document will guide the integration of the system. To avoid interference problems during the integration, it is convenient to start by a preliminary assembly of the critical parts of the system. Once the problems that may appear are solved, the integration of the final system is undertaken step by step.

- Verification of the system

  Following the system verification document, all the requirements and specifications at system level will be verified. In some cases, a partial verification of the system can be of interest, in order to assure the full integration of the system. Usually, a system requirements verification matrix is checked to guarantee that all the scientific requirements are met.

  As in the case of the verification of the subsystems, quite complex setups can be needed to perform these measurements. Nevertheless, each requirement should have its own previously agreed and documented method of verification. When a direct measurement is not possible, other methods can be used. For instance, demonstration, analysis or inspection.

  Some requirements are not verifiable in the laboratory. General requirements or those in relation with safety or control system have to be verified during the commissioning phase at the telescope.

4.7.3 AIV equipment and facilities

Apart from the special equipment or setups that may be required to perform the verification process, it has also to be taken into account the numerous auxiliary systems needed to manipulate, align, rotate, move and transport the different parts of SIDE, during this phase. Some of these auxiliary systems are already available or are just off-the-shelf, but others will need to be designed and will be treated as any other work package in the SIDE planning.

Similarly, during the AIV phase, the engineers may require the development of specific computer programs to control and monitor the different devices (sensors, motors...) needed to test and integrate the different components and subsystems. These programs should be specified at the beginning of the project in order to be incorporated in the planning.

Among the Consortium institutions, it can be ensured the necessary knowledge, infrastructures and instrumentation to assembly, integrate and verify the components and subsystems of SIDE, and the instrument as a whole. At this point it is worth mentioning the large AIV laboratory (see Figure 223) at the IAC headquarters in La Laguna. This facility has two separate sections (clean room and general purpose) and a GTC Nasmyth rotator simulator. Presently, the AIV of OSIRIS is taken place in this laboratory.

Figure 223: AIV building of the IAC in La Laguna. Left, external view. Center, internal view. Right, GTC Nasmyth rotator simulator.

It is being considered the possibility to perform the Dual VIS-NIR spectrograph AIV at the IAA-CSIC headquarters in Granada.

4.8 SIDE weight budget

4.8.1 General

A monitoring of the weights involved with SIDE, even if as a rough estimation, is very important for the project, in order to quickly find any possible problems with GTC weight constraints early enough as to take proper actions to mitigate the risk. At this stage there are so many uncertainties that any reasonable accuracy is impossible, but it seems better to start with the process of monitoring all the components, even if the results are not accurate. It is certainly easier to *correct* a table than *make* a table from scratch.

4.8.2 Weight breakdown

Table 85 shows the estimation of the weights of the various SIDE components. Weights are given in Kilograms.

System	per unit	subtotal
WFC (Nasmyth)	420	420
WFC (Folded Cass)	200	200
LBNL Fiber Positioner (Nasmyth)	200	200
UFL Fiber positioner (Nasmyth)	750	750
UFL Fiber positioner (Folded Cass)	700	700
Robot stowage trolley	200	200
Dual VIS-NIR spectrograph	650	6500
Hi-Res spectrograph	2500	2500
Fiber cable	180	180
Spectrograph room[1]	5000	5000
Calibration system	150	150
Electronics racks	400	400
Detectors controllers	30	630
LN2 system	400	400
Total		**18230**

Table 85 Breakdown of weights for SIDE components.

[1] The spectrograph room weight shown in Section 3.2.4 is only 2000 kg, but in the same section we comment that this will increase due to the higher number of spectrographs.

ANNEXES

A. ACKNOWLEDGEMENTS

We wish to thank all the people, institutions and companies not included within the authors of this document, but who collaborated with us in the work here described, in the (optimistic) hope that nobody gets forgotten.

We acknowledge the help of: Ernesto Sanchez, Dr. Martin Roth, Dr. Christopher Wolf, Dr. Andreas Kelz, Dr. Marc Davis, prof. Harland Epps, the Isaac Newton Group, A. J. Cuesta., Miguel A. Sánchez-Conde, Vicente Sánchez and Héctor Magán Madinabeitia.

We acknowledge the help of G. B. Dalton, I. A. J. Tosh and M. J. Ferlet from the Rutherford Appleton Laboratory.

We acknowledge the help of the following companies: NTE, IDOM, LIDAX.

We acknowledge the interest shown for the project by the following companies: SENER, FRACTAL, TEKNIKER, AVS.

We want to tank the people from GTC for all the support provided during this last year and we thank GTC for the financial support of 30,000 € during this early phase of the project.

We also want to acknowledge the financial support by the Spanish Ministerio de Educación y Ciencia, who granted the project with an "Acción Complementaria" Ref.: AYA2006-28477-E of 150,000 €.

We also thank all the Consortium institutions for the financial and human effort devoted to this project.

We thank the contribution of the people who participated to the workshop "Spectroscopy in Cosmology and Galaxy Evolution 2005-2015", held in Granada, October 3 – 5 2007.

B. LIST OF AUTHORS

INSTITUTO de ASTROFISICA de ANDALUCIA (IAA-CSIC)	**Management, Fiber Positioner, Dual VIS-NIR spectrograph design, Pre-optics, Calibration unit, Mechanics and Logistics, Instrument definition and requirements, System Engineering, Science Case.**
F. Prada	**PI, Instrument definition and requirements, Science case.**
M. Azzaro	**PM, System Engineering, Instrument definition and requirements.**
O. Rabaza	**Dual Spectrograph Optical Design, GTC WFCs Optical Design and ADC considerations, Hi-Res spectrograph design.**
J. Sanchez	**Fiber Positioner, Fiber Positioner Comparison, Spectrographs Optical Requirements, Calibration units, Pseudoslit Configurations, System Engineering.**
M. Ubierna	**Dual Spectrograph Mechanical Design, Fiber Positioner, Logistics and GTC Interfaces, Spectrograph Room, Instrument Mechanical Requirements**

INSTITUTO de ASTROFISICA de CANARIAS (IAC)	**AIV, Fibers, Microlenses, Mechanism control, System engineering, Detectors and controllers**
J. Casares	**Co-I**
C. Martín	**Local Project Manager**
F. Gracia	**Engineers**
E. Joven	
J. L. Rasilla	

INSTITUT D'ESTUDIS ESPACIALS DE CATALUNYA (IEEC)	**Acquisition and Guiding unit**
F. Castander	**Co-I**
X. Xirgu	**Local Project Manager**

INSTITUTO de FISICA de ALTAS ENERGIAS (IFAE)	**Detectors and controllers**
M. Martínez	**Co-I**
L. Cardiel	**Local Project Manager**

INSTITUTO NACIONAL de ASTROFISICA, OPTICA y ELECTRONICA (INAOE)	**Hi-Res spectrograph design**
I. Aretxaga	**Co-I**
E. Carrasco	**Local Project Manager**
J. Castro	**Engineer**

LAWRENCE BERKELEY NATIONAL LABORATORY (LBNL)	**LBNL fiber positioner**
D. Schlegel	**Co-I and Local Project Manager**
W. Ghiorso	**Engineer**

UNIVERSIDAD DE BARCELONA (UB)	
J. Torra	**Co-I**

UNIVERSIDAD COMPLUTENSE DE MADRID (UCM)	**Pipeline data reduction software**
J. Gallego	**Co-I**
A. Castillo	**Local Project Manager**
N. Cardiel	**Engineer**

UNIVERSITY OF FLORIDA (UFL)	**UFL fiber positioner**
S. Eikenberry	**Co-I and Local Project Manager**

IDT	**Instrument definition and requirements**
S. Eikenberry (UFL)	
E. Carrasco (INAOE)	
J. Sánchez del Rio (IAA-CSIC)	
A. Manchado (IAC)	
E. Mediavilla (IAC)	
D. Schlegel (LBNL)	
J. Turner (Gemini)	

SCIENCE TEAM	SIDE Science case
A. Alonso (IMAF) **A. Castro (IAA-CSIC)** **D. Mayya (INAOE)** **M. Rosado (UNAM)** **C. Tadhunter (USheffield)** **M. Villar (IAA-CSIC)**	**Energetic Phenomena**
I. Aretxaga (INAOE) **D.H. Hughes (INAOE)** **R. Pelló (Obs.Midi-Pyrenees)**	**First Objects & the IGM**
R. Gonzalez (IAA-CSIC) **J. M. Vílchez (IAA-CSIC)** **C. Wolf (Oxford)**	**Galaxy Evolution**
F. Figueras (UB) **F. Garzón (IAC)** **J. Maiz (IAA-CSIC)** **D. Martínez (IAC)** **A. Sarajedini (UF)**	**Galactic Structure and the Local Group**
J. Betancort-Rijo (IAC) **F. Castander (IEEC)** **E. Gaztañaga (IEEC)** **M. Martínez (IFAE)** **R. Miquel (IFAE)** **J. Newman (LBNL)** **S. Patiri (IAC)** **M. Plionis (INAOE)** **G. Yepes (UAM)**	**LSS & Cosmological Parameters**
L. M. Lara (IAA-CSIC) **P. J. Gutiérrez (IAA-CSIC)** **L. Kolokolova (UMaryland)** **G. P. Tozzi (Arcetri)** **R. Hueso (UPV)**	**Solar System**
E. Alfaro (IAA-CSIC) **P. Amado (IAA-CSIC)** **J. Casares (IAC)** **S. Eikenberry (UFL)** **A. Herrero (IAC)** **D. Montes (UCM)** **I. Negueruela (UA)** **M. R. Zapatero (IAC)**	**Stellar Physics**

C. SKY BACKGROUND LEVELS

- Extracted from Eikenberry (2007) of 3.10.1.5.5:

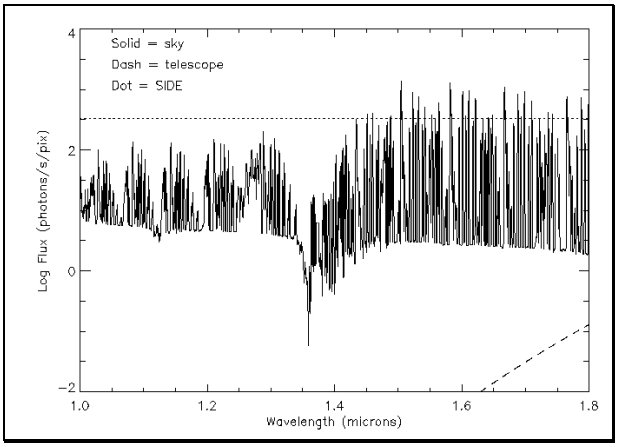

Figure 224 Contributors to SIDE background, including the night sky spectrum, the telescope/fibre (T=283K), and an ambient-temperature (T=283K) spectrograph. Note that the spectrograph dominates background except for a few locations with particularly strong telluric emission**.**

- Extracted from Ferlet (2003) of 3.10.1.5.5:

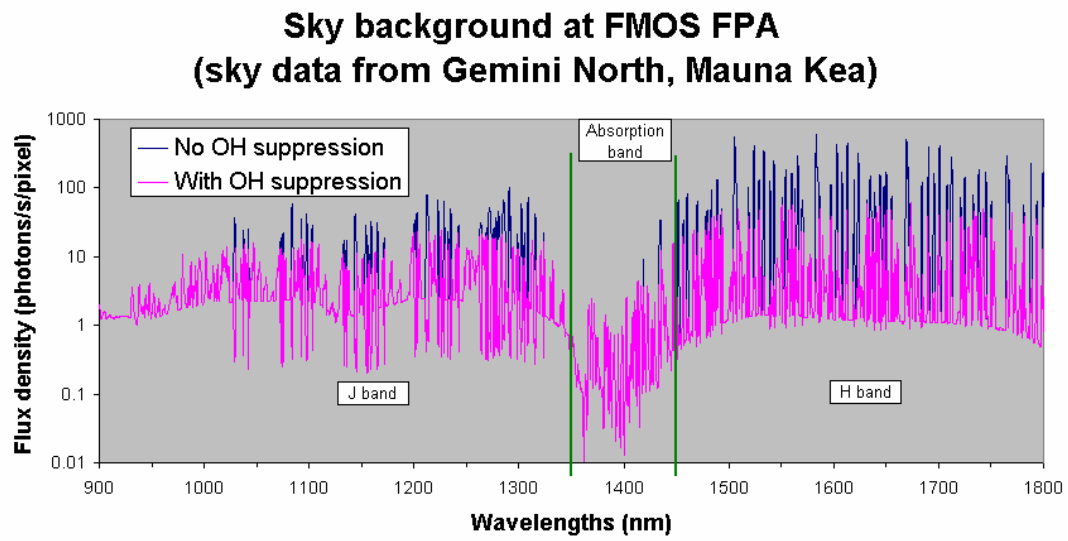

D. ASAP MODEL BACKWARD MODE RESULT

- Spectral dependence of the View Factors (not normalised) coefficients:

Comparison with 2E5rays in backward raytrace (ASAP model)

STATS

0.95um

Object	Rays	Flux	
36	29614	213.8131	SECTION_F
28	29377	212.1019	LENS_5.EDGE
35	28218	203.734	SECTION_E
30	20857	150.5875	FPA.ARRAY
32	18674	134.8263	SECTION_A
29	13659	98.61798	LENS_5.BACK_PLANE
40	9458	68.28676	DET_BACK
34	7825	56.4965	SECTION_D
44	7263	52.43886	SECTION_B
33	6347	45.82534	SECTION_C
24	4964	35.84008	LENS_4.EDGE
25	3425	24.7285	LENS_4.BACK_PLANE
12	2792	20.15824	GRISM.BOTTOM
38	2361	17.04642	EDGE_B_C
42	2219	16.02118	VIS_PORT_OUT
7	1871	13.50862	DICHROIC.EDGE
21	1606	11.59532	LENS_3.EDGE
37	1434	10.35348	EDGE_A_B
11	1156	8.34632	GRISM.RIGHT_SIDE
46	1128	8.14416	SLIT_SUPPORT
10	1060	7.6532	GRISM.LEFT_SIDE
43	994	7.17668	VIS_PORT_TUBE
9	835	6.0287	GRISM.GRATING
47	769	5.55218	SLIT_WALL
18	648	4.67856	LENS_2.EDGE
39	418	3.01796	EDGE_C_D
15	235	1.6967	LENS_1.EDGE
45	105	0.7581	SLIT_BACK
22	53	0.38266	LENS_4.FRONT
1	47	0.33934	SLIT
41	34	0.24548	VIS_PORT_IN
27	10	7.22E-02	LENS_5.BACK
6	5	3.61E-02	DICHROIC.BACK
23	5	3.61E-02	LENS_4.BACK
TOTAL	199477	1440.224	

1.33um

Object	Rays	Flux	
36	28972	209.1778	SECTION_F
28	28805	207.9721	LENS_5.EDGE
35	28351	204.6942	SECTION_E
30	19488	140.7034	FPA.ARRAY
32	18428	133.0502	SECTION_A
29	13544	97.78768	LENS_5.BACK_PLANE
40	8763	63.26886	DET_BACK
34	7909	57.10298	SECTION_D
44	6896	49.78912	SECTION_B
33	6142	44.34524	SECTION_C
24	5001	36.10722	LENS_4.EDGE
9	4120	29.7464	GRISM.GRATING
42	3783	27.31326	VIS_PORT_OUT
25	3442	24.85124	LENS_4.BACK_PLANE
38	2171	15.67462	EDGE_B_C
12	1909	13.78298	GRISM.BOTTOM
43	1826	13.18372	VIS_PORT_TUBE
7	1591	11.48702	DICHROIC.EDGE
21	1560	11.2632	LENS_3.EDGE
37	1347	9.72534	EDGE_A_B
46	1089	7.86258	SLIT_SUPPORT
11	1075	7.7615	GRISM.RIGHT_SIDE
10	1057	7.63154	GRISM.LEFT_SIDE
47	686	4.95292	SLIT_WALL
18	683	4.93126	LENS_2.EDGE
39	381	2.75082	EDGE_C_D
15	203	1.46566	LENS_1.EDGE
45	94	0.67868	SLIT_BACK
22	49	0.35378	LENS_4.FRONT
41	45	0.3249	VIS_PORT_IN
1	45	0.3249	SLIT
27	11	7.94E-02	LENS_5.BACK
3	5	3.61E-02	COLLIMATOR.EDGE
23	5	3.61E-02	LENS_4.BACK
5	3	2.17E-02	DICHROIC.FRONT
6	3	2.17E-02	DICHROIC.BACK
16	3	2.17E-02	LENS_2.FRONT
TOTAL	199487	1440.296	

1.7um

Object	Rays	Flux	
36	29441	212.564	SECTION_F
28	29103	210.1237	LENS_5.EDGE
35	28288	204.2394	SECTION_E
30	20310	146.6382	FPA.ARRAY
32	18929	136.6674	SECTION_A
29	13745	99.2389	LENS_5.BACK_PLANE
40	8943	64.56846	DET_BACK
34	7923	57.20406	SECTION_D
44	7112	51.34864	SECTION_B
33	6239	45.04558	SECTION_C
24	5069	36.59818	LENS_4.EDGE
25	3348	24.17256	LENS_4.BACK_PLANE
42	3053	22.04266	VIS_PORT_OUT
12	2326	16.79372	GRISM.BOTTOM
38	2200	15.884	EDGE_B_C
9	1823	13.16206	GRISM.GRATING
7	1757	12.68554	DICHROIC.EDGE
21	1535	11.0827	LENS_3.EDGE
43	1448	10.45456	VIS_PORT_TUBE
37	1361	9.82642	EDGE_A_B
46	1159	8.36798	SLIT_SUPPORT
10	1040	7.5088	GRISM.LEFT_SIDE
11	1031	7.44382	GRISM.RIGHT_SIDE
47	824	5.94928	SLIT_WALL
18	603	4.35386	LENS_2.EDGE
39	412	2.97464	EDGE_C_D
15	233	1.68226	LENS_1.EDGE
45	95	0.6859	SLIT_BACK
22	53	0.38266	LENS_4.FRONT
1	44	0.31768	SLIT
41	33	0.23826	VIS_PORT_IN
27	14	0.10108	LENS_5.BACK
23	6	4.33E-02	LENS_4.BACK
5	4	2.89E-02	DICHROIC.FRONT
6	4	2.89E-02	DICHROIC.BACK
26	3	2.17E-02	LENS_5.FRONT
TOTAL	199516	1440.506	

Average VF	Rms	Rms/Average
211.85	2.40	1.13%
210.07	2.07	0.98%
204.22	0.48	0.24%
145.98	4.98	3.41%
134.85	1.81	1.34%
98.55	0.73	0.74%
65.37	2.60	3.98%
56.93	0.38	0.67%
51.19	1.33	2.60%
45.07	0.74	1.64%
36.18	0.38	1.06%
24.58	0.36	1.47%
21.79	5.65	25.93%
16.31	12.17	74.60%

1284.85 : total 1.62%

1440.342 : total all

89.2% : fraction of total all

- Results stability check wrt input ray statistics:

ASAP results: large number of source rays for source statistics & final results

NRAYS=2E6 @ 1.33um Ref: 1444 (FPA surface area in mm2)

--- *STATS* *0.5*100*(1/SQRT(NRAYS))*

Object	Rays	Flux		
36	293289	211.7547	SECTION_F	14.66%
28	290399	209.6681	LENS_5.EDGE	14.52%
35	283360	204.5859	SECTION_E	14.17%
30	202556	146.2454	FPA.ARRAY	10.13%
32	190498	137.5396	SECTION_A	9.52%
29	135882	98.10681	LENS_5.BACK_PLANI	6.79%
40	89977	64.9634	DET_BACK	4.50%
34	79069	57.08782	SECTION_D	3.95%
44	70895	51.18619	SECTION_B	3.54%
33	62157	44.87736	SECTION_C	3.11%
24	50521	36.47616	LENS_4.EDGE	2.53%
25	33476	24.16967	LENS_4.BACK_PLANI	1.67%
42	30724	22.18273	VIS_PORT_OUT	1.54%
12	22968	16.5829	GRISM.BOTTOM	1.15%
38	22569	16.29482	EDGE_B_C	1.13%
7	18127	13.08769	DICHROIC.EDGE	0.91%
9	18117	13.08047	GRISM.GRATING	0.91%
21	15630	11.28486	LENS_3.EDGE	0.78%
43	14513	10.47839	VIS_PORT_TUBE	0.73%
37	13931	10.05818	EDGE_A_B	0.70%
46	11569	8.352818	SLIT_SUPPORT	0.58%
11	10705	7.72901	GRISM.RIGHT_SIDE	0.54%
10	10639	7.681358	GRISM.LEFT_SIDE	0.53%
47	8381	6.051082	SLIT_WALL	0.42%
18	6349	4.583978	LENS_2.EDGE	0.32%
39	3881	2.802082	EDGE_C_D	0.19%
15	2112	1.524864	LENS_1.EDGE	0.11%
45	983	0.709726	SLIT_BACK	0.05%
TOTAL	1994996	1440.387		99.75%

NRAYS=3E6 @ 1.33um

--- *STATS* *0.5*100*(1/SQRT(NRAYS))*

Object	Rays	Flux		
36	439264	211.4324	SECTION_F	14.64%
28	435579	209.6587	LENS_5.EDGE	14.52%
35	425144	204.636	SECTION_E	14.17%
30	304436	146.5352	FPA.ARRAY	10.15%
32	285687	137.5107	SECTION_A	9.52%
29	203739	98.06637	LENS_5.BACK_PLANI	6.79%
40	134837	64.90154	DET_BACK	4.49%
34	118531	57.05292	SECTION_D	3.95%
44	106261	51.14696	SECTION_B	3.54%
33	93154	44.83812	SECTION_C	3.11%
24	75842	36.50528	LENS_4.EDGE	2.53%
25	50090	24.10999	LENS_4.BACK_PLANI	1.67%
42	45983	22.13315	VIS_PORT_OUT	1.53%
12	34536	16.62333	GRISM.BOTTOM	1.15%
38	34039	16.3841	EDGE_B_C	1.13%
9	27243	13.11296	GRISM.GRATING	0.91%
7	27231	13.10719	DICHROIC.EDGE	0.91%
21	23557	11.33877	LENS_3.EDGE	0.79%
43	21649	10.42039	VIS_PORT_TUBE	0.72%
37	20872	10.04639	EDGE_A_B	0.70%
46	17229	8.292892	SLIT_SUPPORT	0.57%
10	16150	7.773533	GRISM.LEFT_SIDE	0.54%
11	16067	7.733582	GRISM.RIGHT_SIDE	0.54%
47	12703	6.114377	SLIT_WALL	0.42%
18	9588	4.615024	LENS_2.EDGE	0.32%
39	5836	2.809061	EDGE_C_D	0.19%
15	3205	1.542673	LENS_1.EDGE	0.11%
45	1462	0.703709	SLIT_BACK	0.05%
22	909	0.437532	LENS_4.FRONT	0.03%
TOTAL	2992488	1440.384		99.75%

NRAYS=1E6 @ 1.33um

--- *STATS* *0.5*100*(1/SQRT(NRAYS))*

Object	Rays	Flux		Mean	Rms	Rms/Mean
36	146519	14.65%	SECTION_F	14.65%	0.011%	0.076%
28	145240	14.52%	LENS_5.EDGE	14.52%	0.003%	0.018%
35	141726	14.17%	SECTION_E	14.17%	0.002%	0.017%
30	101233	10.12%	FPA.ARRAY	10.13%	0.013%	0.129%
32	95194	9.52%	SECTION_A	9.52%	0.003%	0.029%
29	68016	6.80%	LENS_5.BACK_PLANE	6.80%	0.005%	0.078%
40	45003	4.50%	DET_BACK	4.50%	0.003%	0.066%
34	39648	3.96%	SECTION_D	3.96%	0.007%	0.186%
44	35369	3.54%	SECTION_B	3.54%	0.004%	0.113%
33	31251	3.13%	SECTION_C	3.11%	0.011%	0.348%
24	25344	2.53%	LENS_4.EDGE	2.53%	0.004%	0.172%
25	16653	1.67%	LENS_4.BACK_PLANE	1.67%	0.004%	0.255%
42	15402	1.54%	VIS_PORT_OUT	1.54%	0.004%	0.242%
12	11500	1.15%	GRISM.BOTTOM	1.15%	0.001%	0.122%
38	11150	1.12%	EDGE_B_C	1.13%	0.010%	0.891%
9	9125	0.91%	GRISM.GRATING	0.91%	0.003%	0.349%
7	9088	0.91%	DICHROIC.EDGE	0.91%	0.001%	0.164%
21	7732	0.77%	LENS_3.EDGE	0.78%	0.006%	0.790%
43	7290	0.73%	VIS_PORT_TUBE	0.73%	0.004%	0.508%
37	6994	0.70%	EDGE_A_B	0.70%	0.002%	0.276%
46	5727	0.57%	SLIT_SUPPORT	0.58%	0.003%	0.516%
10	5325	0.53%	GRISM.LEFT_SIDE	0.54%	0.003%	0.545%
11	5249	0.52%	GRISM.RIGHT_SIDE	0.53%	0.005%	1.022%
47	4163	0.42%	SLIT_WALL	0.42%	0.004%	0.857%
18	3114	0.31%	LENS_2.EDGE	0.32%	0.004%	1.345%
39	1999	0.20%	EDGE_C_D	0.20%	0.003%	1.655%
15	1061	0.11%	LENS_1.EDGE	0.11%	0.001%	0.584%
TOTAL	997442	99.74%				

E. OUT-OF-FIELD INPUT THERMAL STRAY

The spectrograph is fed by fibre with a baselined f/5 numerical aperture. With similar numerical aperture at the input side of the fibre, while being fed by f/17 from sky via telescope (assumed GTC focal ratio at Cassegrain/Nasmyth focus) so that the sky source beam fills ~1% of the numerical aperture of any given fibre. With a low surface emissivity for the telescope optical elements, the in-field thermal emission is low but the fibre can potentially gather a lot more from the f/5 accepted solid angle. Once captured by the fibre, it is dispersed and imaged in-band in the spectrograph. The spectral variations of the thermal stray signal at IR FPA pixel can be expressed, in the valid Wien approximation, as:

$$s_{out-of-field} = \varepsilon . A\Omega_{fibre} . \tau_{fibre+spectro} . QE(\lambda) . \frac{2.c}{R.\lambda^3} . e^{-hc/\lambda kT_{obs}} . \frac{1}{\gamma}$$

where R is the spectrograph chosen spectral resolution. The following assumptions are made: fibre diameter equal to 120um, throughput[1] (for fibre+spectrograph, excluding QE) of 12.5%, emissivity ~1 (cavity approximation). The factor γ expresses the spread of spectral resolution element over ~2.36pixels in spectral direction and about $(1.75/5).d_{fibre}/d_{pixel}$~2.33pixels in the spatial direction so that γ=2.36*2.33=5.5 so as to recover a final value per pixel. Below is plotted this input thermal stray signal level for different resolutions and average observatory enclosure temperature.

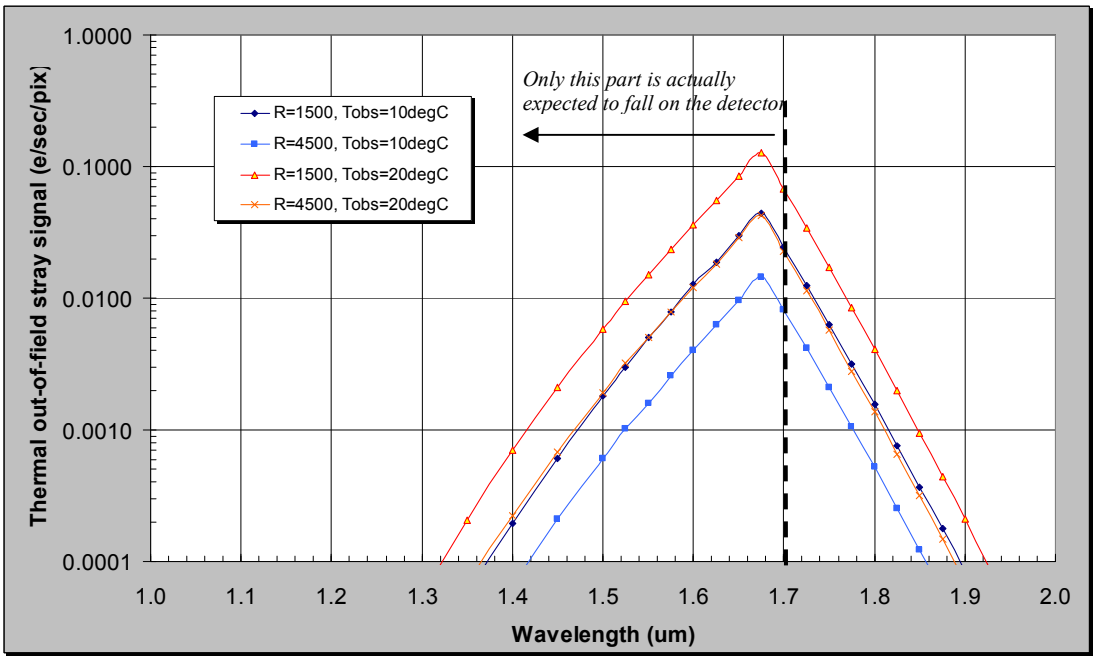

[1] This is just an estimate here. If not representative it can be changed to other values, the results scaled accordingly.

In any resolution mode, a gradient across the IR FPA peaking around the expected longwave part of the spectrum and reaching value in the range of several 10^{-2} to ~0.1e/sec/pix can be expected under the validation of the above assumptions. It is certainly more difficult to maintain and control the observatory enclosure environment temperature than doing the same at the scale of an instrument sub-assembly. So in order to limit sensitivity to external thermal fluctuations around ambient, it could be best preferred to maintain the control on the max total (i.e. observatory+instrument) thermal stray falling onto the detector by having it dominated by the instrumental part. Although from a science sensitivity point of view, the lowest total is preferred, here if deep cooling of instrument assembly is not foreseen or to be avoided then the observatory enclosure out-of-field thermal stray puts a lower limit (around 0.1e/sec/pix typically here) on what one wants to reach in terms of best but stable/controllable thermal stray noise. This justifies the choice of temperature values used in the different cases studied in this report.

This thermal stray source is not an issue for the case of a 1.4um cut-off detector.

F. LIST OF APPLICABLE DOCUMENTS

Document title	Code	Issue
GTC services to the Instruments	DCI/INST/0053-R	3.A
Instrument Rotators – Instrumentation	DCI/STMA/0017-R	1.G
Instrumentation – Telescope Structure	DCI/STMA/0018-R	1.G
Telescope Mechanics - Support Elements	DCI/STMA/0021-R	1.C
Electronic Cabinets	DR/CS-EC/000	1.D
Nasmyth Focal Station Envelope	DR/GTC/001	1.H
Nasmyth Rotator-Instrument Attachment Flanges	DR/I-IN-TL-001/001	1.C
Nasmyth Rotator Rotating Connector Panel	DR/I-IN-TL-001/010	1.B
Telescope Mount Nasmyth Platform	DR/TL-MN-NP/001	2.A
Programming Standards	ESP/CTRL/0042-R	1.B
GTC Control System Software Standards	ESP/CTRL/0045-R	1.C
Instrument Control System Specification	ESP/CTRL/0132-R	1.B
GTC System specification	ESP/STMA/0017-L	1.M
A&G requirements	ESP/OPTI/0029-L	3.A
A&G vignetting	NTE/CCIA/0411-R	1.A
Technical specifications for the fiber positioner for the SIDE spectrograph	NTE-PFS-SP-002	1.1
GTC Telescope Mechanical Design	PUB/TELE/0031-L	1.A
A&G preliminary mechanical design	RPT/OPTI/0093-L	3.A
GTCAO Conceptual Mechanical Design	RPT/OPTI/0244 –R	1.B
GTC coordinate systems	RPT/STMA/0075-R	2.A